ornl

NUREG/CR-4760
ORNL-6187

OAK RIDGE
NATIONAL
LABORATORY

MARTIN MARIETTA

Test of 6-in.-Thick Pressure Vessels. Series 3: Intermediate Test Vessel V-8A—Tearing Behavior of Low-Upper-Shelf Material

R. H. Bryan
B. R. Bass
S. E. Bolt
J. W. Bryson
J. G. Merkle
R. K. Nanstad
G. C. Robinson

Prepared for the U.S. Nuclear Regulatory Commission
Office of Nuclear Regulatory Research
Under Interagency Agreements DOE 40-551-75 and 40-552-75

OPERATED BY
MARTIN MARIETTA ENERGY SYSTEMS, INC.
FOR THE UNITED STATES
DEPARTMENT OF ENERGY

Available from

Superintendent of Documents
U.S. Government Printing Office
Post Office Box 37082
Washington, D.C. 20013-7982

and

National Technical Information Service
Springfield, VA 22161

NUREG/CR-4760
ORNL-6187
Dist. Category RF

Engineering Technology Division

TEST OF 6-IN.-THICK PRESSURE VESSELS. SERIES 3: INTERMEDIATE TEST VESSEL V-8A — TEARING BEHAVIOR OF LOW-UPPER-SHELF MATERIAL

R. H. Bryan
B. R. Bass*
S. E. Bolt
J. W. Bryson
J. G. Merkle
R. K. Nanstad**
G. C. Robinson

*Computing and Telecommunications Division
**Metals and Ceramics Division

Manuscript Completed — April 29, 1987
Date Published — May 1987

Prepared for the
U.S. Nuclear Regulatory Commission
Office of Nuclear Regulatory Research
under Interagency Agreements DOE 40-551-75 and 40-552-75

NRC FIN No. B0119

Prepared by the
OAK RIDGE NATIONAL LABORATORY
Oak Ridge, Tennessee 37831
operated by
MARTIN MARIETTA ENERGY STSYEMS, INC.
for the
U.S. DEPARTMENT OF ENERGY
under Contract No. DE-AC05-840R21400

CONTENTS

LIST OF FIGURES

LIST OF TABLES

FOREWORD

The work reported here was performed at Oak Ridge National Laboratory (ORNL) under the Heavy-Section Steel Technology (HSST) Program, C. E. Pugh, Program Manager. The program is sponsored by the Office of Nuclear Regulatory Research of the U.S. Nuclear Regulatory Commission (NRC). The technical monitor for the NRC is Milton Vagins.

This report is designated HSST Program Technical Report 80. Reports in this series are listed below:

1. S. Yukawa, *Evaluation of Periodic Proof Testing and Warm Prestressing Procedures for Nuclear Reactor Vessels*, HSSTP-TR-1, General Electric Company, Schenectady, N.Y. (July 1, 1969).
2. L. W. Loechel, *The Effect of Testing Variables on the Transition Temperature in Steel*, MCR-69-189, Martin Marietta Corporation, Denver, Colo. (November 20, 1969).
3. P. N. Randall, *Gross Strain Measure of Fracture Toughness of Steels*, HSSTP-TR-3, TRW Systems Group, Redondo Beach, Calif. (November 1, 1969).
4. C. Visser, S. E. Gabrielse, and W. VanBuren, *A Two-Dimensional Elastic-Plastic Analysis of Fracture Test Specimens*, WCAP-7368, Westinghouse Electric Corporation, PWR Systems Division, Pittsburgh, Pa. (October 1969).
5. T. R. Mager and F. O. Thomas, *Evaluation by Linear Elastic Fracture Mechanics of Radiation Damage to Pressure Vessel Steels*, WCAP-7328 (Rev.), Westinghouse Electric Corporation, PWR Systems Division, Pittsburgh, Pa. (October 1969).
6. W. O. Shabbits, W. H. Pryle, and E. T. Wessel, *Heavy-Section Fracture Toughness Properties of A533 Grade B Class 1 Steel Plate and Submerged Arc Weldment*, WCAP-7414, Westinghouse Electric Corporation, PWR Systems Divison, Pittsburgh, Pa. (December 1969).
7. F. J. Loss, *Dynamic Tear Test Investigations of the Fracture Toughness of Thick-Section Steel*, NRL-7056, Naval Research Laboratory, Washington, D.C. (May 14, 1970).
8. P. B. Crosley and E. J. Ripling, *Crack Arrest Fracture Toughness of A533 Grade B Class 1 Pressure Vessel Steel*, HSSTP-TR-8, Materials Research Laboratory, Inc., Glenwood, Ill. (March 1970).
9. T. R. Mager, *Post-Irradiation Testing of 2T Compact Tension Specimens*, WCAP-7561, Westinghouse Electric Corporation, PWR Systems Division, Pittsburgh, Pa. (August 1970).
10. T. R. Mager, *Fracture Toughness Characterization Study of A533, Grade B, Class 1 Steel*, WCAP-7578, Westinghouse Electric Corporation, PWR Systems Division, Pittsburgh, Pa. (October 1970).
11. T. R. Mager, *Notch Preparation in Compact Tension Specimens*, WCAP-7579, Westinghouse Electric Corporation, PWR Systems Division, Pittsburgh, Pa. (November 1970).

12. N. Levy and P. V. Marcal, *Three-Dimensional Elastic-Plastic Stress and Strain Analysis for Fracture Mechanics, Phase I: Simple Flawed Specimens*, HSSTP-TR-12, Brown University, Providence, R.I. (December 1970).

13. W. O. Shabbits, *Dynamic Fracture Toughness Properties of Heavy Section A533 Grade B Class 1 Steel Plate*, WCAP-7623, Westinghouse Electric Corporation, PWR Systems Division, Pittsburgh, Pa. (December 1970).

14. P. N. Randall, *Gross Strain Crack Tolerance of A 533-B Steel*, HSSTP-TR-14, TRW Systems Group, Redondo Beach, Calif. (May 1, 1971).

15. H. T. Corten and R. H. Sailors, *Relationship Between Material Fracture Toughness Using Fracture Mechanics and Transition Temperature Tests*, T&AM Report 346, University of Illinois, Urbana, Ill. (August 1, 1971).

16. T. R. Mager and V. J. McLaughlin, *The Effect of an Environment of High Temperature Primary Grade Nuclear Reactor Water on the Fatigue Crack Growth Characteristics of A533 Grade B Class 1 Plate and Weldment Material*, WCAP-7776, Westinghouse Electric Corporation, PWR Systems Division, Pittsburgh, Pa. (October 1971).

17. N. Levy and P. V. Marcal, *Three-Dimensional Elastic-Plastic Stress and Strain Analysis for Fracture Mechanics, Phase II: Improved Modelling*, HSSTP-TR-17, Brown University, Providence, R.I. (November 1971).

18. S. C. Grigory, *Tests of 6-in.-Thick Flawed Tensile Specimens, First Technical Summary Report, Longitudinal Specimens Numbers 1 through 7*, HSSTP-TR-18, Southwest Research Institute, San Antonio, Tex. (June 1972).

19. P. N. Randall, *Effects of Strain Gradients on the Gross Strain Crack Tolerance of A533-B Steel*, HSSTP-TR-19, TRW Systems Group, Redondo Beach, Calif. (June 15, 1972).

20. S. C. Grigory, *Tests of 6-Inch-Thick Flawed Tensile Specimens, Second Technical Summary Report, Transverse Specimens Numbers 8 through 10, Welded Specimens Numbers 11 through 13*, HSSTP-TR-20, Southwest Research Institute, San Antonio, Tex. (June 1972).

21. L. A. James and J. A. Williams, *Heavy Section Steel Technology Program Technical Report No. 21, The Effect of Temperature and Neutron Irradiation Upon the Fatigue-Crack Propagation Behavior of ASTM A533 Grade B, Class 1 Steel*, HEDL-TME 72-132, Hanford Engineering Development Laboratory, Richland, Wash. (September 1972).

22. S. C. Grigory, *Tests of 6-Inch-Thick Flawed Tensile Specimens, Third Technical Summary Report, Longitudinal Specimens Numbers 14 through 16, Unflawed Specimen Number 17*, HSSTP-TR-22, Southwest Research Institute, San Antonio, Tex. (October 1972).

23. S. C. Grigory, *Tests of 6-Inch-Thick Tensile Specimens, Fourth Technical Summary Report, Tests of 1-Inch-Thick Flawed Tensile Specimens for Size Effect Evaluation*, HSSTP-TR-23, Southwest Research Institute, San Antonio, Tex. (June 1973).

24. S. P. Ying and S. C. Grigory, *Tests of 6-Inch-Thick Tensile Specimens, Fifth Technical Summary Report, Acoustic Emission Monitoring of One-Inch and Six-Inch-Thick Tensile Specimens*, HSSTP-TR-24, Southwest Research Institute, San Antonio, Tex. (November 1972).

25. R. W. Derby, J. G. Merkle, G. C. Robinson, G. D. Whitman, and F. J. Witt, *Test of 6-Inch-Thick Pressure Vessels. Series 1: Intermediate Test Vessels V-1 and V-2*, ORNL-4895, Oak Ridge Natl. Lab., Oak Ridge, Tenn. (February 1974).

26. W. J. Stelzman and R. G. Berggren, *Radiation Strengthening and Embrittlement in Heavy Section Steel Plates and Welds*, ORNL-4871, Oak Ridge Natl. Lab., Oak Ridge, Tenn. (June 1973).

27. P. B. Crosley and E. J. Ripling, *Crack Arrest in an Increasing K-Field*, HSSTP-TR-27, Materials Research Laboratory, Inc., Glenwood, Ill. (January 1973).

28. P. V. Marcal, P. M. Stuart, and R. S. Bettes, *Elastic-Plastic Behavior of a Longitudinal Semi-Elliptic Crack in a Thick Pressure Vessel*, HSSTP-TR-28, Brown University, Providence, R.I. (June 1973).

29. W. J. Stelzman, R. G. Berggren, and T. N. Jones, *ORNL Characterization of Heavy-Section Steel Technology Program Plates 01, 02 and 03*, NUREG/CR-4092 (ORNL/TM-9491), Oak Ridge Natl. Lab., Oak Ridge, Tenn. (April 1985).

30. Canceled.

31. J. A. Williams, *The Irradiation and Temperature Dependence of Tensile and Fracture Properties of ASTM A533, Grade B, Class 1 Steel Plate and Weldment*, HEDL-TME 73-75, Hanford Engineering Development Laboratory, Richland, Wash. (August 1973).

32. J. M. Steichen and J. A. Williams, *High Strain Rate Tensile Properties of Irradiated ASTM A533 Grade B Class 1 Pressure Vessel Steel*, Hanford Engineering Development Laboratory, Richland, Wash. (July 1973).

33. P. C. Riccardella and J. L. Swedlow, *A Combined Analytical-Experimental Fracture Study of the Two Leading Theories of Elastic-Plastic Fracture (J-Integral and Equivalent Energy)*, WCAP-8224, Westinghouse Electric Corporation, Pittsburgh, Pa. (October 1973).

34. R. J. Podlasek and R. J. Eiber, *Final Report on Investigation of Mode III Crack Extension in Reactor Piping*, Battelle Columbus Laboratories, Columbus, Ohio (December 14, 1973).

35. T. R. Mager, J. D. Landes, D. M. Moon, and V. J. McLaughlin, *Interim Report on the Effect of Low Frequencies on the Fatigue Crack Growth Characteristics of A533 Grade B Class 1 Plate in an Environment of High-Temperature Primary Grade Nuclear Reactor Water*, WCAP-8256, Westinghouse Electric Corporation, Pittsburgh, Pa. (December 1973).

36. J. A. Williams, *The Irradiated Fracture Toughness of ASTM A533, Grade B, Class 1 Steel Measured with a Four-Inch-Thick Compact Tension Specimen*, HEDL-TME 75-10, Hanford Engineering Development Laboratory, Richland, Wash. (January 1975).

37. R. H. Bryan, J. G. Merkle, M. N. Raftenberg, G. C. Robinson, and J. E. Smith, *Test of 6-Inch-Thick Pressure Vessels. Series 2: Intermediate Test Vessels V-3, V-4, and V-6*, ORNL-5059, Oak Ridge Natl. Lab., Oak Ridge, Tenn. (November 1975).

38. T. R. Mager, S. E. Yanichko, and L. R. Singer, *Fracture Toughness Characterization of HSST Intermediate Pressure Vessel Material*, WCAP-8456, Westinghouse Electric Corporation, Pittsburgh, Pa. (December 1974).

39. J. G. Merkle, G. D. Whitman, and R. H. Bryan, *An Evaluation of the HSST Program Intermediate Pressure Vessel Tests in Terms of Light-Water-Reactor Pressure Vessel Safety*, ORNL/TM-5090, Oak Ridge Natl. Lab., Oak Ridge, Tenn. (November 1975).

40. J. G. Merkle, G. C. Robinson, P. P. Holz, J. E. Smith, and R. H. Bryan, *Test of 6-In.-Thick Pressure Vessels. Series 3: Intermediate Test Vessel V-7*, ORNL/NUREG-1, Oak Ridge Natl. Lab., Oak Ridge, Tenn. (August 1976).

41. J. A. Davidson, L. J. Ceschini, R. P. Shogan, and G. V. Rao, *The Irradiated Dynamic Fracture Toughness of ASTM A533, Grade B, Class 1 Steel Plate and Submerged Arc Weldment*, WCAP-8775, Westinghouse Electric Corporation, Pittsburgh, Pa. (October 1976).

42. R. D. Cheverton, *Pressure Vessel Fracture Studies Pertaining to a PWR LOCA-ECC Thermal Shock: Experiments TSE-1 and TSE-2*, ORNL/NUREG/TM-31, Oak Ridge Natl. Lab., Oak Ridge, Tenn. (September 1976).

43. J. G. Merkle, G. C. Robinson, P. P. Holz, and J. E. Smith, *Test of 6-In.-Thick Pressure Vessels. Series 4: Intermediate Test Vessels V-5 and V-9 with Inside Nozzle Corner Cracks*, ORNL/NUREG-7, Oak Ridge Natl. Lab., Oak Ridge, Tenn. (August 1977).

44. J. A. Williams, *The Ductile Fracture Toughness of Heavy Section Steel Plate*, NUREG/CR-0859, Hanford Engineering Development Laboratory, Richland, Wash. (September 1979).

45. R. H. Bryan, T. M. Cate, P. P. Holz, T. A. King, J. G. Merkle, G. C. Robinson, G. C. Smith, J. E. Smith, and G. D. Whitman, *Test of 6-in.-Thick Pressure Vessels. Series 3: Intermediate Test Vessel V-7A Under Sustained Loading*, ORNL/NUREG-9, Oak Ridge Natl. Lab., Oak Ridge, Tenn. (February 1978).

46. R. D. Cheverton and S. E. Bolt, *Pressure Vessel Fracture Studies Pertaining to a PWR LOCA-ECC Thermal Shock: Experiments TSE-3 and TSE-4 and Update of TSE-1 and TSE-2 Analysis*, ORNL/NUREG-22, Oak Ridge Natl. Lab., Oak Ridge, Tenn. (December 1977).

47. D. A. Canonico, *Significance of Reheat Cracks to the Integrity of Pressure Vessels for Light-Water Reactors*, ORNL/NUREG-15, Oak Ridge Natl. Lab., Oak Ridge, Tenn. (July 1977).

48. G. C. Smith and P. P. Holz, *Repair Weld Induced Residual Stresses in Thick-Walled Steel Pressure Vessels*, NUREG/CR-0093 (ORNL/NUREG/TM-153), Oak Ridge Natl. Lab., Oak Ridge, Tenn. (June 1978).

49. P. P. Holz and S. W. Wismer, *Half-Bead (Temper) Repair Welding for HSST Vessels*, NUREG/CR-0113 (ORNL/NUREG/TM-177), Oak Ridge Natl. Lab., Oak Ridge, Tenn. (June 1978).

50. G. C. Smith, P. P. Holz, and W. J. Stelzman, *Crack Extension and Arrest Tests of Axially Flawed Steel Model Pressure Vessels*, NUREG/CR-0126 (ORNL/NUREG/TM-196), Oak Ridge Natl. Lab., Oak Ridge, Tenn. (October 1978).

51. R. H. Bryan, P. P. Holz, J. G. Merkle, G. C. Smith, J. E. Smith, and W. J. Stelzman, *Test of 6-in.-Thick Pressure Vessels. Series 3: Intermediate Test Vessel V-7B*, NUREG/CR-0309 (ORNL/NUREG-38), Oak Ridge Natl. Lab., Oak Ridge, Tenn. (October 1978).

52. R. D. Cheverton, S. K. Iskander, and S. E. Bolt, *Applicability of LEFM to the Analysis of PWR Vessels Under LOCA-ECC Thermal Shock Conditions*, NUREG/CR-0107 (ORNL/NUREG-40), Oak Ridge Natl. Lab., Oak Ridge, Tenn. (October 1978).

53. R. H. Bryan, D. A. Canonico, P. P. Holz, S. K. Iskander, J. G. Merkle, J. E. Smith, and W. J. Stelzman, *Test of 6-in.-Thick Pressure Vessels, Series 3: Intermediate Test Vessel V-8*, NUREG/CR-0675 (ORNL/NUREG-58), Oak Ridge Natl. Lab., Oak Ridge, Tenn. (December 1979).

54. R. D. Cheverton and S. K. Iskander, *Application of Static and Dynamic Crack Arrest Theory to TSE-4*, NUREG/CR-0767 (ORNL/NUREG-57), Oak Ridge Natl. Lab., Oak Ridge, Tenn. (June 1979).

55. J. A. Williams, *Tensile Properties of Irradiated and Unirradiated Welds of A533 Steel Plate and A508 Forgings*, NUREG/CR-1158 (ORNL/Sub-79/50917/2), Hanford Engineering Development Laboratory, Richland, Wash. (July 1979).

56. K. W. Carlson and J. A. Williams, *The Effect of Crack Length and Side Grooves on the Ductile Fracture Toughness Properties of ASTM A533 Steel*, NUREG/CR-1171 (ORNL/Sub-79/50917/3), Hanford Engineering Development Laboratory, Richland, Wash. (October 1979).

57. P. P. Holz, *Flaw Preparations for HSST Program Vessel Fracture Mechanics Testing; Mechanical-Cyclic Pumping and Electron-Beam Weld-Hydrogen Charge Cracking Schemes*, NUREG/CR-1274 (ORNL/NUREG/TM-369), Oak Ridge Natl. Lab., Oak Ridge, Tenn. (May 1980).

58. S. K. Iskander, *Two Finite Element Techniques for Computing Mode I Stress Intensity Factors in Two- or Three-Dimensional Problems*, NUREG/CR-1499 (ORNL/NUREG/CSD/TM-14), Computer Sciences Div., Union Carbide Corp. Nuclear Div., Oak Ridge, Tenn. (February 1981).

59. P. B. Crosley and E. J. Ripling, *Development of a Standard Test for Measuring K_{Ia} with a Modified Compact Specimen*, NUREG/CR-2294 (ORNL/Sub-81/7755/1), Materials Research Laboratory, Glenwood, Ill. (August 1981).

60. S. N. Atluri, B. R. Bass, J. W. Bryson, and K. Kathiresan, *NOZ-FLAW: A Finite Element Program for Direct Evaluation of Stress Intensity Factors for Pressure Vessel Nozzle-Corner Flaws*, NUREG/CR-1843 (ORNL/NUREG/CSD/TM-18), Computer Sciences Div., Oak Ridge Gaseous Diffusion Plant, Oak Ridge, Tenn. (March 1981).

61. A. Shukla, W. L. Fourney, and G. R. Irwin, *Study of Energy Loss and Its Mechanisms in Homalite 100 During Crack Propagation and Arrest*, NUREG/CR-2150 (ORNL/Sub-7778/1), University of Maryland, College Park, Md. (August 1981).

62. S. K. Iskander, R. D. Cheverton, and D. G. Ball, *OCA-I, A Code for Calculating the Behavior of Flaws on the Inner Surface of a Pressure Vessel Subjected to Temperature and Pressure Transients*, NUREG/CR-2113 (ORNL/NUREG-84), Oak Ridge Natl. Lab., Oak Ridge, Tenn. (August 1981).

63. R. J. Sanford, R. Chona, W. L. Fourney, and G. R. Irwin, *A Photoelastic Study of the Influence of Non-Singular Stresses in Fracture Test Specimens*, NUREG/CR-2179 (ORNL/Sub-7778/2), University of Maryland, College Park, Md. (August 1981).

64. B. R. Bass, S. N. Atluri, J. W. Bryson, and K. Kathiresan, *OR-FLAW: A Finite Element Program for Direct Evaluation of K-Factors for User-Defined Flaws in Plate, Cylinders, and Pressure-Vessel Nozzle Corners*, NUREG/CR-2494 (ORNL/CSD/TM-165), Oak Ridge Natl. Lab., Oak Ridge, Tenn. (April 1982).

65. B. R. Bass and J. W. Bryson, *ORMGEN-3D: A Finite Element Mesh Generator for 3-Dimensional Crack Geometries*, NUREG/CR-2997, Vol. 1 (ORNL/TM-8527/V1), Oak Ridge Natl. Lab., Oak Ridge, Tenn. (December 1982).

66. B. R. Bass and J. W. Bryson, *ORVIRT: A Finite Element Program for Energy Release Rate Calculations for 2-Dimensional and 3-Dimensional Crack Models*, NUREG/CR-2997, Vol. 2 (ORNL/TM-8527/V2), Oak Ridge Natl. Lab., Oak Ridge, Tenn. (February 1983).

67. R. D. Cheverton, S. K. Iskander, and D. G. Ball, *PWR Pressure Vessel Integrity During Overcooling Accidents: A Parametric Analysis*, NUREG/CR-2895 (ORNL/TM-7931), Oak Ridge Natl. Lab., Oak Ridge, Tenn. (February 1983).

68. D. G. Ball, R. D. Cheverton, J. B. Drake, and S. K. Iskander, *OCA-II, A Code for Calculating Behavior of 2-D and 3-D Surface Flaws in a Pressure Vessel Subjected to Temperature and Pressure Transients*, NUREG/CR-3491 (ORNL-5934), Oak Ridge Natl. Lab., Oak Ridge, Tenn. (February 1984).

69. A. Sauter, R. D. Cheverton, and S. K. Iskander, *Modification of OCA-I for Application to a Reactor Pressure Vessel with Cladding on the Inner Surface*, NUREG/CR-3155 (ORNL/TM-8649), Oak Ridge Natl. Lab., Oak Ridge, Tenn. (May 1983).

70. R. D. Cheverton and D. G. Ball, *OCA-P, A Deterministic and Probabilistic Fracture-Mechanics Code for Application to Pressure Vessels*, NUREG/CR-3618 (ORNL-5991), Oak Ridge Natl. Lab., Oak Ridge, Tenn. (May 1984).

71. J. G. Merkle, *An Examination of the Size Effects and Data Scatter Observed in Small Specimen Cleavage Fracture Toughness Testing*, NUREG/CR-3672 (ORNL/TM-9088), Oak Ridge Natl. Lab., Oak Ridge, Tenn. (April 1984).

72. C. E. Pugh et al., *Heavy-Section Steel Technology Program — Five-Year Plan FY 1983–1987*, NUREG/CR-3595 (ORNL/TM-9008), Oak Ridge Natl. Lab., Oak Ridge, Tenn. (April 1984).

73. D. G. Ball, B. R. Bass, J. W. Bryson, R. D. Cheverton, and J. B. Drake, *Stress Intensity Factor Influence Coefficients for Surface Flaws in Pressure Vessels*, NUREG/CR-3723 (ORNL/CSD/TM-216), Oak Ridge Natl. Lab., Oak Ridge, Tenn. (February 1985).

74. W. R. Corwin, R. G. Berggren, and R. K. Nanstad, *Charpy Toughness and Tensile Properties of Neutron Irradiated Stainless Steel Submerged-Arc Weld Cladding Overlay*, NUREG/CR-3927 (ORNL/TM-9309), Oak Ridge Natl. Lab., Oak Ridge, Tenn. (September 1984).

75. C. W. Schwartz, R. Chona, W. L. Fourney, and G. R. Irwin, *SAMCR: A Two-Dimensional Dynamic Finite Element Code for the Stress Analysis of Moving CRacks*, NUREG/CR-3891 (ORNL/Sub/79-7778/3), University of Maryland, College Park, Md. (November 1984).

76. W. R. Corwin, G. C. Robinson, R. K. Nanstad, J. G. Merkle, R. G. Berggren, G. M. Goodwin, R. L. Swain, and T. D. Owings, *Effects of Stainless Steel Weld Overlay Cladding on the Structural Integrity of Flawed Steel Plates in Bending, Series 1*, NUREG/CR-4015 (ORNL/TM-9390), Oak Ridge Natl. Lab., Oak Ridge, Tenn. (April 1985).

77. R. H. Bryan, B. R. Bass, S. E. Bolt, J. W. Bryson, D. P. Edmonds, R. W. McCulloch, J. G. Merkle, R. K. Nanstad, G. C. Robinson, K. R. Thoms, and G. D. Whitman, *Pressurized-Thermal-Shock Test of 6-in.-Thick Pressure Vessels. PTSE-1: Investigation of Warm Prestressing and Upper-Shelf Arrest*, NUREG/CR-4106 (ORNL-6135), Oak Ridge Natl. Lab., Oak Ridge, Tenn. (April 1985).

78. R. D. Cheverton, D. G. Ball, S. E. Bolt, S. K. Iskander, and R. K. Nanstad, *Pressure Vessel Fracture Studies Pertaining to the PWR Thermal-Shock Issue: Experiments TSE-5, TSE-5A, and TSE-6*, NUREG/CR-4249 (ORNL-6163), Martin Marietta Energy Systems, Inc., Oak Ridge Natl. Lab., Oak Ridge, Tenn. (June 1985).

79. R. D. Cheverton, D. G. Ball, S. E. Bolt, S. K. Iskander, and R. K. Nanstad, *Pressure Vessel Fracture Studies Pertaining to the PWR Thermal-Shock Issue: Experiment TSE-7*, NUREG/CR-4304 (ORNL-6177), Martin Marietta Energy Systems, Inc., Oak Ridge Natl. Lab., Oak Ridge, Tenn. (August 1985).

80. R. H. Bryan, B. R. Bass, S. E. Bolt, J. W. Bryson, J. G. Merkle, R. K. Nanstad, and G. C. Robinson, *Test of 6-in.-Thick Pressure Vessels. Series 3: Intermediate Test Vessel V-8A — Tearing Behavior of Low Upper-Shelf Material*, NUREG/CR-4760 (ORNL-6187), Martin Marietta Energy Systems, Inc., Oak Ridge Natl. Lab., Oak Ridge, Tenn. (May 1987).

81. R. D. Cheverton and D. G. Ball, *A Parametric Study of PWR Pressure Vessel Integrity During Overcooling Accidents, Considering Both 2-D and 3-D Flaws*, NUREG/CR-4325 (ORNL/TM-9682), Martin Marietta Energy Systems, Inc., Oak Ridge Natl. Lab., Oak Ridge, Tenn. (August 1985).

82. E. C. Rodabaugh, *Comments on the Leak-Before-Break Concept for Nuclear Power Plant Piping Systems*, NUREG/CR-4305 (ORNL/Sub/82-22252/3), E. C. Rodabaugh Associates, Inc., Hilliard, Ohio (August 1985).

83. J. W. Bryson, *ORVIRT.PC: A 2-D Finite Element Fracture Analysis Program for a Microcomputer*, NUREG/CR-4367 (ORNL-6208), Martin Marietta Energy Systems, Inc., Oak Ridge Natl. Lab., Oak Ridge, Tenn. (October 1985).

84. D. G. Ball and R. D. Cheverton, *Adaptation of OCA-P, A Probabilistic Fracture-Mechanics Code, to a Personal Computer*, NUREG/CR-4468 (ORNL/CSD/TM-233), Martin Marietta Energy Systems, Inc., Oak Ridge Natl. Lab., Oak Ridge, Tenn. (January 1986).

85. J. W. Bryson and B. R. Bass, *ORMGEN.PC: A Microcomputer Program for Automatic Mesh Generation of 2-D Crack Geometries*, NUREG/CR-4475 (ORNL-6250), Martin Marietta Energy Systems, Inc., Oak Ridge Natl. Lab., Oak Ridge, Tenn. (March 1986).

86. G. D. Whitman, *Historical Summary of the Heavy-Section Steel Technology Program and Some Related Activities in Light-Water Reactor Pressure Vessel Safety Research*, NUREG/CR-4489 (ORNL-6259), Martin Marietta Energy Systems, Inc., Oak Ridge Natl. Lab., Oak Ridge, Tenn. (March 1986).

87. C. Inversini and J. W. Bryson, *ORPLOT.PC: A Graphic Utility for ORMGEN.PC and ORVIRT.PC*, NUREG/CR-4633 (ORNL-6291), Martin Marietta Energy Systems, Inc., Oak Ridge Natl. Lab., Oak Ridge, Tenn.

EXECUTIVE SUMMARY

The test of intermediate test vessel V-8A was the 12th fracture test of a 150-mm-thick steel vessel in the Heavy-Section Steel Technology (HSST) Program at the Oak Ridge National Laboratory. This series of tests is a set of experiments on a scale large enough to simulate realistically important aspects of fracture behavior of reactor pressure vessels. Such experiments are the means by which theoretical models of fracture behavior can be evaluated for possible application to fracture analysis of vessels in nuclear plants.

The V-8A test is concerned with the fracture behavior of the pressure vessel steels that are particularly susceptible to irradiation damage. Several reactor pressure vessels in service contain welds that, because of high copper content, may have their Charpy upper-shelf impact-energy values reduced to relatively low levels by neutron irradiation. Such low-upper-shelf steels are known to exhibit low resistance to a ductile tearing mode of crack propagation in small (25-mm) laboratory specimens. The results of the V-8A test are intended to provide an experimental basis for judging the accuracy of analytical procedures used to evaluate the safety of reactor pressure vessels under conditions of low-upper-shelf toughness.

The test plan was formulated to (1) demonstrate on a large scale the tearing behavior of a low-upper-shelf steel and (2) facilitate the comparisons, based on elastic-plastic fracture mechanics, with experimental results of predictions of stable and unstable tearing. The test required placing a special low-upper-shelf weld seam in a test vessel and generating a large flaw in this seam.

The test vessel was a typical HSST intermediate test vessel with an outside diameter of 990 mm and a thickness of 152 mm. The vessel used for the V-8A test had been tested previously at ORNL and repaired by the Babcock & Wilcox Company by depositing a submerged-arc seam weld especially designed to have the desired properties for the V-8A test. A fatigue-sharpened flaw 280 mm long by 88 mm deep was implanted in the seam. The vessel was extensively instrumented with crack-mouth-opening displacement gages, strain gages, and ultrasonic transducers for detecting the flaw depth throughout the test.

The vessel was heated to an isothermal condition at ~150°C and then pressurized slowly in several stages until unstable tearing was observed. Pauses in pressurization at several pressure levels allowed time for observing stable crack depths. A tearing instability was first observed while the pressure was between 138 and 140.5 MPa. Tearing was interrupted by a slight depressurization, and a second tearing instability was induced by further pressurization, which reached 143 MPa. The crack grew in depth ~6 mm before the first instability. At the end of the test, the flaw was 453 mm long and 101.4 mm deep.

Extensive elastic-plastic finite-element analyses were performed before and after the test. Before the test, estimates of instability pressure were made on the basis of these analyses and measurements of the ductile tearing resistance of four characterization welds. The estimated instability pressures depended on the various measured resistances and fell in the range of 133 to 145 MPa. The estimated instability pressure

based on tearing resistance of the vessel test weld itself measured after the test was 134.5 MPa, which is 4% lower than the actual instability pressure.

The objectives of the test were attained in spite of difficulties with high-pressure, high-temperature seals. The Charpy-impact and tearing-resistance properties of the special seam weld were as desired: impact energy was ~60 J. Ultrasonic transducers and crack-mouth-opening displacement gages performed satisfactorily. Instabilities were arrested, preserving the final crack geometry. Pretest predictions of the instability pressure made by several investigators worldwide were all within —14 to +10% of the observed instability pressure.

This experimental study demonstrated that the V-8A vessel, when pressurized in a ductile state with a large flaw in a region of low tearing resistance, is capable of withstanding a pressure twice the nominal *ASME (American Society of Mechanical Engineers) Code* design pressure. The study also indicated that accurate prediction of instability pressures of a ductile vessel requires, first, methods of analysis that account for plasticity and, second, good representations of the properties of the material with respect to tearing resistance (with proper consideration to scatter) and stress-strain behavior.

TEST OF 6-IN.-THICK PRESSURE VESSELS. SERIES 3: INTERMEDIATE TEST VESSEL V-8A — TEARING BEHAVIOR OF LOW-UPPER-SHELF MATERIAL

R. H. Bryan
B. R. Bass
S. E. Bolt
J. W. Bryson
J. G. Merkle
R. K. Nanstad
G. C. Robinson

ABSTRACT

Tests of several 152-mm-thick vessels were performed to study the behavior of flaws under stress states similar to those in full-scale reactor pressure vessels. The objective of the latest test, V-8A, was to provide accurate quantitative data concerning the growth by ductile tearing and the final ductile tearing instability of a flaw in a low upper-shelf toughness weld located in a cylinder of reactor vessel steel. This test is important because vessels are in service that contain welds that, because of high-copper content, may have their Charpy upper-shelf energy values reduced to relatively low levels by neutron irradiation. The results of the V-8A test are intended to provide an experimental basis for judging the accuracy of vessel fracture safety analysis procedures for low-upper-shelf toughness conditions. The objective of the V-8A test was attained. A tearing instability was observed at a pressure of ~139 MPa (about two times the design pressure). The flaw, which was initially a fatigue-sharpened notch with an approximately elliptical profile, grew in depth and length to 101.4 and 453 mm, respectively. Pretest and posttest fracture mechanics and stress analyses were made by simplified methods, convenient for investigating a wide range of parameters, and by three-dimensional finite-element methods, which modeled the material properties and geometry more precisely. Ductile flaw growth and instability predictions based upon measured J-resistance and tensile properties were made. Results of analyses based on J_R-controlled crack growth agree reasonably well with experimental observations.

---

1. INTRODUCTION

The Heavy-Section Steel Technology (HSST) Program was instituted at Oak Ridge National Laboratory to accelerate investigations of thick-section vessels for water-cooled nuclear reactor service. The program, which is especially concerned with developing the information necessary to assess the influence of flaws on the safety and serviceability of the thick-section components of reactor pressure vessels, developed data on

the characteristics of plates, welds, and forgings in terms of mechanical properties, toughness, inherent flaws, and homogeneity. A major objective is to develop methods by which better estimates can be made of the effects of flaws on the service life and strength of vessels.

Analytical, as well as experimental, methods are being developed for fracture evaluation of structures. A wide variety of specimen types and sizes have been tested under a wide range of loading conditions. Considerable progress have been made in understanding the behavior of flawed structures and in applying small-specimen test results to the analysis and evaluation of large structures.

The importance of the size of test specimens and structures in the proper characterization of flaw behavior was demonstrated in many parts of the program. The confidence in methods of analysis required in safety evaluation of nuclear vessels can be attained only by experience and experiment with appropriately sized structures under loading conditions of interest. Consequently, the HSST Program includes simulated service tests, of which the intermediate vessel tests are a part.

The aim of simulated service testing is to provide, through a series of experiments, a connection between the behavior of structures observed in a laboratory environment and the behavior of full-size components under the wide variety of conditions that constitute the real operating environment. One objective of each intermediate vessel test is to determine the ability of analytical methods to predict actual fracture behavior of a flawed structure under known conditions of material properties and loading. In the planned progression of such tests, analytical methods are confirmed or improved, or their limitations are revealed.

The intermediate vessel tests were originally subdivided into four series:

1. flaws in cylindrical vessels, A 508 class 2 forging steel — two vessels;
2. flaws in cylindrical vessels with longitudinal submerged-arc weld seams, A 508 class 2 forging steel — three vessels;
3. flaws in cylindrical vessels with longitudinal submerged-arc weld seams, A 533 grade B class 1 plate steel — two vessels; and
4. cylindrical vessels with radially attached nozzles, vessels of A 508 class 2 forging steel and A 533 grade B class 1 plate steel, nozzles of A 508 class 2 forging steel — three vessels.

Reports have been prepared on tests in all four series.[1-7] Twelve fracture tests with pressure loading have been performed. The last test, V-8A, is the subject of this report.

The objective of the V-8A test was to provide accurate quantitative data concerning the growth by ductile tearing and final instability of a flaw in a low-upper-shelf toughness weldment located in a cylinder of reactor vessel steel. The motivation for performing this test was that some reactor pressure vessels in service contain welds that, because of high copper content, may have their Charpy upper-shelf energy values reduced to relatively low levels by neutron irradiation. After some period of operation, the toughness of these welds is expected to be degraded to the extent that practical operating temperature limits may not be definable in accordance with current regulatory guidelines. However, no one

has actually demonstrated that a vessel with low toughness does not have adequate resistance to tearing. The results of the V-8A test are intended to provide an experimental basis for judging the accuracy of vessel-fracture safety-analysis procedures for low-upper-shelf toughness conditions.

The purposes for which the V-8A test plan was formulated were to (1) demonstrate the fracture behavior of low-toughness material at upper-shelf temperatures and (2) compare elastic-plastic fracture-mechanics predictions of stable and unstable tearing with full-scale test results. The plan involved the insertion of a special low-upper-shelf weld seam in a test vessel and the placement of a large flaw in this seam. Then, with the vessel heated to the proper temperature, the vessel was pressurized slowly, with intermittent pauses for recording data related to flaw growth, until unstable tearing was detected. After an instability was observed, the vessel was depressurized to preserve the flaw and the vessel for further examination.

Extensive pretest and posttest analyses were performed to estimate stable crack growth and the instability pressure. The test was performed with the expected result. A tearing instability condition was obtained twice and interrupted each time by depressurization.

References

1. R. W. Derby et al., *Test of 6-in.-Thick Pressure Vessels. Series 1: Intermediate Test Vessels V-1 and V-2*, ORNL-4895, Union Carbide Corp. Nuclear Div., Oak Ridge Natl. Lab., February 1974.

2. R. H. Bryan et al., *Test of 6-in.-Thick Pressure Vessels. Series 2: Intermediate Test Vessels V-3, V-4, and V-6*, ORNL-5059, Union Carbide Corp. Nuclear Div., Oak Ridge Natl. Lab., November 1975.

3. J. G. Merkle et al., *Test of 6-in.-Thick Pressure Vessels. Series 3: Intermediate Test Vessel V-7*, ORNL/NUREG-1, Union Carbide Corp. Nuclear Div., Oak Ridge Natl. Lab., August 1975.

4. J. G. Merkle et al., *Test of 6-in.-Thick Pressure Vessels. Series 4: Intermediate Test Vessels V-5 and V-9 with Inside Nozzle Corner Cracks*, ORNL/NUREG-7, Union Carbide Corp. Nuclear Div., Oak Ridge Natl. Lab., August 1977.

5. R. H. Bryan et al., *Test of 6-in.-Thick Pressure Vessels. Series 3: Intermediate Test Vessel V-7A under Sustained Loading*, ORNL/NUREG-9, Union Carbide Corp. Nuclear Div., Oak Ridge Natl. Lab., July 1977.

6. R. H. Bryan et al., *Test of 6-in.-Thick Pressure Vessels. Series 3: Intermediate Test Vessel V-7B*, ORNL/NUREG-38, Union Carbide Corp. Nuclear Div., Oak Ridge Natl. Lab., October 1978.

7. R. H. Bryan et al., *Test of 6-in.-Thick Pressure Vessels. Series 3: Intermediate Test Vessel V-8*, NUREG/CR-0675 (ORNL/NUREG-58), Union Carbide Corp. Nuclear Div., Oak Ridge Natl. Lab., December 1979.

2. TEST VESSEL

2.1 Prior History

The vessel used in the V-8A test was originally procured for the Heavy-Section Steel Technology (HSST) Program as intermediate test vessel V-8. Prior to its preparation for V-8A, vessel V-8 was tested at low temperature in the elastic range with a flaw in the vicinity of a half-bead weld repair.[1]

2.1.1 Original fabrication

The cylindrical test section of vessel V-8 was fabricated of 152-mm-thick steel plate that met American Society for Testing and Materials A 533 grade B class 1 specifications. Vessel configuration is shown in Fig. 2.1. The vessel was fabricated under contract with the

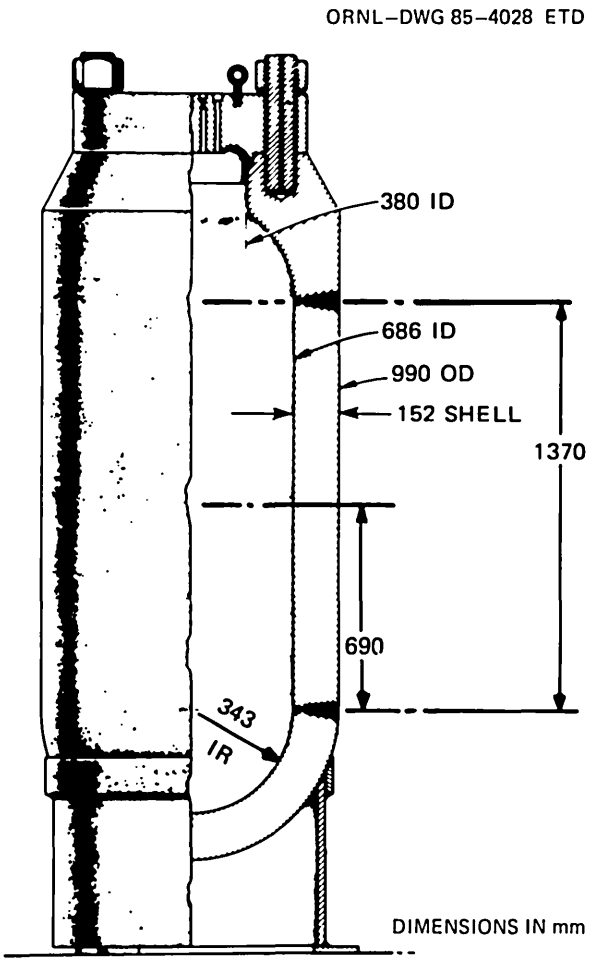

Fig. 2.1. Intermediate test vessel V-8.

Taylor Forge Division of Gulf and Western Products Company, with V-8 being one of four intermediate test vessels using steel plate for the cylindrical courses. Design and procurement of the vessels are described in detail in Ref. 2; principal features pertaining to vessel V-8 are summarized here.

The cylindrical shell courses and prolongations for vessels V-7 through V-10 were fabricated from plate produced by Lukens Steel Company from a single heat identified as B5233-2. Chemical (ladle) analysis reported by the Lukens Mill Certification for this heat is given below.

Material	wt %
C	0.20
Mn	1.23
P	0.015
S	0.017
Si	0.26
Ni	0.49
Mo	0.52

The mechanical test results from specimens representing the shell material are presented in Table 2.1.

Table 2.1. Mechanical test results from Data Trac specimens representing heat B5233-2 shell material[a]

Yield strength (MPa)	Tensile strength (MPa)	Elongation in 51 mm (%)	Longitudinal Charpy V-notch at −12°C (J)	Lateral expansion (mm)	Fracture appearance (% shear)
450	586	26			
432	563	29	125—96—106	1.55—1.93—1.52	70—70—70

[a]Nil-ductility transition temperature as determined by drop-weight tests: −51°C.

2.1.2 Test V-8

To meet the V-8 test objectives, a large repair weld was deliberately performed by the half-bead technique prescribed by Sect. XI of the *ASME Boiler and Pressure Vessel Code*.[3] In such a weldment, one expects locally high residual stresses and material properties within heat-affected zones not typical of weldments that have undergone the normal high-temperature postweld heat treatment. Details of the repair cavity are shown in Fig. 2.2.

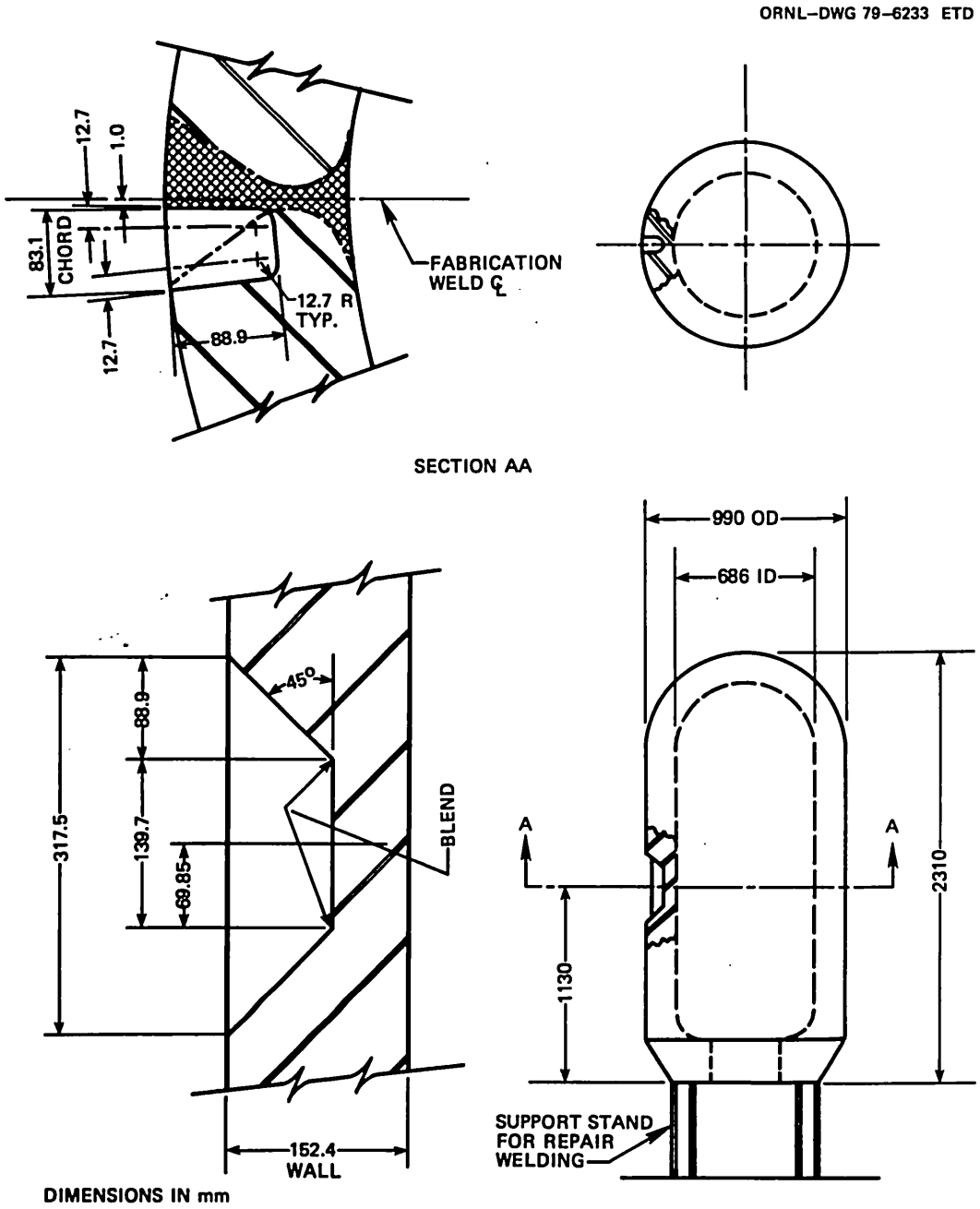

Fig. 2.2. Details of cavity prepared in vessel V-8 for Sect. XI repair welding.

A fatigue-sharpened flaw was implanted in a radial-axial plane of the vessel adjacent to the repair weld in the longitudinal seam weld. In the test, the vessel was cooled to approximately −24°C and hydrostatically pressurized to 65.3 MPa. The flaw propagated by cleavage and arrested, as predicted. Maximum strains in the cylindrical test section outside the flawed region were well within the elastic limits of the material.

2.2 Repair and Modification of Vessel for Test V-8A

The V-8 flaw was flame cut from the vessel, which was then repaired under subcontract with the Babcock & Wilcox Company (B&W). Details of the repair are presented in Ref. 4.

The cavity resulting from the removal of the V-8 flaw (Fig. 2.3) was repaired by welding in a plug of material made from a piece of the prolongation of vessel V-9, and a special seam weld was placed at another location in the vessel for the V-8A test. The plug welding was performed by the manual metal arc process with E8015 electrodes. The arrangement of the special seam weld relative to the cavity repair is shown in Fig. 2.4.

The special seam weld was made by the submerged-arc process with materials and heat treatment designed to produce a seam with low Charpy V-notch impact energy on the upper shelf. B&W made preliminary trial weldments with 95-mm-thick SA 533 grade B class 1 steel base material and welding electrodes of SFA 5.23 type EF-2 material. Material property tests were made with weld-metal specimens from these trial weldments with the objective of selecting a process that would produce the properties suitable for the V-8A vessel test. Upper-shelf Charpy impact energy, yield strength, and the temperature at the onset of the Charpy upper shelf were important to the proper conduct of the test. Three different proportions of Linde 60 and Linde 80 fluxes and three different heat treatments were combined to make nine types of welds to be tested. The specified ranges of acceptable impact energies and yield strengths were 47.5 to 74.6 J and 450 to 620 MPa, respectively. The impact energy was specified so as to be representative of the particular irradiated reactor pressure vessel steels that have unusually low tearing resistance.

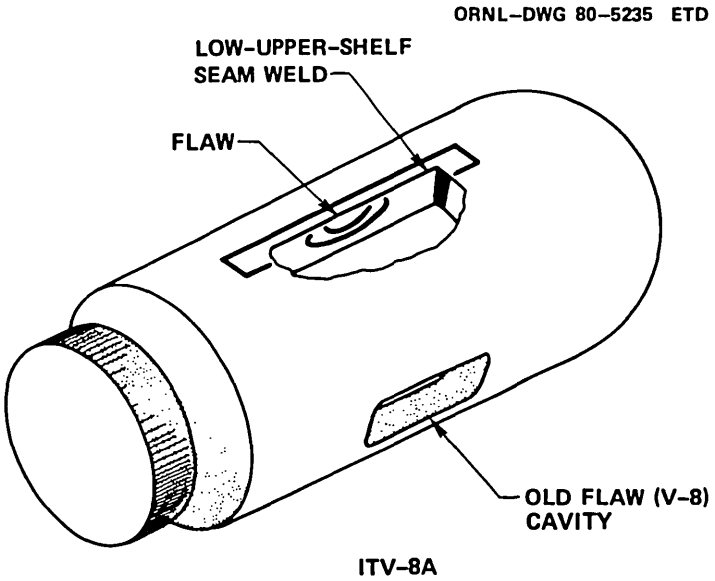

Fig. 2.3. Schematic of vessel V-8A showing location of flaw relative to special seam weld.

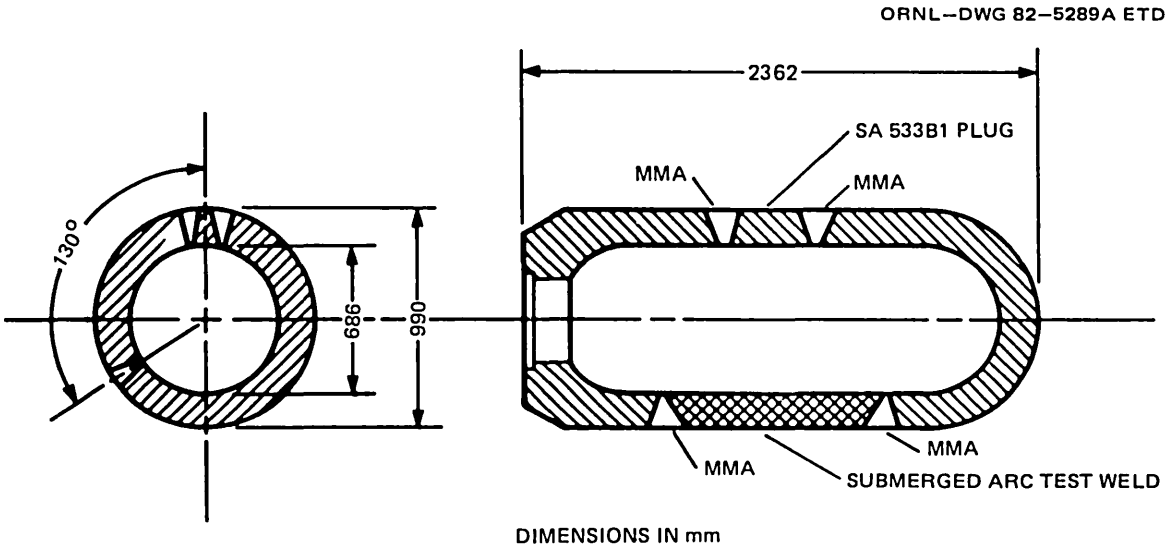

Fig. 2.4. Vessel repair and special seam weld.

Limits on yield strength were specified to provide, at the minimum, adequate strength to attain a tearing instability in the V-8A test before the onset of a local plastic instability. The maximum yield strength was selected to be representative of that of irradiated steel. It was also desired that the temperature at the onset of the Charpy upper shelf be as low as practicable so that an upper-shelf test temperature would introduce no severe demands on the vessel test facility. The nine preliminary weld combinations are given in Table 2.2. The combination represented by weld V822 was selected for the special seam weld of the test vessel. The upper-shelf impact energy, yield strength, and temperature at the onset of the upper shelf were 57.2 J, 461 MPa, and 107°C, respectively, for weld V822.

A trial weld, designated V842, was made in a 152-mm-thick plate of SA 533 grade B class 1 steel. Welding materials and conditions were nearly the same as for weld V822. Tensile, Charpy V-notch, drop weight,

Table 2.2. Weld designations

Flux composition (%)		Mean hold temperature during postweld heat treatment at		
Linde 60	Linde 80	613°C	579°C	552°C
60	40	V811	V812	V813
75	25	V821	V822	V823
90	10	V831	V832	V833

and J-integral tests were made for the V842 weld to confirm the suitability of the welding procedure. The welding parameters and properties of all the welds made in the preliminary investigation are described in detail in Ref. 4.

The special seam weld was deposited in a slot for which dimensional details are shown in Fig. 2.5. The central portion of this weld was made by an automatic submerged-arc process with the parameters given in Table 2.3, which are essentially the same as those used in making the trial weld V842.

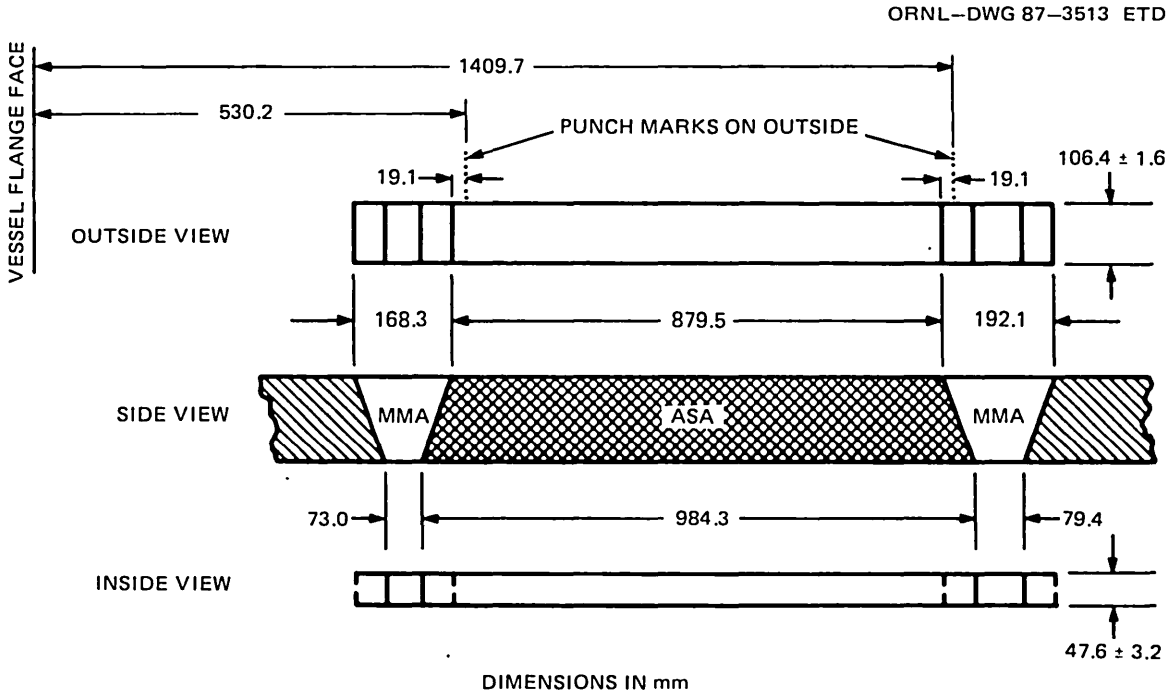

Fig. 2.5. Dimensions at the special seam weld of the vessel.

After the submerged-arc weld was placed, it was cut back at the ends to form cavities for manual metal arc welds used to finish the seam. After the plug weld and the special seam weld were completed and heat treated, radiographic inspection disclosed an unacceptable defect in the manual metal arc portion of the seam weld nearest the vessel flange. The entire seam was removed and replaced, and the vessel was again heat treated. Final dimensions are shown in Fig. 2.5. The conditions of the postweld heat treatments of the vessel are given in Table 2.4.

Table 2.3. Welding parameters for the V-8A special seam weld

Parameter	Value
Preheat temperature, minimum	149°C
Interpass temperature, maximum	260°C
Current	450—500 A
Voltage	30—34 VAC
Travel speed	4.7—5.5 mm/s
Flux	75% Linde 60, 25% Linde 80[a]
Electrode	3.18-mm-diam, SFA 5.23, Mn-Mo-Ni, heat F60853

[a]Linde 60 flux from Lot 0894 was ground to 48XD and mixed with Linde 80 flux from Lot 0592. The first batch of the mixture was used for trial weld V842 and characterization welds V852, V862, V872, and V882. This first batch was also used in the seam weld in the vessel that had to be removed. A second batch, prepared from the same lots of flux, was ground, mixed, and used for the final weld in the vessel and for characterization weld V8102.

Table 2.4. Postweld heat treatment for vessel V-8A

	Original	Final
Heating rate — 316 to 566°C, K/h	31.3	22.7
Hold time at 566 to 593°C, h	50.5	49.8
Average hold temperature, °C	583	581
Cooling rate — 566 to 316°C, K/h	6.8	6.7

2.3 Materials Investigations

2.3.1 Preparation of characterization material and specimens

Essential properties of the special seam weld in which the flaw was implanted and of the base metal of the V-8A vessel barrel were characterized by testing specimens cut from characterization welds, the prolongation of the cylindrical section of intermediate test vessel V-10, and the

special seam weld itself. Specimens from the special seam weld were prepared after the vessel was tested; all other specimen tests were completed before it was tested. The schedule of characterization tests is given in Table 2.5.

Originally four seam welds were made in the prolongation, identified as V10P, of intermediate test vessel V-10 for use in pretest characterization of the special seam weld in vessel V-8A. The layout of these welds is shown in Fig. 2.6. One seam, V872, had radiographic indications of imperfections that made it inappropriate for characterization. Consequently, a fifth seam, V8102, with nominally the same geometry as the welds in the prolongation, was made in a 152-mm-thick plate of SA 533 grade B class 1 steel. All characterization welds were made by the same automatic submerged-arc process applied to the vessel, as indicated by the welding parameters given in Table 2.3. The same heat of electrodes and the same lots of flux were used for both the vessel and the characterization welds. However, as indicated in Table 2.3, a second batch of flux had to be ground and mixed for the final vessel weld and characterization weld V8102. Postweld heat treatment conditions for the characterization welds and the final special seam weld in the vessel are given in Table 2.6. Characterization weld V8102 and a piece of base metal from V10P were heat treated with vessel V-8A during its final postweld heat treatment. The piece of V10P that had received the second postweld heat treatment (called piece V10S1 by B&W) was shipped to Oak Ridge National Laboratory (ORNL) for base metal tensile testing. V10P was originally

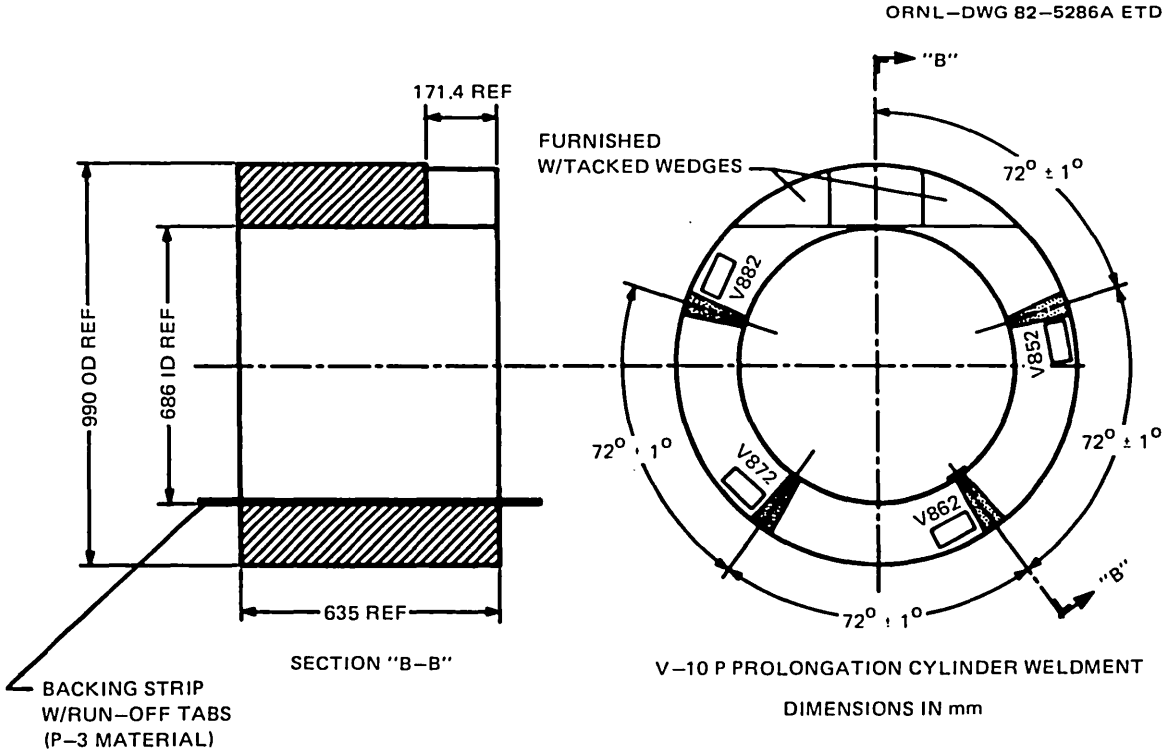

Fig. 2.6. Characterization welds made in vessel V-10 prolongation (welds V852, V862, V872, and V882).

Table 2.5. Types of specimens used for characterization tests

Type	Specimen material[a]	Number
Chemical analysis	V852	3
	V8102	3
Transverse bend	V862	4
	V882	4
Charpy impact	V852	20
	V862	20
	V882	10
	V8102	10
	V8A	20
Drop weight	V862	6
	V882	5
Fracture toughness (IT)	V852	4
	V862	2
	V8102	1
J-integral (J_R)		
1T compact	V852	7
	V862	11
	V882	6
	V8102	6
	V8A	10
2T compact	V852	2
	V862	2
	V882	2
	V8102	4
PCCV	V8102	14
Macrostructure	V852	1
	V8102	1
Tensile[b]	V852	6
	V8102	6
	V8A	4
	V10P	46
Hardness	V10P	2

[a]V852, V862, V882, and V8102 are characterization welds. V8A is a part of the submerged arc portion of the special seam weld in vessel V-8A. V10P is the prolongation of intermediate test vessel V-10.

[b]All specimens had gage diameters of 12.8 mm except that the V8A specimens and 28 of the V10P specimens had gage diameters of 6.4 mm.

Table 2.6. Postweld heat treatment for vessel V-8A and characterization welds

Parameter	Final V-8A seam weld	Welds V852, V862, V872, and V882	Weld V8102
Heating rate — 316 to 566°C, K/h	22.7	20.6	27.8
Hold time at 566 to 593°C, h	49.8	50.0	48.5
Average hold temperature, °C	581	577	576
Cooling rate — 566 to 316°C, K/h	6.7	8.6	6.9

fabricated from the same plate from which the cylindrical test section of vessel V-8A was made.[2] Accordingly, prior to the placement of the special seam weld in vessel V-8A, the vessel and the prolongation had received about the same heat treatment. Childress reported that V-8 and V10P had received the total postweld heat treatments given in Table 2.7 after the austenitizing, quenching, and tempering treatment.[2] The base metal of the V-8A vessel and piece V10S1 of the prolongation simultaneously received a total of 100.3 h of postweld heat treatment in the course of making the special seam weld.

After the V-8A test, the special seam weld was cut from the vessel, and segments of the submerged-arc weld were used for Charpy impact, tensile, and J-integral specimens. The positions of the specimens relative to the flaw and the boundaries of the submerged-arc portion of the special seam weld are shown in Fig. 2.7.

Table 2.7. Postweld heat treatments for V-8 and V10P

Component	Phase of postweld heat treatment	Temperature (°C)	Total time at temperature (h)
V-8	Intermediate	593	4.5
	Final	621	6
V10P	Intermediate	593	7.5
	Final	621	6

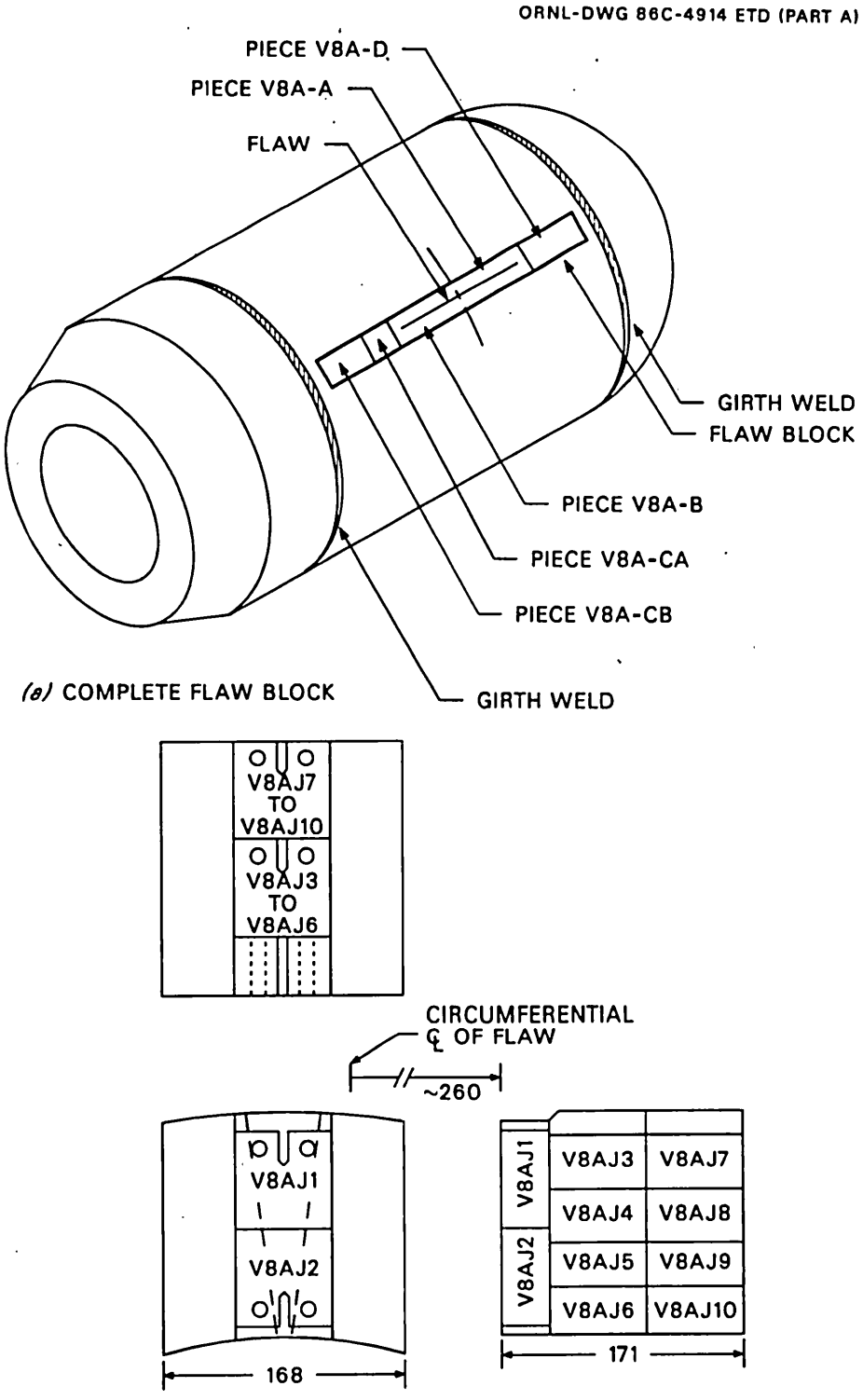

Fig. 2.7. Plan for cutting the special seam weld from vessel V-8A after the test. (*a*) Location of pieces used for J-integral, Charpy impact, and tension tests; (*b*) location of blanks for J-integral specimens; and (*c*) location of blanks for Charpy impact and tensile specimens.

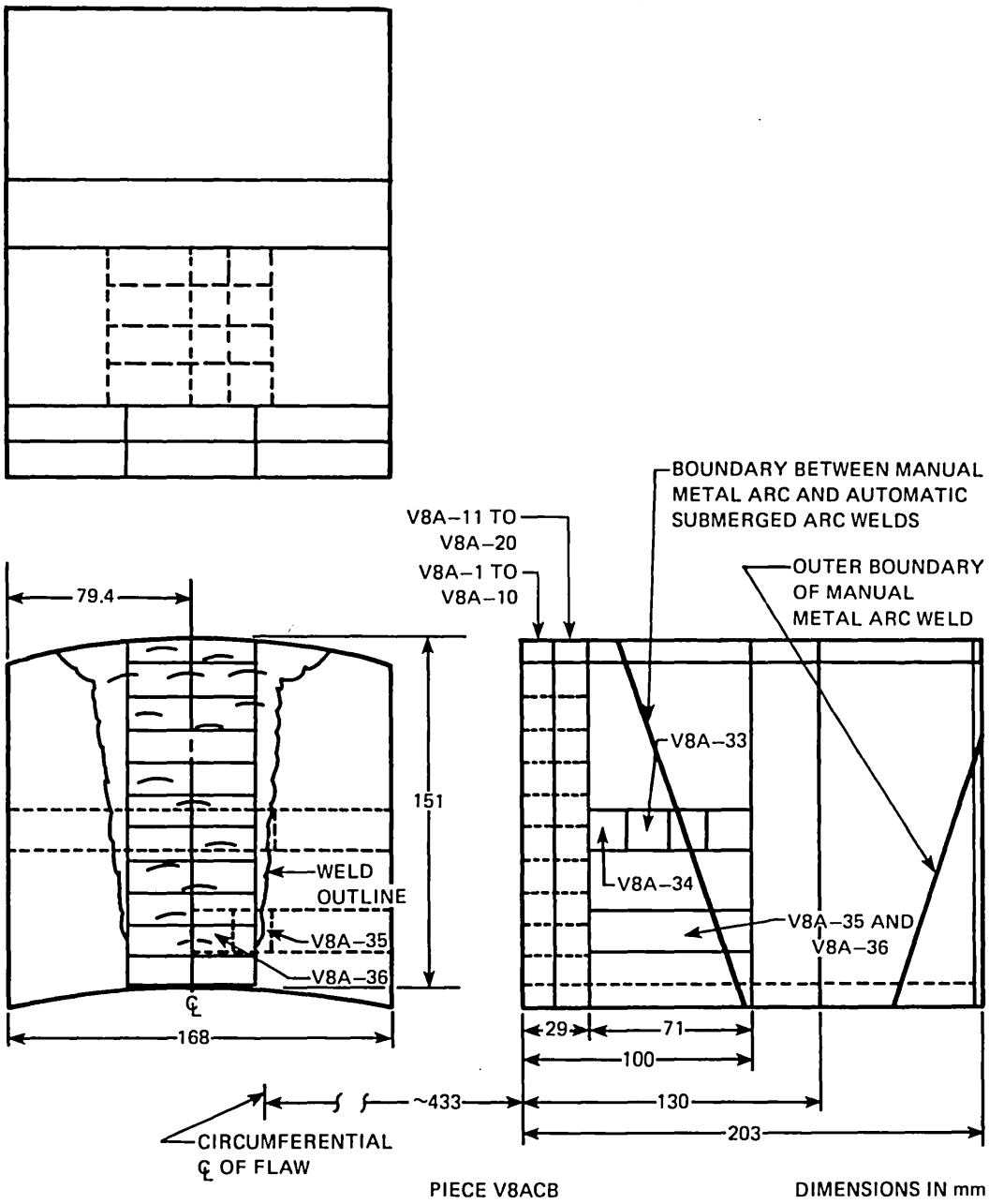

(c) LOCATION OF BLANKS FOR CHARPY AND TENSILE SPECIMENS

Fig. 2.7 (continued)

2.3.2 Material properties

B&W Company performed all testing of the characterization welds.[4] Characteristics and average properties of all of the welds made with the flux mixture used for the vessel are compared in Table 2.8. Figure 2.8 shows a typical cross section of the 152-mm-thick welds. Details of material properties not presented in this chapter are presented in Appendix L of this report and in Ref. 4.

Charpy impact data. Charpy V-notch impact specimens cut from each characterization weld were tested to identify the temperature of the onset of the upper shelf and to determine the upper-shelf impact energy.

Table 2.8. Characteristics and average properties of V-8A characterization and test welds

Weld chemistry	Weld						
	V822	V842	V852	V862	V882	V8102	Vessel V-8A
C	0.06	0.05	0.06			0.06	
Mn	1.61	1.50	1.56			1.52	
P	0.024	0.028	0.031			0.026	
S	0.017	0.016	0.016			0.014	
Si	0.65	0.66	0.71			0.62	
Ni	0.61	0.62	0.63			0.63	
Mo	0.48	0.45	0.48			0.47	
Cu	0.29	0.27	0.25			0.17	
O	0.143	0.143	0.147	0.153	0.147	0.147	
Plate (weld) thickness, mm	95.2	152	152	152	152	152	152
Heat input, kJ/mm	3.6	3.0	3.0	3.0	3.0	3.0	3.0
PWHT							
Heating rate, K/h	33.0	82.2	20.6	20.6	20.6	27.8	22.7
Hold time, h	50.0	52.0	50.0	50.0	50.0	48.5	49.8
Hold temperature, °C	579	584	577	577	577	576	581
Cooling rate, K/h	6.8	5.7	8.6	8.6	8.6	6.9	6.7
Room temperature tension tests[a]							
Yield strength, MPa	461	460	430			478	423[b]
Ultimate tensile strength, MPa	565	568	547			581	525[b]
Elongation, %	24.7	25.8	26.8			22.8	18.6[b]
Reduction of area, %	54.4	55.3	57.8			53.3	53.6[b]
Charpy V-notch tests (100% shear)[c]							
Energy, J	57.2	58.0	66.3	61.8	59.0	50.7	56.3
J_{Ic} at 149°C, kJ/m^2		66.2[d]	70.8	61.5	59.0	43.3	46.6
NDT temperature, °C				−18 or −23	−18		

[a]Specimen axis parallel to welding direction.

[b]Tested at 149°C.

[c]CA orientation in cylindrical weldments and corresponding orientation in other weldments.

[d]Tested at 116 to 121°C.

The highest temperature at which the Charpy fracture appearance indicated <100% shear was 104°C. The impact energies for the specimens that exhibited 100% shear fracture ranged from 48.9 to 76.6 J. Average upper-shelf energies are shown in Table 2.9 for each characterization weld and for a sample of the V-8A special seam weld removed after the vessel test was completed. These upper-shelf energies were well within the specified range of 47.5 to 74.6 J. The Charpy test results for the V-8A seam are shown in Fig. 2.9; a complete tabulation of Charpy data for the welds is in Appendix L.

Tensile properties. The tensile properties of the characterization welds are presented in Table 2.10. After the test of the vessel, tensile properties of a sample of the special seam weld were determined. The results are summarized in Table 2.11. See Fig. 2.7 for locations of specimens in the V-8A weld.

As described earlier in this chapter, tensile characteristics of the base metal were determined at ORNL by testing specimens cut from V10P.

ORNL PHOTO 3397–81A

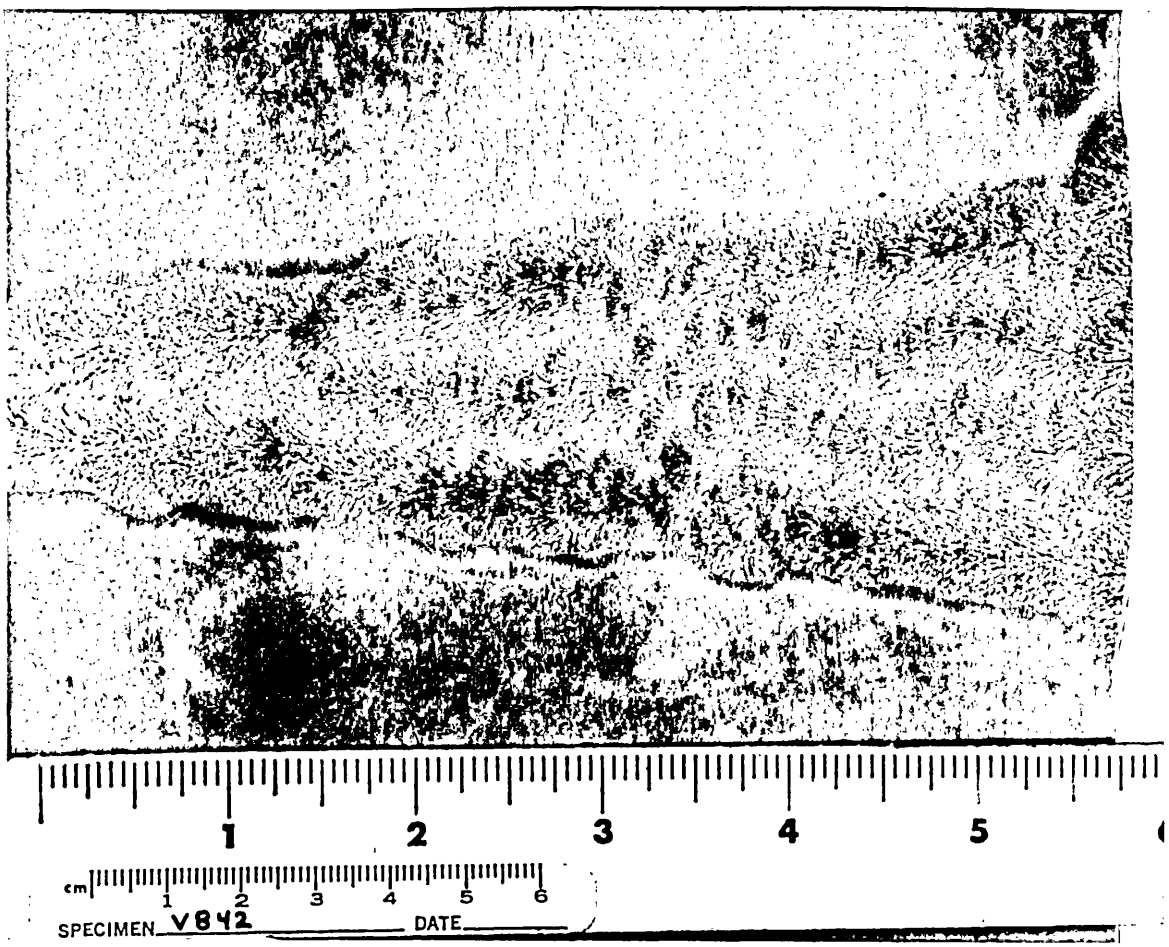

Fig. 2.8. Macrograph of cross section of weld V842. Photograph by the Babcock & Wilcox Company. (Original reduced 28%)

Table 2.9. Mean upper-shelf Charpy impact energy (USE) values of characterization welds[a]

Weld	Specimens with 100% shear	Average temperature (°C)	USE (J)
V852	13	130	66.3
V862	13	129	61.8
V882	10	110	59.0
V8102	10	136	51.7
V8A	4	149	56.3

[a]CA and similar orientation.

Table 2.10. V-8A characterization weld tensile data[a]

Weld	Test temperature (°C)	Stresses (MPa)		Ductility (%)	
		Yield	Ultimate	Elongation	Reduction of area
V852	24	430	547	26.8	57.8
	149	391	498	22.7	53.3
V8102	24	478	581	22.8	53.3
	149	438	534	19.3	50.3

[a]Average of three tests. Axis of specimen parallel to direction of welding.

Two methods of characterizing the tensile properties were used: (1) the determination of the effects of temperature over a range encompassing the proposed V-8A test temperature and (2) the determination of the through-thickness distribution at the proposed test temperature. The tensile specimens used were either 12.8- or 6.4-mm-gage diam and were tested at four test temperatures (22.8, 121, 149, and 177°C).

Results from the 12.8-mm-gage-diam specimens machined from the central region of the 168-mm-thick wall and aligned in either the circumferential (C) or the axial (A) orientation are listed in Table 2.12 and plotted in Fig. 2.10. Three test temperatures (22.8, 121, and 177°C) and three depth locations (0.34, 0.50, and 0.66t) were examined. Each of the results represents the average of three specimens (one from each depth location). The results indicate that the tensile properties decrease

Table 2.11. Tensile properties (6.4-mm-diam specimens, strain rate 0.016/min) of weld metal from the special seam weld in vessel V-8A at 149°C

Specimen No. V8A	Stresses (MPa)		Ductility (%)		Elastic modulus (GPa)
	Yield[a]	Ultimate	Total elongation[b]	Reduction of area	
			Axial orientation[c]		
35	429	525	18.7	54.3	205
36	417	525	18.6	53.0	187
			Circumferential orientation[d]		
34	403	502	16.9	52.9	234
33	401	502	17.3	56.7	231

[a]0.2% offset.

[b]Gage length to gage diameter = 5.

[c]Specimen axis paralel to welding direction.

[d]Specimen axis perpendicular to welding direction.

Table 2.12. Tensile properties[a] of the V-10 prolongation after a postweld heat treatment of 100 h at 560°C

Temperature (°C)	Stresses (MPa)		Ductility (%)		Elastic modulus (GPa)
	Yield[b]	Ultimate	Elongation[c]	Reduction of area	
			C orientation[d]		
22.8	471	617	21.5	67.7	207
121	427	583	18.5	66.6	
177	423	574	18.9	66.0	
			A orientation[e]		
22.8	470	616	19.7	60.7	203
121	436	574	16.4	58.1	
177	421	568	16.4	56.9	

[a]Average of three specimens; strain rate = 0.018/min; 12.8-mm-gage diam.

[b]0.2% offset.

[c]Gage length to gage diameter = 4.

[d]Specimen length perpendicular to vessel axis (A); fracture axial and radial.

[e]Specimen length parallel to A; fracture radial and circumferential.

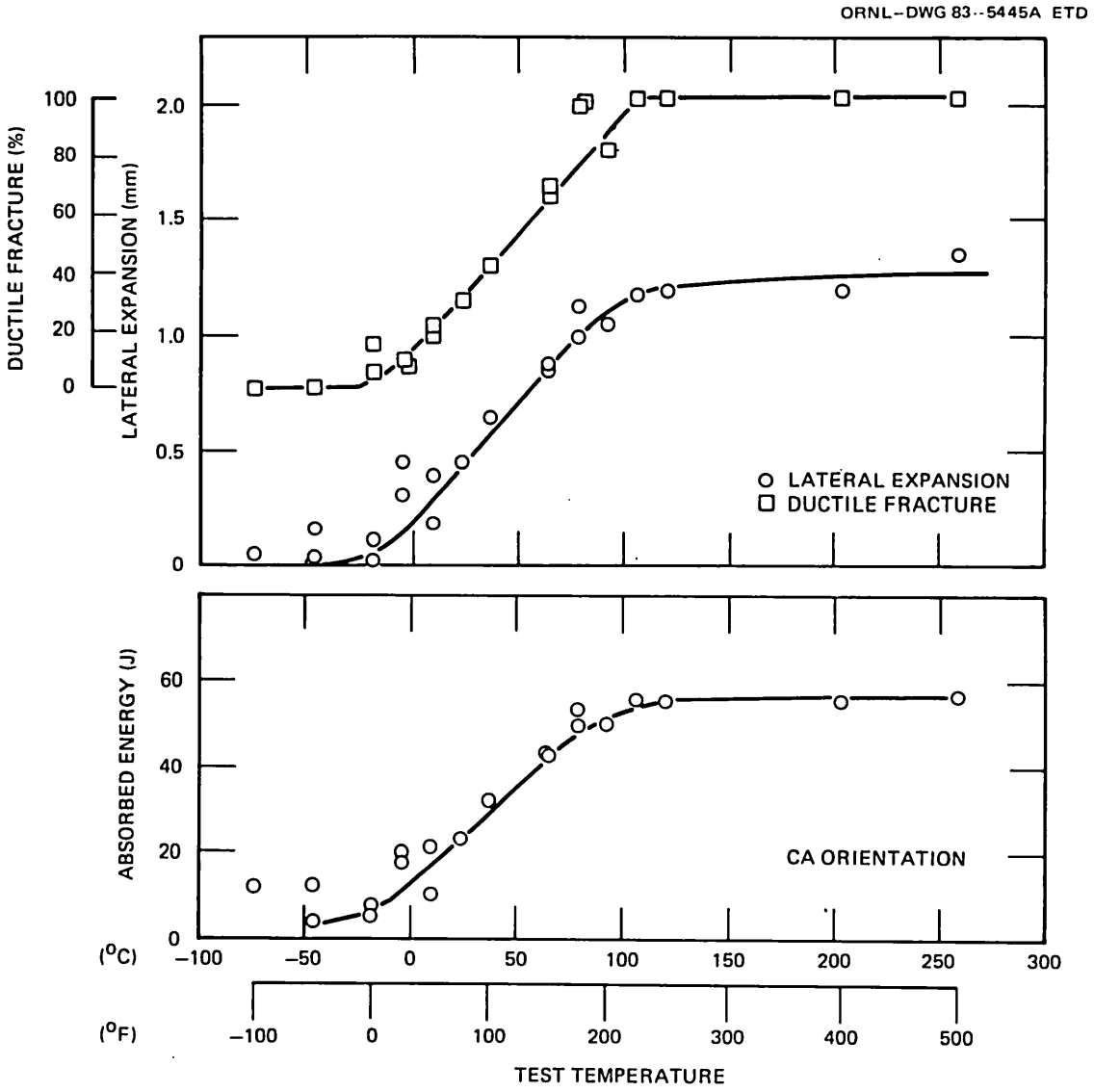

Fig. 2.9. Posttest through-thickness Charpy V-notch impact properties of weld metal from special seam weld in test vessel V-8A. See Fig. 2.7 for locations of specimens.

with increasing test temperature between 23 and 177°C but that the decrease between 121 and 177°C is small, ensuring that the tensile properties remain fairly constant 30°C on either side of the 150°C V-8A test temperature. Specimen orientation appears to affect the total elongation and the reduction of area (ductility) to a greater extent than the yield and ultimate strengths. Results from A-oriented specimens show lower ductility, as measured by both elongation and reduction of area, than C-oriented specimens.

The results from 6.4-mm-gage-diam C- and A-oriented tensile specimens from seven depth locations, 0.05–0.95t, and from tests conducted at 149°C are listed in Table 2.13 and plotted in Fig. 2.11. Each result

Table 2.13. Tensile properties[a] through the thickness of the V10 prolongation at 149°C after a postweld heat treatment of 100 h at 560°C

Depth from outer surface[b]	Stresses (MPa)		Ductility (%)		Elastic modulus (GPa)
	Yield[c]	Ultimate	Elongation[d]	Reduction of area	
			A orientation[e]		
0.05	487	613	17.5	66	202
0.20	424	566	18.0	69	207
0.35	422	566	18.1	62	210[f]
0.50	427	569	17.4	59	211[f]
0.65	425	571	17.1	61	208
0.80	422[f]	562	17.3	62	200
0.95	425[f]	562	18.4	63	221
			C orientation[g]		
0.05	459	594	19.1	72	209
0.20	424	565	19.6	71	209
0.35	430	569	19.8	69	212
0.50	429	573	19.5	69	211[f]
0.65	430[f]	572	19.4[f]	66[f]	206[f]
0.80	424[f]	565	19.3[f]	71[f]	210[f]
0.95	432	570	19.6	71	209

[a]Average of two specimens except as noted; 6.4 mm in diameter; strain rate 0.016/min.

[b]Fraction of 168-mm wall thickness.

[c]0.2% offset.

[d]Gage length/diameter = 4.

[e]Specimen length parallel to vessel axis (A); fracture radial and circumferential.

[f]Property determined from a single specimen.

[g]Specimen length perpendicular to A; fracture axial and radial.

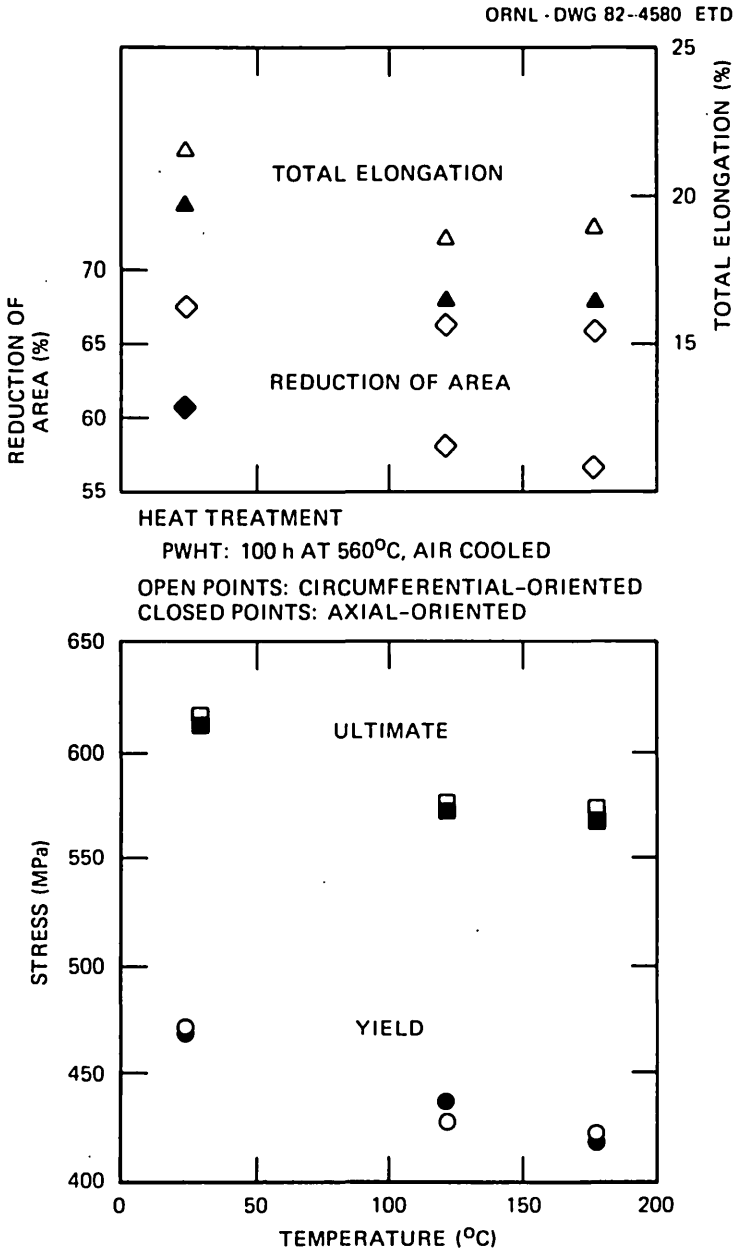

Fig. 2.10. Effect of temperature on tensile properties of prolongation V10P after a PWHT of 100 h at 560°C, air cooled.

represents the average from two specimens unless otherwise noted. The tensile specimens were machined from sections of V10P, which, with a wall thickness of 168 mm, is thicker than the 152-mm wall of V-8A. Fabrication documentation for V-8 (Ref. 2) indicates that the vessel and prolongation were rolled separately from 167-mm-thick (6 9/16-in.) A 533 grade B class 1 plate. This would indicate that the prolongation (V10P) was rolled to the V-8A outside diameter, 991 mm, and that no material

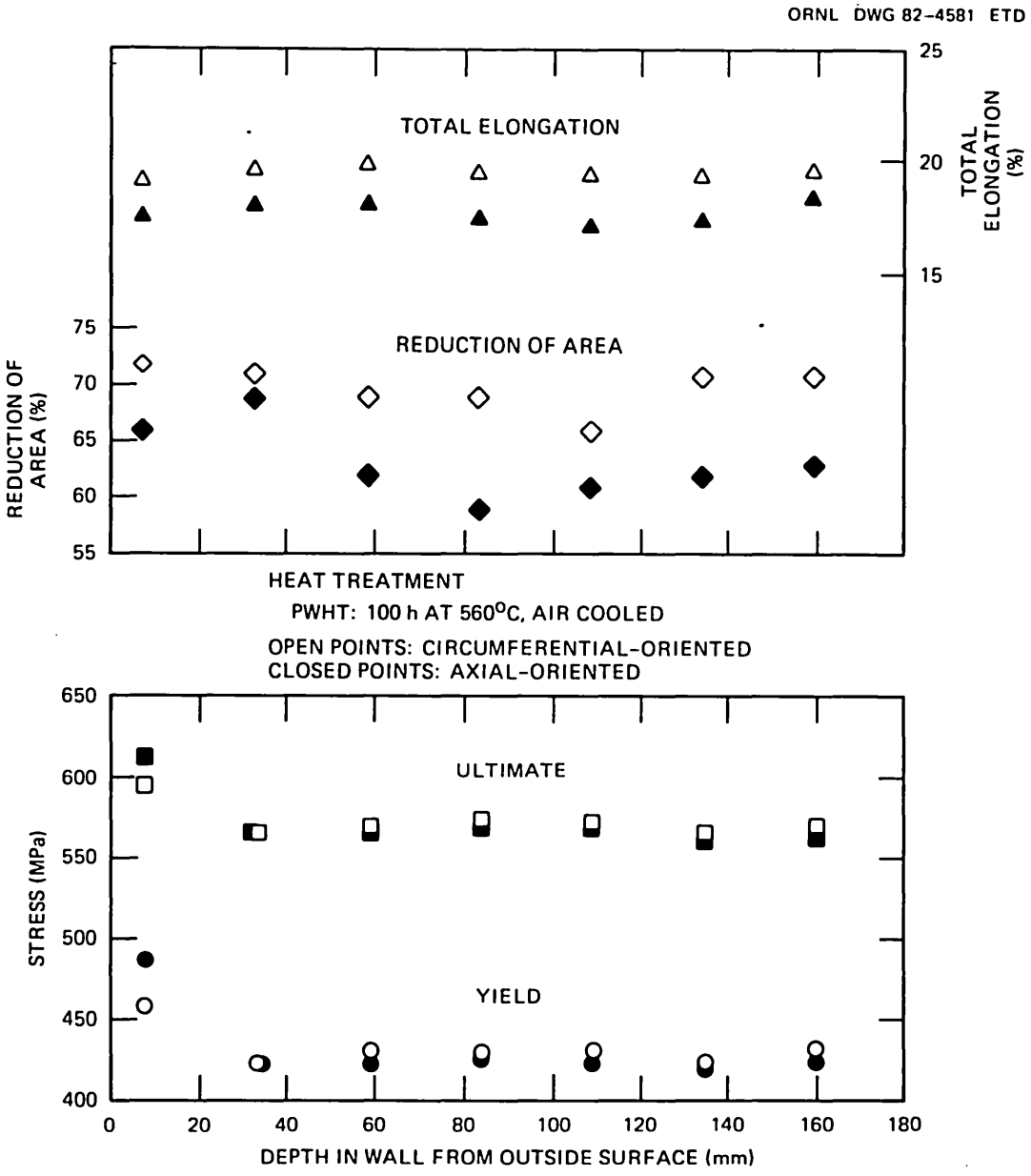

Fig. 2.11. Tensile properties through the thickness of the V10P prolongation.

was removed from either surface. The tensile results indicate higher strengths near the outer surface but not near the inner surface of V10P. Higher strengths would be expected near both surfaces of quenched and tempered material, but the results from the inner surface do not reflect this.

Other than the high strength near the surface, the tensile properties, with the exception of the reduction of area, show little variation over the central region of V10P. The reduction of area results go

through a minimum value at midthickness. The effect of specimen orientation indicates that the A-oriented specimens provide lower values but show the same trends as the C-oriented specimens.

A through-thickness hardness traverse was made to ascertain the trend of tensile strength in greater detail. The results from the hardness measurements are shown in Fig. 2.12. Each point represents the average of two hardness measurements, which were made on the Rockwell B scale. The results indicate that the hardness begins to increase within 19 mm of either surface. It appears to reach a maximum about 6.3 mm from either surface, but that is considered to be caused by the loss of constraint very near the surface when using a large hardness indenter. Since the hardness can be related to the tensile strength,[5] the strengths near the inner surface should have increased as well. The innermost tensile specimens apparently were located close to the depth where tensile strengths begin to increase.

The 6.4-mm-gage-diam specimens from V10P were instrumented for determination of the stress-strain behavior of the base material before the vessel test. One tensile specimen cut from the V-8A seam weld was also used for stress-strain measurements. The true stress-true strain relationships for the two materials are shown in Fig. 2.13. The data on which the stress-strain curves are based are presented in Appendix L.

Fracture toughness. Fracture toughness tests were performed with specimens from three of the characterization welds. None of the results conformed to the validity requirements of the testing standard American Society for Testing and Materials (ASTM) E399 for plane-strain fracture toughness. The values of K_c presented in Table 2.14 are calculated from J at maximum load.

Tearing resistance. The principal effort in characterizing the material of the V-8A special seam weld was to determine its tearing

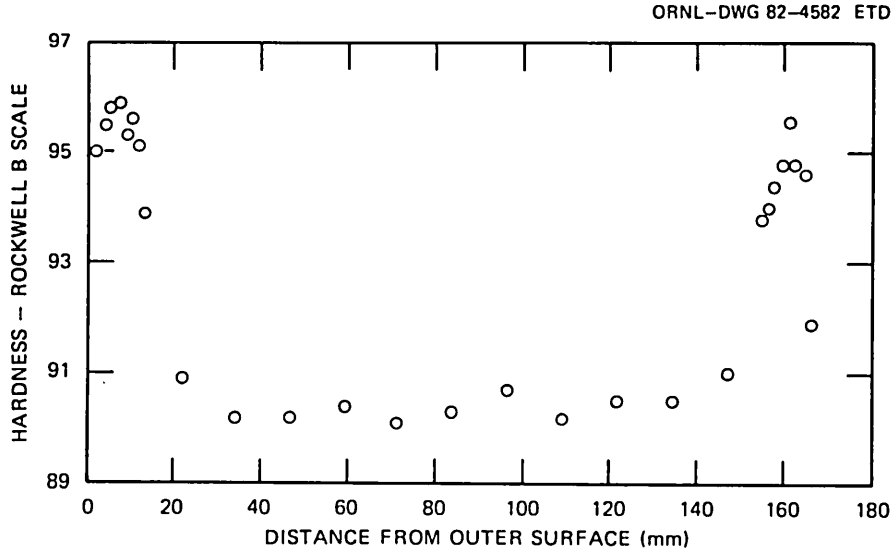

Fig. 2.12. Variation of hardness through the 168-mm-thick wall of prolongation V10P.

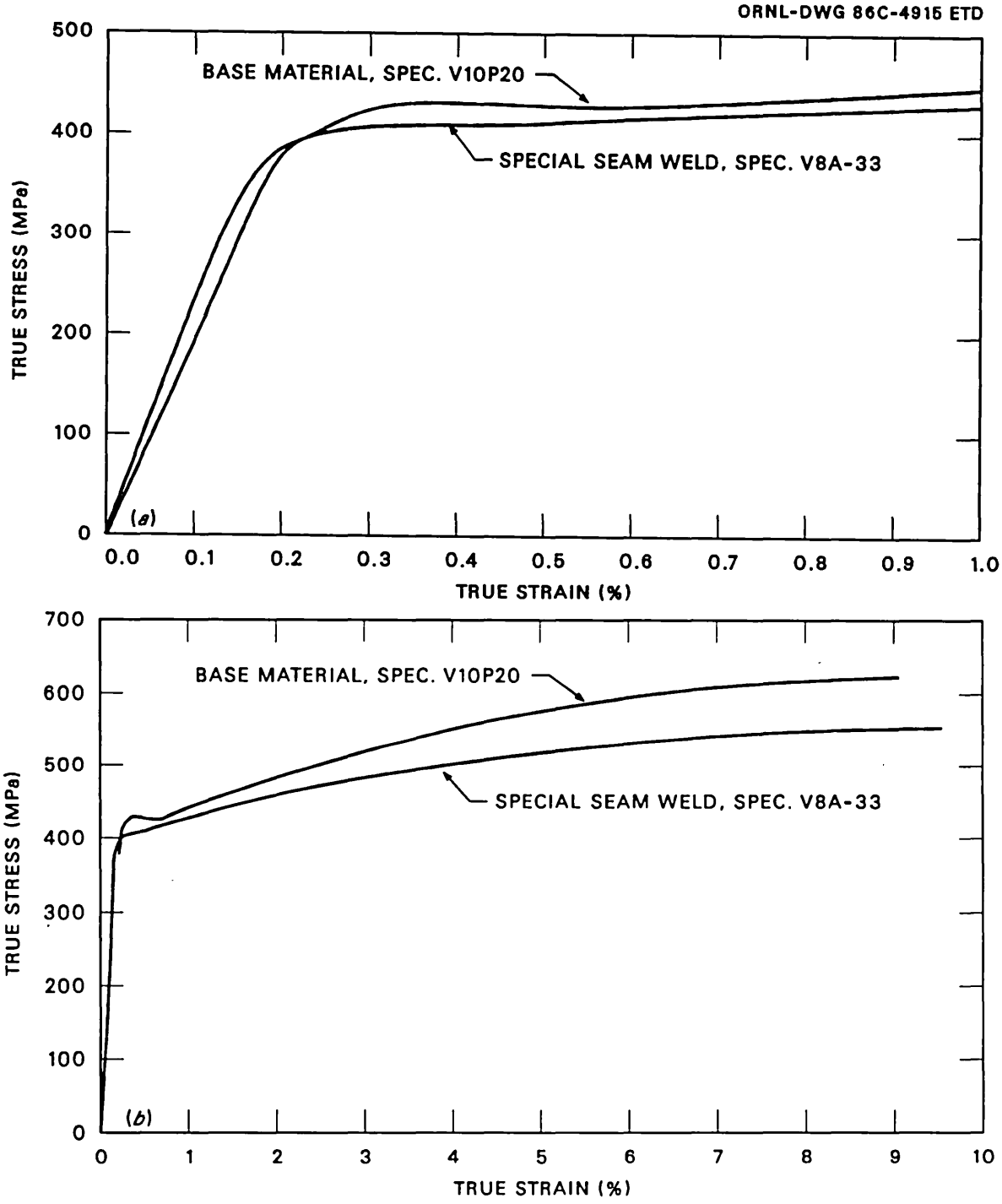

Fig. 2.13. True stress vs true strain for a representative specimen of base material and for the V-8A special seam weld.

Table 2.14. Results of fracture toughness tests of V-8A characterization welds

Weld	Specimen orientation[a]	Test temperature[b] (°C)	J[c] (kJ/m²)	K_c[d] (MPa·√m)
V852	CA	−16	157	180
V852	CA	−15	90	136
V852	CA	−15	148	175
V852	CA	−14	134	166
V862	CR	22	.243	224
V862	CR	22	231	219
V8102	CA[e]	−15	49	101

[a]C — circumferential, A — axial, R — radial.

[b]Average of temperatures at beginning and end of test.

[c]At maximum load; some crack extension might have occurred.

[d]Calculated from J at maximum load.

[e]In the plate weldment, the welding direction corresponds to A and the transverse direction to C.

resistance (J_R) in terms of the J integral. B&W performed the J_R tests for the characterization welds before the vessel was tested and for a portion of the V-8A seam weld after the vessel test. The pretest J_R data, which have been reported in detail in Ref. 4, are summarized here. The posttest data, which are contained in an unpublished report,[6] are presented completely in this chapter and in Appendix L.

Data from each specimen were fitted by a least-squares procedure to the power-law expression

$$J = c(\Delta a)^n , \tag{1}$$

in which J and Δa are tearing resistance and increment of crack depth, respectively, and c and n are parameters determined by the least-squares procedure. A linear least squares fit was made with the transformed variables x and y defined by

$$y = \ell n\ J , \tag{2}$$

and

$$x = \ell n\ (\Delta a) . \tag{3}$$

Equations (2) and (3) transform Eq. (1) into

$$y = Ax + B \ , \qquad (4)$$

with A = n and B = ℓn c.

Fits obtained with the transformed Eq. (4) were compared with direct fits to Eq. (1). Differences in the results of the two methods were very small.

Six options for calculating the power-law parameters were investigated. Two domains of the variable Δa were considered: (1) the Δa domain defined in the standard ASTM E813 for J_{Ic} determination and (2) all points with Δa greater than those defined by the ASTM lower exclusion line. For each Δa domain, three statistical options were considered: (1) J random, (2) Δa random, and (3) both J and Δa random. The significance of these options is illustrated by the typical results shown in Fig. 2.14. The three statistical options produce nearly identical results. The choice of the maximum Δa, on the other hand, affects the resulting J_R curve substantially. Figure 2.14 shows a divergence that is typical of most specimens for the two types of fits. This figure also shows an example of test data that are not well represented by a power-law expression.

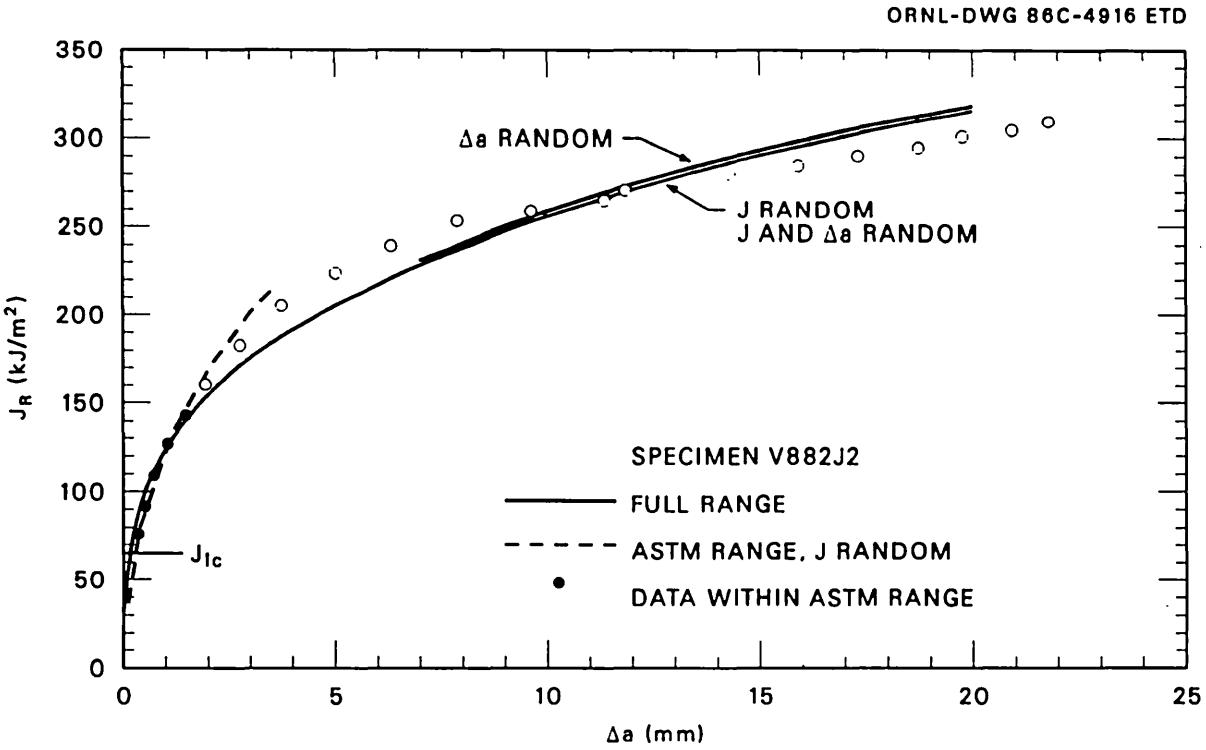

Fig. 2.14. Power-law J_R curves for specimen V882J2. This set of curves represents four different least-squares fits.

Results of the J_R tests are summarized in the power-law curves shown in Figs. 2.15 and 2.16 for all welds. The maximum values of Δa in the tests were ~11 to 13 mm for 25-mm-thick specimens and ~20 to 30 mm for 51-mm-thick specimens. The maximum Δa for the data included in the ASTM range is ~1.5 mm. In all cases, data with Δa below the lower exclusion line (the blunting line plus 0.15 mm) were excluded. Figures 2.15 and 2.16 show that power-law curves fitting only the data within the ASTM range are generally steeper than the corresponding curves fitting data with greater values of Δa. It is plausible that the best J_R curve for analysis is best represented by a composite expression rather than a single power-law expression, as in Eq. (1). Average values of the parameters of the power-law expression for the five welds are given in Table 2.15. Pretest and posttest tearing instability analyses at ORNL were based on power-law curves fitted to the full range of data.

The tearing resistance was variable from weld to weld, as may be observed in Figs. 2.15 and 2.16. However, the range of values for the characterization and V-8A welds was close to that of several irradiated low-upper-shelf welds tested by Loss at the Naval Research Laboratory.[7] This similarity is shown in Fig. 2.17.

The specimens from each weld exhibited variability, as illustrated in Fig. 2.18 for the vessel weld. This figure shows the highest and lowest J_R curves for the set of ten specimens from the vessel weld. The bounding curves are about 20% above and below the mean curve. The $J_R - \Delta a$

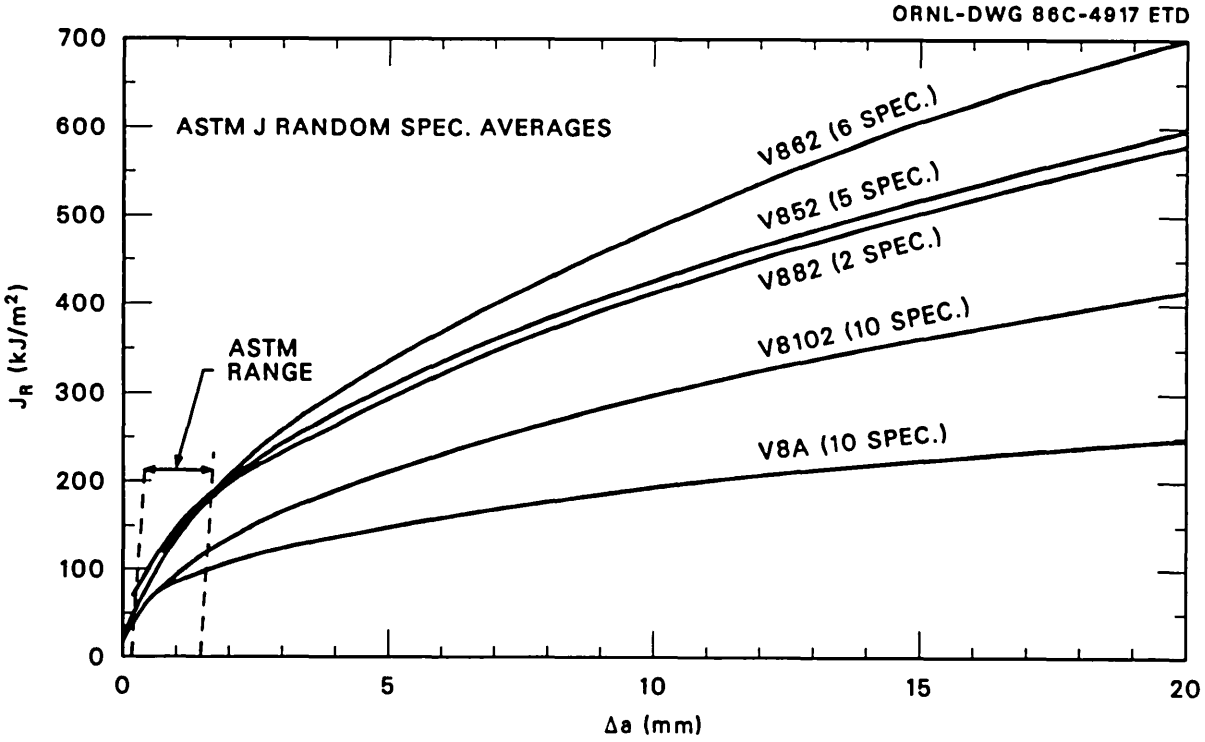

Fig. 2.15. J_R curves for average power-law parameters for each characterization weld and the vessel weld at 149°C. See "ASTM range" column of Table 2.15 for values of parameters.

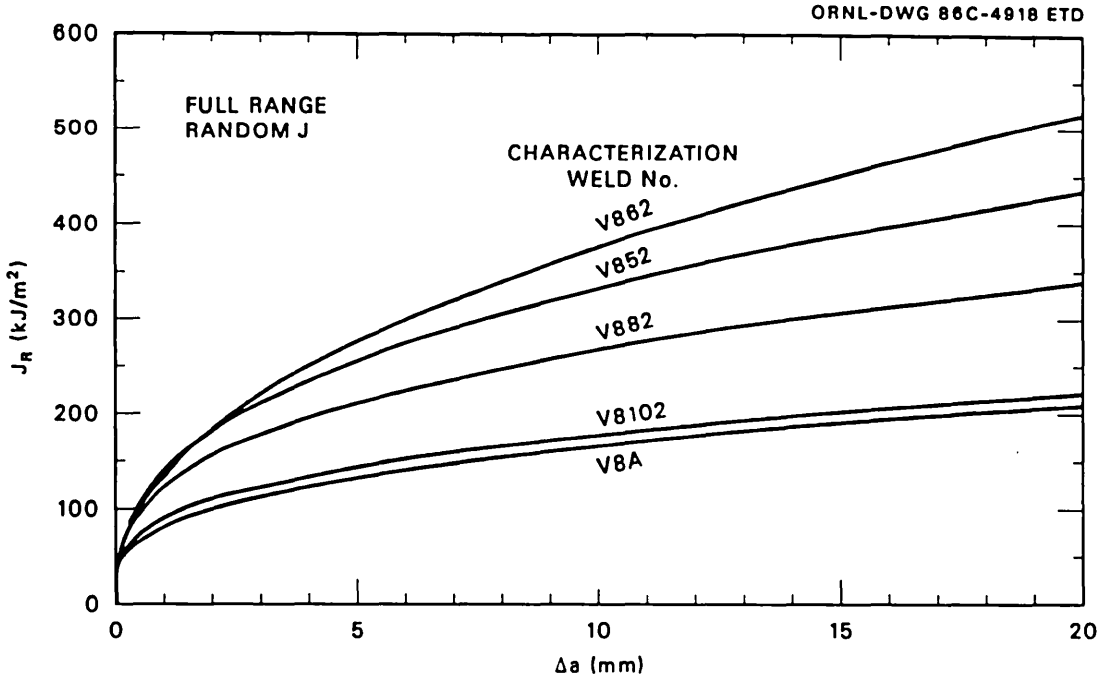

Fig. 2.16. J_R curves for average power-law parameters for each characterization weld and the vessel weld at 149°C. See "Full range" column of Table 2.15 for values of parameters.

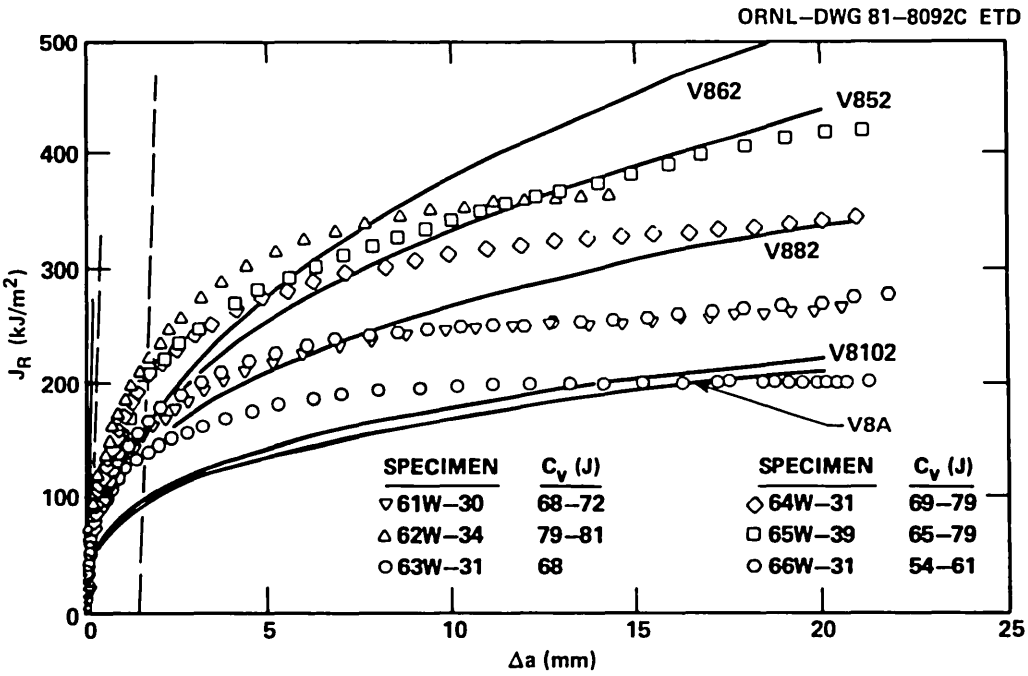

Fig. 2.17. Comparison of tearing resistance data for the V-8A special seam weld; the characterization welds V852, V862, V882, and V8102; and irradiated high-copper welds. Irradiated weld data are from F. J. Loss (Ref. 7).

Table 2.15. J-integral average properties of low-upper-shelf welds at 149°C[a]

Weld	Number of specimens	Orientation[b]	Nominal thickness (mm)	J_{Ic} (kJ/m²)	Power law parameters[c]			
					ASTM range[d]		Full range[d]	
					c	n	c	n
V852	5			70.8	140.6	0.482	137.9	0.386
	2	CA	25	93.2	150.4	0.364	150.1	0.332
	1	CR	25	47.8	112.3	0.588	110.0	0.502
	1	CA	51	70.8	142.6	0.469	142.5	0.360
	1	CR	51	49.2	147.4	0.626	136.6	0.406
V862	6			61.5	137.6	0.547	134.0	0.451
	2	CA	25	67.4	142.0	0.537	137.8	0.431
	2	CR	25	56.9	131.0	0.558	130.9	0.496
	1	CA	51	73.0	144.3	0.464	143.0	0.379
	1	CR	51	47.5	135.0	0.629	123.9	0.471
V882	2			59.0	130.8	0.498	123.0	0.342
	1	CA	51	64.6	126.5	0.422	124.5	0.311
	1	CR	51	53.4	135.0	0.574	121.5	0.372
V8102	10[e]			43.2	96.18	0.484	89.32	0.308
	4	CA	25	42.6	90.01	0.473	86.21	0.340
	2	CR	25	42.1	103.3	0.530	91.46	0.295
	2	CA	51	43.1	97.69	0.488	91.20	0.272
	2	CR	51	45.9	99.96	0.456	91.50	0.294
	14[f]		10	37.4				
V8A	10		25	46.6	83.1	0.364	81.7	0.318
	8	CA	25	47.9	84.7	0.361	83.3	0.314
	2	CR	25	41.2	76.9	0.374	75.3	0.333

[a]All specimens are compact specimens with 20% total side grooves, except for the Charpy V-notch specimens of V8102 material as noted.

[b]C — circumferential, A — axial, R — radial. In plate weldment V8102, the welding direction corresponds to A and the transverse direction to C.

[c]$J = c(\Delta a)^n$ with J in kJ/m² and Δa in mm.

[d]Data ranges: ASTM — only data between ASTM E813 exclusion lines; full — all data with Δa beyond lower exclusion line.

[e]These averages exclude Charpy V-notch data.

[f]Charpy V-notch specimens tested in 3-point bending.

data for individual specimens were fitted well by the power-law expression of Eq. (1) for welds V8102 and V8A. This is indicated by the plot in Fig. 2.19. Root-mean-square deviations from the fitted curves were <7% for most of the specimens from these two welds. The root-mean-square deviations of the ten-specimen mean curves were 11.5 and 13.4% for welds V8102 and V8A, respectively, over the full range of data.

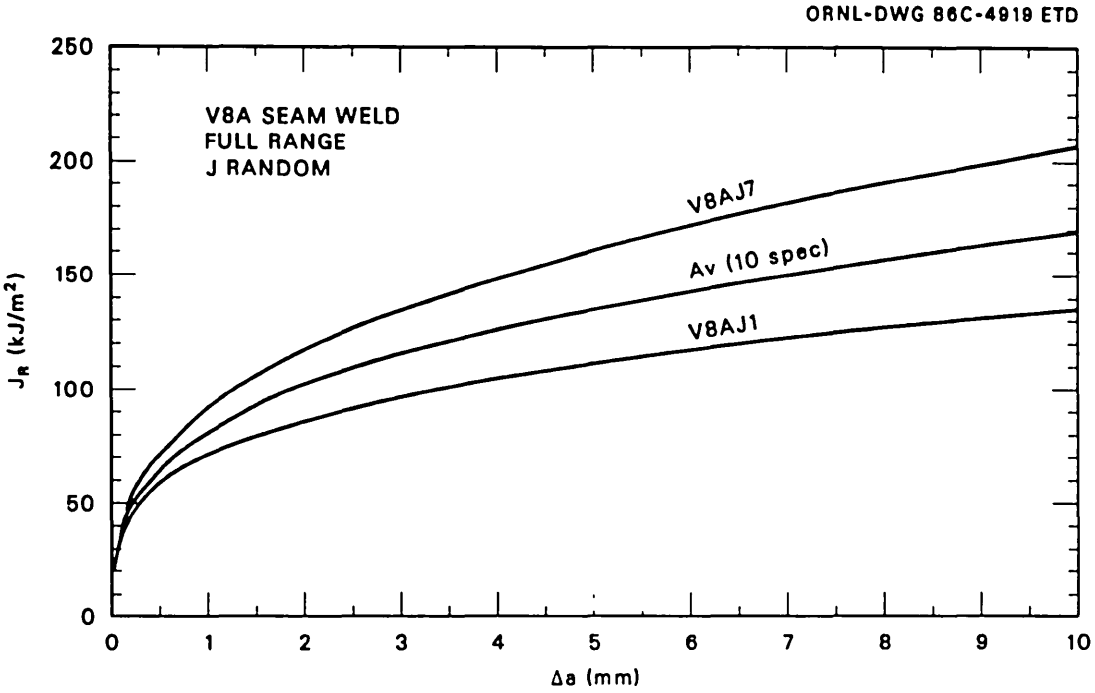

Fig. 2.18. Average J_R curve for the vessel seam weld (V8A) compared with the highest and lowest curves from the set of ten specimens. These fits were made with the full range of data with Δa greater than that on the lower ASTM exclusion line.

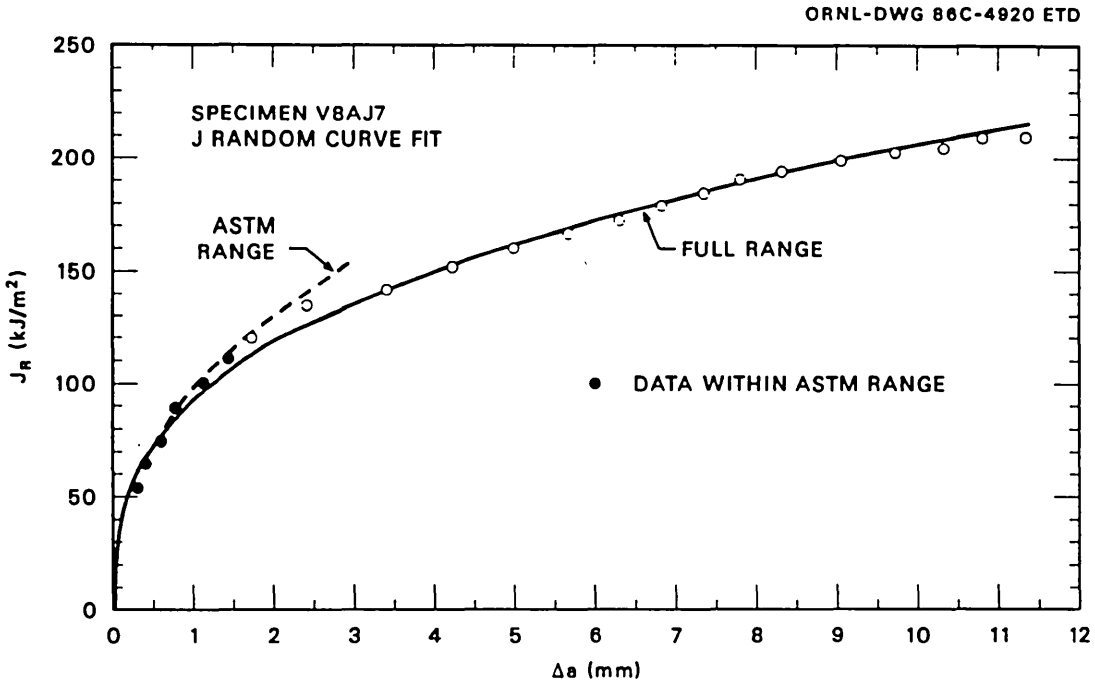

Fig. 2.19. Fits of J — Δa data for specimen V8AJ7 from the vessel seam weld.

2.4 Flaw Preparation

Preparation of a flaw in the V-8A vessel involved, first, machining a notch in the vessel with a profile that approximated a semiellipse and, second, cyclically pressurizing the notch to extend it by fatigue to produce a sharpened, semielliptical crack front. Flawing the vessel was preceded by prototypic trials of the procedure with weldments incorporating full-scale seams of low-upper-shelf material. The procedures used for flawing are described in detail in Ref. 8.

Two flawing trials were performed, the first with a 600-mm-long by 422-mm-wide by 150-mm-thick weldment prepared by B&W using the procedures and materials already described for the characterization welds. The size of the flaws in the trails was chosen to be identical to the flaw in the vessel in the V-8 test.[1] The machined notch had a surface length of 205.7 mm and a depth of 51.1 mm. The notch was sealed by a gasketed steel block and pressurized at a rate of 30 to 35 cycles per minute from atmospheric pressure to some maximum pressure, p_{max}. In this trial, p_{max} was 105.5 MPa for the first 5,900 cycles and 106.9 to 107.6 MPa for 27,200 cycles for a total of 33,100 cycles.

Ultrasonic monitoring by a transducer aimed at the center of the notch indicated about 5 mm of flaw growth after about 24,000 cycles. About 11 mm growth was apparent after 30,000 cycles. Two other transducers 90 mm from the center indicated no definite growth until near the end of the cycling, when growth of only 2 to 3 mm was apparent. At locations 50 mm from the center, there was 6 mm of growth. After 33,100 cycles the flaw had apparently grown 13 mm.

The plate was cut, chilled, and broken open for direct measurement of the fatigue crack extension. The notch and fracture surfaces are shown in Fig. 2.20. This photograph shows that crack extension at the deepest point was about as had been estimated from ultrasonic measurements (~13 mm), but growth was highly asymmetrical. Because this was an undesirable crack shape for the test vessel, additional trials were planned.

The spare characterization seam weld, V872, was used for the second trial. The machined notch in weld V872 was 203 mm long at the surface by 51 mm deep. Cyclic pressurization was applied for 65,700 cycles at ~32 cycles per minute with an average peak pressure of ~83 MPa. Pressurization had to be terminated because the fatigue crack extended beyond the seal. The indications of flaw growth from ultrasonic observations are compared with direct measurement of the final fatigued crack in Fig. 2.21. The fatigue crack surfaces are shown in Fig. 2.22.

On the basis of preliminary fracture analyses discussed in Chap. 5, dimensions of the machined notch in the vessel and tentative objectives for fatigue crack extension of the notch were selected. Machining and cyclic pressurization of the notch were accomplished by procedures used in the two earlier trials of the flaw preparation procedure. The objective of the procedure was to produce a fatigue-sharpened flaw of approximately semielliptical profile.

The machining operations consisted of first machining a flat on the vessel, centered on the special low-upper-shelf seam weld, as shown in Fig. 2.23. Then a notch of dimensions and shape shown in Fig. 2.24 was

ORNL–PHOTO 7655–81A

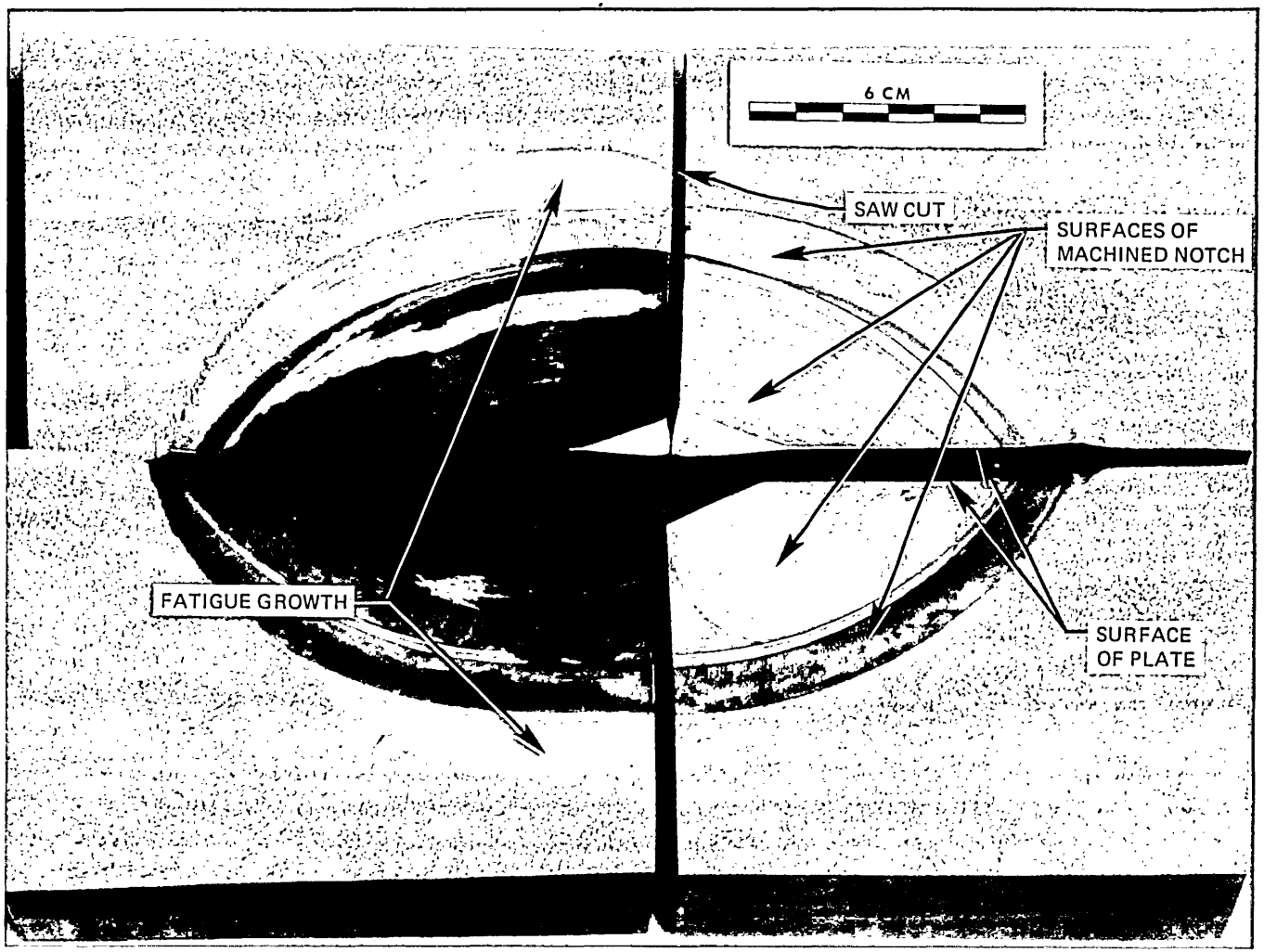

Fig. 2.20. Fatigue crack growth in V-8A flawing practice piece in first trial.

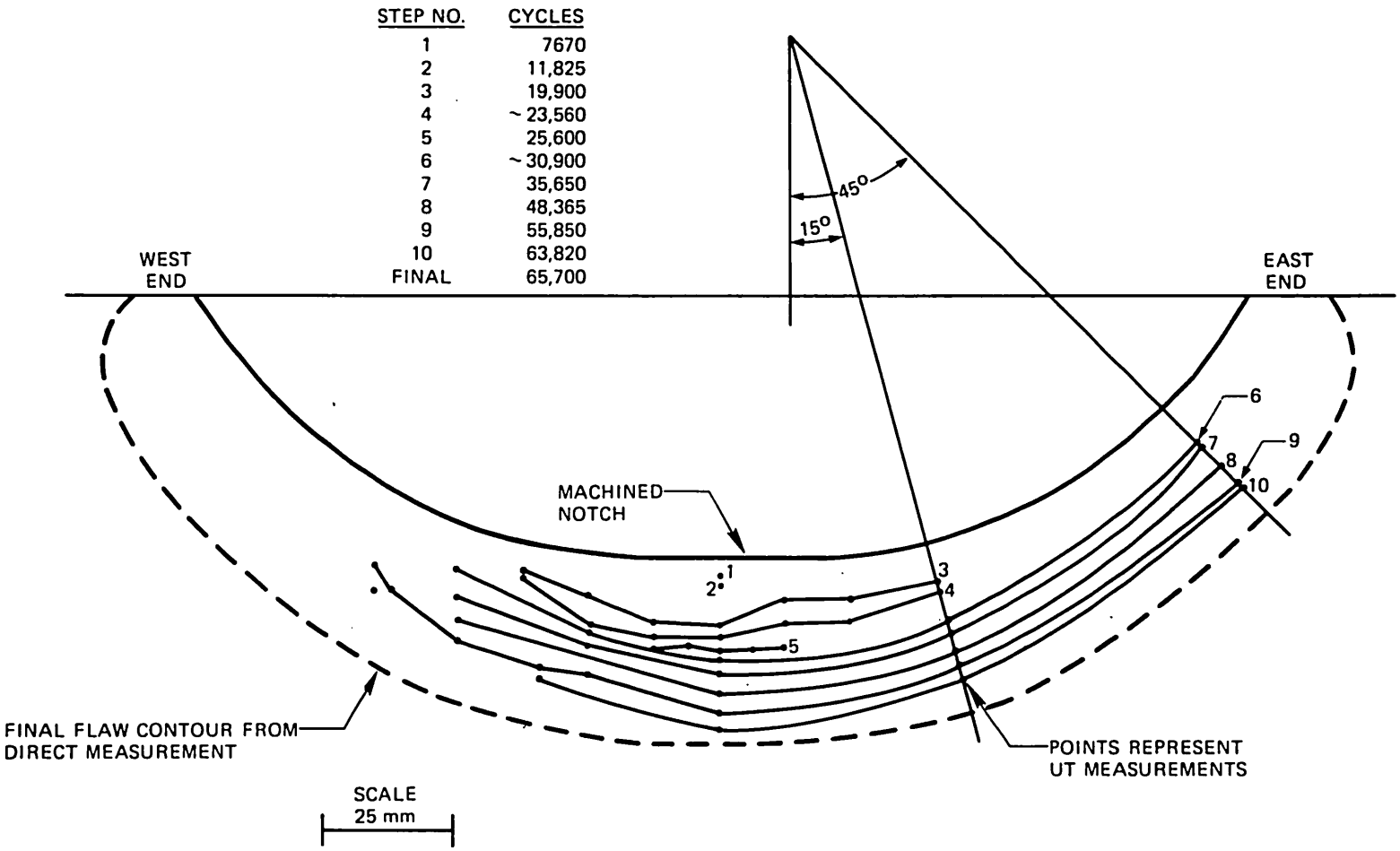

Fig. 2.21. Flaw growth observed ultrasonically for various stages of fatigue cycling in weld V872.

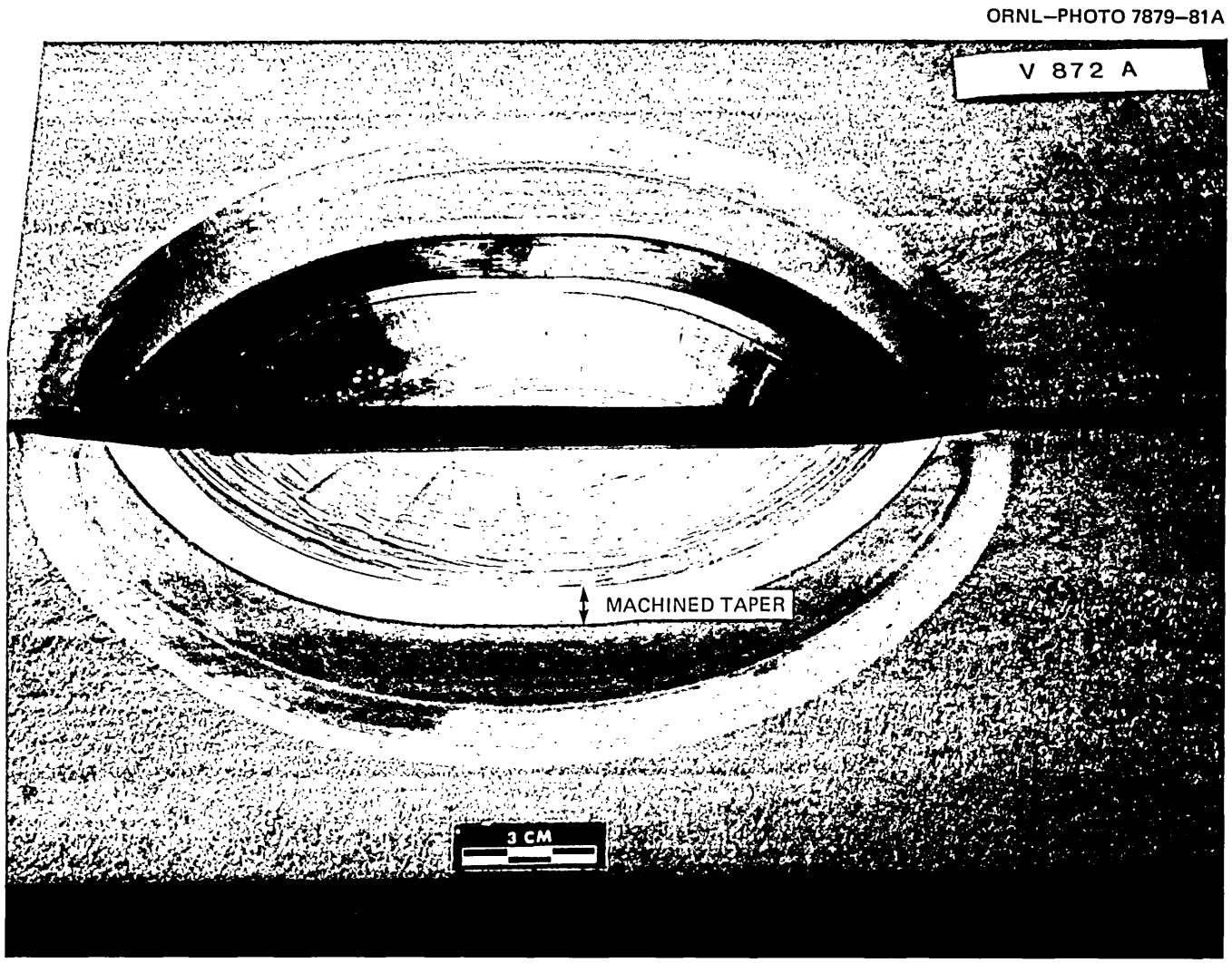

Fig. 2.22. Halves of fatigue-grown flaw in weld V872.

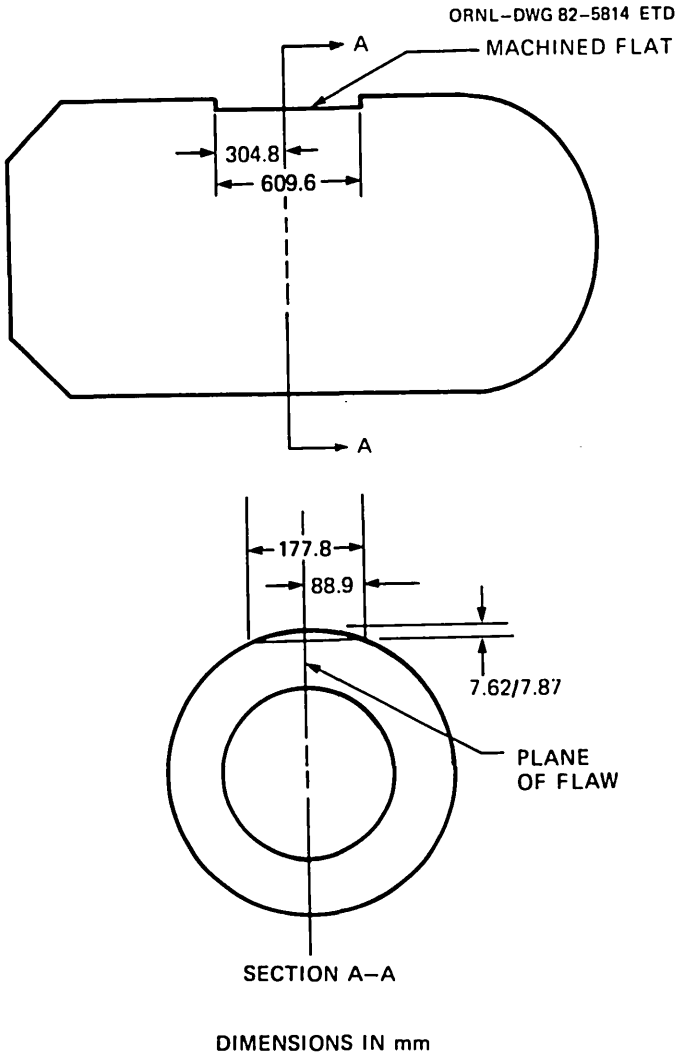

Fig. 2.23. Dimensions of machined flat at flaw site in vessel V-8A.

cut in a radial-axial plane of the vessel in the center of the special seam weld.

The fatigue sharpening of the notch was initiated with the objective of attaining crack growth of 22 mm at the deepest point of the flaw. However, the depth actually accepted was contingent on the profile of the flaw maintaining a reasonable shape. This was a special concern, because in the flawing trials both asymmetrical crack growth and unexpectedly rapid growth had been observed.

The vessel was instrumented with ultrasonic transducers mounted on the inside surface of the vessel in positions, shown in Fig. 2.25, from which measurements of crack growth could be observed. Pressurization apparatus was mounted as shown in Fig. 2.26 so that high pressure could be applied to the machined notch.

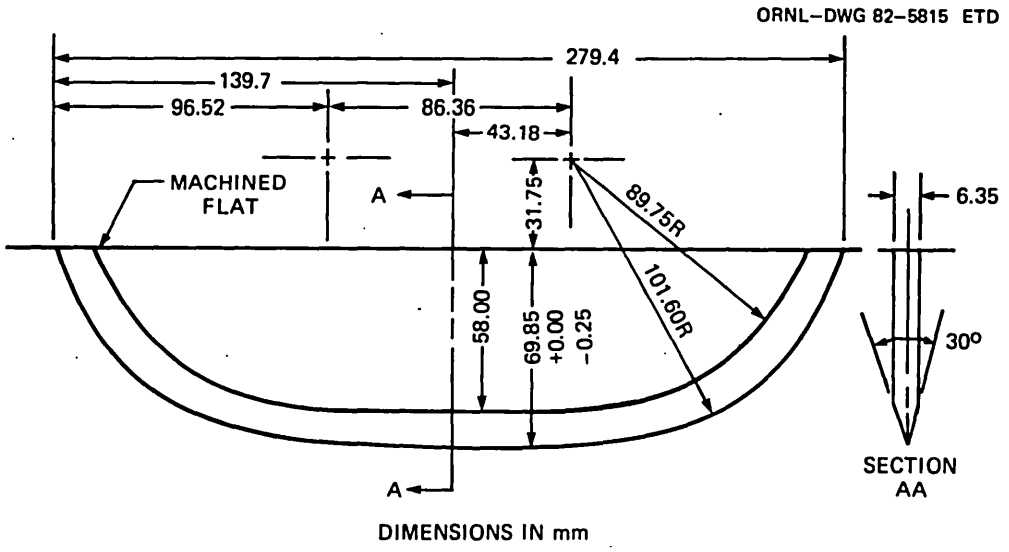

Fig. 2.24. Sectional view of a radial-axial plane of the vessel that shows the configuration of the V-8A machined notch.

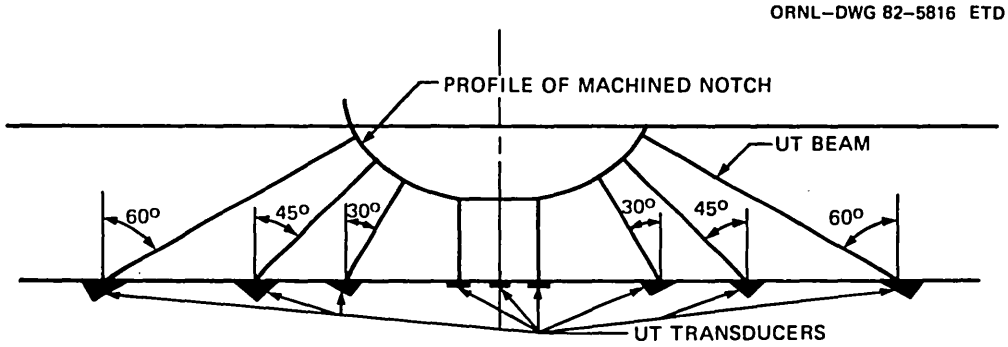

Fig. 2.25. Profile of the V-8A machined notch with locations of ultrasonic transducers used to measure fatigue crack growth.

Pressure was applied cyclically to the notch, and ultrasonic measurements were made continuously. The maximum pressure p_{max} in each cycle was limited to keep K_I well below K_{Ic}. Intermittently, the pressure cycles were changed to produce beach marks on the fatigued fracture surface. The schedule of p_{max} vs number of cycles is given in Fig. 2.27.

The successive observations of crack growth during pressurization are presented in Figs. 2.27 and 2.28. The process was stopped after 105,331 cycles with an indicated crack growth of 21.3 mm at the center of the flaw. This implied a total crack depth of 91.2 mm. Figure 2.29 is a view of the machined notch and a portion of the surrounding machined flat.

ORNL PHOTO 8132-82A

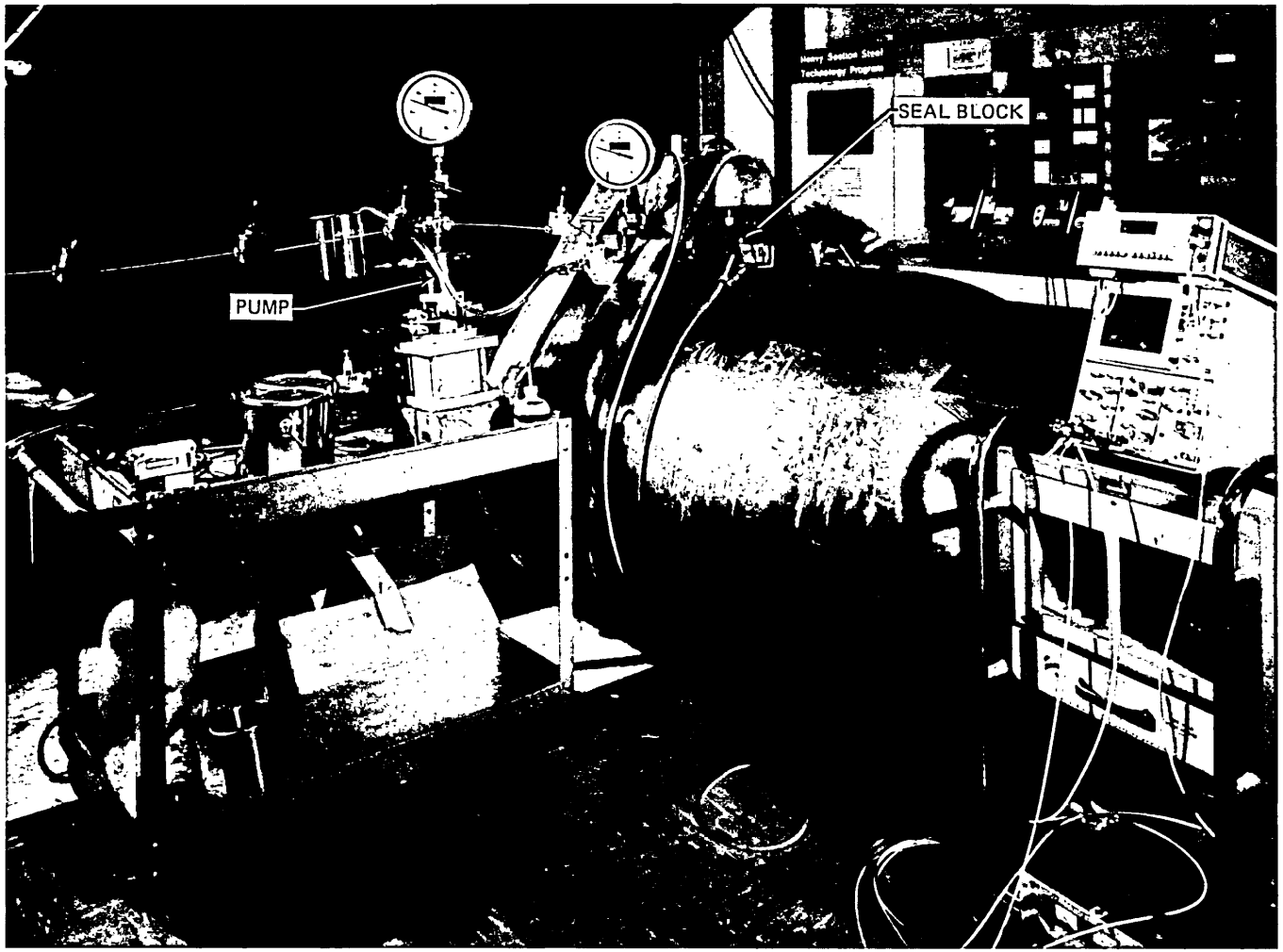

Fig. 2.26. Intermediate test vessel V-8A with apparatus used to cyclically pressurize the machined notch.

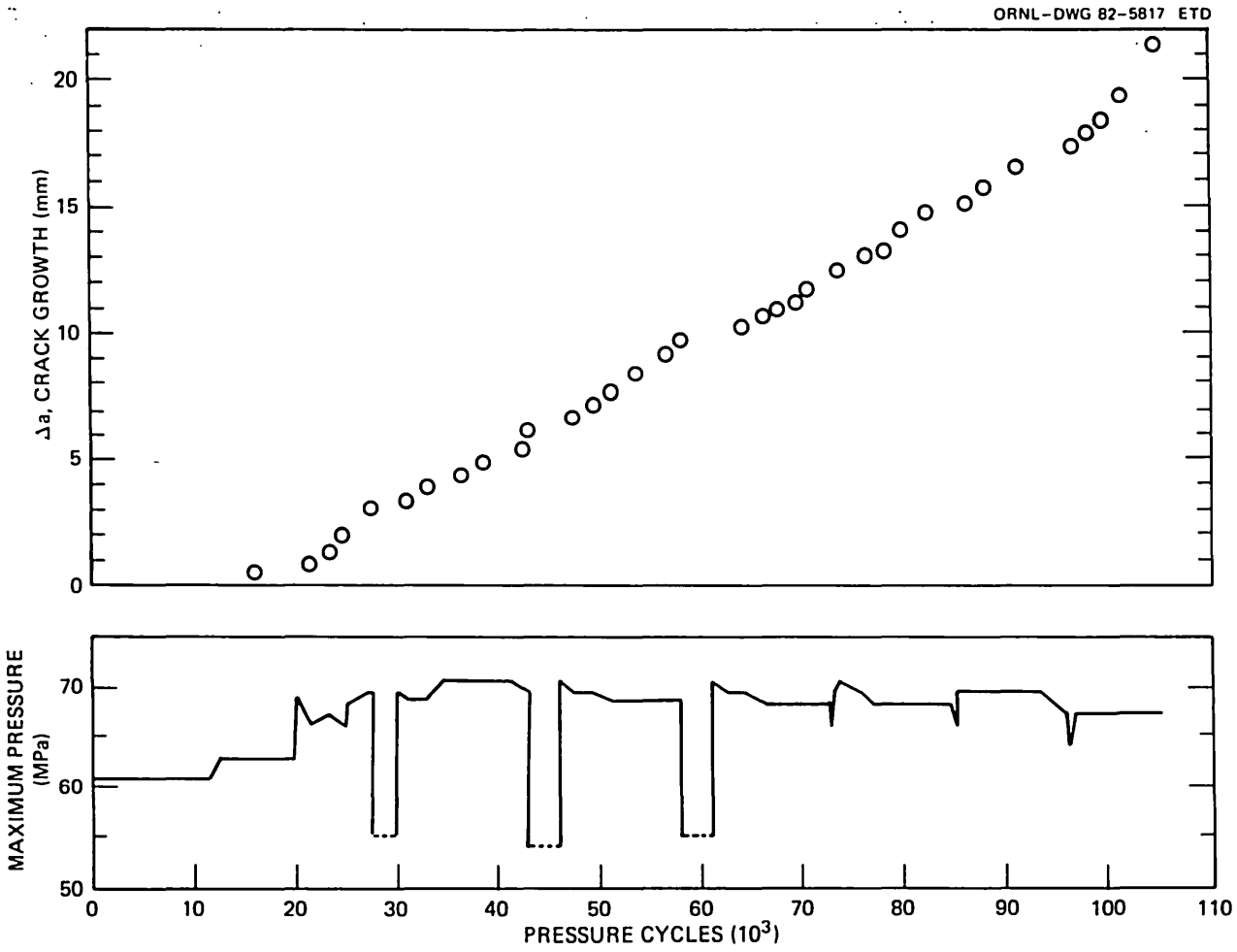

Fig. 2.27. Maximum cyclic pressure p_{max} and crack growth Δa at deepest point of flaw vs number of cycles.

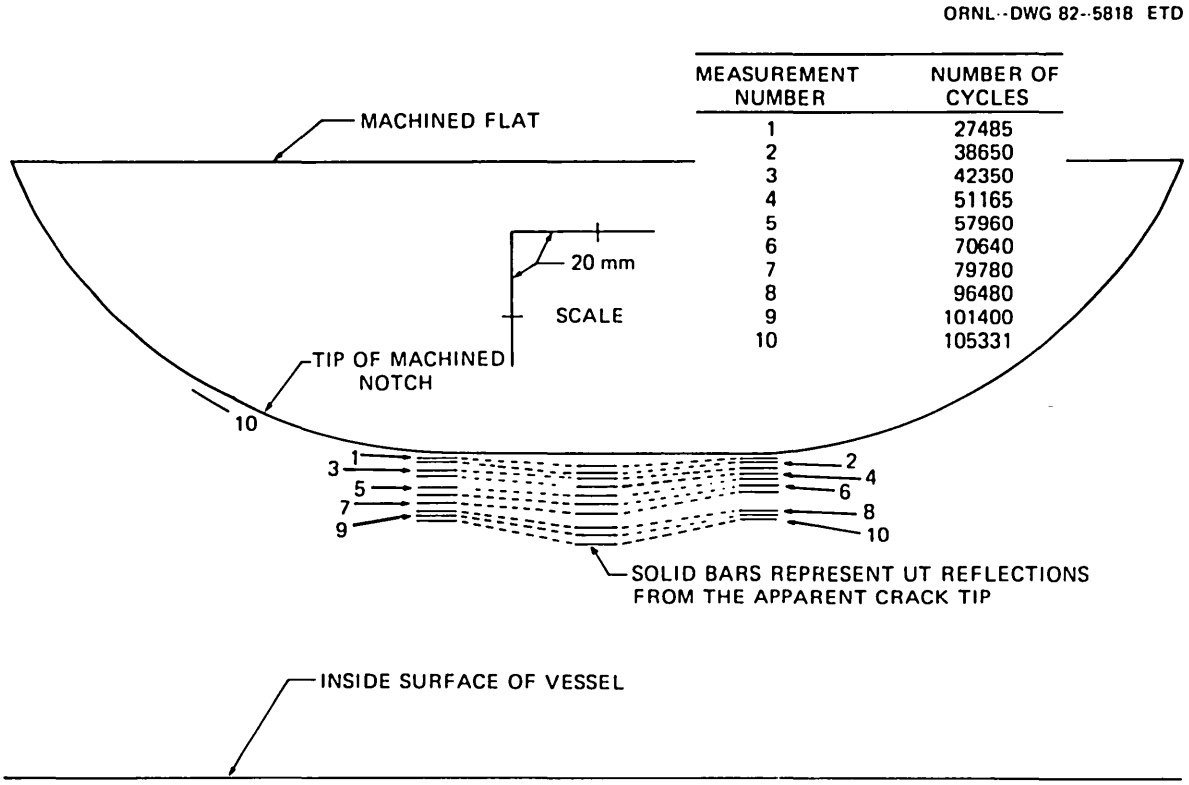

Fig. 2.28. Scale plot of locations of ultrasonic reflections from the crack tip at several stages of crack growth.

ORNL PHOTO 8136–82A

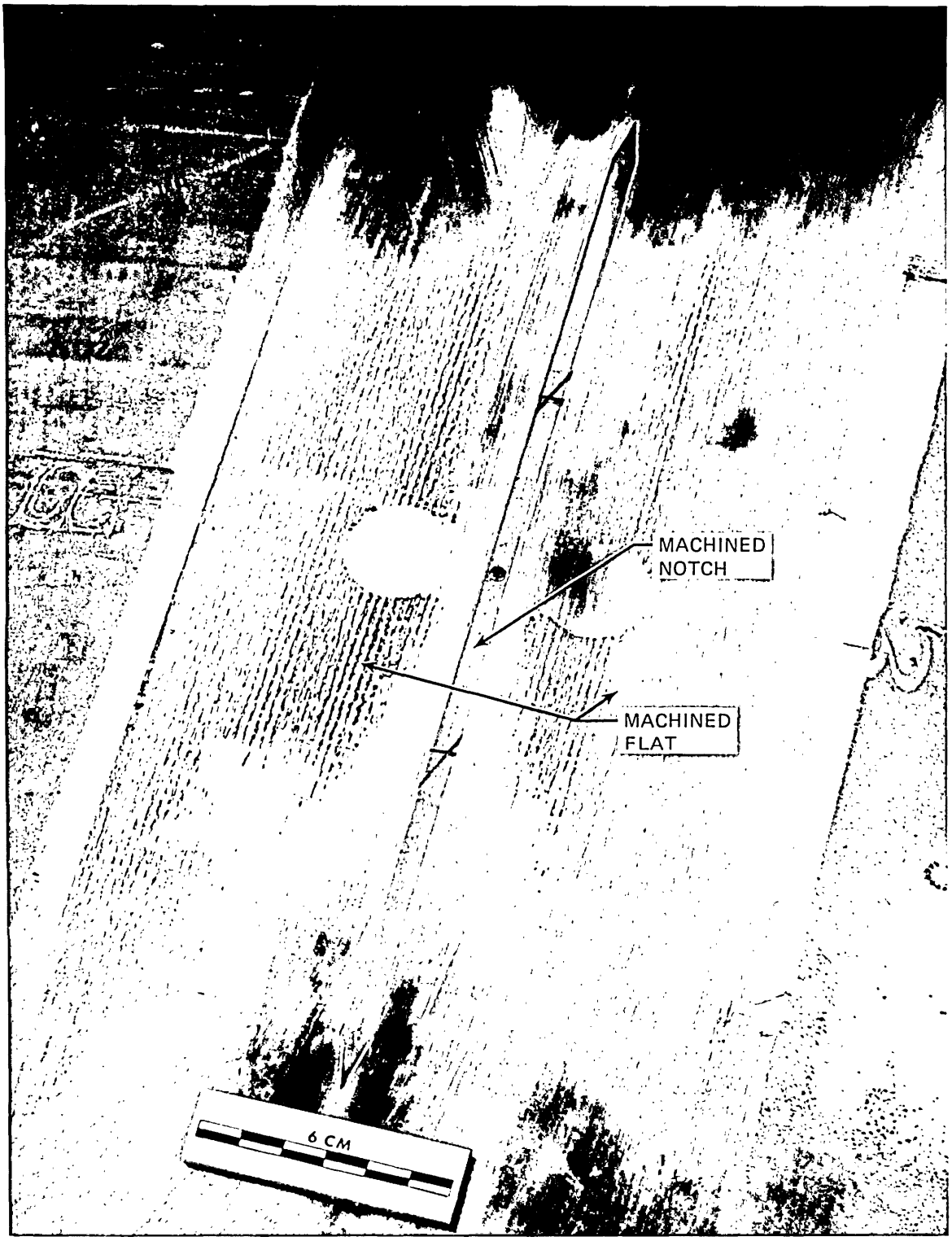

Fig. 2.29. Machined and fatigue-sharpened flaw in vessel V-8A.

References

1. R. H. Bryan et al., *Test of 6-in.-Thick Pressure Vessels. Series 3: Intermediate Test Vessel V-8*, NUREG/CR-0675 (ORNL/NUREG-58), Union Carbide Corp. Nuclear Div., Oak Ridge Natl. Lab., December 1979.

2. C. E. Childress, *Fabrication and Mechanical Test Data for the Four 6-in.-Thick Intermediate Test Vessels Made from Steel Plate for the Heavy-Section Steel Technology Program*, Documentary Report 5, ORNL/TM-5074, Union Carbide Corp. Nuclear Div., Oak Ridge Natl. Lab., January 1976.

3. "Rules for In-Service Inspection of Nuclear Power Plant Components," *ASME Boiler and Pressure Vessel Code, Section XI, Subsubarticle IWB-4420*, 1974 Ed. with Summer and Winter 1975 Addenda, American Society of Mechanical Engineers, New York.

4. H. A. Domian, *Vessel V-8A Repair and Preparation of Low Upper-Shelf Weldment*, ORNL/Sub/81-85813/1, prepared for Oak Ridge Natl. Lab. by the Babcock & Wilcox Company, Alliance, Ohio, June 1982.

5. Lyman Taylor (ed.), *Heat Treatment, Cleaning, and Finishing*, Vol. 2, 8th ed., pp. 670—72, American Society for Metals, Metals Park, Ohio, 1964.

6. H. A. Domian and R. J. Futato, *J-Integral Test Results of HSST-ITV8A Low Upper Shelf Weld — Final Report*, Babcock & Wilcox Company, Research and Development Div., Alliance, Ohio, February 1983.

7. F. J. Loss, "Toughness and Ductile Shelf Properties of Irradiated Low-Shelf Weld Metals," Nuclear Regulatory Commission 8th Water Reactor Safety Research Information Meeting, Gaithersburg, Maryland, October 27—31, 1980.

8. P. P. Holz, *Flaw Preparations for HSST Program Vessel Fracture Mechanics Testing: Mechanical-Cyclic Pumping and Electron-Beam Weld-Hydrogen-Charge Cracking Schemes*, NUREG/CR-1274 (ORNL/NUREG/TM-369), pp. 6—10, Union Carbide Corp. Nuclear Div., Oak Ridge Natl. Lab., May 1980.

3. DEVELOPMENT OF SPECIAL FEATURES

To conduct the V-8A test with the flawed material in a ductile state required that the test vessel be maintained at about 150°C, a temperature higher than that of any previous intermediate vessel test. This temperature exceeded that on which the safety evaluation of the test facility was based. Consequently, new high-pressure seals had to be developed and tested; ultrasonic transducers capable of withstanding the high-temperature and -pressure environment had to be developed, manufactured, and tested; and ballast to reduce the quantity of fluid in the test vessel had to be designed and fabricated.

3.1 High-Pressure Seals

Two types of seals are necessary for the intermediate test vessels: a large-diameter seal (or seals) between the closure head and the closure flange of the vessel and a 17-mm-diam seal between the head and the instrumentation penetration fitting (Fig. 3.1). In all earlier vessel tests, O-ring seals of Viton were used and performed satisfactorily, because temperatures did not exceed 100°C. At the 150°C temperature of the V-8A test, the reliability of Viton was questionable; at the ~300°C temperatures planned for the pressurized-thermal-shock test series,[1] a new seal arrangement was definitely necessary.

Among the early development activities of the Heavy-Section Steel Technology (HSST) Program was the development and validation of procedures for installing strain gages, thermocouples, and transducers in the interior of the test vessel and the routing of the instrument leads for these sensors through the pressure boundary to a data acquisition system. Crucial to these procedures was the validation testing of lead-through seal assemblies (Fig. 3.2), procured from Autoclave Engineers, that accommodated the penetration of instrumentation leads through the pressure boundary. The vendor rated the fitting for operation at 206 MPa and 204°C and hydrostatically tested each fitting at 310 MPa and room temperature. Oak Ridge National Laboratory subsequently performed validation tests at 276 MPa and 93°C on selected assemblies. Each fitting permits the passage of six 1.70-mm-diam stainless-steel-sheathed, magnesium oxide insulated, three-wire cable assemblies. The closure covers of the intermediate test vessels are machined to receive ten Autoclave lead-through seal assemblies (see Fig. 3.1); therefore, provisions have been made for the passage of 60 individual cables from the interior of the vessels. Except for failures experienced on the first intermediate vessel test, the reuse of refurbished fittings on subsequent intermediate vessel tests has been eminently successful.

While preparations were being made for the V-8A test, work was also undertaken to develop seals that would be reliable in pressurized-thermal-shock tests. In the existing lead-through seal assemblies, components that were suspected to be unreliable at the anticipated higher test temperatures were Viton O-rings, nylon packing, and phenolic backups to the packing (shown in Fig. 3.2).

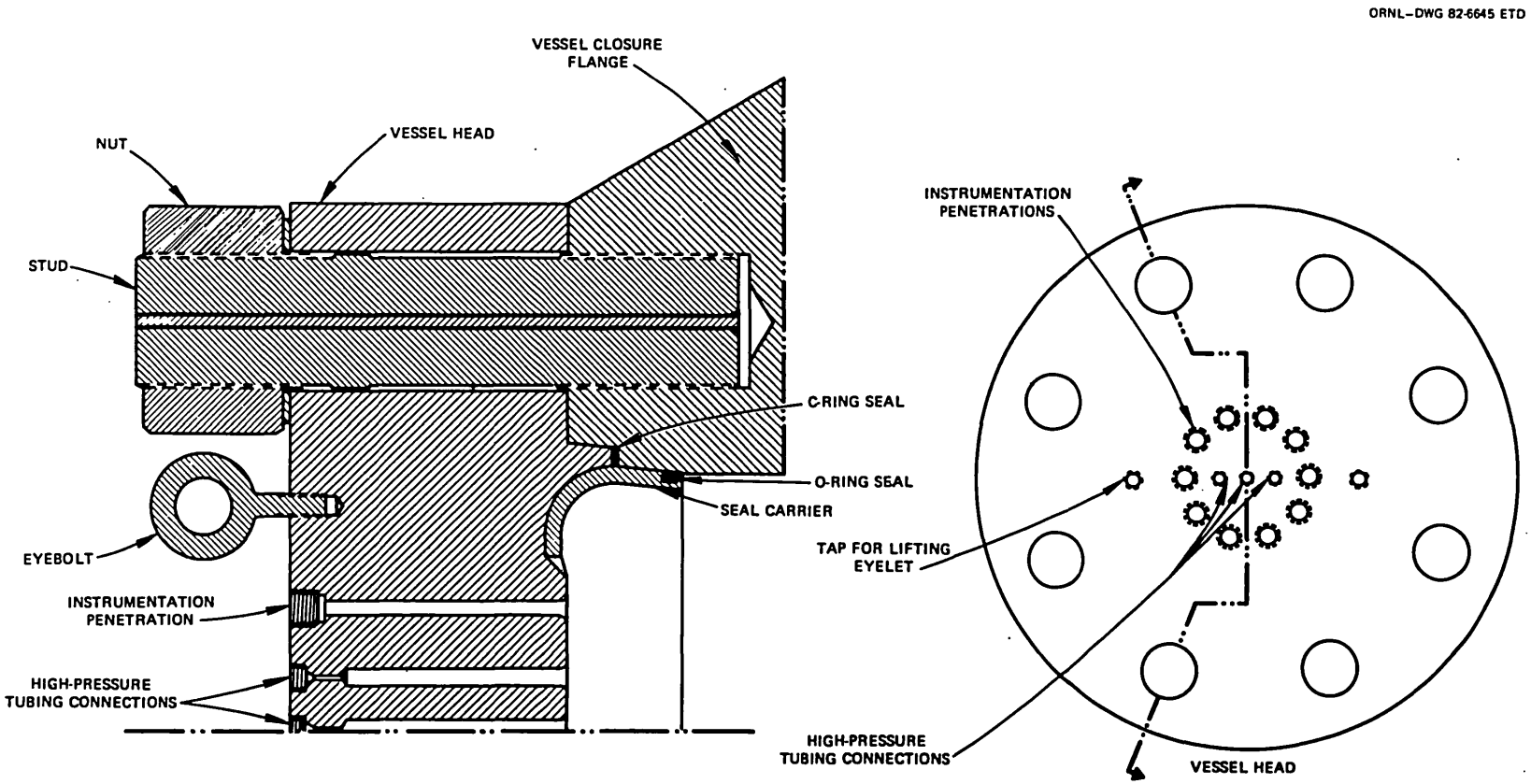

Fig. 3.1. Intermediate test vessel head and access opening assembly showing locations of seals for closure and instrumentation penetrations.

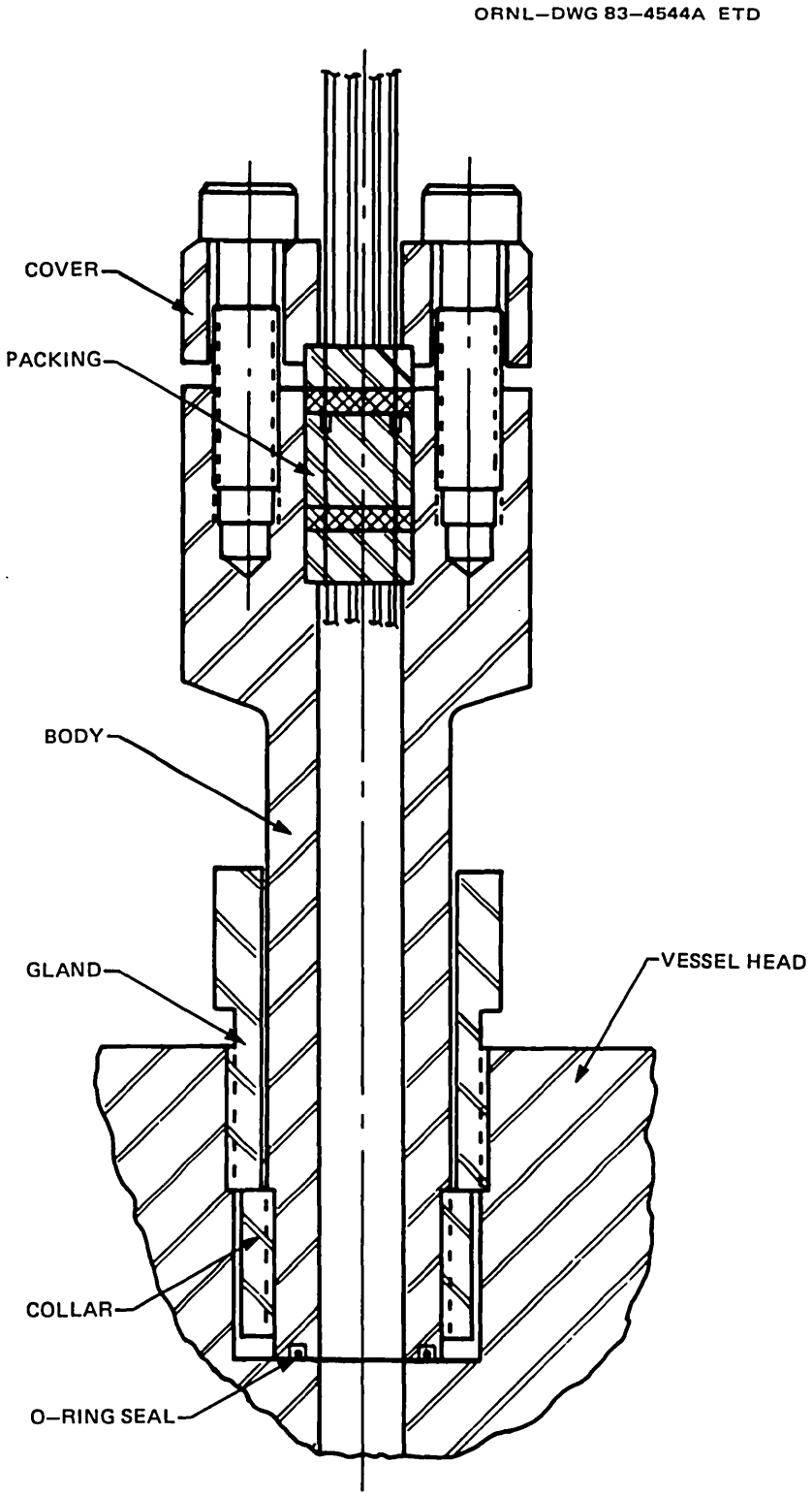

Fig. 3.2. Cross section of unmodified instrument lead penetration assembly.

To overcome these apparent deficiencies, the packing was redesigned to use "lava" as shown in Fig. 3.3; the O-ring (Fig. 3.2) was changed from Viton to Kalrez, an elastomer recently developed by DuPont for operation at temperatures up to 315°C. The redesign was then subjected to a validation test consisting of a pressure test to 207 MPa at room temperature followed by heating to and holding at 290°C, while cycling between 14 and 140 MPa.

The redesigned fittings failed the validation test. After passing the pressure test at room temperature, the O-ring failed repeatedly at pressures varying from 76 to 86 MPa at 290°C as shown in Fig. 3.4. No leakage through the packing was evident. The unusually low failure pressure of the O-ring raised doubt as to the suitability of the fittings for operation at 150°C, the projected temperature of operation for the V-8A test.

A series of tests at 150°C was conducted on the fitting, with both Viton and Kalrez O-rings and a packing designed and manufactured by Autoclave. The cyclic peak pressure was varied in each test with cyclic pressurization continuing until the O-ring failed. In no test did the packing fail. The results are summarized in Fig. 3.4.

The number of cycles to failure corresponding to V-8A test conditions was ~40, indicating that the fitting as designed was unsatisfactory for both the V-8A test and the pressurized-thermal-shock test series. Evidently, the deformation of the fitting with pressure loading produces too great a gap for either a Vitron or Kalrez O-ring to bridge, when temperatures exceed ~90°C. Both Viton and Kalrez compositions experience considerable compression set and loss of strength at temperatures from 150 to 300°C, and the O-rings without backup are unsatisfactory.

Graphite-filled Teflon seals with a "C" cross section and a metal-spring core were selected as a replacement for both the large and small O-rings, and prototypes of the smaller seal were tested successfully in an autoclave vessel at temperatures up to 290°C. Both types of Teflon seals were manufactured by Bal Seal Engineering Company.

A seal test fixture (Fig. 3.5), consisting of a vessel head and a mockup of the mating part of the vessel closure flange, was fabricated for proof testing a full set of seals in the actual test-vessel geometry. This set includes one large seal and ten of the small instrumentation-penetration seals. In this fixture, both the large Viton O-ring of the original design and the large Bal Seal (shown in Fig. 3.1) were tested successfully for V-8A conditions, namely, at least 100 pressure cycles to 200 MPa at 150°C.

The small seals were persistently unreliable in performance; some seals leaked sporadically and, during or after installation, shifted from their proper position. The design of the penetration assembly was modified and tested again. It turned out that the position of the seal on its seating surface in the head was critical to proper function, and a device to prevent the expulsion of the metal spring from the C-ring was necessary.

The instrumentation penetration assemblies were modified by the addition of retaining sleeves and shim sleeves as shown in Fig. 3.6. A full set of assemblies, including the retaining sleeves but without shim

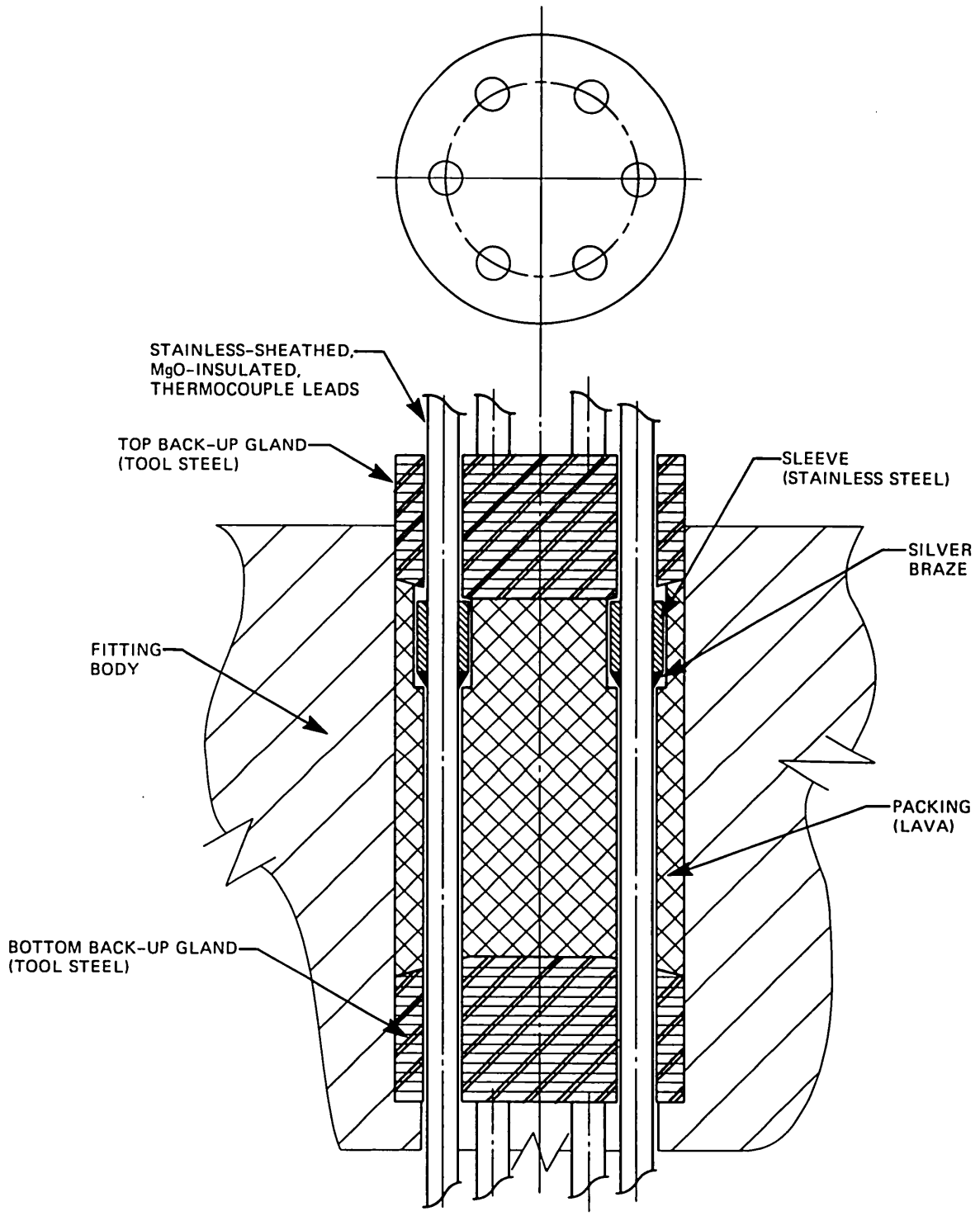

Fig. 3.3. Packing concept for instrument lead penetration.

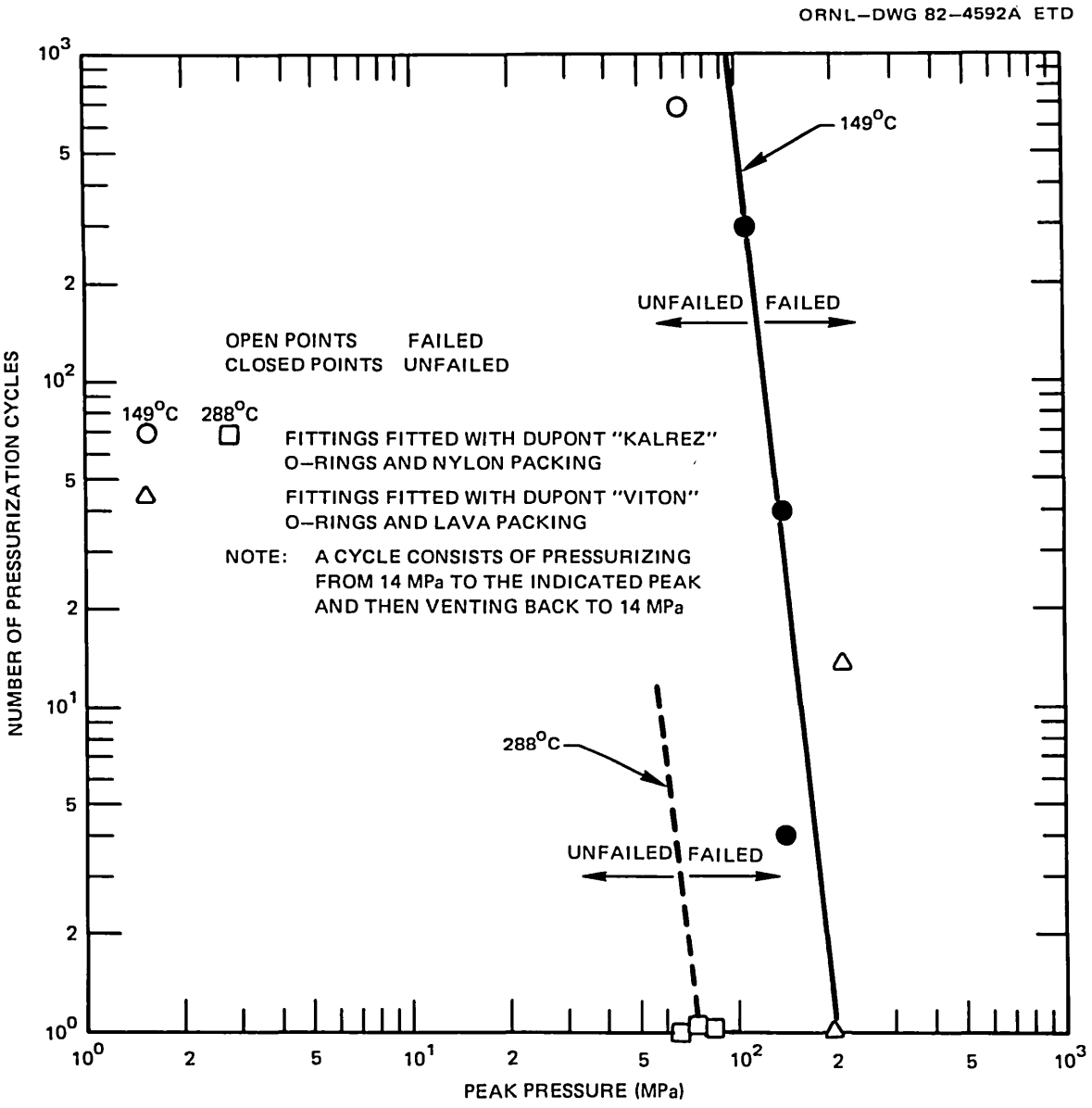

Fig. 3.4. Cyclic pressure failure test of O-rings in Autoclave instrument lead-through fittings. Unfailed-failed line for 288°C data is assumed to be parallel to the 149°C line.

sleeves, was tested in the seal test fixture at ~150°C by cyclic pressurization between ~50 and 200 MPa. The set of seals endured 25 cycles at 105°C and 87 cycles at 150°C without irreversible failure. There were a few instances of leakage with subsequent sealing. Inspection of the assemblies after the test showed that the gap between the retaining sleeve and the bore of the hole through the vessel head was excessive in some locations. This resulted in a part of the seal being extruded inward, probably during heatup.

K–25 PHOTO 82–0636A

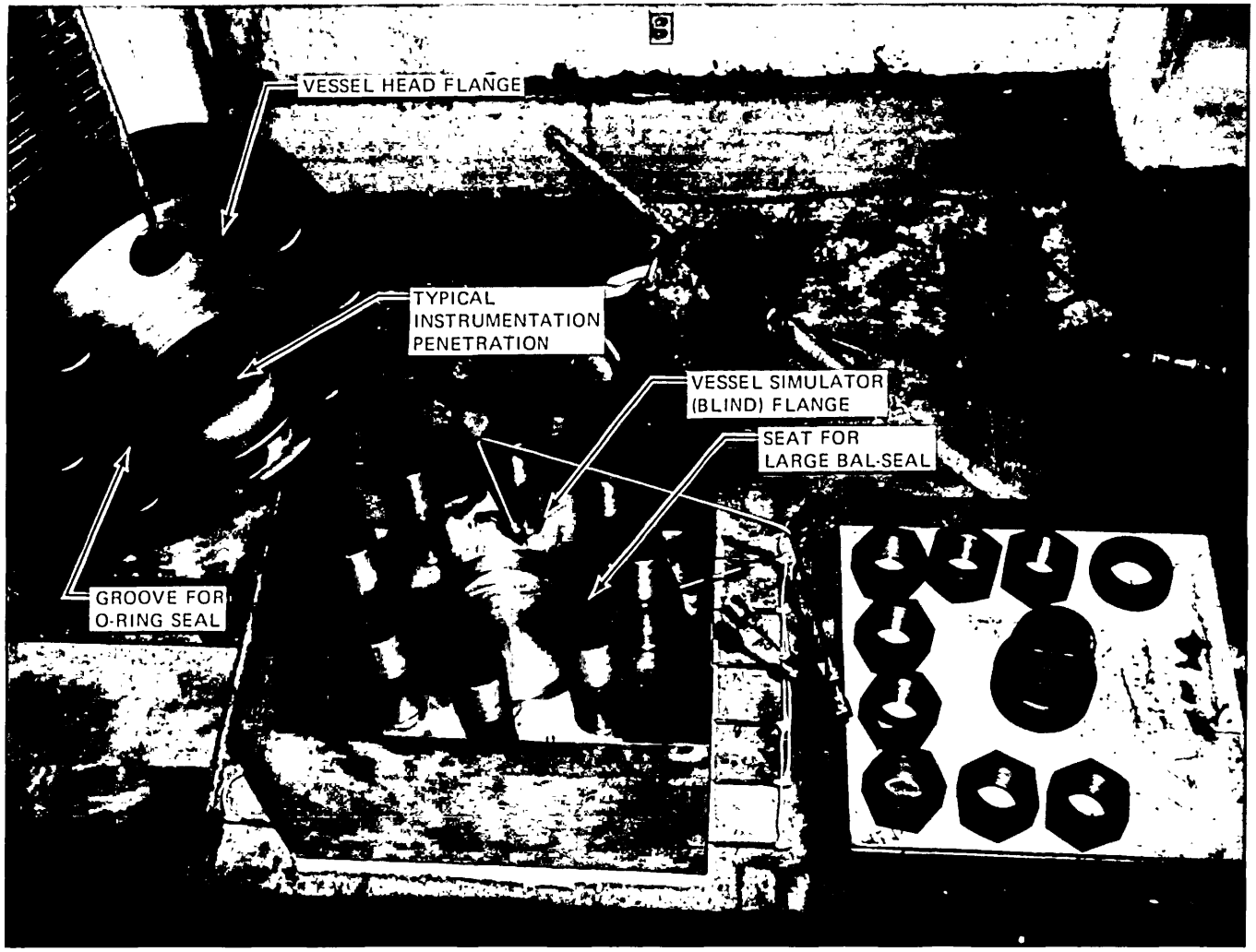

Fig. 3.5. Seal test fixture.

ORNL DWG 82-6646 ETD

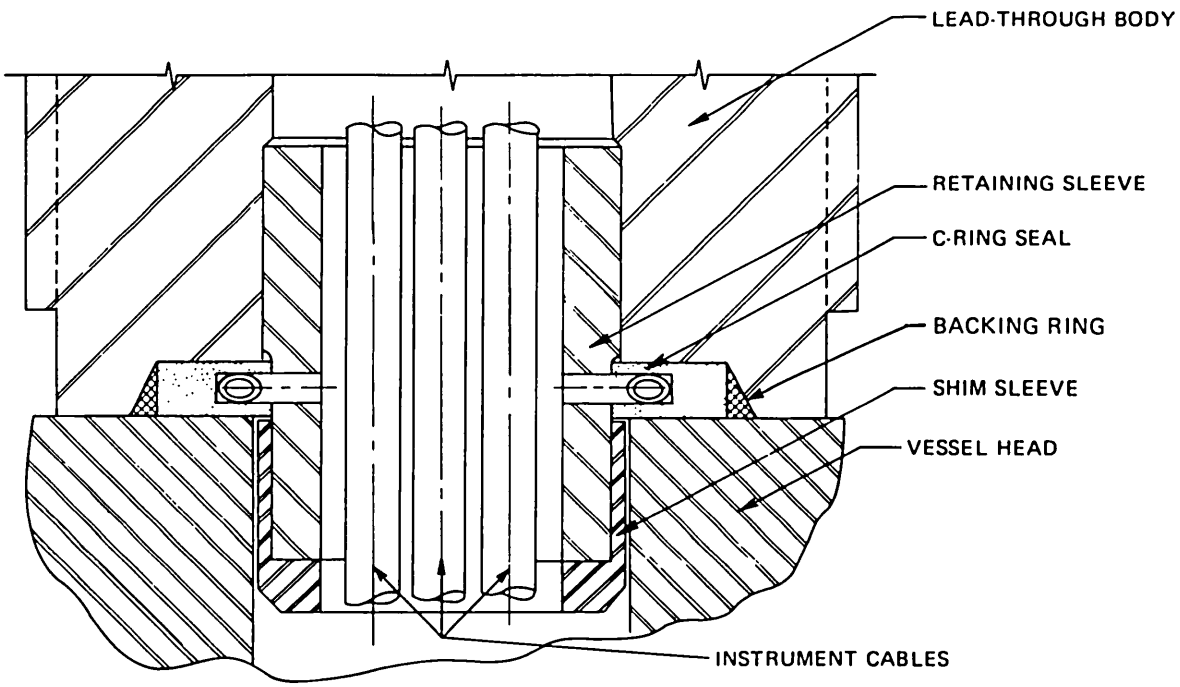

Fig. 3.6. Details of C-ring seal assembly for instrument penetration.

Before installation of the assemblies in the head of vessel V-8A, the diameter and concentricity of each hole relative to the penetration assembly were gaged. Shim sleeves were machined to dimensions that would reduce the gap to 0.1 to 0.2 mm. The V-8A closure included both a large Viton seal and a large Bal Seal, although either one alone would have been satisfactory.

3.2 High-Temperature Ultrasonic Transducers

The ultrasonic transducers for V-8A were designed and manufactured by Search Units Systems, Inc. (SUSI), especially for prolonged use at 150°C. The performance of each transducer was demonstrated at 150°C and atmospheric pressure by the manufacturer. Tests under pressure in a mixture of ethylene glycol and water were conducted at Oak Ridge National Laboratory (ORNL). The transducers experienced a number of problems. Waterproofing a cable connection that could withstand high pressure was difficult, and this problem temporarily obscured the fact that the transducer assembly itself was damaged during pressurization. Incorporation of an integral sheathed cable obviated the waterproofing problem, and design changes were made by SUSI to enhance the integrity of the bonding between the piezoelectric transducer and the wear face on one side and the damping medium on the other.

Transducer assemblies of modified design also failed the pressurized proof tests. Through consultation with SUSI, a structural modification to the assembly was developed and proved to be satisfactory in proof tests of prototypes. Subsequently, a complete set of transducers was tested under cyclic pressurization to 200 MPa at 150°C. As shown in Fig. 3.7, each transducer was held in place in the V-8A test vessel by a bracket that maintained proper contact force between the transducer and the vessel. All modified transducers responded satisfactorily during the proof tests and survived the V-8A test.

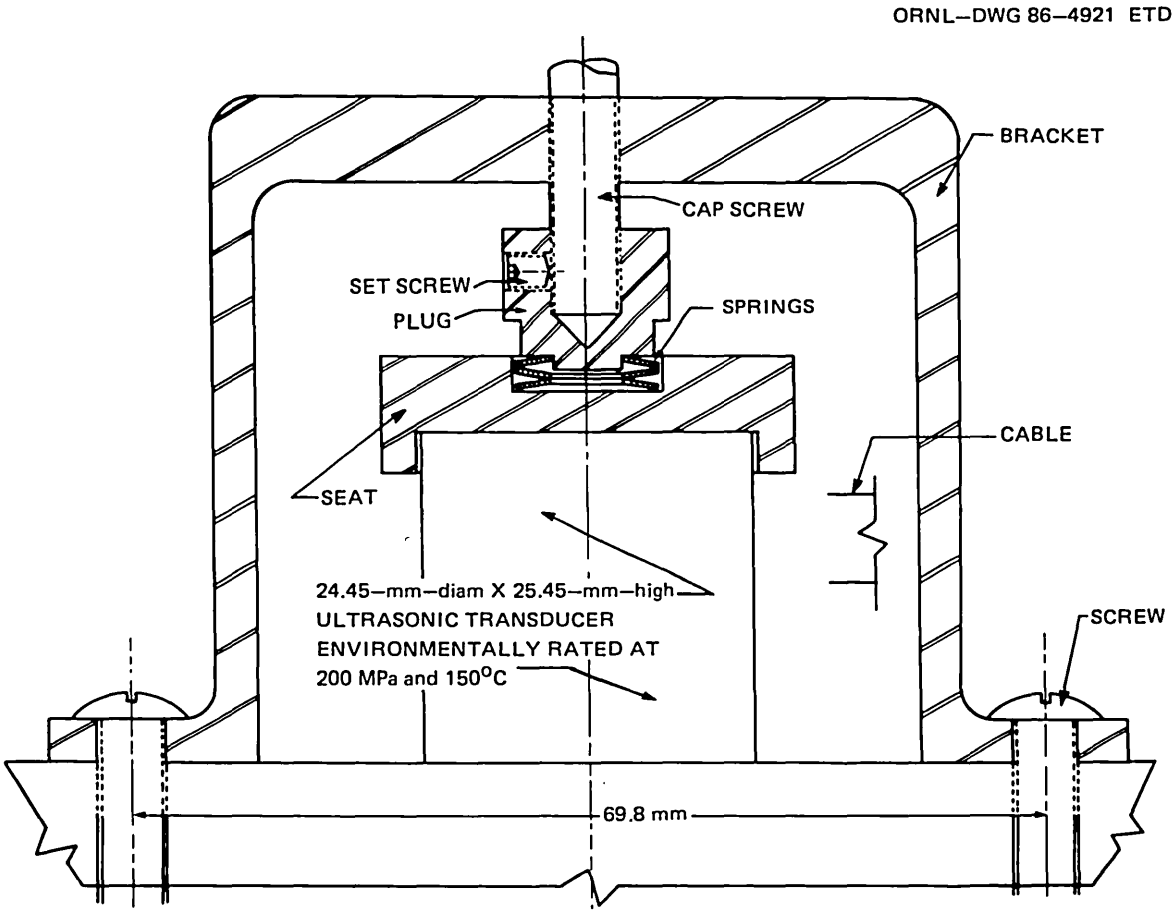

Fig. 3.7. Assembly for holding ultrasonic transducer in vessel V-8A.

3.3 Ballast

In the initial design and development of the equipment and facilities to test intermediate test vessels, C. L. Segaser assessed the potential hazards.[2] This assessment concluded that the test cell could withstand the impact of a missile with an energy as high as 7.81×10^6 J

without penetration of the thinnest (weakest) reinforced concrete wall section.

From test plans of vessel V-8A and pressurized-thermal-shock vessels, it was evident that the former safety criteria, although quite conservative for the ten tests already performed in the cell, would be inadequate because of the strong effect of the elevated temperature of these tests on the contained energy of the pressurizing medium.

To compensate for the increased heat energy content for test V-8A and the prospective tests, ballast in the form of graphite segments was designed and fabricated to fill the test vessels, leaving a calculated void volume of 10.4%. Estimates of the compressibility of the pressurizing fluid as a function of temperature were determined by using the energy-volume coefficients derived by Gibson and Loeffler[3] and by using the *American Society of Mechanical Engineers (ASME) Steam Tables*.[4] Figures 3.8 and 3.9 show the pressure-specific-volume curves for water and ethylene glycol, respectively, for temperatures of 25, 148.9, and 287.8°C. The curves at 148.9 and 287.8°C for water in Fig. 3.8 were extrapolated from ASME Steam Table data by curve fitting as shown.

Figure 3.10 was developed by integrating the area under the curves of Figs. 3.8 and 3.9 with the pressurization fluid considered to consist of a mixture of equal weights of ethylene glycol and water. Estimates of the heat energy available were made by determining the internal energy change for an isentropic process for a liquid on the saturation curves, corresponding to temperatures of 148.9°C for V-8A and 287.8°C for pressurized-thermal-shock tests, expanding down to atmospheric pressure. The ethylene glycol and water were assumed to act independently. Thermodynamic properties for ethylene glycol were premised on the data collection of Curme et al.[5] An efficiency of 50% was considered to be representative of good reciprocating steam engine design[6] and to be a conservative upper bound for missile propulsion, because the fluid following vessel rupture is unconfined.

The total energy potentially available for missile propulsion was considered to be the summation of pressurization energy, heat energy, and strain energy. Segaser's calculation[2] of strain energy as a function of pressure was used without revision. Figure 3.11 shows the summation of energy as a function of test pressure for the V-8A test. The total available energy is far below the value of 7.81×10^6 J calculated by Segaser[2] and validated by the Union Carbide Corporation—Nuclear Division safety committees. Figure 3.12 shows the total energy available at 287.8°C for pressurized-thermal-shock tests. Again the total available energy for all test pressures is considerably less than the approved value of 7.81×10^6 J.

The analysis of test cell designs for missiles with energies up to 7.81×10^6 J, as performed by Segaser[2] and approved by the safety committees, incorporated a conservatism not currently required in safety assessments.[7] Namely, no partitioning of energy was originally assumed to occur; although violating dynamics principles, all available energy was assumed to propel a single missile. Current Nuclear Division safety standards provided rational rules for the partitioning of energy to vessel fragments following a vessel rupture. It was concluded that the combination of the various conservatisms provided an ample safety margin for missile resistance of the test cells as employed for the V-8A test and other tests.

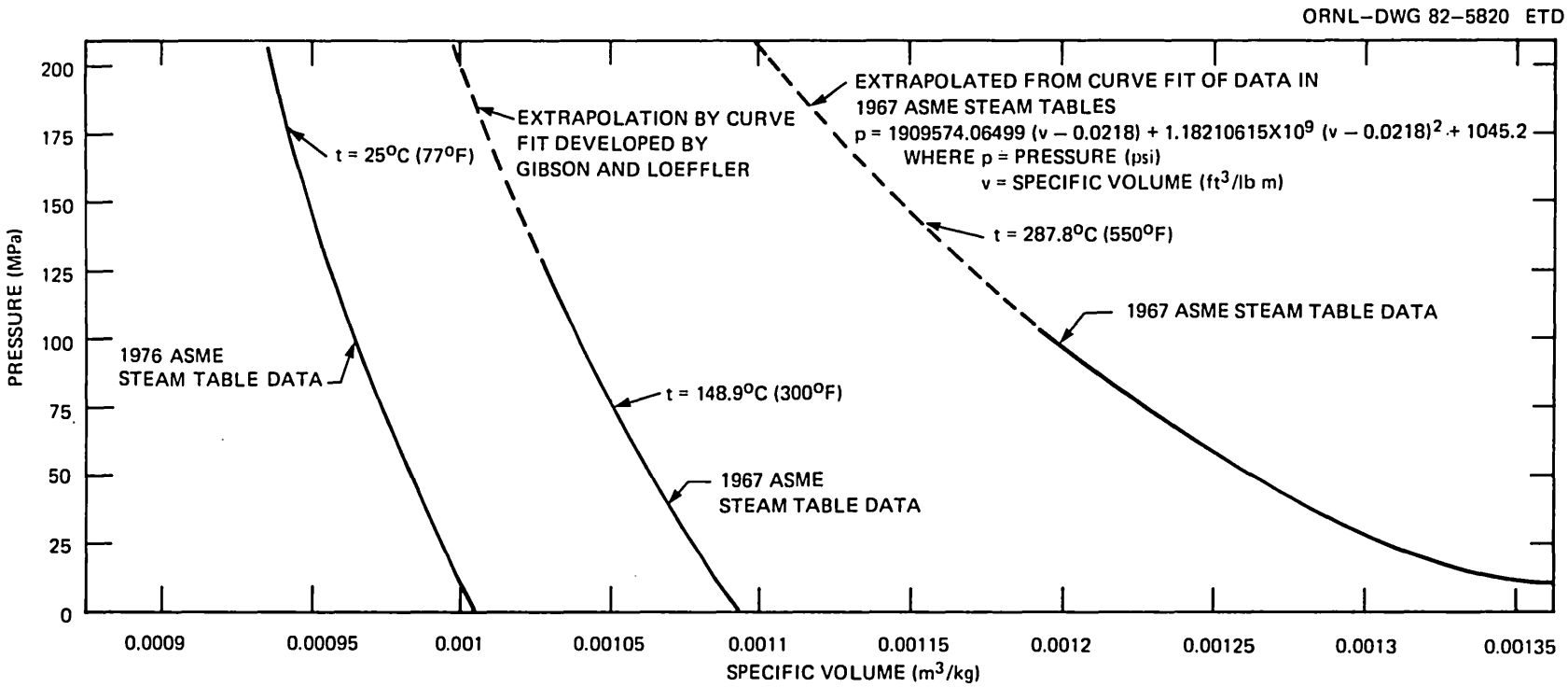

Fig. 3.8. Pressure vs specific volume for water.

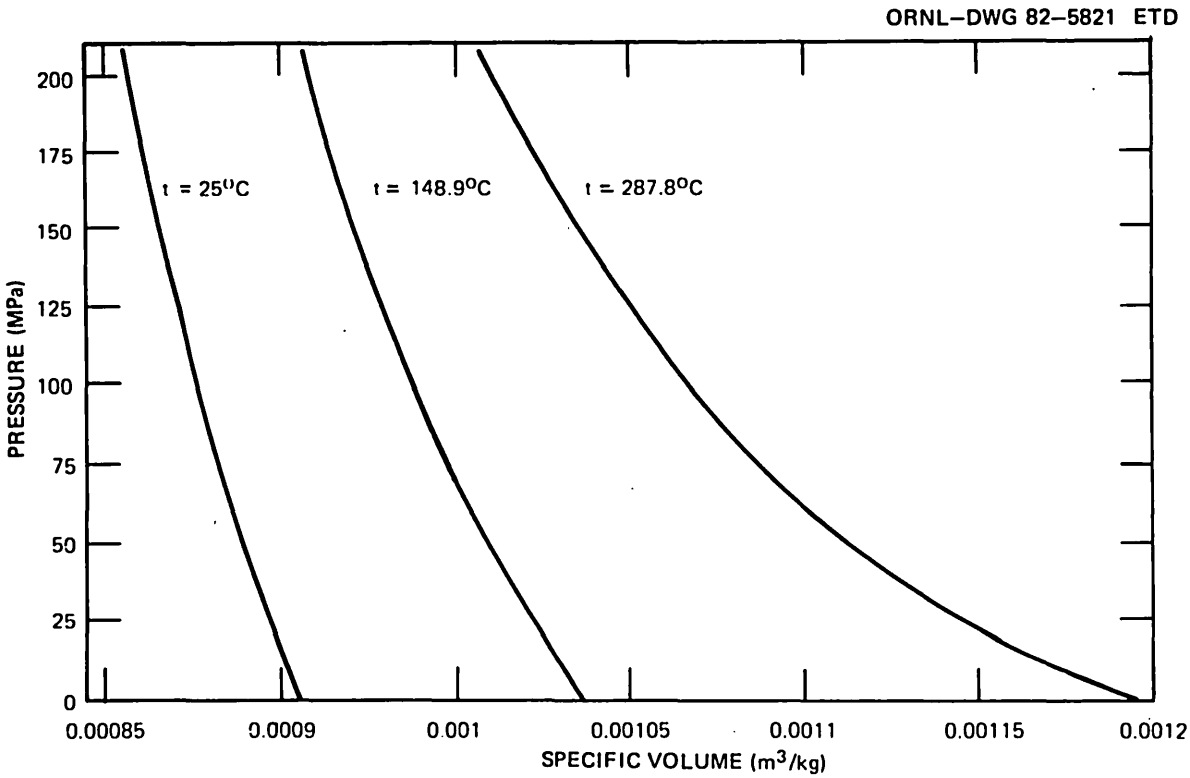

Fig. 3.9. Pressure vs specific volume for ethylene glycol.

Because of the elevated temperatures of the V-8A and other prospective tests, vessel failure will be accompanied by a considerable release of vapor with consequent pressure loading of the cells. The amount of vapor has been estimated by assuming an isenthalpic expansion of the 50% by weight mixture of ethylene glycol and water down to cell pressure. The fluids were considered to expand independently; thermodynamic properties for ethylene glycol were taken from Curme[5] and for water from the *ASME Steam Tables*.[4] The vapor released was assumed to fill the cell, and the total pressure was estimated by Dalton's law to be the sum of the partial pressures. Although considerable leak paths exist around personnel and chase entries, the cells were assumed to be leaktight for conservatism. Under these assumptions, the failure of the V-8A test vessel in the Heavy-Section Steel Technology cell results in a calculated wall loading of 13.23 kPa. Similarly, failure of a vessel in the pressurized-thermal-shock series in the prestressed-concrete reactor-vessel cell results in calculated wall loading of 46.9 kPa. The weakest section of the concrete walls of both the cells was analyzed by yield line theory.[8] The minimum load to failure was estimated to be 193.1 kPa. The cells therefore have a margin of safety for pressure loading exceeding a factor of 4.

The graphite ballast used in the V-8A vessel was divided into segments of a practical size for manual installation. A plexiglass scale model of the vessel and graphite (Fig. 3.13) was made to assist in the design of fixtures for keeping the segments aligned during assembly of the ballast and movement of the vessel.

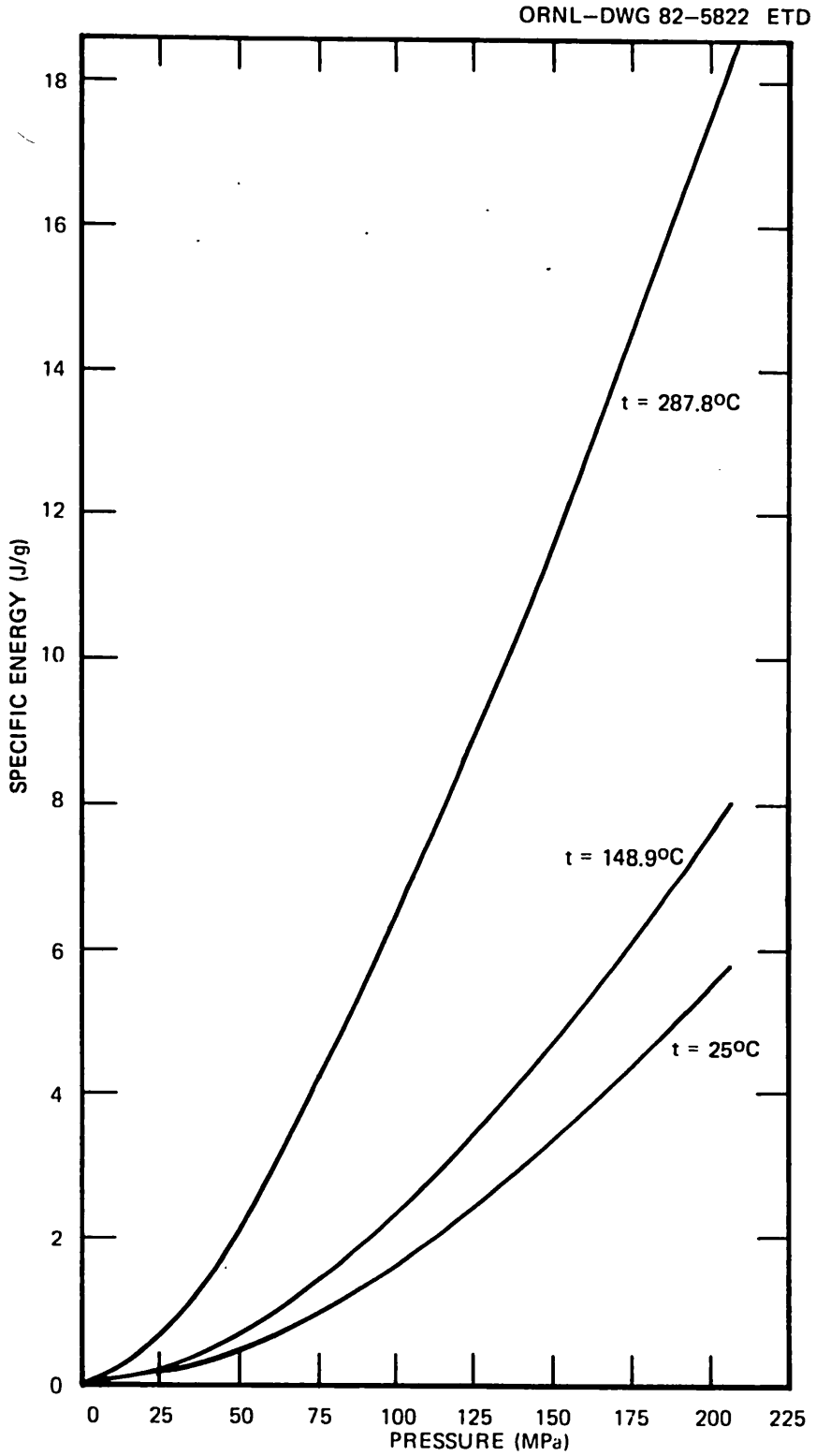

Fig. 3.10. Energy to compress 50% by weight ethylene glycol-water mixture.

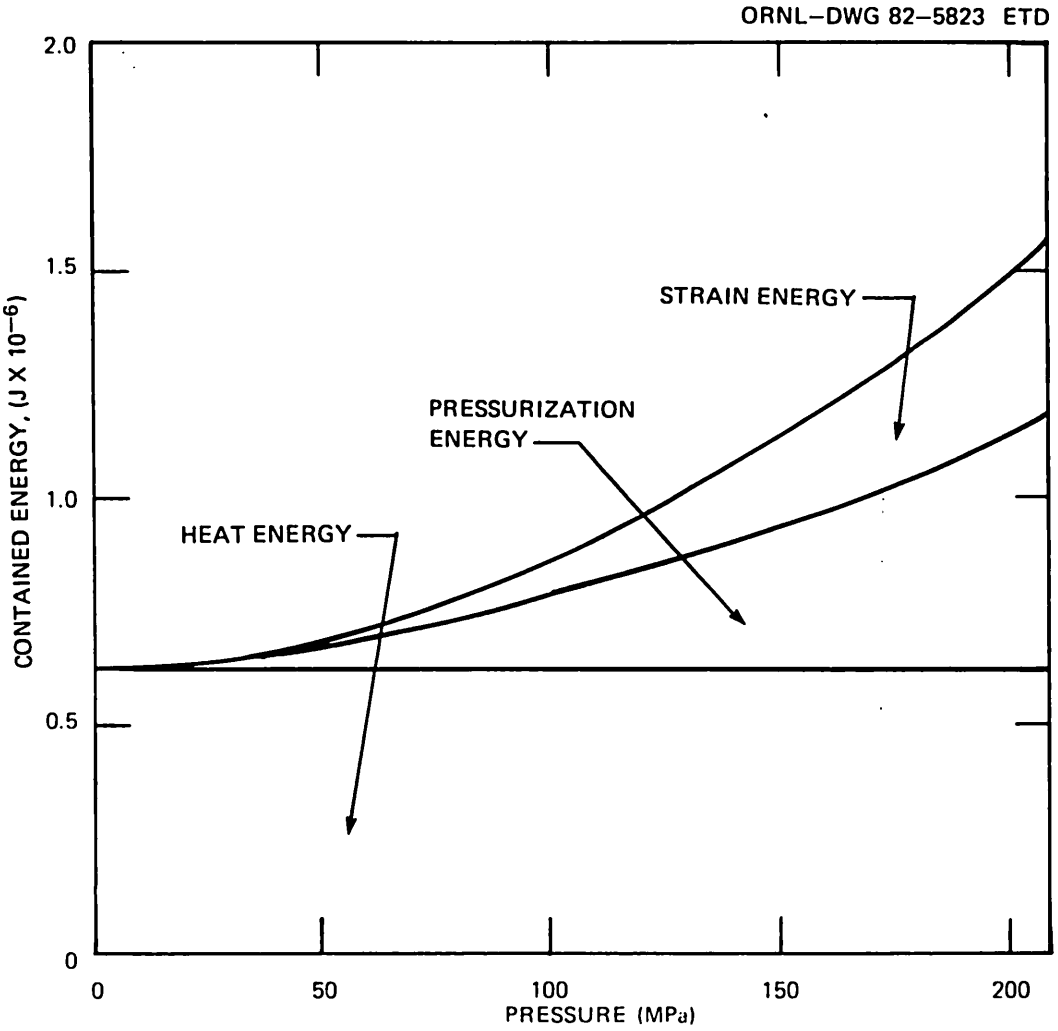

Fig. 3.11. Available energy to produce missiles in intermediate vessel test V-8A.

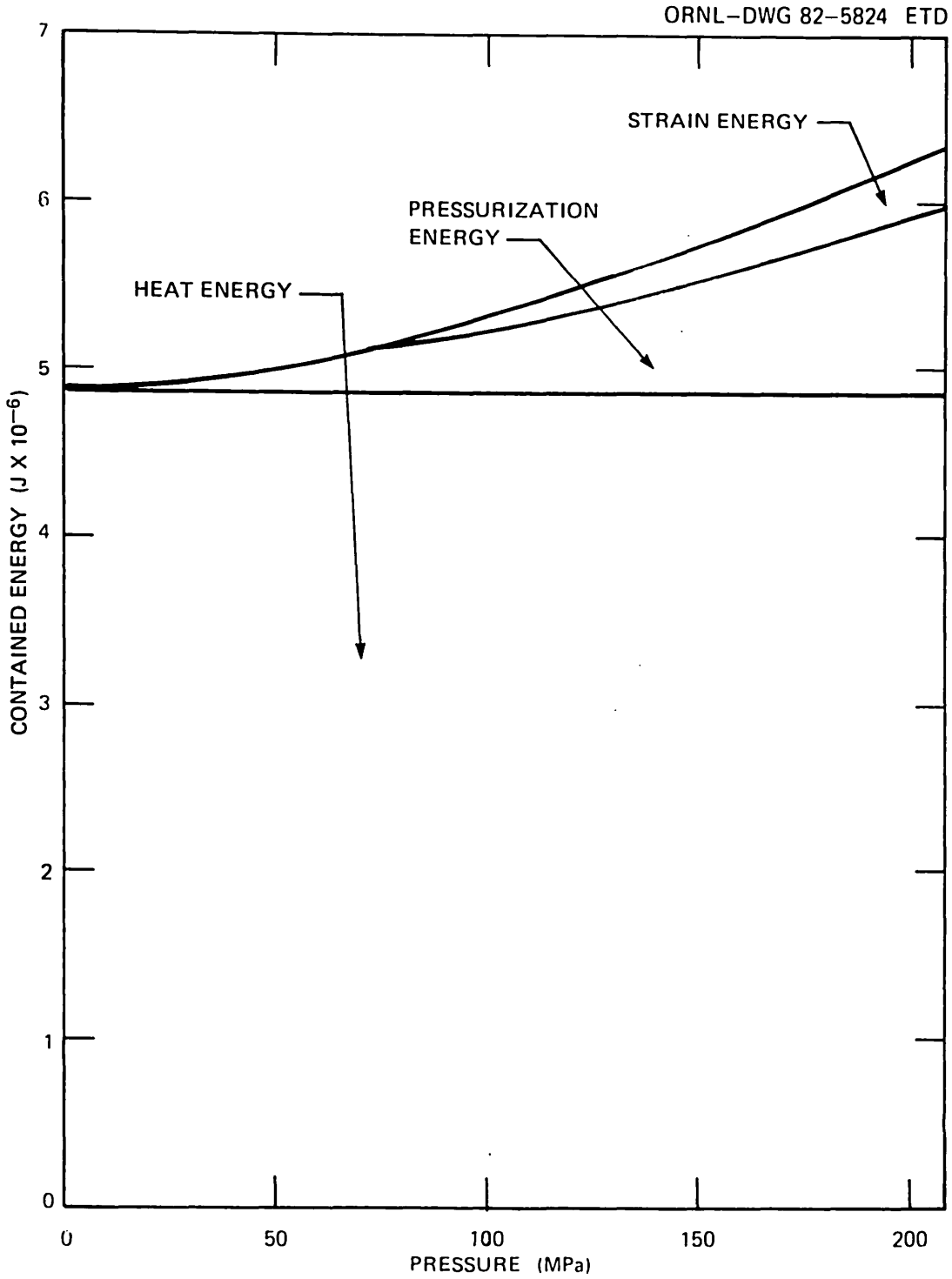

Fig. 3.12. Available energy to produce missiles in pressurized-thermal-shock experiments.

ORNL PHOTO 7402–81

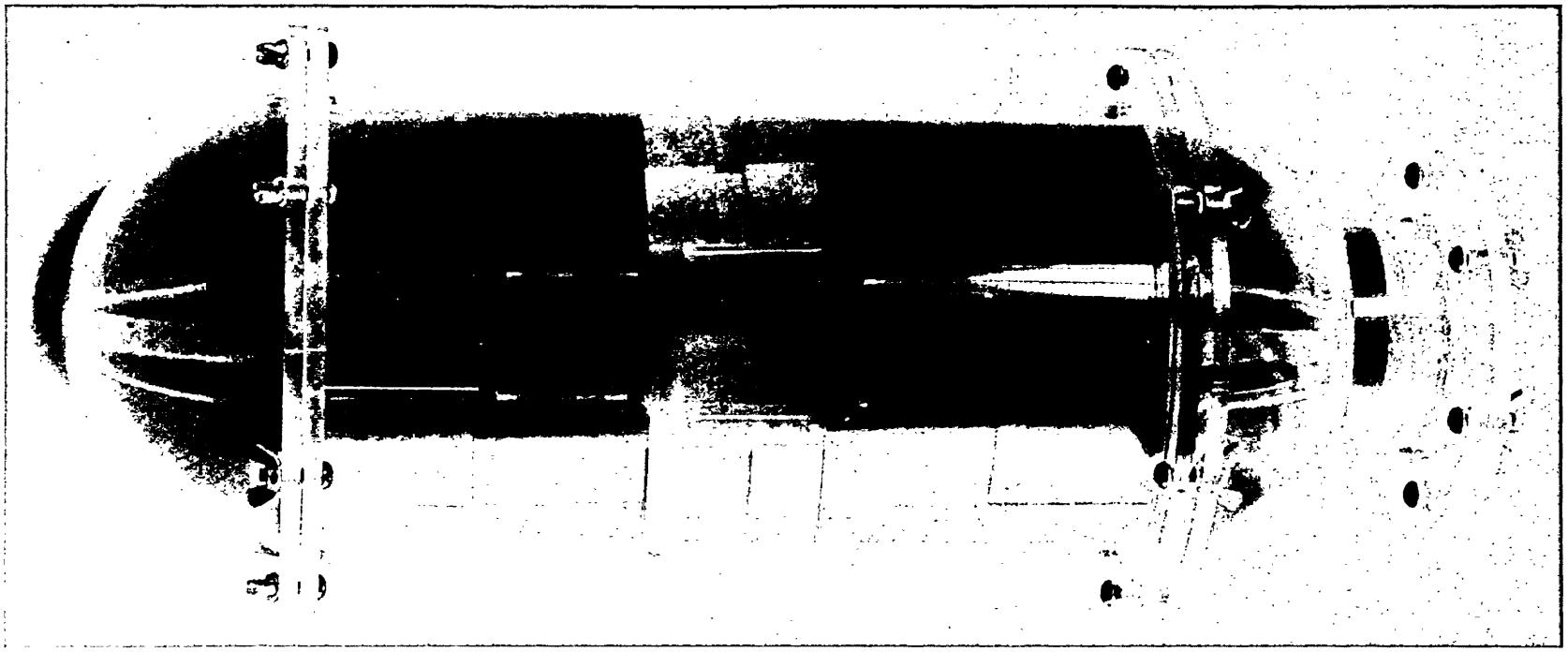

Fig. 3.13. One-fifth scale plexiglass model of test vessel V-8A with graphite ballast.

References

1. R. H. Bryan et al., *Pressurized-Thermal-Shock Test of 6-in.-Thick Pressure Vessels. PTSE-1: Investigation of Warm Prestressing and Upper-Shelf Arrest*, NUREG/CR-4106 (ORNL-6135), Martin Marietta Energy Systems, Inc., Oak Ridge Natl. Lab., April 1985.

2. C. L. Segaser, *System Design Description of the Intermediate Vessel Tests for the Heavy-Section Steel Technology Program*, ORNL/TM-2849, Union Carbide Corp. Nuclear Div., Oak Ridge Natl. Lab., Revised July 1973.

3. R. E. Gibson and O. H. Loeffler, "Pressure-Volume-Temperature Relations in Solution. V. The Energy-Volume Coefficients of Carbon Tetrachloride, Water and Ethylene Glycol," *J. Am. Chem. Soc.* 64, 898–906 (April 1941).

4. C. A. Meyer et al., "Thermodynamic and Transport Properties of Steam," *ASME Steam Tables*, 4th ed., The American Society of Mechanical Engineers, New York, 1979.

5. George O. Curme (ed.), *Glycols*, Reinhold Publishing Co., New York, 1952.

6. R. T. Kent, *Kent's Mechanical Engineering Handbook*, 11th ed., Table 7, pp. 7–26, John Wiley & Sons, New York, 1945.

7. The Ad Hoc Committee for High Pressure Safety, *Safety Standards for High Pressure System Facilities*, Y/GA-23, Union Carbide Corp. Nuclear Div., Oak Ridge Y-12 Plant, April 1981.

8. George Winter et al., *Design of Concrete Structures*, 7th ed., p. 239, McGraw-Hill, New York, 1964.

4. VESSEL TEST AND RESULTS

4.1 Test Facility

The test site for intermediate test vessel V-8A was the same as that used for several other intermediate vessels.[1-5] The hydraulic testing facility is located at the old power plant adjacent to the Oak Ridge Gaseous Diffusion Plant (ORGDP), where the vessels were pressurized to failure in a concrete-bunkered cell that was converted from an old steam turbine foundation. A sectional view of the test cell is shown in Fig. 4.1, and a top view of intermediate test vessel V-8A in the cell can be seen in Fig. 4.2. The criteria for site selection and design, along with a detailed description of the test facility, are given in Ref. 6.

The testing facility is equipped with systems for filling, heating or cooling, and pressurizing the test vessel. The systems that perform these functions are capable of controlling the vessel temperature between −29 and 177°C and pressurizing the vessel to 345 MPa. The pressurizing system and test vessel were filled with a mixture of 58% ethylene glycol and 42% demineralized water (by volume).

The vessel was equipped with six groups of tubular electrical heaters distributed on three levels along the cylindrical section of the test vessel, as shown in Fig. 4.3. Thus, at each level there were two groups of heaters; each group covered essentially 180° of the vessel circumference. Power was supplied to each group by a Variac power control. Each of the four groups at the upper and lower levels was connected to produce 5.9 kW at the maximum setting; the two groups in the middle were capable of producing 4.4 kW each.

4.2 Instrumentation and Data Acquisition System

Instrumentation was planned to provide as much information as could reasonably be obtained on the state of stress of the test vessel and the size and shape of the flaw at various stages of the test. Special aspects of instrumentation design for this test were concerned with

1. reliability and performance of sensors designed to function under high pressure (to ~200 MPa) at temperatures up to 150°C, which is higher than any temperature previously attained in intermediate vessel tests;
2. detection of tearing or structural instability; and
3. synchronized recordings of widely varying types of measurements.

The instrumentation plan adopted was based on the use of methods and devices that were well developed in terms of objective and quantitative interpretation of data and were adaptable to the vessel test environment.

The sensor and data acquisition features of the V-8A instrumentation are presented in Table 4.1. These include the features necessary for test control, evaluation of test results during the test, and data recording for posttest evaluation and analysis.

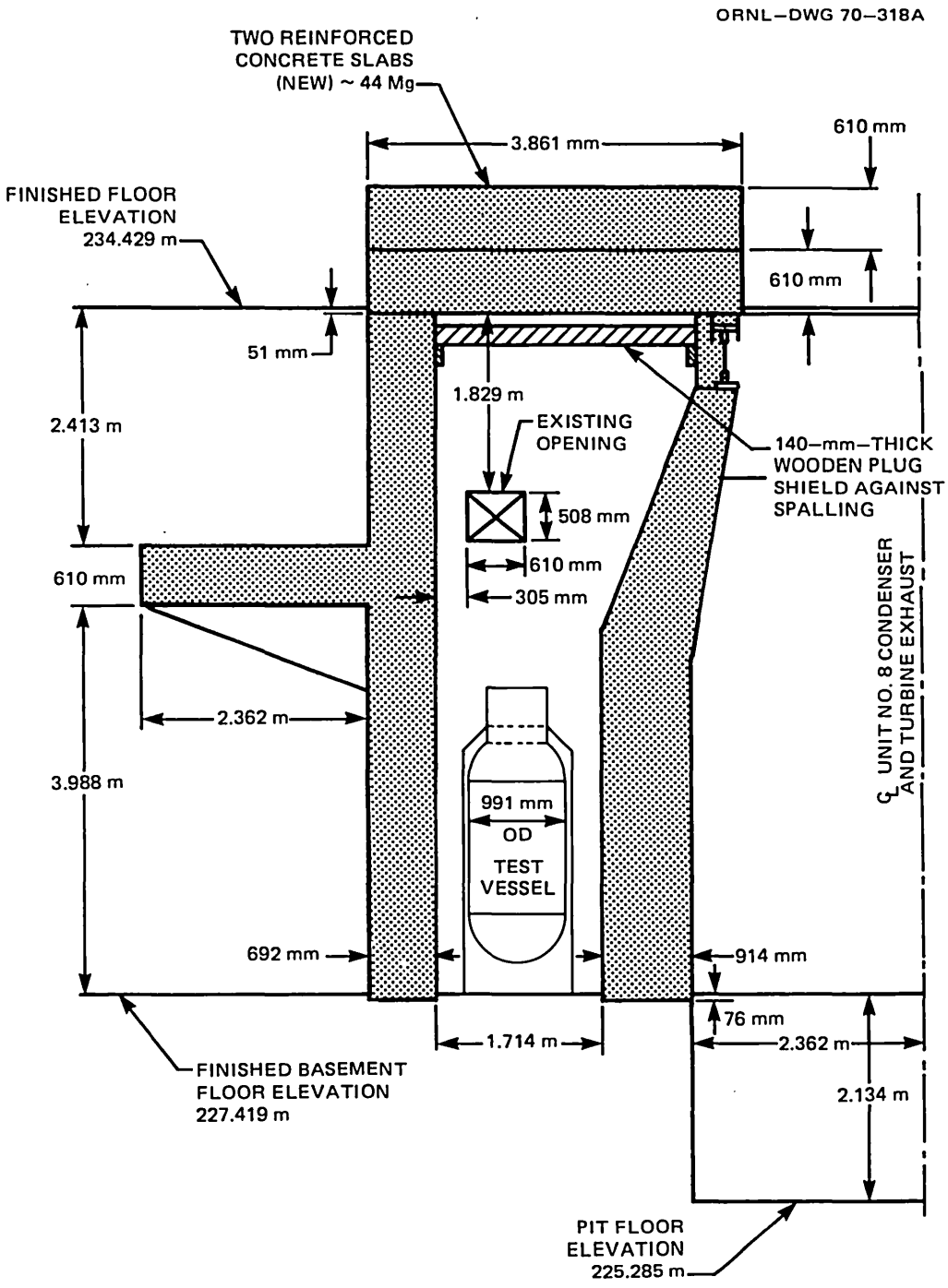

Fig. 4.1. Sectional view of intermediate vessel test cell.

K–25 PHOTO 82–2288A

Fig. 4.2 View of vessel V-8A from top of test cell before connections and thermal insulation were completed.

K–25 PHOTO 82–2287A

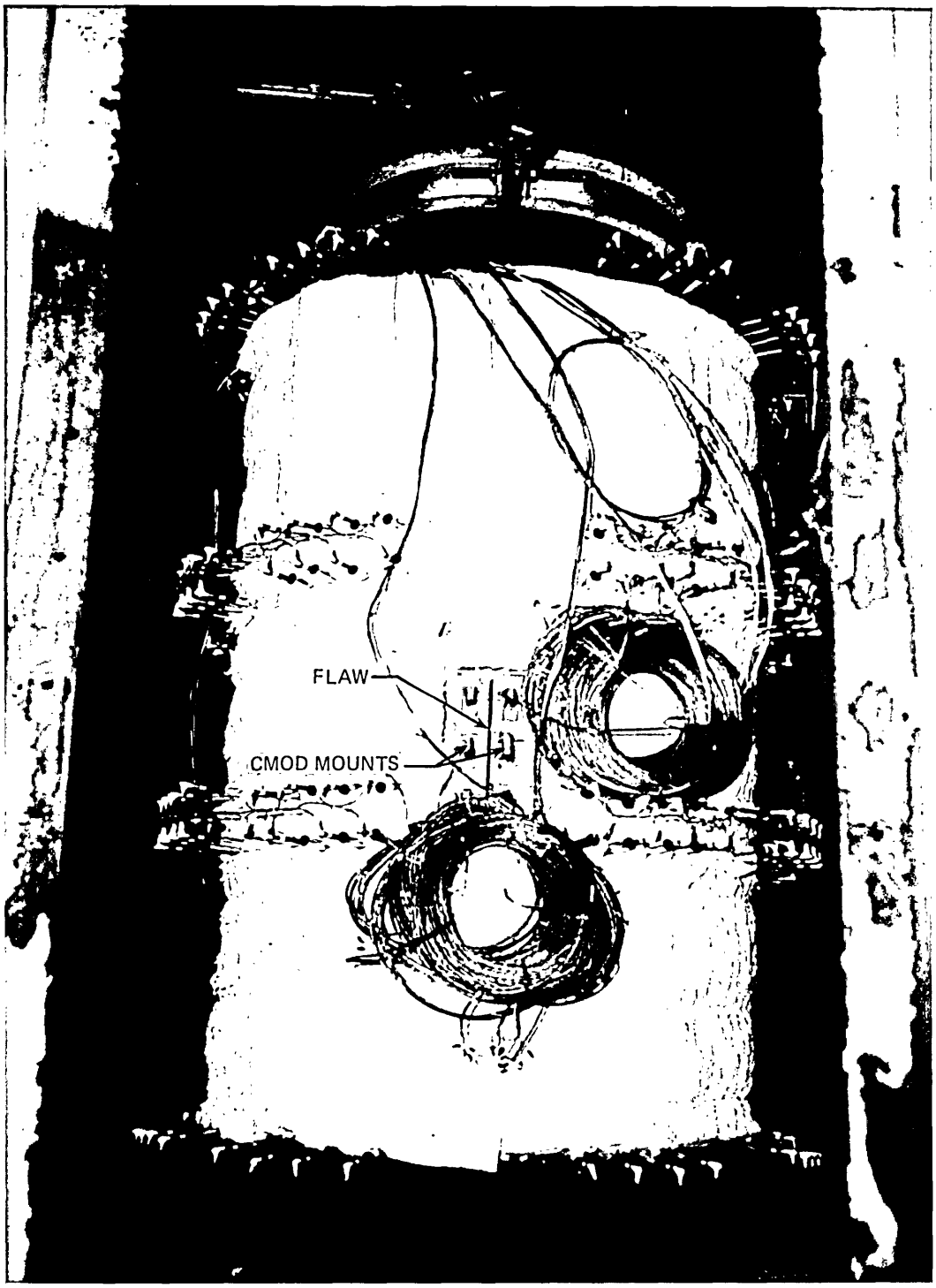

Fig. 4.3. Vessel V-8A in test cell before instrumentation cables and electrical heaters were connected.

Table 4.1. V-8A instrumentation output assignments

Variable and sensor number prefix	Location of sensors on vessel	Number of sensors	Primary recording device[a]	Secondary output	
				Device[a]	Number of channels
Temperature	Inside	4	CCDAS		
TE	Outside	13	CCDAS		
	Outside	16	Strip chart[b]		
Pressure	Static line	2	CCDAS	Plotter	1
PE				Strip chart	1
				Digital display	1
		1	Video tape	Visual	1
Strain	Inside — F[c]	41	CCDAS	Strip chart	1
XE	Outside — F[d]	42	CCDAS	Strip chart	2
	Inside — other	8	CCDAS	Plotter	1
	Outside — other	13	CCDAS	Plotter	1
	Outside	3	Vishay[e]		
CMOD	Crack mouth	4	CCDAS (8 channels)	Plotter	4
ZT				Strip chart	1
				Digital display	1
Instability, $\dot{v}$ = d/dt ln (CMOD/p^2)	[f]	1	Strip chart Digital display	CCDAS	1
XM					
Ultrasonic	Inside — F[c]	7	Video tape[g]	Oscilloscope	
UT					

[a]CCDAS: computer-controlled data acquisition system with time base; scanning rate is 10,000 points/s; recording rate is variable; strip chart: variable vs time; Vishay: printed paper tape on manual command; plotter: variable plotted vs pressure.

[b]At heater control panel.

[c]Inside vessel near flaw.

[d]Outside vessel near flaw.

[e]A Vishay-Ellis strain recording system was used to record data independently of the CCDAS to save essential data if the CCDAS failed.

[f]Derived from sensors specified for CMOD (ZT151) and pressure (PE30).

[g]Video section of tape records UT signal; audio section records time code.

Strain gages, crack-mouth-opening-displacement (CMOD) gages, and ultrasonic transducers mounted on the vessel provided the information on states of stress, deformation, and crack depths necessary for interpretation of the experiment. Locations of these sensors are described in Figs. 4.4 and 4.5 and Table 4.2.

Pressure and temperature indications were used for control. In addition, a CMOD-pressure variable was produced by a special electronic module and used as an indicator of incipient instability so that the vessel could be depressurized promptly to interrupt the tearing instability. The variable selected for indication of instability is the time derivative

$$\dot{v} = \frac{dv}{dt} = \frac{d}{dt} \ln (CMOD/p^2) ,$$

where CMOD is crack-mouth-opening displacement and p is pressure. The use of a logarithmic derivative provided a signal amplitude that was reasonably independent of the absolute magnitude of pressure and CMOD, which were expected to vary widely.

The test was planned with the expectation that estimates of crack size and shape could be made from CMOD measurements and ultrasonic (UT) observations of the crack tip at each of several stages of the test. CMOD measured during small decrements of pressure was output to plotters displaying CMOD vs p. The elastic response of CMOD could be correlated with precalculated CMOD changes for various crack sizes. The resolution of the UT and CMOD measurements of crack depth was expected to be on the order of 1 mm.

All measurements made during the test were recorded for posttest investigation. The principal recording media were magnetic tapes for digital data produced by a computer-controlled data acquisition system (CCDAS) and video tapes for UT data. The records on the two types of tapes were synchronized by writing a time code on the UT tapes by a time code generator set to the CCDAS clock time. The data recording scheme presented in Table 4.1 provided redundancy, diversity, and dispersion of sensors, recording devices, and other apparatus to minimize the adverse impact of equipment malfunctions.

Generally the test would not have proceeded if the CCDAS was not functioning properly, but if the CCDAS had failed after the test had reached a point of no return, there were independent recordings of pressure, all CMODs, and some strains. Also two magnetic tapes of the CCDAS data were written simultaneously to protect against accidental loss of those records.

The two pressure transducers (PE30 and PE31) were on a static line penetrating the head of the vessel (Fig. 4.6). Pretest calibrations indicated that the outputs had maximum nonlinearities of 0.30 and 0.28% of full scale between 0 and 200 MPa.

CMOD gages were HITEC Corporation Proximic gages, which measured displacement by sensing capacitance changes of the gage. The installation of these gages on the test vessel is shown in Fig. 4.7. Model HPC-375, which has a nominal range of 0 to 6.35 mm, was used for sensor ZT151. The other three sensors were model HPC-150, which has a nominal

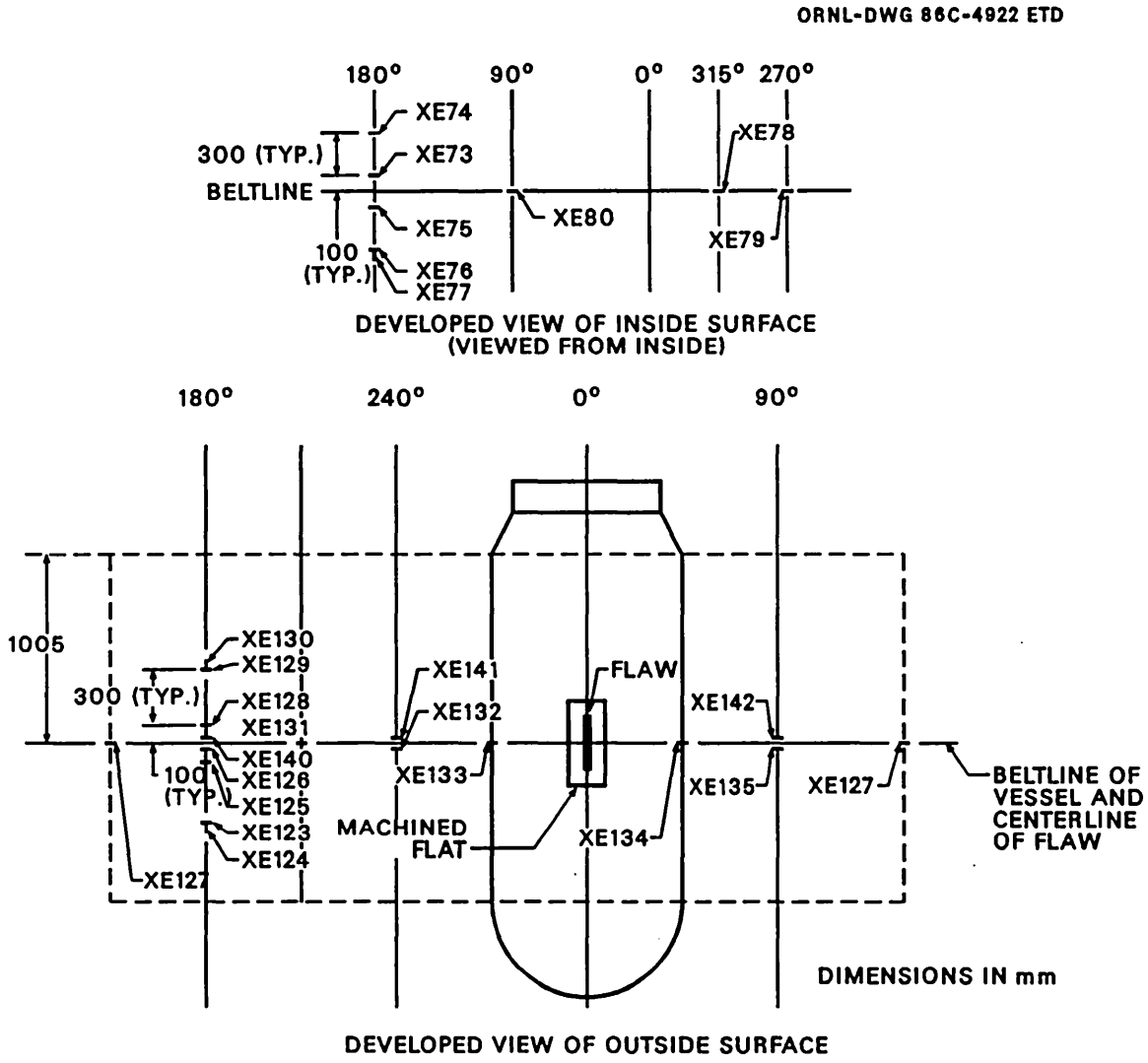

Fig. 4.4. Locations of sensors remote from flaw. See Fig. 4.5(a) for definition of coordinate system.

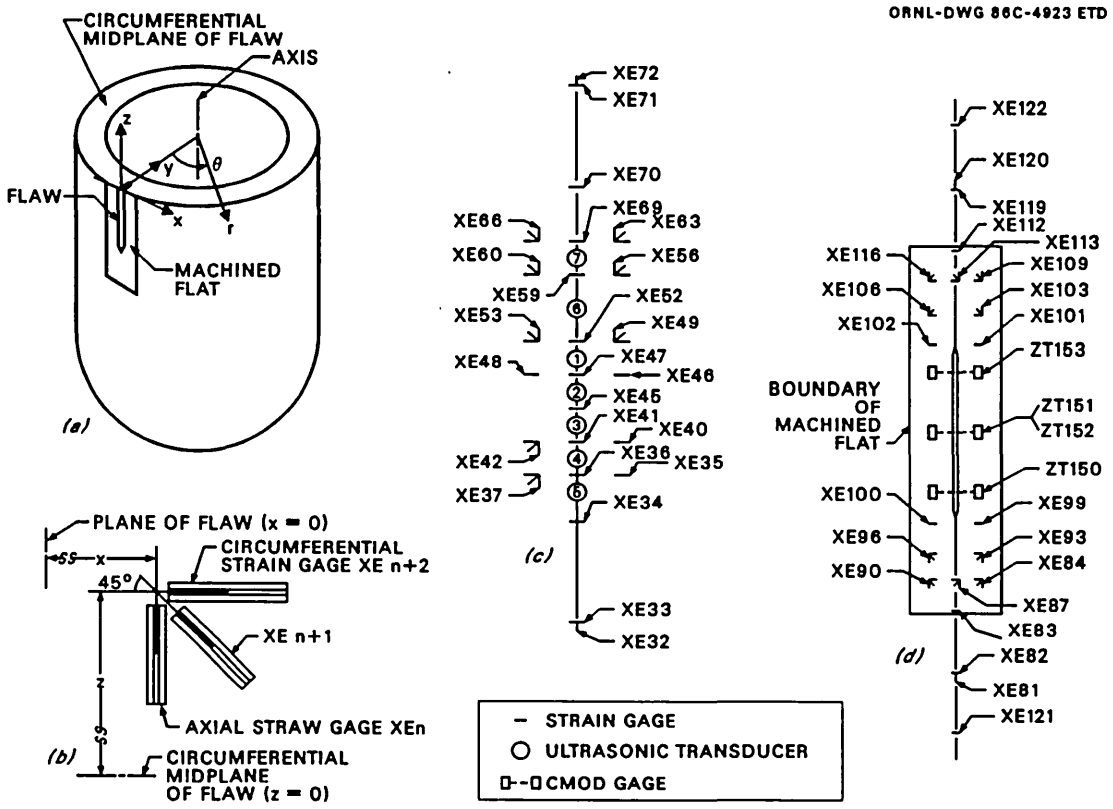

Fig. 4.5. Locations of sensors near flaw. See Table 4.2 for coordinates of sensors. (*a*) Definition of coordinate system used for sensor locations and features of the fracture surface, (*b*) arrangement of strain gage rosettes, (*c*) sensors on inside surface, and (*d*) sensors on outside surface.

Table 4.2. Coordinates of sensors near flaw[a]

Inside strain gage No. XE	Coordinate (mm)		Outside strain gage No. XE	Coordinate (mm)		Sensor	Coordinate, z (mm)
	x	z		x	z		
32	0	−413	81	0	−413	CMOD ZT[b]	
33	0	−400	82	0	−400	150	−100
34	0	−250	83	0	−300	151	0
35	73	−175	84[c]	51	−250	152	0
36	0	−175	87[c]	−13	−250	153	100
37[c]	−60	−175	90[c]	−51	−250		
40	73	−125	93[c]	51	−200	Ultrasonic	
41	0	−125	96[c]	−51	−200	UT	
42[c]	−60	−125	99	38	−150	1	0
45	0	−75	100	−38	−150	2	−50
						3	−100
46	73	−25	101	38	150	4	−150
47	0	−25	102	−38	150	5	−200
48	−73	−25	103[c]	51	200	6	75
49[c]	60	25	106[c]	−51	200	7	150
52	0	25	109[c]	51	250		
53[c]	−60	25	112	0	300		
56[c]	60	125	113[c]	−13	250		
59	0	125	116[c]	−51	250		
60[c]	−60	125	119	0	400		
63[c]	60	175	120	0	413		
66[c]	−60	175	121	0	−500		
69	0	175	122	0	500		
70	0	250					
71	0	400					
72	0	413					

[a]See Fig. 4.5(*a*) for definition of the coordinate system.

[b]Supports for CMOD gages are at x = −38 and +38 mm. Axes of sensors are 25.4 mm from the machined flat surface, except for ZT151, which is 50.8 from the surface.

[c]Only the number of the axial gage in a rosette is listed. See Fig. 4.5(*b*) for definition of other gage numbers and of coordinates.

ORGDP PHOTO
K/PH 82–2747A

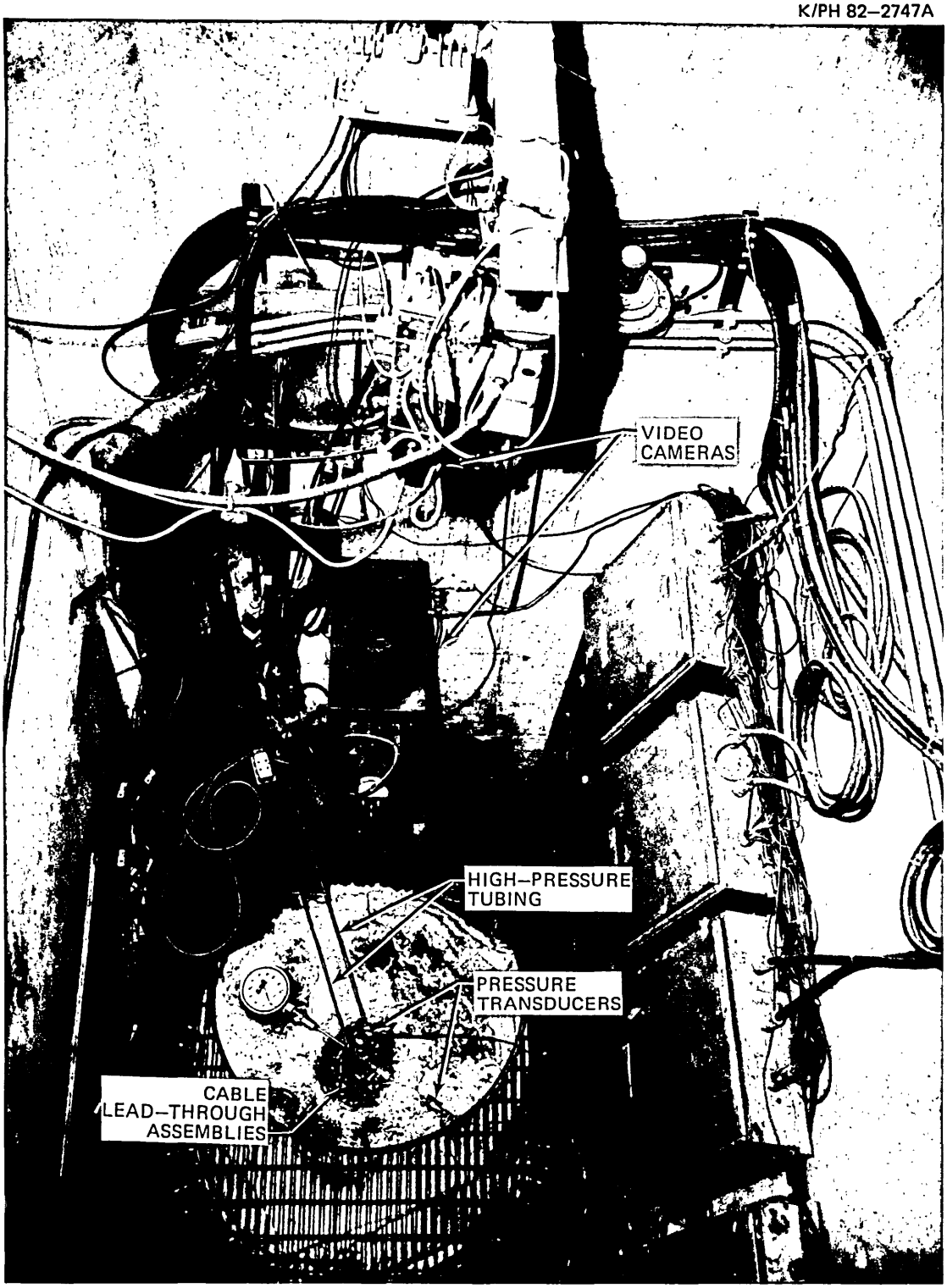

Fig. 4.6. Top of vessel V-8A in test cell with all equipment installed and connected.

ORGDP PHOTO
K/PH 82–2567A

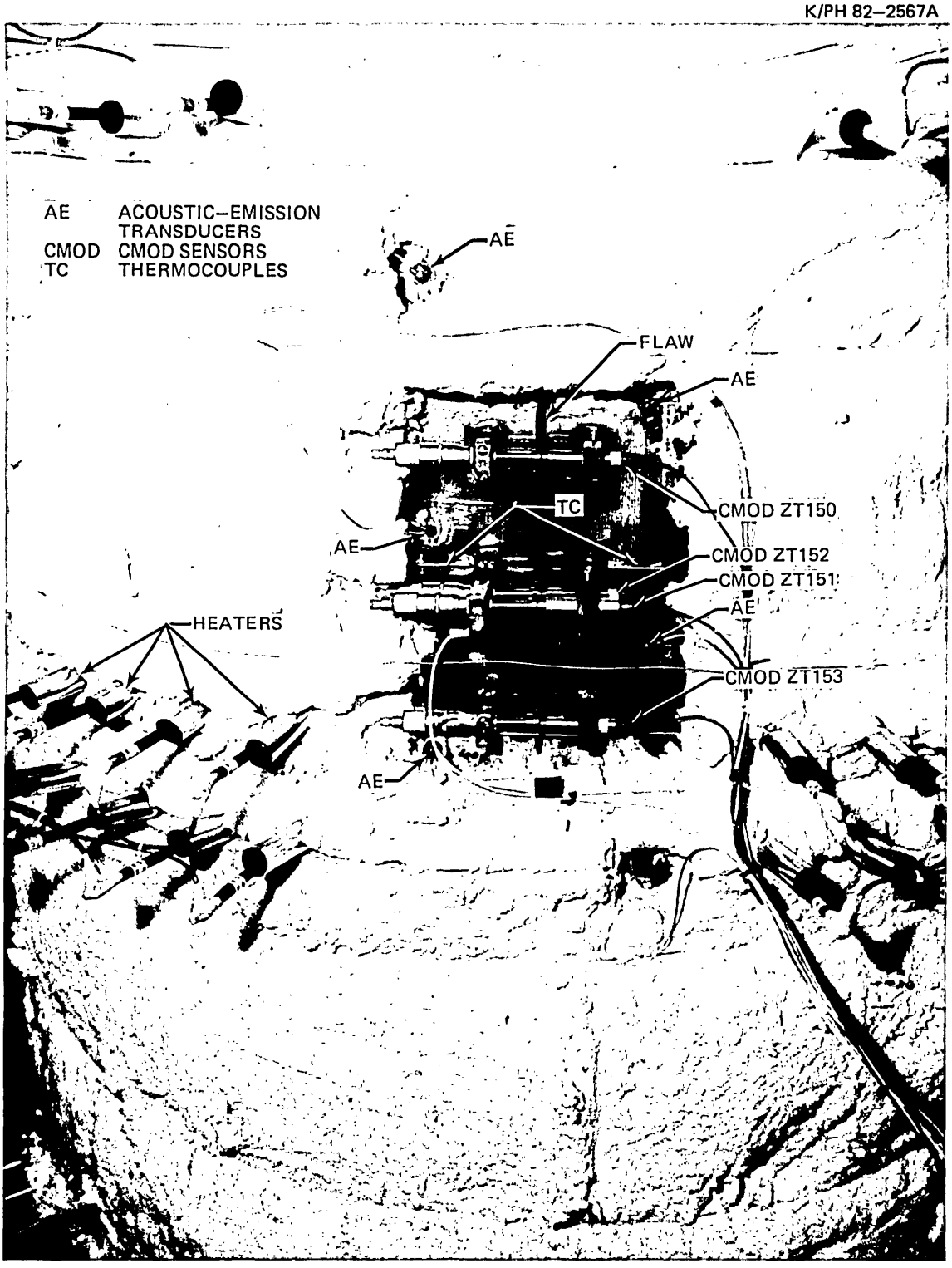

Fig. 4.7. Instrumentation attached to the vessel in the vicinity of the flaw.

range of 0 to 2.54 mm. A CMOD sensor consisted of an active (HITEC) element and a target supported on a micrometer drive, as shown in Fig. 4.8 for sensors ZT151 and ZT152. Sensors ZT150 and ZT153 were each on a separate mount similar to the one shown in this figure. The micrometer permitted calibration of each gage in place. Output of the gages deviated from linearity by <1% of the maxima of the recorded ranges, which were 5.44 mm for ZT151 and 3.09 mm for the other three gages.

The strain gages were weldable Ailtech gages with a nominal 25 mm gage length. Types SG125-01H-26-6S and SG125-09F-15-6S were applied to the inside and outside surfaces, respectively. The gages were essentially identical except for the length of the integral stainless-steel-sheath cable.

Seven pulser-receiver UT transducers were located on the inside surface of the vessel in the plane of the flaw, as shown in Fig. 4.5. A cross-sectional view of this arrangement is shown in Fig. 4.9. The pulse signals to all transducers were triggered by a pulse-synchronizing signal to reduce interference among sensors. The signal frequency was 5 MHz, and the pulse repetition rate was about 1000 Hz. Reflected signals from each transducer were recorded on a separate magnetic tape cassette by a video recorder. An instantaneous video display of each output could be monitored by means of three oscilloscopes. Provisions were made for playback and display of segments of any tape during extended pauses during the test. During active testing periods, a time code was written on the sound track of each video tape, so that each UT event could be associated with the times of events recorded by the CCDAS.

Six acoustic emission sensors for monitoring the activity of the flaw were attached to the vessel in the vicinity of the flaw (Fig. 4.7). No useful data were recorded by the acoustic emission system because of a failure of the signal processor.

Video cameras were set up to monitor critical areas of the test system. A monitor in the control room displayed a view of the region around the head of the test vessel.

4.3 Test Procedures

4.3.1 Vessel preparation

The test vessel was assembled in six steps: (1) installation of internal instrumentation, (2) installation of graphite ballast, (3) attachment of the closure head, (4) installation of external instrumentation, (5) sealing of cable penetrations, and (6) installation of electrical heaters and insulation. Figure 4.10 shows the inside of vessel V-8A after the internal instrumentation was installed and with two of seven courses of the graphite ballast in the vessel.

Figures 4.11 and 4.12 show external views of the vessel after completion of the assembly except for thermal insulation. Details of instrumentation near the fatigue-sharpened flaw are shown in Figs. 4.5 and 4.11. Weldable strain gages and thermocouples are covered with pieces of split tubing for protection against damage in handling. Figure 4.12 is an overall view of the vessel 90° from the flaw. The vessel is in the frame used for lifting and transporting the vessel.

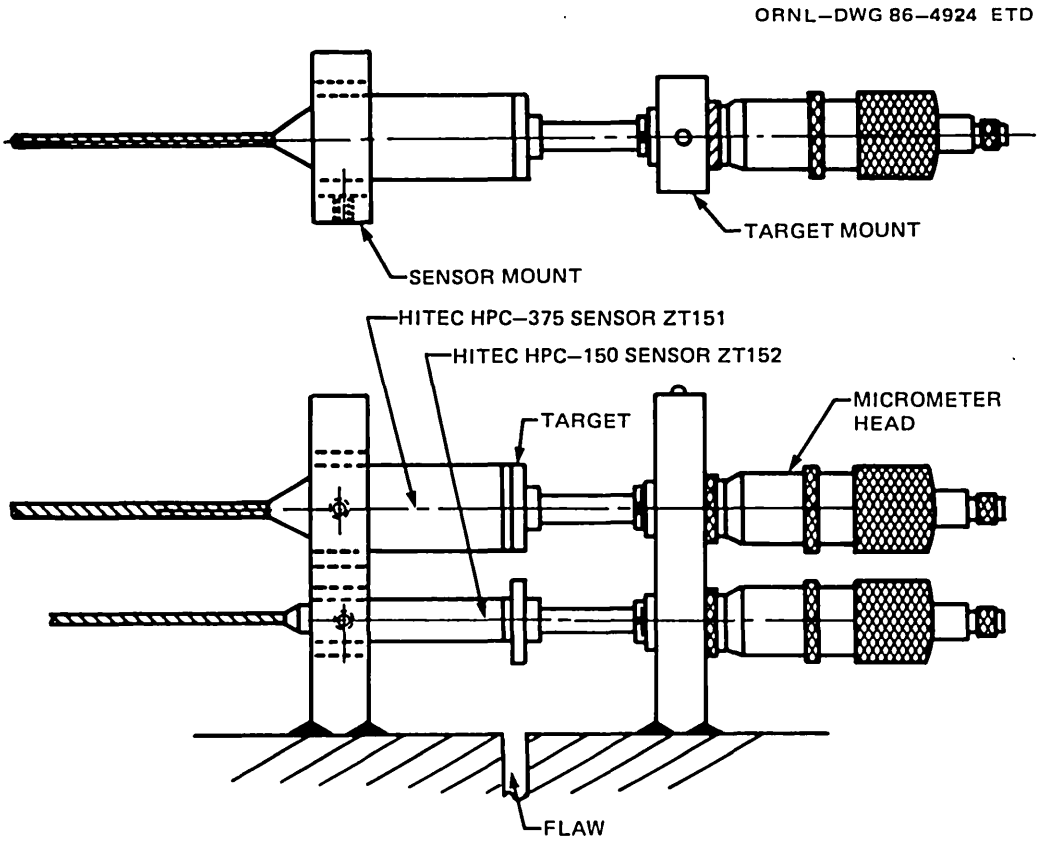

Fig. 4.8. CMOD sensor assembly for ZT151 and ZT152. The mounts for ZT150 and ZT153 were similar.

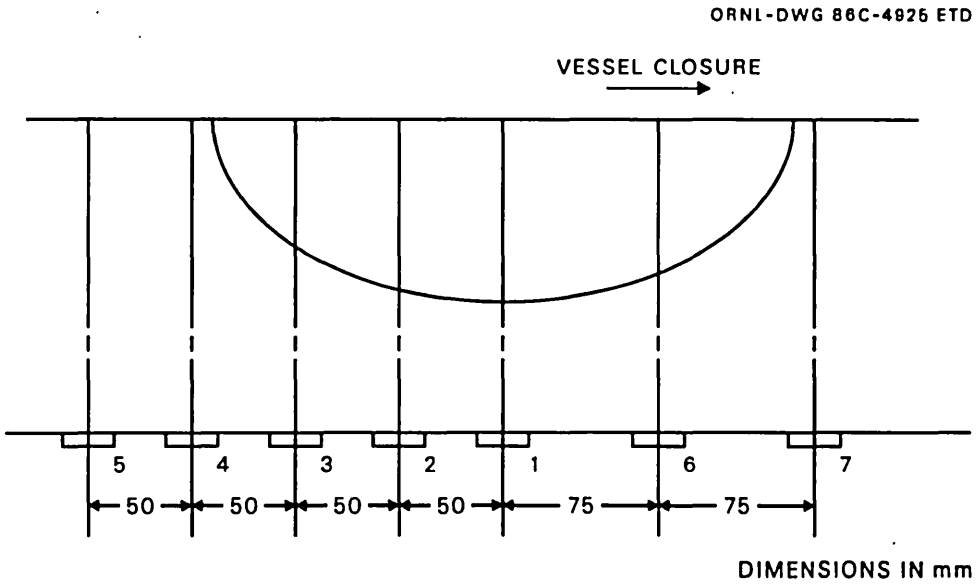

Fig. 4.9. Section of flawed region showing locations of UT transducers.

ORNL–PHOTO 8404–82A

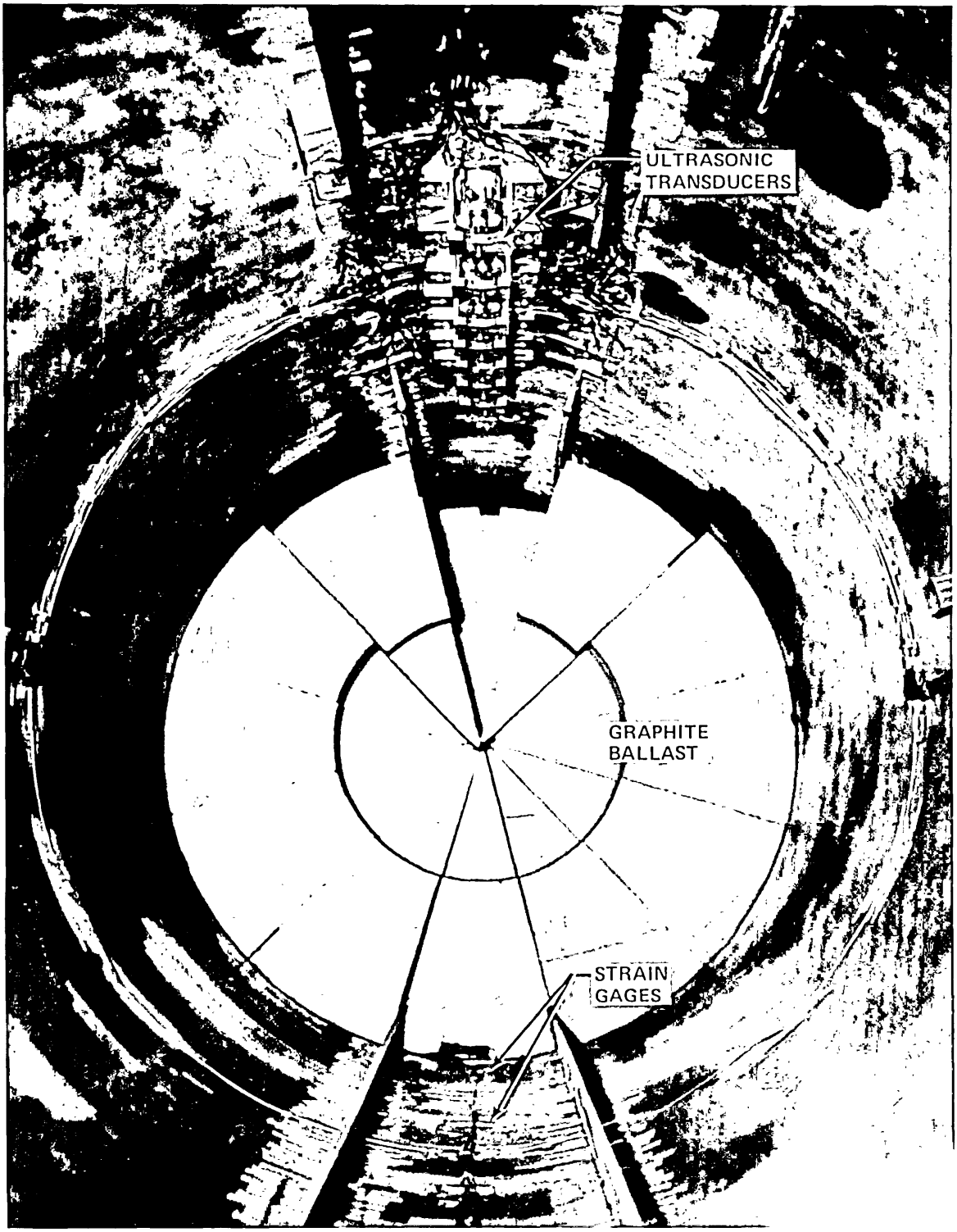

Fig. 4.10. Internal instrumentation and graphite ballast. Instrumentation is complete, and about one-third of graphite is in place.

ORNL–PHOTO 8502–82

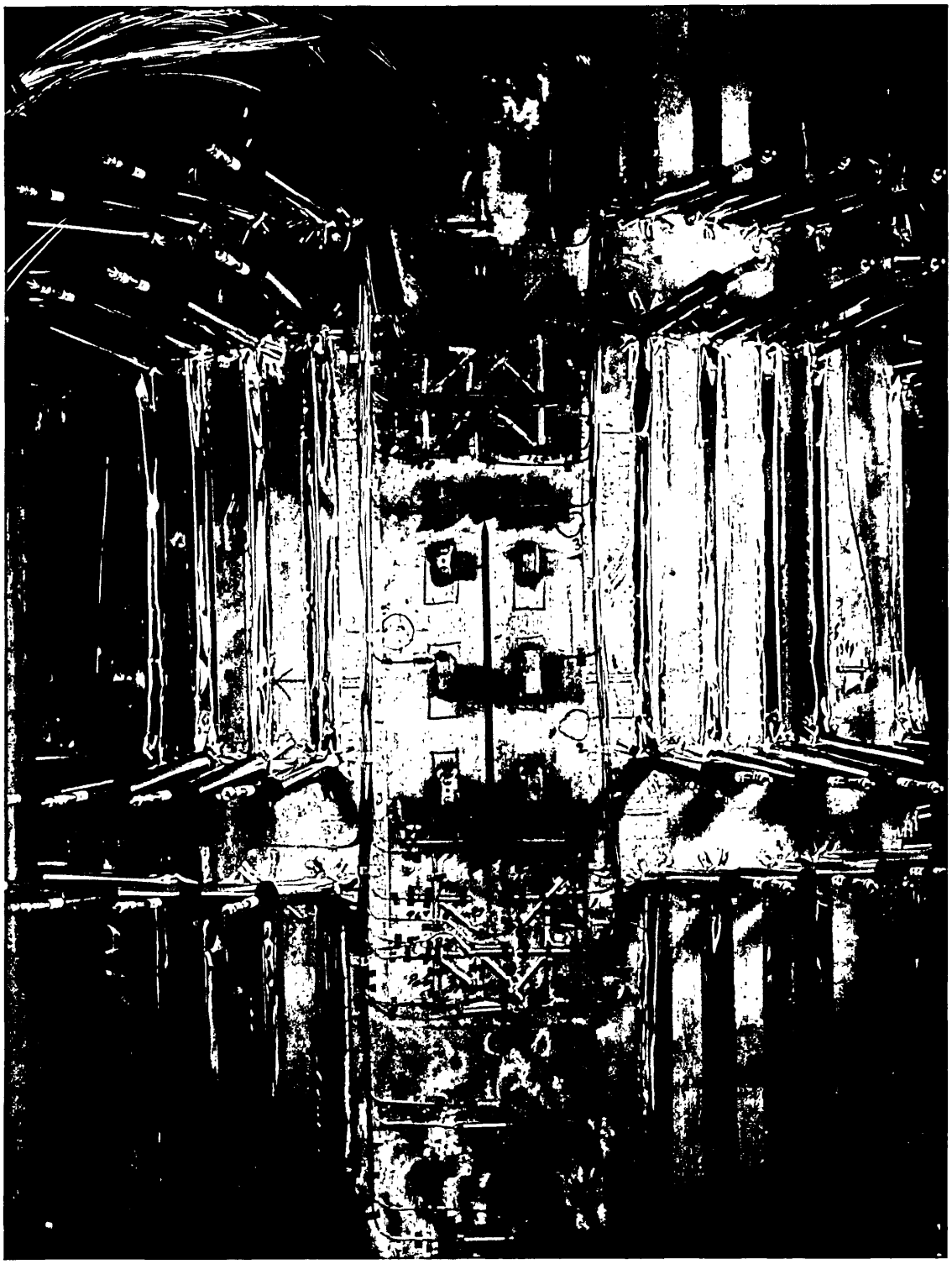

Fig. 4.11. Instrumentation, CMOD fixtures, and electrical heaters applied near the flaw on the outside surface.

ORNL–PHOTO 8503–82

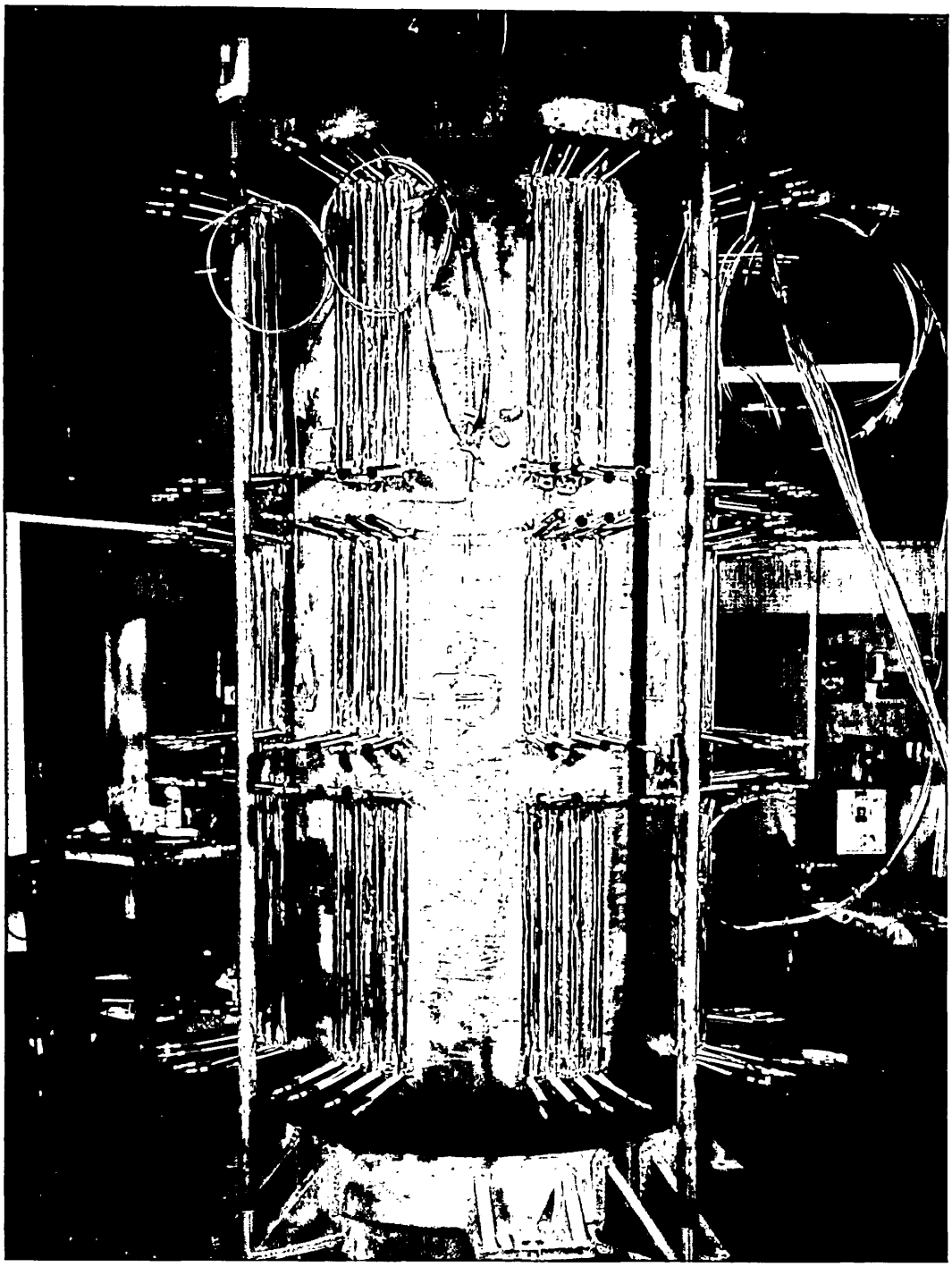

Fig. 4.12. View of sensors and electrical heaters from the 90° side. The 16 heaters shown here on each of the 3 levels were connected to a single variable power source for each level. Heaters on the opposite side were similarly arranged so that separate power control was exercised for six areas.

Installation of thermal insulation on the vessel was completed after the vessel was placed in the test cell. CMOD assemblies were attached to the mounts after completion of other work in the vicinity of the flaw, as shown in Fig. 4.7.

4.3.2 Pressure testing

The vessel test consisted of a heatup phase and a high-pressure phase. All test equipment was operable at the commencement of the heatup phase, about 48 h prior to the scheduled high-pressure phase. The objective of the heatup phase was to bring the vessel to a thermal steady state condition with temperatures in the test section of the vessel at or slightly above 150°C. The temperature history during this phase is shown in Fig. 4.13.

The electrical power applied to the vessel heaters was about 12 kW initially and was subsequently reduced to about 1250 W before initiation of the high-pressure phase on August 11, 1982. When vessel temperatures reached 90°C, the vessel was pressurized to ~5 MPa. Thereafter, during the heatup, pressure was maintained between 2 and 6 MPa to suppress vapor formation. When the high-pressure test began, temperatures in the region of the flaw were ~157°C except on the uninsulated outside surface at the flaw (see Fig. 4.7), where the temperature was 150°C.

During the high-pressure phase, pressure transducer PE31 exhibited a drift of the order of 1 MPa while at atmospheric pressure. For this reason, the pressures generally used in discussion of results in this report are those indicated by transducer PE30. The variance of the two indications was never >1.5 MPa.

The pressurization phase of the test consisted of

1. slowly increasing pressure to several designated ascending levels,
2. interrupting pressurization and unloading slightly for the purpose of recording elastic CMOD changes,
3. continuing pressurization until unstable tearing was detected,
4. rapidly unloading to interrupt unstable tearing,
5. repressurizing after interrupted tearing to confirm instability, and
6. rapidly unloading to prevent a burst.

During this phase of the test, all data except acoustic emission were recorded synchronously for posttest interpretation to provide evidence of the conditions at the onset of stable tearing and the onset of a tearing or local plastic instability.

4.4 Test Results

The pressurization of the vessel proceeded as shown in Fig. 4.14. An apparent tearing stability was observed between 138.0 and 140.5 MPa. The instability was interrupted and reinitiated before the final depressurization. As planned, the vessel did not rupture.

The pressurization phase proceeded through 16 increments of pressure, as indicated by Fig. 4.14. The desired objective of inducing and interrupting a tearing instability was attained. However, leaking seals

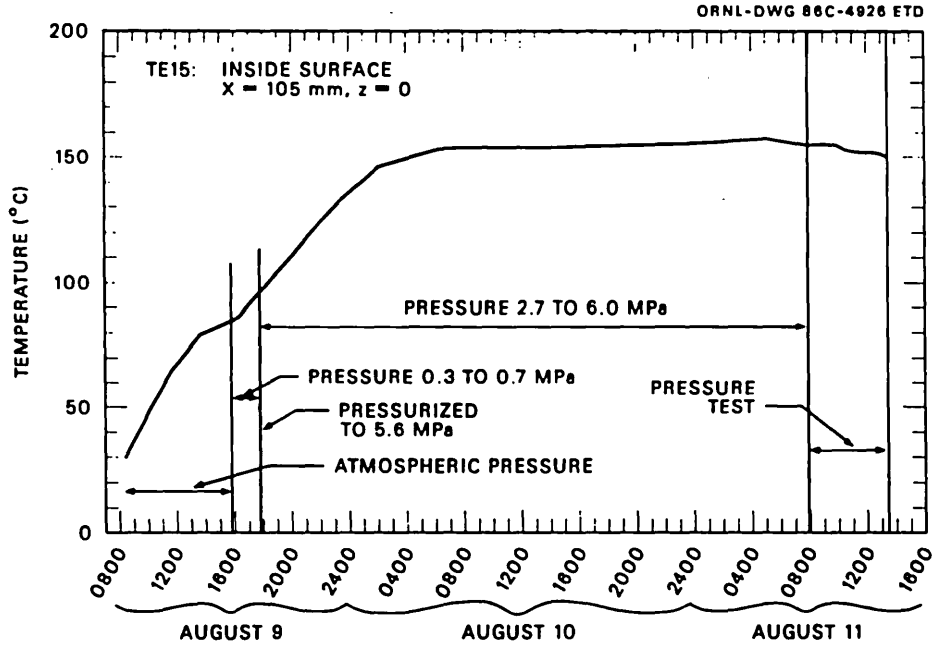

Fig. 4.13. Temperature time history of V-8A during heatup and pressurization test, August 9—11, 1982.

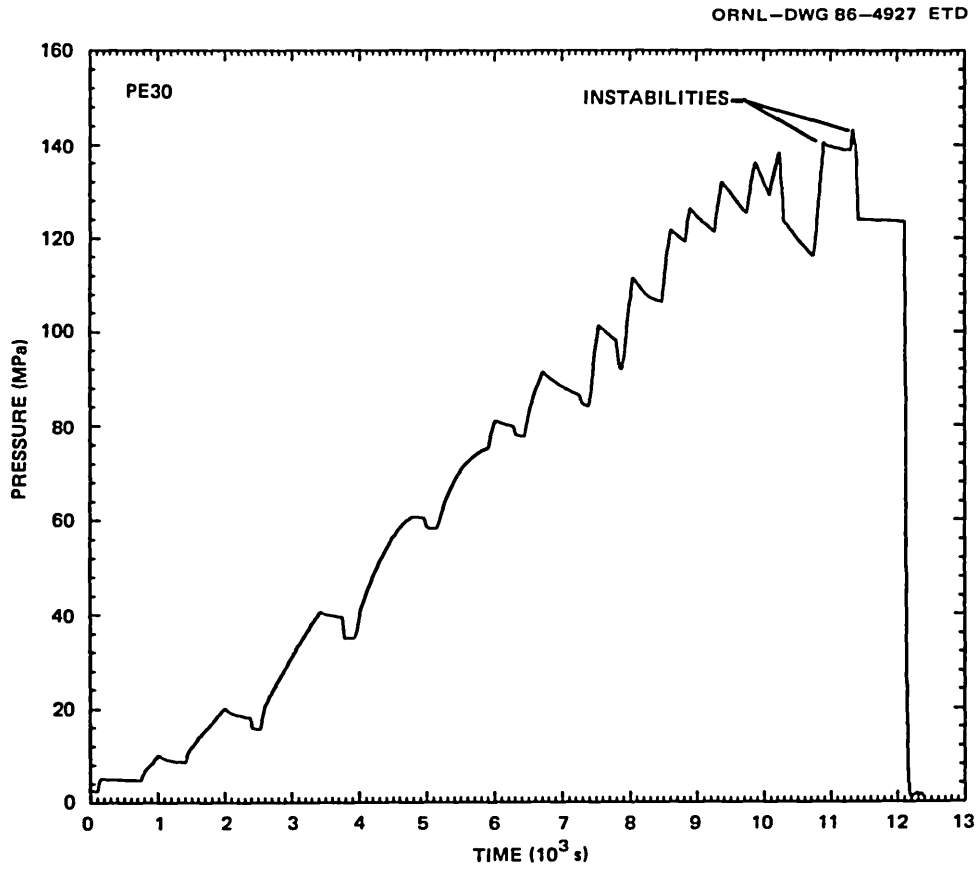

Fig. 4.14. Pressure vs time during V-8A test.

in some of the cable penetrations in the head prevented sustained periods of reasonably constant pressure after a pressure of 80 MPa was reached. This prevented any deliberate assessment of flaw size during the test, either from CMOD measurements or UT observations. Data displays nevertheless gave clear indications of incipient and progressive tearing instabilities. The principal results of the test are presented here and in Chap. 5. A complete record of pressure, temperature, strain, and CMOD data is presented in Appendix M. Appendix N presents details of fracture surfaces.

4.4.1 Temperature

As indicated by Fig. 4.13, the temperature of the test vessel was stable for several hours before the pressurization phase of the test. Figure 4.15 shows the downward temperature trends during the 3 1/2 h test. The entire vessel cooled by about 5 K. The coldest part of the vessel was the uninsulated portion of the outside surface around the flaw. Here the temperature stayed between 146 and 150°C. The temperatures through the wall of the vessel near the flaw are shown to have been between 146 and 158°C (Fig. 4.15).

4.4.2 Strain

The states of stress developed in the test section of the vessel are indicated by measurements of strain on the inside and outside surfaces of the vessel. The strain history of the test is summarized in Figs. 4.16–4.19, which generally show strains at or near the beltline of the vessel ($z = 0$). Strains remote from the flaw, that is, at 180°, are shown in Fig. 4.16. This indicates that, at maximum pressure, the outside surface was well below the yield strain; and the inside surface was close to yielding. (See Fig. 2.13 for the stress-strain relationships for the V-8A material.) Inside and outside surface strains at points 90° from the flaw reached similar magnitudes, as shown in Fig. 4.17. However, these strains differ from their respective strains at 180° in the directions that reflect the effects of the vessel bulging around the flaw.

Inside surface strains at or near the beltline of the vessel at several azimuthal points, shown in Figs. 4.17 and 4.18(*a* and *b*), indicate only a slight asymmetry relative to the plane of the flaw. The suppression of the strain immediately beneath the flaw [0°, Fig. 4.18(*a*)] at pressures <110 MPa is the consequence of bending of the ligament at that section.

Localization of bending near the flaw is clearly evident in comparing inside surface strains 50 mm on either side of the flaw (Fig. 4.19) with strains 45° and 90° from the flaw (Figs. 4.17 and 4.18). At pressures above 110 MPa, the large changes in strain at the 50-mm points (Fig. 4.19) indicate that the bulging is principally within 100 mm of the flaw and is slightly asymmetric. Strain changes immediately beneath the flaw are much smaller than nearby strains and finally become negative immediately prior to maximum pressure (Fig. 4.19).

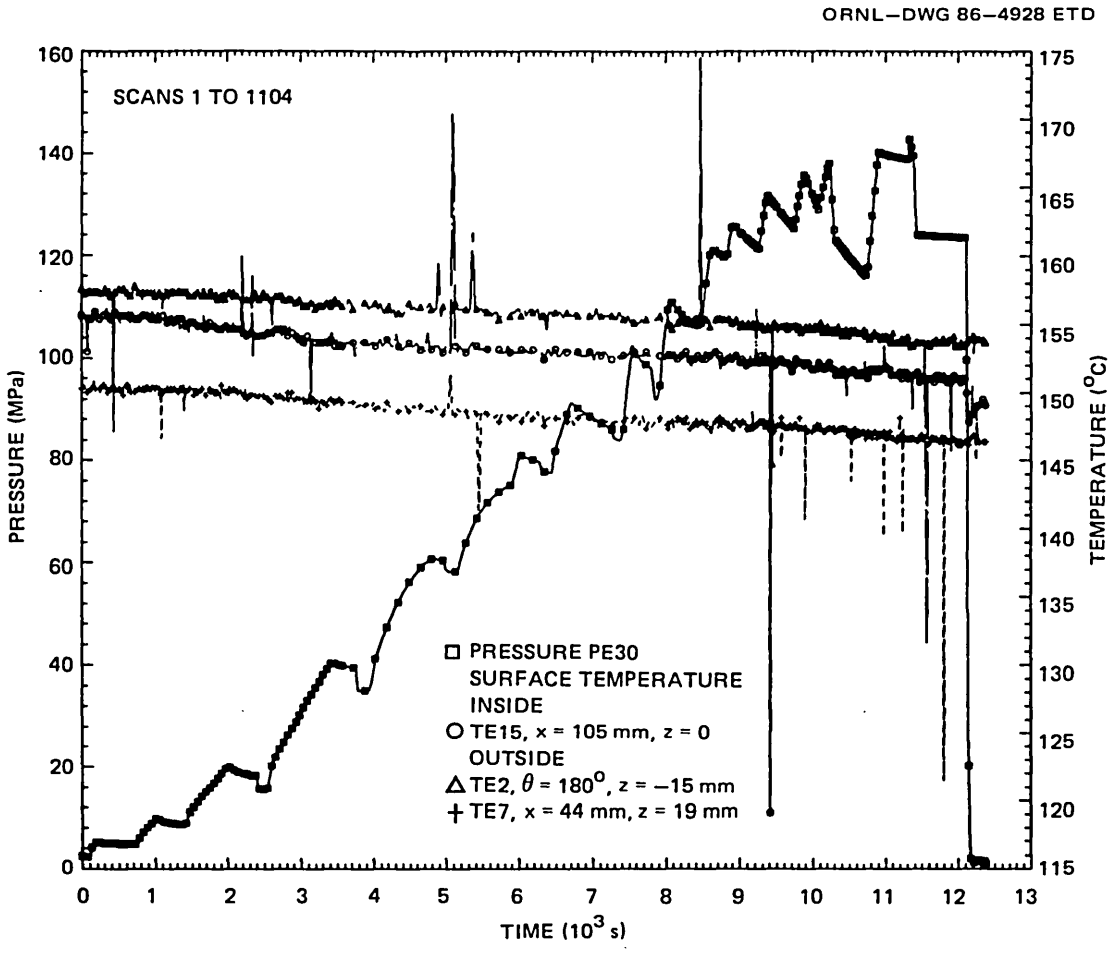

Fig. 4.15. Pressure and temperature vs time during V-8A test.

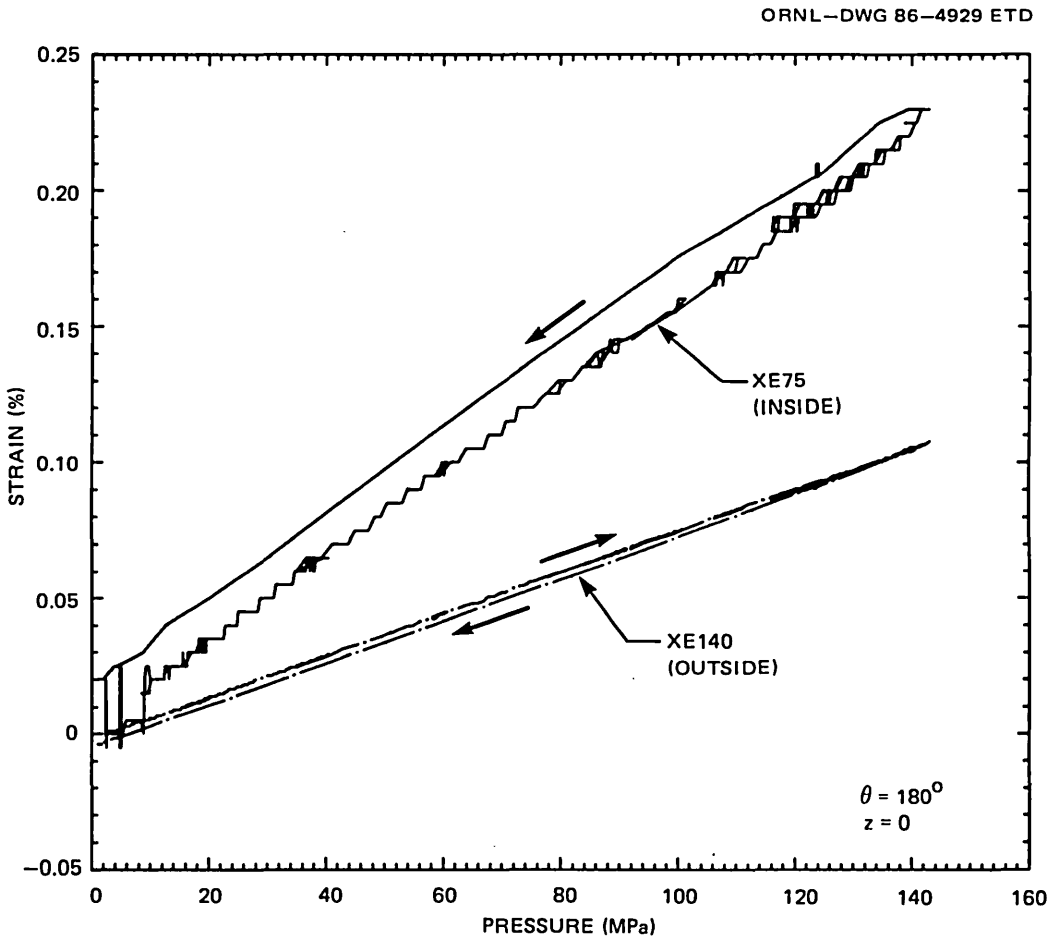

Fig. 4.16. Inside and outside surface strain vs pressure at the beltline at θ = 180°.

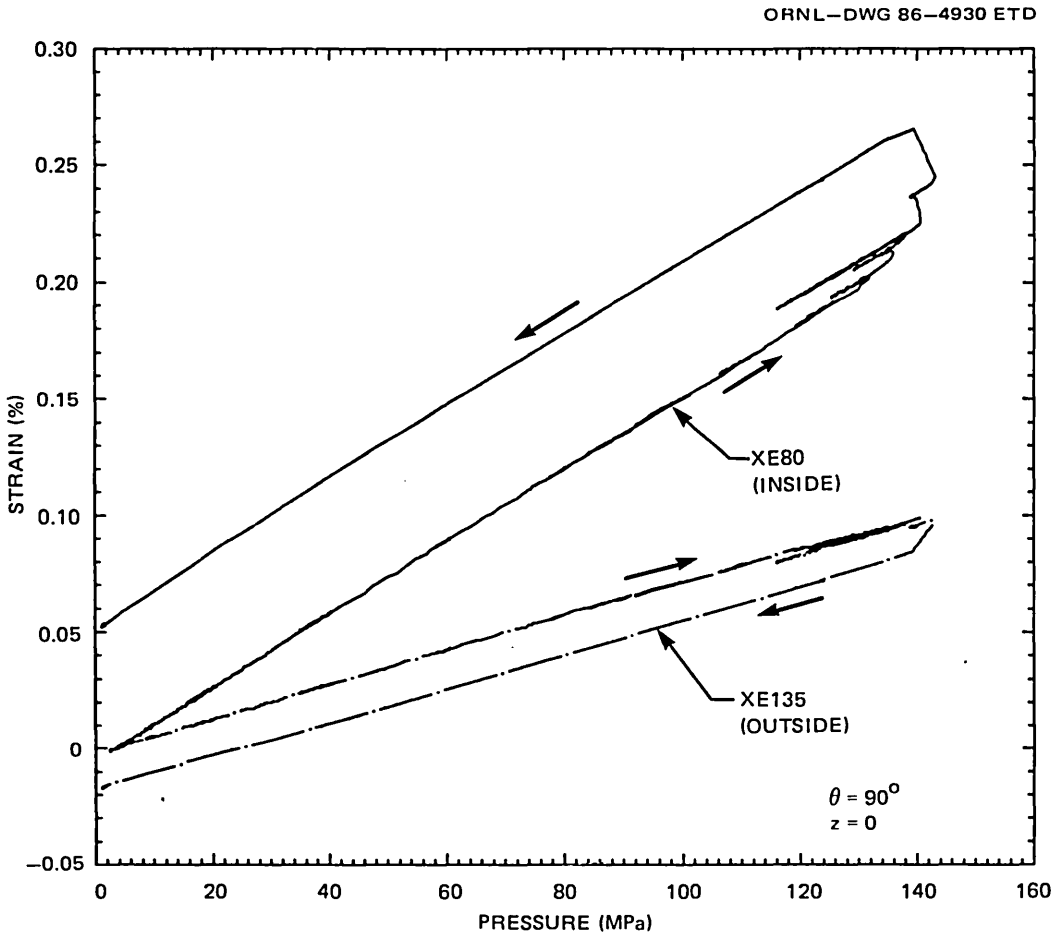

Fig. 4.17. Inside and outside surface strain vs pressure at the beltline at θ = 90°.

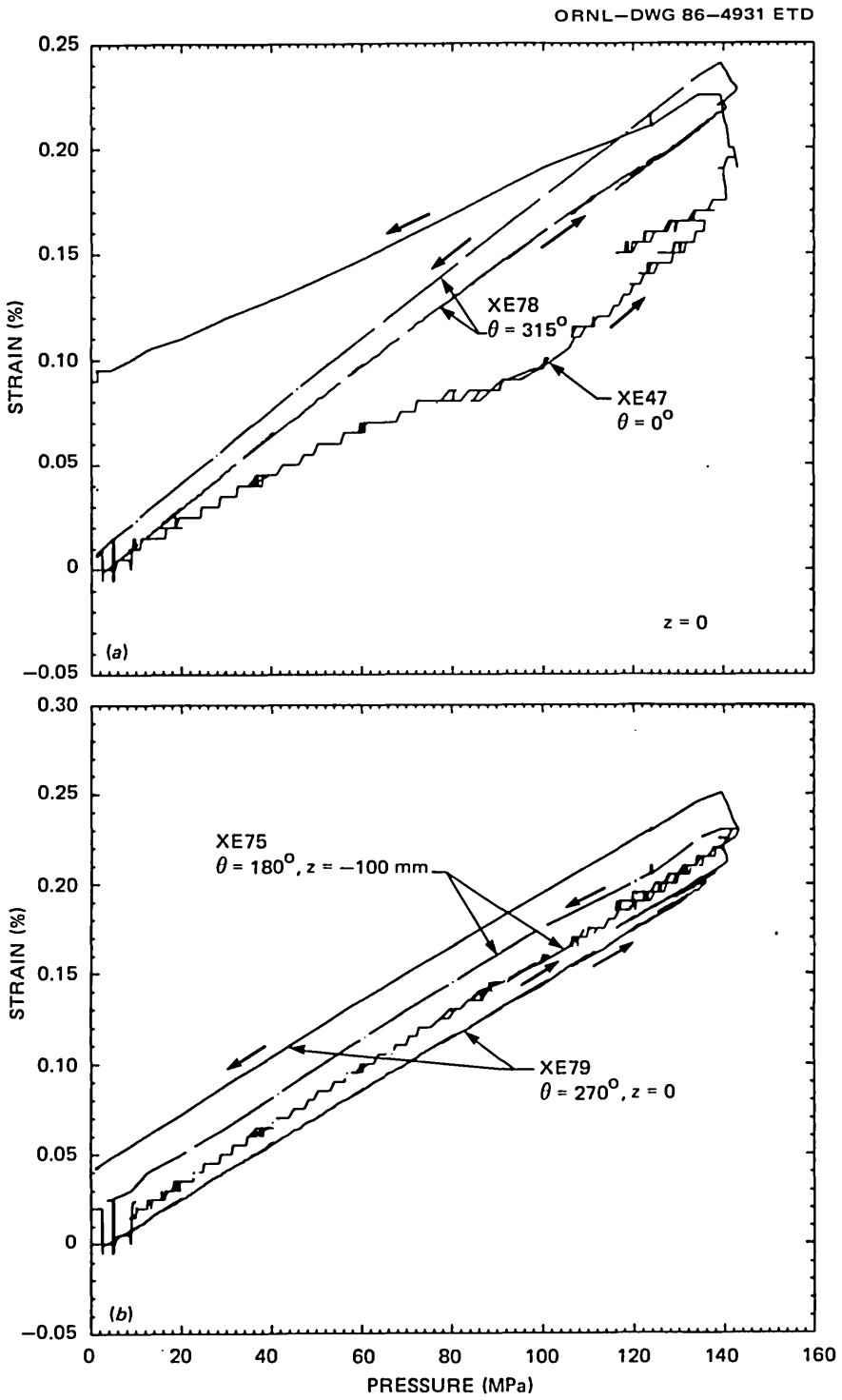

Fig. 4.18. Inside surface strain vs pressure at or near the beltline at various azimuths. (*a*) θ = 0 and 315°, (*b*) θ = 180 and 270°.

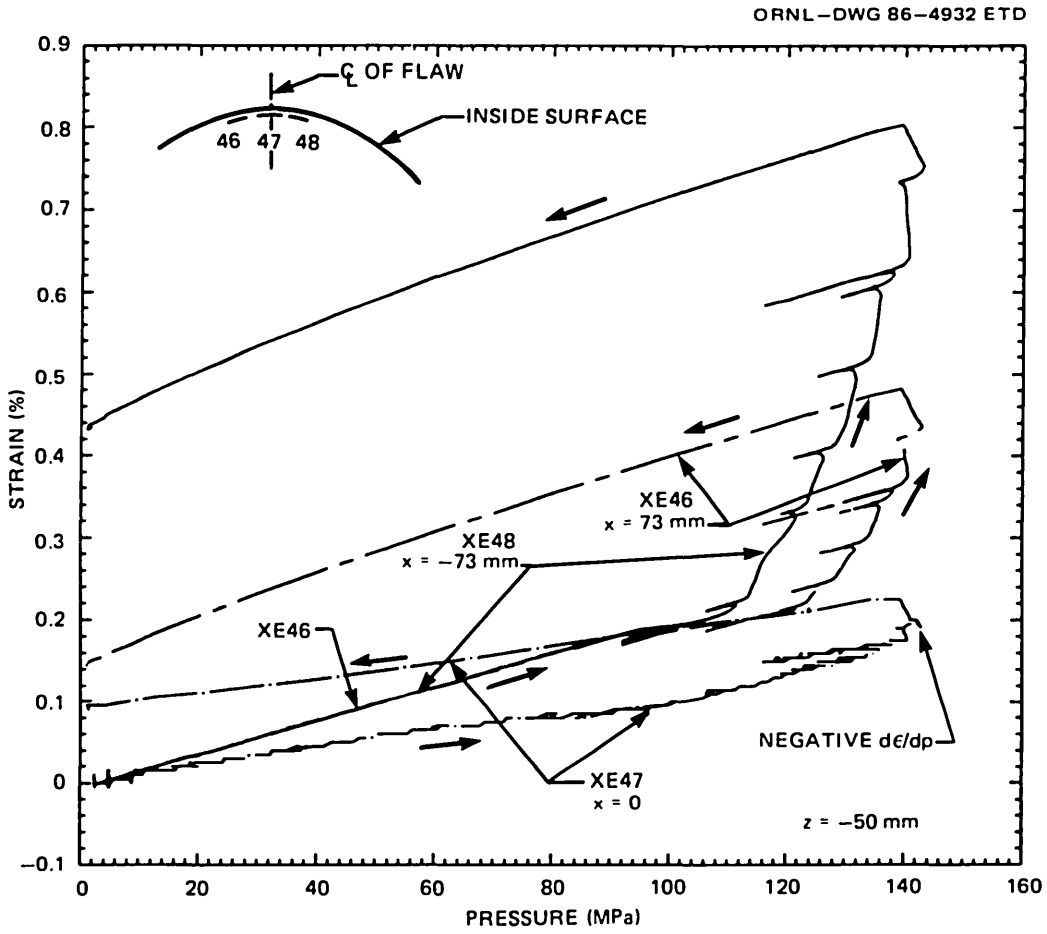

Fig. 4.19. Inside surface strain vs pressure in or near the plane of the flaw.

4.4.3 Crack-mouth-opening displacement

Three CMOD sensors, ZT150, ZT152, and ZT153, were located at positions z = —100, 0, and 100 mm, respectively, from the center of the flaw. The centerlines of these three sensors were 25.4 mm from the outside surface of the vessel. The fourth CMOD sensor, ZT151, was mounted at z = 0 mm, 50.8 mm from the surface. Figure 4.20 shows the typical displacement of the crack mouth throughout the test for the 16 increments of pressure. Figure 4.21 shows CMOD as a function of pressure. The effect of yielding near the flaw is clearly seen in increment 8, when pressure first exceeded 93 MPa. Sensor ZT151 is the only CMOD gage that did not exceed its recordable range in the test. The other three sensors reached their recordable limit of 3.1 mm during the 16th increment and remained beyond this limit thereafter, even with complete unloading. This observation is consistent with the residual displacement of 3.9 mm measured by ZT151 (Fig. 4.21).

4.4.4 Stable crack tearing

CMODs were recorded to provide a basis for calculating changes in stable crack depth and to identify the onset of tearing instability. UT pulse-echo signals of surface and crack-tip reflections were recorded to provide direct measurements of crack-tip locations at each of seven points along the length of the crack.

Plans to calculate crack depth from CMOD were not realized. Values of dCMOD/dp needed to be determined precisely at each increment of pressure. Because of excessive seal leakage, pressure could not be maintained at constant levels long enough to make precise observations of stable displacements. From previous experience with vessel tests, it was expected that constant loads would have to be maintained for periods ranging from a few seconds to a few hundreds of seconds. At higher pressures, which involve larger regions of plasticity, it requires longer times for strains and displacements to approach steady state values after load changes.

To illustrate the problem encountered in the V-8A test, pressure and CMOD changes are shown in Fig. 4.22 for three increments. At low pressures, as shown in Figs. 4.22(*a* and *b*), CMOD responded promptly to changes in pressure. The short periods of nearly constant pressure before and after the unloading phases appear to be satisfactory for computing dCMOD/dp. In the next increment, shown in Fig. 4.22(*c*), however, the pressure is never constant; because the ratio of dCMOD/dt to dp/dt changes with time during the unloading phase, there is no unambiguous indication of a steady state dCMOD/dp.

During increment 10, in which the pressure reached 120 MPa for the first time, the lagging of CMOD variations relative to pressure variations is clear, as shown in Fig. 4.23. At this stage of the test it would have been useful to have depressurized the vessel and held pressure constant for a few minutes to determine whether stable tearing had occurred, but excessive seal leakage precluded that procedure. This step was not taken because a dense cloud of water vapor, emanating from the

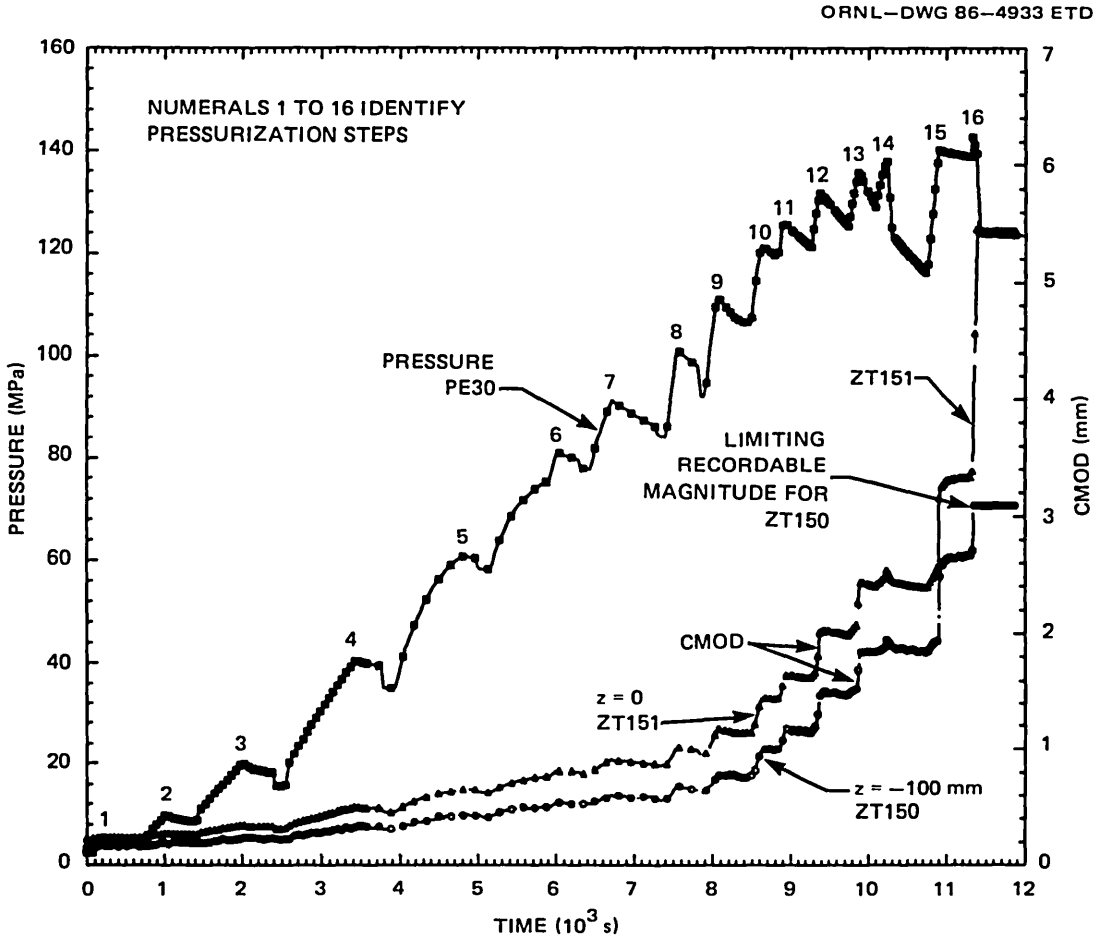

Fig. 4.20. Pressure and CMOD vs time during all 16 increments of pressure.

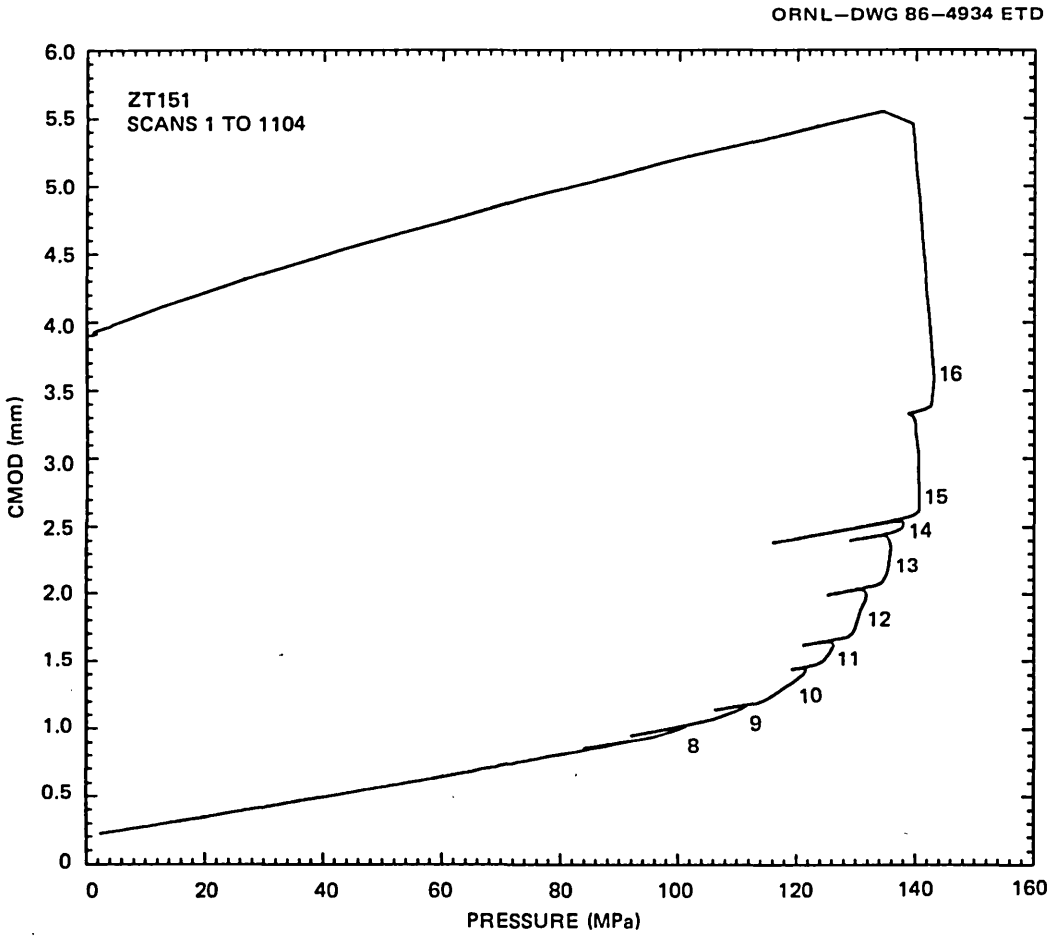

Fig. 4.21. CMOD at center of flaw vs pressure for entire test.

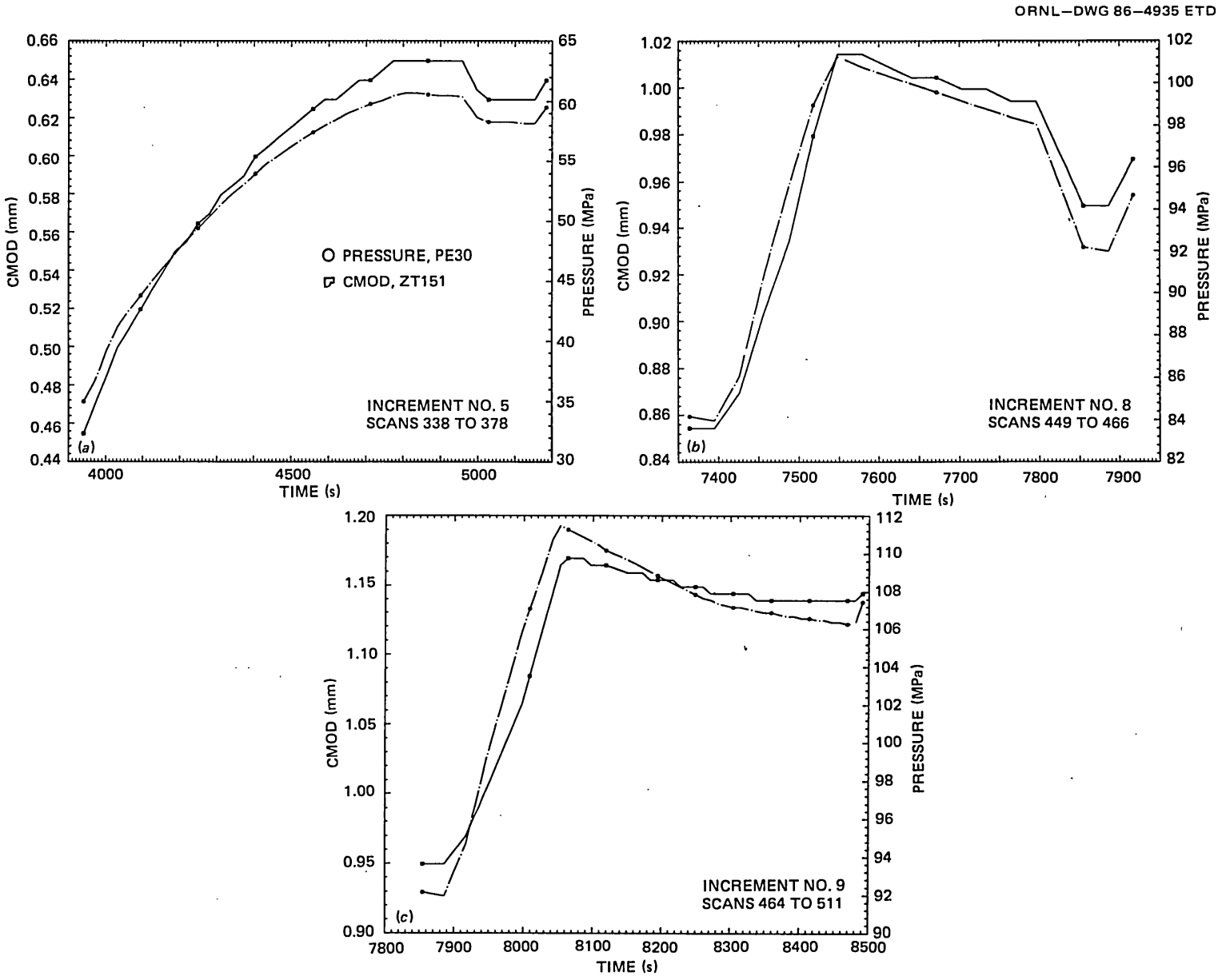

Fig. 4.22. Pressure and CMOD vs time for intervals illustrating prompt response of displacement to changes in load. (*a*) Pressure increment 5, (*b*) increment 8, and (*c*) increment 9.

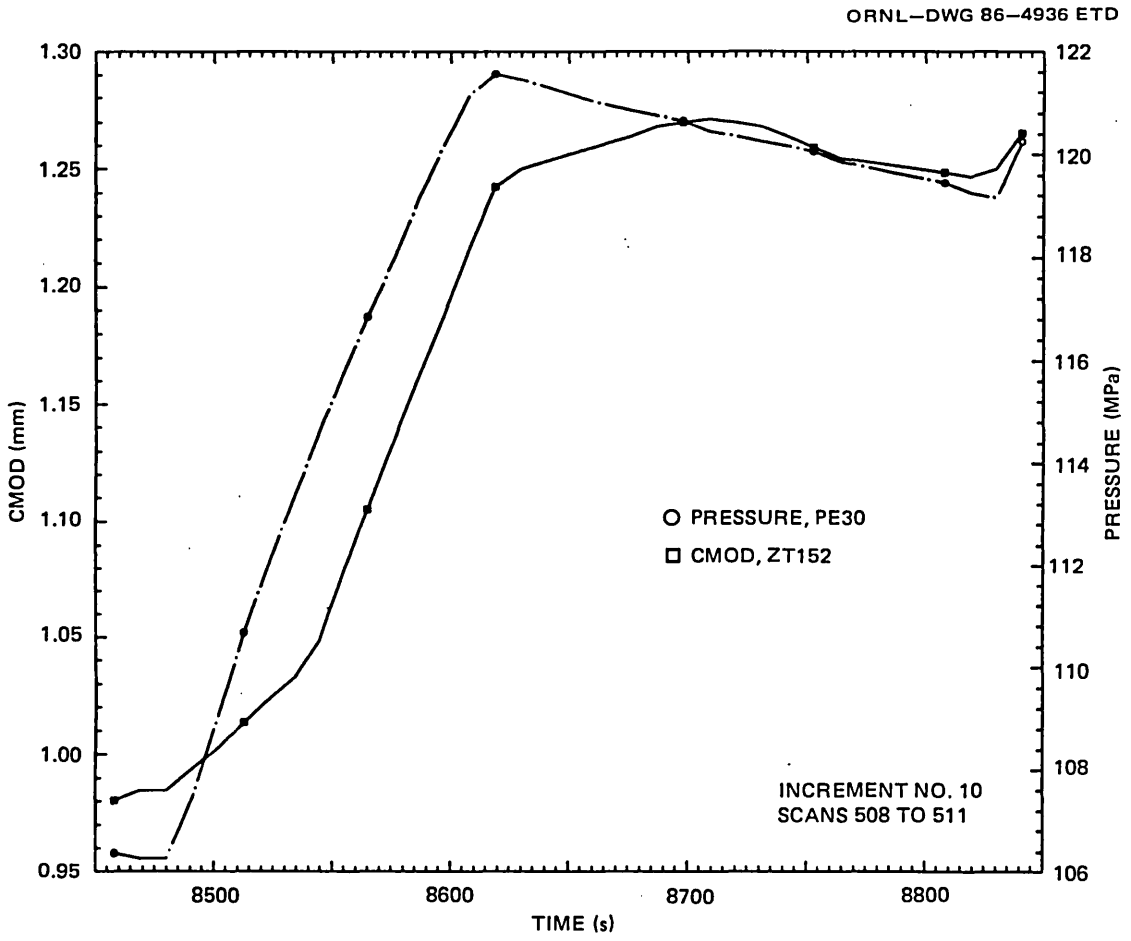

Fig. 4.23. Pressure and CMOD vs time for pressure increment 10, which illustrates delayed response of displacement for changes in load.

vessel head, was observed on the video monitor. It was decided to proceed with the test as quickly as possible to minimize the risk of a complete failure of a seal before a tearing instability could be produced.

The first positive indication of stable tearing came from UT observations during the 12th and 13th increments, identified in Fig. 4.20. A careful reexamination of recorded data indicated that, at a location near the center of the crack (at transducer No. 2), the crack grew in depth ~6 mm. In this time period, the pressure peaks were ~132 and 136 MPa, as shown in Fig. 4.20. The other transducers near the center of the flaw (Nos. 1, 3, and 6) indicated no change during this phase of the test. The next change in crack depth was observed ultrasonically during the 15th increment of pressure, when changes in depth of 1.4 and 4 mm were noted by transducers No. 2 and 6, respectively. This crack growth coincided with the incidence of the first tearing instability, which is discussed in the next section. Therefore, it is likely that the stable growth did not include most of the change observed in this increment.

The UT observations for the entire test are summarized in Table 4.3 and Fig. 4.24. The appearance of the flaw surface after the test (Fig. 4.24) has no features that conclusively demarcate areas associated with separate phases of stable tearing. There was no indication of lengthwise crack growth prior to the start of tearing instability.

Figure 4.24 shows that the UT observation of the initial tip of the crack was accurate at transducer position 1, where the crack depth varied only slightly over the width of the transducer. The observations were less accurate at positions 3 and 6. In each of these positions, however, the reflection from the tip of the crack nearest one edge of the transducer accurately represents the initial location of the crack. The other initial and final crack locations will be discussed in the last section of this chapter.

Fortuitously, the instability indicator $\dot{v}$, described in Sect. 4.2, gave indirect evidence of the portion of the test in which stable tearing occurred. When the vessel is in a predominantly elastic state with no tearing, the magnitude of the fluctuations of $\dot{v}$ will be theoretically proportional to $1/p$ times the fluctuations of $\dot{p}$. This is evident in the early record of $\dot{v}$ vs time in Fig. 4.25, from t = 0 to 5000 s. The figure shows the record of $\dot{v}$ as a function of time throughout the 16 increments of pressurization. The fluctuations of $\dot{v}$ were remarkably low from t = 5000 to 9000 s, the latter time coinciding with the start of the period during which UTs indicated the first crack growth. The sudden increase in amplitude at 9000 s and its persistence thereafter is possibly associated with a continual crack-growth process that started during the 12th pressure increment. A portion of the strip-chart recording of $\dot{v}$ and CMOD vs time for the 15th and 16th increments is shown in Fig. 4.26. This continuous recording shows the two peaks in $\dot{v}$ that mark the instabilities. The earlier peak did not appear in the CCDAS record because it fell within the 6-s interval between two successive data scans.

Values of the derivative dCMOD/dp as a function of pressure during pressure increments were examined for evidence of tearing. These values are shown in Fig. 4.27 for pressure increments 8–15. For each of these increments, except 8, two values are shown joined by a line. The lower of the two values represents dCMOD/dp at the start of the pressurization increment. In increments 9–15, for which Fig. 4.23 shows a typical CMOD

Table 4.3. Summary of UT observations of locations of crack tip[a]

Pressure increment No.	Time (s)	Transducer No. 1	2	3	4	5	6	7
		Axial distance (z) of transducer from center of flaw (mm)						
		0	−50	−100	−150	−200	75	150
1 to 12	0 to 9263	a = 85.5	76.4	66.5			80.5	
12	9263 to 9441		a change 2.8 mm					
13	9681 to 10,101		a change 2.8 mm					
15	10,750 to 10,921		a change 1.4 mm Amplitude[b]	Amplitude[b]			a change ~4 mm	
16	11,336 to 11,411		a change 9.9 mm	a change ~19 mm			a change ~11 mm	
16	11,337					a = 42.5[c]		
	After 11,411	a = 94.5	93.4	84.5		42.5	94.5	

[a]Initial and final crack depths are based on the posttest measurement of the unnecked wall thickness at the flaw of 141.3 mm; crack depth a in mm.

[b]Amplitude of the signal reflected from the crack tip increased.

[c]First indication of a reflection.

ORNL PHOTO 6781–83B

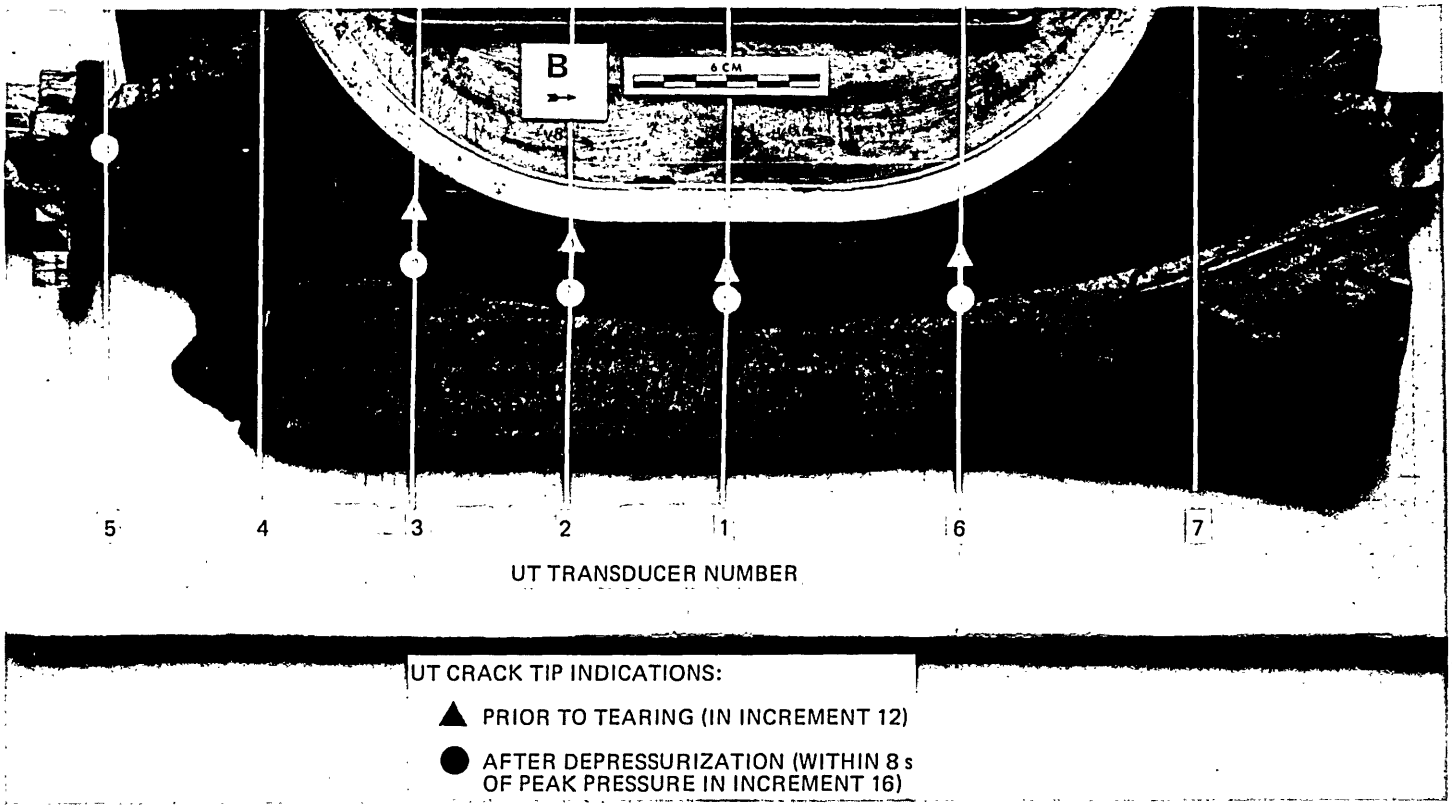

Fig. 4.24. Initial and final crack-tip locations indicated by ultrasonic observations.

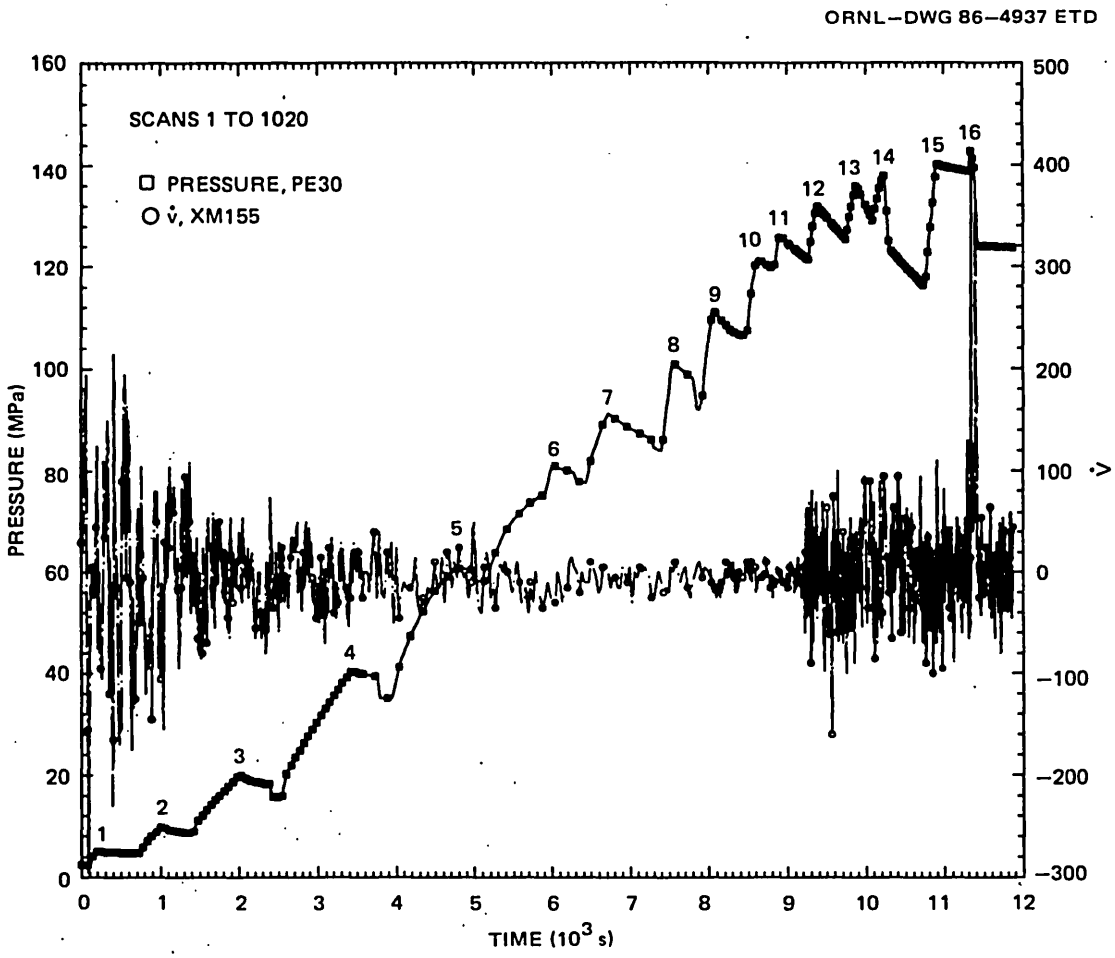

Fig. 4.25. Pressure and $\dot{v}$ vs time for all loading increments.

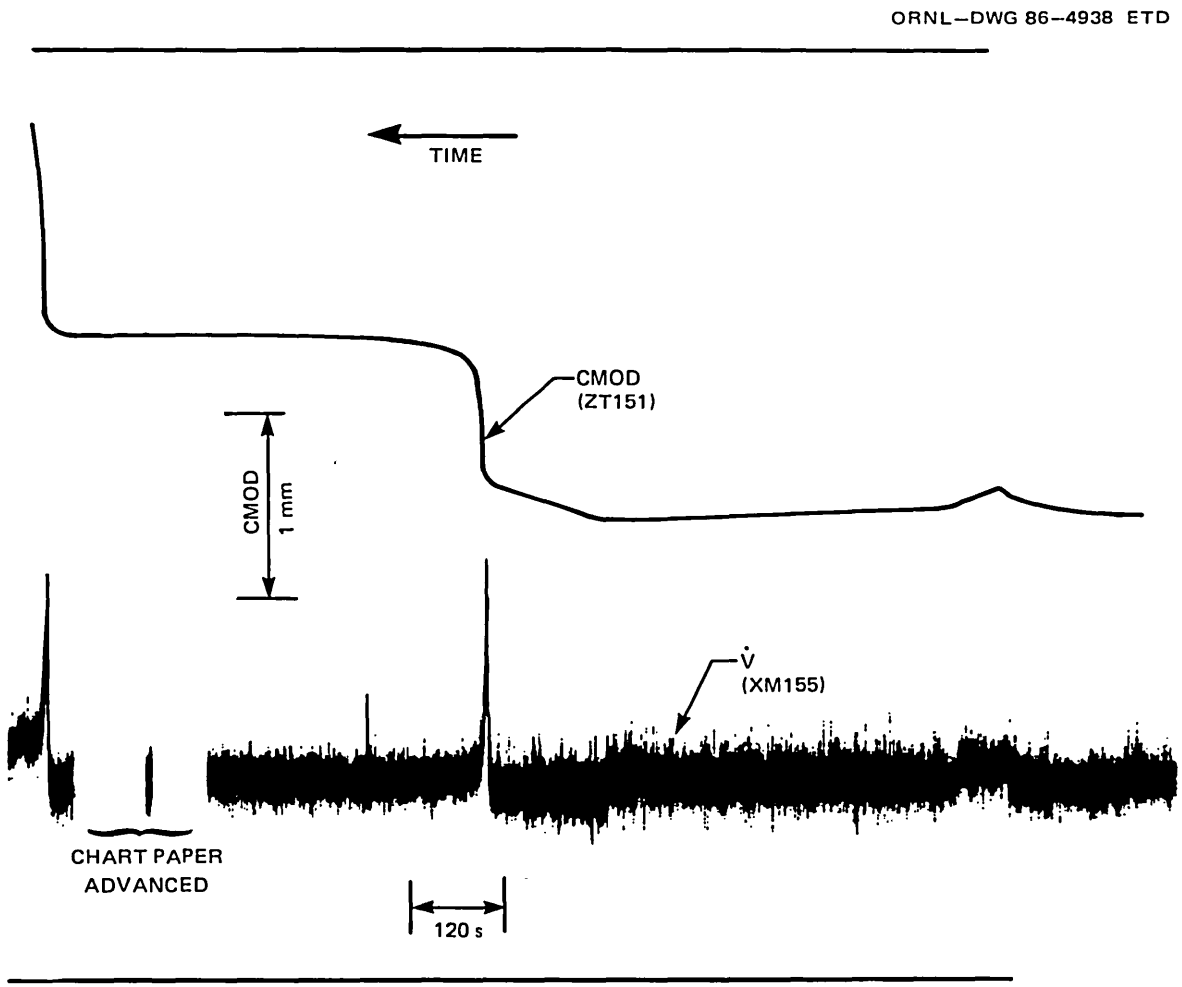

Fig. 4.26. Strip-chart record of CMOD and $\dot{v}$ during pressurization increments 15 and 16.

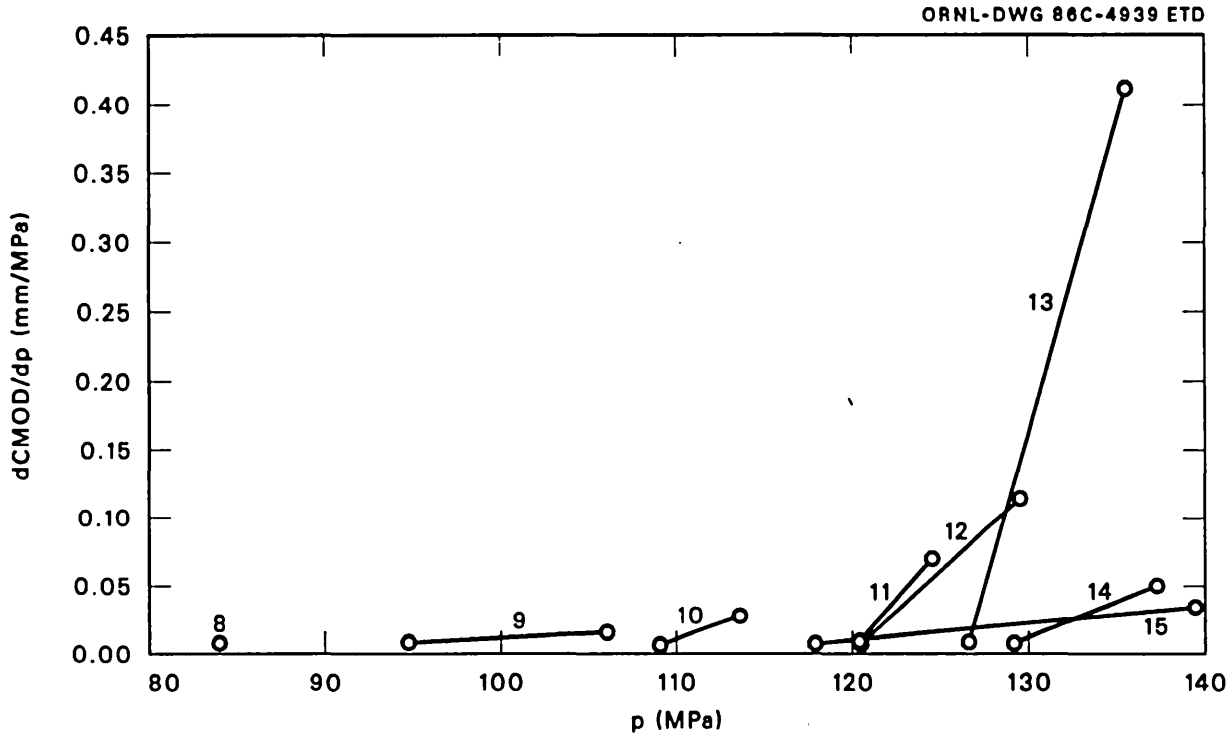

Fig. 4.27. dCMOD/dp vs pressure for pressurization increments 8–15.

response, the rate of change of CMOD is low in the early part of the increment and distinctly higher later. The large values of dCMOD/dp, shown in Fig. 4.27 for increments 12 and 13, suggest that most of the stable tearing occurred during those two increments.

4.4.5 Tearing instability

A condition of incipient instability exists when changes in displacements persist while the loading is constant. In this test, pressure was never constant long enough to apply this simple definition of instability. CMODs were the principal indicators of instability.

Two instability occurrences inferred from the V-8A test data are identified in Fig. 4.28, which shows CMOD and pressure vs time for portions of pressurization increments 15 and 16. In each instability the CMOD increased suddenly; after the onset of the rapid change in CMOD, dCMOD/dp was much greater than before; and the positive change in CMOD persisted for a significant time during the subsequent depressurization.

The instability events are unambiguous, but the loadings that caused unstable tearing are not precisely known. In the preceding section it was observed that displacement changes lagged pressure changes after increment 9. One can observe in Fig. 4.29(*a*) that the rapid decrease in CMOD after pressure increment 14 is 6 to 12 s later than the pressure drop. Figure 4.29(*b*) shows a similar effect for a more moderate pressure drop, for which the lag is ~24 s.

Just prior to the time of the pressure peak in increment 15, dCMOD/dp was ~0.035 mm/MPa, a value not strongly suggestive of tearing (see Fig. 4.27). Thereafter, the large change in CMOD is the result of unstable tearing. During the 24 s preceding the pressure peak, the pressure rose from 136.5 to 140.5 MPa. The flaw had been stable during the preceding increment, which reached 138.0 MPa. These observations indicate that the load causing the first tearing instability could have been any value between 138.0 and 140.5 MPa. However, dCMOD/dt decreased remarkably by the time the load dropped to 140.0 MPa. It is quite likely that the slow increase in CMOD during the following 300 s was principally the result of yielding of the vessel in the region of the flaw.

The second unstable change in CMOD occurred in the 16th pressurization increment at t = 11,333 to 11,338 s, as shown in Fig. 4.30. The pressure increased from 142.6 to 143.0 MPa in this time interval. Fifteen seconds before this manifestation of a tearing instability, the pressure was between 140.0 and 140.7 MPa.

4.4.6 Posttest examination of flaw

After the test the outside surface was visibly deformed at both ends of the flaw, and short tears from the ends were evident, as shown in Fig. 4.31. The tears ran about 14 and 4 mm from the top and bottom ends, respectively, of the flaw.

A block of material containing the V-8A flaw was removed from the test vessel [Fig. 2.7(*a*)], chilled in liquid nitrogen, and split along the fracture plane by wedge-loading the machined opening of the flaw. This splitting did not uncover the fracture surfaces at the two ends of

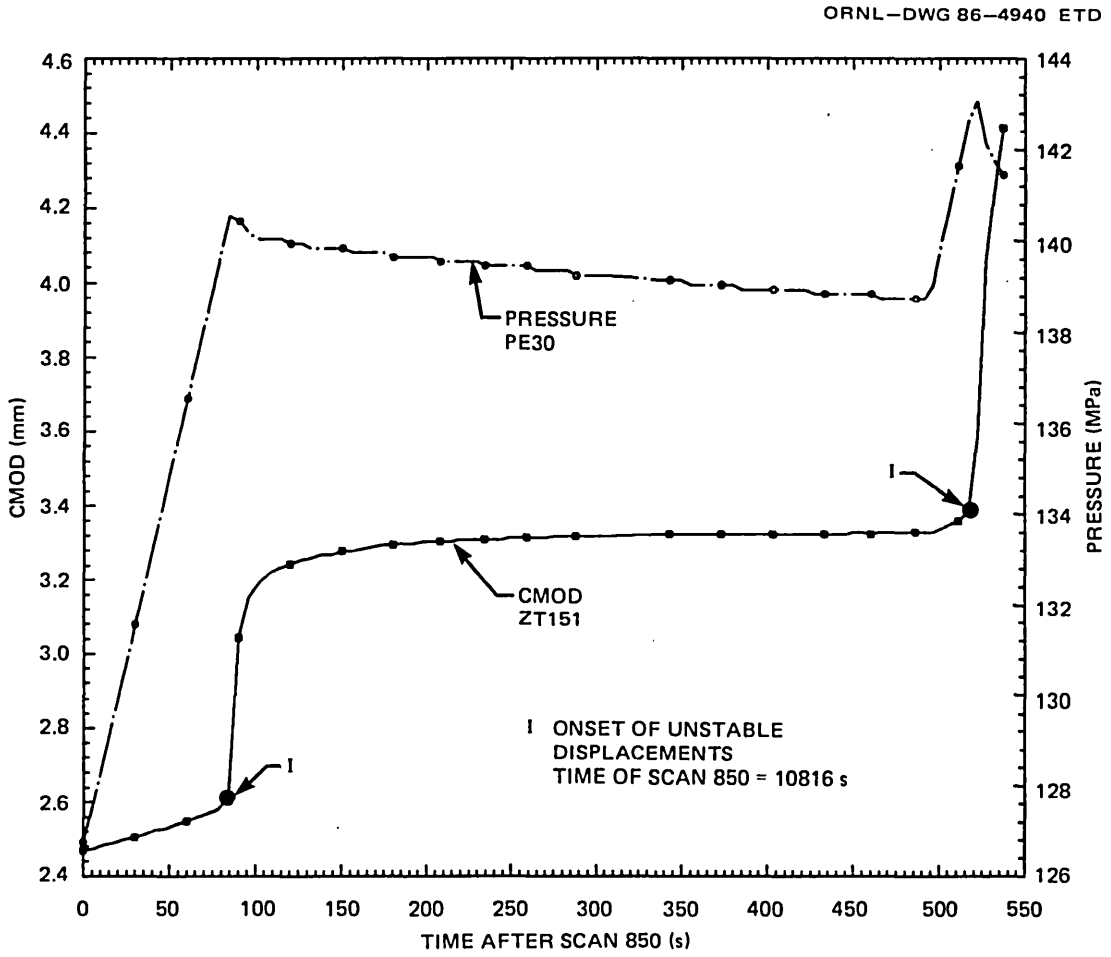

Fig. 4.28. CMOD and pressure vs time during pressurization increments 15 and 16.

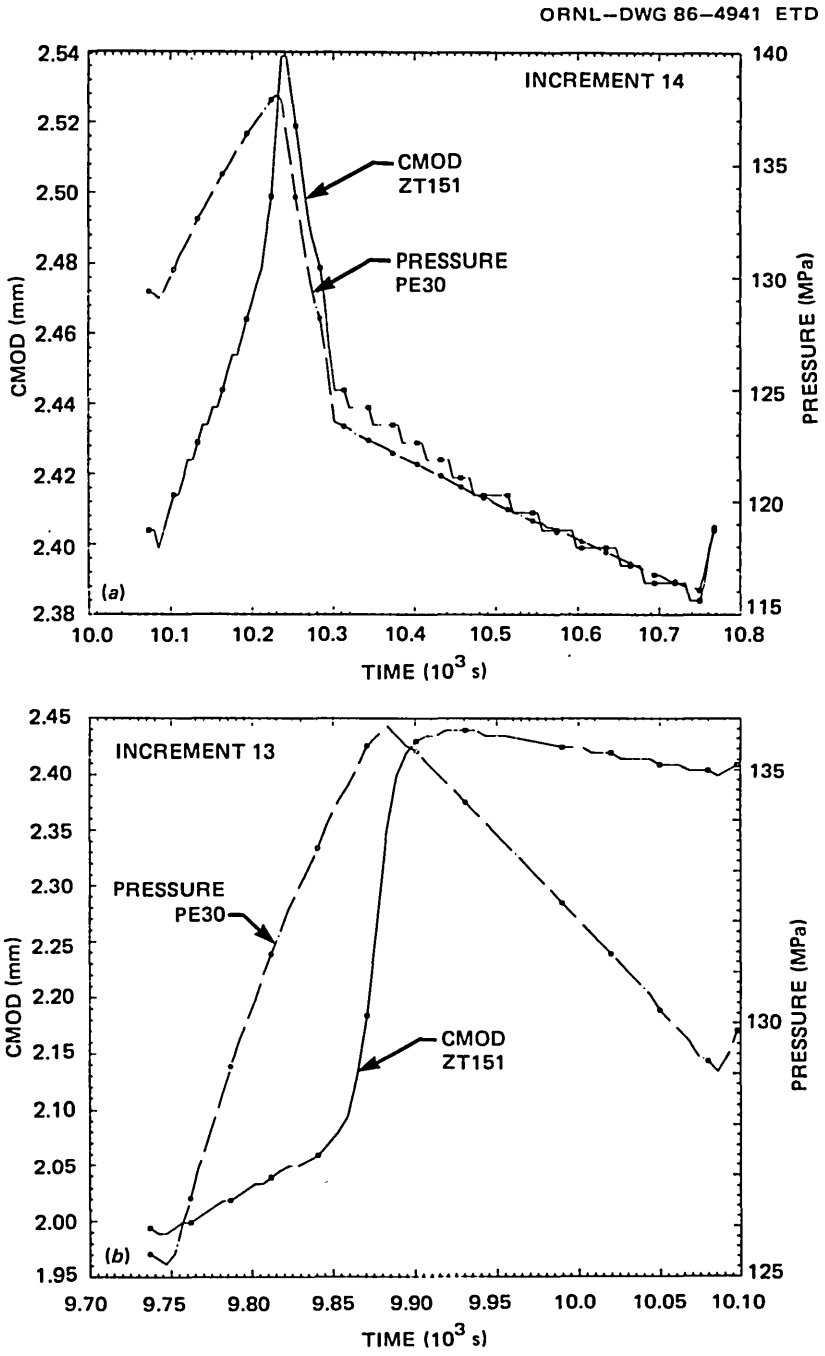

Fig. 4.29. CMOD and pressure vs time for two pressurization increments: (*a*) 14 and (*b*) 13. Peak pressures preceded peak CMODs by 6 to 24 s.

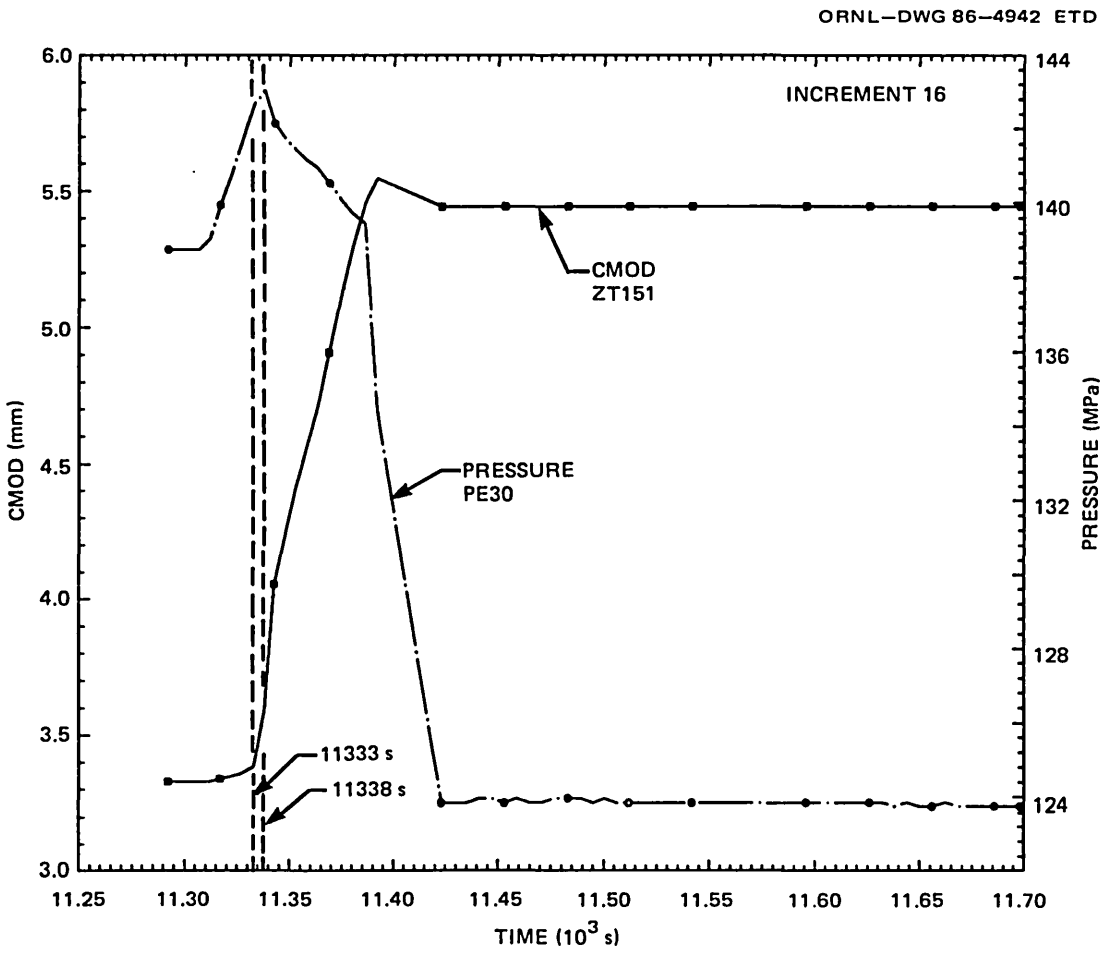

Fig. 4.30. CMOD and pressure vs time for pressurization increment 16.

ORNL PHOTO 5691–86

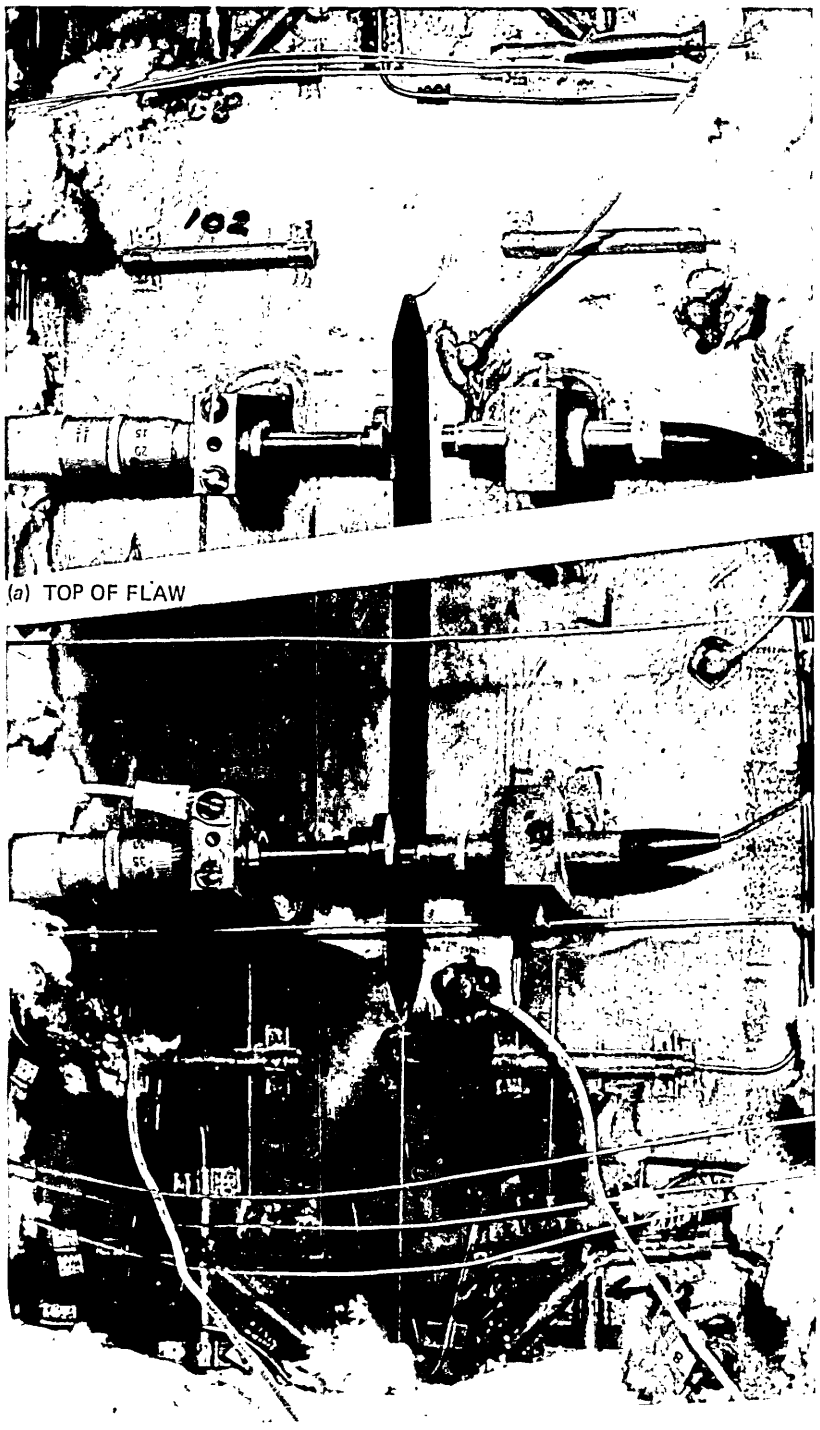

(*a*) TOP OF FLAW

(*b*) BOTTOM OF FLAW

Fig. 4.31. Posttest photographs of the outside surface of the vessel at the ends of the flaw. In (*a*) a short tear and deformation (a depression) at the top end of the notch is visible; in (*b*) the deformation at the end of the notch can be seen more clearly.

the flaw. Therefore, it was necessary to resection the two halves of the split block, chill the pieces in liquid nitrogen, and wedge apart the unopened portions of the fracture surfaces. This process produced about 20 fragments containing some portion of the fracture surfaces developed during the V-8A test.

The two complete fracture surfaces were reconstructed so that precise measurements of the flaw could be made. Photographs of the matching surfaces, labeled surface A and surface B, are shown in Figs. 4.32 and 4.33. The widths of saw cuts were measured and accounted for in reassembly of the surfaces. The V-8A flaw attained a depth of 101.4 mm and a length of 453.0 mm.

Measurements of the locations of features of fracture surface B were made under a low-power microscope with a scale graduated in 0.5-mm units. Important features are described here; a larger set of flaw photographs and additional dimensional information are given in Appendix N.

The entire ductile fracture surface consists of large relatively smooth areas interrupted by a few bands of shear tears from one to a few millimeters wide (Fig. 4.33). Except at the intersections of the flaw with the outside surface of the vessel, the shear bands are axially oriented. With oblique illumination, the fracture surface appears striated parallel to the fatigue crack front as illustrated in Fig. 4.34. Neither the striations nor the shear bands have been correlated with specific phases of the pressure loading during the test. Additional details on features shown in Fig. 4.34 are in Appendix N.

Features of the ductile fracture corresponding to particular phases of tearing are illustrated by the photograph in Fig. 4.35 and by a cross section of this part of the flaw in Fig. 4.36. Cross section 3-3, which contains crack features I, J, and H (Fig. 4.35), lies 5 mm from the centerline of UT transducer No. 2. This is the only transducer that sensed crack growth prior to the onset of the first tearing instability. At this section the crack grew stably by ~6 mm, according to the UT observation. The total crack growth indicated ultrasonically (i.e., after unstable tearing ceased) was 17 mm, which compares well with the directly measured value of 13.6 mm at this section. If one assumes that the changes in crack depth indicated ultrasonically are correct, this implies that the deepest stable crack front segment lay ~3 mm deeper than the feature at point J. Three other transducers (Nos. 1, 3, and 6) sensed crack-tip positions at both the beginning and end of the test, and one (No. 5) sensed a position only after tearing ceased. Shown in Fig. 4.24, these final positions are all at a shear band rather than the final crack tip. This may be a fortuitous coincidence. The reflection indicated by transducer 5 was evidently from the more distant tip of the crack or some nearby feature.

ORNL PHOTO 6782-83

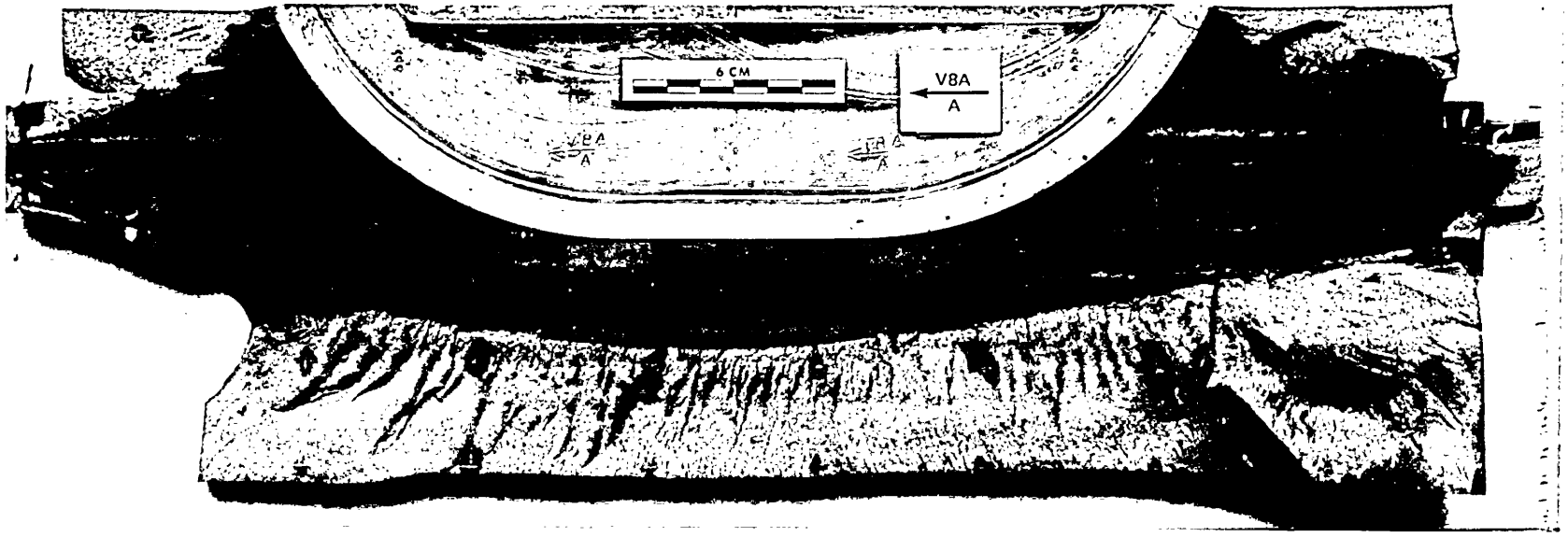

Fig. 4.32. Photograph of the composite of fracture surface A. The arrow points toward the vessel closure. Lighter areas are brittle fracture zones generated in breaking the block.

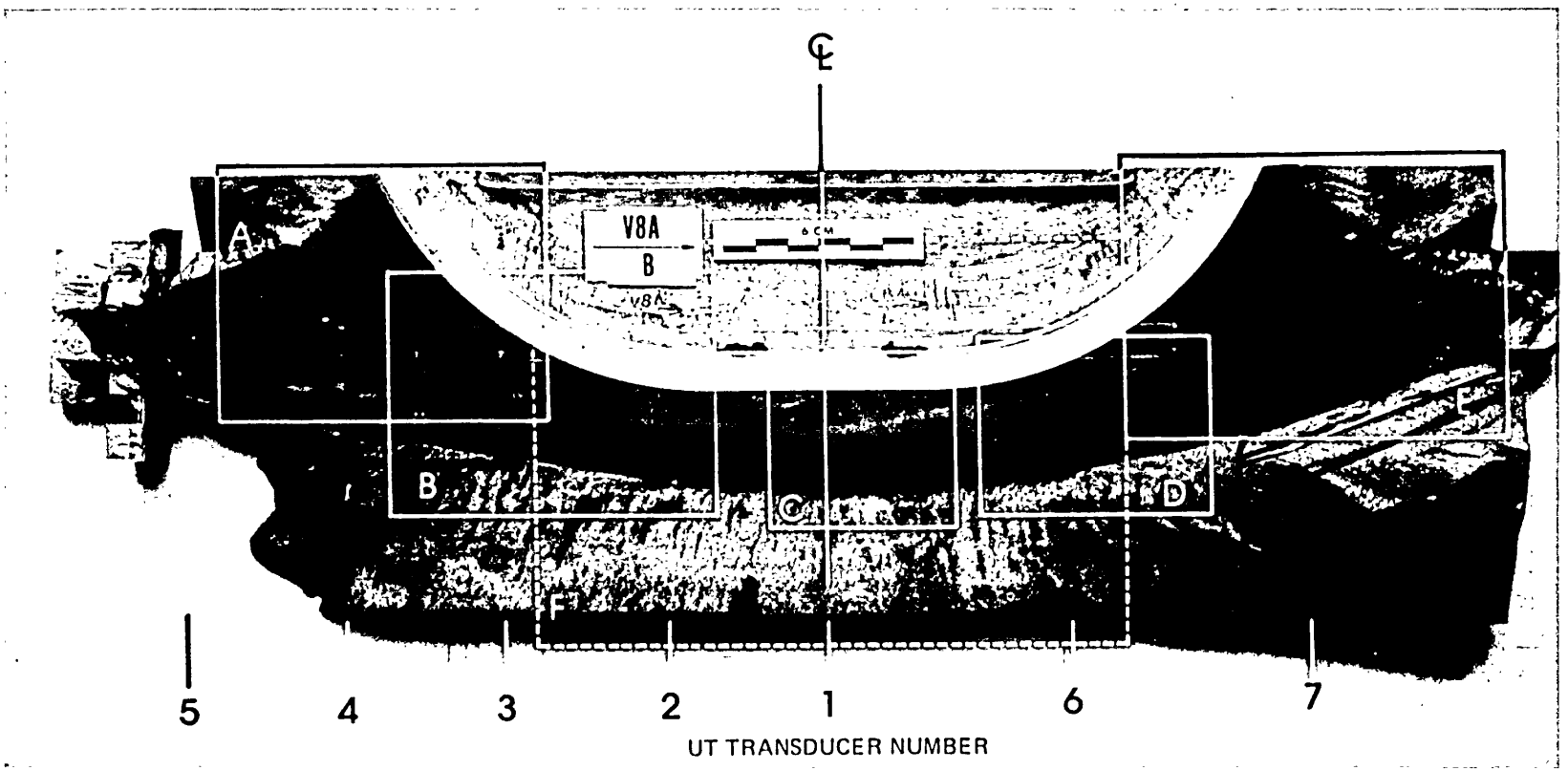

Fig. 4.33. Photograph of the composite of fracture surface B. The arrow points toward the vessel closure. Areas shown in more detail in subsequent figures are identified here. Lighter areas are brittle fracture zones generated in breaking the block.

M&C PHOTO Y187558A

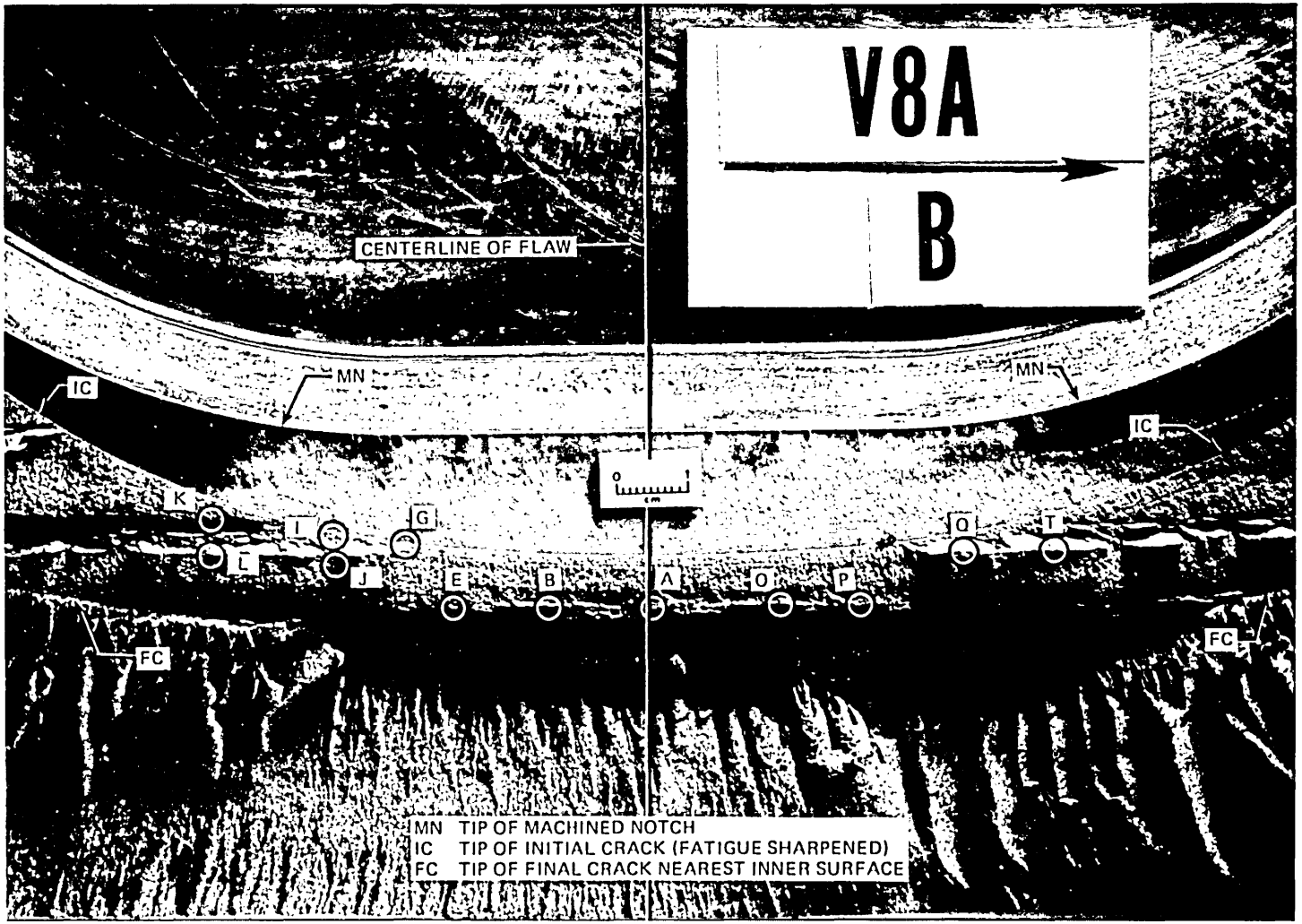

Fig. 4.34. Area F of fracture surface B (of Fig. 4.33), showing a portion of the fracture surface from the deepest part of the flaw. Labeled features are described in detail in Appendix N.

M&C PHOTO Y187562B

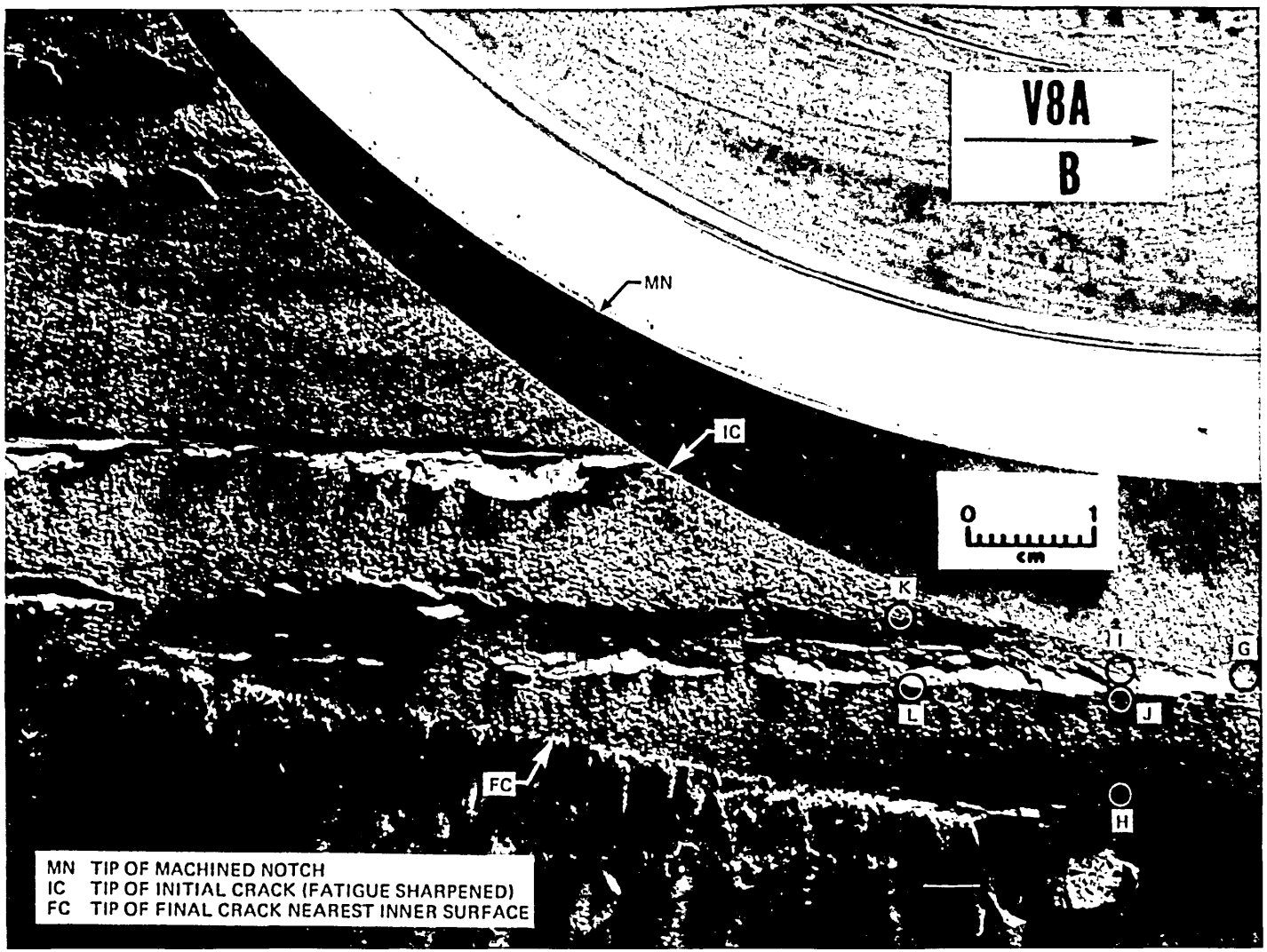

Fig. 4.35. Area B of fracture surface B (of Fig. 4.33), showing features of the fracture surface that have been correlated with ultrasonic observations made during the test.

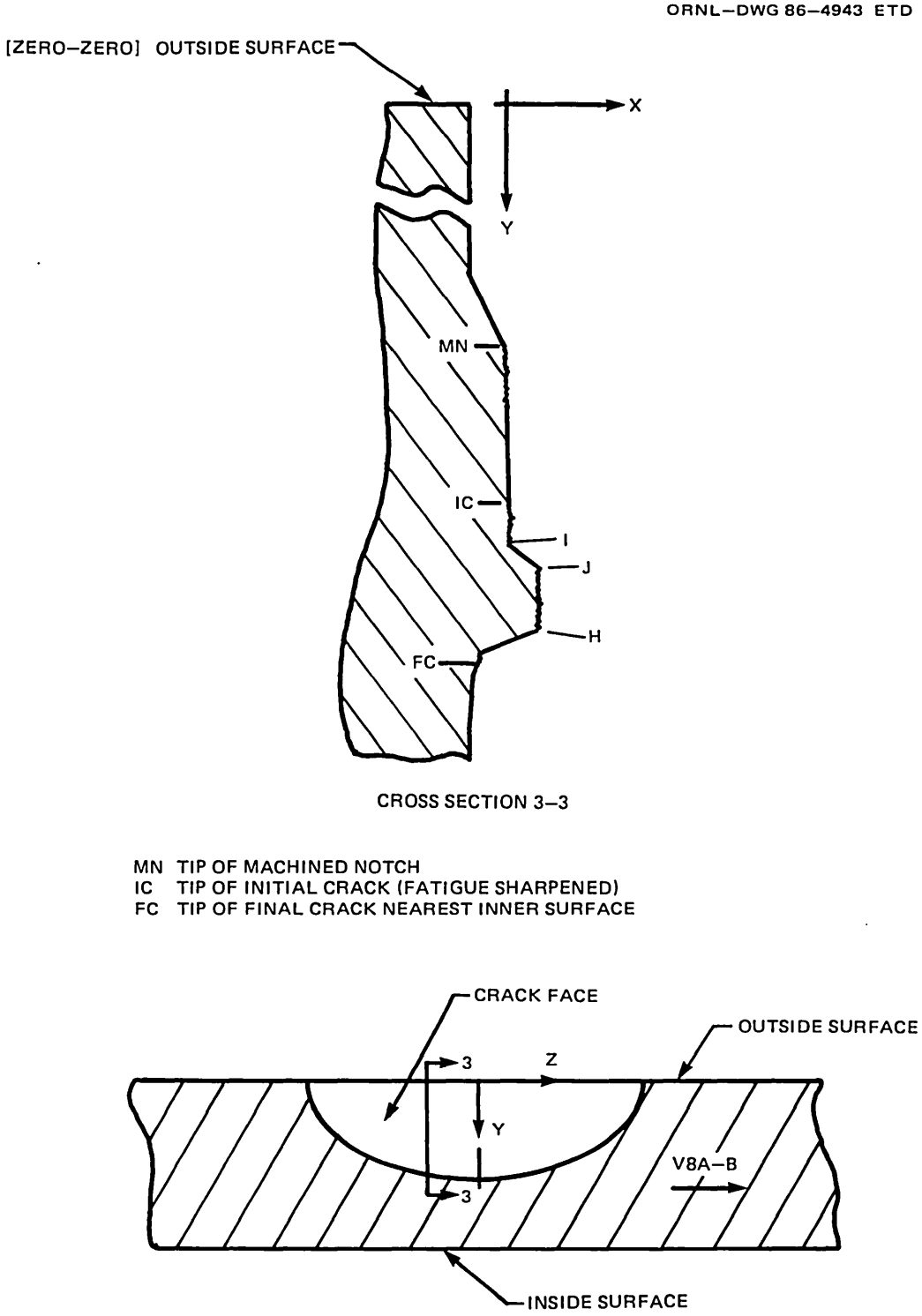

Fig. 4.36. Cross section of area B of fracture surface B shown in Fig. 4.35.

References

1. R. W. Derby et al., *Test of 6-in.-thick Pressure Vessels. Series 1: Intermediate Test Vessels V-1 and V-2*, ORNL-4895, Union Carbide Corp. Nuclear Div., Oak Ridge Natl. Lab., February 1974.

2. R. H. Bryan et al., *Test of 6-in.-thick Pressure Vessels. Series 2: Intermediate Test Vessels V-3, V-4, and V-6*, ORNL-5059, Union Carbide Corp. Nuclear Div., Oak Ridge Natl. Lab., November 1975.

3. J. G. Merkle et al., *Test of 6-in.-thick Pressure Vessels. Series 3: Intermediate Test Vessel V-7*, ORNL/NUREG-1, Union Carbide Corp. Nuclear Div., Oak Ridge Natl. Lab., August 1976.

4. J. G. Merkle et al., *Test of 6-in.-thick Pressure Vessels. Series 4: Intermediate Test Vessels V-5 and V-9*, ORNL/NUREG-7, Union Carbide Corp. Nuclear Div., Oak Ridge Natl. Lab., August 1977.

5. R. H. Bryan et al., *Test of 6-in.-thick Pressure Vessels. Series 3: Intermediate Test Vessel V-7B*, ORNL/NUREG-38, Union Carbide Corp. Nuclear Div., Oak Ridge Natl. Lab., October 1978.

6. C. L. Segaser, *System Design Description of the Intermediate Vessel Tests for the Heavy-Section Steel Technology Program*, ORNL/TM-2849, Union Carbide Corp. Nuclear Div., Oak Ridge Natl. Lab., June 1970, revised July 1973.

5. FRACTURE ANALYSIS

5.1 Development of Test Plan

5.1.1 Objectives

It was essential to the attainment of the vessel V-8A test objective that tearing controlled by the tearing resistance (J_R) curve of the material be distinguished from tearing promoted by a general or local plastic instability. Generally, as pressure is increased, the flaw will begin to tear at a load determined by the J_{Ic} of the material and continue to tear stably until a pressure is reached at which the flaw will continue to grow without further increase in load. This tearing instability can be produced in two ways. If tearing resistance is high enough, a flaw of a given size may not be prone to tear unstably until a local or general plastic instability develops, in which case the flawed region would deform without an increase in load. In this instance, the strain field around the flaw changes with time even if the flaw size and applied load do not. If, on the other hand, tearing resistance is low enough, a tearing instability will occur at a flaw size and applied load that cannot cause a plastic instability. In both cases, tearing eventually ensues, but in the latter situation the state of stress that caused the tearing instability is more clearly defined and is easier to determine.

In planning the V-8A test, both cases were considered so that observations of fracture could be attributed to the proper causes. Analyses were made to define structural instabilities as well as tearing instabilities based on the material properties of the characterization welds and the base metal. Selection of the V-8A flaw geometry and decisions on the placement of vessel instrumentation were made as a consequence of the preliminary analyses described here.

In all of the pretest analyses for vessel V-8A and all but two of the posttest analyses, the J_R curves of the test material were based on J_D, a deformation plasticity calculation of the J-integral for the test specimens including a reduction for crack growth. In two of the posttest analyses, the J_R curves were based on J_M, a modified calculation of the J-integral with a smaller reduction for crack growth. The use of J_M eliminates negative slopes (which did not occur in the V-8A data) and reduces size effects in J_R data. However, evaluations of its use for the tearing instability analysis of flawed structures are just beginning. The mathematical selection between J_D and J_M is discussed in Appendix K.

5.1.2 Preliminary analyses

Preliminary analyses were made to investigate structural instabilities caused by yielding and to verify the accuracy of numerical methods of fracture analysis in the linear-elastic range. Two types of analyses were used to investigate structural instabilities without tearing. First, the pressure-strain relationship of an unflawed cylinder, with the assumption of the trilinear stress-strain curve[1] shown in Fig. 5.1, indicated the pressure (p_{GY}) at which the test vessel would yield through the

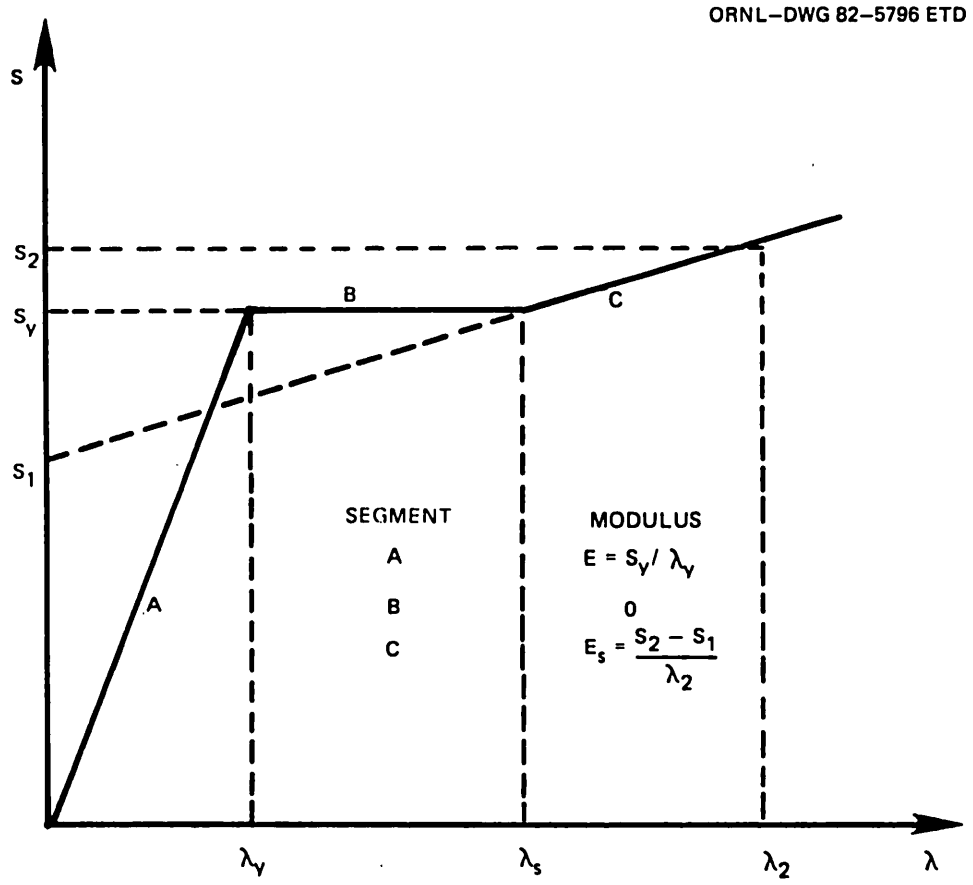

Fig. 5.1. Stress and strain parameters defining a linearized stress-strain relationship.

thickness. Figure 5.2, which is based on the values of tensile properties in Table 5.1, shows that at $p = p_{GY}$ the vessel will expand without further application of load until strain-hardening begins. This type of limited instability had to be avoided in the V-8A test if a J_R-controlled instability was to be detected. Second, a local plastic instability analysis[2] of a flawed cylinder was made to estimate the pressure at which the vessel wall near the flaw would reach a limit load without tearing.

Initial linear-elastic fracture analyses of vessel V-8A were performed by two methods for the set of semielliptical flaw geometries defined in Table 5.2. The first method used the three-dimensional (3-D) computer programs, ORMGEN,[3] ADINA,[4] and ORVIRT[5] to calculate the strain-energy release rate G by a virtual crack extension procedure. The second method is based on the equations formulated by Raju and Newman[6] for surface cracks in finite plates under tension and bending. In the latter method, the circumferential stress distribution given by Lamé's solution for the cylinder is approximated by a linear distribution fit over the depth of the flaw.

The results of the two methods are compared in Figs. 5.3–5.5, in which the G values calculated with ORVIRT have been converted to the

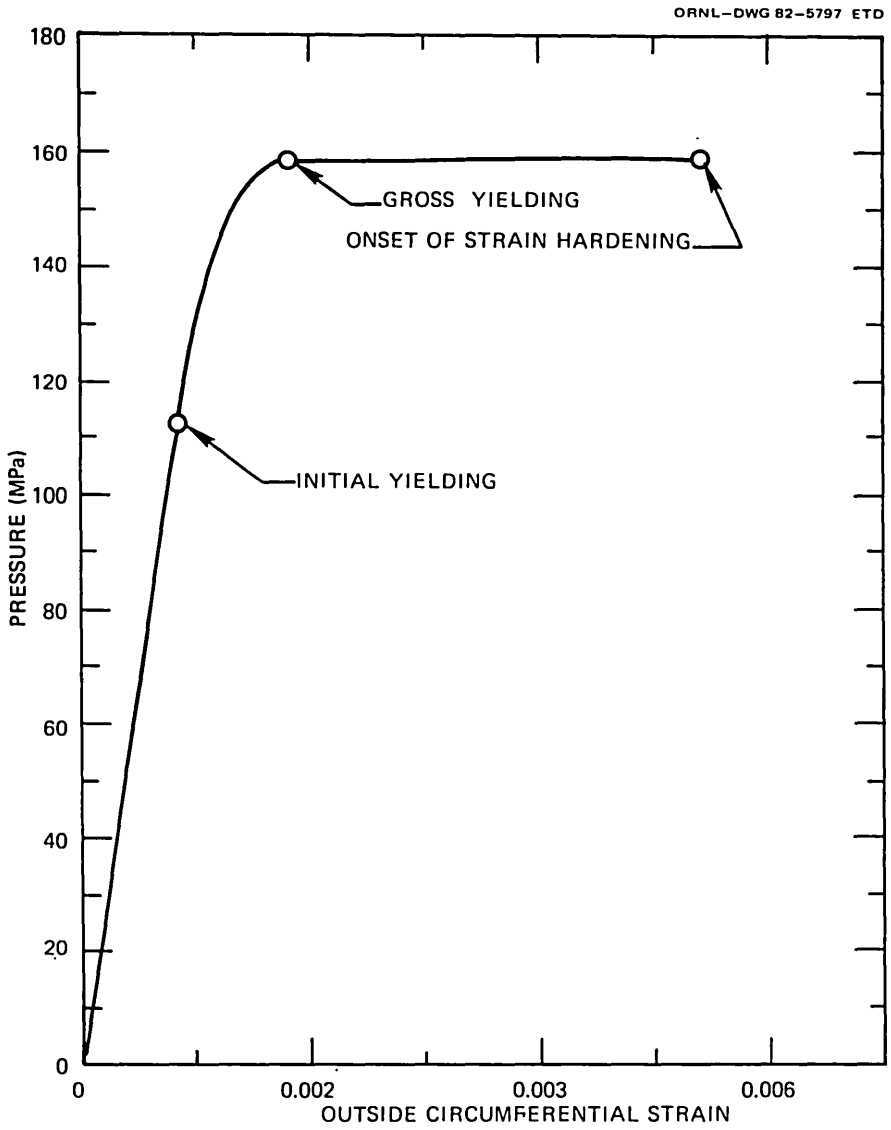

Fig. 5.2. Pressure vs outside circumferential strain for a cylinder of V-8A geometry with properties given in Table 5.1.

stress intensity factor K_I by

$$K_I = \sqrt{\frac{EG}{(1 - \nu^2)}}\ , \qquad (1)$$

where E is Young's modulus and ν is Poisson's ratio. It is evident from these figures that the Raju-Newman K_I distributions are similar to those given by ORVIRT, and agreement is quantitatively good for shallow cracks.

Table 5.1. Material properties used in preliminary TM, local plastic instability, and gross yield calculations for vessel V-8A

Property	Value
Poisson's ratio, ν	0.3
Uniaxial yield strength, σ_{yu}, MPa[a]	413.7
Tensile strength, σ'_{ult}, MPa	551.6
Young's modulus, E, GPa	206.8
TM, E_s, GPa	2.068
Yield strain, λ_y	0.002 (0.00208 for p — ε curve)
Hardening strain, λ_s	0.012

[a]Biaxial yield strength, $\sigma_y = 1.04\ \sigma_{yu}$ = 430.2 MPa.

Table 5.2. Parameters for preliminary LEFM analyses of V-8A flaws

Pressure, MPa	10
Poisson's ratio, ν	0.3
Young's modulus, GPa	200
Inside radius, m	0.3429
Outside radius, m	0.4953

Flaw geometry[a]

a/w	a/b	a (mm)	b (mm)
0.4	0.6	60.96	101.60
	0.7		87.09
	0.8		76.20
0.5	0.6	76.20	127.00
	0.7		108.86
	0.8		95.25
0.6	0.6	91.44	152.40
	0.7		130.63
	0.8		114.30

[a]w = thickness = 152.4 mm; a = flaw depth; b = half length of semielliptical flaw.

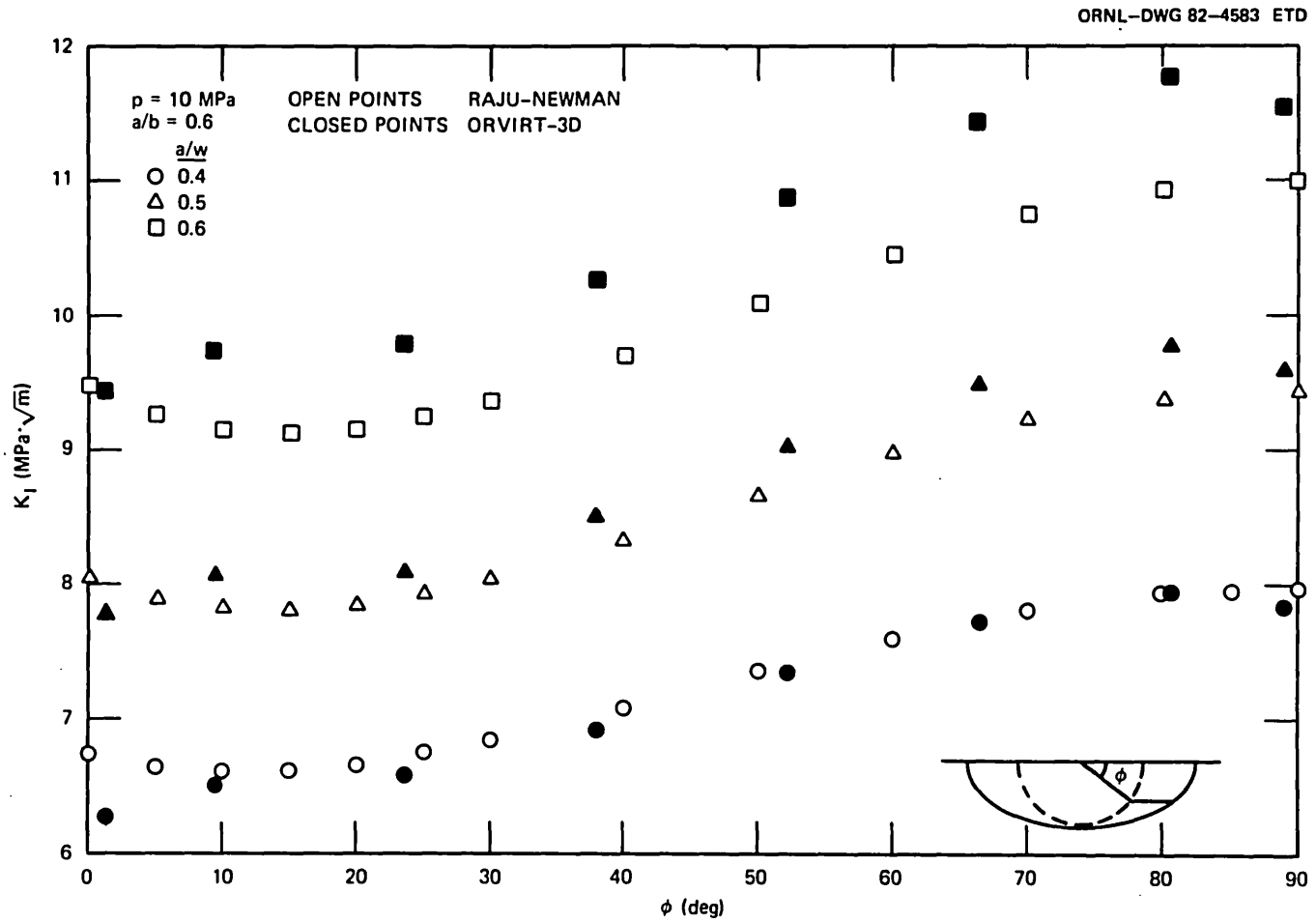

Fig. 5.3. Comparisons of results of elastic ORVIRT and Raju-Newman calculations for p = 10 MPa and a/b = 0.6.

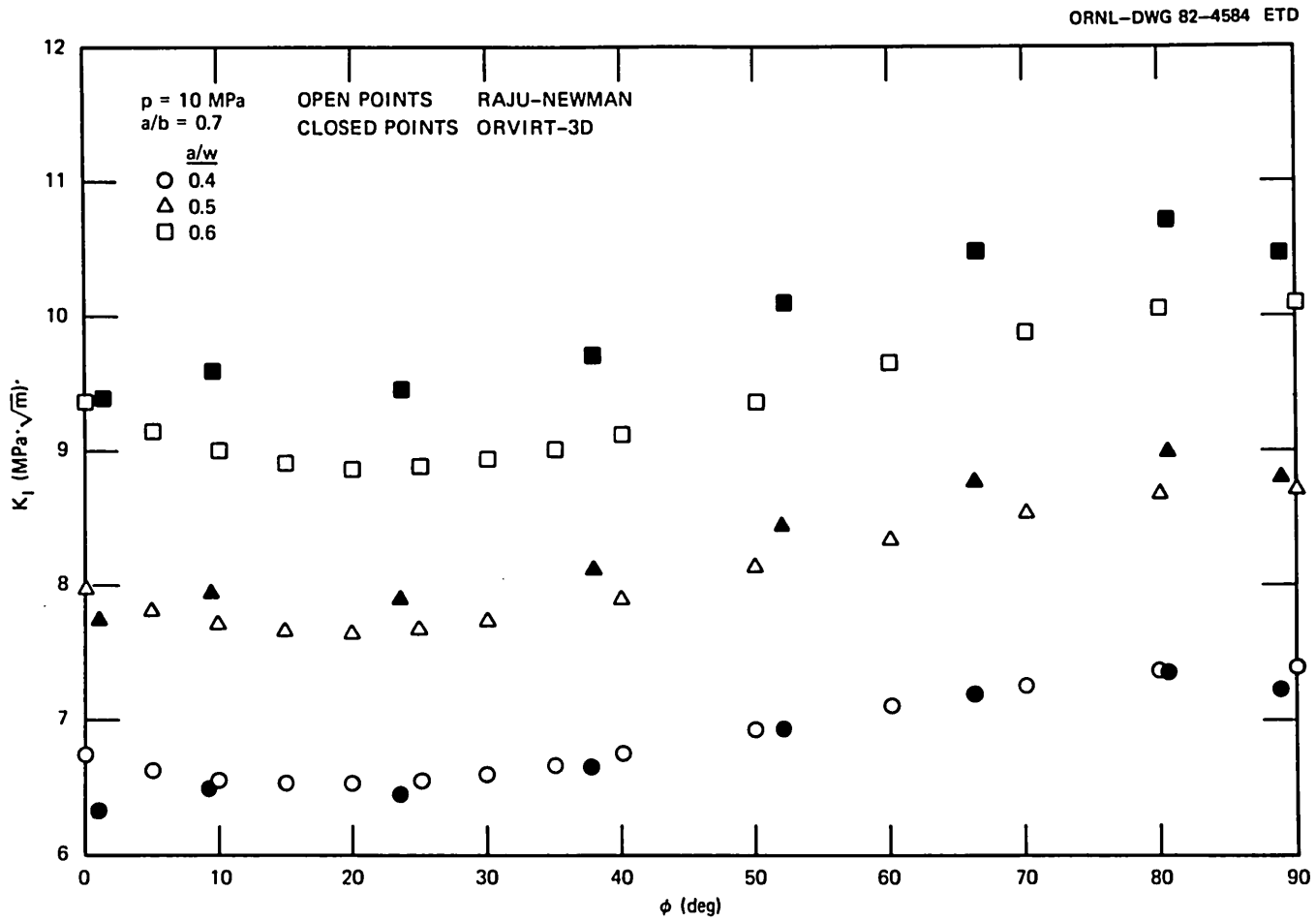

Fig. 5.4. Comparison of results of elastic ORVIRT and Raju-Newman calculations for p = 10 MPa and a/b = 0.7.

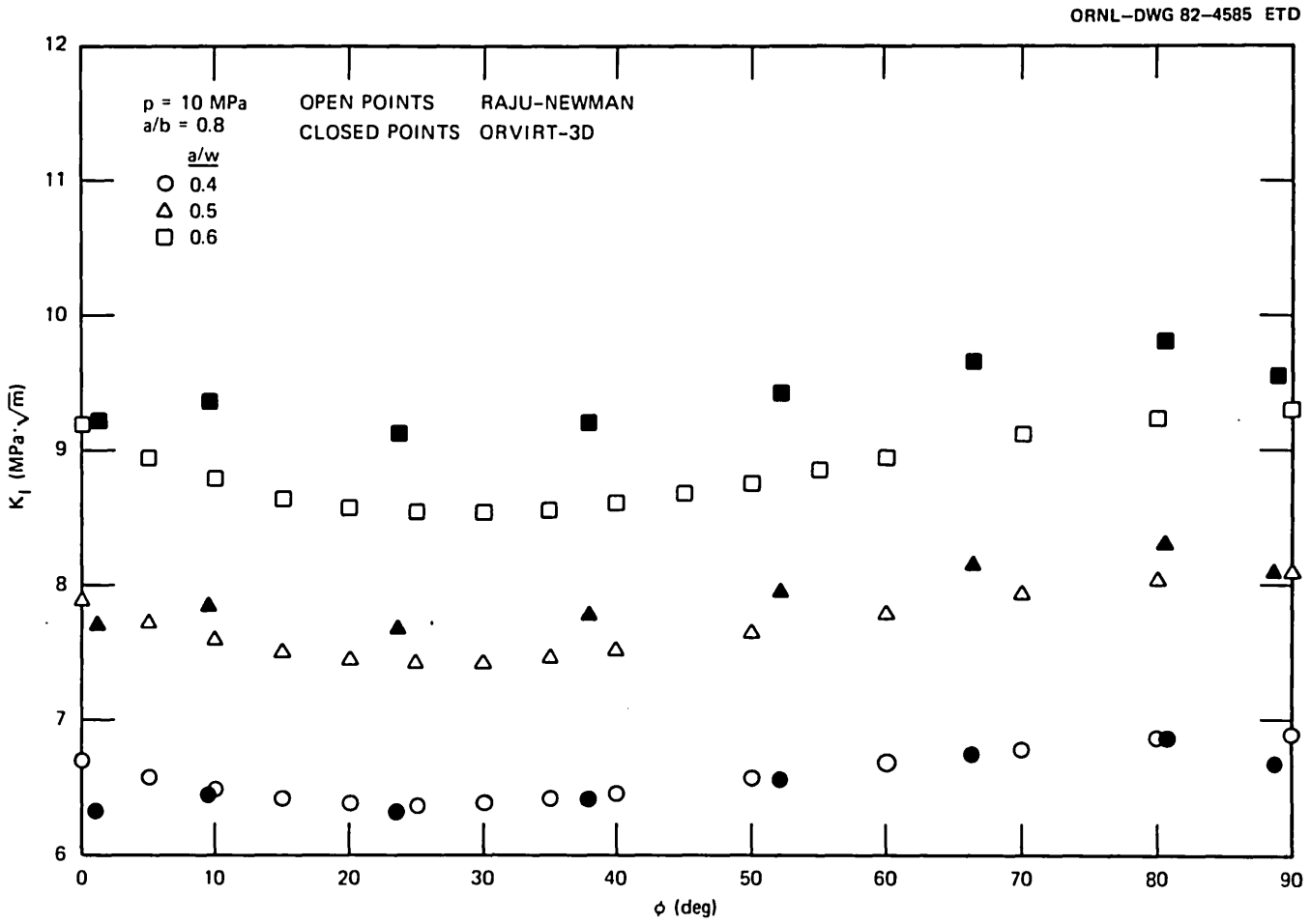

Fig. 5.5. Comparison of results of elastic ORVIRT and Raju-Newman calculations for p = 10 MPa and a/b = 0.8.

5.2 Tearing Instability Analysis

5.2.1 Overview of methods

Estimates of J_R-controlled tearing were made based upon measured tearing resistance and the J-integral J_I (or G, the 3-D generalization of J_I) calculated by two methods: the tangent modulus (TM) method of elastic-plastic fracture-mechanics analysis (EPFM) (see Appendix A for details) and the ORMGEN,[3] ADINA,[4] and ORVIRT[5] computer programs for performing finite-element EPFM analysis. The basis for determining the progression of J_R-controlled tearing is illustrated in Fig. 5.6. If a flaw has an initial depth a_0, then at some pressure p_1, the condition $J_I = J_R$ is satisfied when $a = a_1$ and $J_I = J_{R1}$. In this particular instance (Fig. 5.6) at a constant pressure p_1, a virtual increment in crack depth

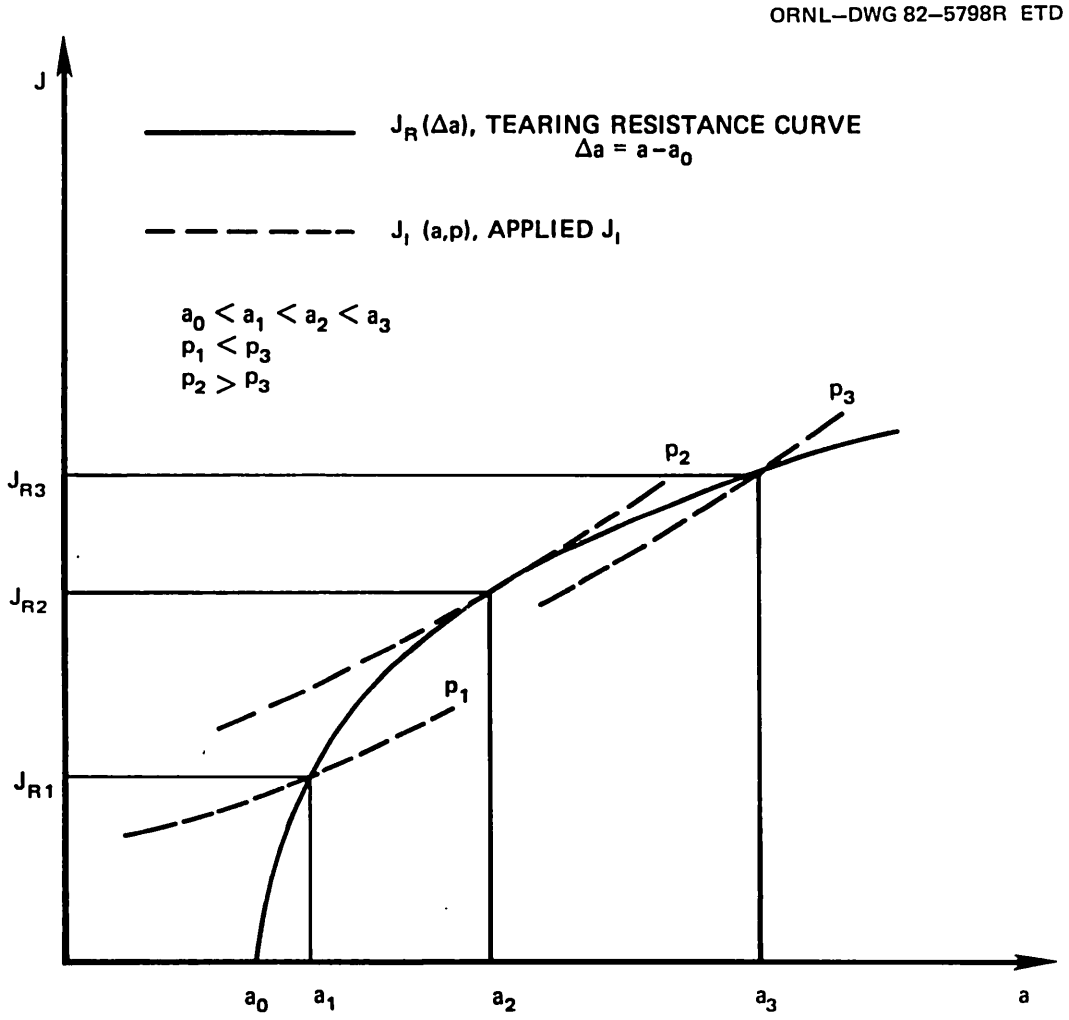

Fig. 5.6. Schematic for determination of J_R-controlled crack depth and tearing instability pressure of a vessel.

beyond a_1 would cause J_R to increase more than J_I with the result that $J_R > J_I$. This implies that more energy would be required to generate the virtual extension than could be supplied by the strain energy released; thus, a_1 is a stable crack depth. At crack depths a_2 and a_3, a virtual extension would result in J_I becoming greater than J_R, the necessary condition for a tearing instability. Pressure p_2 is the maximum pressure determined by this procedure for which $J_I = J_R$ and is therefore defined as the tearing instability pressure.

The ORVIRT analysis computes strain energy release rate directly. The TM method is convenient for a direct calculation of J_I on the assumption that K_I and J_I are related by

$$K_I^2 = EJ_I \ . \tag{2}$$

Then, for linear-elastic conditions, K_I is either given by the Raju-Newman equations[6] or by

$$K_I = C\sigma\sqrt{\pi a} \ , \tag{3}$$

where C is the elastic shape factor, a is crack depth, and σ is the appropriate stress for a surface crack.[7,8] In the TM analysis, it is convenient to use a form of Eq. (3) that expresses the relationship between K_I and the hoop strain λ at the outside surface of the unflawed cylinder. For elastic conditions, this relationship is

$$\lambda = \frac{(1 - \nu/2)K_I}{CE\sqrt{\pi a}} = \frac{(1 - \nu/2)}{C}\sqrt{\frac{J_I}{\pi E a}} \ , \tag{4}$$

where λ is related to pressure by the Lamé solution,

$$p = \frac{E(r_o^2/r_i^2 - 1)}{(2 - \nu)}\lambda \ . \tag{5}$$

For strains larger than the yield strain λ_y of Fig. 5.1, the expression for λ is more complicated but generally of the form (see Appendix A)

$$\lambda = f(C, a, J_I, \lambda_y, \lambda_s) \ . \tag{6}$$

In this case, the pressure is obtained from the nonlinear relationship between p and λ shown in Fig. 5.2.

In applications of the TM method to estimating a tearing instability pressure, tearing resistance may be represented by the power-law expression

$$J_R = c(\Delta a)^n \ , \tag{7}$$

where Δa = the crack extension, $a - a_0$. Critical pressure as a function of crack depth is then calculated for a given a_0 as follows:

1. calculate J_R (Δa) over a range of Δa values,
2. let $J_I = J_R$,
3. calculate λ by Eq. (4) or (6) as appropriate, and
4. determine p by Eq. (5) or Fig. 5.2 as appropriate.

5.2.2 Flaw-sizing calculations

The initial fracture-mechanics computations performed for the purpose of selecting a flaw size for vessel V-8A employed the TM method, as described in detail in Appendix A. For subsequent pretest calculations, three J_R curves were selected from preliminary Babcock & Wilcox (B&W) characterization data for vessel V-8A.[9] The power-law parameters corresponding to high, medium, and low values are given in Table 5.3. Results of tearing instability computations are shown in Fig. 5.7 for an initial crack depth a_0 = 91.44 mm. The gross yield pressure and local plastic instability pressures[2] shown in Fig. 5.7 were based on the parameters of Table 5.1, which were the best estimates of tensile properties available at the time. The high J_R case gave strains in excess of gross yield but

Table 5.3. J_R-curve power-law parameters for preliminary tearing instability estimates[a] for flaw sizing

Designation	Specimen No.	c	n
	V852J5	136.33	0.4071
	V862J5	123.72	0.4722
High	Average	130.03	0.4397
Medium	V882J2	124.38	0.3119
Low	V8102J7	92.45	0.2798

[a]Parameters obtained by least-squares fit to B&W data[9] for all points beyond the lower exclusion line. Both J_R and Δa considered random. $J_R = c(\Delta a)^n$, with J_R in kJ/m^2 and Δa in mm.

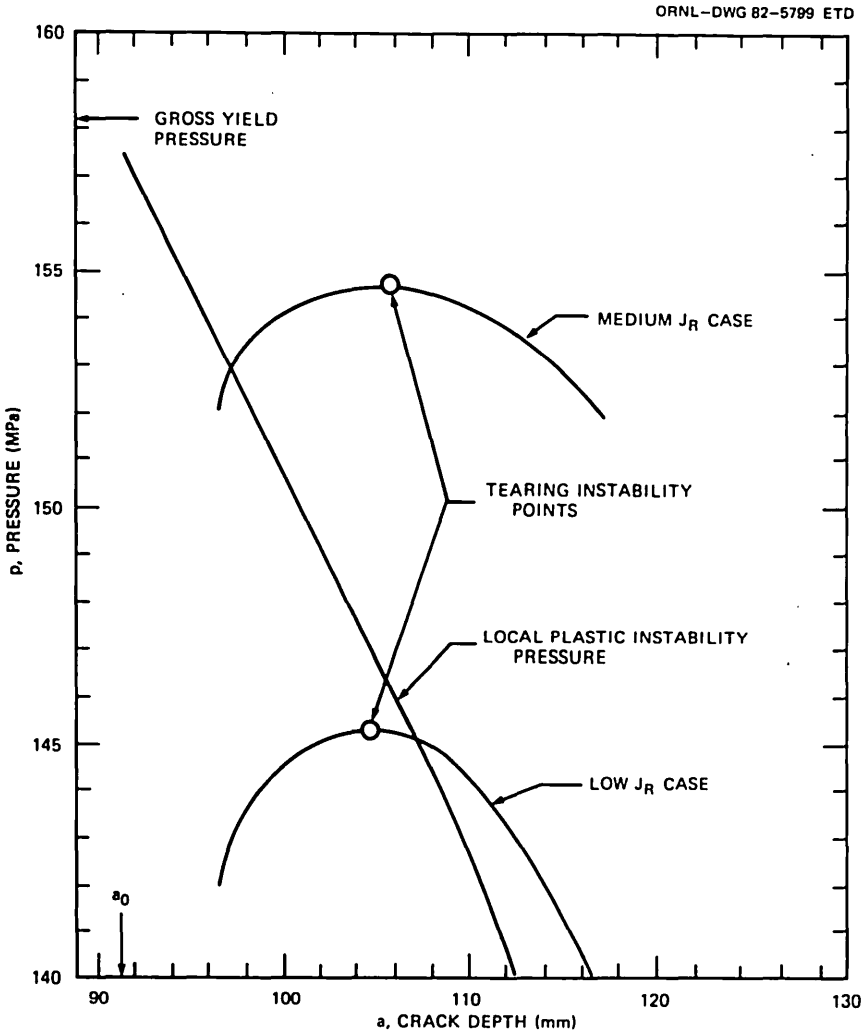

Fig. 5.7. J_R-controlled crack depth vs pressure and local plastic instability pressure of vessel V-8A based on properties given in Table 5.1 and J_R-curve parameters in Table 5.3.

below the strain hardening range. The other two cases indicate tearing instability pressures of 145.3 and 154.7 MPa at crack depths of ~104.7 and 105.7 mm, respectively. The higher pressure is lower than the gross yield pressure, 158.21 MPa. For the conditions assumed, Fig. 5.7 shows that a local plastic instability would precede a tearing instability in the medium J_R case.

The decision to machine the flaw notch in the vessel to a depth of 70 mm and a length of 280 mm was based on the conclusion that, if the vessel toughness were actually as high as the high-J_R case, the vessel would attain gross yield prior to flaw instability, a condition that would certainly impair the quality and usefulness of test data.

5.2.3 Evaluation of ORVIRT models

While the vessel was being flawed, the first set of ADINA and ORVIRT 3-D elastic-plastic calculations of G were made. The flaw geometry and cases analyzed are defined in Fig. 5.8 and Table 5.4. Initial ADINA-ORVIRT computations using an incremental plasticity model were abandoned because of the excessive expense of the computations. Deformation plasticity theory[10] was used in all the ORVIRT computations shown in Table 5.4.

The first case, V8EP1, was analyzed with a Ramberg-Osgood stress-strain law

$$\frac{\varepsilon}{\varepsilon_y} = \frac{\sigma}{\sigma_y} + \alpha\left(\frac{\sigma}{\sigma_y}\right)^n \quad , \tag{8}$$

for which the parameters are defined in Table 5.4 and Fig. 5.9. The parameter values for case V8EP1 were taken from the work of Shih et al.[11] at General Electric Company, because measured values[12] for V-8A were not available at the time.

Results of ORVIRT case V8EP1 for a particular pressure are shown in Fig. 5.10 in terms of $J_I(\phi)$, in comparison with previous linear-elastic analyses performed with ORVIRT and with the Raju-Newman equations.[6] Generally, at pressures below about 75 MPa, there is little difference between ORVIRT linear-elastic and elastic-plastic distributions $J_I(\phi)$.

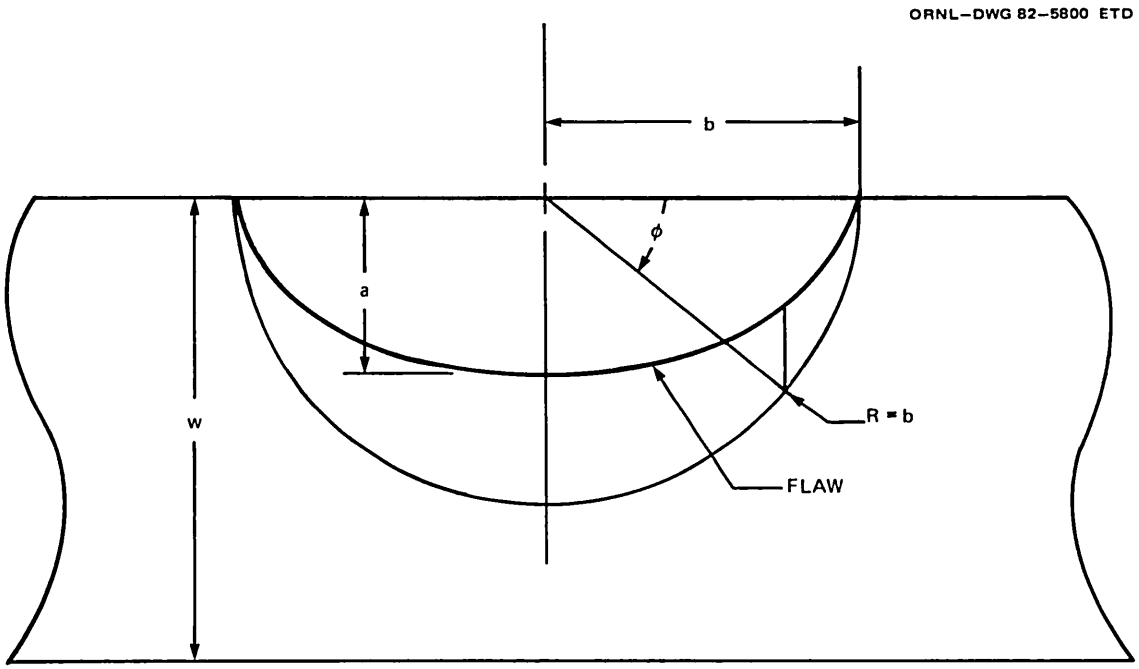

Fig. 5.8. Definition of semielliptical flaw geometry for analyses of vessel V-8A.

Table 5.4. ORVIRT-3D elastic-plastic computations for vessel V-8A

Case No.	a (mm)	b (mm)	E (MPa)	σ_y (MPa)	Ramberg-Osgood parameters[a]		Piecewise linear $\sigma - \varepsilon$ representative curve No.
					n	α	
V8EP1	101.60	152.40	206,843	427.5	9.7[b]	1.115[b]	
V8EP2	101.60	152.40	209,600	401.3	7.0[c]	2.020[c]	
V8EP3	101.60	152.40	209,600	430.2			1[d]
V8EP4	101.60	152.40	209,600	427.5			2[d]
V8EP5	96.52	152.40	209,600	427.5			2[d]
V8EP6	91.44	139.70	209,600	427.5			2[d]
V8EP7	96.52	139.70	209,600	427.5			2[d]
Large deformation[e]	101.60	152.40	209,600	427.5			2[d]

[a] $\varepsilon/\varepsilon_y = \sigma/\sigma_y + \alpha(\sigma/\sigma_y)^n$; $\varepsilon_y = \sigma_y/E$.

[b] Ref. 11.

[c] V-8A data by Stelzman (Ref. 12).

[d] Curves in Fig. 5.9(a).

[e] ADINA only run for large deformations.

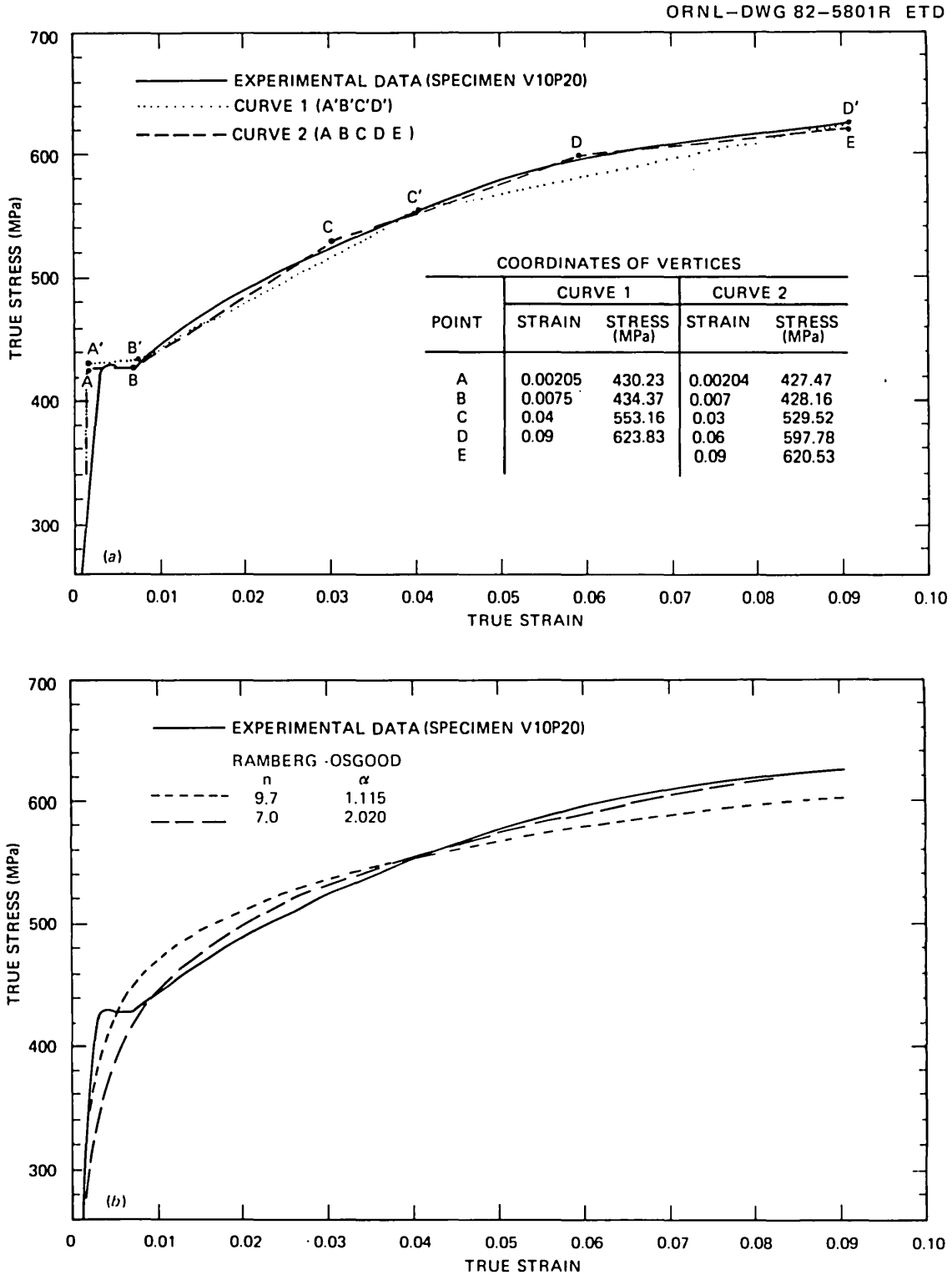

Fig. 5.9. Uniaxial true stress-strain curve of tensile specimen V10P20 tested at 149°C. The four stress-strain relationships used in ORVIRT analyses are also shown. (*a*) Piecewise linear, (*b*) Ramberg-Osgood.

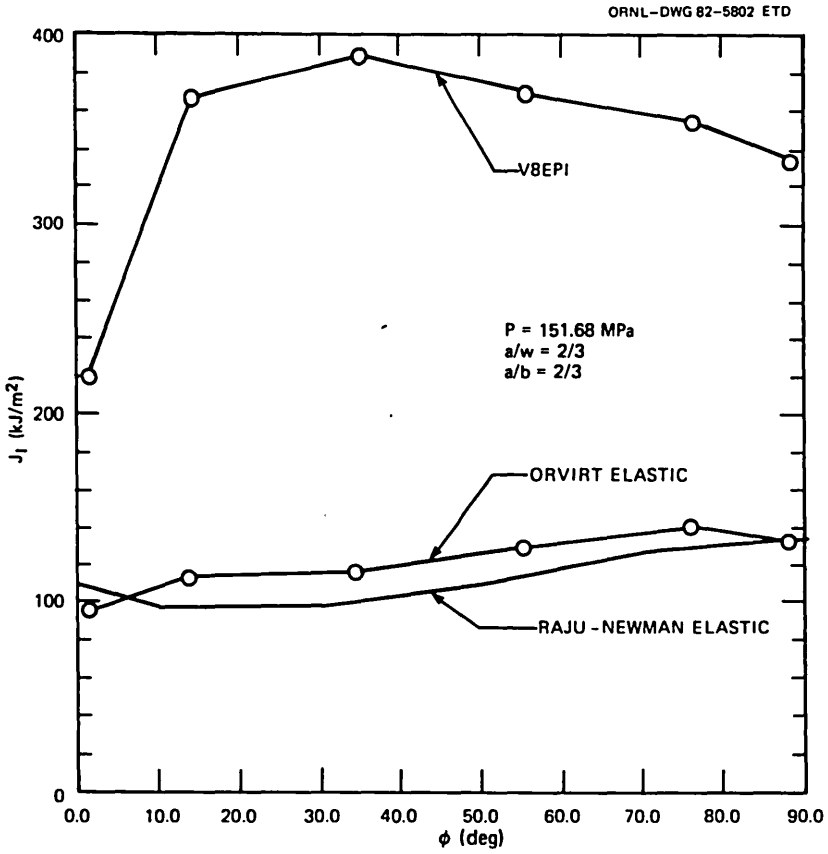

Fig. 5.10. Results of ORVIRT case V8EP1 (elastic-plastic) compared with linear-elastic values from ORVIRT and Raju-Newman expressions.

At higher pressures, such as the one on which Fig. 5.10 is based, the linear-elastic result can be a very poor representation of J_I. The elastic-plastic analyses all show a shifting of the peak of the $J_I(\phi)$ distribution with increasing pressure.

Another factor investigated is the influence of variations of the stress-strain relationship on calculated deformations and J_I. ORVIRT cases V8EP1, 2, 3, and 4 were based on four different stress-strain relationships but with the same crack geometry. The assumptions are shown graphically in comparison with experimental data in Fig. 5.9. The crack-mouth-opening displacements (CMODs) shown in Fig. 5.11 indicate the importance of an accurate stress-strain representation. Here two different Ramberg-Osgood cases, V8EP1 and 2, are compared with a case (V8EP3) based on a closer fitting piecewise linear stress-strain representation. Figure 5.11 shows that the Ramberg-Osgood parameters that gave a poorer overall representation of the stress-strain curve produced CMOD values closer to those of case V8EP3. This result led to the conclusion that the stress-strain representation in the strain range near initial yielding is very important. Consequently, it was decided that the Ramberg-Osgood law, although convenient for computations, could not be used in the V-8A analysis because it lacks accuracy near the initial yield point.

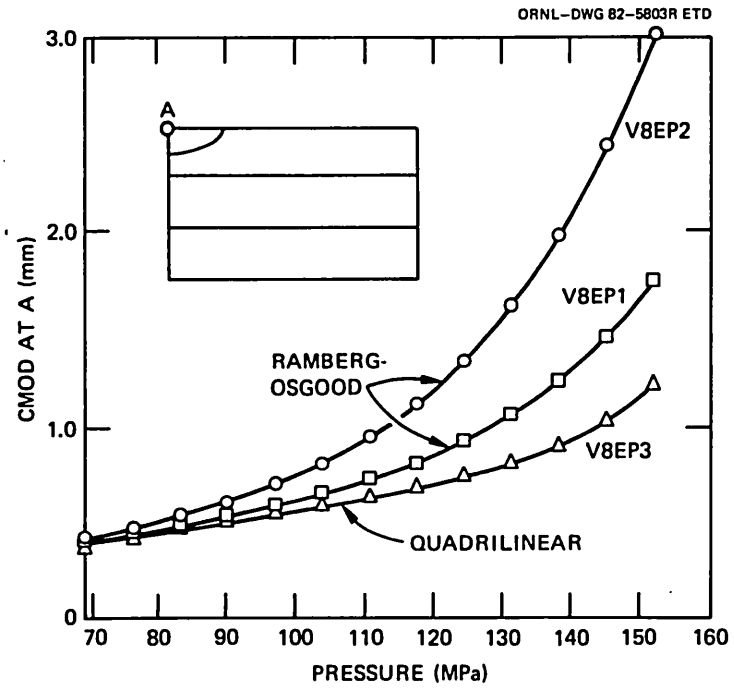

Fig. 5.11. Comparison of CMOD calculated by ORVIRT for three stress-strain relationships: two Ramberg-Osgood cases and one piecewise linear case. Note relatively large overestimate of displacement in V8EP2 case, using Ramberg-Osgood parameters that give best overall fit to stress-strain curve.

ORVIRT elastic-plastic calculations were next made for a set of four crack geometries and a single stress-strain representation, the piecewise linear curve 2 of Fig. 5.9. The results of these four cases, V8EP4 to 7, are presented in Figs. 5.12–5.17. The crack depths and lengths include some of the cases previously analyzed by linear-elastic fracture mechanics (LEFM) and the TM method. Figures 5.12–5.15 show that the maximum in the J_I (ϕ,p) distribution shifts from near $\phi = 90°$ in the elastic range to near $\phi = 35°$ after yielding. Curves of CMOD and near outside surface circumferential strain vs pressure are shown in Figs. 5.16 and 5.17, which imply a gross yield pressure >165 MPa. This value is in contrast to the one shown in Fig. 5.2 but is a natural consequence of using the Von Mises yield criterion, which tends to produce an overestimate of the gross yield pressure. Neither is there any clear indication of a local plastic instability developing near the flaw, but this is also a natural consequence of using an analysis based on assumptions of small strain and small displacement.

To show the influence of the assumed stress-strain relationship on J_I, curves of J_I vs pressure were drawn for three of the stress-strain cases (V8EP2, 3, and 4) identified in Table 5.4 and two values of ϕ (88.27° and 34.62°). [Note that, in Figs. 5.12–5.15, the maxima in J_I (ϕ,p) occur at $\phi \simeq 35°$.] The results are shown in Figs. 5.18 and 5.19, which show a substantial difference between the Ramberg-Osgood case

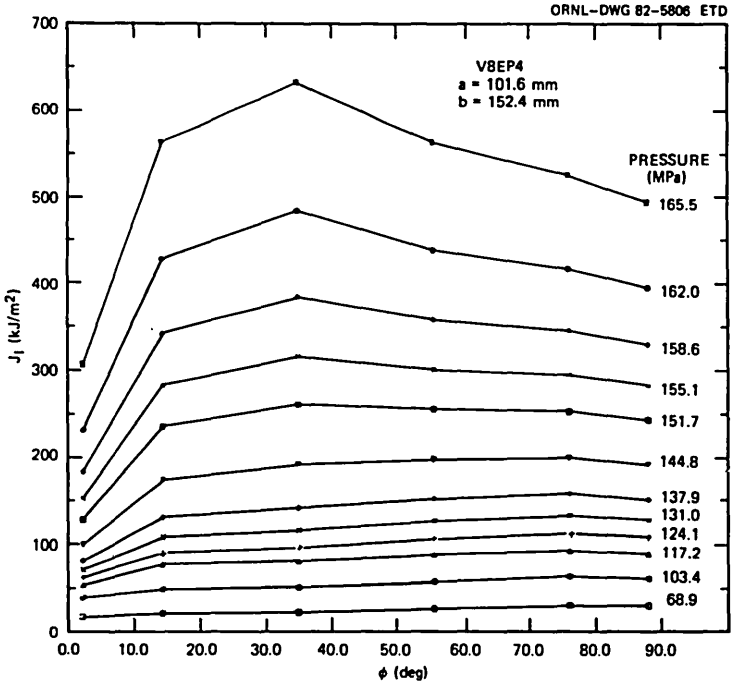

Fig. 5.12. J_I vs ϕ and p for ORVIRT case V8EP4.

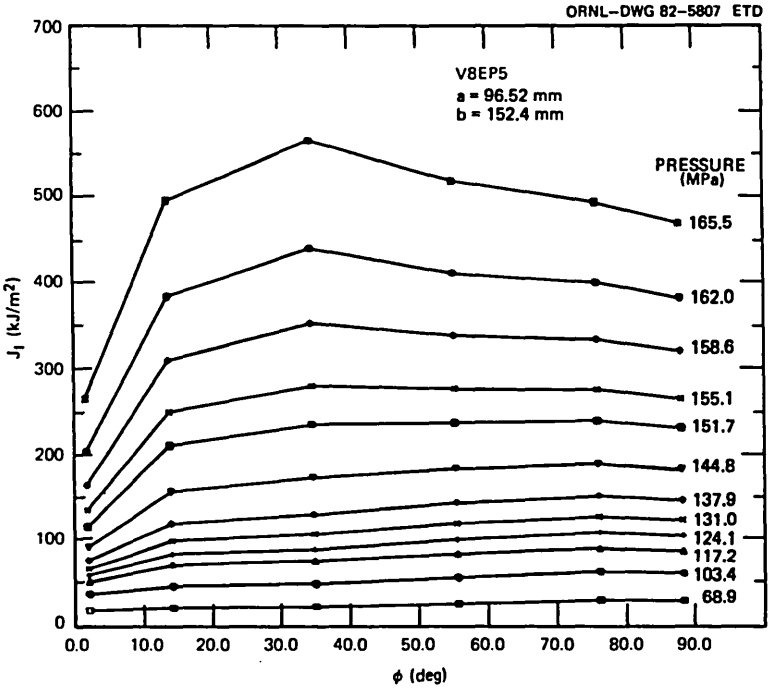

Fig. 5.13. J_I vs ϕ and p for ORVIRT case V8EP5.

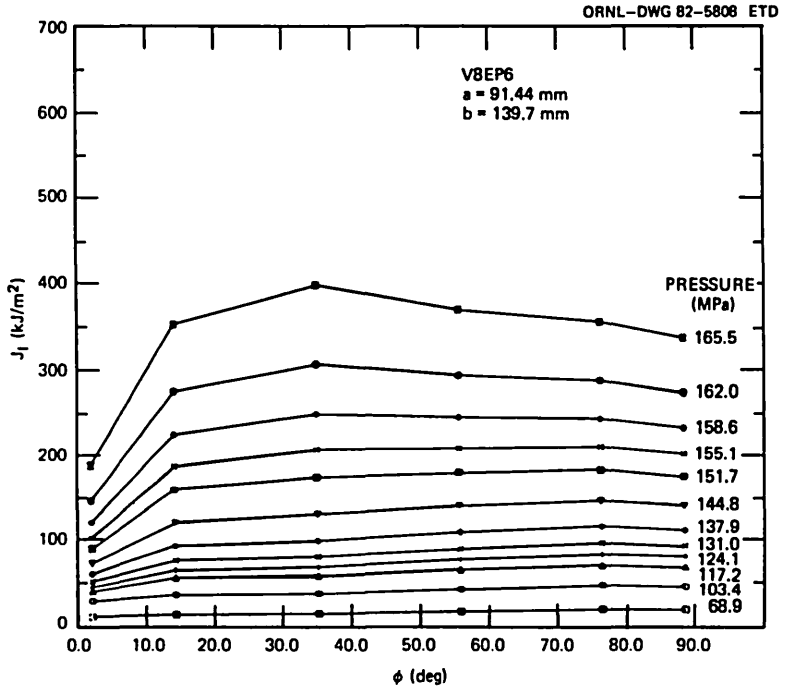

Fig. 5.14. J_I vs ϕ and p for ORVIRT case V8EP6.

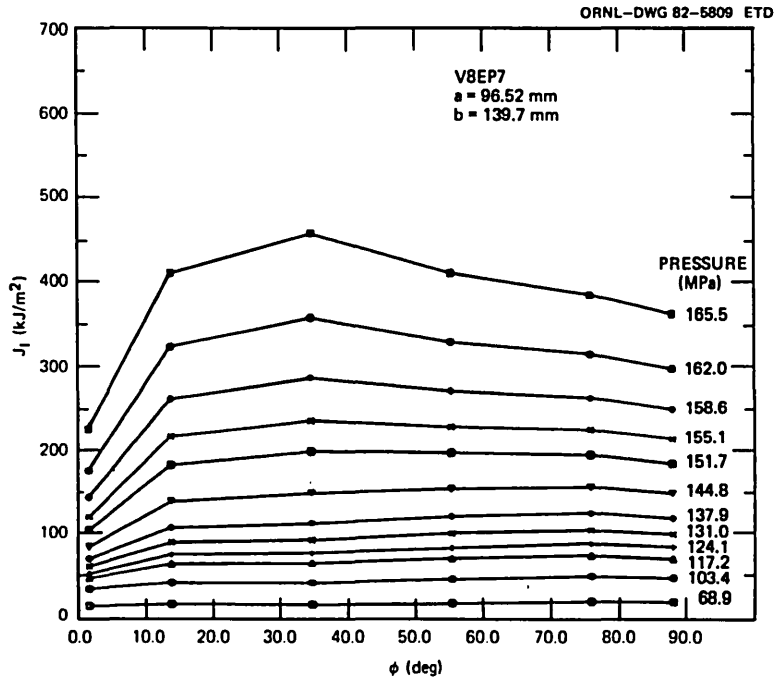

Fig. 5.15. J_I vs ϕ and p for ORVIRT case V8EP7.

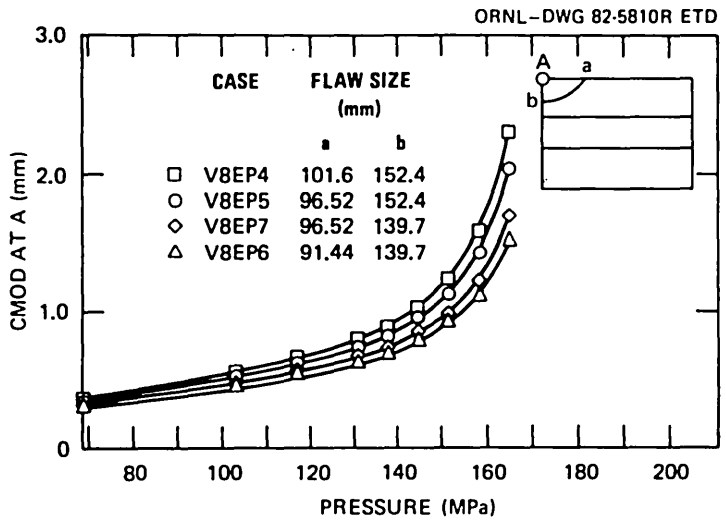

Fig. 5.16. CMOD vs p for four different crack geometries. Tendency toward local plastic instability is shown by increasing slope (dCMOD/dp) with increasing pressure and crack size.

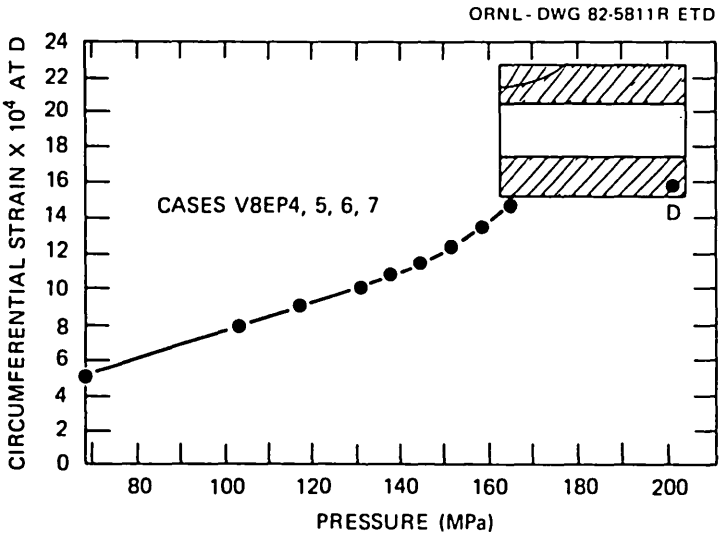

Fig. 5.17. Outside circumferential strain vs p at point remote from flaw.

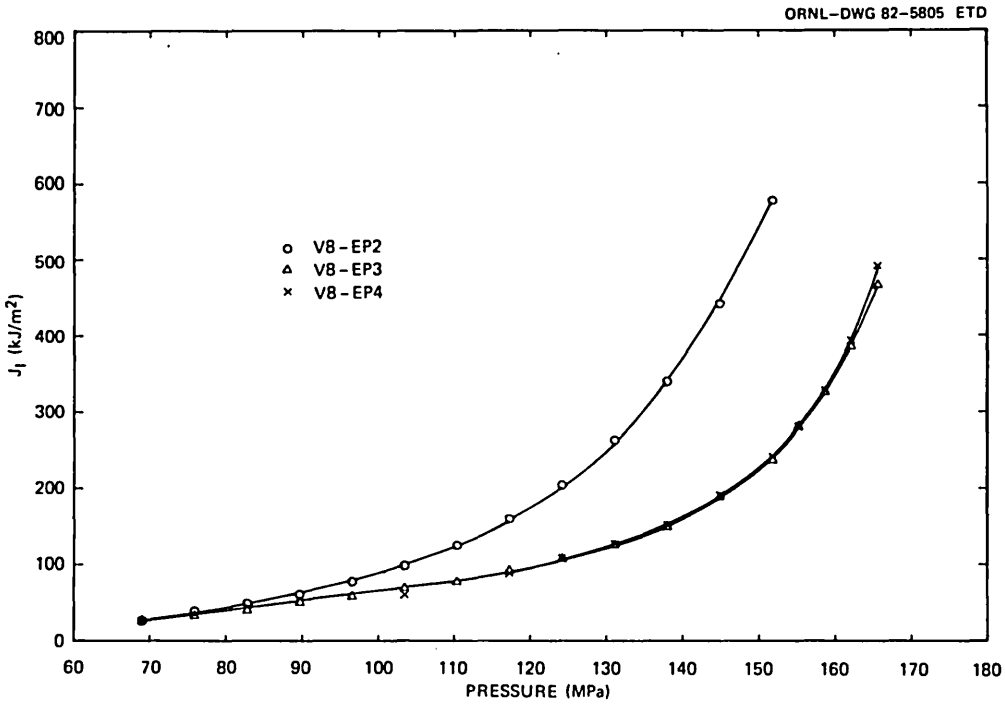

Fig. 5.18. J_I at $\phi = 88.27°$ vs p, a comparison of three ORVIRT cases with parameters producing the best fits to the stress-strain curve.

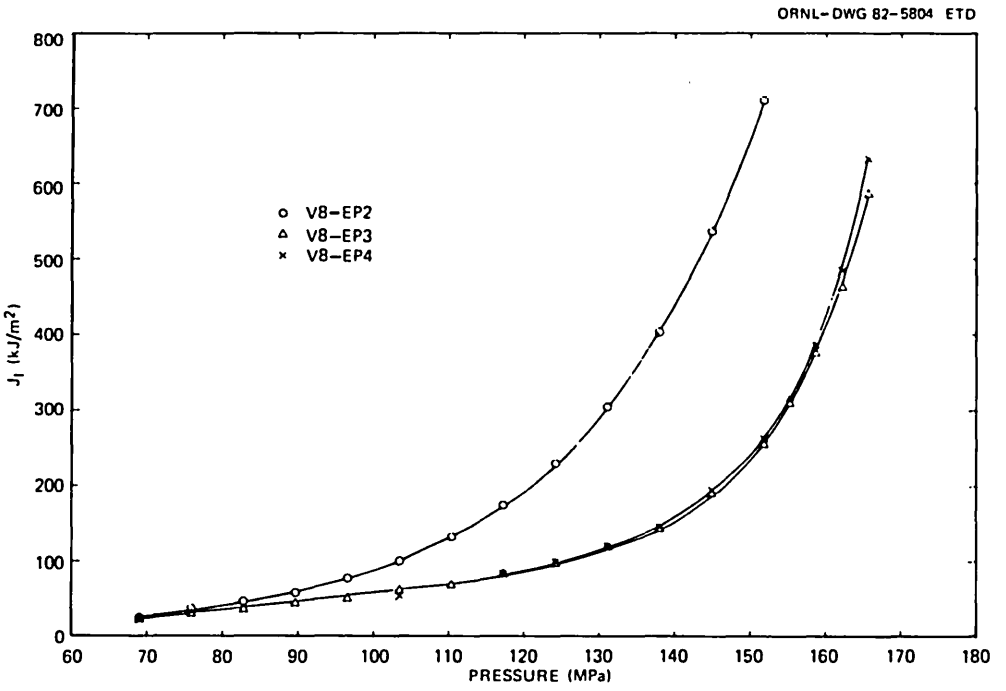

Fig. 5.19. J_I at $\phi = 34.62°$ vs p, a comparison of three ORVIRT cases with parameters producing the best fits to the stress-strain curve.

(V8EP2) that corresponds to the best overall fit to the stress-strain curve and the two more accurate piecewise linear fits (V8EP3 and 4), which produced nearly identical results. The other Ramberg-Osgood case (V8EP1), which corresponded to a better fit to the stress-strain curve near initial yielding as shown in Fig. 5.9(*b*), produced values of J_I vs pressure that lie between case V8EP2 and cases V8EP3 and 4. It is clear that, as fully plastic conditions are approached, a Ramberg-Osgood stress-strain representation that overestimates the nominal strain will also overestimate J_I; this overestimation may be substantial. An accurate EPFM calculation for loads near the gross yield load requires an accurate representation of the stress-strain curve near initial yielding.

5.2.4 Pretest estimates of J_I vs p

For the final pretest analyses at Oak Ridge National Laboratory (ORNL) a set of 3-D ADINA finite-element calculations was carried out with a deformation plasticity material model based on the stress-strain relationship given by curve 2 of Fig. 5.9(*a*). The associated strain-energy-release-rate calculations were performed with the ORVIRT computer program. Crack geometries and loads analyzed are summarized in Table 5.5.

Table 5.5. Semielliptical flaw geometries for final ADINA-ORVIRT pretest analyses[a]

ORVIRT case No.	Semielliptical flaw dimensions (mm)	
	Depth, a	Length, 2b
V8EP-8	93	280
V8EP-9	98	280
V8EP-10	98	290
V8EP-11	103	280
V8EP-12	108	280
V8EP-13	108	290
V8EP-14	108	300
V8EP-15	113	280
V8EP-16[b]	103	280

[a]Pressure loads of 105, 140, 150, and 155 MPa were applied in each case, except in V8EP8 the 150-MPa load was omitted. The 105-MPa load induced essentially the same results with linear-elastic and elastic-plastic models.

[b]This flaw had the shape of the pseudoellipse

$$\left(\frac{y}{a}\right)^3 + \left(\frac{z}{b}\right)^3 = 1 \ .$$

A flat area was machined on the side of the vessel to be flawed, as shown in Figs. 2.23 and 2.29. This flat was included in the finite-element model of the vessel. The dimensions of the cylindrical model are shown in Fig. 5.20. The results of these cases (V8EP8 to 16) are presented in Figs. 5.21–5.29 in terms of $J_I(\phi,p)$. The J_I peaks sharply around ϕ = 20° to 30° at higher pressures (140 to 155 MPa) in contrast to the J_I distribution for pressures producing no large-scale yielding ($\lesssim$105 MPa).

The final set of pretest analyses performed by means of the ADINA and ORVIRT programs was based on the stress-strain relationship used in cases V8EP4 to 7 but used a more refined mesh. A comparison of corresponding $J_I(\phi,p)$ plots from the penultimate and final sets (e.g., Figs. 5.15 and 5.21) shows that the finer mesh used in the later set of analyses produced significantly higher values of J_I.

The magnitude of the differences in J_I for essentially the same crack dimensions indicates the necessity of proper modeling studies prior to important application of the elastic-plastic finite-element calculations. The models used in these two sets are described in Table 5.6 and Fig. 5.30. The model used in the final set (V8EP8 to 16) has about 60% more elements and nodes than the earlier model. The final pretest model was the largest one that was practical to use in ADINA computations on the IBM 3033 computer available for the pretest analysis. Further aspects of modeling are discussed in the Sect. 5.4 on posttest calculations.

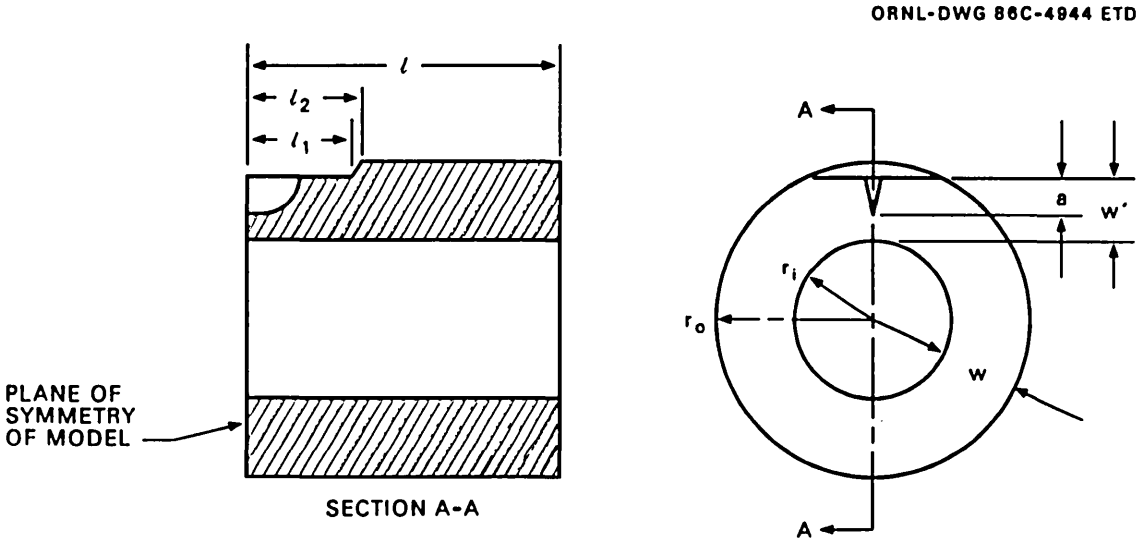

r_o	495.00
r_i	343.00
w	152.00
w'	144.25
ℓ	1016.00
ℓ_1	304.80
ℓ_2	325.00

Fig. 5.20. Geometry of the ADINA model of the V-8A vessel.

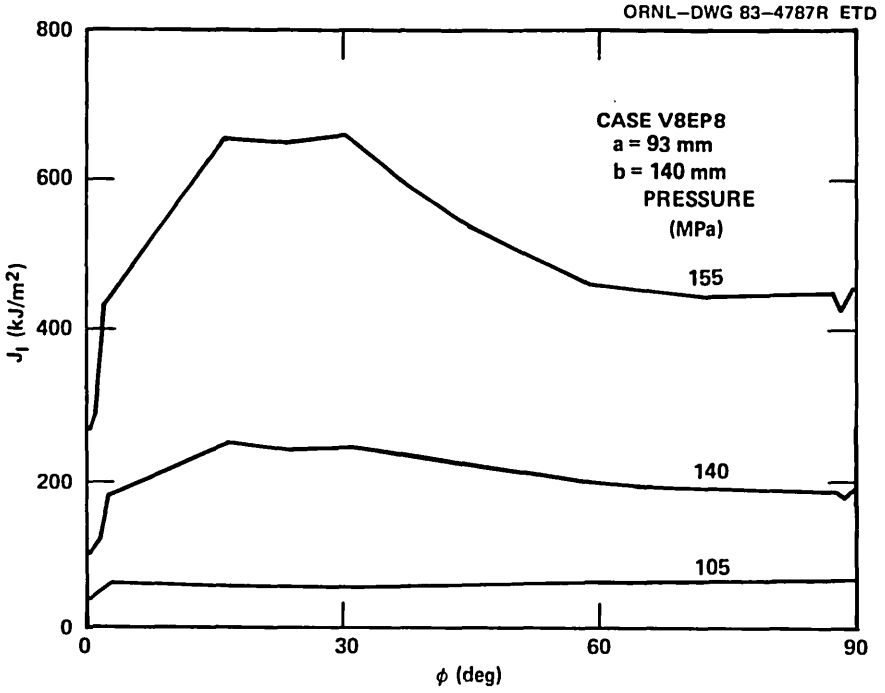

Fig. 5.21. J_I vs ϕ and p for case V8EP8 (a = 93 mm, b = 140 mm).

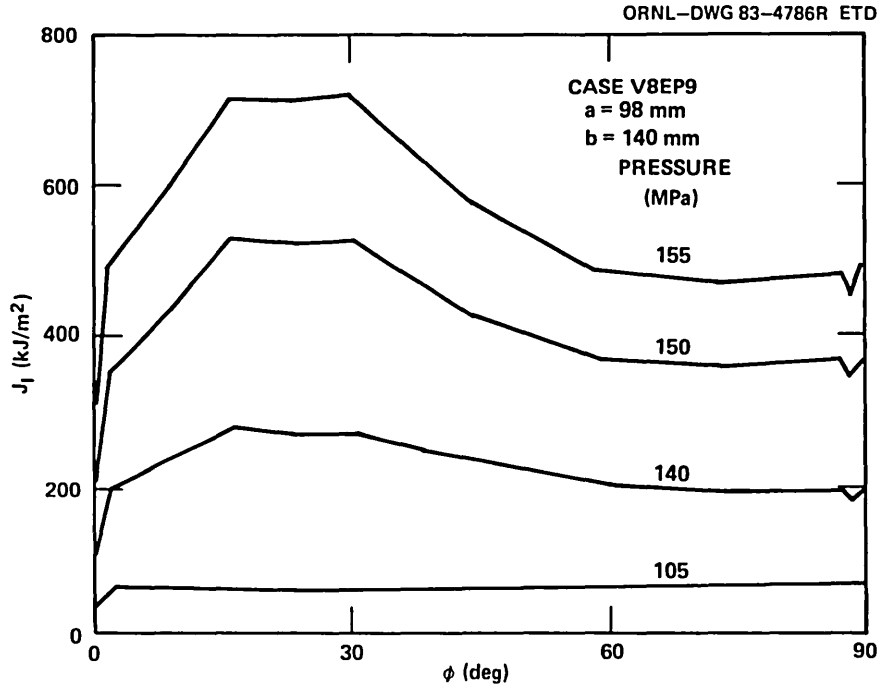

Fig. 5.22. J_I vs ϕ and p for case V8EP9 (a = 98 mm, b = 140 mm).

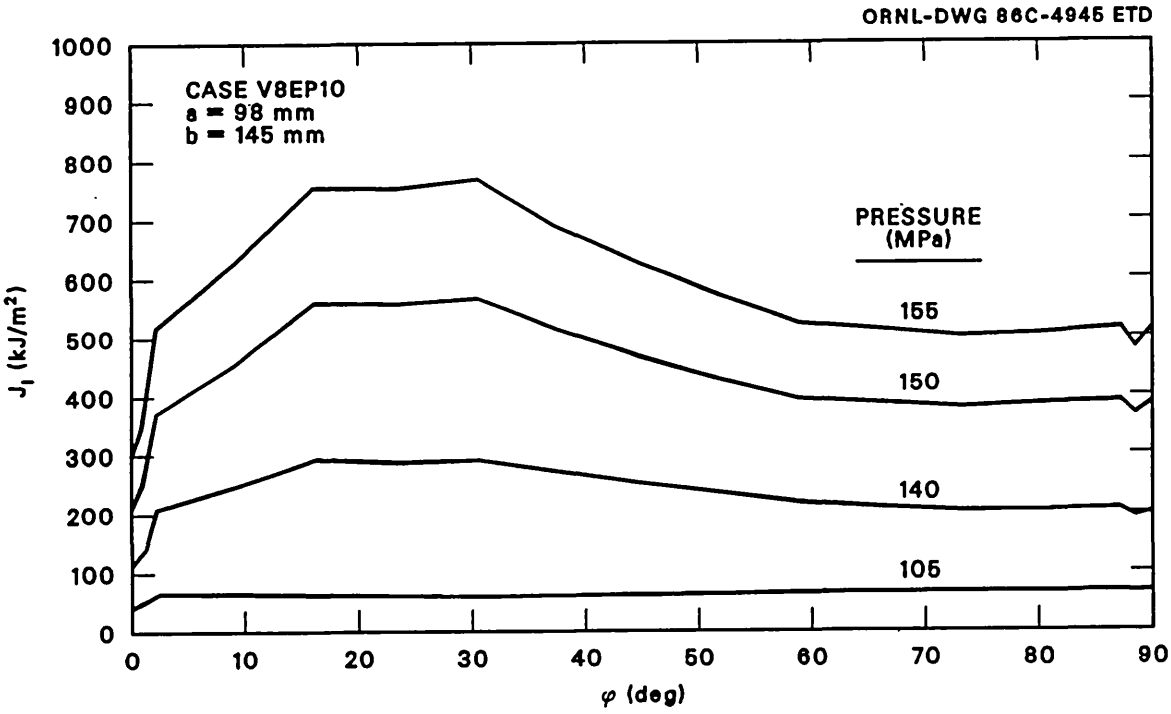

Fig. 5.23. J_I vs ϕ and p for case V8EP10 (a = 98 mm, b = 145 mm).

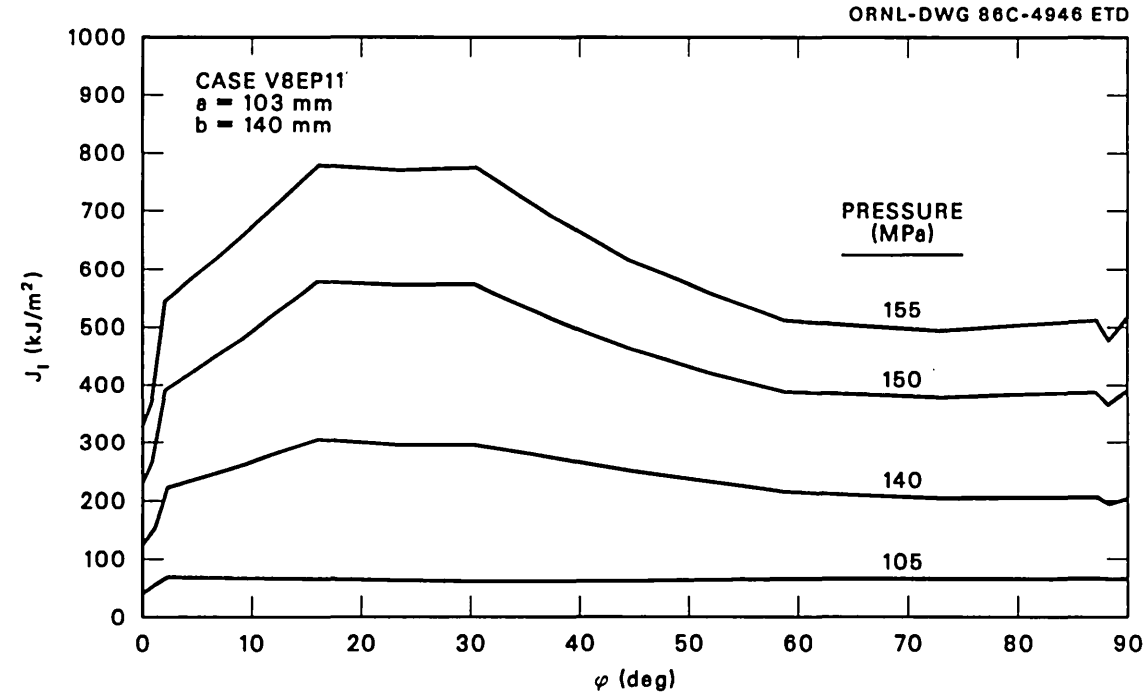

Fig. 5.24. J_I vs ϕ and p for case V8EP11 (a = 103 mm, b = 140 mm).

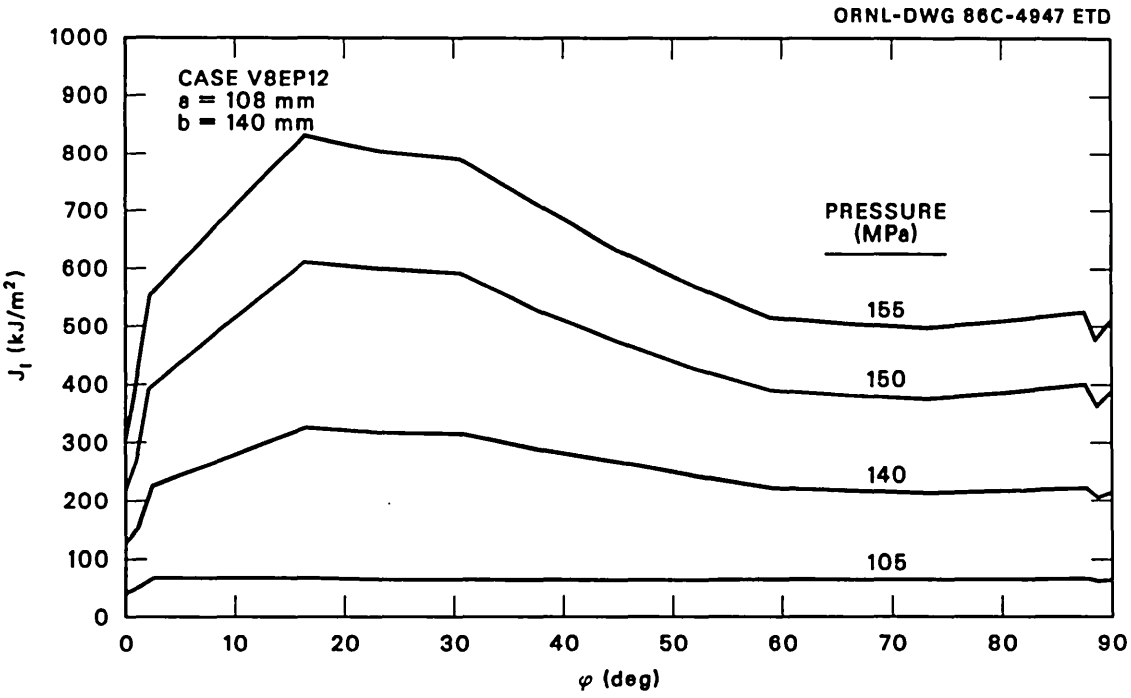

Fig. 5.25. J_I vs ϕ and p for case V8EP12 (a = 108 mm, b = 140 mm).

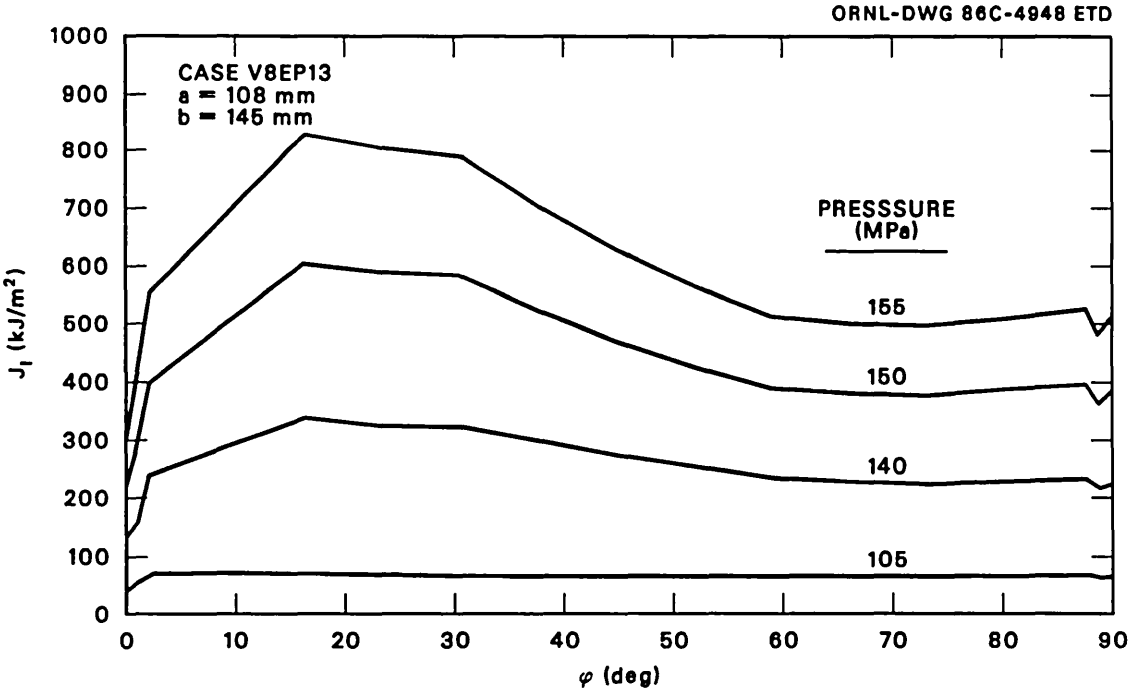

Fig. 5.26. J_I vs ϕ and p for case V8EP13 (a = 108 mm, b = 145 mm).

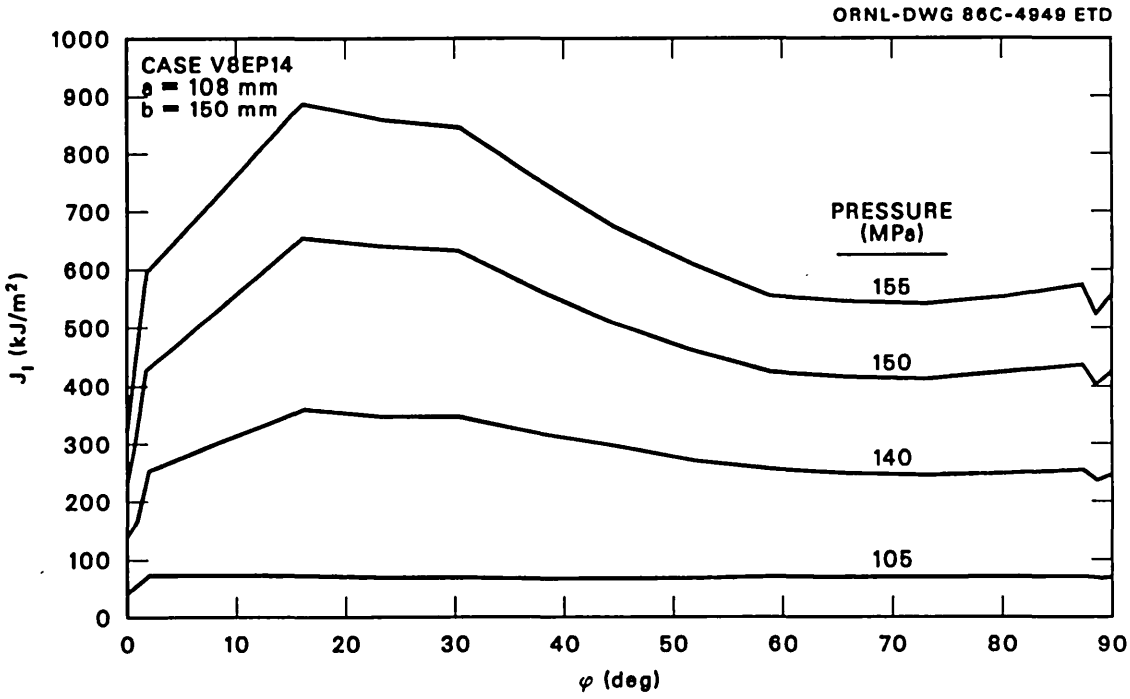

Fig. 5.27. J_I vs ϕ and p for case V8EP14 (a = 108 mm, b = 150 mm).

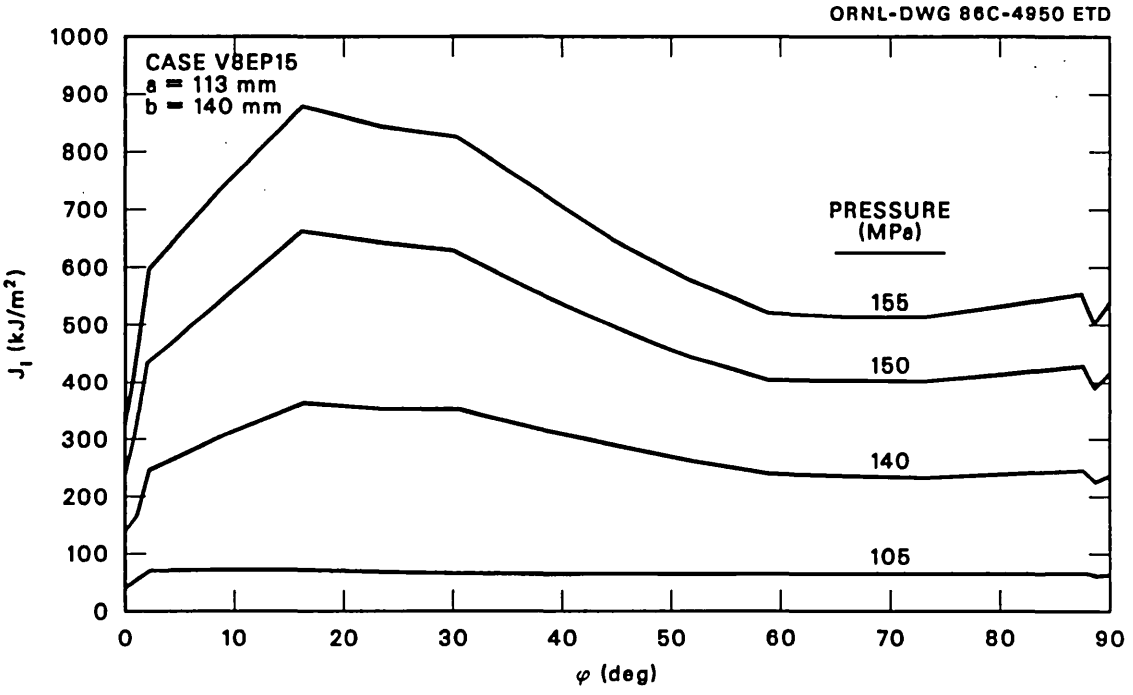

Fig. 5.28. J_I vs ϕ and p for case V8EP15 (a = 113 mm, b = 140 mm).

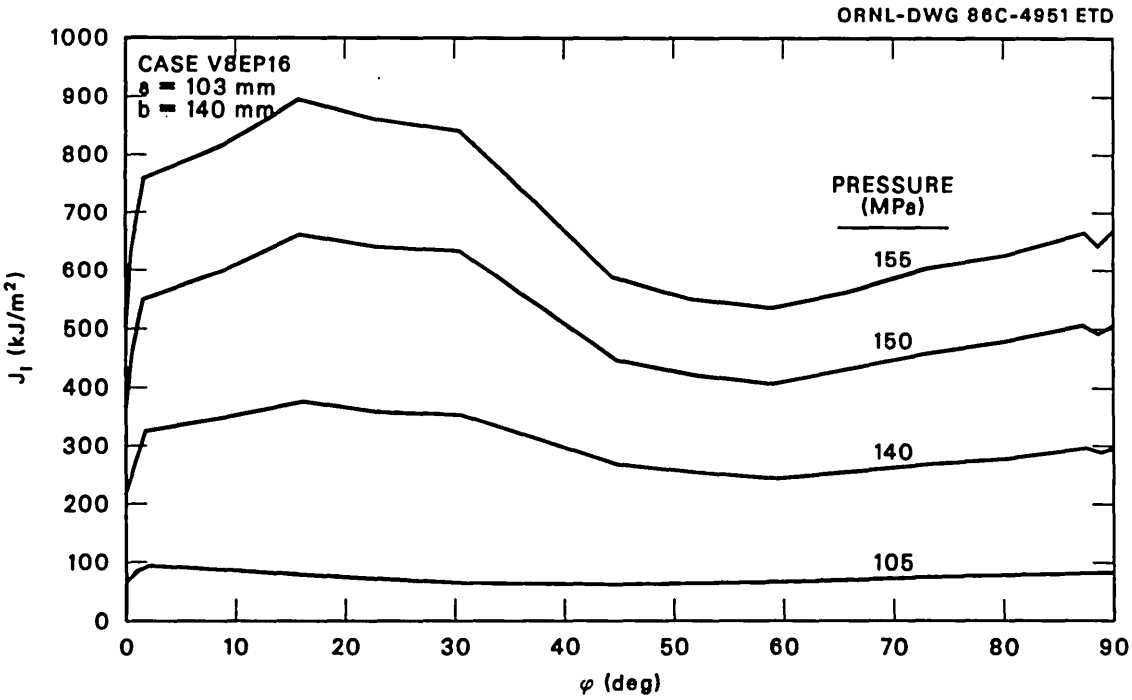

Fig. 5.29. J_I vs ϕ and p for case V8EP16 (a = 103 mm, b = 140 mm).

Table 5.6. Characteristics of finite-element models used in analysis of V-8A

Parameter	Cases		
	V8EP1 to 7[a]	V8EP8 to 16[b]	V8EP20 to 23[c]
Total number of elements	303	496	520
Number of crack-tip elements	96	128	128
Number of regular elements	207	368	392
Number of nodes	1678	2652	2760
Number of segments on crack front	6	8	8

[a]Preliminary elastic-plastic pretest analyses.

[b]Final elastic-plastic pretest analyses.

[c]This series of posttest cases is described in Sect. 5.4.

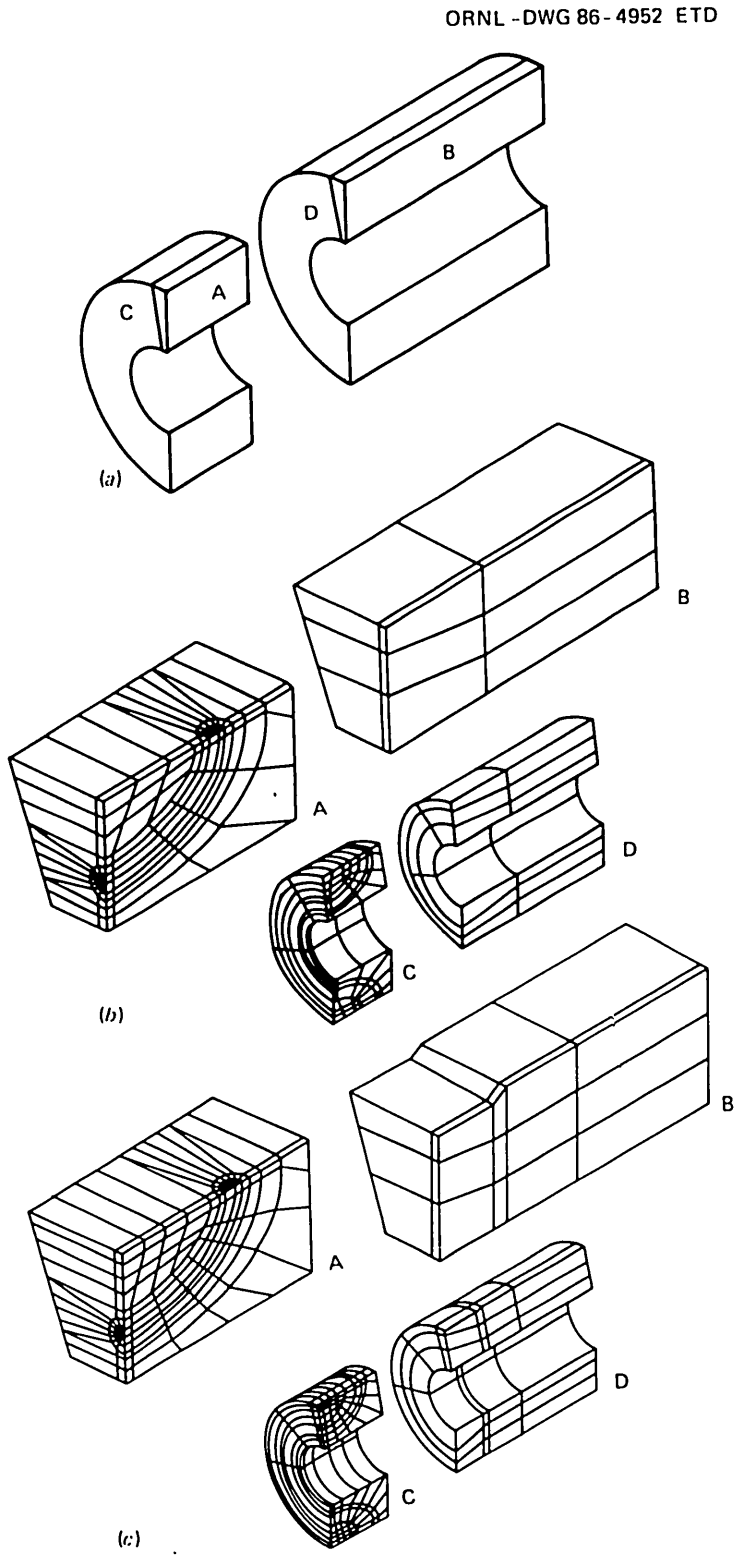

Fig. 5.30. Finite-element model used in ORMGEN-ADINA-ORVIRT pretest analyses of vessel V-8A. (*a*) Definition of parts of model, (*b*) model used in cases V8EP1 to 7, and (*c*) model used in cases V8EP8 to 16.

5.2.5 Pretest instability estimates

Three independent ORNL predictions of instability pressure were made on the basis of the pretest J_R curves of Fig. 2.15 for the characterization weld data from which these curves were obtained. These pretest analyses were based also on a crack depth of 91.2 mm, which had been determined by pretest ultrasonic (UT) measurements, and a directly measured total length of 280 mm. The results of the ORNL predictions are included in the discussion of the pretest analysis round robin in Sect. 5.3.

J_I was determined in the ORNL analyses by two methods — the TM method of Merkle[2] and the virtual-crack-extension technique of the ORVIRT program for calculating the strain-energy-release rate.

The final pretest stability analyses were based on the set of ORVIRT strain-energy-release-rate calculations described in Sect. 5.2.4 and J-resistance curves for each of the characterization welds. The power-law parameters determined by least-squares fitting of J_R data over the full range of Δa measurements were used in these analyses, as given in Table 5.7 for the four characterization welds and the V-8A seam weld.

Table 5.7. Average power-law parameters for the V-8A characterization welds and seam weld[a]

Weld	Number of specimens	c	n
V852	5	137.9	0.386
V862	6	134.0	0.451
V882	2	123.0	0.342
V8102	10	89.32	0.308
Vessel seam	10	81.7	0.318

[a] $J_R = c(\Delta a)^n$ with J_R in kJ/m^2 and Δa in mm.

Because the ductile tearing of the crack is a process that absorbs energy over the entire crack front, some simplification of $J_I(\phi,a,b,p)$ was required to represent the state of the crack by a function of a (or Δa) and p only. This was done by averaging the value of $J_I(\phi,a,b,p)$ around the crack front. In these particular computations $J_{I\ AV}(a,b,p)$ was calculated as the average of the minimum and maximum values of $J_I(\phi,a,b,p)$ with points of low accuracy near the free surface excluded. Further mesh refinements would have to be made to determine whether the J_I values near the surface are physically reasonable, but such refinements were not feasible during this study. The average values are given in Table 5.8. Furthermore, the independent variables a and b were assumed to be related, for a given initial crack geometry defined by a_0

Table 5.8. Average values of J_I used in final pretest stability analyses[a]

Geometric parameters (mm)		Pressure (MPa)	$J_{I\ AV}(a,b,p)$[a] (kJ/m^2)	ADINA-ORVIRT case
a	b			
93	140	105	58.9	V8EP8
		140	212.7	
		155	544.0	
98	140	105	62.2	V8EP9
		140	230.8	
		150	438.8	
		155	587.7	
98	145	105	64.1	V8EP10
		140	244.9	
		150	464.8	
		155	619.8	
103	140	105	64.7	V8EP11
		140	249.3	
		150	470.6	
		155	626.2	
108	140	105	64.4	V8EP12
		140	261.9	
		150	482.0	
		155	642.5	
108	145	105	67.5	V8EP13
		140	273.8	
		150	479.8	
		155	644.5	
108	150	105	69.7	V8EP14
		140	292.2	
		150	521.8	
		155	692.6	
113	140	105	67.9	V8EP15
		140	291.6	
		150	514.9	
		155	673.0	

[a] $J_{I\ AV}(a,b,p)$ is an average of $J_I(\phi,a,b,p)$ with respect to ϕ. The values tabulated are the average of the maximum and minimum values of J_I, with points nearest each end of the flaw ($\phi < 2.37°$) excluded. This approximation to $J_{I\ AV}$ differs from

$$J_{I\ AV} = \frac{2}{\pi} \int_0^{\pi/2} d\phi\ J_I(\phi,a,b,p)$$

by ~4% or less.

and b_0, to an effective increment in crack size defined by

$$\Delta a_{eff} = \frac{\Delta a + \Delta b}{2} , \tag{9}$$

where $\Delta a = a - a_0$ and $\Delta b = b - b_0$. A preliminary graphical solution based on the average J_R curve for weld V8102 is shown in Fig. 5.31. By the graphical interpolation shown in Fig. 5.32, the predicted instability conditions are p = 130 MPa and Δa = 8.4 mm. The results of a more precise numerical solution, based on cases V8EP-8, -9, -11, -12, and -15 for which the virtual strain-energy-release rates are the highest, are shown in Figs. 5.33–5.36. The average J_I (p, Δa_{eff}) was determined from this set of cases by nonlinear interpolation with respect to pressure (p) and linear interpolation with respect to crack increment (Δa_{eff}). With these assumptions, the instability point for each J_R curve was determined by numerical solution of

$$J_I (p, \Delta a) = J_R(\Delta a) , \tag{10}$$

with the condition that Δa be unique. The four figures, 5.33–5.36, show

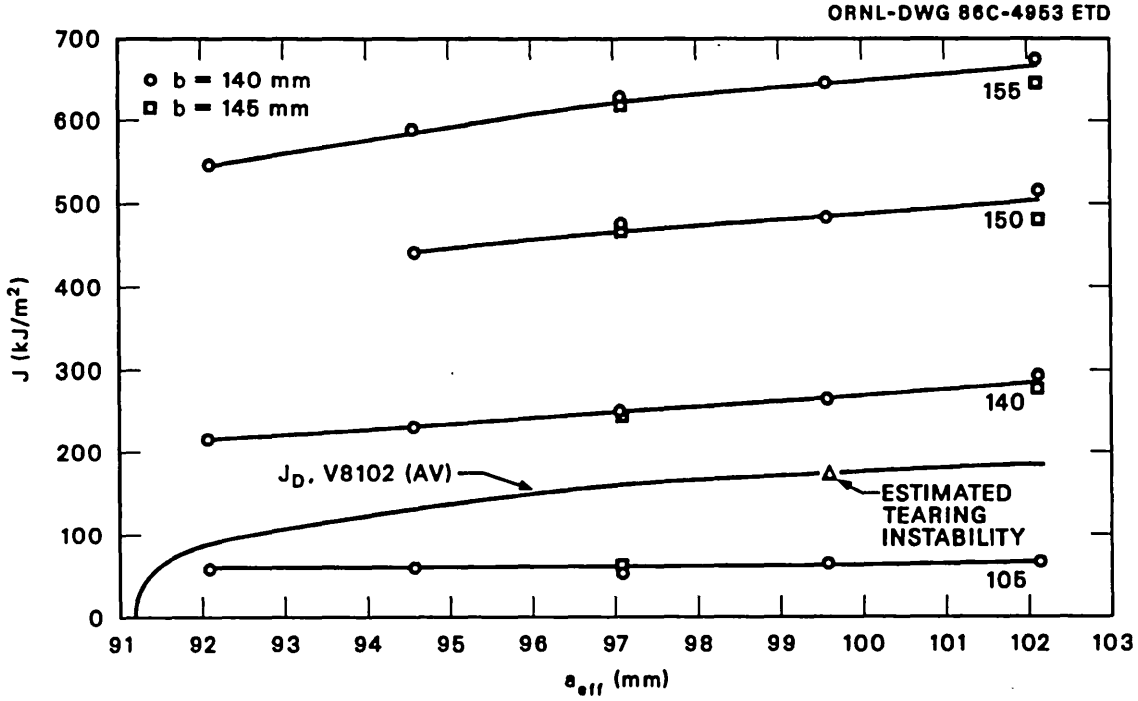

Fig. 5.31. Graphical tearing instability solution for vessel V-8A, based on elastic-plastic finite-element analysis and the average J_D resistance curve for characterization weld V8102.

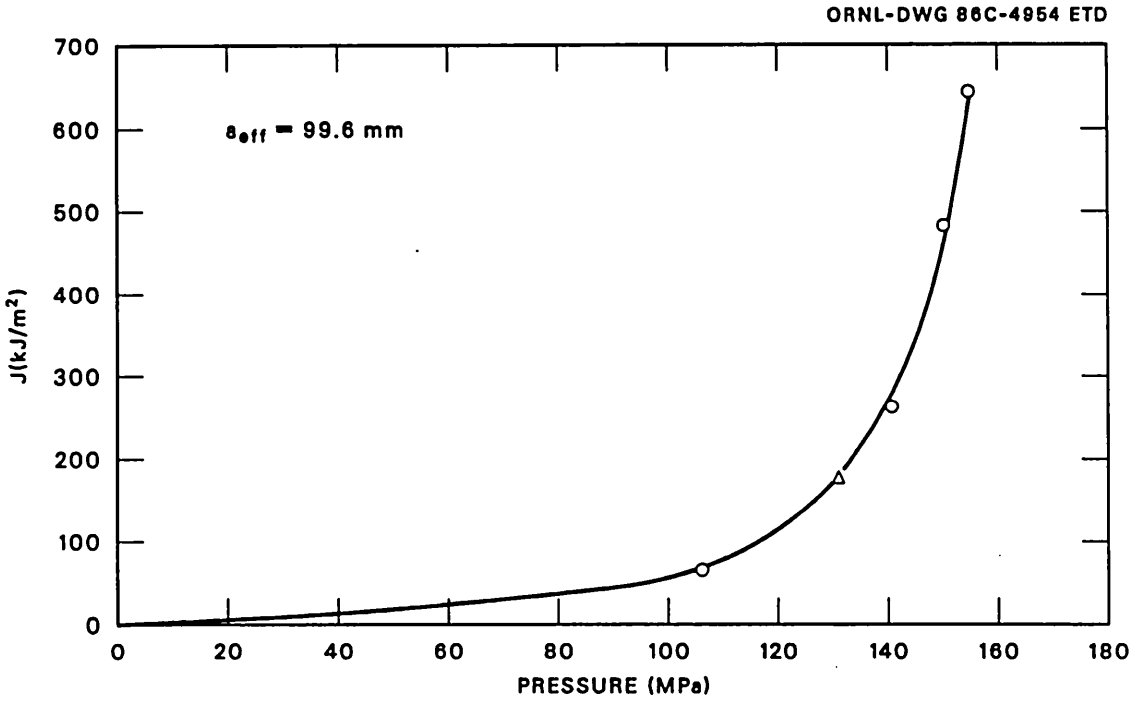

Fig. 5.32. Graphical interpolation for pressure at tearing instability based on the instability solution shown in Fig. 5.31.

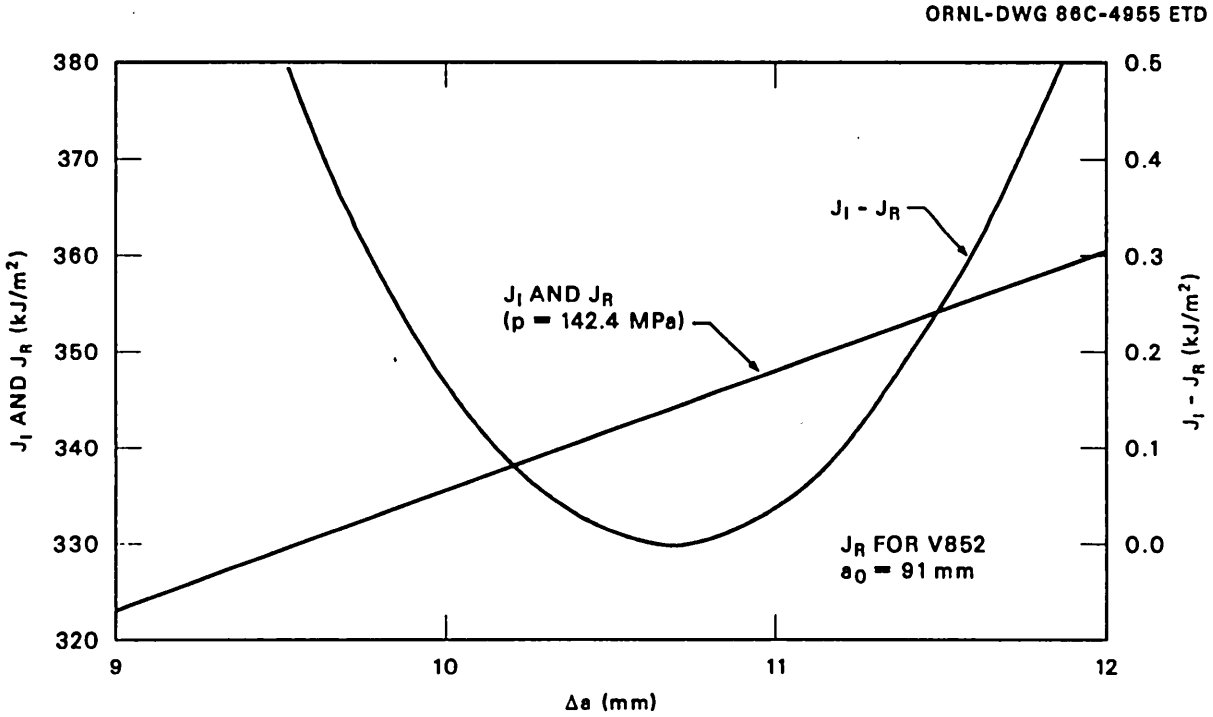

Fig. 5.33. J_I, J_R, and $J_I - J_R$ vs Δa for the instability pressure based on characterization weld V852.

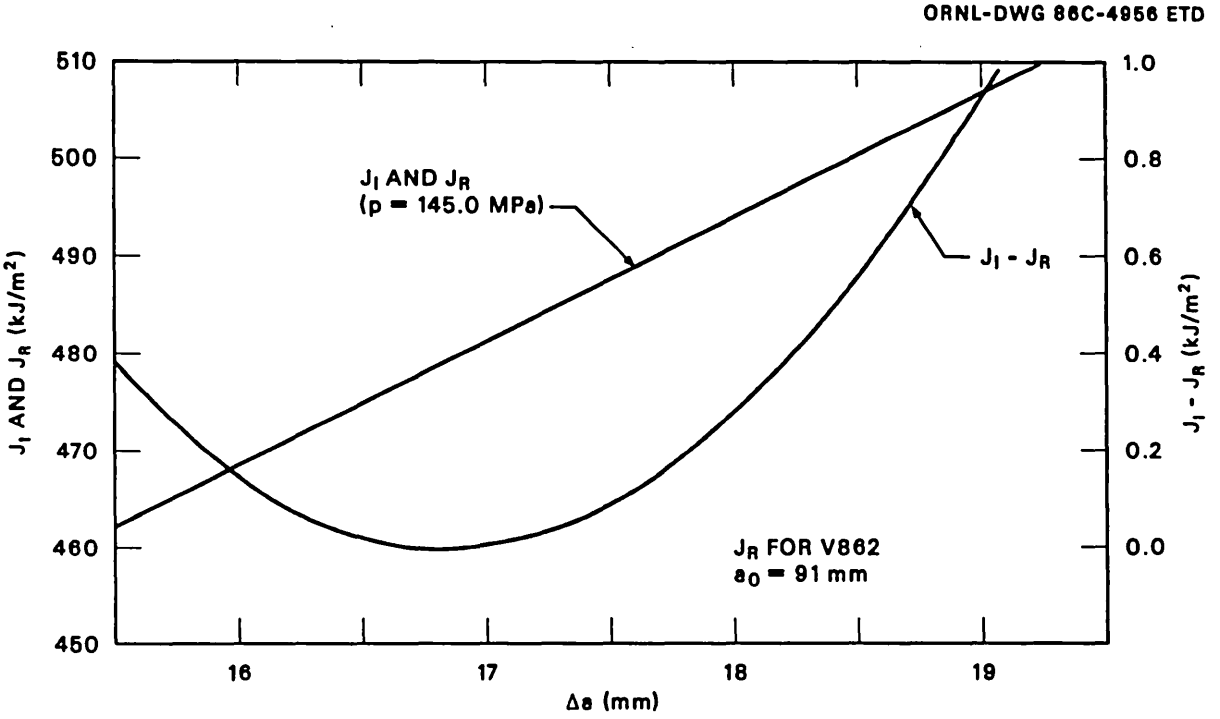

Fig. 5.34. J_I, J_R, and $J_I - J_R$ vs Δa for the instability pressure based on characterization weld V862.

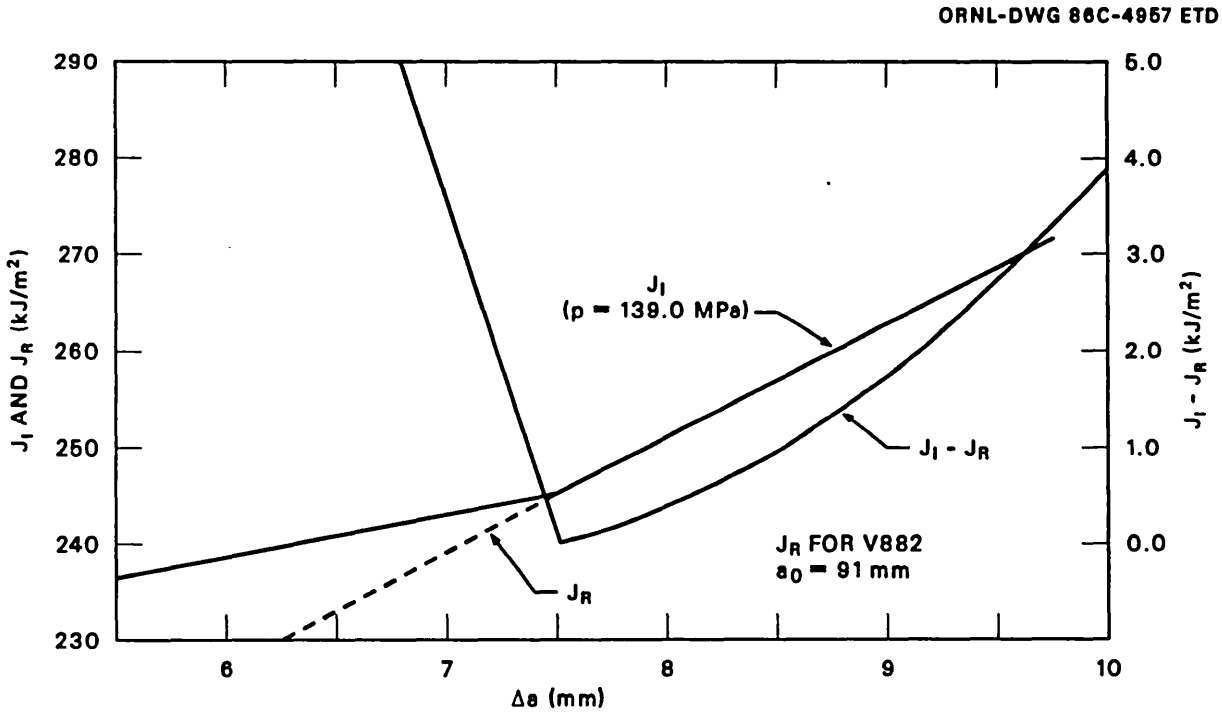

Fig. 5.35. J_I, J_R, and $J_I - J_R$ vs Δa for the instability pressure based on characterization weld V882.

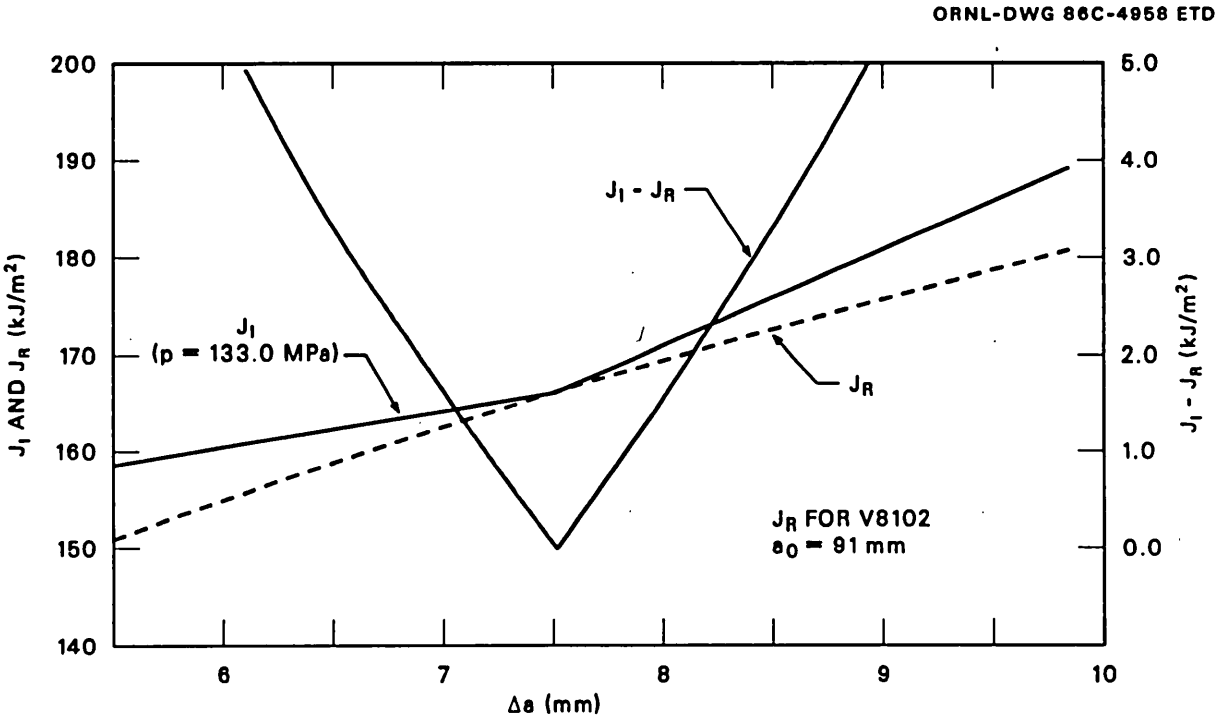

Fig. 5.36. J_I, J_R, and $J_I - J_R$ vs Δa for the instability pressure based on characterization weld V8102.

the instability solutions based on the J_R resistance curves for the four characterization welds, V852, V862, V882, and V8102, respectively. For weld V8102, Fig. 5.36 shows that the predicted instability conditions are p = 133 MPa and Δa = 7.5 mm. Thus the preliminary graphical solution and the more precise numerical solution are in good agreement.

5.3 Pretest Analysis Round Robin

Because of the widespread international interest in the reliability of analysis methods for ensuring the safe operation of reactor pressure vessels, the Nuclear Regulatory Commission asked ORNL to implement a pretest analytical round robin for the test of intermediate vessel V-8A. Following the performance of flaw-sizing calculations, notch machining, and fatigue sharpening by cyclic pressurization, a complete package of pretest analysis information (see Appendix B) was mailed to a distribution list of all parties indicating an interest in the round robin. Because the purpose of the round robin was to facilitate the objective evaluation of analytic methods, including the time required to implement them in a realistic engineering situation, the time provided, 5 weeks, was considered reasonable. Because the problem involved the ductile tearing of a flaw under elastic-plastic conditions, the analysts were asked to estimate the nominal pressure-strain curve for the vessel, the variation of flaw dimensions with pressure, and the pressure at flaw-tearing instability.

Pretest analyses were based on the estimated size of the fatigue-sharpened flaw and the material properties of the characterization welds. A summary of the results of the pretest analytical round robin is shown in Table 5.9. Note that all but the lowest of the estimated instability pressures were within 10% of the actual instability pressure, and the lowest was only 14% low. The predicted estimates of flaw growth prior to instability range from 7 to 15 mm, while the UT-indicated value is 5 mm. The three estimates received from the United Kingdom (see Appendix C) were all performed by the R6 Method, which has developed from a generalization of the through-crack strip yield equation for a plate under tension. The assumptions involved in the UK analyses included (1) completely ductile crack extension, (2) material properties falling within the scatter bands of the characterization data, (3) material properties unaffected

Table 5.9. Vessel V-8A pretest analytical round-robin results for ductile flaw instability

Organization	Method	P (MPa)	λ (%)	Δa[a] (mm)
National Bureau of Standards	Simplified Line Spring	153	0.126	12
ORNL	TM and J_R curve	150	0.133	10
IWM, Freiburg	(Not specified)	147		15
ORNL	ORVIRT and J_R curve	147		10
CERL	R6	141	0.108	7
ORNL	Experimental results	140	0.12	5
ORNL[b]	ORVIRT J_R curve	139		8
AERE	R6	128		7
National Nuclear	R6	121	0.092	7

[a]Prior to instability.

[b]Based on the J_R curve for weld V882. Unpublished pretest predictions based on welds V852, V862, and V8102 were p = 143, 145, and 133 MPa and Δa = 11, 17, and 8 mm, respectively.

by intermittent partial unloading or sustained loading, (4) the crack acting as a sharp planar defect, and (5) pressure reduced at initial through-thickness flaw instability to prevent axial flaw instability. It was noted that there might be a potential for time-dependent effects to promote a flaw instability if the pressure was held constant close to flaw instability.[13]

The estimate by the Simplified Line Spring Model,[14] performed by National Bureau of Standards (NBS), Boulder, Colorado (see Appendix D), was particularly complete. It included estimates of both the CMOD and the crack-tip-opening displacement (CTOD), as well as the pressure-strain curve and the flaw instability pressure. The CMOD estimate was in good agreement with the elastic-plastic finite-element calculations performed at ORNL, although both estimates underpredicted the measured values near flaw instability, probably because of axial flaw growth.

The method of analysis used by IWM Freiburg (see Appendix E) was also based on the R6 Method, but the result was presented as a plot of pressure vs current crack size. Three curves were prepared, corresponding to the estimated mean and extremes of R-curve behavior. Instability was defined by the maximum load point on the plot of pressure vs current crack depth.

The calculations performed at ORNL by the ORGMEN-ADINA-ORVIRT programs,[3-5] the results of which are discussed in Sect. 5.2.5, proved to be quite accurate, including indications of a propensity for axial crack tunneling. The diverseness of the resistance curves accounts for most of the scatter in the ORNL predictions of the instability pressure. However, stable flaw growth predictions were not very sensitive to the choice of a J_R curve.

In general, it was observed from the estimates submitted that a lower bound R-curve provided the best estimate of flaw instability pressure, unless other deliberate conservatisms were introduced. Crack-opening displacements and strains for partial yielding were estimated, and good accuracy was obtained by algebraically direct approximations as well as by numerical methods. It was demonstrated that engineering methods are available for analyzing 3-D flaw problems involving elastic-plastic behavior, at least for flaws in plain plates and cylinders.

5.4 Posttest Calculations

5.4.1 Posttest R-curve measurements

After the V-8A test, measurements were made of the initial and final flaw dimensions, and J_R tests were made on specimens of material cut from the vessel. The pretest measurements of the flaw dimensions were reasonably accurate, as indicated by the pretest and posttest values given in Table 5.10. Results of the J_R specimen tests for the vessel[15] are given in terms of J_D (the deformation-theory interpretation of tearing resistance tests) in Fig. 2.15 and Table 5.7, which show that the V-8A weld seam had tearing resistance similar to that of weld V8102, the characterization weld with the lowest tearing resistance. Appendix L includes the J_D data of Ref. 15 and tabulated values and plots of the modified resistance (J_M) curves for the V-8A special seam weld.

Table 5.10. Flaw geometry measurements made posttest on actual fracture surfaces

Measurement	Dimensions (mm)	
	Pretest	Posttest
Wall thickness (w) at flawed section		
Initial	144.5	141.3[a]
Final		140.0[b]
Flaw depth (a)		
Initial	91.2	87.8
Final[c]		101.4
Flaw length (2b)		
Initial	280.0	280.0
Final[c]		453.0

[a]Largest value measured. Unnecked section was probably slightly thicker.

[b]At center of flaw. See Table N.1 (Appendix N) for other measurements.

[c]These are dimensions after the test was completed. See Sect. 4.4.6 and Appendix N for a detailed description of the final flaw geometry.

5.4.2 ORNL ORVIRT calculations

A tearing instability analysis based on the principles discussed in Sect. 5.2.5 was performed. The pretest series of ORVIRT calculations of J-applied, V8EP8—V8EP15, was used in conjunction with the initial flaw depth measured posttest (Table 5.10) and the J_D tearing resistance determined posttest from the V-8A weld seam (Table 5.7). The $J_I - J_R$ relationships in this analysis are shown graphically in Fig. 5.37. The calculated instability conditions are p = 134.5 MPa and Δa = 12.5 mm.

An approximate graphical analysis using the J_M tearing resistance curve for specimen V8AJ4 was also constructed, as shown in Fig. 5.38. Despite the fact that specimen V8AJ4 had relatively low tearing resistance compared with the other V-8A test weld specimens and that two tearing instabilities were produced in the test of vessel V-8A, none is predicted in Fig. 5.38. Thus, it appears that further analytical investigations are necessary before J_M resistance curves can be used with confidence in conjunction with J-applied curves calculated by deformation theory for the safety analyses of structures.

Comparison between pretest analyses and experimental measurements indicated a need to improve the accuracy of CMOD and circumferential strain calculations. In this regard, the development of crack tunneling

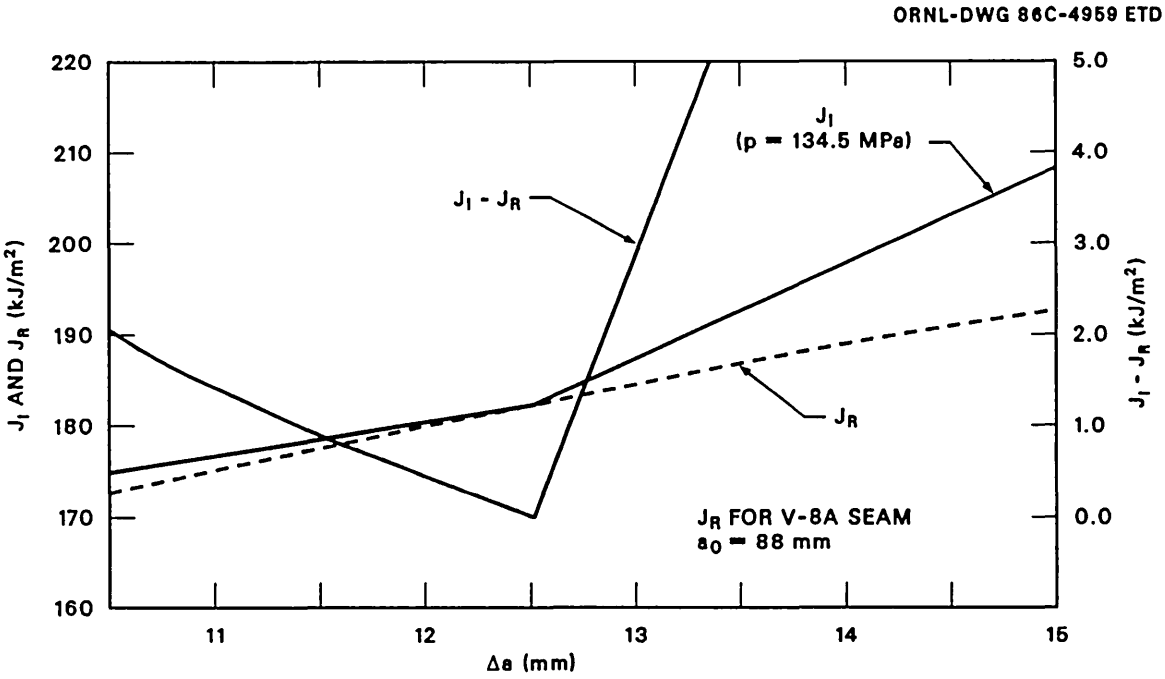

Fig. 5.37. J_I, J_R, and $J_I - J_R$ vs Δa for the instability pressure based on the seam weld in vessel V-8A.

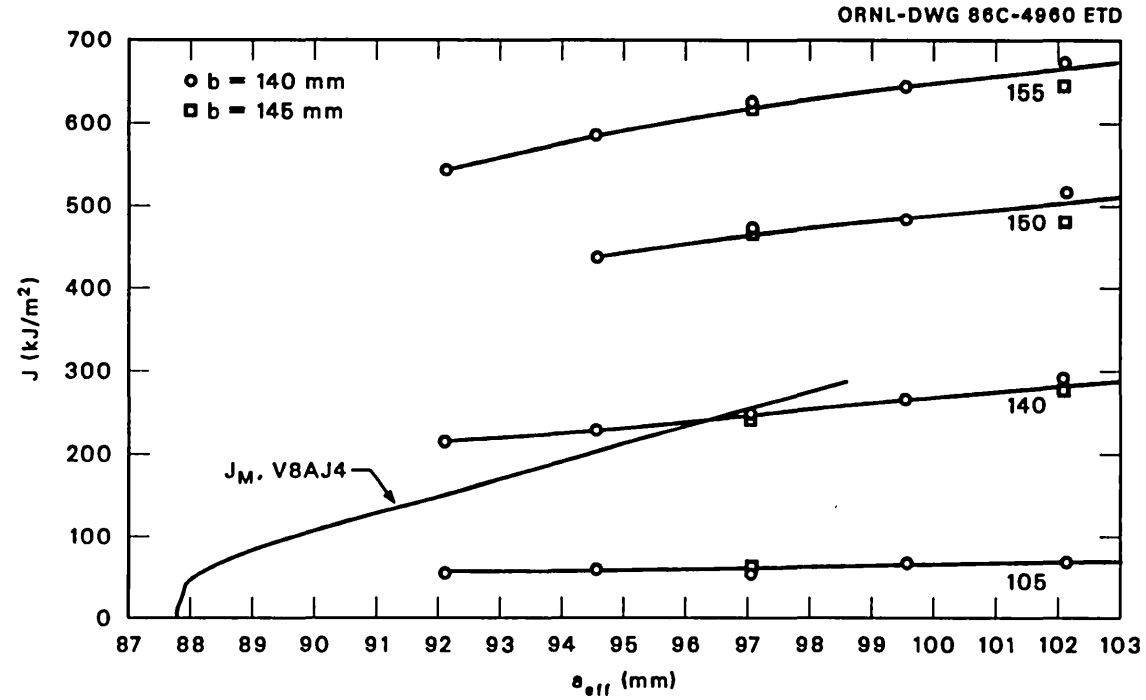

Fig. 5.38. Graphical tearing instability diagram for vessel V-8A based on elastic-plastic finite-element analysis and the J_M resistance curve for test weld specimen V8AJ4. Note that no tearing instability is predicted within the range of experimental J_M data.

by stable tearing beneath the vessel surface made it necessary to consider departures from semielliptical crack shape as a possibly important factor in improving the accuracy of CMOD calculations.

Posttest fracture analyses of the V-8A test were made at ORNL on the basis of direct measurements of approximate flaw geometry and material properties. Figure 5.39 illustrates the series of four crack profiles that were analyzed with the ORMGEN-ADINA-ORVIRT system. Profile 1 is the initial configuration and profile 4 the final configuration. The ORMGEN-generated finite-element model of profile 4 is depicted in Fig. 5.40. The dimensions and geometrical features of the cylinder for this series are identical to those of the final pretest series, V8EP8 to 16. The finite-element models of the two series are similar, the only differences being crack shape, the inclusion of an additional layer of elements (through the thickness) in parts B and D of the model shown in Fig. 5.30(*c*), and the consequential shifting of element boundaries within parts A and C to accommodate the additional layer. Attributes of the mesh for the posttest series are included in Table 5.6 for comparison with earlier models.

This series of four ORMGEN-ADINA-ORVIRT calculations is the basis of only qualitative comparisons of analysis and experiment, excluding the onset of tearing instability. Results from these four analyses are presented in Figs. 5.41–5.45 for $J_I(\phi,p)$ and in Fig. 5.46 for CMOD. These analyses indicate that the peak values of J_I associated with the initial profile for $\phi \approx 20°$ and $p_o > 135$ MPa are reduced relative to the maximum-depth values at $\phi = 90°$ as the crack profile progressively takes on the canoelike shape of the final configuration. This is illustrated by the family of $J_I(\phi,p)$ curves shown in Fig. 5.45 for the progression of four crack profiles at a single pressure, 135 MPa (near which most of the tearing occurred in the test). Profile 1 (semiellipse) shows a relatively high driving force for crack extension in the directions of $10° < \phi < 20°$; progressive canoeing (profiles 2–4) appears to diminish this tendency. These analytical results agree qualitatively with the experimental observations that little, if any, axial crack growth occurred

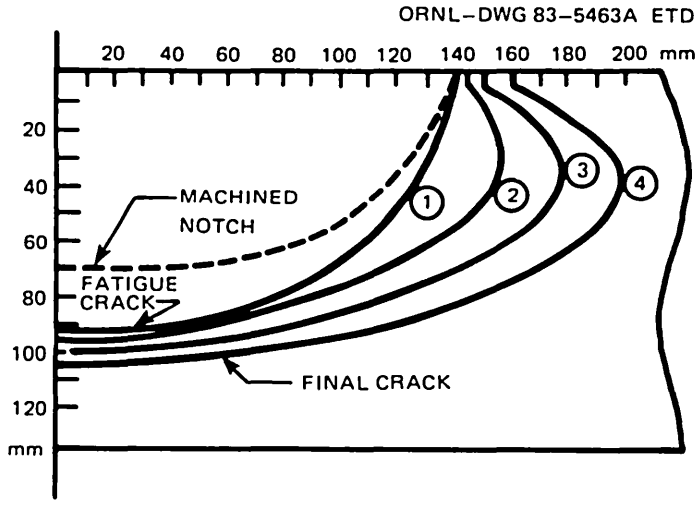

Fig. 5.39. Four crack profiles subjected to posttest analysis using ORMGEN-ADINA-ORVIRT.

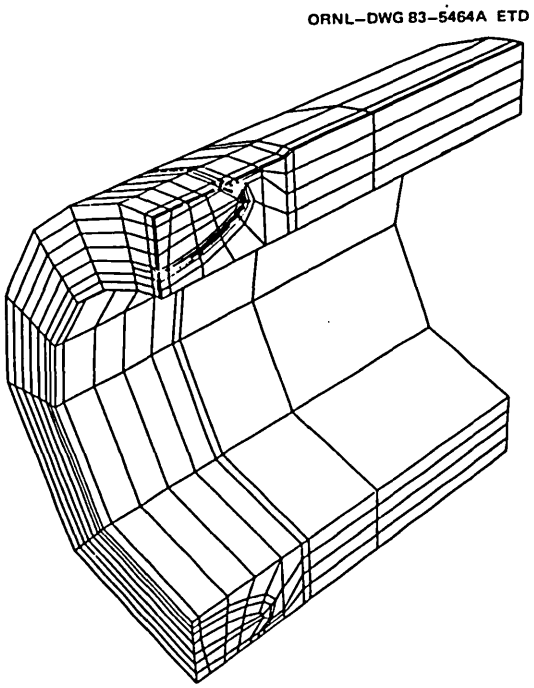

Fig. 5.40. Schematic of finite-element model generated by ORMGEN for final crack configuration (profile 4).

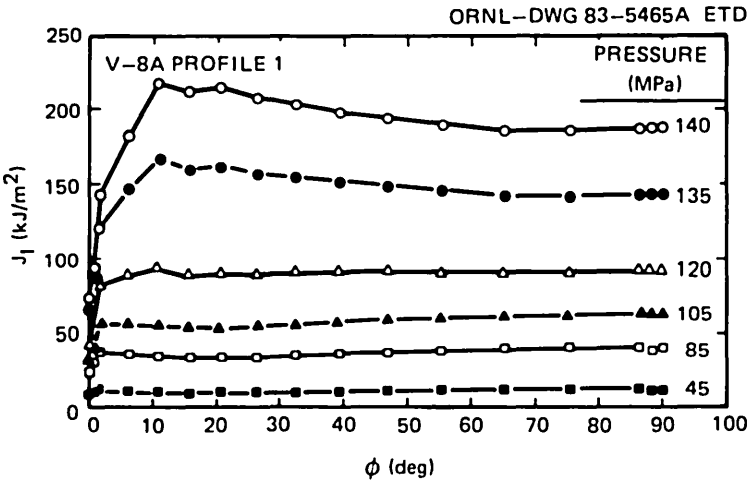

Fig. 5.41. J_I vs ϕ and p for initial crack (profile 1), case V8EP23.

at pressures below ~138 MPa, while extensive canoeing occurred at or above this pressure. It is not known whether the variations in J_I with ϕ when $\phi \lesssim 10°$ are physically real or an artifact of the numerical method.

The comparisons between measured and computed CMOD values in Fig. 5.46 reflect that the stress-strain curve of Fig. 5.9(*a*) (curve 2) used to model the vessel material is overly stiff near the yield stress in the elastic region. An adjusted stress-strain curve that more accurately reflects the posttest measured properties of the V-8A vessel material in the elastic region near the yield point is depicted in Fig. 5.47.

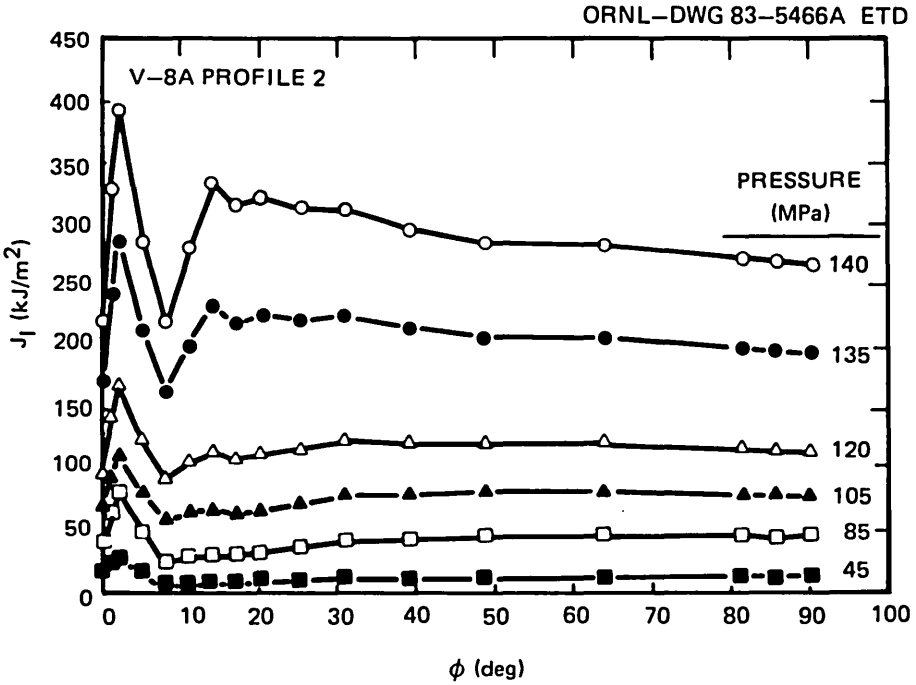

Fig. 5.42. J_I vs ϕ and p for intermediate crack (profile 2), case V8EP22.

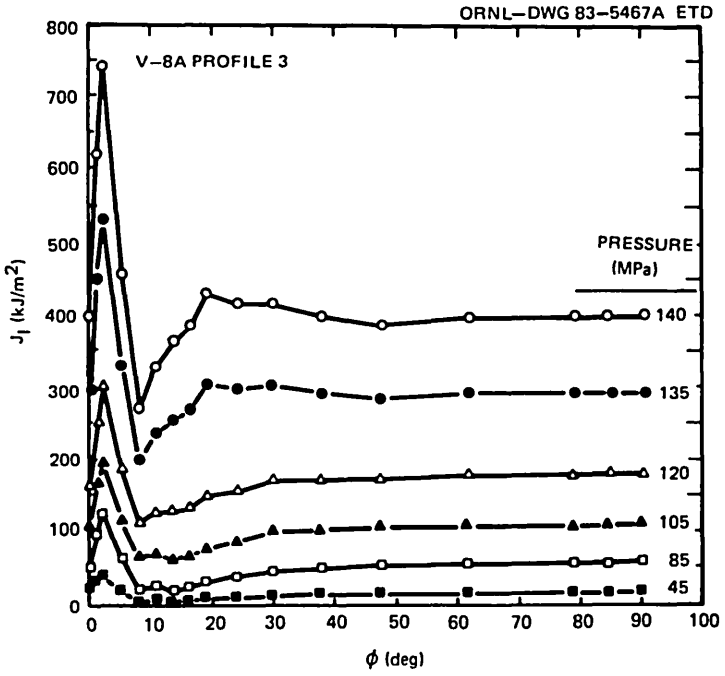

Fig. 5.43. J_I vs ϕ and p for intermediate crack (profile 3), case V8EP21.

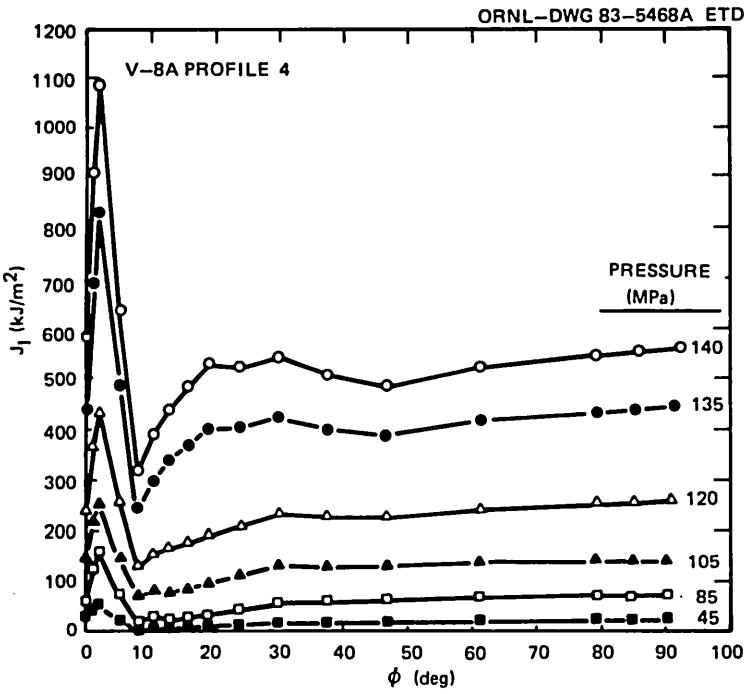

Fig. 5.44. J_I vs ϕ and p for final crack (profile 4), case V8EP20.

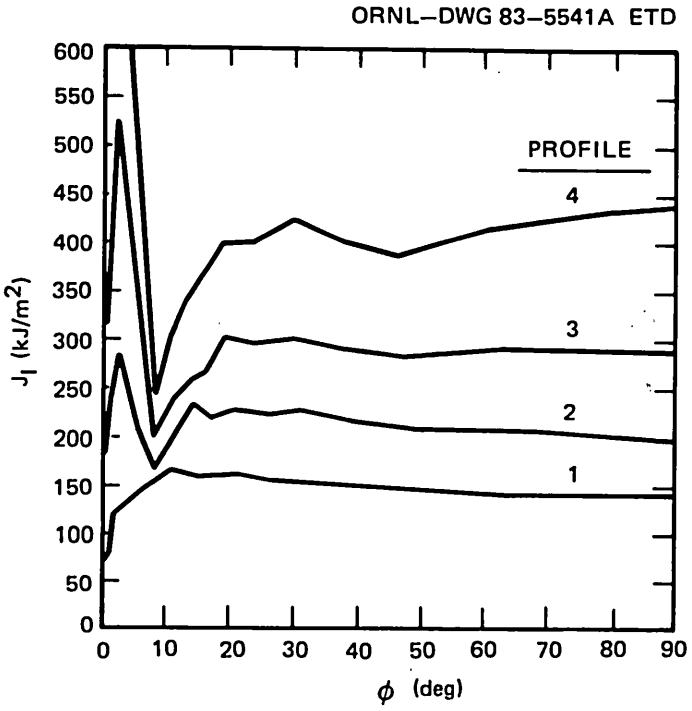

Fig. 5.45. J_I vs ϕ for profiles 1–4 for p = 135 MPa.

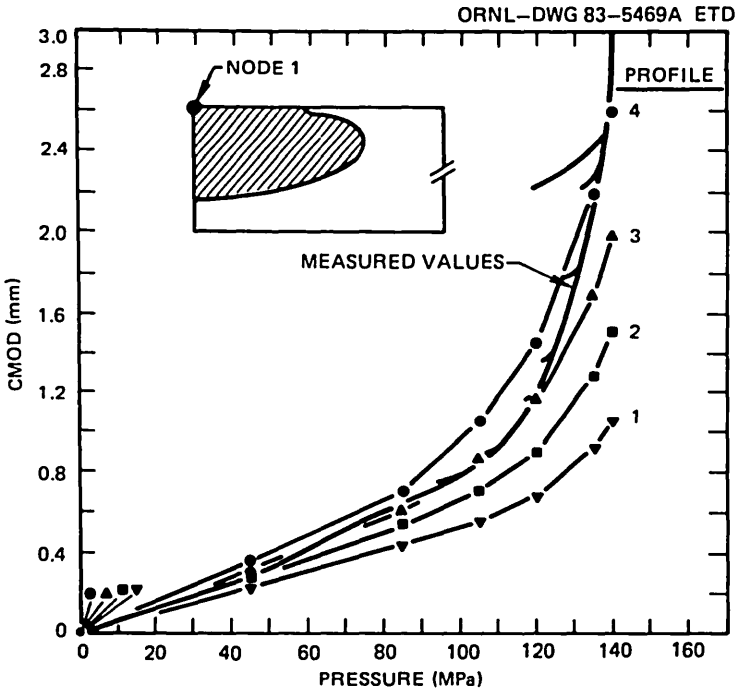

Fig. 5.46. A comparison of measured CMOD with computed CMOD for four crack profiles.

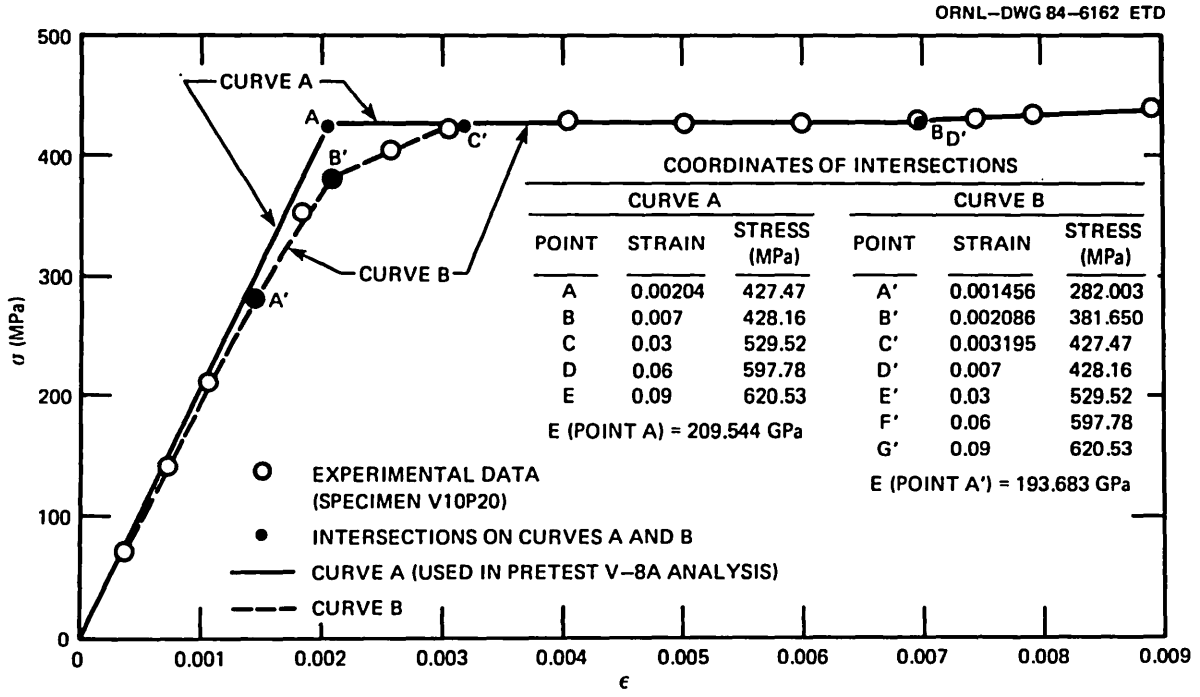

Fig. 5.47. Stress-strain relationships used in earlier V-8A analyses (curve A) and in present analysis (curve B).

This stress-strain curve was used with 3-D finite-element models that better approximate the initial and final crack configurations in a repetition of the stress analyses described above. Computed results from this second set of analyses are compared with measured data in Fig. 5.48 (for CMOD) and in Fig 5.49 (for inner- and outer-surface hoop strain) and indicate improved agreement with the experimental data.

The posttest series of finite-element analyses, when compared with corresponding pretest analyses, is a further illustration of the sensitivity of $J_I(\phi,p)$ to details of the finite-element mesh (see Sect. 5.2.4). Figures 5.21 and 5.41 show $J_I(\phi,p)$ for semielliptical cracks of approximately the same geometry. The differences at low pressure (<105 MPa), at

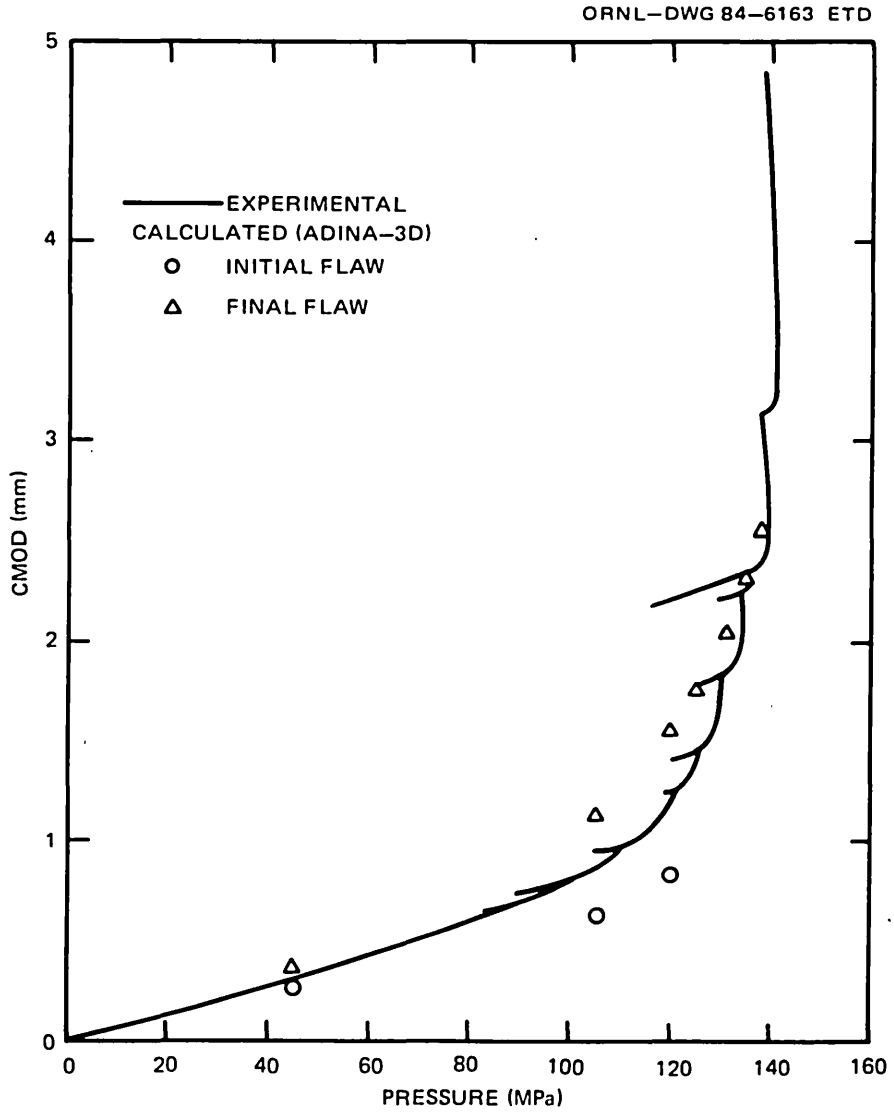

Fig. 5.48. Comparison of measured and calculated values of CMOD in V-8A at center of flaw. Almost all crack growth occurred above 120 MPa.

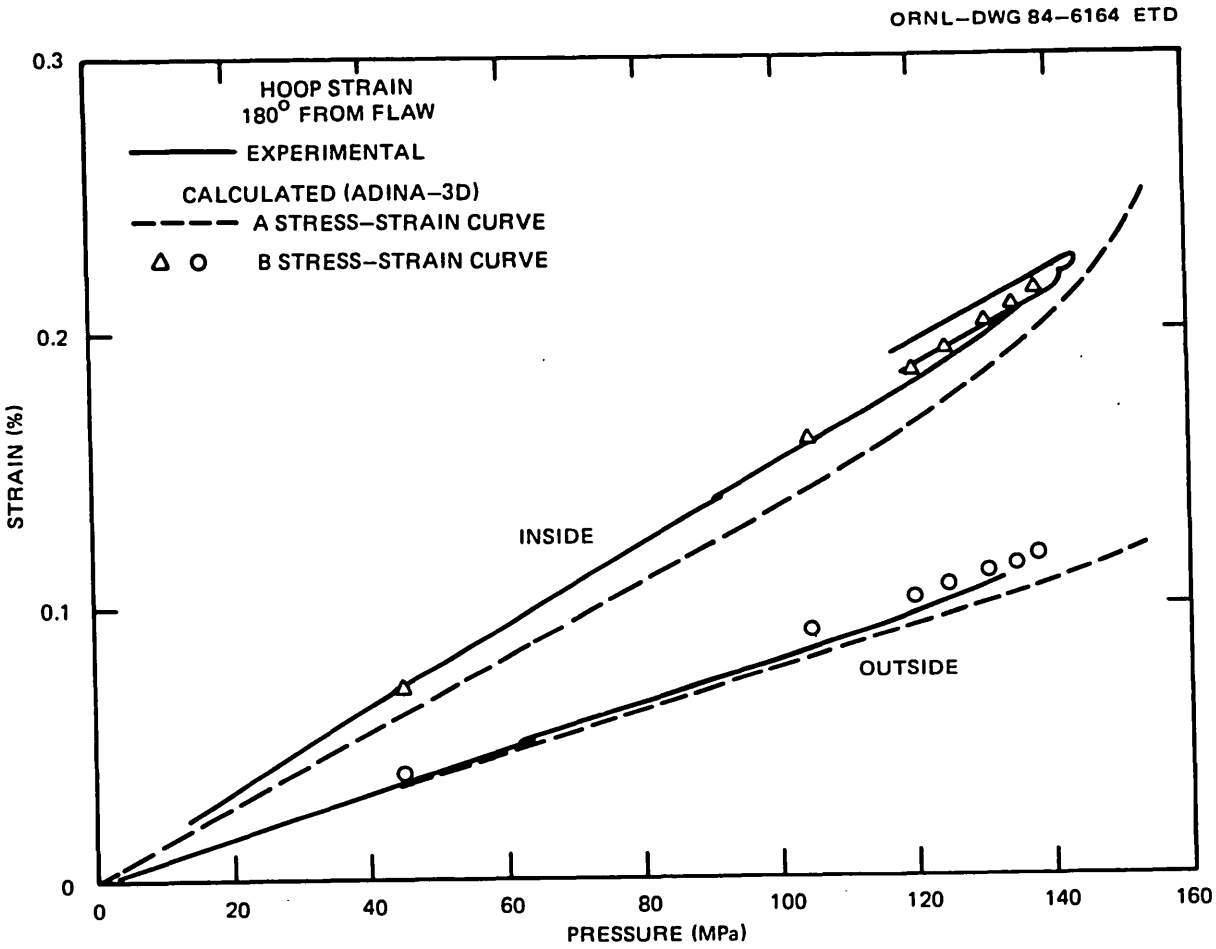

Fig. 5.49. Comparison of measured and calculated values of hoop strain 180° from flaw in V-8A.

which the unflawed cylinder is essentially elastic, are negligible. However, at 140 MPa the maxima in J_I are quite different, 217 vs 248 kJ/m^2 for the posttest (Fig. 5.41) and pretest (Fig. 5.21) cases, respectively. The disparities caused by differences in the refinement of the mesh are large when plasticity becomes extensive, as it was during the last three pressurization cycles of the test. Inside- and outside-surface strain measurements (Appendix M) show that the ligament of the crack was fully plastic and large plastic zones extended from the ends of the crack on the outside surface. Further analyses of the initial crack with the ORMGEN-ADINA-ORVIRT system are necessary to determine whether the latest mesh refinement gives a reasonably accurate representation of $J_I(\phi,p)$.

5.4.3 Other posttest calculations

Several additional posttest analyses of vessel V-8A were made or received from others. Collectively these analyses led to valuable additional clarifications of both the physical and calculational aspects of tearing instability analysis.

Posttest analyses of vessel V-8A by the J-T diagram procedure were developed by both ORNL (see Appendix F) and by a group of cooperating organizations in the UK (see Appendix G). The ORNL analyses described in Appendix F were of the simplest type, assuming a linear J-T applied line. Although it was possible to obtain an accurate estimate of the tearing instability pressure by using the measured lower bound R-curve, the corresponding estimate of crack extension at instability was not accurate, because of the neglect of increasing crack size in the basic method. Some of the UK calculations in Appendix G also used straight J-T applied lines, but others deliberately omitted this assumption, thereby developing excellent examples of the nonlinearity that occurs in J-T applied curves when the applied load approaches a crack-size-dependent fully plastic load. Appendix G states that there are methods other than the J-T diagram procedure by which it is easy to consider both the increase in crack size caused by stable tearing and crack-size-dependent limit loads.

For both power-law stress-strain curves and R6 estimates of J-applied, the nonlinear J-T applied curves developed numerically in Appendix G provided the motivation for development of a mathematical expression for the J/T ratio for the R6 method, which is presented in Appendix H. This solution confirms the general nonlinearity of J-T applied curves, when the variables of load and crack size are not arbitrarily separated, and eliminates the need for potentially inaccurate numerical differentiation to obtain the values of T-applied for the R6 method.

A posttest analysis of V-8A by the Deformation Plasticity Failure Assessment Diagram (DPFAD) procedure was performed by the B&W Company, the fabricator of the V-8A test weld. This analysis is described in Appendix I, which utilizes approximate solution curves based on elastic-plastic J estimates for a through crack in a flat plate. In these calculations, unlike the ORNL graphical analysis, an improvement in accuracy was obtained by changing from a J_D (deformation J) to a J_M (modified J) resistance curve. A straightforward explanation of the DPFAD curve, as a graphical device for solving the nonlinear equation that determines the load satisfying the equation $J_{mat} = J_{appl}$ for a given current crack size, is developed in Appendix J. An explanation of the physical and mathematical bases for the deformation and modified J parameters is developed in Appendix K. Because the DPFAD analysis in Appendix I used an analytical model that was an indirect approximation (a through crack in a flat plate), conclusions cannot be drawn on this basis alone concerning the relative merits of using J_M vs J_D resistance curves for tearing instability calculations. An evaluation of this matter requires additional calculations and a comparison of the analytical assumptions underlying the calculation of J for a flawed vessel and the CT toughness specimen.

5.4.4 Discussion of posttest calculations

Table 5.11 summarizes all the posttest tearing-instability calculations made for vessel V-8A. The individual results are listed in order of decreasing calculated pressure, thereby displaying the relative accuracy of the methods used with respect to the experimental results. The

Table 5.11. Vessel V-8A posttest calculations and experimental results for ductile flaw instability

Organization	Method	Pressure (MPa)	Outside circumferential strain (%)	Δa (mm)	Details in Appendix
IWM, Freiburg	R6	145		9.0	E
ORNL	TM ($2b_0$ = 279.4 mm)	145		13.3	
ORNL	TM ($2b_0$ = 304.8 mm)	144	0.12	12.7	A
ORNL	J-T	140	0.26	28.2	F
RNL	J-T	140		15.0	G
ORNL	Experimental results	140	0.12	5.0	
B&W	DPFAD; J_M	139		7.6	I
CERL	J-T and R6; $a = a_0$	136		5.0	G
ORNL	ORVIRT and J_R curve	134.5		12.5	
B&W	DPFAD; J_D	132		5.1	I
CERL	J-T and R6; $a = a_0 + 6$ mm	130		5.0	G

TM calculations are pretest estimates based on an R-curve for weld V8102, the characterization weld known from posttest data to best represent the vessel test material. In the case of the J-T calculations made by ORNL, only the calculation based on the measured R-curve for weld V8102 is shown, because the other calculations were made primarily for the auxiliary purpose of evaluating R-curve parameter correlations with Charpy impact energy. The range of estimated instability pressures shown in Table 5.11 is less than the range for the pretest calculations shown in Table 5.9, as expected. Also noteworthy are the overestimates of Δa at instability made by the J-T method, because of the neglect of this factor in the calculation of J. In addition, there is a scarcity of strain estimates, with one accurate but the other inaccurate because of the excess strain near yielding estimated by the Ramberg-Osgood equation. In fact, the only analyses of vessel V-8A that included accurate strain estimates were the Simplified Line Spring and TM estimates. As shown in Appendix A, the TM method also produced accurate posttest estimates of both load and strain at instability for vessels V-1, -3, and -6. The series of J-T calculations contained in Appendix F also produced accurate values of instability load and strain for vessels V-1, -3, and -6, but, as indicated above, the same method did not produce an accurate strain estimate for vessel V-8A.

In Table 5.11, the highest and lowest calculated pressures are 3.6% above and 7.1% below the measured instability pressure. Moreover, all but the last two results listed are within ±4% of the measured result. The main reason for the improvement in accuracy with respect to pretest calculations is the use of J_R curves near the lower bound of the measured scatter band, although the DPFAD-J_M analysis is an exception to this observation. Because the use of a J_M resistance curve in conjunction with a 3-D elastic-plastic calculation of J did not produce an instability estimate, it is clear that numerical precision alone does not lead to accuracy. More work is needed on this issue.

Six different methods of analysis were used for pretest or posttest analyses of V-8A, and it is instructive to compare these methods of analysis with regard to some of their basic features. Five basic features are directly related to the completeness, accuracy, and ease of execution of the analytical procedures:

1. considers plastic instability,
2. considers effects of increasing crack size on calculated value of J,
3. can directly calculate the load corresponding to specified values of crack size and toughness,
4. relates load to nominal strain by using a numerically or analytically exact elastic-plastic stress and strain analysis solution, and
5. provides solution for J.

A comparison of the six methods of analysis used for vessel V-8A with regard to the five analytical features listed above is shown in Table 5.12. Except for load-strain considerations, an almost steadily increasing progression of factors is considered by the different analytical methods. Note, however, as shown by the last line in Table 5.12, that nonlinear numerical methods for calculating J cannot solve for unknown loads. The footnote in Table 5.12 indicates that the J analysis

Table 5.12. Comparison of features included in analytical methods used to make tearing instability estimates for vessel V-8A

Method	Plastic instability	Crack extension	Load calculation	Load vs strain	Exact J
J-T					
R6	x			[a]	
Line spring	x			[a]	
DPFAD	x	x	x		
TM	x	x	x	x	
ORVIRT	x	x		x	x

[a] J analysis is based on a fixed relationship between nominal stress and a load.

is based on a fixed relationship between a nominal stress and the load. Nominal strain at the flaw location is not calculated directly, but it can be determined from a separate stress analysis of the uncracked structure. However, the stress calculated at the flaw location by the stress analysis may not be the same as the nominal stress used to calculate J, because of either stress gradients or yielding or both.

5.5 Evaluation of Results

The tearing instability analyses performed on intermediate test vessel V-8A by ORNL and by others consisted of pretest analyses, including premachining flaw design calculations, and posttest calculations. A variety of analytical procedures were employed; each differed partially in detail from the others, but all aimed at predicting a load at instability with respect to current crack size caused by ductile tearing of the crack. All the analyses were based on J-integral resistance curve data for the test material, and all attempted to predict, in some fashion, a load maximum as a function of current crack size.

Not all the analyses performed by others were described completely, so that it was not always possible to fully explain the results or to determine exactly why one result differs from another. However, after reviewing all the analytical results, it is possible to make a general statement of the problem and to identify the numerous important features of an elastic-plastic tearing instability analysis.

The basic analytical problem in an elastic-plastic tearing instability analysis is to formulate an equation that is nonlinear to an arbitrary power in the load, relating the load and the current crack size to the tearing resistance of the material, which is itself a function of the crack size increase, and then to solve the equation for the load. Furthermore, by either differentiation or repeated calculations over a range of current crack sizes, a load maximum is to be determined.

Some of the most important features of a tearing instability analysis were discussed in the preceding section. A more complete listing of important features follows.

A. LEFM

1. The source and exact expressions for the LEFM shape factor in the expression for K_I, and
2. the reference stress for calculating the linear-elastic value of K_I.

B. EPFM and plastic instability

1. Consideration of the load that will cause local plastic instability near the crack;
2. the mathematical expression for the local plastic instability load;

3. the mathematical expression for J and its rearrangements for determining an assessment curve or a J-T applied curve, where used (analytical or numerical);
4. the method for load determination as a function of current crack size and tearing resistance —
   (a) analytical,
   (b) numerical iteration, and
   (c) graphical (e.g., failure assessment curves); and
5. method for determining the relationship between load, nominal stress, and nominal strain at the location of the flaw.

C. Material properties

1. The shape of the stress-strain curve used for analysis and its comparison to the actual material stress-strain curve,
2. choice of the crack extension correction for reducing R-curve data (J_M or J_D),
3. consideration of the temperature dependence of the elastic modulus, and
4. choice of the plane-stress or plane-strain values of the elastic modulus.

D. Tearing instability analysis

1. Method for determining the tearing instability load
   (a) successive load determinations using Δa as the independent variable; and
   (b) diagrams — (1) J_R tangency and (2) J-T intersection with separate load calculation;
2. variability of the loading parameter in the equation for J with crack size through the crack-size dependence of the local plastic instability load;
3. assumption regarding crack size and shape changes during stable tearing, especially for loads approaching the limit load of the flawed region; and
4. in the case of the J-T diagram, the linearity or nonlinearity of the J-T applied curve, either for a fixed crack size because of D.2 or because of updating the crack size.

References

1. R. H. Bryan et al., *Test of 6-in.-Thick Pressure Vessels, Series 2: Intermediate Test Vessels V-3, V-4, and V-6*, ORNL-5059, Union Carbide Corp. Nuclear Div., Oak Ridge Natl. Lab., November 1975.

2. J. G. Merkle, "Explanation of Analytical Bases for Low Upper Shelf Vessel Toughness Evaluations," *Resolution of the Reactor Vessel*

Materials Toughness Safety Issue, U.S. Nuclear Regulatory Commission, NUREG-0744, Vol. 2, Appendix C, September 1981.

3. B. R. Bass and J. W. Bryson, *Applications of Energy Release Rate Techniques to Part-Through Cracks in Plates and Cylinders, Volume 1. ORMGEN-3D: A Finite Element Mesh Generator for 3-Dimensional Crack Geometries*, NUREG/CR-2997, Vol. 1 (ORNL/TM-8527/V1), Union Carbide Corp. Nuclear Div., Oak Ridge Natl. Lab., December 1982.

4. K. J. Bathe, *ADINA — A Finite Element Program for Automatic Dynamic Incremental Nonlinear Analysis*, Report 82448-1, Massachusetts Institute of Technology, Cambridge, Mass., September 1975 (revised December 1978).

5. B. R. Bass and J. W. Bryson, *Applications of Energy Release Rate Techniques to Part-Through Cracks in Plates and Cylinders, Vol. 2. ORVIRT: A Finite Element Program for Energy Release Rate Calculations for 2-Dimensional and 3-Dimensional Crack Models*, NUREG/CR-2997, Vol. 2 (ORNL/TM-8527/V2), Union Carbide Corp. Nuclear Div., Oak Ridge Natl. Lab., February 1983.

6. J. C. Newman, Jr. and I. S. Raju, "Analysis of Surface Cracks in Finite Plates Under Tension or Bending Loads," NASA Technical Paper 1578 (1979).

7. J. G. Merkle, "Stress Intensity Factor Estimates for Part-Through Surface Cracks in Plates Under Combined Tension and Bending," *Quart. Prog. Rep. on Reactor Safety Programs Sponsored by the Division of Reactor Safety Research for July–September 1974*, ORNL-TM-4729, Union Carbide Corp. Nuclear Div., Oak Ridge Natl. Lab., November 1974.

8. F. W. Smith and M. J. Alavi, "Stress-Intensity Factors for a Part-Circular Surface Flaw," *Proceedings of the First International Conference on Pressure Vessel Technology, Delft, The Netherlands*, III, pp. 793–800, ASME, New York, 1969.

9. H. A. Domian, *Vessel V-8 Repair and Preparation of Low Upper Shelf Weldment*, NUREG/CR-2676 (ORNL/Sub/81-83813/1), Babcock & Wilcox Company, Alliance Research Center, Alliance, Ohio, June 1983.

10. A. Mendelson, *Plasticity: Theory and Application*, MacMillan, New York, 1968.

11. C. F. Shih et al., *Methodology for Plastic Fracture, Fifth Quarterly Report, May 1, 1977 to August 31, 1977*, General Electric Company, Schenectady, N.Y., Nov. 1, 1977.

12. W. J. Stelzman and R. K. Nanstad, "Prolongation V-10P Studies," pp. 92–98 in *Heavy-Section Steel Technology Program Quart. Prog. Rep. October–December 1981*, NUREG/CR-2141, Vol. 4 (ORNL/TM-8252), Union Carbide Corp. Nuclear Div., Oak Ridge Natl. Lab., April 1982.

13. S. J. Garwood, *Time-Dependent Ductile Crack Extension of Reactor Pressure Vessel Steels under Contained Yielding Conditions — Interim Report*, Paper No. 1, presented at a seminar sponsored by HM Nuclear Installation Inspectorate, held at the Electric Power Research Institute, Palo Alto, California, July 16, 1982.

14. P. B. King, "Elastic Plastic Analysis of Surface Flaws Using a Simplified Line — Spring Model," paper to be published in *Engineering Fracture Mechanics*.

15. H. A. Domian and R. J. Futato, *J-Integral Test Results of HSST-ITV8A Low Upper Shelf Weld — Final Report*, Babcock and Wilcox Company, Alliance Ohio 44601, February 1983.

6. CONCLUSIONS

Intermediate test vessel V-8A was successfully tested with a semi-elliptical outside surface flaw in a special seam weld of material having low tearing resistance (i.e., low-upper-shelf material). The primary objective of the test was to observe and record the tearing behavior of the flaw while the vessel was loaded incrementally through phases of stable tearing and into a tearing instability.

The special seam weld, as fabricated, had the properties desired. The Charpy impact energy on the ductile upper shelf was low, as is common to irradiated high-copper welds; the tearing resistance of the special seam weld was also representative of that of irradiated high-copper welds.

The desired tearing conditions were attained. Stable tearing was observed at pressures at least as high as 138 MPa. Tearing instability was induced twice and, in each case, was terminated as planned by unloading. The test was terminated without rupturing the vessel, and the final fracture surface was preserved.

On the basis of flaw geometry, material properties, and loading conditions, pretest and posttest analyses were made to estimate the marginal conditions for tearing instability. The pretest analyses, all based on a slightly erroneous estimate of initial crack depth, tended to overestimate the extent of stable crack growth; some underestimated and some overestimated the instability pressure.

Posttest analyses performed on the basis of correct information relating to crack size and material properties are more instructive of the merits of the various methods of analysis. The test results indicate that a good analysis of tearing instability of a pressure vessel should take into account, at least implicitly, the following factors:

1. conditions of local and general plastic instability;
2. a good representation of the shape of the stress-strain properties of the flawed material, especially near the yield point;
3. for methods using J_I, a representation based on elastic-plastic analysis;
4. in the case of elastic-plastic finite-element analysis, the need for sufficient mesh refinement to preclude excessive numerical errors; and
5. scatter of data in tearing resistance curves.

Tearing resistance curves in terms of J as a function of Δa are useful in estimating conditions of tearing instability. However, the advantages of using the J_M parameter instead of the J_D parameter are ambiguous, because the accuracy of an approximate analysis was improved by using J_M but the accuracy of a more precise numerical analysis was not. Nevertheless, this test suggests that estimates of instability may, in fact, be within the range of common engineering uncertainties. However, the test data should be a basis for improving the interpretation of tearing resistance data and their methods of application.

ACKNOWLEDGMENTS

The authors gratefully acknowledge the essential contributions of H. A. Domian and coworkers of the Babcock & Wilcox Company Alliance Research Center for work on vessel fabrication and material characterization; T. M. Cate for work on instrumentation, controls, and data acquisition systems; K. K. Klindt and J. E. Batey for ultrasonic applications; G. D. Whitman for guidance and advice; P. P. Holz (deceased) for his many direct contributions to our group; and M. Vagins of the U.S. Nuclear Regulatory Commission for support, encouragement, and guidance.

Appendix A

ELASTIC-PLASTIC TEARING INSTABILITY ANALYSES FOR INTERMEDIATE TEST VESSELS BY THE TANGENT MODULUS METHOD

A complete method of analysis for estimating margins of safety against ductile fracture should include an elastic-plastic stress and strain analysis of the uncracked structure; a local plastic-instability analysis for the region surrounding the flaw; a J-integral resistance curve; and an elastic-plastic relationship among strain (or load), crack size, and the crack extension parameter. To avoid inaccuracies caused by abrupt changes in the strain-hardening tangent modulus, the latter relationship should be based on strain rather than stress. In addition, agreement with vessel test data and ease of interpreting the calculated results in a physical sense clearly are important features of a method of fracture analysis to be used for evaluating safety margins.

A method of elastic-plastic fracture analysis applicable before gross yielding is called linear-elastic fracture mechanics (LEFM) based on strain.[1] This method has been verified by the test results obtained in the transition temperature range from Heavy-Section Steel Technology (HSST) vessels V-2 and V-4. The data for these vessels indicated that the fracture strain for a flaw in a vessel cylinder can be accurately estimated by LEFM, provided that yielding does not progress completely through the vessel wall. After through-thickness yielding has occurred, the method becomes increasingly conservative as strain increases. It appears that this method works in the case of a vessel cylinder partly because little or no plastic strain occurs in the axial direction, tangential to the crack tip, and, therefore, a condition of full transverse restraint is maintained along the crack front even after partial yielding has occurred. When applying LEFM based on strain, the failure strain is calculated directly as if it were a totally elastic strain, and the corresponding pressure is then determined from the nonlinear pressure strain curve for the flaw location, ignoring the presence of the flaw.[1] A calculated pressure vs outside surface circumferential strain curve for an intermediate test vessel is shown in Fig. A.1.

The more general method of elastic-plastic fracture analysis to be applied here is the tangent modulus method, previously applied by Oak Ridge National Laboratory (ORNL) to several sets of HSST Program test specimens, including small-scale steel model pressure vessels,[1] intermediate tensile specimens,[1] and intermediate test vessels with nozzle corner cracks.[2] This method of fracture analysis was originally developed from Neuber's equation[3] for the inelastic stress and strain concentration factors for a sharp notch,

$$K_\sigma K_\varepsilon = K_t^2 , \qquad (A.1)$$

by writing the left-hand side of Eq. (A.1) in incremental form. In Eq. (A.1), K_σ and K_ε are the inelastic stress and strain concentration factors, respectively, and K_t is the theoretical elastic stress concentration factor. The incremental form of Eq. (A.1) is

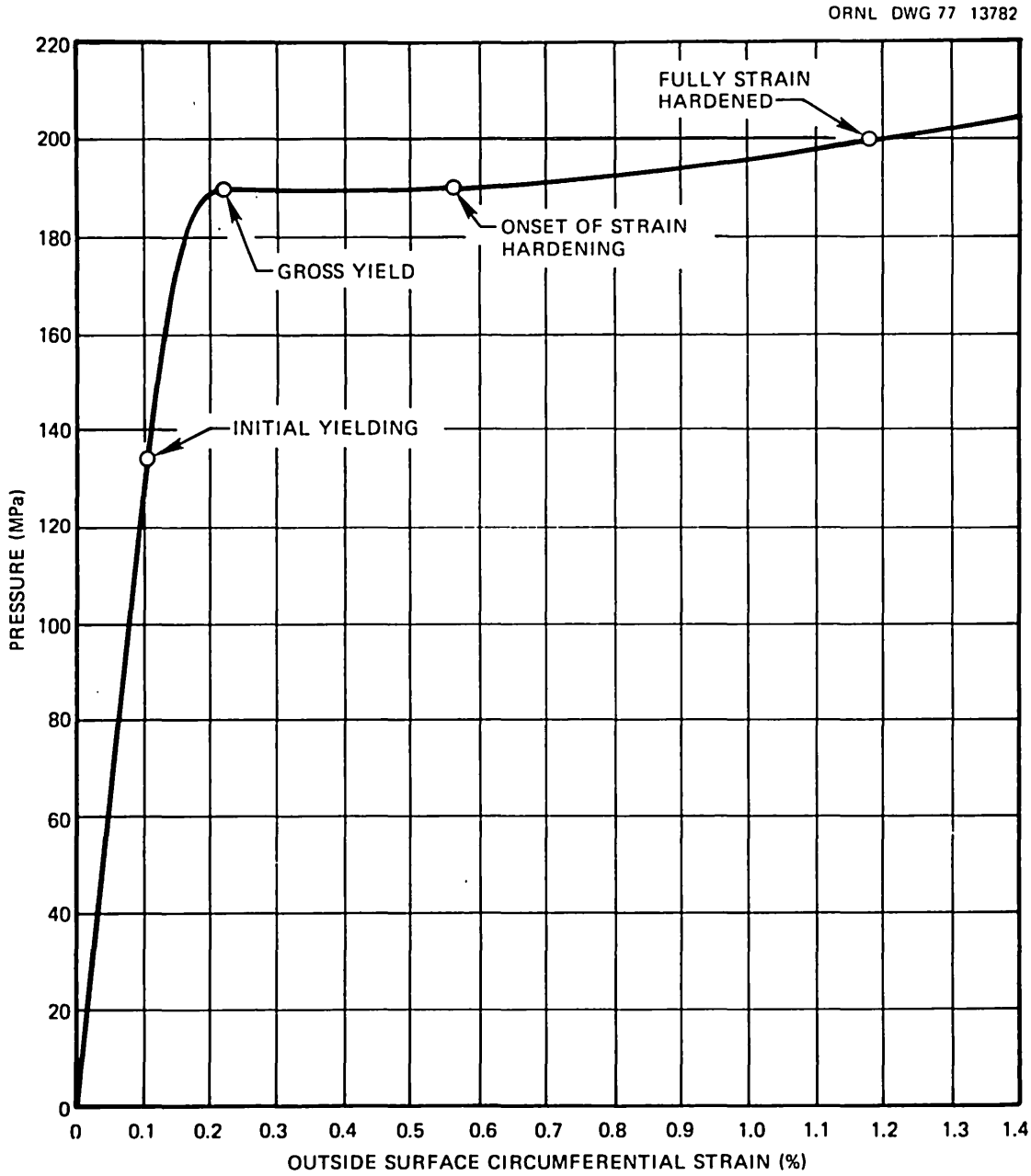

Fig. A.1. Calculated pressure vs outside circumferential strain curve for intermediate test vessel.

$$\left(\frac{d\sigma}{dS}\right)\left(\frac{d\varepsilon}{d\lambda}\right) = K_t^2 \ , \tag{A.2}$$

where σ and S are the peak and the nominal stresses, respectively, and ε and λ are the peak and the nominal strains, respectively. Additional analysis has shown that Eq. (A.2) can be derived by differentiating the results of a J-integral analysis of an elastic region containing a sharp notch with a reduced modulus zone surrounding the notch tip.[4] Although derived from elastic analysis, Eq. (A.2) is applicable, as an approximation, to elastic-plastic analysis because of the linearity of the flow rule that governs the plastic strain increments in incremental plasticity. According to the incremental theory of plasticity,[5,6] the plastic strain increments at a point are linearly proportional to the effective stress increment and inversely proportional to the strain-hardening tangent modulus. The latter quantity varies from point to point and also changes between load increments with the total effective plastic strain.

The working form of Eq. (A.2) is obtained by using the substitutions

$$\frac{d\sigma}{d\varepsilon} = E_s \ , \tag{A.3}$$

$$\frac{dS}{d\lambda} = E_g \ , \tag{A.4}$$

and the equation

$$K_t = 2C\sqrt{\frac{a}{\rho}} \ , \tag{A.5}$$

where E_s is the strain-hardening tangent modulus, E_g is the gross section tangent modulus in the plane of the flaw, ρ is the crack-tip root radius, and, as shown by Creager and Paris,[7] C is the LEFM shape factor in the expression for K_I. The result after rearrangements is the incremental expression

$$d\varepsilon\sqrt{\rho} = 2C\sqrt{a}\sqrt{\frac{E_g}{E_s}}\,d\lambda \ . \tag{A.6}$$

Note that, although neither $d\varepsilon$ nor ρ can be determined separately, their product can be determined from the quantities appearing on the right-hand side of Eq. (A.6). The integration of Eq. (A.6) is facilitated by approximating the stress-strain curve with a series of connected straight-line segments, as shown in Fig. A.2. The tangent modulus E_g is considered to be the average tangent modulus across the section containing the flaw. In the case of tensile loading, for strain increments in the strain range below the yield strain, E_g has the value of E. For strain increments in the strain-hardening range, E_g has the value of E_s. For strain increments in the transition range between the yield strain λ_Y and the strain at the onset of strain hardening λ_s, the tangent modulus E_g is assigned a

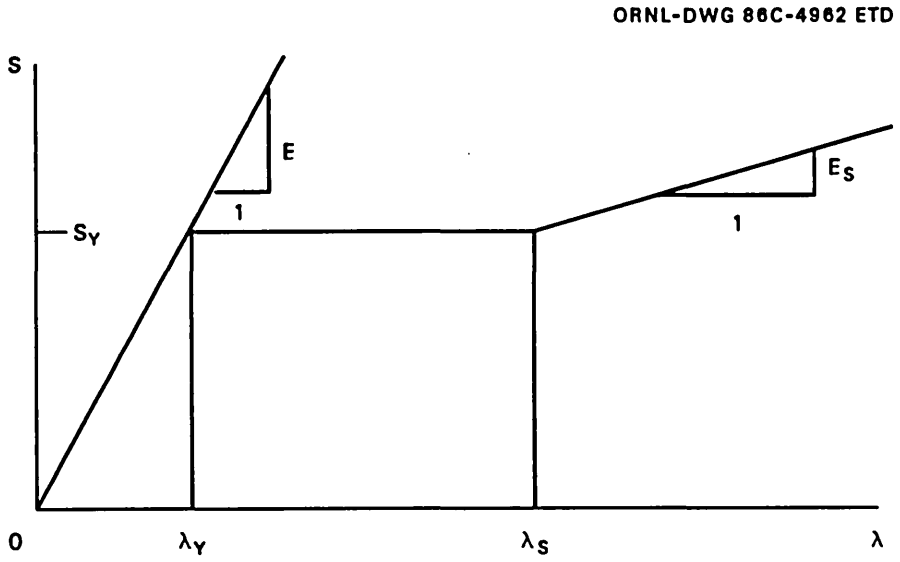

Fig. A.2. Piecewise linear representation of tensile stress-strain curve.

value determined by the strain gradient caused by the eccentricity of the net section.[1] For a linearly varying strain distribution, it can be shown that the average tangent modulus across a plane section is the ratio of the stress difference to the strain difference between the two surface points at the ends of the section. In the transition range of strain, the average tangent modulus changes continually with strain. However, to simplify the analysis, the average tangent modulus is estimated as the ratio of the stress difference across the section as a result of bending, when initial yielding just occurs at the cracked surface, divided by the difference between the strain at the onset of strain hardening and the bending strain at the opposite unyielded surface. Thus, in the transition range of strain,

$$E_g = \frac{\left(\frac{\Delta S_b}{S}\right) S_Y}{\lambda_s - \left(1 - \frac{\Delta S_b}{S}\right) \lambda_Y} , \qquad (A.7)$$

where S is the nominal net section stress at the cracked surface, ΔS_b is the stress difference across the section as a result of bending, λ_Y is the yield strain, and λ_s is the strain at the onset of strain hardening. Equation (A.7) describes conditions just before the onset of strain hardening at the cracked surface, assuming that the stress and strain at the back surface remain constant in the elastic range as yielding progresses inward from the cracked surface. The term $(\Delta S_b/S)$ in Eq. (A.7) is estimated by finding the fractional linear stress decrease across the net section that, considering the area removed by the crack but not the

crack-tip stress concentration, still maintains the line of action of the applied load at the midpoint of the gross section. Therefore, taking the moment of the linearly varying net section stress distribution about the back surface of the specimen, treating the stress that would have acted over the area of the crack as being a uniform tensile stress equal to the linearly varying net section stress acting at the centroidal depth of the crack, and equating the resulting moment arm to t/2 gives

$$\frac{\Delta S_b}{S} = \frac{1}{(1 - k_1) + \dfrac{1}{6\left(\dfrac{A_c}{A_1}\right)(2k_1 - 1)}} . \tag{A.8}$$

In Eq. (A.8), k_1 is the fractional distance of the crack area centroid from the back surface, A_c is the crack area, and A_1 is the effective gross section area. In the case of a surface-cracked tensile specimen, the difference between net and gross section areas causes actual differences between net and gross section strains, as well as a net section stress gradient. In the case of a pressure vessel cylinder, the effective gross section area is estimated only for the purpose of estimating the stress gradient near the flaw caused by the eccentricity of the flaw area, but the net and gross section strains are otherwise assumed to be equal. For a semielliptical surface crack, the crack area is given by

$$A_c = \frac{\pi ab}{2} , \tag{A.9}$$

and the distance ratio k_1 is given by

$$k_1 = 1 - \frac{4}{3\pi}\left(\frac{a}{t}\right). \tag{A.10}$$

For a surface crack in a vessel cylinder, the effective width of the area affected by the crack is estimated to be about five times the thickness, so

$$A_1 = 5t^2 . \tag{A.11}$$

The value of the elastic shape factor C for a single part-through surface crack can be estimated by any one of the several approximate methods available, or it can be calculated by the finite-element method. However, for simply and directly performing a series of calculations covering a range of crack sizes, shapes, and stress gradients, it is convenient to have a set of algebraic equations that explicitly consider back surface effects, crack shape, and stress gradients. Two recently developed sets of equations of this type are the equations fit to the present *American Society of Mechanical Engineers* (*ASME*) *Code* Sect. XI

Appendix A curves by Cipolla[8] and the equations fit to an extensive series of three-dimensional finite-element calculations by Newman and Raju.[9] Another older but simpler set of equations developed at ORNL,[10] based partly on photoelastic experimental data obtained at Virginia Polytechnic Institute,[11] was used for making the tangent modulus calculations presented in this report. These equations have also been used by ORNL for analyzing the run-arrest behavior of an initially semicircular part-through surface crack located in a thick-walled steel test cylinder subjected to thermal shock loading.[12] The basic equation of LEFM is written in the conventional form

$$K_I = C\sigma_s\sqrt{\pi a} \ , \tag{A.12}$$

where σ_s is the elastically calculated surface stress at the flaw location. Referring to Fig. A.3, the factor C for a semielliptical part-through surface crack is represented semiempirically by the expression[10]

$$C = \frac{M_1 M_2}{\Phi} \ F(\theta) \ , \tag{A.13}$$

where M_1 and M_2 are the front- and back-face free surface magnification factors, respectively, and the factors $F(\theta)$ and Φ are taken from the analytical solution for a buried elliptical crack under uniform tension.[13]

The factors M_1 and M_2 are given by[10]

$$M_1 = \psi_0(\theta) - \left(1 - \frac{\sigma_0}{\sigma_s}\right)\left(\frac{2a}{t}\right) \psi_1 \ (\theta) \ , \tag{A.14}$$

$$M_2 = \left[\frac{\tan(\pi a/2t)}{\pi a/2t}\right]^{1/2} \left[1 + \left(\frac{a}{t}\right)^{5/2} \sin\theta\right] , \tag{A.15}$$

where

$$\psi_0(\theta) = 1.211 - 0.186(\cos\theta)^{1/2} \ , \tag{A.16}$$

$$\psi_1(\theta) = 0.18 + 0.54\left(\frac{a}{b}\right)\cos\theta \ . \tag{A.17}$$

The factor $F(\theta)$ is given by

$$F(\theta) = \left[1 - \frac{1 - \left(\frac{a}{b}\right)^2}{1 + \left(\frac{b}{a}\right)^2 \cot^2\theta}\right]^{1/4} . \tag{A.18}$$

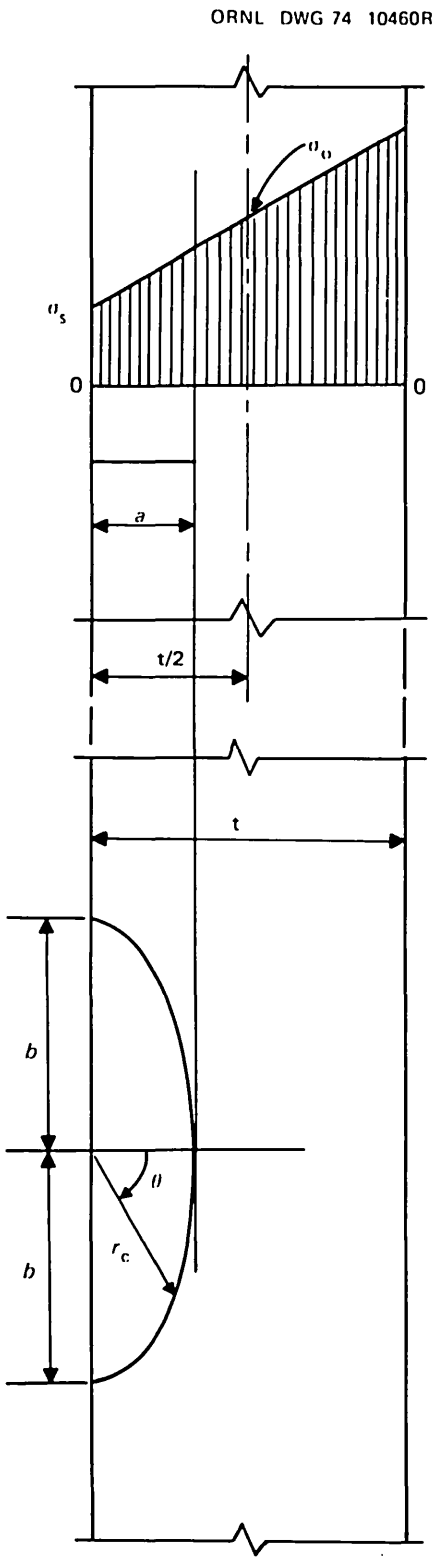

Fig. A.3. Definition of terms associated with the analysis of a semielliptical surface crack.

The elliptical integral Φ in Eq. (A.13) can be calculated with sufficient accuracy by using the empirical equation[14]

$$\Phi^2 = 1 + 4.593 \left(\frac{a}{2b}\right)^{1.65} . \tag{A.19}$$

For an external surface flaw of the shape used in the intermediate test vessels, the maximum value of K_I occurs at the deepest point of the flaw, for which $\theta = 0°$. In addition, by fitting a straight line to the elastic stress distribution in the outer portion of the vessel wall,[15] $\sigma_0/\sigma_s = 2.10/1.84 = 1.196$. Consequently, for the intermediate test vessels, the equations for M_1, M_2, and $F(\theta)$ at $\theta = 0°$ become

$$M_1 = 1.025 + 0.391 \left(\frac{a}{t}\right) \left[0.18 + 1.08 \left(\frac{a}{2b}\right)\right] , \tag{A.20}$$

$$M_2 = \left[\frac{\tan(\pi a/2t)}{\pi a/2t}\right]^{1/2} , \tag{A.21}$$

$$F(\theta) = 1 . \tag{A.22}$$

For elastic-plastic calculations based on toughness measured in terms of a J-integral resistance curve, the value of J corresponding to a given amount of stable crack growth can be determined from the resistance curve or from an empirical equation for estimating the curve from Charpy and tensile data, if a measured resistance curve is not available. For subsequent calculations, it is convenient to convert the value of J into an equivalent value of K_c, using the equation

$$K_c = \sqrt{EJ} . \tag{A.23}$$

The value of nominal strain in the vessel wall required to develop the same level of toughness can be calculated by integrating Eq. (A.6) after first expressing the toughness quantity appearing on the left-hand side of Eq. (A.6) in terms of its equivalent value of K_c. This conversion is based on the premise that strain hardening occurs immediately at the notch tip and that the notch-tip fracture strain is independent of whether the nominal strain is above or below the yield strain. Assuming nominally elastic conditions, the nominal fracture strains determined from Eqs. (A.6) and (A.12) can be equated, resulting in the conversion[4]

$$\varepsilon_f\sqrt{\rho} = \left(\frac{2}{\sqrt{\pi}} \sqrt{\frac{E}{E_s}}\, \lambda_Y\right) \left(\frac{K_c}{S_Y}\right) , \tag{A.24}$$

which, for an estimated modulus ratio $E/E_s = 100$, then becomes

$$\varepsilon_f\sqrt{\rho} = 11.284\ \lambda_Y\left(\frac{K_c}{S_Y}\right). \tag{A.25}$$

When the nominal fracture or tearing strain λ_f is below the yield strain, LEFM based on strain is the appropriate method of analysis. The outside surface circumferential strain is then given by

$$\lambda_f = \frac{K_c}{MC\left(\frac{\sigma_s}{p}\right)\sqrt{\pi a}}, \tag{A.26}$$

where M is the modulus relating pressure to elastic strain and (σ/p) is the ratio of the elastically calculated outside surface circumferential stress to the pressure. For the intermediate test vessels, $(\sigma_s/p) = 1.84$, and $M = 1320$ MPa $(\%)^{-1}$.

When the nominal strain is in the transition range $(\lambda_Y < \lambda_f < \lambda_s)$, integrating Eq. (A.6) gives

$$\varepsilon_f\sqrt{\rho} = 2C\sqrt{a}\left[\sqrt{\frac{E}{E_s}}\,\lambda_Y + \sqrt{\frac{E_g}{E_s}}\,(\lambda_f - \lambda_Y)\right]. \tag{A.27}$$

Solving Eq. (A.27) for λ_f and then using Eq. (A.25), the fracture or tearing strain in the transition range of strain is given by

$$\lambda_f = \lambda_Y + \frac{\dfrac{5.642\ \lambda_Y\left(\frac{K_c}{S_Y}\right)}{C\sqrt{a}} - \sqrt{\frac{E}{E_s}}\,\lambda_Y}{\sqrt{\frac{E_g}{E_s}}}. \tag{A.28}$$

When the nominal strain is in the strain-hardening range $(\lambda_f > \lambda_s)$, integrating Eq. (A.6) gives

$$\varepsilon_f\sqrt{\rho} = 2C\sqrt{a}\left[\sqrt{\frac{E}{E_s}}\,\lambda_Y + \sqrt{\frac{E_g}{E_s}}\,(\lambda_s - \lambda_Y) + (\lambda_f - \lambda_s)\right]. \tag{A.29}$$

Solving Eq. (A.29) for λ_f and then using Eq. (A.25), the fracture or

tearing strain in the strain-hardening range is given by

$$\lambda_f = \lambda_s + \left[\frac{5.642\ \lambda_Y \left(\frac{K_c}{S_Y}\right)}{C\sqrt{a}} - \sqrt{\frac{E}{E_s}}\ \lambda_Y - \sqrt{\frac{E_g}{E_s}}\ (\lambda_s - \lambda_Y) \right] . \qquad (A.30)$$

Note that Eq. (A.26) for the elastic range takes the effects of biaxiality into account; Eqs. (A.27)—(A.30), however, are based on a uniaxial state of stress. Consequently, for a cylinder the occurrence of yielding may be indicated by Eq. (A.28) for the transition range, but is not yet indicated by Eq. (A.26) for the elastic range. For the calculations to be discussed here, as an approximation the applicable range of strain was determined by uniaxial calculations, with biaxiality then being taken into account for those cases indicated to be in the elastic range.

Once a strain for fracture or stable tearing has been calculated, the corresponding load can be determined from the load-strain diagram. In the case of the HSST Program intermediate test vessels, the pressure-strain diagram is shown in Fig. A.1. For calculating pressures from strains beyond the range of the curve shown in Fig. A.1, the equation for the fully strain-hardened portion of the pressure-strain curve is

$$p = 177.5 + 19.3\lambda \quad (\lambda > 1.4\%) , \qquad (A.31)$$

where the pressure p is in megapascals and the strain λ is in percent. A similar diagram can be calculated analytically for a vessel of given dimensions and material properties.

If, under rising load, the presence of a crack in a ductile metal does not cause failure because of brittle or ductile crack advance, it will eventually cause the region of yielding surrounding the crack to grow until it reaches free surfaces; then large plastic strains will begin to develop in the yielded region. The cross section of the yielded region surrounding the flaw will contract as tensile stretching takes place in the direction perpendicular to the plane of the flaw. Eventually, an effective load-bearing area surrounding the crack will reach a plastic-instability condition and begin to neck. Referring to Fig. A.4, it has been found possible to estimate the plastic-instability pressure for a trapezoidal area bordering a part-through surface crack in the cylinder of a pressure vessel by[15,16]

$$P_f = \frac{\left(1 - \frac{A_c}{A}\right) \sigma_\theta^*}{\left(\frac{r_i}{t}\right)} , \qquad (A.32)$$

where σ_θ^* is the plastic-instability flow stress for a thin-walled cylinder under internal pressure, estimated as ~1.07 times the average of the yield and the ultimate tensile stresses; A_c is the crack area; A is the

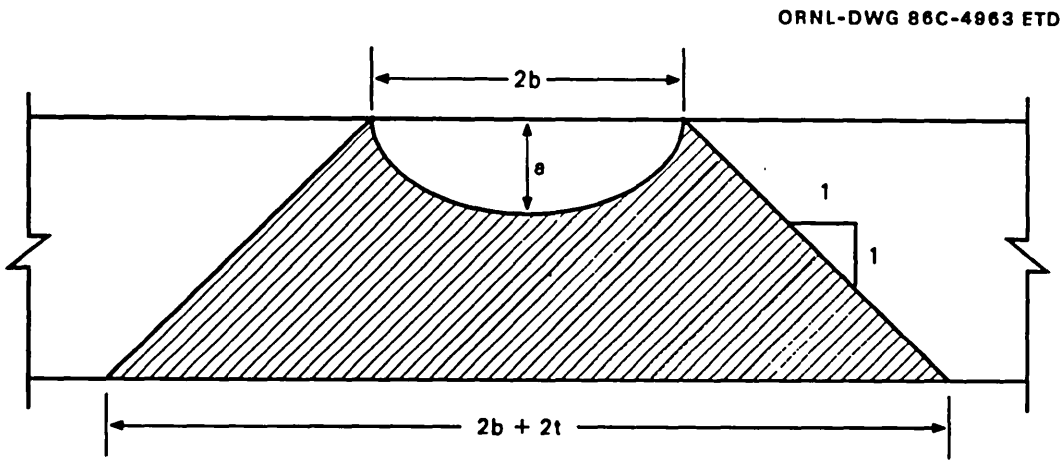

Fig. A.4. Effective load-bearing area governing local plastic instability near a surface flaw.

effective load-bearing area; and r_i and t are the inside radius and thickness of the vessel cylinder, respectively. Treating the crack border as a semiellipse, the crack area is given by Eq. (A.9), and treating the effective load-bearing area as a trapezoid,

$$A = (2b + t)t \ . \qquad (A.33)$$

The original development of Eqs. (A.32) and (A.33) for estimating local plastic-instability conditions for part-through surface cracks in vessel cylinders is given in Appendix C of Ref. 15. Calculated results for the HSST Program intermediate pressure vessel tests are summarized in Ref. 16.

Applying the above method of analysis to the intermediate test vessels shows that the results are improved by considering possible crack shape changes during stable crack growth. Because there is only a moderate stress gradient in the vessel walls, it was found reasonable to assume that only one crack dimension would change until the shape ratio a/2b became equal to 0.36, after which it would remain constant; this is the value of a/2b for which the elastically calculated values of K_I at the deepest point and at the surface of a shallow semielliptical part-through surface crack in a uniform tensile field are approximately equal.[10]

The foregoing equations can be used for a crack stability analysis by using the amount of stable crack growth as the independent variable and plotting curves of strain and load vs current crack size. These curves will reach maxima at the onset of tearing instability, as shown schematically in Fig. A.5. The following is the procedure for making the calculations.

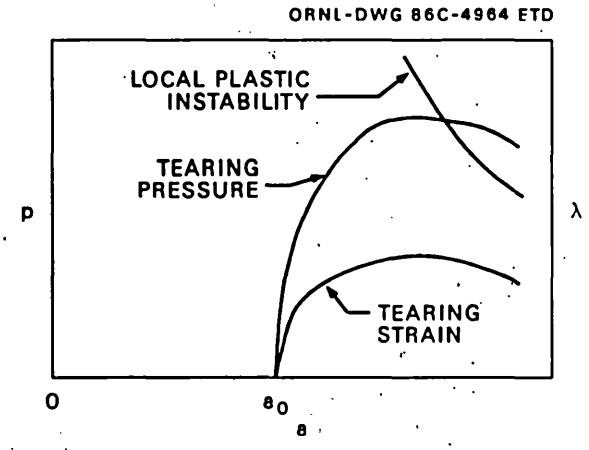

Fig. A.5. Schematic diagram of graphical output from a tearing and local plastic instability analysis.

1. Assume the value of Δa.
2. Calculate J from a measured or empirically estimated resistance curve.
3. Determine the current crack depth a and the crack shape ratio a/2b.
4. Determine the LEFM shape factor — C, for example — by using Eqs. (A.13)—(A.19). For the intermediate test vessels, these equations reduce to Eqs. (A.19)—(A.22), plus Eq. (A.13).
5. Determine the effective tangent modulus in the transition range of strain, using Eqs. (A.7)—(A.11).
6. Convert the current value of J to its equivalent K_c value, using Eq. (A.23).
7. Determine the nominal tearing strain required to develop the calculated value of K_c from Eqs. (A.26), (A.28), or (A.30).
8. Determine the corresponding tearing pressure from the pressure-strain diagram. For the intermediate test vessels, use Fig. A.1 or Eq. (A.31).
9. Calculate the pressure for local plastic instability, using Eqs. (A.9), (A.32), and (A.33).
10. Plot the tearing strain, tearing pressure, and local plastic-instability pressure vs current crack size, as shown in Fig. A.5. It is convenient to use two vertical scales, reading the tearing strain from the right-hand scale and the two pressures from the left-hand scale.
11. If the peak of the tearing-strain curve precedes the intersection of the two pressure curves, use the peak strain and pressure values as an estimate of the conditions at the onset of tearing instability. Note that this solution will be identical to one based on the tangency of a J- vs crack-size curve with the J_R curve.
12. If the two pressure curves intersect before the tearing-strain curve reaches its maximum, use the conditions at the intersection point as a conservative estimate of failure conditions, especially if the vessel wall is fully yielded.

Because tearing instability occurs at the maximum point of the pressure vs crack-size curve, it follows that a calculation for any assumed current crack size provides a lower bound to the tearing-instability pressure, provided that the local plastic-instability pressure is still higher.

In the absence of experimental resistance curve data for vessels V-1, -3, and -6, it was assumed that the R-curves for these vessels could be represented by the power law

$$J = 175.13\ c \left(\frac{\Delta a}{25.4}\right)^m , \tag{A.34}$$

where J is in kilojoules per square meter; Δa is in millimeters; and the parameters c and m could be estimated by correlation with upper-shelf Charpy V-notch (CVN) impact energy and tensile flow stress data, using[17,18]

$$c = -0.144 \left(\frac{CVN}{135.58}\right) + 5.382 \left(\frac{CVN}{135.58}\right)^2 , \tag{A.35}$$

$$x = c + 1.5 \left(\frac{\bar{\sigma}}{689.48}\right) , \tag{A.36}$$

$$m = \frac{0.473\ x^3}{14.42 + x^3} , \tag{A.37}$$

where CVN is in joules and the flow stress $\bar{\sigma}$, which is in megapascals is defined here as the average of the yield and ultimate tensile stresses. The input data for analyzing vessels V-1, -3, and -6 are given in Tables A.1 and A.2. The analytical results are given numerically in Table A.3 and graphically in Figs. A.6—A.8. A comparison between measured and calculated results is shown in Table A.4, which indicates good agreement. Note from Table A.3 that vessel V-1 appears to have reached maximum load by tearing instability; vessels V-3 and V-6, however, both reached maximum load by simultaneous tearing and local plastic instability.

Although the tangent modulus method of analysis does involve approximations, it also has several advantages, including ease of considering flaw size and shape variations; the applicability of elastic geometry factors because of the incremental nature of the analysis; the completeness of the solution in terms of both strain and load; explicit consideration of local plastic-instability effects; and for plotting the results, a graphical method that is independent of the analysis method and has clear physical significance. Because of these advantages, the tangent modulus method was used for the vessel V-8A flaw design calculations performed before machining the crack starter notch. The input data used for these calculations were identical to those used for vessels V-1, -3, and -6, except for the material tensile stress values and the use of measured

Table A.1. Test and material conditions for intermediate test vessels V-1, -3, and -6

Vessel	Test temperature (°C)	Initial flaw size (mm)		Material tested	Upper-shelf CVN (J)
		a_0	$2b_0$		
1	54	65.0	209.6	A 508-2	122
3	54	53.6	215.9	Weld	170
6	88	47.5	133.4	Weld	170

Table A.2. Material properties and vessel dimensions for intermediate test vessels V-1, -3, and -6

Item	Symbol	Value
Elastic modulus	E	207 GPa
Strain-hardening tangent modulus	E_s	2.07 GPa
Yield stress	S_Y	496 MPa
Yield strain	λ_Y	0.24%
Strain at onset of strain hardening	λ_s	1.20%
Ultimate tensile stress	σ'_{ult}	641 MPa
Flow stress	$\bar{\sigma}$	569 MPa
Cylinder plastic-instability stress	σ^*_θ	609 MPa
Inside radius	r_i	342.9 mm
Wall thickness	t	152.4 mm
Pressure-strain modulus	M	1320 MPa $(\%)^{-1}$

tearing resistance curves. Because differences between base and weld metal tensile properties were small, the base metal properties of characterization section V802 at 121°C (Ref. 19) listed in Table A.5 were used because they govern the overall deformation of the cylinder. Because tearing instability was desired before gross yielding, the elastic, perfectly plastic, pressure-strain curve extending to gross yield shown in Fig. A.9 was plotted by using a yield stress elevated 4% above the uniaxial value to allow for biaxiality effects.[2]

Table A.3. Tearing and plastic-instability analysis results for HSST intermediate test vessels V-1, -3, and -6

Vessel	J-R parameters		Δa (mm)	a (mm)	b (mm)	$\frac{a}{2b}$	C	$\frac{\Delta S_b}{S}$	$\sqrt{\frac{E_g}{E_s}}$	J (kJ/m²)	λ (%)	p (MPa)	p_f (MPa)	Remarks
	c	m												
1	4.257	0.4352	11.2	76.2	105.9	0.360	0.942	0.349	2.83	522	0.610	190	209	
			15.2	80.3	111.5	0.360	0.962	0.368	2.90	597	0.625	190	204	Tearing instability
			17.8	82.8	115.1	0.360	0.976	0.380	2.95	638	0.624	190	201	
			25.4	90.4	125.5	0.360	1.022	0.410	3.05	746	0.596	190	192	
			50.0	115.1	159.8	0.360	1.265	0.457	3.20	1001	0.395	190	162	
3	8.267	0.4652	16.5	70.1	108.0	0.325	0.944	0.349	2.83	1185	1.486	206	213	
			21.3	74.9	108.0	0.347	0.947	0.354	2.85	1335	1.595	208	210	
			22.4	75.9	108.0	0.352	0.948	0.355	2.86	1364	1.610	209	208	$p \sim p_f$
			23.4	77.0	108.0	0.357	0.949	0.356	2.86	1390	1.621	209	208	
			32.8	86.4	119.9	0.360	0.996	0.395	3.00	1630	1.335	203	197	
			46.7	100.3	139.4	0.360	1.098	0.439	3.15	1923	1.051	197	180	
6	8.267	0.4652	8.1	55.6	78.0	0.356	0.866	0.235	2.36	852	2.15	219	232	
			16.3	63.8	89.4	0.356	0.893	0.286	2.58	1176	2.29	222	223	$p \sim p_f$
			32.5	80.0	112.3	0.356	0.964	0.372	2.92	1624	1.80	212	204	

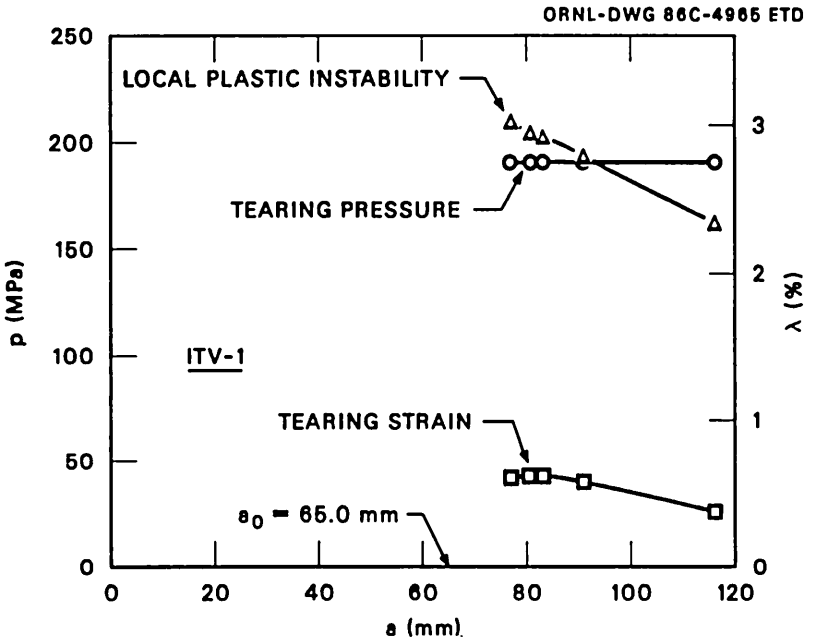

Fig. A.6. Results of tearing and local plastic instability analysis for intermediate test vessel ITV-1.

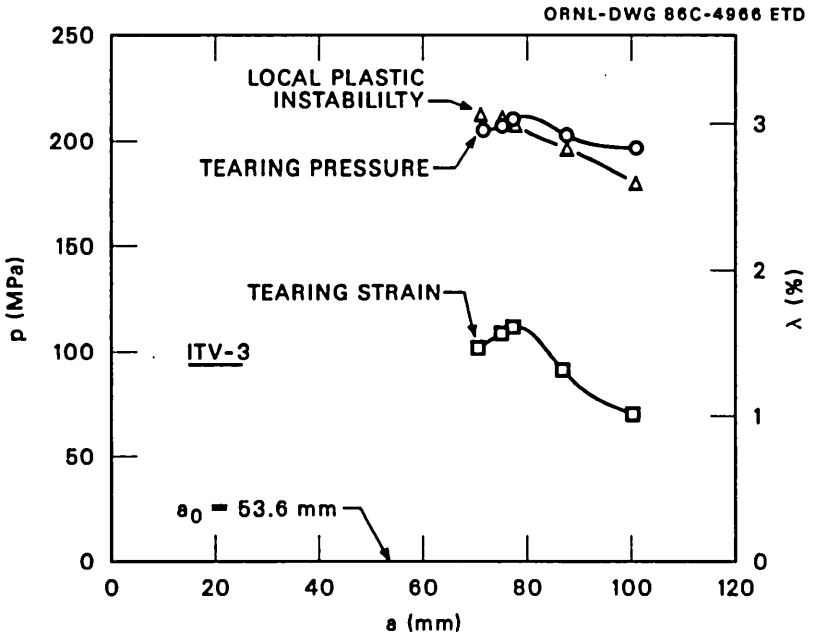

Fig. A.7. Results of tearing and local plastic instability analysis for intermediate test vessel ITV-3.

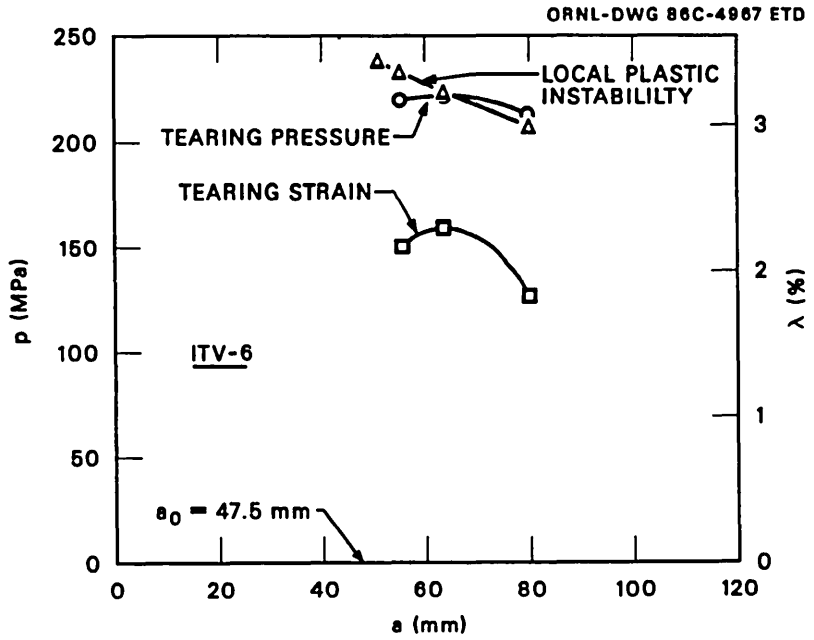

Fig. A.8. Results of tearing and local plastic instability analysis for intermediate test vessel ITV-6.

Table A.4. Comparison of measured and calculated failure conditions for intermediate test vessels V-1, -3, and -6

Vessel	Failure conditions					
	Actual		Calculated			
	p (MPa)	λ (%)	p (MPa)	λ (%)	J (kJ/m^2)	Δa (mm)
1	199	0.92	190	0.63	597	15.2
3	214	1.47	209	1.61	1364	22.4
6	220	2.0	222	2.29	1176	16.3

Four different tearing resistance curves were used for the V-8A flaw design calculations. The first two curves were fit over different crack extension ranges to the data from one trial weld specimen[20] (specimen V842J1), and these curves were used before the characterization weld data became available. The other two curves represented the extremes of the characterization weld data[19] (the average of the two specimens V862J5 and V852J5 and specimen V8102J7). The ranges of variation of the characterization weld data are shown in Fig. A.10. All four of the R-curves used were represented by power-law equations having the form given by Eq. (A.34). The material and specimen identities and power-law parameters of the V-8A flaw design R-curves are given in Table A.6.

Table A.5. Tensile stress and strain properties of base metal section V802 at 121°C used for vessel V-8A flaw design calculations

Item	Symbol	Value
Yield stress	S_Y	414 MPa
Ultimate tensile stress	σ'_{ult}	552 MPa
Cylinder plastic-instability stress	σ^*_θ	517 MPa
Yield strain	λ_Y	0.2%

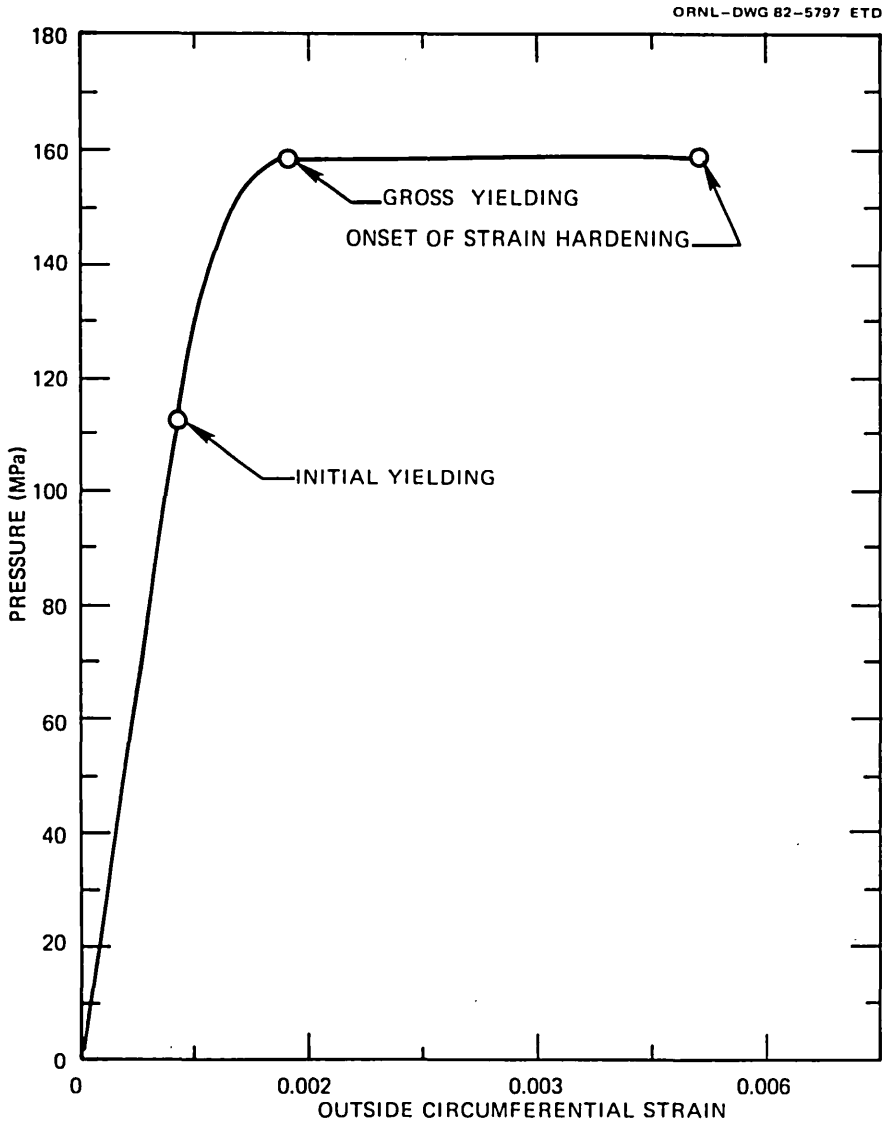

Fig. A.9. Calculated pressure vs outside circumferential strain curve for intermediate test vessel V-8A.

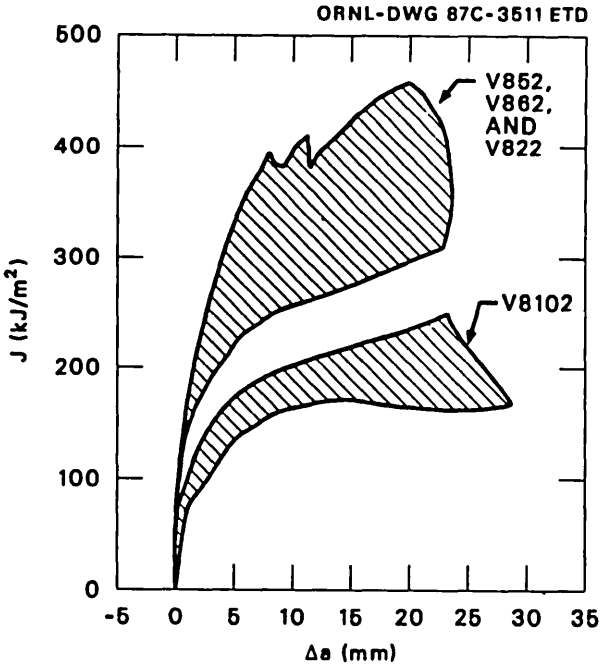

Fig. A.10. Scatter bands of R-curves for vessel V-8A characterization welds.

Table A.6. Material and R-curve specimen identities and power-law parameters used for vessel V-8A flaw design analysis

Weld designation	Specimen No.	Power law Parameters c	m
Characterization welds V862 and V852	Average of V862J5 and V852J5	3.079	0.4397
Trial weld V842	V842J1 $0.28 < \Delta a < 1.5$ mm	2.147	0.3687
Trial weld V842	V842J1 $0.28 < \Delta a < 13.2$ mm	1.512	0.2687
Characterization weld V8102	V8102J7	1.305	0.2798

The flaw size for vessel V-8A was selected by choosing trial dimensions for the fatigue-sharpened flaw; performing tearing instability estimates; and upon achieving a satisfactory result, subtracting the estimated amount of fatigue crack growth during flaw sharpening to obtain the machined notch dimensions. The main criterion was that incipient vessel failure should occur before gross yielding so that the test result could be definitely attributable only to flaw instability, and not also to the large strains that accompany gross yielding. For trial fatigue-sharpened flaw dimensions of a_0 = 91.44 mm and $2b_0$ = 304.80 mm, the tearing and local plastic-instability results are shown in Table A.7 and Fig. A.11. These results indicated that flaw instability would most likely occur before gross yielding and that tearing and local plastic instability would occur nearly simultaneously. This result was considered satisfactory, thus leading to a choice of machined notch dimensions of a_m = 69.85 mm and $2b_m$ = 279.40 mm.

The calculations shown in Table A.7 were used as the basis for one of the pretest failure pressure estimates for vessel V-8A made by ORNL. Using the second lowest of the R-curves to be moderately conservative,

Table A.7. Summary of flaw-sizing calculations for HSST intermediate vessel V-8A[a]

Δa (mm)	a/2b	Item	Lower bound (V8102J7)	Low (V842J1)	High (V842J1)	Upper bound (V862J5 and V852J5)	Plastic-instability pressure (MPa)
0	0.3						158
5.08		J, kJ/m^2	146	172	208	266	
		p, MPa	142	147	152	157	154
	0.317	λ, %	0.177	0.128	0.140	0.159	
10.16		J, kJ/m^2	177	207	268	360	
		p, MPa	144	150	155	159	150
	0.333	λ, %	0.123	0.133	0.151	0.221	
12.70		J, kJ/m^2	188	220	291	398	
		p, MPa	144	150	156	159	148
	0.342	λ, %	0.124	0.133	0.154	0.237	
20.32		J, kJ/m^2	215	249	346	489	
		p, MPa	143	148	155	159	141
	0.360	λ, %	0.120	0.129	0.153	0.244	
25.40		J, kJ/m^2	229	265	376	539	
		p, MPa	139	145	154	159	136
	0.360	λ, %	0.114	0.123	0.147	0.222	

[a]Trial initial flaw dimensions: a_0 = 91.44 mm and $2b_0$ = 304.80 mm.

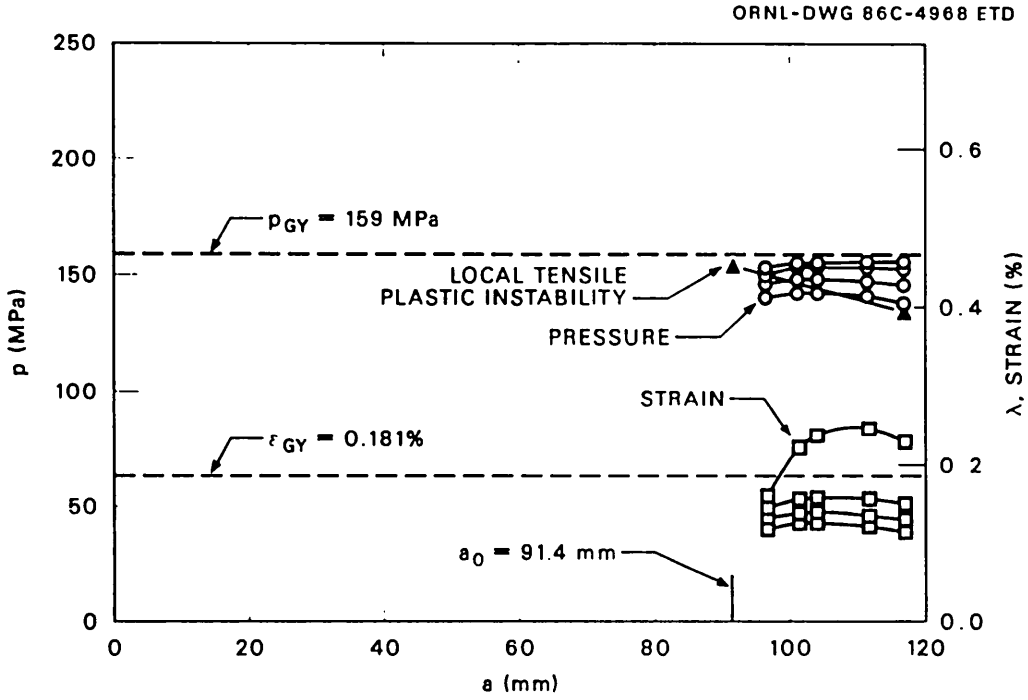

Fig. A.11. Results of tearing and local plastic instability flaw design calculations for intermediate test vessel V-8A.

the failure conditions were estimated to be

$$p = 150 \text{ MPa},$$
$$\lambda = 0.133\%,$$
$$\Delta a = 10.2 \text{ mm}.$$

In posttest analysis it is clear that the lowest of the four R-curves most nearly represented the vessel. The failure conditions for this R-curve are

$$p = 144 \text{ MPa},$$
$$\lambda = 0.122\%,$$
$$\Delta a = 10.2 \text{ mm}.$$

The estimated amount of stable crack growth at instability lies between the 5 mm estimated by ultrasonics at the beginning of instability and the postinstability value of 14.5 mm measured directly by posttest examination of the flaw.[21] Furthermore, as shown by Fig. A.11, the instability load is rather insensitive to small variations in the Δa value, and, for a given R-curve, calculational errors are always conservative.

In summary, the tangent modulus method of analysis has been applied with accurate results to the posttest analysis of vessels V-1, -3, and -6 and with equal accuracy to the flaw design calculations for vessel V-8A. The analysis results can be directly interpreted in a physical sense, thus aiding in the development of a better understanding of the problem.

References

1. R. H. Bryan et al., "*Test of 6-Inch-Thick Pressure Vessels, Series 2: Intermediate Test Vessels V-3, V-4, and V-6*," ORNL-5059, Union Carbide Corp. Nuclear Div., Oak Ridge Natl. Lab., November 1975.

2. J. G. Merkle, "An Approximate Method of Elastic-Plastic Fracture Analysis for Nozzle Corner Cracks," pp. 674–702 in *Elastic-Plastic Fracture*, ASTM STP 668, American Society for Testing and Materials, Philadelphia, 1979.

3. H. Neuber, "Theory of Stress Concentration for Shear Strained Prismatical Bodies with Arbitrary Nonlinear Stress-Strain Law," *J. Appl. Mech., ASME*, 544–50 (December 1961).

4. J. G. Merkle, "An Application of the J-Integral to the Elastic-Plastic Analysis of Blunting Cracks," pp. 3–24 and 56–58 in *Heavy-Section Steel Technology Program Quart. Prog. Rep. October–December 1979*, ORNL/NUREG/TM-380, Union Carbide Corp. Nuclear Div., Oak Ridge Natl. Lab., May 1980.

5. A. Mendelson, *Plasticity: Theory and Application*, Macmillan, New York, 1968.

6. J. G. Merkle, *An Engineering Approach to Multiaxial Plasticity*, ORNL-4138, Union Carbide Corp. Nuclear Div., Oak Ridge Natl. Lab., July 1967.

7. M. Creager and P. C. Paris, "Elastic Field Equations for Blunt Cracks with Reference to Stress Corrosion Cracking," *Int. J. Fract. Mech.* 3, 247–52 (1967).

8. R. C. Cipolla, *Computational Method to Perform the Flaw Evaluation Procedure as Specified in the ASME Code, Section XI, Appendix A; Part 1: General Description and Background*, EPRI NP-1181, Part 1, Failure Analysis Associates, Palo Alto, Calif., September 1979.

9. J. C. Newman and I. S. Raju, "Stress-Intensity Factors for Internal Surface Cracks in Cylindrical Pressure Vessels," *J. Pressure Vessel Tech., ASME* 102, 342–46 (November 1980).

10. J. G. Merkle, "Stress Intensity Factor Estimates for Part-Through Surface Cracks in Plates Under Combined Tension and Bending," pp. 3–22 and 31–32 in *Heavy-Section Steel Technology Program Quart. Prog. Rep.* July–September 1974, ORNL-TM-4729, Vol. II, Union Carbide Corp. Nuclear Div., Oak Ridge Natl. Lab., November 1974.

11. C. W. Smith, "Use of Three-Dimensional Photoelasticity in Fracture Mechanics," *Exp. Mech.* 13(12), 539–44 (December 1973).

12. R. D. Cheverton, *Pressure Vessel Fracture Studies Pertaining to a PWR LOCA-ECC Thermal Shock: Experiments TSE-1 and TSE-2*, ORNL/NUREG/TM-31, Union Carbide Corp. Nuclear Div., Oak Ridge Natl. Lab., September 1976.

13. G. R. Irwin, "Crack-Extension Force for a Part-Through Crack in a Plate," *J. Appl. Mech., ASME*, 651–54 (December 1962).

14. R. A. Rawe, "Fracture Mechanics and Safe Life Design," DAC 59591, Douglas Missile and Space Systems Division, Santa Monica, Calif., January 11, 1968.

15. R. W. Derby et al., *Test of 6-Inch-Thick Pressure Vessels. Series 1: Intermediate Test Vessels V-1 and V-2*, ORNL-4895, Union Carbide Corp. Nuclear Div., Oak Ridge Natl. Lab., February 1974.

16. J. G. Merkle, G. D. Whitman, and R. H. Bryan, *An Evaluation of the HSST Program Intermediate Pressure Vessel Tests in Terms of Light-Water-Reactor Pressure Vessel Safety*, ORNL-TM-5090, Union Carbide Corp. Nuclear Div., Oak Ridge Natl. Lab., November 1975.

17. J. R. Dougan, *Relationships Between Charpy V-Notch Impact Energy and Fracture Toughness*, ORNL/TM-7921, Union Carbide Corp. Nuclear Div., Oak Ridge Natl. Lab., March 1982.

18. J. G. Merkle and R. E. Johnson, "Example Calculations Illustrating Methods for Analyzing Ductile Flaw Stability in Nuclear Pressure Vessels," *Int. J. Pressure Vessels and Piping* 18, 35–53 (1985).

19. H. A. Domian, *Vessel V-8 Repair and Preparation of Low Upper Shelf Weldment*, NUREG/CR-2676 (ORNL/Sub/81-85813/1), Babcock & Wilcox Company, Alliance Research Center, Alliance, Ohio, June 1982.

20. P. P. Holz and R. H. Bryan, "Intermediate Test Vessel V-8A," pp. 97–102 in Heavy-Section Steel Technology Program Quart. Prog. Rep. January–March 1981, ORNL/TM-7822, Union Carbide Corp. Nuclear Div., Oak Ridge Natl. Lab., June 1981.

21. R. H. Bryan et al., "Experimental Investigation of Tearing Behavior of a Flaw in a Thick Pressure Vessel," paper presented at the SMIRT Post-Conference Seminar No. 6, Integrity of Reactor Pressure Boundary, Monterey, Calif., August 29–30, 1983.

Appendix B

PRETEST ANALYSIS INFORMATION FOR HSST PROGRAM INTERMEDIATE TEST VESSEL V-8A*

R. H. Bryan† P. P. Holz†
J. G. Merkle†

B.1 Purpose of the Test

The test of Heavy-Section Steel Technology (HSST) Program intermediate test vessel V-8A is the twelfth ultimate strength test of a deliberately flawed intermediate test vessel to be conducted by the HSST Program at the Oak Ridge National Laboratory. The objective of the V-8A test is to provide accurate quantitative data concerning the growth by ductile tearing and final instability of a flaw in a low-upper-shelf toughness weldment located in a cylinder of reactor vessel steel. The reason for this test is that there are vessels in service containing welds that, because of high copper content, may have their Charpy upper-shelf energy values reduced to relatively low levels by neutron irradiation.[1] At present, Title 10 of the *Code of Federal Regulations*[2] (10 *CFR* 50) specifies that if the Charpy upper-shelf energy level of a vessel material falls below 68 J (50 ft-lb), either a special fracture safety analysis must be performed, showing that an adequate margin of safety still exists, or else the vessel must be annealed for the vessel to remain in service. However, the procedures for performing the required analysis and the basis for determining what constitutes an adequate margin of safety are not specified in 10 *CFR* 50. In an effort to provide guidance on these matters, the Nuclear Regulatory Commission convened a panel of consultants whose recommendations are contained in Ref. 1. However, although it does contain recommended analysis methods and safety factors, Ref. 1 does not contain enough example calculations to make clear the probable consequences of applying its recommendations to vessels in service. In addition, there are no comparisons with test data on experimental pressure vessels containing flaws in low-upper-shelf toughness weldments because no such vessels have yet been tested. Thus, the primary purpose of the V-8A test is to provide experimental data, now lacking, that are needed to resolve an anticipated question of safety with regard to some reactor pressure vessels now in service.

The vessel to be used for the low-upper-shelf toughness test was tested previously as vessel V-8. Because only two run-arrest events and no nominal yielding occurred in the V-8 test, the vessel was available for additional testing. Therefore, the vessel has been repaired by welding in the region of the original V-8 flaw, a special low-upper-shelf

---

*This appendix is an edited version of the pretest information sent on June 23, 1982, to 50 persons who had expressed interest in performing pretest predictions of the behavior of the V-8A flaw.

†Oak Ridge National Laboratory, Oak Ridge, TN 37831.

toughness longitudinal test weld was placed 130° from the original flaw location, and the vessel stress was relieved to make it ready for additional tests as vessel V-8A. The previous history of the vessel is documented in Refs. 3 and 4, and a copy of Ref. 4 is furnished here as Enclosure 1. Preparations for the vessel V-8A test have been documented in successive HSST Program quarterly progress reports, beginning with ORNL/NUREG/TM-347,[5] dated October 1979.

B.2 Low-Upper-Shelf Toughness Trial Welds

A subcontract was awarded to the Babcock & Wilcox (B&W) Company, Alliance Research Center, Alliance, Ohio, to repair vessel 8, develop a procedure for producing a low-upper-shelf toughness weld, place such a weld in the vessel, and determine the properties of the low shelf weld by using additional weld material prepared for the purpose. The work performed by B&W is described in detail in Ref. 6, a copy of which is furnished here as Enclosure 2.

Three preliminary trial welds were made in 95.3-mm-thick (3 3/4-in.) A 533 B, class 1 steel plate, each using a copper-clad Mn-Mo-Ni weld wire and different proportions of Linde 60 and Linde 80 fluxes. Each preliminary trial weld was trisected, with each section being given one of three postweld heat treatments, thus producing nine different combinations of conditions (see Enclosure 2). The preliminary trial welds were designated by the symbol "V8," followed by a weld number (1, 2, or 3), and a heat treatment number (1, 2, or 3). Upon selection of the second flux combination (a 75% Linde 60, 25% Linde 80 mixture) and the second heat treatment (50 h at 566 to 593°C), based on Charpy impact and tensile data, a fourth trial weld, designated "V842" was prepared. J-integral resistance curve specimens, as well as tensile, Charpy, drop weight, and other metallurgical specimens, were prepared from trial weld V842. All of the test results obtained for trial weld V842 are documented in Appendix C of Enclosure 2 and discussed on pp. 12—15 of Enclosure 2. Tensile and Charpy impact data were also obtained for base metal specimens taken from a piece of the V-8 prolongation designated "V802," which was subjected to the same postweld heat treatment as weld V842. Table B.1 shows a tabulation of data[7] obtained from preliminary trial weld V822, trial weld V842, and base metal section V802.

The resistance curve data obtained by B&W for trial weld V842 are shown in Fig. B.1 (see also Fig. 11 of Enclosure 2). Power-law curve fitting parameters for each set of data,[8] based on the equation

$$J = c(\Delta a)^n \ , \qquad (1)$$

are listed in Table B.2. As a check on the reasonableness of these results, the power-law curve fit to the data for specimen V842J1 was compared graphically with the data for irradiated low-upper-shelf toughness weld material previously obtained by Loss.[9] The results, shown in Fig. B.2, demonstrate that the resistance curve data for trial weld V842

Table B.1. Vessel V-8A, B&W ASA low-upper-shelf weldment experimentation[a]

Designation	Target range	Base metal — V802	Weld — V822	Trial weld V842
Material thickness, mm	152	152	95	152
Welding current, A			575 ± 15	475 ± 25
Welding voltage, V ac			32 ± 2	32 ± 2
Welding speed, mm/min			305 ± 1	305 ± 1
Heat input, kJ/mm	2950		3620	2990
Postweld heat treatment				
Heatup rate, maximum, K/h	55	78	28	83
Hold temperature and time, °C, h	566–593, 48–52	588, 58	580, 50	584, 52
Cooling rate, K/h	5–7.5	6.9	6.1	5.1
CVN impact tests				
Upper-shelf absorbed energy, 93 to 149°C, J	54–68 47.5–74.5 acceptable		57.2	57.6
Upper-shelf lateral expansion, 93 to 149°C, mm			1.2	1.3
Temperature at upper shelf (100% shear), °C	66–93		107	99
Tensile properties				
Yield stress, room temperature, MPa	448–620	452.0	461.3	459.9
Yield stress, 121°C, MPa		413.7		419.9
Ultimate stress, room temperature, MPa	551–690	598.5	564.7	568.1
Ultimate stress, 121°C, MPa		549.5		519.2
Elongation, room temperature, %	18 min.	27.8	24.7	25.8
Elongation, 121°C, %		25.7		24.3
Reduction in area, room temperature, %		70.4	54.4	55.3
Reduction in area, 121°C, %		70.0		53.5
Drop-weight NDT temperature, °C				−12

[a]Base material — SA 533, grade B, class I
Wire — 1/8-in.-diam Mn-Mo-Ni type SFA 5.23, EF-2
Flux — 75% Linde 60 and 25% Linde 80
Preheat — 140°C min; interpass 260°C max

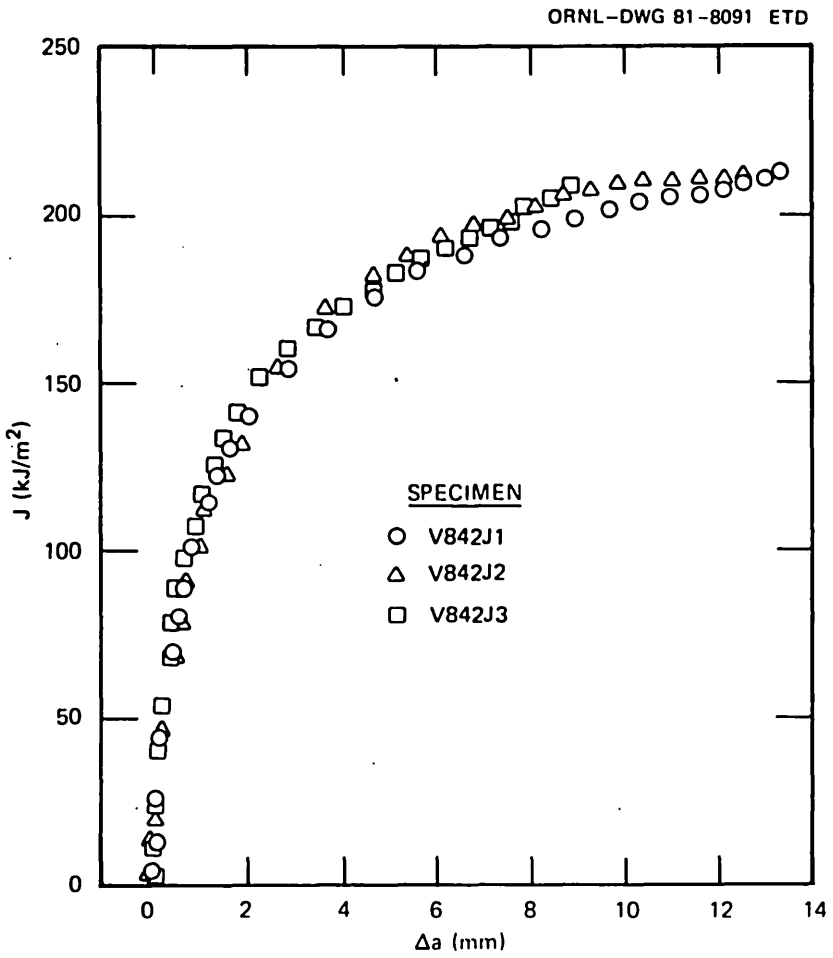

Fig. B.1. J-Integral resistance curve data from three unloading compliance tests of IT compact specimens of B&W trial weld V842.

Table B.2. Power-law parameters n and c from least-squares fit of J-Δa data from B&W trial weld V842 with J considered as a random variable

Specimen	Δa range (mm)	n	c [kJ•m^{-2}/(mm)^n]
J1	0.282–1.509[a]	0.3687	114.10
J2	0.278–1.713[a]	0.3692	109.83
J3	0.246–1.642[a]	0.3606	120.26
J1	0.282–13.193	0.2687	111.06
J2	0.278–12.380	0.2948	108.73
J3	0.246–8.753	0.2824	115.95

[a]Exclusion range for J_{Ic} determination.

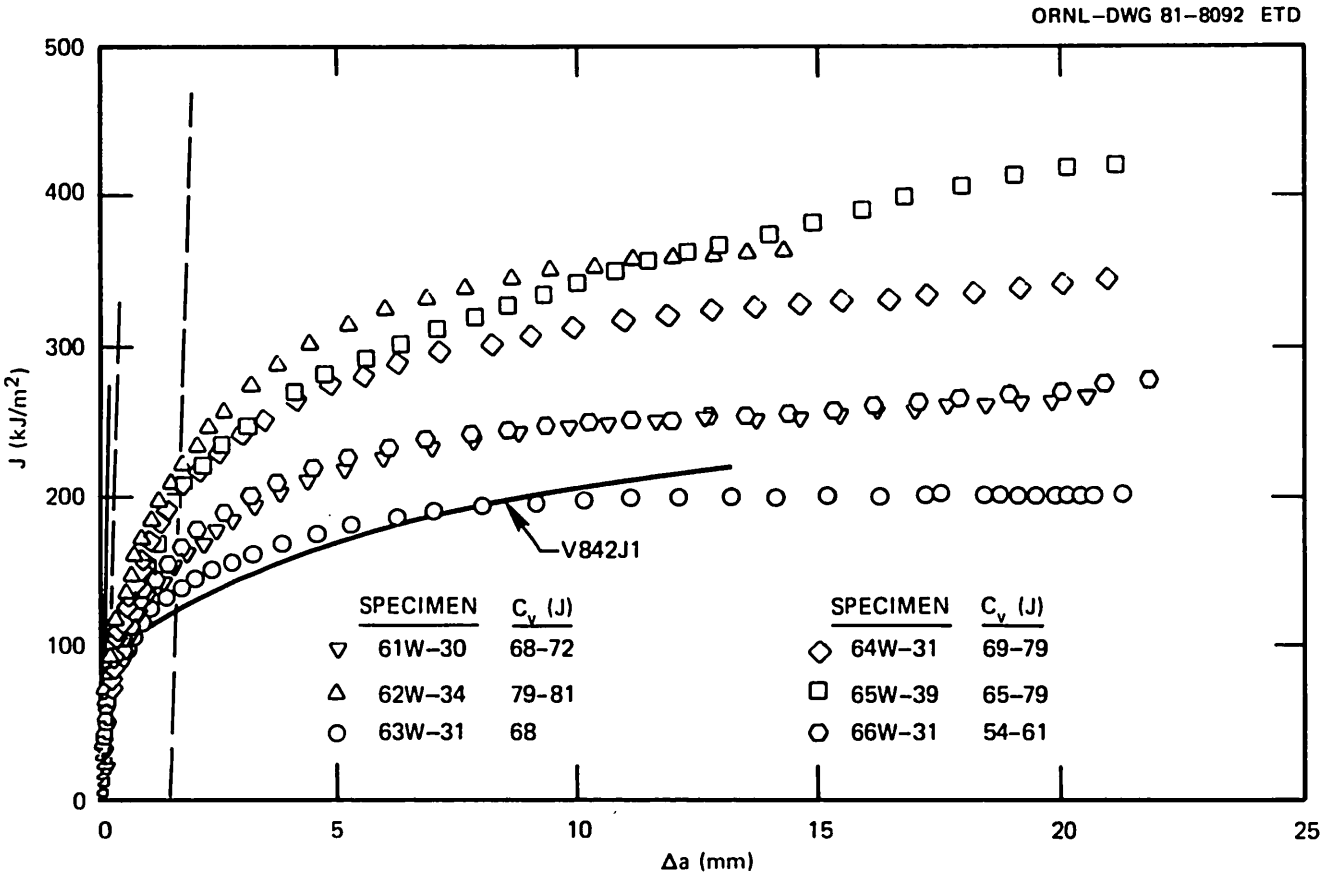

Fig. B.2. Comparison of power-law curve fit to J-R data from B&W trial weld V842 with results of tests of 1.6T compact specimens of irradiated welds.

are consistent with the existing data for irradiated low-upper-shelf toughness weld metal.

Based on the satisfactory test results obtained for trial weld V842, a low-upper-shelf toughness test weld was placed in vessel V-8A by the same procedure, as discussed in Sect. 4 of Enclosure 2. Because of nondestructive examination/test indications, the test weld in vessel V-8A had to be remade twice, once before and once after the vessel was postweld heat treated. Consequently, the vessel received double the originally intended postweld heat treatment, totalling ~100 h at 566 to 593°C (1050 to 1100°F). Because vessel V-8A has been adequately stress relieved following welding and is to be tested in the upper-shelf temperature range, residual stresses are not expected to have a significant effect on the test results.[3]

B.3 Vessel Geometry

The overall geometry of vessel V-8, being used for the V-8A test, is shown on p. 1 of Enclosure 2. The details of the low-upper-shelf toughness test weld are shown on pp. 7 and 36 of Enclosure 2. The test weld tapers through the thickness of the vessel, from an outside width of 106.4 mm (4 3/16 in.) to an inside width of 47.6 mm (1 7/8 in.), and consists of an 879.5-mm-long (34 5/8-in.) automatic submerged arc (ASA) test section, flanked by short tapered manual metal arc (MMA) end sections.

B.4 Preparations for Testing

Vessel V-8A is scheduled to be tested in August 1982. The test temperature will be 150°C (302°F). An up-to-date summary of preparations for testing is given in Enclosure 3, which is excerpted from draft portions of the *HSST Program Quarterly Progress Report for January–March 1982*. The depth of the fatigue-sharpened flaw is estimated to be 91.19 mm (3.59 in.), based on the ultrasonic data taken during flaw sharpening, which are shown in Fig. B.3. There was no measurable fatigue crack growth on the surface during crack sharpening.

Note that the cylinder prolongation used for making characterization welds for the V-8A test was V-10 prolongation (see Enclosure 2) because of the previous use of V-8 prolongation for the V-8 test. The V-7, -8, -9, and -10 vessel cylinders and prolongations were originally fabricated together from A 533 grade B class 1 steel plate,[10] so portions of these prolongations are interchangeable, provided that they receive the same subsequent heat treatments as the vessel being characterized.

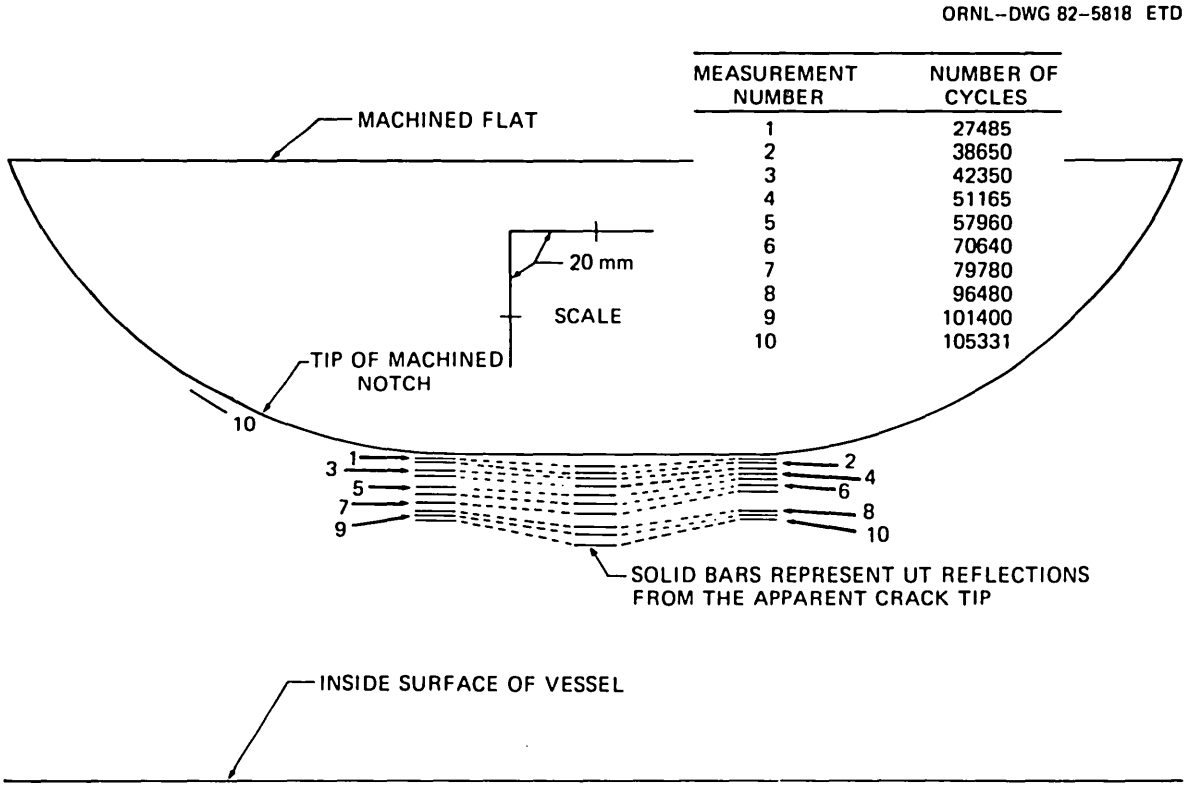

Fig. B.3. Scale plot of locations of UT reflections from the crack tip at several stages of crack growth during flaw sharpening in vessel V-8A.

B.5 Input Data for Analysis

A. Flaw geometry

1. Machined flaw dimensions:
   (see Fig. 5.21 of Enclosure 3)
   a = 69.85 mm (2.75 in.)
   2b = 279.40 mm (11.00 in.)
2. Fatigue-sharpened flaw dimensions:
   (see Fig. B.3 and Fig. 5.25 of Enclosure 3)
   a = 91.19 mm (3.59 in.)
   2b = 279.40 mm (11.00 in.).

B. Test temperature: 150°C (302°F).

C. Material properties of low-shelf test weld

1. Material: (see Sect. 4.0 of Enclosure 2).
2. NDT: (see p. D-4 of Enclosure 2)
   −17.8°C (0°F).

3. CVN data: (see Sects. 3.2 and D.6 of Enclosure 2). The upper-shelf Charpy impact energy of the V-8A test weld material is estimated to be 59 J (43.5 ft-lb) (see p. 57 of Enclosure 2).
4. RT_{NDT}: The RT_{NDT} of the V-8A test weld cannot be determined by standard methods because the Charpy upper-shelf impact energy is <68 J (50 ft-lb). However, using the mil lateral expansion curves in Sect. 3.2 of Enclosure 2 and the drop weight NDT value of −17.8°C (0°F), the RT_{NDT} of the test weld is not less than about −6.7°C (20°F).
5. Fracture toughness data below the upper shelf: (see p. 25 of Enclosure 2).
6. Tensile data:
   (a) Stress-strain curve: (not available).
   (b) Yield stress, ultimate stress, elongation after fracture, and reduction of area after fracture: (see p. 20 of Enclosure 2).
   (c) Specimen gage length: 50.8 mm (2.00 in.).
   (d) Specimen diameter: 12.7 mm (0.500 in.).
7. J-integral resistance curves: All of the B&W J-integral resistance curve test results are summarized in Table 6 of Enclosure 2. The R-curves that are most directly applicable to the V-8A test are those obtained at 149°C (300°F). These data are plotted in Figs. 21–23 of Enclosure 2. Note that the data shown in the second half of Fig. 21 were obtained from side-grooved, precracked Charpy specimens (see discussion in Appendix E of Enclosure 2). The original load, displacement, unloading compliance, and crack-length data for the J_R specimens are recorded on a magnetic tape, from which the values can be furnished on request.

   Power-law resistance curves plotted by using the arithmetic mean values of the fitting parameters for all of the specimens of each characterization weld at 149°C (300°F) are plotted in Fig. 5.19 of Enclosure 3, and the values of the average fitting parameters are listed in Table 5.4 of Enclosure 3. Note that these values do not exactly coincide with the values for trial weld V842 listed in Table B.2.

D. Material properties of vessel cylinder base metal

1. Tensile stress-strain curve: A true stress vs true strain curve for the V-8A vessel cylinder base metal, at 149°C (300°F), is given in Fig. B.4.
2. Other data are given in Table B.1, Enclosure 1, and Enclosure 2.

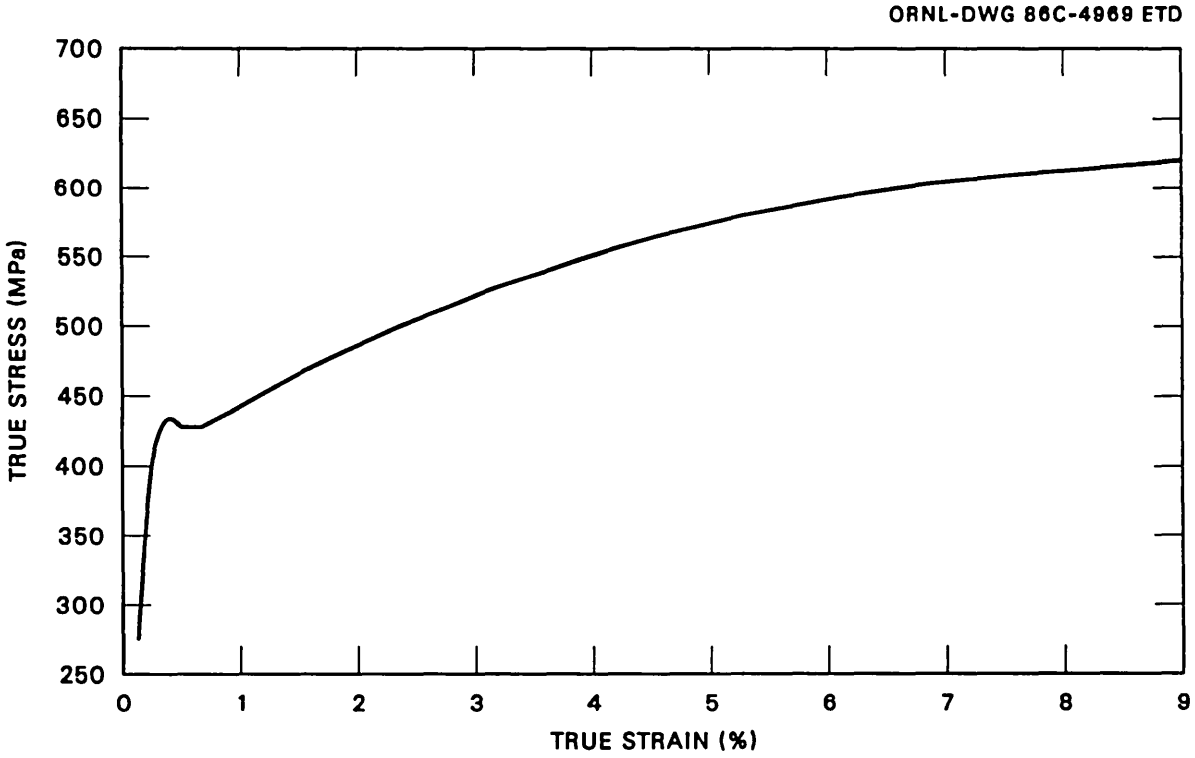

Fig. B.4. True stress-strain curve for vessel V-8A base metal at 149°C (specimen V10P20).

Enclosures*

1. Reference 4 (ASME paper on V-8).
2. Reference 6 (B&W draft report).
3. R. H. Bryan, "Preparation for Intermediate Vessel Test V-8A," pp. 82—109 and 118—119 in *Heavy-Section Steel Technology Program Quart. Prog. Rep. for January—March 1982*, ORNL/TM-8369/V1, Union Carbide Corp. Nuclear Div., Oak Ridge Natl. Lab., August 1982 (draft with analysis results deleted).

*Not included in this appendix.

References

1. R. Johnson, *Resolution of the Reactor Vessel Materials Toughness Safety Issue*, NUREG-0744, Vols. 1 and 2 for comment, U.S. Nuclear Regulatory Commission, September 1981.

2. 10 *CFR* Chap. I, Appendix G.

3. R. H. Bryan et al., *Test of 6-in.-Thick Pressure Vessels. Series 3: Intermediate Test Vessel V-8*, ORNL/NUREG-58, Union Carbide Corp. Nuclear Div., Oak Ridge Natl. Lab., December 1979.

4. R. H. Bryan et al., "Test of Thick Vessel with a Flaw in Residual Stress Field," *J. Pressure Vessel Tech., ASME* 103(1), 85–93 (February 1981).

5. G. D. Whitman and R. H. Bryan, *Heavy-Section Steel Technology Program Quart. Prog. Rep. April–June 1979*, ORNL/NUREG/TM-347, Union Carbide Corp. Nuclear Div., Oak Ridge Natl. Lab., October 1979.

6. H. A. Domian, *Vessel V-8 Repair and Preparation of Low Upper-Shelf Weldment*, NUREG/CR-2676 (ORNL/Sub/81-85813/1), Babcock and Wilcox Company, Alliance Research Center, Alliance, Ohio, June 1982 (January 1982 draft).

7. G. D. Whitman and R. H. Bryan, *Heavy-Section Steel Technology Program Quart. Prog. Rep. for October–December 1980*, ORNL/NUREG/TM-437, Union Carbide Corp. Nuclear Div., Oak Ridge Natl. Lab., March 1981.

8. G. D. Whitman and R. H. Bryan, *Heavy-Section Steel Technology Program Quart. Prog. Rep. for January–March 1981*, ORNL/NUREG/TM-7822, Union Carbide Corp. Nuclear Div., Oak Ridge Natl. Lab., June 1981.

9. F. J. Loss, "Toughness and Ductile Shelf Properties of Irradiated Low-Shelf Weld Metals," NRC 8th Water Reactor Safety Research Information Meeting, Gaithersburg, Md., October 27–31, 1980.

10. C. E. Childress, *Fabrication and Mechanical Test Data for the Four 6-Inch-Thick Intermediate Test Vessels Made from Steel Plate for the Heavy Section Steel Technology Program*, ORNL/TM-5074, Union Carbide Corp. Nuclear Div., Oak Ridge Natl. Lab., January 1976.

Appendix C

RESULTS OF PRETEST ANALYSES OF HSST VESSEL V-8A*

C.1 Introduction

This note coordinates the results of the following three establishments:

1. National Nuclear Corporation Ltd., Leicester;
2. UK Atomic Energy Authority, AERE, Harwell; and
3. Central Electricity Generating Board (CEGB), CERL, Leatherhead.

All three establishments adopted the CEGB procedure, R6, to perform their analyses. Each analysis was performed independently, and the results are presented in Tables C.1—C.3. Judgments concerning the use of input data are included where appropriate in the footnotes of each table, and the different ways of treating the data are responsible for the small differences in the predictions. Some reservations are expressed about the test, deriving mainly from the possibility of excessive scatter in the low-toughness weld metal properties and the potential for time-dependent effects to promote an instability if the pressure is held close to instability. Nevertheless, each organization has performed analyses based upon assumptions that exclude any events that cannot be predicted from the available data base.

The R6 procedure is, of course, primarily concerned with avoiding failure rather than predicting it. Consequently, for this exercise, each establishment has performed a lower-bound estimate that is intended to be a conservative R6 analysis to define the pressure below which failure would be avoided. Best-estimate analyses have also been performed in an attempt to predict the actual pressure crack-size relationships obtained during the test.

However, despite the fact that the information provided in the pretest package† is more comprehensive than in most practical situations, there is an uncertainty in the predictions that is larger than usual. This uncertainty arises because the test is to be performed on a specially prepared low-toughness weld metal. Because of the material, several unexpected events that cannot be predicted from the data package available may arise. Four of these are important and have been identified below.

C.2 Possibility of Cleavage Instability

Two 1-in.-thick specimens of weld V8102 were unstable with a toughness below 150 MPa$\cdot\sqrt{m}$ at 24°C. The remaining specimens of this weld were

---

*Coordinated by I. Milne, CERL, Kelvin Avenue, Leatherhead, Surrey, United Kingdom.

†Appendix B of this report.

Table C.1. Predictions by National Nuclear Corporation[a,b]

	Lower bound[c]	Best estimate[d]
Initiation pressure, P_i, MPa	67	88
Instability pressure, P_F, MPa	107	121
Crack depth increase at P_F, mm	6.6	6.8

Best-estimate pressure crack growth prediction[d]

P (MPa)	Δa (mm)
88	0
106	0.5
114	1.0
119	2.0
121	6.8

Pressure strain prediction[e]

P (MPa)	Strain (%)
105	0.078
120	0.091
130	0.104

[a]Using CEGB R6 method.

[b]Note the vessel thickness was taken as the thickness of the flattened test section, 144 mm.

[c]Using lower-bound parameters from Table 5.4 (Enclosure 3), lower-bound J_{1C}, lowest flow stress of $1/2(\sigma_y + \sigma_u)$ for V852 at 300°F, K solutions for a semielliptical surface defect in a flat plate, and plastic limit pressure given by

$$P \text{ limit} = \sigma_{flow} \frac{t}{r} \frac{\left(\frac{t}{a} - 1\right)}{\left(\frac{t}{a} - \frac{1}{m}\right)},$$

where r is the mean radius and $m = (1 + 0.263\ l^2/rt)^{1/2}$, l being the crack length and t the wall thickness at the flattened section.

[d]As for (c) but using mean parameters from Table 5.4 (Enclosure 3) and mean flow stress for V852 and V8102 at 300°F.

[e]Strains calculated assuming elastic perfectly plastic material.

Table C.2. Predictions by U.K. Atomic Energy Authority (AERE)[a,b]

	Lower bound[c]	Best estimate[d]
Initiation pressure, P_i, MPa	63.9	89.5
Instability pressure, P_F, MPa	111.5	128.0
Crack depth increase at P_F, mm	8.0	7.0

Best-estimate pressure crack growth prediction[d]

P (MPa)	Δa (mm)
113.7	1
121.2	2
124.5	3
126.3	4
127.3	5
127.8	6
127.97	7

[a]Using CEGB R6 method.

[b]Vessel thickness was taken as 152.4 mm.

[c]Using lower-bound parameters from Table 5.4 (Enclosure 3), lower-bound J_{1C}, lowest flow stress of $1/2(\sigma_y + \sigma_u)$ for V852 at 300°F, K solutions based upon those of Emery and Segedin, and plastic limit pressure given by

$$P \text{ limit} = \sigma_{flow} \left(\frac{r_o}{r_i} - 1\right) \left(1 - \frac{A_c}{A}\right),$$

where A_c is the area of the crack and A is the vessel area containing the crack. The crack aspect ratio was kept constant.

[d]As for (c) but using mean parameters from Table 5.4 (Enclosure 3) mean J_{1C} and mean flow stress for V852 and V8102 at 300°C.

Table C.3. Predictions by CERL[a,b]

	Lower bound[c]	Best estimate[d]
Initiation pressure, P_i, MPa	66	104
Instability pressure, P_F, MPa	119	141
Crack depth increase at P_F, mm	5	7

Best-estimate pressure crack growth prediction[d]

P (MPa)	Δa (mm)
104	0
130	1
136	2
140	4
141	6
141	7

Strain at failure (%)	
Lower bound	0.091
Best estimate	0.108

[a]Using CEGB R6 method.

[b]Vessel thickness taken as 152.4 mm.

[c]Using bounding line to lowest R curve for all test welds, lowest flow properties for V852 at 300°C, K solutions for a semielliptical defect in a flat plate, and plastic limit pressure given by

$$P \text{ limit} = 1.04\sigma_{flow} \frac{\left(\frac{t}{a} - 1\right)}{\left(\frac{t}{l} - \frac{l}{m}\right)} \ln \frac{r_o}{r_i} .$$

The crack aspect ratio was kept constant with Δa increasing.

[d]Using mean of parameters from Table 5 (Enclosure 3), mean J_{1C}, mean flow stress for V852 and V8102 at 300°F, K solutions based upon those of Emery and Segedin, and plastic limit pressure given by expression above. The crack length was kept constant as Δa increased.

tested at 150°C, and although fully ductile at this temperature, they had the lowest resistance curves of the four test welds. In view of (1) size and triaxiality effects on the ductile-brittle transition, (2) the scatter in toughness of the welds, and (3) the fact that the transition temperature has not been established, the possibility of a ductile-brittle transition cannot be disregarded. The probability of such an event is small. It will, however, be larger if the postweld heat treatment has not reduced the residual stress to an insignificant level and if dynamic effects follow a ductile instability.

C.3 Crack Shape

Prefatiguing was performed at a relatively high K max, and fatigue crack extension was exclusively in the through-thickness direction. It is anticipated that ductile tearing will progress from the sharpened crack tip mainly through the shell thickness and spread axially to accommodate this extension. Crack propagation axially at the outer surface is unpredictable.

C.4 Loading

Pressurization is expected to be hydraulic. It is intended that the pressure is to be held constant to detect incipient flaw instability. Under these circumstances, there is a possibility of time-dependent plastic flow that may have the effect of reducing the plastic limit load or the resistance curve, thus promoting the instability.

C.5 Resistance Curves

Data are available from 10-, 25-, and 50-mm plane- and side-grooved specimens of the four test welds, and there is considerable variation in these data from weld to weld. Crack extensions beyond a maximum of 3 mm violate the criteria for J-controlled growth, making crack extension predictions increasingly uncertain.

The analyses have been performed using the following assumptions.

1. All crack extensions before instability are ductile.
2. All material properties of the weld fall within the scatter bands for the four test welds.
3. Intermittent partial unloading and sustained loading do not significantly affect the material properties.
4. The crack acts as a sharp planar defect.
5. The pressure is reduced on ligament breakthrough so that axial extension of the through-thickness crack is prevented.

Events that involve a serious departure from these assumptions are not predicted, even though they may occur over the range of pressures or

crack extensions predicted by the analyses. If such events do occur, it is hoped that a full posttest inspection and data base will be made available for further analysis.

C.6 Reference Data

The explanatory notes for the tables in this appendix contain references to Enclosure 3, which is the third enclosure to the Oak Ridge National Laboratory pretest information package (see Appendix B of this report).

Appendix D

PRETEST ANALYSIS OF INTERMEDIATE TEST VESSEL V-8A BY NBS, BOULDER*

D.1 Prediction Procedure

1. Use simplified line-spring model,[1] modified for remote bending stress, to calculate J-integral (J), dJ/da (a is crack depth), crack-mouth-opening displacement (CMOD), and crack-tip-opening displacement (CTOD) from the known flaw dimensions, wall thickness, and material properties, as a function of pressure p.

   1.1 Use the elastic relationship between hoop stress and pressure found in Timoshenko[2] to find stress vs position. Then for use in the line-spring model, approximate the actual stress distribution as a membrane component σ_m and a bending component σ_b. The linearized membrane and bending stress values calculated for ITV-8A are $\sigma_m = 2.2827\ p$ and $\sigma_b = 0.5523\ p$.

   1.2 The unknown quantities are calculated. dJ/da is obtained by numerical differentiation. Results, including r_y, plastic zone radius at crack ends, are given in Table D.1 and plotted vs pressure in Figs. D.1–D.3.

2. Plot applied dJ/da vs applied J, both from part 1 above. On the same plot, graph material dJ/da vs J (see Fig. D.4). Instability is predicted where the applied (J, dJ/da) curve intersects the material (J, dJ/da) band.

---

*Analyst: D. T. Read, National Bureau of Standards, Boulder, Colo.

Table D.1. Calculated results for fracture mechanics tearing-instability analysis of ITV-8A

p (MPa)	σ_m (MPa)	σ_b (MPa)	CTOD (mm)	CMOD (mm)	J (kJ/m^2)	dJ/da (MPa)	r_y (mm)
69	157	38	0.050	0.529	31	0.25	
103	236	57	0.075	0.794	69	0.55	
138	315	76	0.228	1.214	155	2.89	21.34
145	331	80	0.288	1.333	182	3.27	29.21
152	346	84	0.358	1.477	213	3.72	39.12
159	362	88	0.439	1.656	249	4.36	52.32
165	378	91	0.544	1.889	294	5.17	70.61
172	393	95	0.681	2.212	354	6.40	97.03
179	409	99	0.879	2.692	438	8.23	137.67
186	425	103	1.204	3.505	576	11.51	208.28

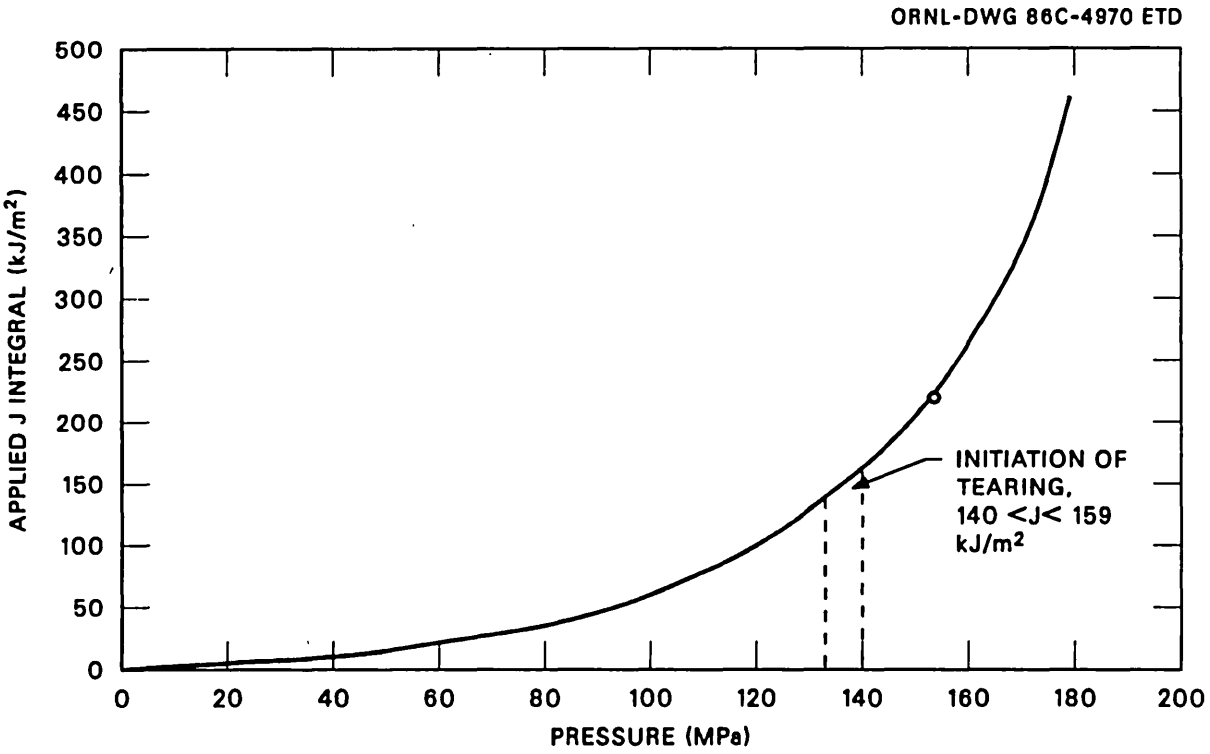

Fig. D.1. Applied J vs pressure estimate for ITV-8A.

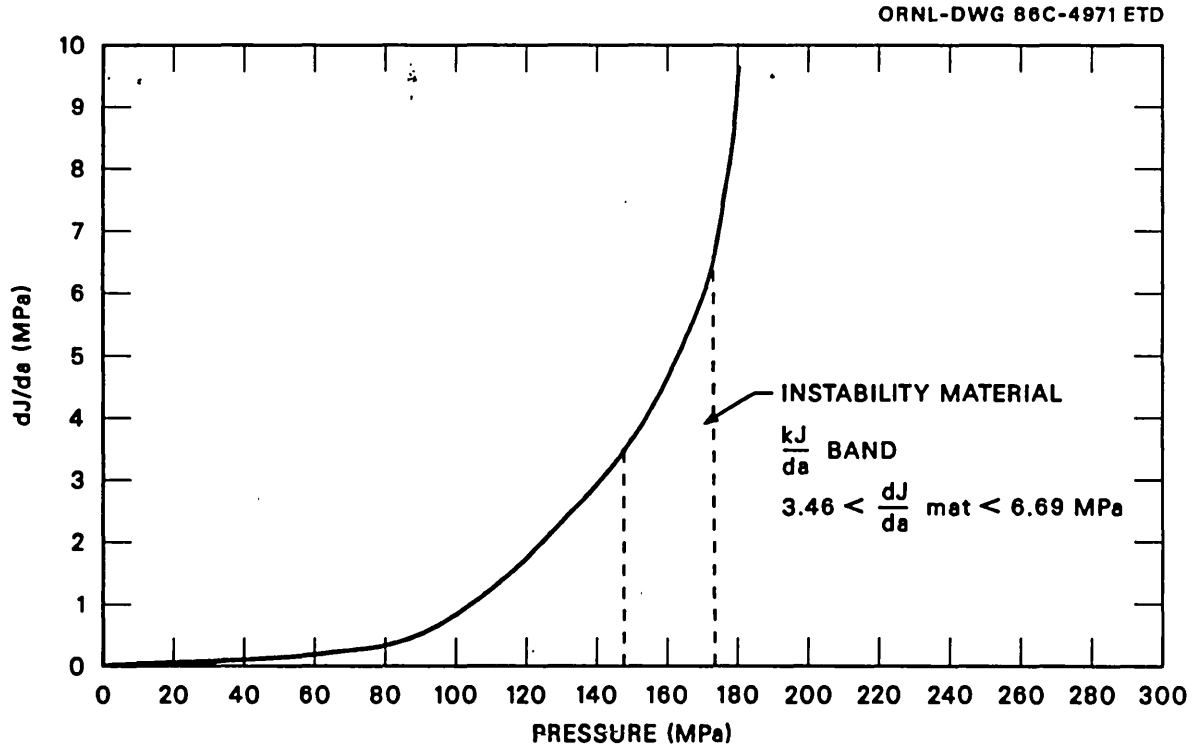

Fig. D.2. Applied dJ/da vs pressure estimate for ITV-8A.

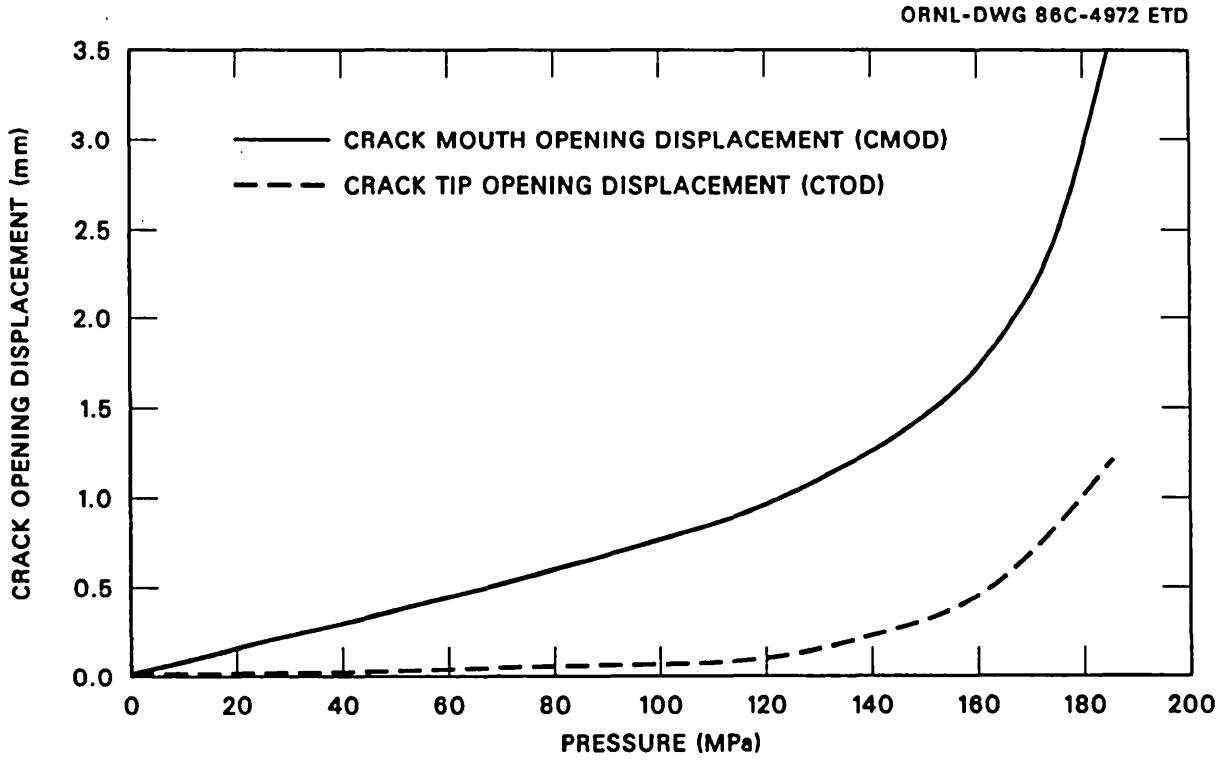

Fig. D.3. Crack-opening-displacement estimates for ITV-8A.

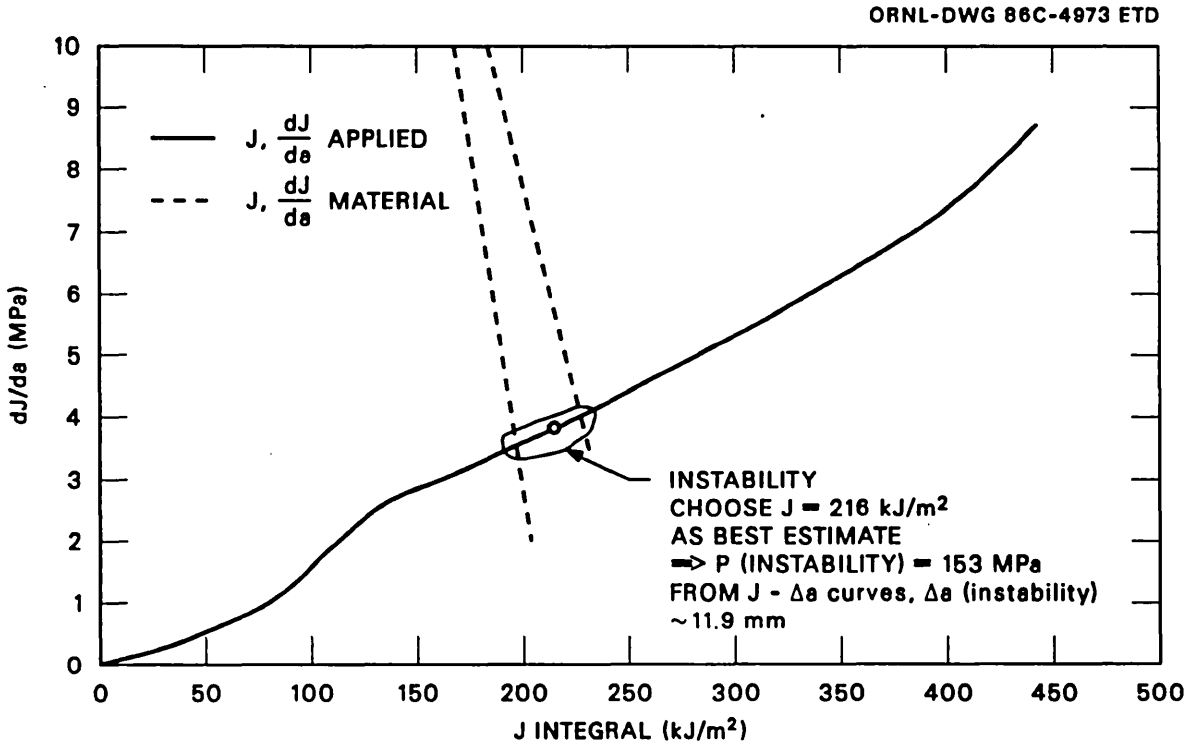

Fig. D.4. Instability diagram plotted in terms of dJ/da vs J for ITV-8A.

3. The graph of CMOD vs pressure, Fig. D.3, can be used for further verification of the analysis because CMOD is being measured. CTOD is also provided for reference.
4. Pressure vs change in crack length, as given in Table D.2, is obtained by using the plot of J vs p in Fig. D.1 and the material J-Δa curve.
5. Hoop strain vs pressure, calculated from the formula for elastic, perfectly plastic behavior[3] is given in Table D.3 and Fig. D.5.

Table D.2. Flaw-depth change vs pressure estimate for ITV-8A

p (MPa)	J (kJ/m^2)	Δa (mm)
131	131	0
138	155	2.54
145	182	4.32
152	213	9.40
159	249	Large

Table D.3. Inside and outside surface circumferential strain vs pressure estimates for ITV-8A

p (MPa)	Inside (%)	Outside (%)	Remarks
34	0.049	0.027	
69	0.099	0.054	
103	0.148	0.081	
128	0.184	0.100	Initial yield
138	0.198	0.108	
152	0.229	0.124	
165	0.262	0.141	
179	0.337	0.178	

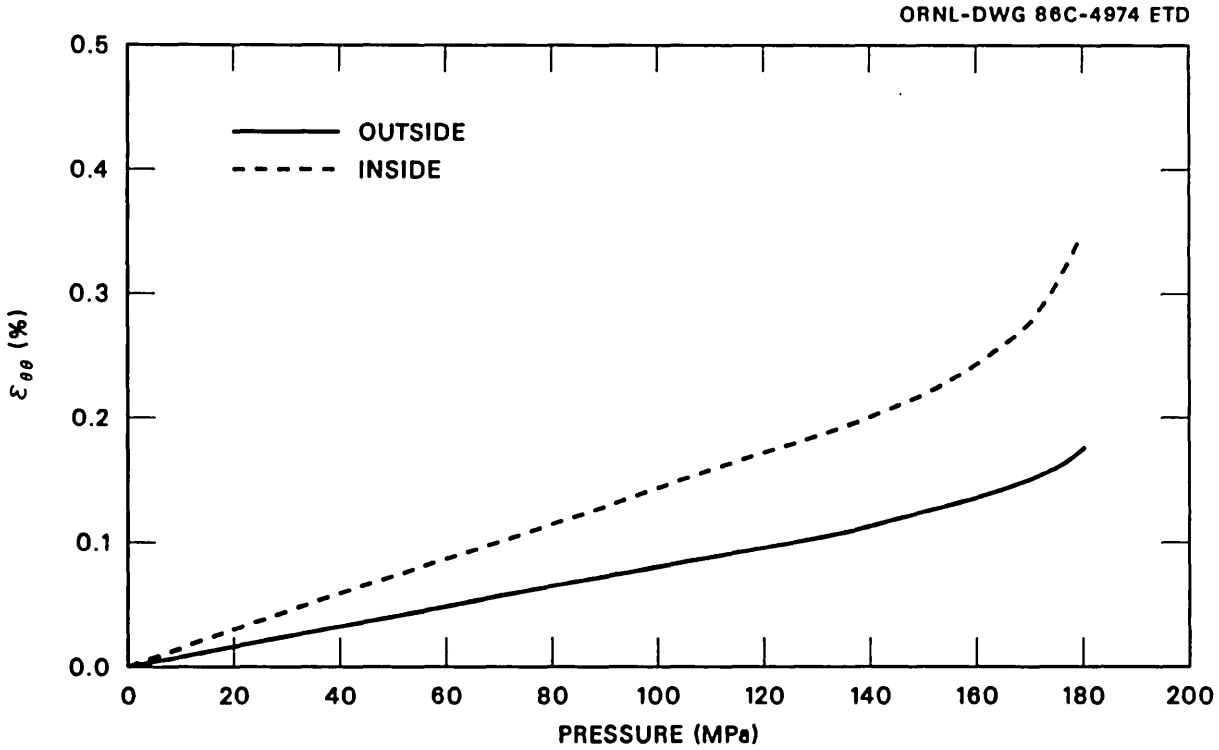

Fig. D.5. Estimated inside and outside surface circumferential strain vs pressure curves for ITV-8A.

D.2 Results

Instability is predicted at 153 MPa and Δa = 11.9 mm (Δa indicates increase in defect depth). No significant changes in defect length before instability are anticipated.

References

1. R. B. King, "Elastic-Plastic Analysis of Surface Flaws Using a Simplified Line-Spring Model," *Eng. Fract. Mech.* 18(1), 217–31 (1983).

2. S. Timoshenko and N. Goodier, *Theory of Elasticity*, 2d ed., McGraw-Hill, New York, 1951, p. 60.

3. L. M. Kachanov, *Foundations of the Theory of Plasticity*, North-Holland, Amsterdam, 1971, p. 127.

Appendix E

PRETEST AND POSTTEST ESTIMATES FOR ITV-8A BY IWM, FREIBURG*

E.1 Pretest Analysis

The analysis was performed numerically according to the Failure Assessment Diagram procedure modified by Milne[1] for strain hardening and shown schematically in Fig. E.1. The coordinates of the failure assessment curve in Fig. E.1 are parametric functions of the equivalent flat-

*Analyst: Dr. L. Hodulak, Fraunhofer — Institut for Werkstoffmechanik.

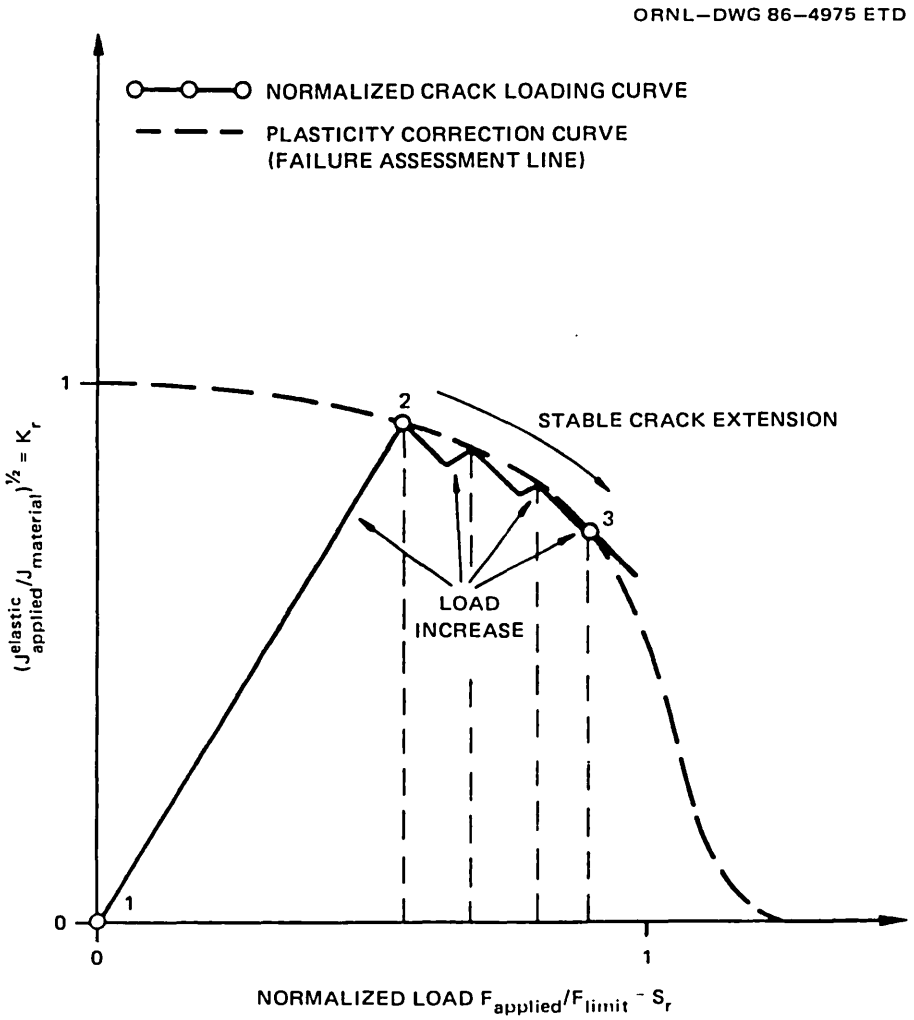

Fig. E.1. R-6 failure assessment diagram curve, considering strain hardening.

plate stress ratio σ/σ_y, according to the equations

$$K_r = \frac{\sigma}{\sigma_y}\left[\frac{8}{\pi^2}\ln\sec\left(\frac{\pi}{2}\,\frac{\sigma}{\sigma_y}\right)\right]^{-1/2} , \tag{E.1}$$

$$S_r = \frac{\sigma}{\sigma_y} + (1 - K_r{}^{1/2})\left(\frac{\sigma_u}{\sigma_y} - 1\right) . \tag{E.2}$$

To obtain the elastically calculated value of $J_{applied}$, the stress-intensity factor K was calculated from interpolation formulae[2] developed for surface cracks in plates under tension with additional corrections for the wall curvature[3] and for a stress gradient (derived from Ref. 4). The equations are

$$J = K_I^2\left(\frac{1 - \nu^2}{E}\right) , \tag{E.3}$$

$$K_I = F\,\sigma\sqrt{\frac{\pi a}{Q}} , \tag{E.4}$$

$$Q = 1 + 1.464\left(\frac{a}{c}\right)^{1.65} , \tag{E.5}$$

$$F = F_1F_2 , \tag{E.6}$$

$$F_1 = M_1 + M_2\left(\frac{a}{t}\right)^2 + M_3\left(\frac{a}{t}\right)^4 , \tag{E.7}$$

$$F_2 = 0.95 + 0.715\left(\frac{a}{t}\right)^6 , \tag{E.8}$$

$$M_1 = 1.13 - 0.09\left(\frac{a}{c}\right) , \tag{E.9}$$

$$M_2 = -0.54 + \frac{0.89}{0.2 + \frac{a}{c}} , \tag{E.10}$$

$$M_3 = 0.5 - \frac{1}{0.65 + \frac{a}{c}} + 14\left(1 - \frac{a}{c}\right)^{24} , \tag{E.11}$$

$$\sigma = \sigma_K - \sigma_L \frac{\left(0.44 - 0.12\,\frac{a}{c}\right)}{\left(1.12 - 0.08\,\frac{a}{c}\right)}\,, \tag{E.12}$$

$$\sigma_K = p\,\frac{\left[1 + \frac{r_o^2}{(r_o - a)^2}\right]}{\left[\left(\frac{r_o}{r_i}\right)^2 - 1\right]}\,, \tag{E.13}$$

$$\sigma_L = \sigma_K - \frac{2p}{\left[\left(\frac{r_o}{r_i}\right)^2 - 1\right]}\,. \tag{E.14}$$

S_r was calculated in the same way as in Ref. 5:

$$S_r = \frac{\sigma}{\sigma_F}\,\frac{\left(\frac{t}{a} - \frac{1}{m}\right)}{\left(\frac{t}{a} - 1\right)}\,, \tag{E.15}$$

$$m = \left[1 + 0.263\,\frac{c^2}{r_i t}\right]^{1/2}\,, \tag{E.16}$$

$$\sigma = p\,\frac{r_i}{t}\,, \tag{E.17}$$

$$\sigma_F = \frac{\sigma_u + \sigma_y}{2}\,. \tag{E.18}$$

Additional input data are as specified (see Appendix B of this report), and, also, E = 195 GPa and a/c = constant. The results are shown in Table E.1 and Fig. E.2. Instability is predicted at a pressure of 147 MPa and with a flaw growth of 15 mm, using the J_R curve for characterization weld V842.

Table E.1. Pretest estimates for vessel V-8A using three sets of material data[a]

Weld V8102		Weld V842		Weld V852	
Pressure (MPa)	Crack depth (mm)	Pressure (MPa)	Crack depth (mm)	Pressure (MPa)	Crack depth (mm)
99.8	91.2	93.4	91.2	100.8	91.2
112.8	91.7	116.1	91.7	124.7	91.7
119.4	92.2	123.9	92.2	133.8	92.2
123.8	92.7	128.5	92.7	139.2	92.7
127.2	93.2	131.8	93.2	143.0	93.2
129.7	93.7	134.3	93.7	145.8	93.7
131.8	94.2	136.3	94.2	148.0	94.2
133.5	94.7	137.9	94.7	149.7	94.7
135.0	95.2	139.2	95.2	151.2	95.2
136.3	95.7	140.3	95.7	152.3	95.7
137.4	96.2	141.3	96.2	153.4	96.2
138.4	96.7	142.2	96.7	154.2	96.7
139.3	97.2	142.9	97.2	155.0	97.2
140.1	97.7	143.5	97.7	155.6	97.7
140.8	98.2	144.1	98.2	156.2	98.2
141.4	98.7	144.6	98.7	156.6	98.7
141.9	99.2	145.1	99.2	157.0	99.2
142.4	99.7	145.4	99.7	157.4	99.7
142.8	100.2	145.8	100.2	157.7	100.2
143.2	100.7	146.1	100.7	158.0	100.7
143.6	101.2	146.3	101.2	158.2	101.2
143.9	101.7	146.5	101.7	158.4	101.7
144.2	102.2	146.7	102.2	158.6	102.2
144.4	102.7	146.9	102.7	158.7	102.7
144.6	103.2	147.0	103.2	158.8	103.2
144.8	103.7	147.1	103.7	158.9	103.7
145.0	104.2	147.2	104.2	158.9	104.2
145.1	104.7	147.3	104.7	158.9	104.7
145.2	105.2	147.3	105.2	159.0	105.2
145.3	105.7	147.3	105.7	159.0	105.7
145.4	106.2	147.4	106.2		
145.4	106.7				
145.4	107.2				
145.4	107.9				

[a]Pressure at tearing instability: 145.4 MPa, Δa = 16.7 mm; 147.4 MPa, 15.0 mm; 159.0 MPa, 14.5 mm.

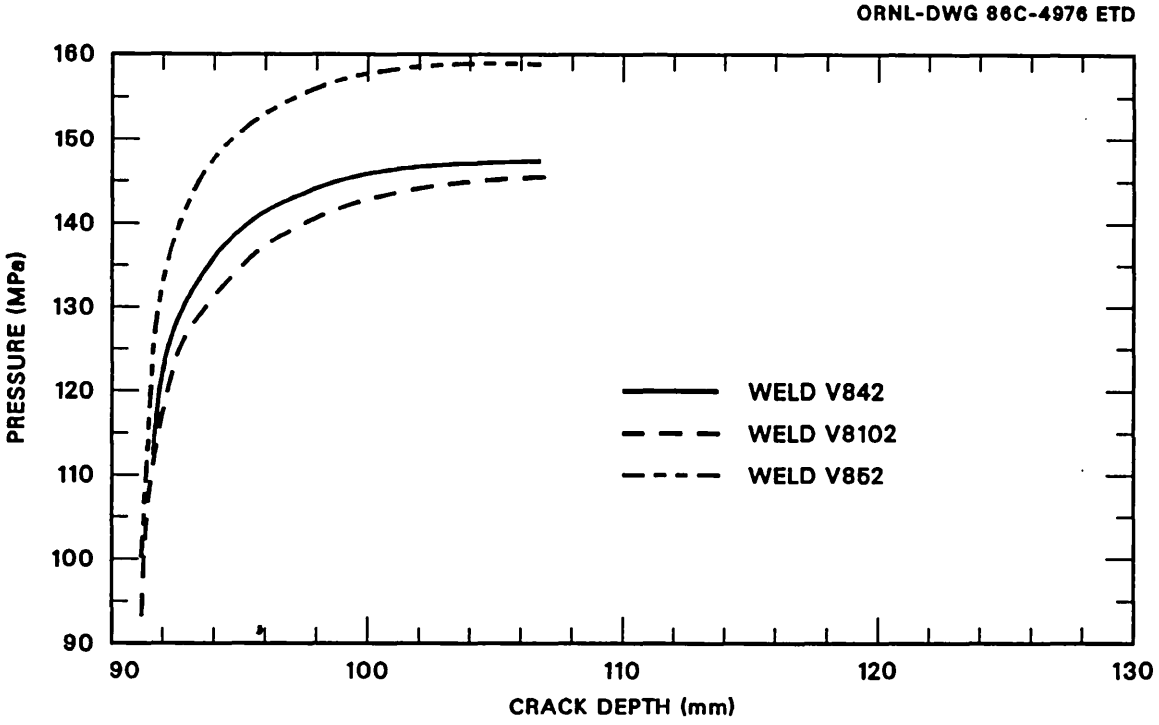

Fig. E.2. Pretest pressure vs current crack size estimates for ITV-8A based on three different J-R curves.

E.2 Posttest Analysis

Using the Failure Assessment Diagram as for pretest estimates, but with an improved iteration procedure, the calculations for ITV-8A have been repeated. With material input data of weld V842 and with an initial crack depth of 88 mm, the best estimates are maximum pressure = 145 MPa, and stable crack extension = 9 mm.

When comparing these calculated values with the experimental data (140 MPa, 15 mm), note the influence of material input data. Figure E.3 shows that the ratio of maximum loads calculated for welds V852 and V8102 is 1.10 as a result of different J_R curves (Fig. E.4) and of different tensile data. The dependence of the failure predictions on material tensile data alone (for constant J_R curve) can be seen in Fig. E.5. Although for the extreme cases V852 and V8102 the ratio of flow stresses $\sigma_F = (\sigma_u + \sigma_y)/2$ is 1.09, the ratio of maximum loads is 1.05.

The results in Figs. E.3 and E.5 were obtained by assuming uniform crack shape (i.e., a/c = const.) during stable crack extension. In Fig. E.6 the influence of the lateral crack growth on maximum load is examined (four different crack-growth modes are analyzed in Fig. E.6). Obviously, the highest maximum load is obtained for constant crack length. This load is ~6% higher than that for the approximate final crack shape

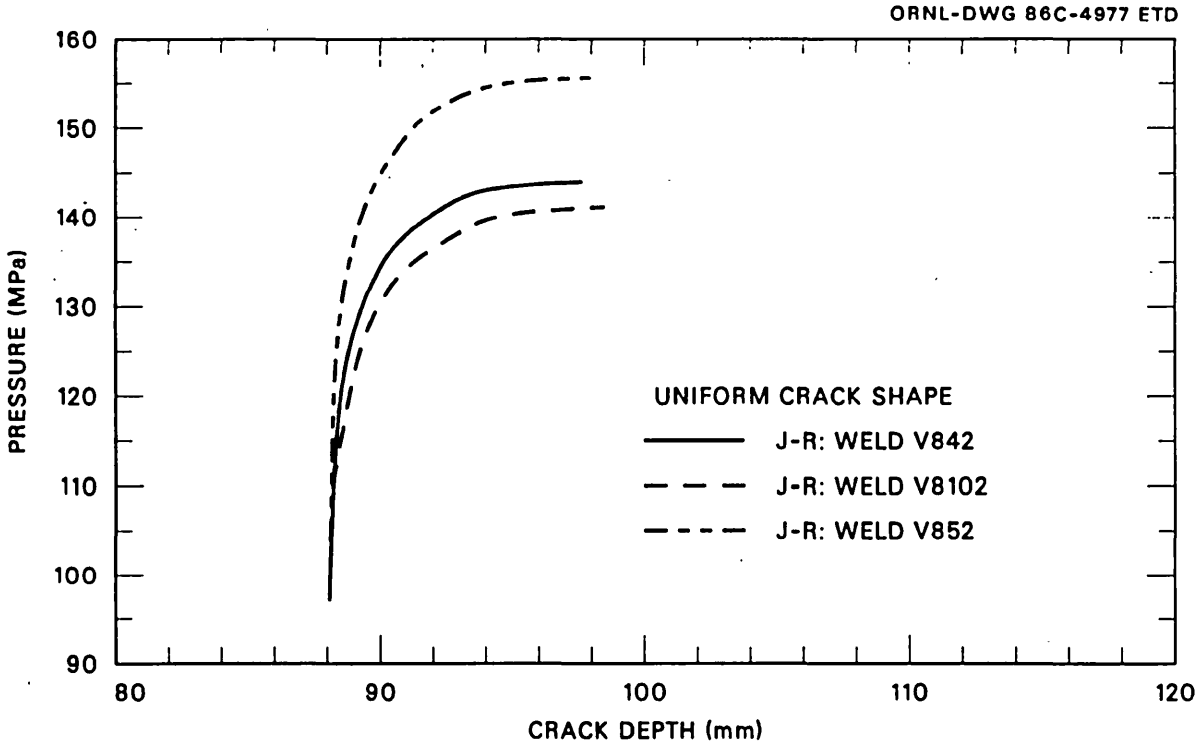

Fig. E.3. Posttest pressure vs current crack size estimates for ITV-8A based on three different J-R curves.

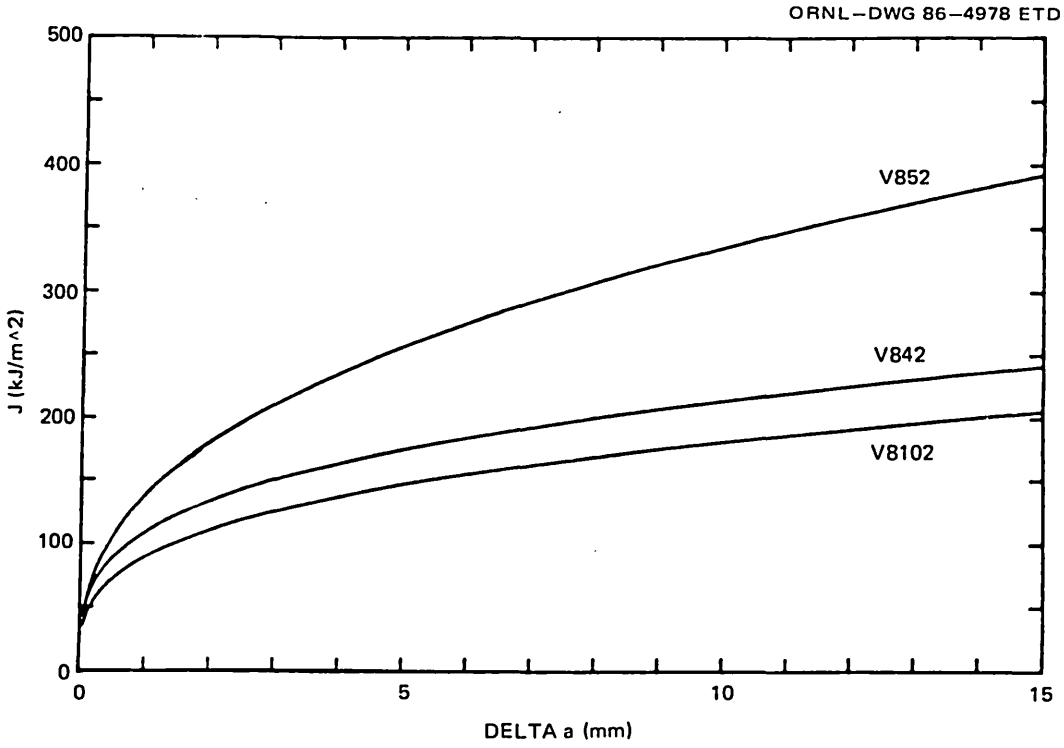

Fig. E.4. J-integral tearing resistance curves for characterization welds V852, V842, and V8102.

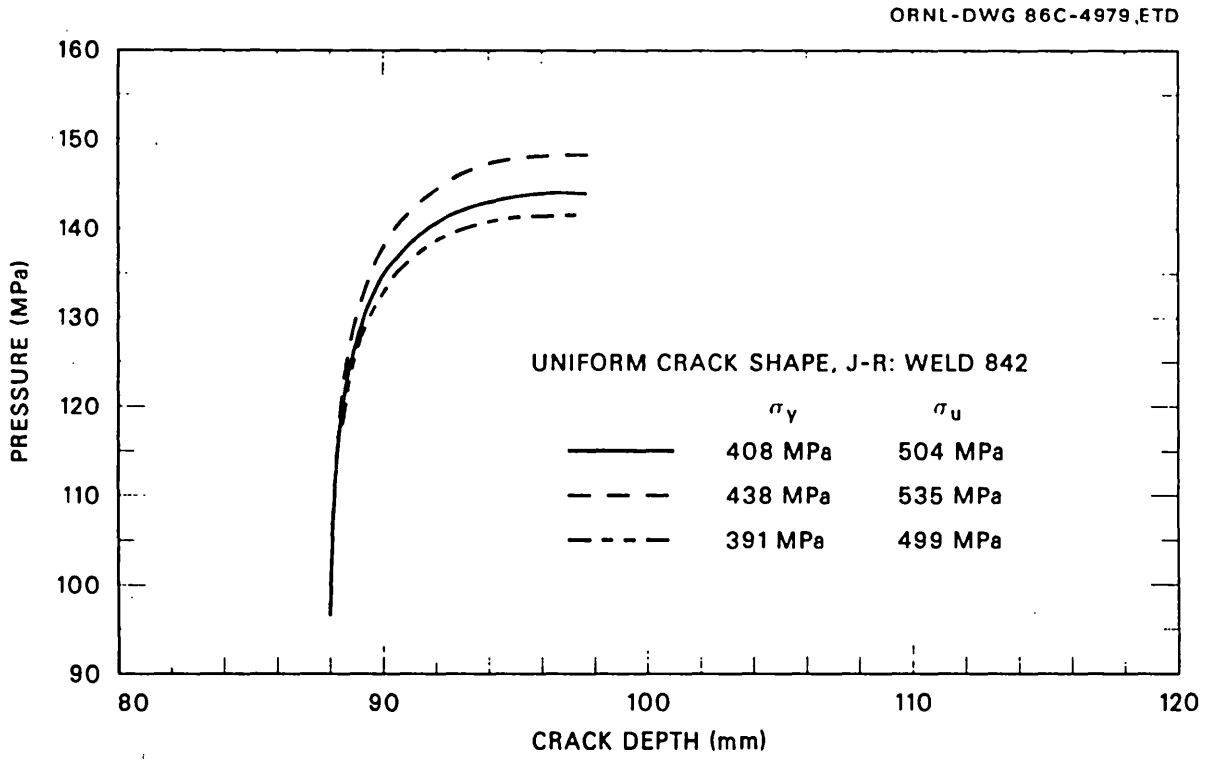

Fig. E.5. Effect of tensile properties on pressure vs current crack size curves for ITV-8A.

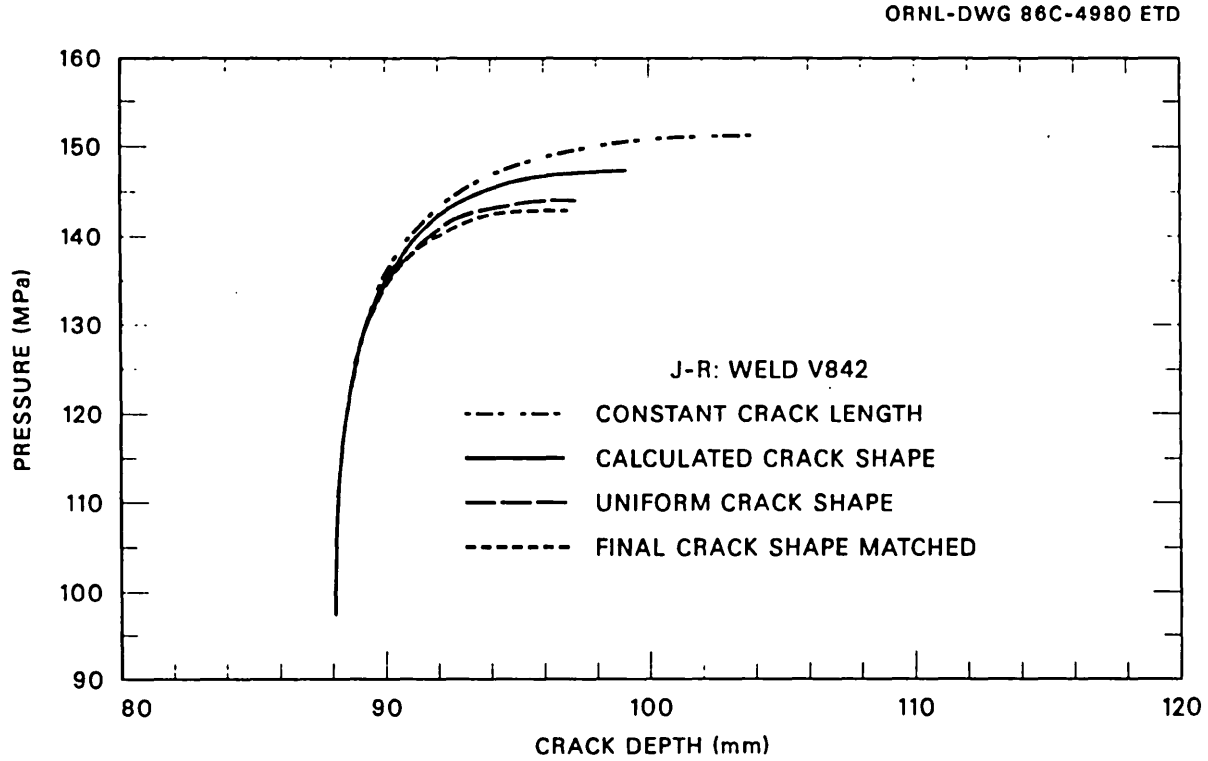

Fig. E.6. Effect of crack shape variation on pressure vs current crack size curves for ITV-8A.

found on the fracture surface. To model the canoe-shaped crack contour by a semiellipse, the mean lateral crack extension $\overline{\Delta c}(\overline{\Delta c} \approx \Delta c_{max}/2)$ is coupled to the extension into the depth by $\overline{\Delta c} = 2 \times \Delta a$ during stable crack growth. At $\Delta a = 15$ mm, then, the final maximum crack extension of $\Delta c_{max} = 72.5$ mm is just slightly underestimated.

In one case (full line in Fig. E.6) lateral crack extension was calculated step-by-step by using the same J_R curve as for the depth direction. The final stable crack extension for this case is $\Sigma a = 11$ mm and $\overline{\Delta c} = 8$ mm. A comparison of this result with the experimental findings suggests that possibly for the calculation of crack growth in the length direction, a lower J_R curve than for the depth direction should be used.

References

1. G. G. Chell and I. Milne, "Ductile Tearing Instability Analysis: A Comparison of Available Techniques," pp. 179—205 in *2nd International Symposium on Elastic Plastic Fracture Mechanics, Philadelphia, October 1981*, Vol. II, ASTM STP 803, American Society for Testing and Materials, Philadelphia, 1983.

2. J. C. Newman and I. S. Raju, *Eng. Fract. Mech.* 15, 185—92 (1981).

3. A. S. Kobayshi et al., *J. of Pressure Vessel Tech., Trans. ASME* 99(1) (February 1977).

4. L. Hodulak and J. G. Blauel, *Ermüdungsrißwachstum unter thermisch induzierten Beanspruchungen*, Vorträge der 14, Sitzung des AK Bruchvorgänge, DVM, Berlin, 1982, pp. 151—58.

5. R. P. Harrison et al., *Assessment of the Integrity of Structures Containing Defects*, CEGB Report R/H/R6-Rev. 2, Central Electricity Generating Board, Great Britain.

Appendix F

J-T CALCULATIONS FOR HSST PROGRAM INTERMEDIATE TEST VESSELS V-1, -3, -6, AND -8A

One of the methods of tearing-instability analysis that could have been used for the flaw design and pretest analyses of ITV-8A is the J-T diagram method suggested by Paris and Johnson.[1,2] This method was not used for pretest calculations at ORNL because of some simplifications in the method, the effects of which were unknown for low-shelf material. In particular, the method does not include the effect of increasing crack size on the applied valve of J, which is inherently unconservative.[3] Also, although the method produces a direct estimate of J at the point of tearing instability, auxiliary methods not specified must be applied to estimate the corresponding load and nominal strain. Although such methods — using vessels V-1, -3, and -6 as examples — had been developed and demonstrated before the V-8A test, they were not used for pretest calculations on V-8A because of their approximate natures. For the V-8A test it was necessary to estimate the values of load and crack extension at instability as accurately as possible, and the methods chosen for doing so, namely the Tangent Modulus Method[3-5] (see Appendix A) and the ORMGEN-ADINA-ORVIRT program[5,6] (see Chap. 5), were considered the most appropriate for this purpose. However, it is worthwhile to examine the posttest J-T diagram solutions for vessels V-1, -3, -6, and -8A to compare analytical and experimental results and to help evaluate the approximations included in the J-T diagram solutions.

Although the J-T diagram is a graphical method of tearing-instability analysis, an analytical solution can also be developed if the R-curve is represented by an equation permitting a closed-form solution. Such is the case for a power-law R-curve, for which[3,7]

$$J = 175.13\ c \left(\frac{\Delta a}{25.4}\right)^m \quad (kJ/m^2) , \tag{F.1}$$

where Δa is in millimeters. It is convenient to normalize the value of J in Eq. (F.1) by writing

$$y = \frac{J}{\left(\frac{\sigma_0^2}{E}\right)} \quad (mm) , \tag{F.2}$$

where (σ_0^2/E) is in megapascals and σ_0 is a characteristic tensile stress that must be defined. Consequently,

$$y = \phi \left(\frac{\Delta a}{25.4}\right)^m \quad (mm) , \tag{F.3}$$

where

$$\phi = \frac{175.13\ c}{\left(\frac{\sigma_0^2}{E}\right)} \quad \text{(mm)} \ . \tag{F.4}$$

For this case, the material J-T curve can be plotted by using the equation

$$y = 25.4 \left(\frac{\phi \cdot m^m}{25.4}\right)^{\frac{1}{1-m}} \cdot \left(\frac{1}{T}\right)^{\frac{m}{1-m}} , \tag{F.5}$$

where

$$T = \frac{\partial y}{\partial a} \ . \tag{F.6}$$

The analytical solution applied here is developed from the equation for the applied value of J,[1,2]

$$J_{appl} = \frac{\sigma_0^2}{E}\, a \left\{ F\left(\frac{\sigma}{\sigma_0}\right) \right\} G \ , \tag{F.7}$$

where, for the intermediate test vessel materials and plane strain,[1,2,7]

$$F\left(\frac{\sigma}{\sigma_0}\right) = \frac{\pi \left(\frac{\sigma}{\sigma_0}\right)^2}{1 - \frac{G}{6}\left(\frac{\sigma}{\sigma_0}\right)^2} \qquad \text{where } \frac{\sigma}{\sigma_0} < \frac{2}{3} \ , \tag{F.8}$$

$$F\left(\frac{\sigma}{\sigma_0}\right) = 3.3 \left(\frac{\sigma}{\sigma_0}\right)^2 + 3.5 \left(\frac{\sigma}{\sigma_0}\right)^{10.7} \qquad \text{where } \frac{\sigma}{\sigma_0} > \frac{2}{3} \ , \tag{F.9}$$

$$G = \frac{M_m^2}{Q} \ , \tag{F.10}$$

with the values of M_m^2 and Q being estimated, by approximation, from the elastic solution. In Eq. (F.7) it is assumed for simplicity that the factors F and G do not vary with crack size. Consequently, from Eq. (F.6),

$$T_{appl} = \left\{ F\left(\frac{\sigma}{\sigma_0}\right) \right\} G \ , \tag{F.11}$$

so that, neglecting changes in crack size,

$$\frac{y_{appl}}{T_{appl}} = a_0 \ . \tag{F.12}$$

From Eq. (F.3),

$$\frac{y_{mat}}{T_{mat}} = \frac{\Delta a}{m} \tag{F.13}$$

so that equating the right-hand sides of Eqs. (F.12) and (F.13) gives, at instability,

$$\Delta a = m a_0 \ , \tag{F.14}$$

and from Eq. (F.3),

$$y_{inst} = \phi \left(\frac{m a_0}{25.4}\right)^m \ . \tag{F.15}$$

Thus, from Eq. (F.12),

$$T_{inst} = \frac{y_{inst}}{a_0} \ , \tag{F.16}$$

and from Eq. (F.11),

$$F\left(\frac{\sigma}{\sigma_0}\right) = \frac{T_{inst}}{G} \ . \tag{F.17}$$

The nominal stress level (σ/σ_0) is determined by solving Eqs. (F.8) and (F.9). Thus, for Eq. (F.8),

$$\left(\frac{\sigma}{\sigma_0}\right) = \frac{1}{\sqrt{\frac{\pi}{F} + \frac{G}{6}}} \ , \tag{F.18}$$

and for Eq. (F.9),

$$\frac{\sigma}{\sigma_0} = \left[\frac{\left\{F\left(\frac{\sigma}{\sigma_0}\right)\right\} - 3.5\left(\frac{\sigma}{\sigma_0}\right)^{10.7}}{3.5}\right]^{1/2} \qquad \text{where } \frac{\sigma}{\sigma_0} < 1 \ , \tag{F.19}$$

$$\left(\frac{\sigma}{\sigma_0}\right) = \left[\frac{\left\{F\left(\frac{\sigma}{\sigma_0}\right)\right\} - 3.3\left(\frac{\sigma}{\sigma_0}\right)^{2}}{3.5}\right]^{\frac{1}{10.7}} \qquad \text{where } \frac{\sigma}{\sigma_0} > 1 \ . \tag{F.20}$$

Equation (F.18) provides a direct solution. Equations (F.19) and (F.20) are solved by successive approximation. The nominal strain is determined from the equation of the stress-strain curve[1,2]

$$\frac{\varepsilon}{\varepsilon_0} = \left(\frac{\sigma}{\sigma_0}\right) + 1.115\left(\frac{\sigma}{\sigma_0}\right)^{9.7} \ , \tag{F.21}$$

where

$$\varepsilon_0 = \frac{\sigma_0}{E} \ . \tag{F.22}$$

The pressure is estimated by assuming

$$p = p_{GY}\left(\frac{\sigma}{\sigma_0}\right) \ , \tag{F.23}$$

where

$$p_{GY} = \frac{\sigma_0}{\frac{R_i}{t} + \frac{1}{2}} \ . \tag{F.24}$$

In the absence of resistance curve data for vessels V-1, -3, and -6, power-law R-curve parameters for Eq. (F.1) were estimated by correlation with upper-shelf Charpy V-notch impact energy and tensile flow stress data, using[7]

$$c = -0.114\left(\frac{CVN}{135.58}\right) + 5.382\left(\frac{CVN}{135.58}\right)^2 , \qquad (F.25)$$

$$x = c + 1.5\left(\frac{\bar{\sigma}}{689.48}\right) , \qquad (F.26)$$

$$m = \frac{0.473\ x^3}{14.42 + x^3} , \qquad (F.27)$$

where the flow stress $\bar{\sigma}$ is defined here as the average of the yield and ultimate tensile stresses. Note that in this analysis, the value of σ_0 is taken to be the uniaxial yield stress rather than the flow stress, consistent with the numerical values (but not the nomenclature) used by Paris and Johnson.[1,2] The values of σ_0, $\bar{\sigma}$, and E were taken as 496 and 569 MPa and 207 GPa, respectively.[8,9] The CVN impact energy for vessel V-1 was 122 J,[8] and for V-3 and -6 it was 170 J.[9] The values of M_m and Q were estimated from the curves given in Sect. XI, Appendix A of the *ASME Code for Nuclear Vessels*.[10] The inside radius R_i of the intermediate test vessels is 342.90 mm, and the wall thickness t is 152.40 mm. From the given values of σ_0 and E, the value of ε_0 is 0.24%, and the value of σ_0^2/E is 1.191 MPa. The calculated results for vessels V-1, -3, and -6 are summarized in Tables F.1 and F.2, and the J-T solutions are shown graphically in Fig. F.1. The agreement between analysis and experiment is good.

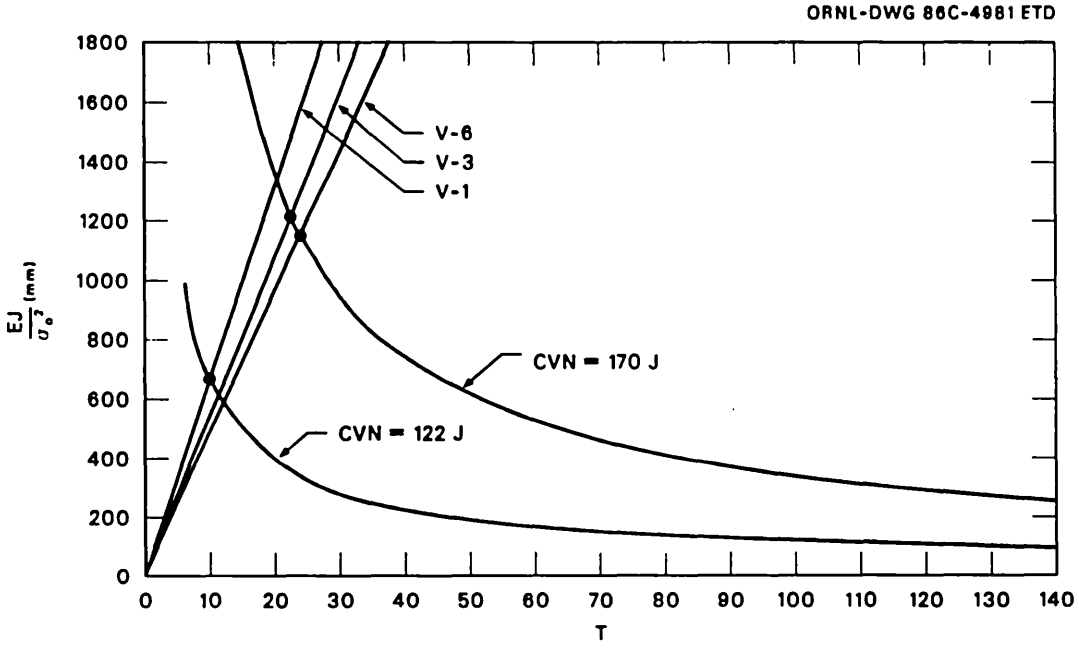

Fig. F.1. J-T diagram for HSST intermediate test vessels V-1, -3, and -6.

Table F.1. J-T diagram calculations for intermediate test vessels V-1, -3, and -6

Vessel	CVN (J)	c	m	a_0 (mm)	l_0 (mm)	G	Δa (mm)	$J_{inst.}$ (kJ/m2)	$T_{inst.}$	$\left(\frac{\sigma}{\sigma_0}\right)$
V-1	122	4.257	0.4352	65.0	209.6	0.829	28.2	782	10.1	1.08
V-3	170	8.267	0.4652	53.6	215.9	0.956	24.9	1435	22.5	1.17
V-6	170	8.267	0.4652	47.5	133.4	0.659	22.1	1357	24.0	1.23

Table F.2. Comparison of calculated and measured tearing-instability pressures for intermediate test vessels V-1, -3, and -6

Vessel	Calculated		Measured	
	p (MPa)	ε (%)	p (MPa)	ε (%)
V-1	196	0.85	199	0.92
V-3	212	1.52	214	1.47
V-6	222	2.25	220	2.0

Four posttest calculations were made for vessel V-8A, using three different R-curves with otherwise identical analysis procedures. The input and results are summarized in Tables F.3 and F.4. Note that other calculations had agreed best with the vessel V-8A test results when based on the lowest of the four characterization weld (V8102) R-curves shown in Fig. 2.16 and that the lowest curve is closest to the posttest characterization data. Furthermore, the decreases in Charpy upper-shelf impact energy and tearing resistance for the characterization welds are nearly consistent (see Table 2.6 and Fig. 2.17). Consequently, the properties of characterization weld V8102 were used as input. All tensile specimens for characterization weld V8102 were oriented in the welding direction, which corresponds to the axial direction in the vessel. Material properties for the vessel V-8A test weld, measured posttest, are shown in Table F.3 for comparison with the values for characterization weld V8102 used for the calculations. The first R-curve used was the J_D-based power-law R-curve estimated by correlation with Charpy and tensile data according to Eqs. (F.25)—(F.27). The results for this R-curve were conservative because the correlation tends to be conservative for low-shelf materials. The second R-curve used was the average measured power-law R-curve for characterization weld V8102 (see Fig. 2.16 and Table 2.13). The result for this R-curve was quite accurate in terms of the calculated instability pressure, which agrees with the measured value of 140 MPa, although the calculated strain exceeds the measured value of 0.12%. The third R-curve used, estimated by a correlation with Charpy data recently proposed by MEA,[11] was a J_M-based power-law R-curve for weld metal at large crack extension. In this case, the value of T_{inst}, calculated by using the J_M-based R-curve, is higher than the values estimated in the two J_D-based calculations, and the calculated instability pressure is slightly unconservative.

Because the MEA J_M-CVN weld metal correlation resulted in an overestimate, a fourth calculation was done, using a companion base metal correlation that predicts lower R-curves at large crack extensions for low-shelf materials. This calculation proved to be slightly conservative and quite accurate in terms of instability pressure. The reason for the

Table F.3. Input data for J-T calculations on intermediate test vessel V-8A

Item	Symbol	Value
Flaw depth	a_0	91.19 mm
Flaw length	l_0	279.40 mm
Charpy upper-shelf impact energy	CVN	
V8102		51.7 J
V-8A		57.0 J
Yield stress	σ_0	
V8102		438 MPa
V-8A		423 MPa
Nominal ultimate stress	σ'_{ult}	
V8102		534 MPa
V-8A		525 MPa
Flow stress	$\overline{\sigma}$	
V8102		486 MPa
V-8A		474 MPa
Inside radius	R_i	342.90 mm
Wall thickness	t	152.40 mm

difference between the weld metal and base metal correlations is not known and should be investigated.

Note that the estimates of crack extension and the associated toughness for the most accurate instability pressure estimate in Table F.4 are too high. This is a consequence of the crack size not being updated as the applied value of J is increased and is, therefore, an inherent limitation of the standard J-T diagram procedure. Thus, if a standard J-T diagram solution is accurate compared with experimental data, it is probably because either Δa is small or there are compensating effects somewhere in the calculation.

Table F.4. J-T diagram calculation results for intermediate test vessel V-8A

Material and R-Curve	c	m	G	Δa (mm)	$J_{inst.}$ (kJ/m^2)	$T_{inst.}$	$\frac{\sigma}{\sigma_0}$	$\frac{\varepsilon}{\varepsilon_0}$	p (MPa)	ε (%)
V8102, J_D-CVN, $\bar{\sigma}$ Corr. (Ref. 7)	0.738	0.1355	0.8563	12.4	117	1.39	0.69	0.72	110	0.15
V8102, Meas. Avg.	1.381	0.3080	0.8563	28.2	249	2.95	0.88	1.20	140	0.26
V8102, J_M-CVN Weld Corr. (Ref. 11)	2.029	0.3628	0.8563	33.0	391	4.63	0.96	1.74	153	0.37
V8102 J_M-CVN B. M. Corr. (Ref. 11)	1.223	0.3072	0.8563	27.9	221	2.61	0.85	1.09	136	0.23

References

1. R. Johnson, *Resolution of the Task A-11 Reactor Vessel Materials Toughness Safety Issue*, NUREG-0744, Vols. 1 and 2, Rev. 1, U.S. Nuclear Regulatory Commission, Washington, D.C., October 1982.

2. P. C. Paris and R. E. Johnson, "A Method of Application of Elastic-Plastic Fracture Mechanics to Nuclear Vessel Analysis," pp. 5—40 in *Elastic-Plastic Fracture: Second Symposium*, ASTM STP 803, Vol. II, American Society for Testing and Materials, Philadelphia, 1983.

3. J. G. Merkle, "Explanation of Analytical Bases for Low Upper Shelf Vessel Toughness Evaluations," Appendix C in *Resolution of the Task A-11 Reactor Vessel Materials Toughness Safety Issue*, NUREG-0744, Vol. 2, Rev. 1, by R. Johnson, U.S. Nuclear Regulatory Commission, Washington, D.C., October 1982.

4. J. G. Merkle, "Crack Stability Analysis for Vessel Tests in the Upper Shelf Temperature Range," paper presented at the NRC Eighth Water Reactor Safety Research Information Meeting, Gaithersburg, Md., October 27—31, 1980.

5. B. R. Bass et al., "Applications of Energy Release Rate Techniques to Part-Through Cracks in Experimental Pressure Vessels," *J. Pressure Vessel Tech., ASME* 104, 308—16 (November 1982).

6. R. H. Bryan et al., "Experimental Investigation of Tearing Behavior of a Flaw in a Thick Pressure Vessel," paper presented at the SMIRT Post Conference Seminar No. 6, Integrity of Reactor Pressure Boundary, Monterey, Calif., August 29—30, 1983.

7. J. G. Merkle and R. E. Johnson, "Example Calculations Illustrating Methods for Analyzing Ductile Flaw Stability in Nuclear Pressure Vessels," *Int. J. Pressure Vessel Piping* 18, 35—53 (1985).

8. R. W. Derby et al., *Test of 6-Inch-Thick Pressure Vessels. Series 1: Intermediate Test Vessels V-1 and V-2*, ORNL-4895, Union Carbide Corp. Nuclear Div., Oak Ridge Natl. Lab., February 1974.

9. R. H. Bryan et al., *Test of 6-Inch-Thick Pressure Vessels. Series 2: Intermediate Test Vessels V-3, V-4 and V-6*, ORNL-5059, Union Carbide Corp. Nuclear Div., Oak Ridge Natl. Lab., November 1975.

10. *ASME Boiler and Pressure Vessel Code*, Sect. XI, Div. 1, Rules for Inservice Inspection of Nuclear Power Plant Component, Appendix A: Analysis of Flaw Indications, American Society Mechanical Engineers, New York, 1980.

11. A. L. Hiser, *Correlation and Prediction of Reactor Pressure Vessel Materials Upper Shelf Fracture Toughness*, Materials Engineering Associates, Inc., Lanham, Md. (to be published as an EPRI report).

Appendix G

UK LIGHT WATER REACTOR STUDY GROUP RESPONSE TO NRC REPORT NUREG-0744 (FOR COMMENT DRAFT)*

G.1 Introduction

The following discussion is taken from correspondence between the United Kingdom (UK) Atomic Energy Authority and the U.S. Nuclear Regulatory Commission (NRC), dated January 28, 1983, and subsequently forwarded by the NRC to the American Society of Mechanical Engineers Working Group on Flaw Evaluation for review.

The Light Water Reactor Study Group has considered the proposals in NUREG-0744,[1] first, in relation to the conclusions reached in the second Marshall Report[2] concerning a pressurized water reactor (PWR) yet to be fabricated in the United Kingdom and, second, in relation to the low-upper-shelf energy problem that was specifically addressed by the A-11 Task Group. Although the Study Group does not expect that the methodology presented in NUREG-0744, or its equivalent, will need to be invoked for any UK PWR vessel, it was, nevertheless, felt that some comment upon this document may be helpful to NRC. Accordingly, the communication that follows discusses first, in a general way, the relevance to a UK PWR vessel; then the specific problem raised by the A-11 issue; second, some conclusions on the J-T methodology in its present stage of development; and, finally, details of the calculations upon which the preceding comments are based.

G.1.1 General relevance of NUREG-0744 proposals in relation to conclusions reached in the second Marshall Report

We note that the A-11 issue is due to low postirradiation upper-shelf toughness values. We do not expect that this would be a relevant concern in the case of a PWR vessel fabricated to meet the essential recommendations of the second Marshall Report.[2] This is because forged ring construction would eliminate all welds in the irradiated beltline region and steel composition limits would be restricted to ensure initially high-upper-shelf fracture toughness properties and very low susceptibility to neutron irradiation damage. Thus, we expect that even at end of life, properties will not have changed significantly; consequently, there will be no requirement to invoke a methodology to deal specifically with low-upper-shelf toughness.

---

*Compiled by L. M. Davies (Secretary to the LWRSG), Atomic Energy Technical Branch, United Kingdom Atomic Energy Authority, AERE Harwell.

G.1.2 Specific comments on NUREG-0744 proposals in relation to the beltline flaw problem addressed by the A-11 Task Group

We recognize that NUREG-0744[1] addresses a regulatory issue, namely, that of establishing the means of demonstrating the existence, or otherwise, of adequate safety margins with regard to the continued operation of those nuclear reactor pressure vessels that, as a result of neutron irradiation embrittlement of beltline region welds, may eventually fail to meet the 68-J (50-ft-lb) Charpy V-notch upper-shelf energy criterion of 10 *CFR* 50, Appendixes G and H.[3] We further recognize that there are several important technical aspects of Task A-11. Our comments and supporting calculations are restricted, however, to Subtasks A, B, and C, as listed under Item 2, "Plan for Problem Resolution," in Appendix A of NUREG-0744 (for comment).[1]

First, by way of preliminary comment, we endorse the assertion in Sect. 4.1 on p. J-10 that the first priority in resolving concerns in connection with the A-11 issues is to "Establish analysis methods and criteria applicable to system Emergency and Faulted Conditions which occur at and near upper shelf temperatures." We, therefore, find it surprising that the methodology presented in NUREG-0744, presumably as a means of addressing this point, is restricted to the more narrowly defined problem of avoiding failure by tearing instability with respect to a flaw situated in the beltline region of a reactor pressure vessel of "low upper-shelf energy" material and subjected only to pressure loading. Although we certainly appreciate the necessity of establishing pressure-temperature limits in connection with this particular mode of failure, we do not agree with the general relevance of a methodology based on a tearing modulus approach and considering only primary (pressure) loading to the case of level C and D transients with possible high secondary (thermal) loading where, depending in particular upon the shift in RT_{NDT} with irradiation, transition region toughness properties may apply. To this extent, we note that the "safe region" marked on the J-T diagram in Fig. 3 on p. B-10 of NUREG-0744 is only safe for a given temperature provided ΔRT_{NDT} is not so large that either (1) brittle fracture occurs when $K_{Ic} = (E' J_{app})^{1/2} < (E' J_{Ic})^{1/2}$ or (2) cleavage instability intervenes following a small amount of stable, ductile crack extension when $J_{app} > J_{Ic}$.

Second, by way of more-detailed comment, we would like to make the following points.

1. We note that although the J-T analysis developed in response to Subtask B is intended to deal with limited amounts of ductile crack extension, it is only broadly consistent with the accepted conditions for J-controlled crack growth being met. In particular, adoption of $\omega \simeq 5$ is not a sufficient condition for this to strictly be the case, and we suggest that, where possible, the appropriate limits be marked on the material J-T curve.
2. We endorse the comments on p. B-40 of NUREG-0744 regarding the need to establish a statistically more significant lower-bound correlation between Charpy V-notch upper-shelf energy and J_{50} values and note that this is particularly relevant with respect to irradiated materials with values of $C_v < 68$ J. Moreover, we note that because

upper-shelf toughness (C_v) and fracture toughness (J_{Ic}; T_{mat} for a given value of J_{mat}) properties are a function of temperature, J_{50} will be a function of temperature. In particular, we would expect J_{50} to decrease with temperature, at least until reaching a minimum, the position and value of which may depend upon material composition and loading rate. We assume that this will be taken into account in any lower-bound correlation that may be formally established.

3. We note that the approximate methods developed for calculating J_{app}/T_{app} for the problem addressed in NUREG-0744 lead to a linear relationship between these two quantities as a direct result of (1) calculating J_{app} by separating the variables of load and geometry and not normalizing the load with respect to a crack-size dependent reference load and (2) ignoring the effect of crack growth when $J_{app} > J_{Ic}$. However, alternative methods could equally be used, and we have found that those based on the CEGB R6 analysis[4] and the estimation scheme of Shih et al.[5] do not, in general, lead to proportionality between J_{app} and T_{app}; moreover, for the cases we have examined, the slope dJ_{app}/dT_{app} is always <8.76 kJ/m^2 (<50 lb/in.) at sufficiently high loads (corresponding to plastic collapse), and we would expect this to be observed regardless of the means of generating J. (See further analysis and discussion in Appendix H of this report.)
4. We note that for small amounts of crack growth to instability, although the shape of the applied J-T curve does not change, the load sensitivity of this curve does.
5. We note that no specific guidance is given as to how secondary (e.g., thermal) stresses should be treated in calculating J_{app}.
6. We assume that the intent of the safety margin with respect to levels C and D transients proposed on p. 6-1 of NUREG-0744 is to limit J_{app} to $1/2\ J_{50}$.
7. We note from our calculations that a safety factor of 2 on J_{app} with respect to J_{50} does not imply a similar safety margin in terms of the corresponding values of pressure loading; nor does it properly acknowledge the factor of safety existing with respect to the pressure estimated to cause instability.
8. We further note from our calculations that because the J-T methodology in NUREG-0744 is specific to materials with low-upper-shelf toughness properties, the possibility exists that if it were applied more generally, then, depending upon the material J_R-curve, flow properties, postulated defect size, etc., this could result in the value of pressure loading corresponding to $J_{app} = 1/2\ J_{50}$ being in excess of that estimated to correspond to the onset of plastic collapse — for example, in the case of a part-through surface crack. We assume that the need to check on this possibility would be emphasized in any Code requirements.
9. We note that application of J-T methodology to problems other than those that were specifically addressed by the A-11 Task Group — including thermal shock, etc. — can only be justified after appropriate validation.

10. We note that surveillance specimens used for obtaining irradiated material J_R-curve data (e.g., 1T-CT) have only a limited J capacity as defined by the ω criterion. Therefore, they cannot sustain sufficient ductile crack extension to ensure the absence of a transition to cleavage before loss of J-controlled crack growth. On a J-T diagram, cleavage will appear as a cutoff to the material J-T curve at the appropriate level of J (Fig. G.1). Because the intersection of the J/T = 8.76 kJ/m^2 (50 lb-in.$^{-1}$) line with the material J-T curve is only a very rough approximation to the ω = 5 limit for a 1TCT specimen, it may not adequately screen out mode conversion before loss of J control, should it occur. Moreover, the linear extrapolation of the material J-T curve proposed in Appendix B of NUREG-0744 as a conservative estimate of material behavior beyond the ω limit also ignores this potential mode transition.

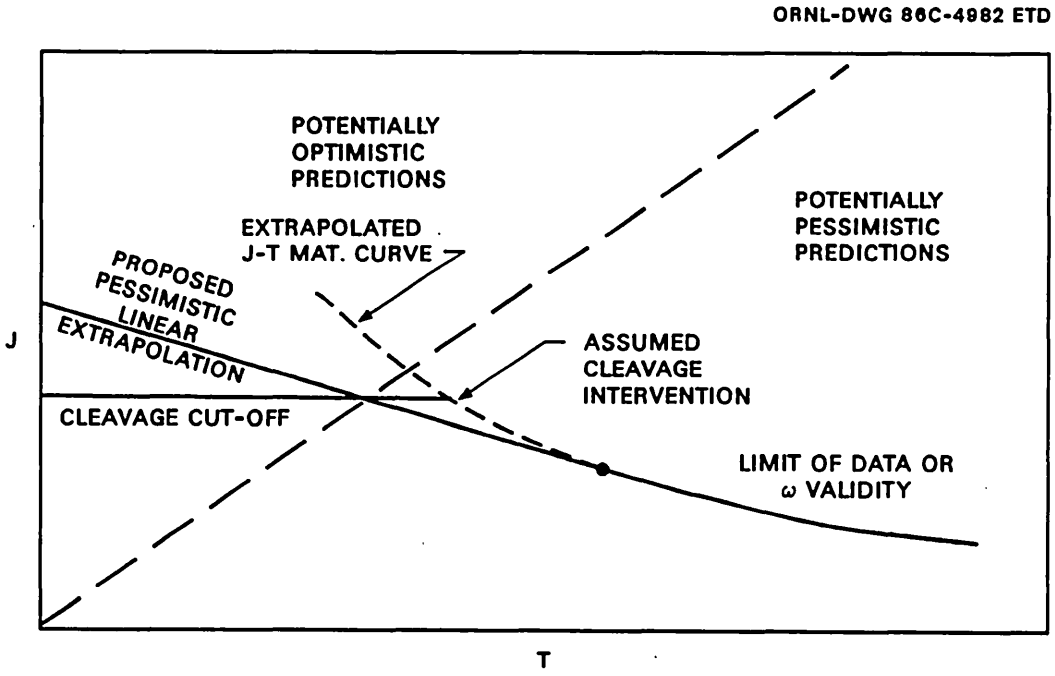

Fig. G.1. Schematic representation of potential for unconservative predictions in presence of ductile-cleavage transition.

G.1.3 Conclusions on J-T methodology in its present stage of development

We recognize the usefulness of the form of analysis developed by the A-11 Task Group in providing the means for defining screening criteria to guard against failure in limited circumstances where

1. the defect geometry is that of a semielliptical surface crack, a/2c > 1/6, in the beltline region of a PWR vessel;

2. the vessel is loaded by pressure only;
3. the material has a low resistance to tearing, and crack extension is fully ductile, leading only to tearing instability; and
4. proper account is taken in the analysis of crack extension and the sensitivity of J with applied load.

We further recognize that after additional development the analysis may be applicable in more-general circumstances. However, we believe that alternative methods that already serve this purpose exist.

G.1.4 J-T analysis for intermediate vessel test V-8A*

Calculations were made by the formulas listed below to establish J-T diagrams, with straight J-T applied lines, for vessel V-8A for two cases. Case I is a lower-bound case based on the J-T material curve for characterization weld V8102. Calculated results are listed in Table G.1, and the instability solution is shown graphically in Fig. G.2. Based on the actual J-T material curve, tearing instability is predicted at a pressure of 140 MPa, with about 15 mm of stable crack growth. Case II is an upper-bound case based on characterization weld V862. Calculated results are listed in Table G.2, and the instability diagram is shown in Fig. G.3. The instability solution for the actual material J-T curve is off scale, although a solution based on a linear extrapolation of the J-T material curve from near the J(50) intersection point lies on the diagram.

Note that for an outside surface flaw the use of an elastically calculated reference stress equal to the inside surface circumferential stress represents a conservation in this analysis. In addition, the variation of the geometry factor G with crack depth is considered.

The input data and equations used are listed below.

Vessel dimensions

$r_1 = 495.3$ mm

$r_0 = 342.9$ mm

$t = 152.4$ mm

Flaw dimensions

$a = 91.15$ mm, $a/t = 0.598$

$\ell = 279.4$ mm, $a/\ell = 0.326$

*D. P. G. Lidbury, RNL.

Table G.1. Calculated loading parameters for lower-bound (Case I) tearing-instability analysis of vessel V-8A

P (MPa)	σ (MPa)	σ/σ_0	$\varepsilon/\varepsilon_0$	J_{app} (kJ/m^2)
40	113.6	0.23	0.23	15
50	142.1	0.28	0.28	23
60	170.5	0.34	0.34	33
70	198.9	0.40	0.40	45
80	227.3	0.45	0.45	60
90	255.7	0.51	0.51	76
100	284.1	0.57	0.57	95
110	312.5	0.63	0.63	116
120	340.9	0.68	0.70	141
125	355.1	0.71	0.74	156
130	369.3	0.74	0.78	172
135	383.5	0.77	0.83	190
140	397.7	0.80	0.89	212
145	412.0	0.82	0.96	238
150	426.2	0.85	1.05	269

$J_{app} = J_{Ic} \approx 45$ kJ/m^2, P ≈ 70 MPa

$J_{app} = J_{50} \approx 110$ kJ/m^2, P ≈ 110 MPa, $\varepsilon \approx 0.10\%$[a]

$J_{app} = 1/2\ J_{50} \approx 55$ kJ/m^2, P ≈ 80 MPa, $\varepsilon \approx 0.07\%$[a]

$J_{app} = J(L) \approx 160$ kJ/m^2, P ≈ 125 MPa, $\varepsilon \approx 0.12\%$[a]

$P_{(limit)} = 160$ MPa

[a]Outside surface circumferential strain.

Table G.2. Calculated loading parameters for upper-bound (Case II) tearing-instability analysis of vessel V-8A

P (MPa)	σ (MPa)	σ/σ_0	$\varepsilon/\varepsilon_0$	J_{app} (kJ/m^2)
40	113.6	0.27	0.27	15
50	142.1	0.33	0.33	23
60	170.5	0.40	0.40	33
70	198.9	0.47	0.47	46
80	227.3	0.54	0.54	61
90	255.7	0.60	0.61	78
100	284.1	0.67	0.68	98
110	312.5	0.74	0.78	123
120	340.9	0.80	0.91	157
125	355.1	0.84	1.00	181
130	369.3	0.87	1.12	210
135	383.5	0.90	1.27	247
140	397.7	0.94	1.48	296
145	412.0	0.97	1.77	359
150	426.2	1.00	2.15	444

$J_{app} = J_{Ic} \approx 45$ kJ/m^2, P ≈ 70 MPa

$J_{app} = J_{50} \approx 260$ kJ/m^2, P ≈ 135 MPa, $\varepsilon \approx 0.12\%$[a]

$J_{app} = 1/2\ J_{50} \approx 130$ kJ/m^2, P ≈ 110 MPa, $\varepsilon \approx 0.10\%$[a]

$J_{app} = J(L) \approx 360$ kJ/m^{2}m, P ≈ 145 MPa, $\varepsilon \approx 0.13\%$[a]

$P_{(limit)} = 136$ MPa

[a]Outside surface circumferential strain.

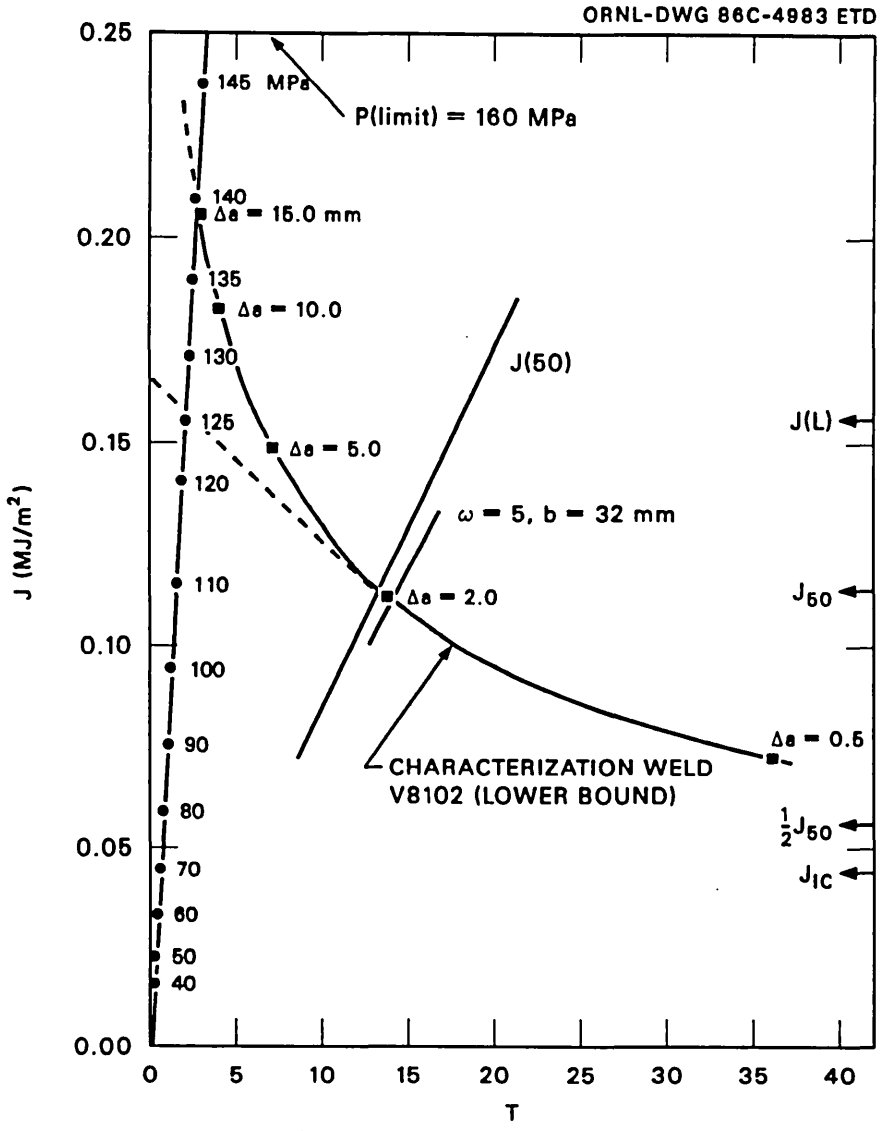

Fig. G.2. J-T analysis diagram for intermediate vessel test V-8A: Case I (lower bound).

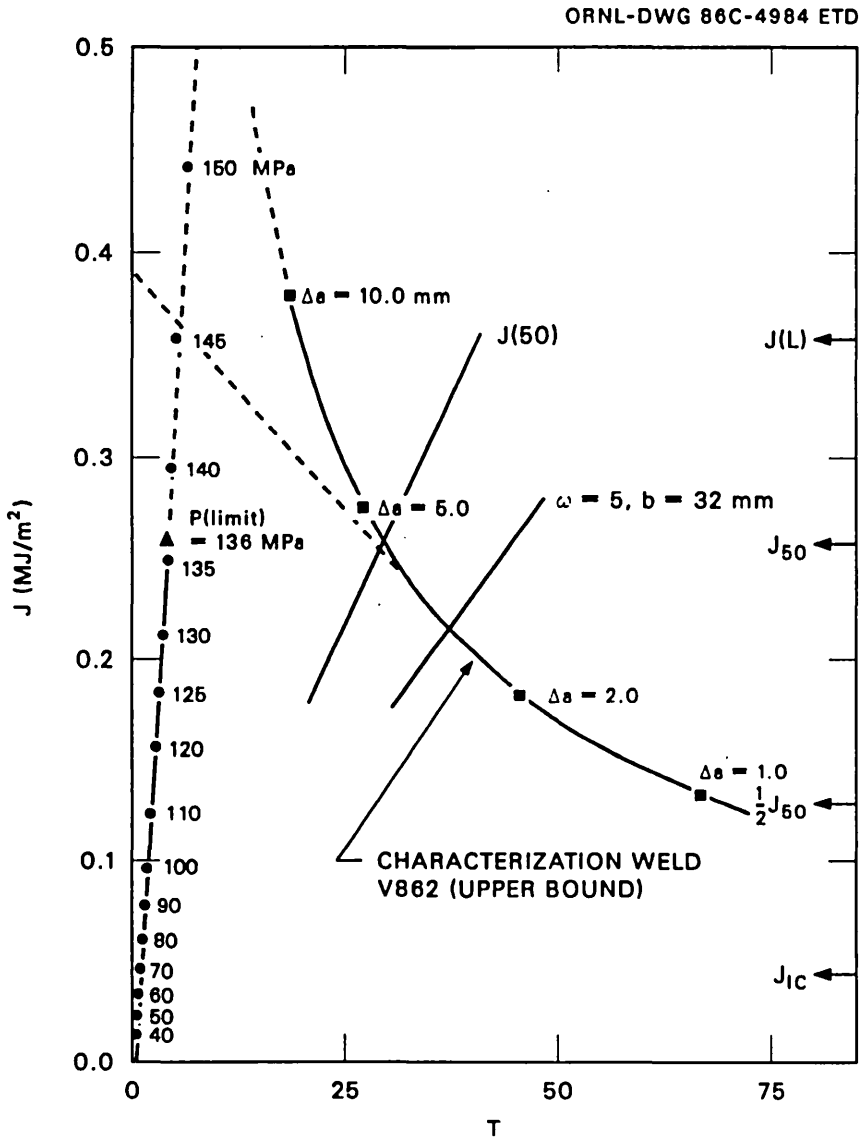

Fig. G.3. J-T analysis diagram for intermediate vessel test V-8A: Case II (upper bound).

Materials data

Case I

log (J/89.0) = 0.308 log (Δa/1.0) , (charac. weld V8102 avg)*

J in kJ/m^2

Δa in mm

$J_{Ic} = 45\ kJ/m^2$

$\sigma_0 = 500$ MPa

$E = 2.1 \times 10^5$ MPa

$C_{vu} = 50.7$ J

$\varepsilon/\varepsilon_0 = \sigma/\sigma_0 + 1.115\ (\sigma/\sigma_0)^{9.7}$

Case II

log (J/134.0) = 0.451 log (Δa/1.0) , (charac. weld V862 avg)*

J in kJ/m^2

Δa in mm

$J_{Ic} = 45\ kJ/m^2$

$\sigma_0 = 425$ MPa

$E = 2.1 \times 10^5$ MPa

$C_{vu} = 61.8$ J

$\varepsilon/\varepsilon_0 = \sigma/\sigma_0 + 1.115\ (\sigma/\sigma_0)^{9.7}$

Stress analysis

Assume thick cylinder formula for $\left(\sigma_{\theta\theta}\right)_{max}$,

$$\sigma = \frac{(r_1^2 + r_0^2)}{(r_1^2 - r_0^2)} \cdot P = 2.841\ P \quad \text{(stress at inside surface)} , \qquad (G.1)$$

where r_0 and r_1 are inside and outside radii, respectively.

$$\frac{J_{app} \text{ and the stress factor } \{\ \}}{J_{app} = \frac{\sigma_0^2 a}{E}\ [M_m^2/Q]\ \{\text{stress}\}} , \qquad (G.2)$$

*See Table 5.4 in Enclosure 3 of Appendix B.

$$\{\ \} = \frac{\pi\ (\sigma/\sigma_0)^2}{1 - \frac{1}{6}\ (\sigma/\sigma_0)^2} \qquad \text{when } \sigma/\sigma_0 < 2/3\ , \tag{G.3}$$

$$\{\ \} = 3.3\ (\sigma/\sigma_0)^2 + 3.5\ (\sigma/\sigma_0)^{10.7} \qquad \text{when } \sigma/\sigma_0 > 2/3\ . \tag{G.4}$$

Strictly speaking, the use of Eqs. (G.3) and (G.4) is limited to $a/t < 1/2$ in NUREG-0744.

LEFM shape factor

$$\begin{aligned} Q &= 1 + 1.464\ (a/c)^{1.65} \\ &= 1.724\ , \end{aligned} \tag{G.5}$$

$$M_1 = 1 + 0.12\ (1 - a/2c)^2\ , \tag{G.6}$$

$$p = 1.6 + 3(a/c)^3 + 8(a/c)(a/t)^5 + 0.008\ (c/a)\ , \tag{G.7}$$

$$\begin{aligned} M_m &= M_1 + (\sqrt{Qc/a} - M_1)\ (a/t)^p \\ &= 1.187\ , \end{aligned} \tag{G.8}$$

$$M_m^2/Q = 0.817\ .$$

$(J/T)_{app}$

$$(J/T)_{app} = \frac{\sigma_0^2 a}{E}\left[1 + \frac{\frac{a}{t}\ [\ ]^1}{[\ ]}\right]\ , \tag{G.9}$$

where, conservatively, $[\ ]^1 = \partial/\partial_{(a/t)}[\ ]$, (G.10)

giving

$$(J/T)_{app} = \frac{\sigma_0^2 a}{E}\ [0.71] \tag{G.11}$$

$$= 81\ \text{kJ/m}^2 \qquad \text{when } \sigma_0 = 500\ \text{MPa}\ , \tag{G.12a}$$

$$= 69\ \text{kJ/m}^3 \qquad \text{when } \sigma_0 = 425\ \text{MPa}\ . \tag{G.12b}$$

Plastic collapse

$$P_{(limit)} = 1.04\ \sigma_0\ \frac{(t/a - 1)}{\left(t/a - \frac{1}{m}\right)}\ \ln\left(\frac{r_1}{r_0}\right)\ , \qquad (G.13)$$

where

$$r = 1/2\ (r_1 + r_0)\ , \qquad (G.14)$$

$$m = \left(1 + 0.263\ \frac{\ell^2}{rt}\right)^{1/2} \qquad (G.15)$$

$$= 1.14954\ ,$$

$$P_{(limit)} = 160.2\ \text{MPa} \quad \text{when } \sigma_0 = 500\ \text{MPa (Case I)}\ , \qquad (G.16a)$$

$$= 136.2\ \text{MPa} \quad \text{when } \sigma_0 = 425\ \text{MPa (Case II)}\ . \qquad (G.16b)$$

G.2 Comparison of J-T Plots for Different Geometries*

G.2.1 Introduction

There are three possible ways of performing a structural integrity analysis using a J-T diagram. The first, labeled type A, was proposed in Appendix B of NUREG-0744.[1] This is the simplest J-T form of analysis and is intended to provide a lower-bound solution to the specific problem of tearing from semielliptical flaws in the beltline of PWR vessels in their end-of-life degraded condition. There is, however, a clear intent to apply this type of solution to a wide class of problems.

This "lower bound" solution used the concept of the J(50) line, where the applied J-T curve is taken to have the form

$$J = 8.76\ T\ \text{kJ/m}^2\ \text{(or 50 T lb/in.)}\ . \qquad (G.17)$$

The "instability" condition is defined by the intersection of the J(50) line with the J-T material curve, the latter obtained from the J-resistance curve at the point $J_{app} = J_{50}$. This provides a level of J-applied, notionally at instability, that is meant to be consistent with J-controlled crack growth criteria applied to the J-resistance curve and, by

*I. Milne, CERL.

implication, the crack extension at that point. The corresponding pressure can be obtained by performing an independent calculation using a simplified expression for J.

The second, labeled type B, is more complicated but, nevertheless, more accurate and is applicable to all categories of problems. In this instance, an explicit evaluation of J-applied is obtained as a function of load at the initial crack length of interest. T_{app} is then obtained from

$$T_{app} = \left[\frac{dJ}{da}\right]_{app} \frac{E'}{\sigma_0^2} , \qquad (G.18)$$

and the definitive J-T applied curve is plotted out. The instability condition is defined by the intersection of this curve with the J-T material curve, from which the instability load and instability crack extension can be determined.

In general, this definitive version of the J-T plot is a curve rather than a straight line, and being explicitly related to J-applied, it takes appropriate account of variations as a result of geometry, crack size and shape, and material flow properties. The analysis, however, is still approximate because there is no allowance for crack extension in the applied value of J. To make the analysis exactly equivalent to a rigorous J-applied/J-resistance analysis, the applied J-T curve has to be updated to allow for crack extension when J-applied exceeds J_{Ic} resistance. This third method, labeled type C, is considered unnecessary for small amounts of crack extension and is more easily achieved by performing a conventional J analysis using a J-a plot. Nevertheless, it is the only way that a J-T diagram can be used to produce an exact solution, so it is included in this discussion as the third form of J-T analysis, labeled type C.

Of these three forms of analysis, types B and C are complicated by the need to calculate J and dJ/da as a function of load to define the load sensitivity of the structure. Because of these complications, these two types of solution do not lend themselves readily to codified procedures, and the simplicity of the J-T diagram is lost. It follows that for any problem where either of these two forms of analysis is necessary, there are simpler and more-accurate solutions than the J-T plot. The type A form of J-T diagram is very simple and readily codified. The only complication results from the need to define the load at instability or the load-J relationship. Assuming that this can be done satisfactorily using the relationships in Appendix B of NUREG-0744[1] via the equation

$$J = \frac{\sigma_0^2 a}{E} \{\text{stress}\} [\text{geometry}] , \qquad (G.19)$$

where {stress} refers to a simple function of the ratio of applied stress to the yield or flow stress and [geometry] refers to a geometric correction factor, then the applicability of this form of J-T diagram depends

only upon the J(50) curve actually representing the true applied J-T curve pessimistically. The analyses discussed below investigate this aspect of J-T diagrams.

G.2.2 Geometries and loading

To obtain an indication of how widely applicable the J-T methodology is, four geometries were chosen for investigation:

1. a 25-mm compact tension specimen with crack depth a = 0.6 W, where W is the specimen width;
2. a pressurized cylinder containing an internal axial extended crack of depth a equal to one-half of the wall thickness t;
3. the Heavy-Section Steel Technology (HSST) test vessel geometry V8A;
4. two semielliptical flaws in the beltline of a PWR vessel, 30 and 90 mm deep, respectively, subject to pressure loading. This geometry was taken from Chap. 6.7 of the second Marshall Report,[2] using Fig. 6.7.13 as the basis for the analysis. Consequently, in addition to the pressure loading, a small residual stress of 50 MPa was also considered to be acting on the vessel.

Explicit solutions for J are available in the literature for the first two geometries, and this allowed a comparison to be made between J-T plots generated from the explicit solutions and J-T plots implied from the R6 equation and J(50). For the second two geometries, explicit J solutions are not available, so only J-T plots implied from the R6 formula were used for comparisons here. It is contended that plots obtained by using the J-design curve[6] would give similar comparisons up to loads that produce a level of stress in the uncracked ligament equal to the flow stress.

Note that for the first three cases the structures are subjected to mechanical loading only. For case 4 there is a small, constant residual stress of 50 MPa applied, but the J-T curve is still plotted as a function of applied mechanical load (pressure). Extension to the problems of an increasing thermal stress, or a thermal stress variable with time, has not been made because the J(50) philosophy has yet to be applied to this form of loading.

G.2.3 Calculations of J and T from definitive estimates of J and from R6 procedures

The GE estimation scheme for J was used for this calculation.[5] J was calculated as a function of applied load for three different crack sizes, a, a + a′, and a − a′, where a is the crack size of interest and a′ is a small fraction of this. The slope was then determined graphically and T obtained by using Eq. (G.18).

In the next case, J was inferred from the R6 diagram,[4] using the equation

$$J = \frac{K_I^2}{E' S_r^2} \left[\frac{8}{\pi^2} \ln \sec \frac{\pi}{2} S_r \right] , \qquad (G.20)$$

where $E' = E/(1 - \nu^2)$, E being Young's modulus and ν, Poisson's ratio. J was calculated for three different crack lengths as a function of applied load, as described above, and from this, T was determined.

One similarity between the GE estimation scheme[5] and R6[4] is that in both cases, the plasticity effects are obtained by using an equation for J in which the load is normalized to a crack-size dependent reference load. For R6 this is required to be the plastic limit load of the remaining uncracked ligament, and work hardening is taken into account by using the flow stress of the material. For the GE scheme the reference load is defined as the yield limit of the remaining uncracked ligament, and work-hardening effects are incorporated by using the parameters of a power law stress-strain curve. In most, but not all, cases the GE reference load is of an identical form to the R6 limit load, with the flow stress replaced by the yield stress. Hence, for consistency in the comparisons, the GE form of reference load was adopted in the calculation of S_r, although in practice a different form of plastic limit load may be preferred in some cases.

Results for the compact specimen are shown in Fig. G.4 and for a long internal axial crack in a pressurized cylinder, in Fig. G.5. Note that the J-T curves for these two explicit solutions undergo a decrease in slope with increasing J, rather than remain straight. (This phenomenon is discussed in detail in Appendix H.) Approximate results are shown in Fig. G.6 for vessel V-8A and in Fig. G.7 for two part-through cracks in a PWR vessel, both based on the R6 method. As shown in Fig. G.6, the predicted tearing-instability pressure for vessel V-8A is between 130 and 136 MPa, with an amount of stable crack extension (estimated from Fig. G.2) to be slightly over 5 mm.

G.3 Sample Calculations for PWR Beltline*

G.3.1 Introduction

Results of sample calculations applying the NUREG-0744[1] proposals to calculate limiting pressures for a range of defects in the PWR beltline region are given below. First, J-T (material) diagrams are produced and limits to J (applied) obtained. Second, J vs pressure is calculated and limiting pressures were estimated. Finally, results are compared with those obtained by using the Central Electricity Generating Board (CEGB) R6 procedure,[4] assuming the same material properties.

G.3.2 J-T (material) curves

Power law R-curve data obtained from characterization welds for the HSST V-8A test (see Table 2.13 and Fig. 2.16) have been used to obtain

---

*C. J. Gardner, AERE.

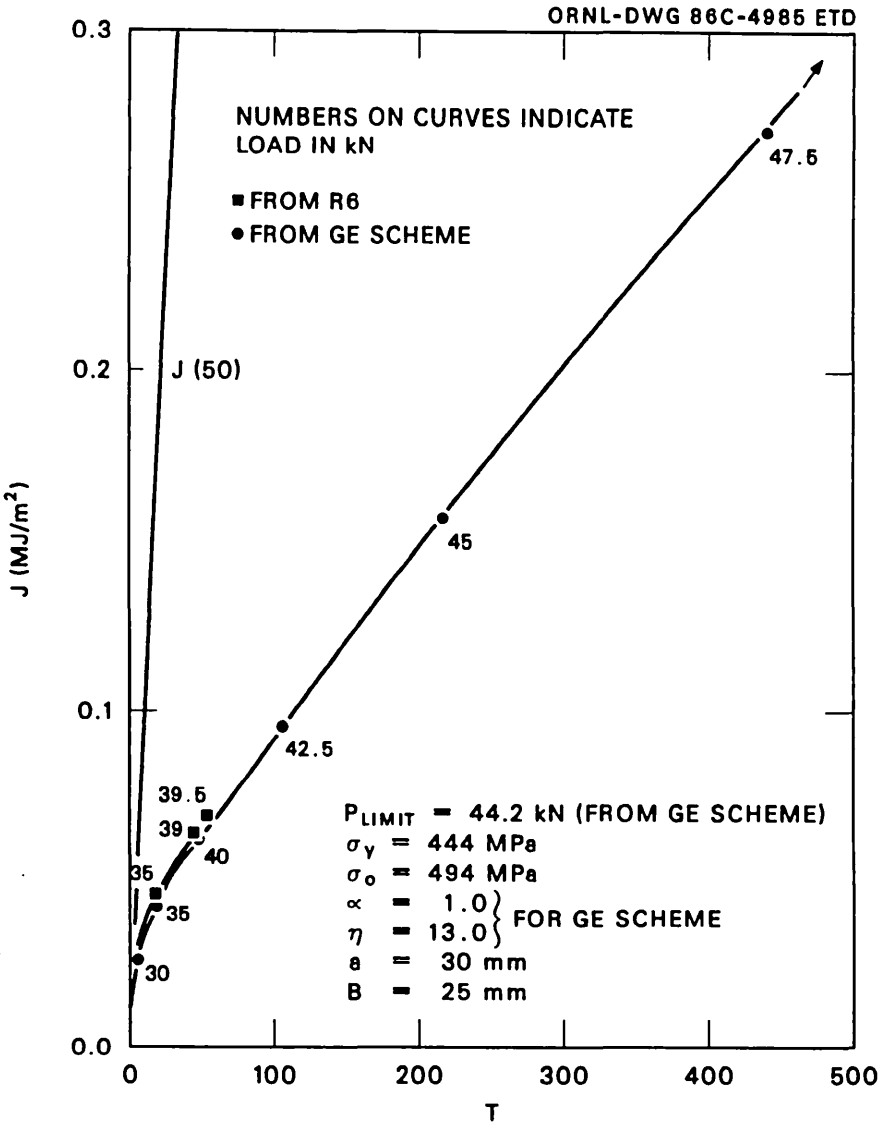

Fig. G.4. J-T applied curves for 25-mm CT specimen.

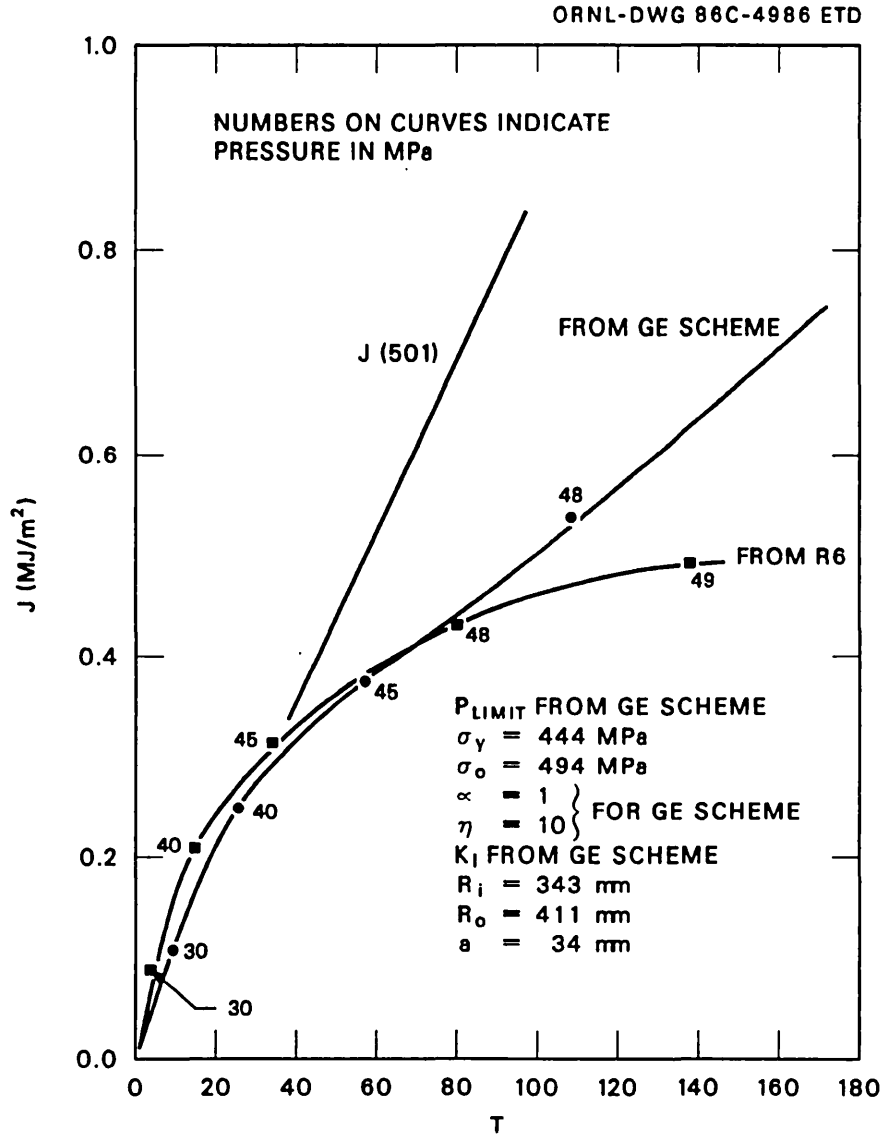

Fig. G.5. J-T applied curves for extended axial internal crack in a pressurized cylinder.

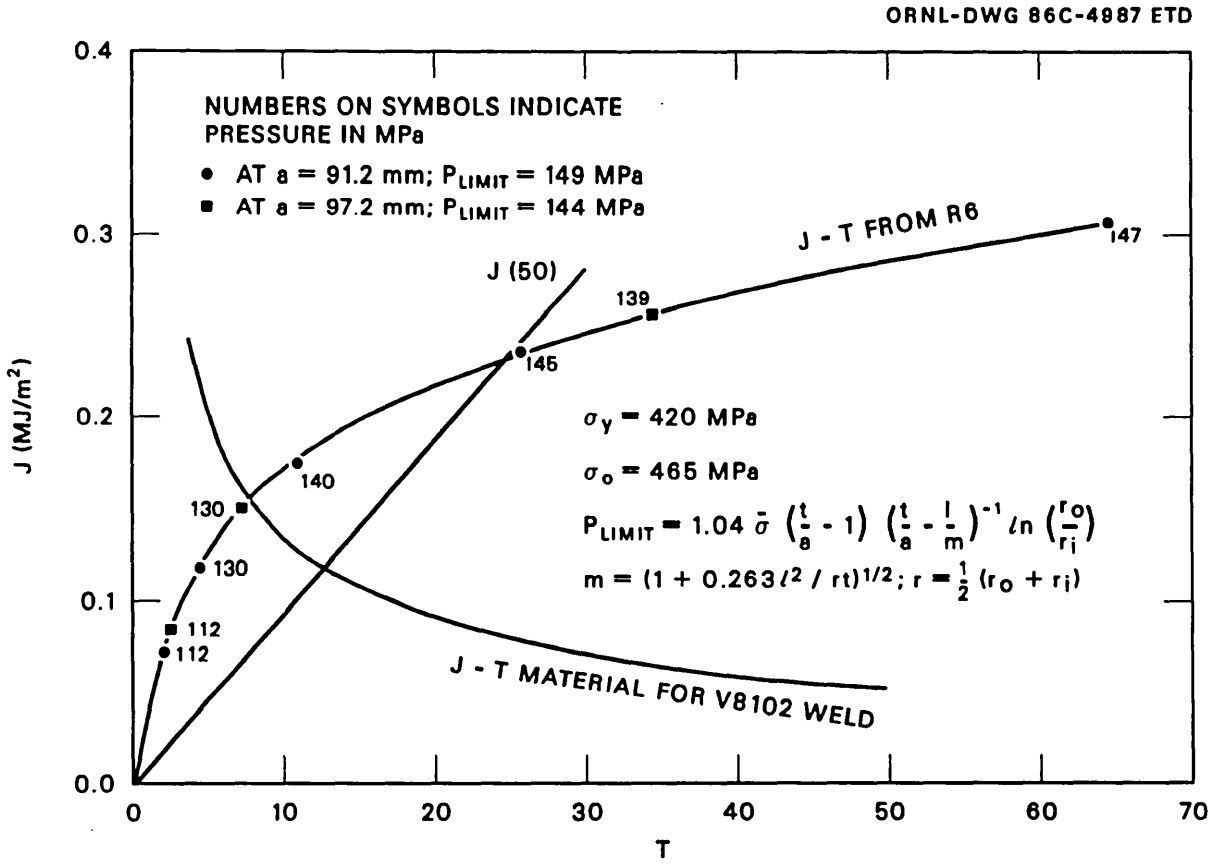

Fig. G.6. J-T analysis diagram for intermediate test vessel V-8A, showing linear J(50) J-T applied line and nonlinear R-6 J-T applied curve that decreases in slope with increasing J due to effect of crack size on plastic limit load.

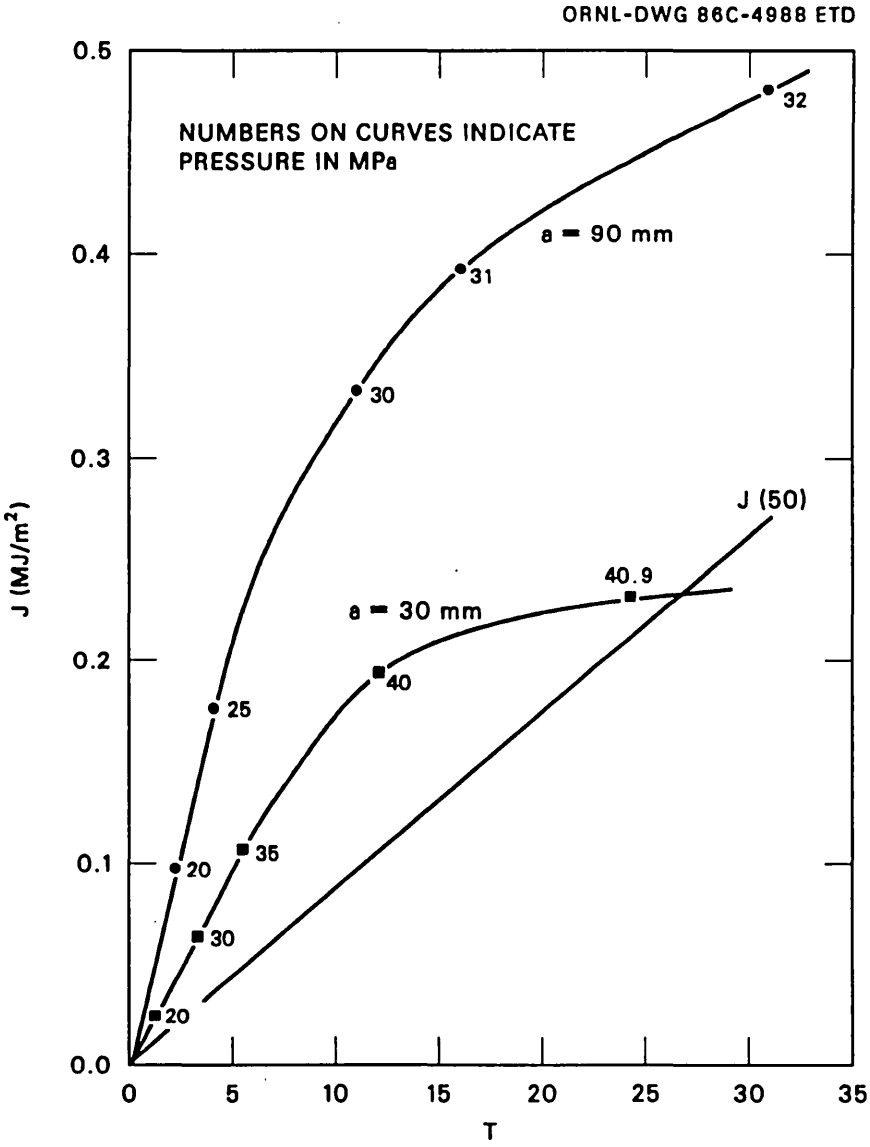

Fig. G.7. J-T applied curves for two beltline flaws with $a/\ell = 1/6$ in a PWR vessel subject to pressure only.

J-T (material) curves. Two cases have been considered:

1. Upper bound (based on weld V862)

$$J = 134\ (\Delta a)^{0.4509} \quad (kJ/m^2)$$

$$\sigma_0 = 425\ MPa \qquad (G.21)$$

Mean upper-shelf energy = 61.8 J

2. Lower bound (based on weld V8102)

$$J = 89\ (\Delta a)^{0.308} \quad (kJ/m^2)$$

$$\sigma_0 = 500\ MPa \qquad (G.22)$$

Mean upper-shelf energy = 50.7 J

In both cases, the upper-shelf energy is below 68 J, so these data should be representative of low USE material. The resulting J-T curves are shown in Fig. G.8. By reference to these curves, the various limitations on J (applied) may be determined. The following limitations on J (applied) are considered for calculations of limiting pressures.

1. "$\omega = 5$" limit suggested in NUREG-0744[1];

   (b = 32 mm has been assumed).

2. "$J_{app} = 1/2J_{50}$" limit. This limitation is assumed to be the intent of the requirement in NUREG-0744 that T_{app} be no greater than one-half the value of T at the intersection of the material J/T curve with the J/T = 8.76 kJ/m^2 (50 lb/in.) for levels C and D transients.

G.3.3 Calculation of J_{app}

J_{app} has been calculated by the method suggested in NUREG-0744 for the surface flaw, using Eq. (G.2), but in which the "geometry bracket" [ ] is given by M_m^2/Q from ASME Sect. XI, Appendix A.[7] The "stress bracket { } depends on the strain-hardening law for the material and the stress level in the remaining ligament. Only one set of power-law strain-hardening data has been given in NUREG-0744, and this has been assumed to be typical and is, therefore, used in these calculations for determining { } from Eqs. (G.3) and (G.4).

The stress level σ is assumed to be $10 \cdot P$, where P is the vessel internal pressure. This method is, therefore, restricted to pressure loading only.

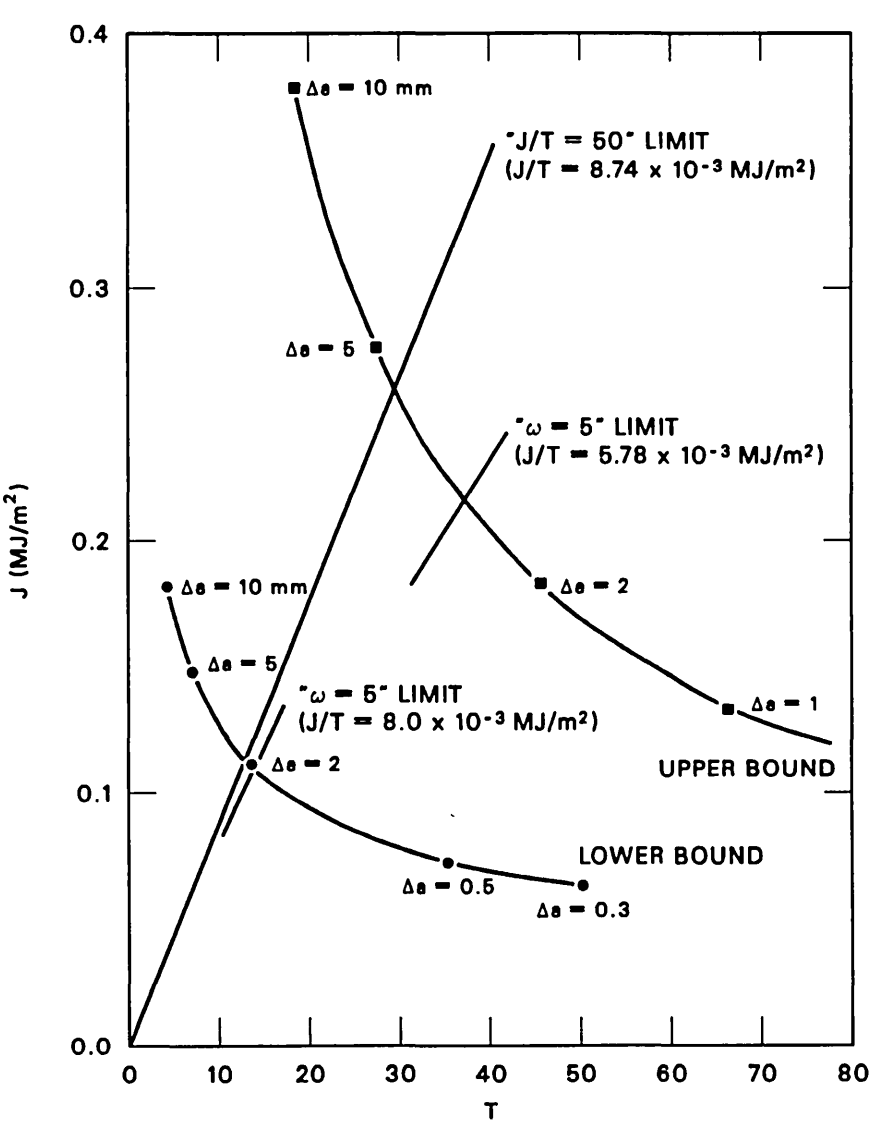

Fig. G.8. Upper and lower bound J-T material curves and limiting lines for J/T = 8.74 kJ/m^2 and ω = 5, for intermediate vessel V-8A.

If required, T_{app} may be estimated from the equation

$$T_{app} = \left(\frac{dJ}{da}\right)_{app} \frac{E}{\sigma_0^2} , \qquad \text{(G.23)}$$

where dJ/da is determined by evaluating J at a small distance on either side of the crack size of interest.

G.3.4 Calculation of limiting pressures

Because J_{app} is known, the pressures corresponding to the above two limitations on J_{app} may be determined. In addition, a check on plastic collapse of the ligament is considered desirable. Although this is recognized in Appendix C of NUREG-0744 (p. C-18), it is not stated in the main body of the report. In these calculations, the following expression for limit load, applicable to an internal flaw, has been used:

$$P_{limit} = \frac{\sigma_0 \, [R_o/R_i - 1] \, [1 - A_c/A]}{1 + [R_o/R_i - 1] \, A_c/A} , \qquad (G.24)$$

where A_c is the area of the flaw and A is the trapezoidal effective load-bearing area of the region containing the flaw.

G.3.5 Results

Limiting pressures for the upper- and lower-bound R-curves considered are given in Tables G.3 and G.4, respectively, for a range of defect sizes. In addition to the NUREG-0744 calculations,[1] the CEGB R6 procedure[4] has been used to obtain limiting pressures corresponding to 2-mm crack growth (the limit used in the second Marshall report[2]) at ultimate instability. (Note that the limit corresponding to ultimate instability requires extrapolation of the method beyond the limits on crack growth recommended in R6.)

In Fig. G.9 the lower-bound J-T curve from Fig. G.8 is shown enlarged. The J-T (applied) curve for a 1/4-thickness (54-mm) defect* is shown based on a flow stress of 500 MPa. This is one of the solutions listed in Table G.4. The J-T (material) curve has been extended up to a point corresponding to 15-mm ductile crack extension (significantly beyond the limits of J-controlled crack growth). Thus, neglecting such limitations, the onset of instability for this case (defined as the intersection of the two curves) is predicted to occur just below the plastic collapse pressure of 42.8 MPa after almost 15 mm of ductile crack growth.

In Fig. G.10 the R6 ductile crack-growth analysis[4] is illustrated, again for the same 1/4-thickness defect. The procedure followed, given in Appendix 5 of R6, requires evaluation of K_r and S_r as a function of crack growth Δa for an arbitrary constant applied load. From this, the load factor F is evaluated as a function of Δa. The maximum tolerable load (called the instability load in Tables G.3 and G.4) is the product of the applied load and the maximum value of F, subject to the usual restrictions on Δa. In general for the cases considered here, the maximum value of F has been found to lie outside the J-controlled crack-growth regime, as indicated by the values of Δa at instability in Tables G.3 and G.4. [Note that the instability pressure estimated by the R6

*Although not stated, it is apparently assumed that $a/\ell = 1/6$.

Table G.3. Comparison of R6 and NUREG-0744 limiting pressures, PWR beltline region upper-bound R curve

(Flow stress = 425 MPa)

Defect size (mm)	R6 predictions				NUREG-0744 predictions		
	Initiation (MPa)	Δa = 2 mm (MPa)	Instability (MPa)	Δa at instability (mm)	ω = 5 limit (MPa)	J_{app} = 1/2 J_{50} limit (MPa)	Limit load (MPa)
25	33.8	39.2	39.4	4	> Limit load	> Limit load	40.0
54 (t/4)	24.9	33.1	34.6	7	> Limit load	34.6	36.4
100	17.2	24.7	27.2	10	29.6	23.6	29.8
150[a]	12.9	18.5	20.9	9	18.0	13.5	22.5
	Pressures relative to J_{app} = 1/2 J_{50} value						
25							
54 (t/4)	0.72	0.96	1.0			1.0	1.05
100	0.73	1.05	1.15		1.25	1.0	1.26
150[a]	0.96	1.37	1.50		1.33	1.0	1.67

[a]This defect size is beyond the current recommended limit of the analysis procedure.

Table G.4. Comparison of R6 and NUREG-0744 limiting pressures, PWR beltline region lower-bound R curve

(Flow stress = 500 MPa)

Defect size (mm)	R6 predictions				NUREG-0744 predictions		
	Initiation (MPa)	Δa = 2 mm (MPa)	Instability (MPa)	Δa at instability (mm)	ω = 5 limit (MPa)	J_{app} = 1/2 J_{50} limit (MPa)	Limit load (MPa)
25	31.3	41.0	42.5	7	45.1	37.4	47.1
54 (t/4)	21.8	31.1	34.2	12	34.2	25.4	42.8
100	14.7	21.8	25.2	>15	21.8	15.6	35.0
150[a]	11.0	16.3	16.8	>15	13.8	9.0	26.4
Pressures relative to J_{app} = 1/2 J_{50} value							
25	0.84	1.10	1.14		1.21	1.0	1.26
54 (t/4)	0.86	1.22	1.35		1.35	1.0	1.69
100	0.94	1.40	1.62		1.4	1.0	2.24
150[a]	1.22	1.81	2.09		1.533	1.0	2.93

[a]This defect size is beyond the current recommended limit of the analysis procedure.

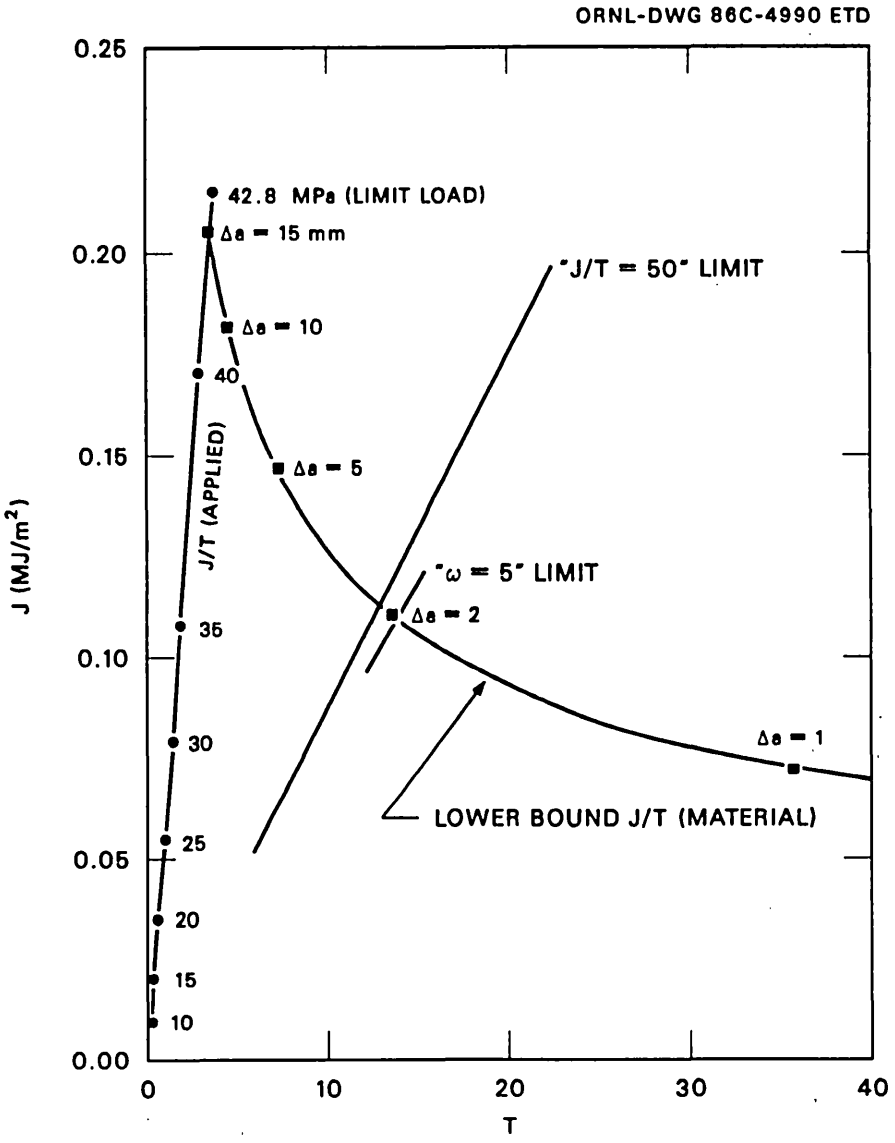

Fig. G.9. J-T analysis diagram for a quarter thickness defect (a = 54 mm, a/ℓ = 1/6) in a PWR vessel.

method, which updates the crack size and its effect on limit load, is 34.2 MPa (see Fig. G.10 and Table G.4); however, the instability pressure estimated by the straight line J-T applied curve, which neither updates the crack size nor considers limit load, is ~41.5 MPa. This illustrates the potential unconservation brought about by not updating the crack size and its effect on limit load. Note also that the J_{50}, $\omega = 5$, and lower-bound J-T material curve portions of Figs. G.2, G.6, G.8, and G.9 are in agreement, as they should be.]*

*Comments in brackets added by ORNL.

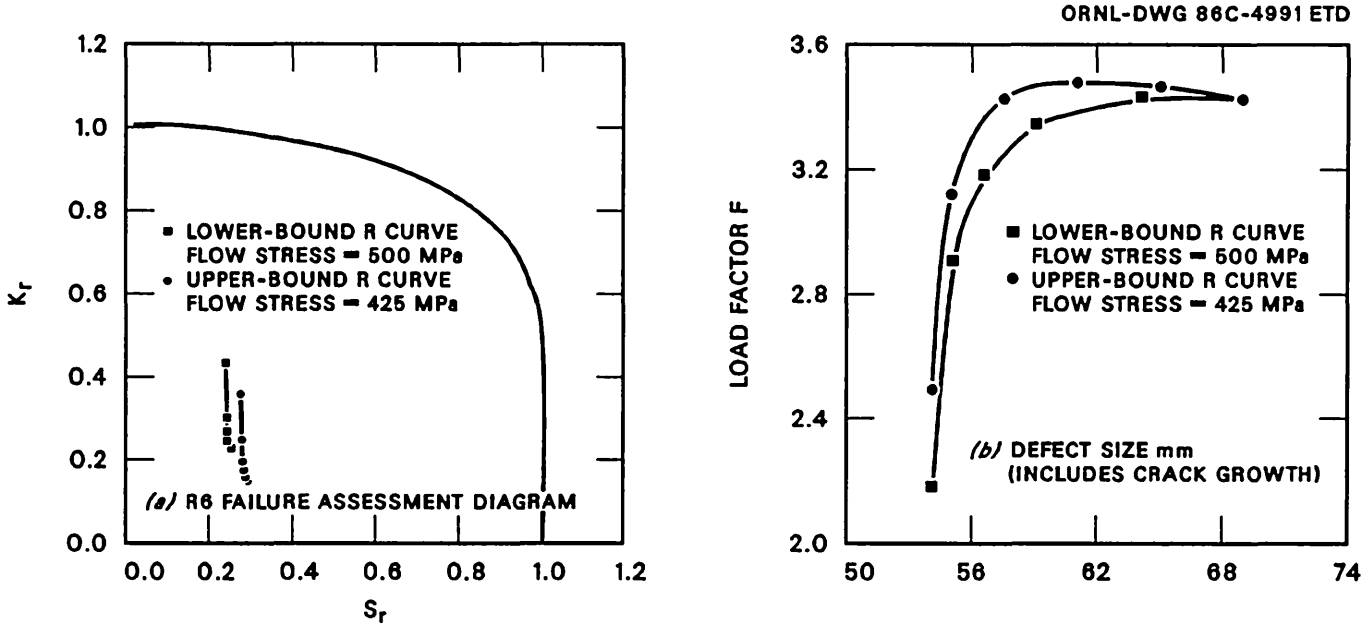

Fig. G.10. Results of R-6 ductile crack growth tearing instability analysis for quarter thickness defect (a = 54 mm, a/ℓ = 1/6) in a PWR vessel; nominal applied load is 10 MPa.

References

1. R. Johnson, ed., *Resolution of the Reactor Vessel Materials Toughness Safety Issue*, NUREG-0744, for comment, two volumes, U.S. Nuclear Regulatory Commission, September 1981.

2. W. Marshall, ed., *An Assessment of the Integrity of PWR Pressure Vessels, Second Report of the Study Group*, two volumes, United Kingdom Atomic Energy Authority, March 1982.

3. *Code of Federal Regulations*, Title 10 (Energy), Chapter I (Nuclear Regulatory Commission), Part 50 (Domestic Licensing of Production and Utilization Facilities), published separately for the Office of the Federal Register, National Archives and Records Service, General Services Administration, by the U.S. Government Printing Office, 1979.

4. R. P. Harrison et al., *Assessment of the Integrity of Structures Containing Defects*, R/H/R6-Rev. 2, Central Electricity Generating Board, Research Division, London, April 1980.

5. V. Kumar, M. D. German, and C. G. Shih, *An Engineering Approach for Elastic-Plastic Fracture Analysis*, EPRI NP-1931, Electric Power Research Institute, Palo Alto, Calif., July 1981.

6. F. M. Burdekin and M. G. Dawes, "Practical Use of Linear Elastic and Yielding Fracture Mechanics with Particular Reference to Pressure Vessels," pp. 28–37 in *Practical Application of Fracture Mechanics to Pressure-Vessel Technology*, The Institution of Mechanical Engineers, London, 1971.

7. Appendix A, "Analysis of Flaw Indications," in Section XI, Division 1, "Rules for Inservice Inspection of Nuclear Power Plant Components," *ASME Boiler and Pressure Vessel Code*, American Society Mechanical Engineers, New York, 1980.

Appendix H

CAUSES OF NONLINEAR J-T APPLIED CURVES AND EQUATIONS FOR THE R6 METHOD

As observed in Appendix G, in the J-T-diagram approach to tearing-instability analysis,[1,2] the J-T applied curve will be a straight line only if the crack length is not updated and the variables of load and crack size in the expression for J are separable. The latter influence is the strongest, especially under force-controlled loading as the load approaches a crack-size-dependent, fully plastic load, near which the slope of the J-T applied curve can decrease substantially (e.g., Figs. G.4–G.7). Two common methods of estimating J, for which the variables of crack size and load are not separable because of a crack-size-dependent, fully plastic load, are the R6 method,[3] for which

$$J = J_e \left[\frac{2 \ln \sec \left(\frac{\pi}{2} S_r \right)}{\left(\frac{\pi}{2} S_r \right)^2} \right] , \tag{H.1}$$

and the GE-EPRI method,[4] which for a flawed cylinder as an example, estimates J from

$$J = \frac{C^2(a_e)\ P^2 \left(\frac{\sigma}{P} \right)^2 \pi a \left(\frac{a_e}{a} \right)}{E'} + \alpha\ \sigma_0\ \varepsilon_0 a \left(1 - \frac{a}{t} \right) h_1\ S_r^{n+1} . \tag{H.2}$$

In both cases,

$$S_r = \frac{P}{P_0} , \tag{H.3}$$

where P_0 is a crack-size-dependent, fully plastic load. Paris[1,2] simplified Eq. (H.2) by replacing S_r with (σ/σ_0), where σ_0 is the flow stress, which is a material property not dependent on crack size; by neglecting the plastic zone size correction to J_e; and by assuming that C^2 can be factored from the product $h_1 (1 - a/t)$, leaving the remaining ratio independent of a/t. The result, after some elementary substitutions, was

$$J = \sigma_0\ \varepsilon_0\ a \left\{ F \left(\frac{\sigma}{\sigma_0} \right) \right\} G , \tag{H.4}$$

where

$$F\left(\frac{\sigma}{\sigma_0}\right) = \left\{\psi^* \left(\frac{\sigma}{\sigma_0}\right)^2 + \alpha\, G^* \left(\frac{\sigma}{\sigma_0}\right)^{n+1}\right\} \neq f\left(\frac{a}{t}\right), \tag{H.5}$$

$$G = C^2 \quad . \tag{H.6}$$

For Eq. (H.4), if the crack size is not updated, J-T is constant independent of load level, but for Eqs. (H.1) and (H.2) it is not. The causes are the crack-size dependence of the denominator P_0 in the term S_r and in the case of Eq. (H.2), the probably lesser effect of the plastic zone correction in J_e.

While nonlinear J-T applied curves were shown in Appendix G, the coordinates of these curves were determined numerically. However, in the case of the R6 method, an analytical approach to plotting the J-T applied curve can also be developed. In the case of the R6 method, it is convenient to rewrite Eq. (H.1) in the form

$$J = \frac{8G\left(\frac{\sigma}{P}\right)^2 P_0^2\, a}{\pi E'} f\left(\frac{P}{P_0}\right), \tag{H.7}$$

where

$$f\left(\frac{P}{P_0}\right) = \ln \sec\left(\frac{\pi}{2}\frac{P}{P_0}\right) . \tag{H.8}$$

The applied tearing modulus T, at constant load, is defined by[1,2]

$$T = \frac{\left(\frac{\partial J}{\partial a}\right)_P}{\left(\frac{\sigma_0^2}{E}\right)}, \tag{H.9}$$

so that

$$\frac{T}{J} = \frac{\left(\frac{\partial\, \ln J}{\partial a}\right)_P}{\left(\frac{\sigma_0^2}{E}\right)} . \tag{H.10}$$

From Eq. (H.7),

$$\ln J = \ln \left[\frac{8\left(\frac{\sigma}{P}\right)^2}{\pi E'} \right] + \ln a + \ln G + 2 \ln P_0 + \ln f\left(\frac{P}{P_0}\right), \qquad \text{(H.11)}$$

so that

$$\left(\frac{\partial \ln J}{\partial a}\right)_P = \frac{1}{a} + \frac{\partial \ln G}{\partial a} + 2\,\frac{\partial \ln P_0}{\partial a} - \frac{\partial \ln f\left(\frac{P}{P_0}\right)}{\partial \ln\left(\frac{P}{P_0}\right)} \cdot \frac{\partial \ln P_0}{\partial a}. \qquad \text{(H.12)}$$

Modifying Eq. (H.12) slightly,

$$\left(\frac{\partial \ln J}{\partial a}\right)_P = \frac{1}{a}\left\{1 + \left(\frac{a}{t}\right)\frac{G'}{G} + \left(\frac{a}{t}\right)\left[2 - \frac{\left(\frac{P}{P_0}\right)\partial f\left(\frac{P}{P_0}\right)}{f\left(\frac{P}{P_0}\right)\partial\left(\frac{P}{P_0}\right)}\right]\frac{\partial \ln P_0}{\partial\left(\frac{a}{t}\right)}\right\}. \qquad \text{(H.13)}$$

Notice that when the fully plastic load P_0 is independent of crack size, T/J becomes

$$\frac{T}{J} = \frac{1 + \left(\frac{a}{t}\right)\frac{G'}{G}}{\left(\frac{\sigma_0^2}{E}\right) a}. \qquad \text{(H.14)}$$

It is convenient to define

$$\psi\left(\frac{P}{P_0}\right) = \left[2 - \frac{\left(\frac{P}{P_0}\right)}{f\left(\frac{P}{P_0}\right)} \frac{\partial f\left(\frac{P}{P_0}\right)}{\partial\left(\frac{P}{P_0}\right)}\right], \qquad \text{(H.15)}$$

and

$$\lambda\left(\frac{a}{t}\right) = \left(\frac{a}{t}\right)\frac{\partial \ln P_0}{\partial\left(\frac{a}{t}\right)}, \qquad \text{(H.16)}$$

so that Eq. (H.13) becomes

$$\left(\frac{\partial \ln J}{\partial a}\right)_P = \frac{1}{a}\left\{1 + \left(\frac{a}{t}\right)\frac{G'}{G} + \psi\left(\frac{P}{P_0}\right) \cdot \lambda\left(\frac{a}{t}\right)\right\} \tag{H.17}$$

and

$$\frac{T}{J} = \frac{1 + \left(\frac{a}{t}\right)\frac{G'}{G} + \psi\left(\frac{P}{P_0}\right) \cdot \lambda\left(\frac{a}{t}\right)}{\left(\frac{\sigma_0^2}{E}\right)^a} \cdot \tag{H.18}$$

Note that both ψ and λ will be negative, so their product is positive. Using Eq. (H.8),

$$f\left(\frac{P}{P_0}\right) = -\ln \cos\left(\frac{\pi}{2}\,\frac{P}{P_0}\right) , \tag{H.19}$$

so that

$$\psi\left(\frac{P}{P_0}\right) = 2 - \frac{\left(\frac{\pi}{2}\,\frac{P}{P_0}\right)\tan\left(\frac{\pi}{2}\,\frac{P}{P_0}\right)}{\ln \sec\left(\frac{\pi}{2}\,\frac{P}{P_0}\right)} \cdot \tag{H.20}$$

For a part-through crack in a pressurized cylinder, the value of P_0 is estimated by the R6 method[3,5] with the equation (modified for a thick-walled cylinder)

$$P_0 = 1.04\,\sigma_0\,\frac{\left(\frac{t}{a} - 1\right)}{\left(\frac{t}{a} - \frac{1}{m}\right)}\ln\left(\frac{R_0}{R_i}\right) , \tag{H.21}$$

where m is the elastic bulging factor for a through crack of length ℓ, given by

$$m = \sqrt{1 + 0.263\,\frac{\ell^2}{Rt}} , \tag{H.22}$$

and R is the mean radius of the cylinder. In the case of Eqs. (H.21) and (H.22), the value of λ is given by

$$\lambda\left(\frac{a}{t}\right) = -\left(\frac{a}{t}\right)\left\{\frac{1}{\left(1-\frac{a}{t}\right)} - \frac{\frac{1}{m^s}}{\left[1-\left(\frac{a}{t}\right)\left(\frac{1}{m}\right)\right]}\right\} , \tag{H.23}$$

where

$$s = \begin{cases} 1 \text{ for constant crack length} \\ \\ 3 \text{ for constant crack shape .} \end{cases} \tag{H.24}$$

In the United Kingdom, comments on NUREG-0744 (see Appendix G), an expression used for G was

$$G = \frac{M_m^2}{Q} , \tag{H.25}$$

where[6,7]

$$M_m = M_1 + \left(\sqrt{\frac{Q}{\frac{a}{b}}} - M_1\right)\left(\frac{a}{t}\right)^P \quad \text{(Ref. 6)} , \tag{H.26}$$

$$M_1 = 1 + 0.12\left(1-\frac{a}{2b}\right)^2 \quad \text{(Ref. 7)} , \tag{H.27}$$

$$Q = 1 + 1.464\left(\frac{a}{b}\right)^{1.65} \quad \text{(Ref. 6)} , \tag{H.28}$$

$$p = 1.6 + 3\left(\frac{a}{b}\right)^3 + 8\left(\frac{a}{b}\right)\left(\frac{a}{t}\right)^5 + \frac{0.008}{\left(\frac{a}{b}\right)} , \tag{H.29}$$

$$b = \frac{\ell}{2} . \tag{H.30}$$

For this case and the assumption of constant crack shape,

$$\frac{G'}{G} = \frac{2\,\frac{\partial M_m}{\partial\left(\frac{a}{t}\right)}}{M_m} . \tag{H.31}$$

Consequently,

$$\frac{G'}{G} = 2\left(1 - \frac{M_1}{M_m}\right)\left[\frac{p}{\left(\frac{a}{t}\right)} + 40\left(\frac{a}{b}\right)\left(\frac{a}{t}\right)^4 \ln\left(\frac{a}{t}\right)\right] . \qquad \text{(H.32)}$$

Using a value of $(\sigma/P) = 2$ and the above equations produces values of J and T approximating those indicated by the R6 curve for vessel V-8A in Fig. G.6 of Appendix G in this report.

References

1. R. Johnson, *Resolution of the Task A-11 Reactor Vessel Materials Toughness Safety Issue*, NUREG-0744, Rev. 1, U.S. Nuclear Regulatory Commission, October 1982.

2. P. C. Paris and R. E. Johnson, "A Method of Application of Elastic-Plastic Fracture Mechanics to Nuclear Vessel Analysis," pp. 5—40 in *Elastic-Plastic Fracture: Second Symposium*, ASTM STP 803, Vol. II, American Society Testing and Materials, Philadelphia, 1983.

3. R. P. Harrison et al., *Assessment of the Integrity of Structures Containing Defects*, R/H/R-6-Rev. 2, Central Electricity Generating Board, Research Department, London, April 1980.

4. V. Kumar, M. D. German, and C. F. Shih, "Elastic-Plastic and Fully Plastic Analysis of Crack Initiation, Stable Growth and Instability in Flawed Cylinders," pp. 306—53 in *Elastic-Plastic Fracture: Second Symposium*, ASTM STP 803, Vol. I, American Society Testing and Materials, Philadelphia, 1983.

5. J. F. Kiefner et al., "Failure Stress Levels of Flaws in Pressurized Cylinders," pp. 461—81 in *Progress in Flaw Growth and Fracture Toughness Testing*, ASTM STP 536, American Society Testing and Materials, Philadelphia, 1973.

6. J. C. Newman, *A Review and Assessment of the Stress-Intensity Factors for Surface Cracks*, NASA TM 78805, National Aeronautics and Space Administration, Langley Research Center, Hampton, Va., November 1978.

7. A. S. Kobayashi and W. L. Moss, "Stress Intensity Magnification Factors for Surface-Flawed Tension Plate and Notched Round Tension Bar," pp. 31—45 in *Fracture*, Chapman and Hall, 1969.

Appendix I

ANALYSIS OF HSST INTERMEDIATE VESSEL V-8A TEST BY THE DEFORMATION PLASTICITY FAILURE ASSESSMENT METHOD*†

I.1 Introduction

Oak Ridge National Laboratory (ORNL) conducted the intermediate vessel V-8A test in August 1982; the results are reported in Refs. 1 and 2. Before and after the test, flaw-sizing measurements were made and reported. The weldment for this test vessel simulated a low-upper-shelf energy weld and was made by Babcock & Wilcox (B&W) Nuclear Equipment Division under contract from ORNL.

Even though the test conditions and the geometric parameters — namely, thickness-to-radius ratio, flaw shape, location, and flaw depth — are different from the typical pressurized-water reactor (PWR) vessel configuration, it was suggested by the Nuclear Regulatory Commission (NRC) staff that B&W analyze this test by using the deformation plasticity failure assessment diagram approach (DPFAD)[3] to benchmark this approach. Based on available material information from ORNL and Ref. 4, it is demonstrated here that the DPFAD approach predicts the instability pressure of the V-8A test vessel quite well, given the material toughness properties of the crack-tip location of the actual vessel.

I.2 Upper-Shelf Fracture Analysis

I.2.1 Problem definition

The configuration of the intermediate test vessel V-8A is shown in Fig. I.1. This is a thick (152.40-mm), cylindrical vessel with a thickness-to-inside radius ratio t/R_i of 0.444. A schematic view of the vessel V-8A and the machined flaw are shown in Fig. I.2. A semielliptical surface flaw was machined from the outside of the vessel with initial dimensions of depth (a_0) of 91.44 mm and a surface length (ℓ) of 279.40 mm. This vessel was internally pressurized to produce ductile tearing to obtain experimental data for the evaluation of elastic-plastic fracture mechanics analysis methods.

---

*B&W document BAW-1814, November 1983.

†J. M. Bloom and K. K. Yoon, Babcock & Wilcox Co., Alliance, Ohio, and Lynchburg, Va.

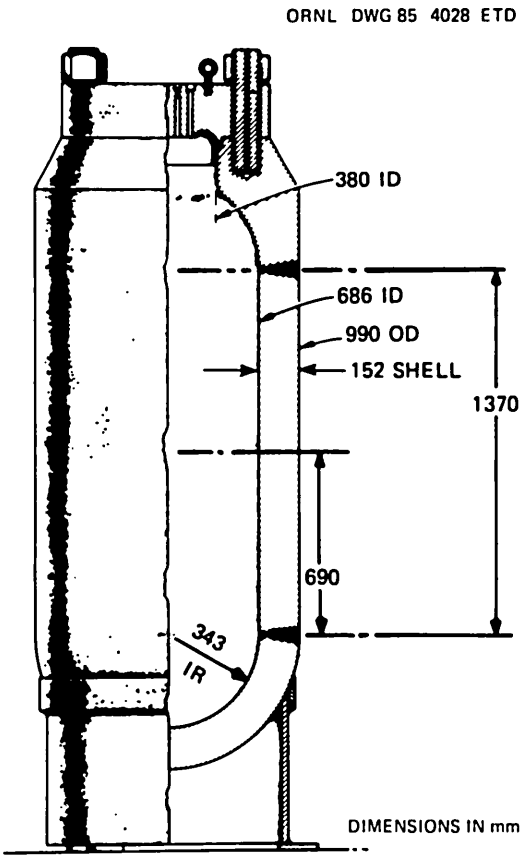

Fig. I.1. Intermediate test vessel V-8A.

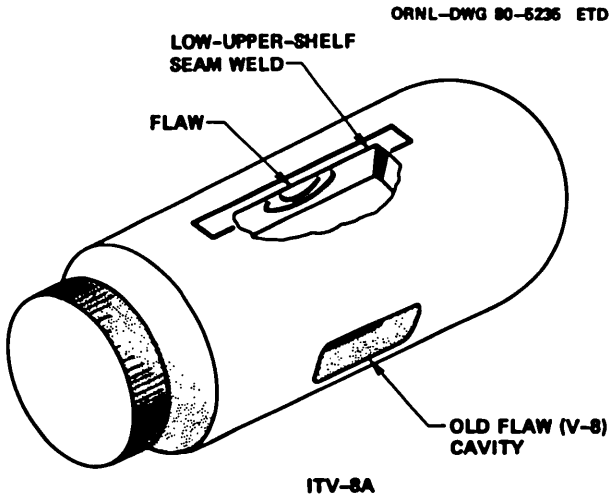

Fig. I.2. Schematic view of vessel V-8A.

I.2.2 Material properties of the weld

The following mechanical properties were obtained from Refs. 4 and 5.

Young's Modulus E	199.26 GPa
Poisson's Ratio ν	0.3
Yield stress σ_0	413.69 MPa
Stress-strain relationship (Ramberg-Osgood)	

$$\frac{\varepsilon}{\varepsilon_0} = \frac{\sigma}{\sigma_0} + \alpha \left(\frac{\sigma}{\sigma_0}\right)^n , \qquad \text{(I.1)}$$

where $\alpha = 1.78$ and $n = 10.225$.

The J_{IR} curve for the experimental weld in vessel V-8A was obtained from posttest compact specimen testing at the B&W Alliance Research Center under contract[4] from ORNL. Based on its orientation and location as shown in Fig. I.3, specimen V8AJ2 was chosen to be representative of the actual material behavior at the crack tip location ($a_0/t = 0.60$) in the V-8A test vessel.

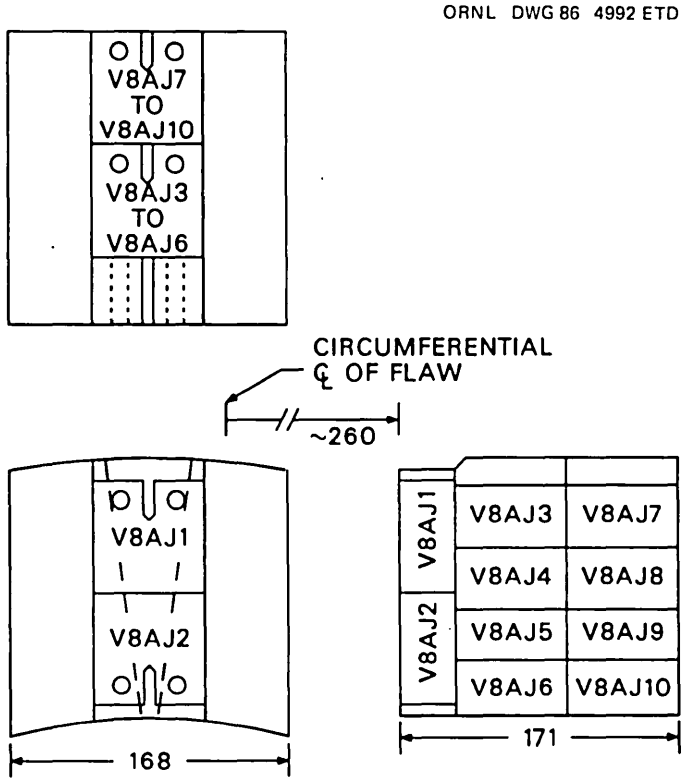

Fig. I.3. Cutting diagram for specimens V8AJ1—V8AJ10 taken from piece V8A-CA; specimen notches are located on centerline of weld.

The J_{IR} curve was derived from test data by using both the deformation (J_D) expression found in ASTM Standard E813-81, as well as the modified (J_M) expression proposed by Ernst.[6] An equation of the following form was used to curve fit both sets of J_{IR} data:

$$J_R\ (\Delta a) = A_1\ (A_2 + \Delta a)^{A3} + A_4 \Delta a + A_5\ , \qquad (I.2)$$

where Δa = crack extension (mm),

$$J_R(\Delta a) = J_{IR}\ (kJ/m^2)\ .$$

The J_{IR} data are listed in Table I.1, and both the data and the fitted

Table I.1. J_{IR} data for specimen V8AJ2

Δa (mm)	E813 J_D (kJ/m^2)	J_M (kJ/m^2)
0.07	2	2
−0.04	5	5
−0.01	11	11
0.04	19	19
0.07	27	27
0.15	37	37
0.25	48	49
0.42	59	61
0.63	70	73
0.94	80	85
1.30	90	99
2.25	95	112
2.64	104	124
3.16	114	140
3.61	123	155
4.14	136	173
4.65	146	191
5.23	155	208
5.80	162	226
6.32	169	242
7.08	177	263
7.99	177	282
8.68	180	299
9.20	186	317
9.56	193	333
9.92	200	349
10.46	203	368
10.95	207	384

curves are presented graphically in Fig. I.4. The fitted curves have the equations

$$J_D = 90.75 + 11.01\ (\Delta a) - \frac{84.85}{(1.062 + \Delta a)^2} \quad (kJ/m^2)\ , \tag{I.3}$$

and

$$J_M = 51.93 + 29.55 - \frac{1.921}{(0.1938 + \Delta a)^2} \quad (kJ/m^2)\ . \tag{I.4}$$

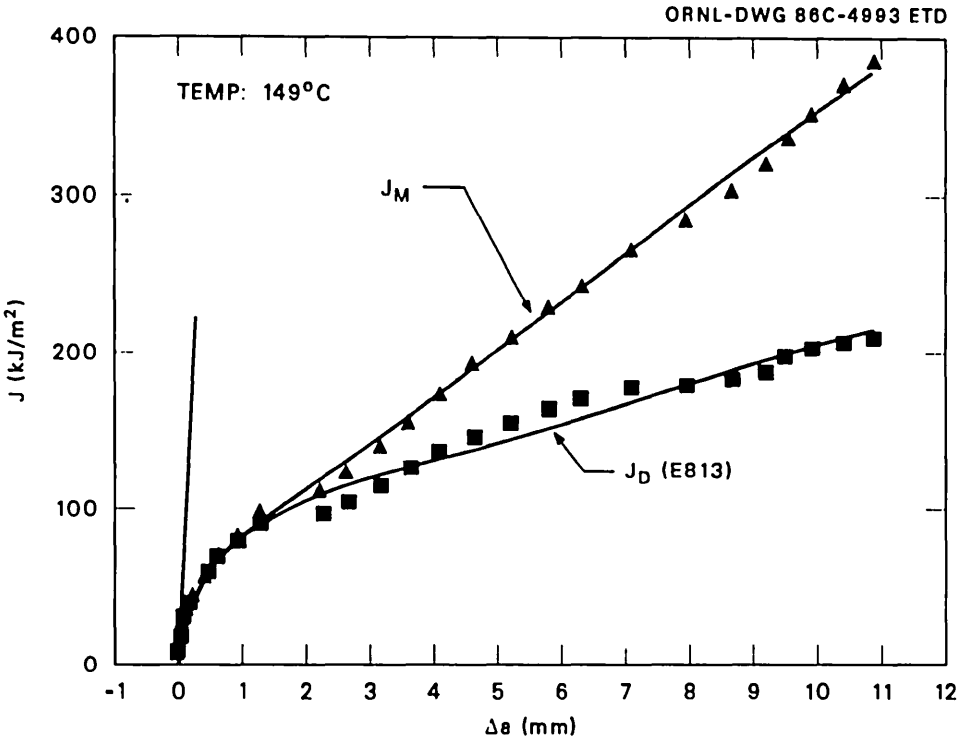

Fig. I.4. J_{IR} curves for specimen V8AJ2.

I.2.3 Deformation plasticity failure assessment diagram (DPFAD) approach

The DPFAD approach for analyzing stable crack growth consists of the following steps.*

*The mathematical basis of the DPFAD approach and its identification as a graphical method for solving the nonlinear equation that determines the load corresponding to a given toughness and crack size are discussed more fully in Appendix J of this report.

Step 1. DPFAD curve generation

The general approach is to obtain the J-integral response for the flawed structure of interest. For a material whose true stress—true strain behavior can be presented by a Ramberg-Osgood power law (Eq. I.1), the J-integral response can be determined from the sum of its elastic response and its fully plastic response. This sum is then normalized with respect to the "elastic" J-integral of the structure defined by

$$J_I^e = K_I^2 \frac{(1 - \nu^2)}{E} , \tag{I.5}$$

where K_I is the linear-elastic fracture mechanics (LEFM) stress-intensity factor. The normalized J-response is then defined by

$$J/J_I^e = 1/K_r^2 = f(S_r) . \tag{I.6}$$

Equation (I.6) defines the boundary between stable and unstable crack growth for a flawed structure in terms of a stress-intensity factor/fracture toughness ratio K_r (the ordinate) and an applied stress/plastic collapse stress ratio $S_r = \sigma/\sigma_l$ (the abscissa). In general, the DPFAD curve is dependent on the material tensile stress-strain properties, structural geometry, and flaw shape and depth. For ferritic nuclear-grade reactor pressure vessels, it was demonstrated that the DPFAD curve could be conservatively represented by a function only of the flaw depth-to-wall thickness ratio, as discussed in Ref. 7 and the next section of this report.

Step 2. Assessment point evaluation

For a given applied pressure, structural configuration, flaw geometry, and material toughness, an assessment point can be calculated in terms of the $K_r - S_r$ coordinates.

The assessment point coordinates will be denoted by K_r' and S_r' to differentiate them from the DPFAD curve coordinates that are independent of the arbitrary load magnitude used to locate the assessment points. The locus of assessment points for stable crack growth (ductile tearing) can be calculated, corresponding to the assumed crack extensions, using the following definitions of K_r' and S_r':

$$K_r'(a_0 + \Delta a) = \sqrt{J_I^e (a_0 + \Delta a)/J_R(\Delta a)} , \tag{I.7}$$

and

$$S_r' = (a_0 + \Delta a) = \sigma/\sigma_l (a_0 + \Delta a) , \tag{I.8}$$

where J_I^e, J_R, and σ_1 are functions of the amount of stable crack growth. For a constant pressure of 68.95 MPa and material toughness given in Table I.1, the locus of assessment points for assumed crack extensions of from 0.18 to 30.5 mm are shown in Fig. I.5 for the V-8A vessel.

In applications such as the present one, where Δa is sufficiently less than a_0, the DPFAD curve, as defined by Eq. (I.6) with $a = a_0$, becomes a conservative lower-bound approximation for the exact failure assessment diagram curve with $a = a_0 + \Delta a$.

Step 3. Tearing-instability calculations

Tearing-instability or maximum-pressure estimates for the V-8A test vessel were determined by dividing the distance from the origin to the DPFAD curve passing through the assessment point of interest by the distance to the assessment point itself (see Fig. I.5). The ratio, denoted by "SF," times the assumed constant pressure gives the equilibrium pressure of the vessel. The point at which this pressure becomes a maximum identifies the predicted tearing-instability pressure of the vessel.

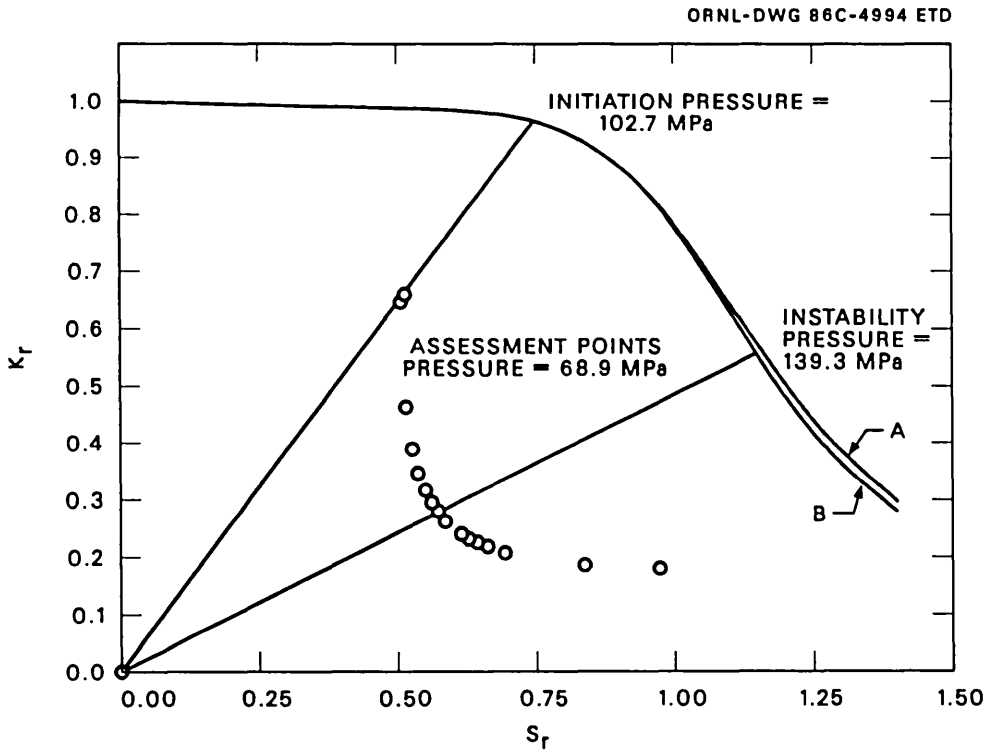

Fig. I.5. Prediction of ductile tearing of HSST V-8A vessel test; assumed pressure of 68.9 MPa for modified J integral (J_M) resistance curve.

I.2.4 DPFAD curves

Failure assessment diagram curves for nuclear-grade pressure vessels with flaw depth-to-vessel wall thickness ratios a/t ranging from 0.0 to 0.75 were developed in Ref. 7 and are shown in Fig. I.6. These curves were generated from plane-strain center-cracked-plate geometries for a/b = 0.0, 0.25, 0.50, and 0.75 for strain-hardening parameters of $\alpha = 1$, $n = 10$, and $\sigma_0 = 413.69$ MPa.

The selection of the center-cracked-plate geometry was made because the FAD curves for this geometry conservatively lower bound all other geometries considered in Ref. 7.

The V-8A vessel is a very thick-walled cylindrical shell (the wall thickness-to-radius ratio $t/R_i = 0.444$). For this geometry, elastic-plastic J-integral has not been generated,[8] and, therefore, generation of a specific DPFAD for this geometry has not been performed.

The first choice for the DPFAD curve is to use the curves of Ref. 7 shown in Fig. I.6. Specifically, the DPFAD curve for $0.50 \leq a/t < 0.75$ was chosen because $a_0/t = 0.60$ for the V-8A test vessel; this curve is designated as DPFAD-A. Alternately, to see if there is any variation with respect to the specific strain-hardening behavior of the V-8A material, a DPFAD curve was generated using the center-cracked-panel solution from the *Plastic Fracture Handbook*[8] for a crack length-to-plate width ratio of 0.625. The DPFAD expression for this curve, designated as DPFAD-B, is given in Appendix B of Ref. 3. These two DPFAD curves are

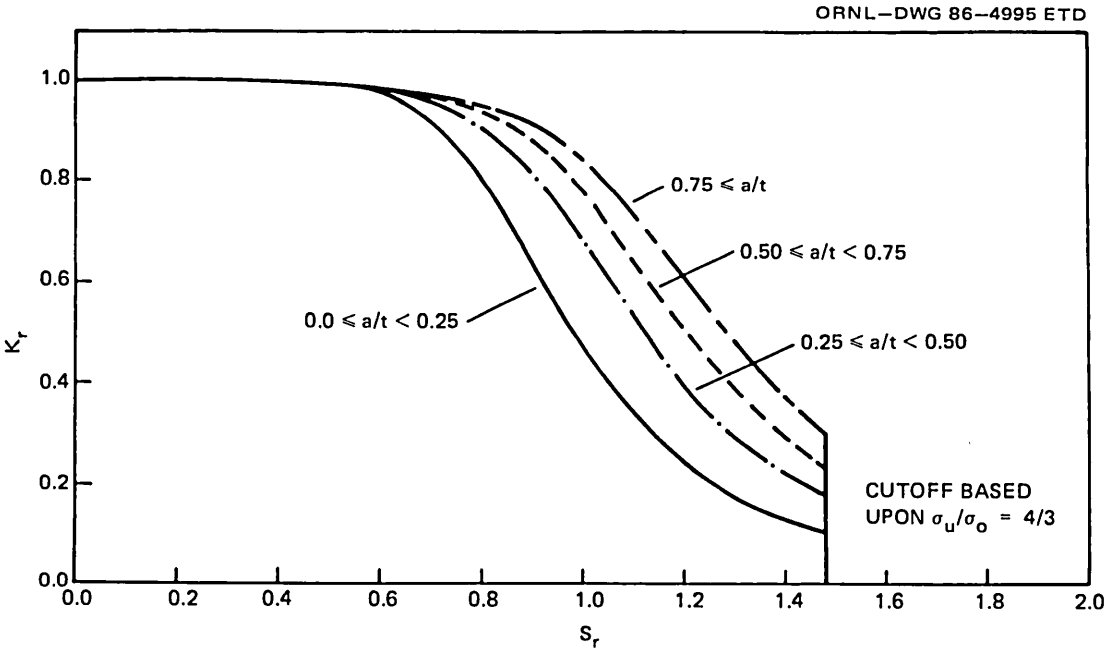

Fig. I.6. Failure assessment curves for center cracked plate in plane strain, using stress-strain parameters for nuclear-grade pressure vessel steels ($\alpha = 1$, $n = 10$, $\sigma_0 = 413.69$ MPa).

shown in Fig. I.5, and values of their coordinates are given in Tables I.2 and I.3. Note both from the figure and the tables that the two curves are almost identical.

Table I.2. DPFAD points for nuclear-grade pressure vessels, based on Ref. 7 (Curve A)

α = 1.000 t = 152.40 mm
n = 10 a = 76.20 mm
h_1 = 1.520 a/t = 0.500

S_r	K_r
0.000	1.000
0.200	0.998
0.400	0.992
0.600	0.982
0.800	0.944
0.900	0.887
1.000	0.785
1.100	0.646
1.200	0.501
1.400	0.280

Table I.3. DPFAD points for center-cracked-plate (Curve B)

α = 1.780 t = 152.40 mm
n = 10.225 a = 95.25 mm
h_1 = 0.863 a/t = 0.625

S_r	K_r
0.000	1.000
0.200	0.998
0.400	0.992
0.600	0.982
0.800	0.944
0.900	0.884
1.000	0.777
1.100	0.632
1.200	0.483
1.400	0.264

I.2.5 Evaluation of assessment points for the V-8A test vessel

The expressions for the calculation of the assessment points are given by Eqs. (I.7) and (I.8), where the stress terms σ and σ_l are the same constant times the applied pressure P and the limit pressure P_l. The K_I expression used was developed from the Raju and Newman[9] expression for a semielliptical surface flaw in a flat plate of infinite width. The applied stress was set equal to the hoop stress σ_θ acting at the outside surface of a thick-walled pressure vessel under internal pressure P. The K_I expression is

$$K_I = \sigma_\theta \sqrt{\frac{\pi a}{Q}} F\,(a/\ell,\ a/t)\ , \tag{I.9}$$

where the flaw shape parameter (Q) was approximated by

$$Q = 1 + 4.593\,(a/\ell)^{1.65}\ . \tag{I.10}$$

Note that Eq. (I.9) applies to the deepest point of the flaw. The factor F is given by

$$F = M_1 + M_2\,(a/t)^2 + M_3\,(a/t)^4\ , \tag{I.11}$$

where

$$M_1 = 1.13 - 18\ a/\ell\ ,$$

$$M_2 = -0.54 + 0.445/(0.1 + a/\ell)\ , \tag{I.12}$$

$$M_3 = 0.5 - \frac{1}{(0.65 + 2a/\ell)} + 14\left(1 - \frac{2a}{\ell}\right)^{24}\ ,$$

$$\sigma_\theta = \frac{2P}{(R_o/R_i)^2 - 1}\ , \tag{I.13}$$

where R_o = outside radius and R_i = inside radius.

The K_I expression used with the defined expression for σ_θ is consistent with a recommendation made by J. Merkle on predicting Heavy-Section Steel Technology (HSST) vessel behavior.

The plastic collapse pressure or limit load pressure for a thick-walled vessel with an external longitudinal semielliptical flaw is

$$P1 = \frac{2}{\sqrt{3}} \frac{(t - a^*)\,\sigma_0}{R_i} , \tag{I.14}$$

where[10]

$$a^* = \frac{a\,[1 - (1 + \ell^2/2t^2)^{-1/2}]}{1 - a/t\ (1 + \ell^2/2t^2)^{-1/2}} , \tag{I.15}$$

and where a and $\ell/2$ are the semiminor and semimajor axes of the actual crack, a* is the equivalent depth of a continuous crack, and σ_0 is the reference yield strength.

Assessment point calculations and tearing-instability calculations were performed by using the computer program FADAP.

I.3 Results and Conclusions

The assessment points using both the J-modified J_{IR} curve and the ASTM E813-81 J_{IR} curve are given in Tables I.4 and I.5. These points are based on a constant, applied pressure of 68.95 MPa. Figure I.5 presents graphically the J-modified results; the ASTM E813 results would be similar. The ratio factors "SF1" and "SF2" are based on the distances of the

Table I.4. FADAP output — J modified

Δa (mm)	J_M (kJ/m²)	S'_r	K'_r	Curve A		Curve B	
				SF1	PC1 (MPa)	SF2	PC2 (MPa)
0.18	44	0.516	0.641	1.489	102.69	1.490	102.73
1.27	89	0.524	0.457	1.827	125.98	1.822	125.60
2.54	127	0.534	0.385	1.932	133.23	1.924	132.63
3.81	164	0.544	0.341	1.983	136.74	1.972	135.99
5.08	202	0.555	0.311	2.009	138.52	1.996	137.64
6.35	240	0.566	0.288	2.020	139.25	2.006	138.30[a]
7.62	277	0.578	0.270	2.020	139.31[a]	2.006	138.28
8.89	315	0.591	0.256	2.014	138.88	1.998	137.77
11.43	390	0.618	0.234	1.987	136.98	1.969	135.74
12.70	427	0.633	0.225	1.967	135.64	1.948	134.35
13.97	465	0.648	0.218	1.945	134.09	1.925	132.74
15.24	502	0.665	0.211	1.920	132.35	1.899	130.96
17.78	577	0.701	0.200	1.862	128.41	1.841	126.95
25.40	802	0.840	0.178	1.648	113.65	1.629	112.30
30.48	953	0.973	0.168	1.478	101.88	1.464	100.97

[a]Instability points.

Table I.5. FADAP output — E813 J

Δa (mm)	J_M (kJ/m²)	S'_r	K'_r	Curve A		Curve B	
				SF1	PC1 (MPa)	SF2	PC2 (MPa)
0.18	38	0.516	0.688	1.405	96.87	1.406	96.92
1.27	89	0.524	0.455	1.830	126.16	1.824	125.78
2.54	112	0.534	0.410	1.890	130.32	1.883	129.79
3.81	129	0.544	0.385	1.908	131.57	1.899	130.95
5.08	144	0.555	0.368	1.912	131.85[a]	1.902	131.17[a]
6.35	159	0.566	0.353	1.909	131.60	1.898	130.86
7.62	174	0.578	0.341	1.900	130.98	1.888	130.20
8.89	188	0.591	0.331	1.887	130.08	1.875	129.26
11.43	216	0.618	0.314	1.851	127.63	1.838	126.75
12.70	230	0.633	0.307	1.829	126.14	1.816	125.23
13.97	244	0.648	0.300	1.806	124.51	1.792	123.58
15.24	258	0.665	0.295	1.780	122.74	1.766	121.79
17.78	286	0.701	0.284	1.724	118.88	1.710	117.88
25.40	370	0.840	0.262	1.525	105.13	1.508	104.00
30.48	426	0.973	0.251	1.369	94.40	1.353	93.27

[a]Instability points.

assessment points to the DPFAD-A curve (SFI) and the DPFAD-B curve (SF2). As explained previously, the DPFAD-A curve was taken from Ref. 7, a generic, ferritic, nuclear pressure vessel FAD curve for $0.50 \leq a/t < 0.75$; the DPFAD-B curve was generated from a center-cracked panel with an initial crack length-to-plate width ratio of 0.625 for the strain-hardening constants of the V-8A vessel weld material of $\alpha = 1.78$, $n = 10.225$, and $\sigma_0 = 413.69$ MPa.

The products of the applied pressure (68.95 MPa) and the "SF" ratios give the predicted tearing pressures "PC1" and "PC2" (see Tables I.4 and I.5) vs crack growth. The maximum values of "PC1" and "PC2" are the predicted ductile tearing-instability pressures for the vessel and for each DPFAD and J_R-curve combination. For the J-modified J_{IR} curve, the DPFAD analysis predicts an instability pressure of 138.3 to 139.3 MPa for 6.4 to 7.6 mm of crack extension, depending on which FAD curve is used. If the ASTM E813-81 calculated J_{IR} curve is used, the instability pressure is predicted to be 131.2 to 131.9 MPa for 5.1 mm of crack growth. These values are to be compared with the experimental results of 140 MPa for the instability pressure and 5 mm for the amount of stable crack growth before the instability point.

This report has demonstrated that the DPFAD approach can predict the tearing-instability pressure of a flawed pressure vessel, provided that the material toughness property in terms of a J_{IR} curve is known. The J_{IR} curve used in this analysis was based on tests of a compact specimen made from the weld metal at the crack-tip location of the actual HSST V-8A test vessel.

References

1. J. G. Merkle, "Preliminary Results of International Round Robin on ITV-8A," pp. 301—06 in *Proceedings of USNRC 10th Water Reactor Safety Research Information Meeting*, NUREG-CP0041, Vol. 4, U.S. Nuclear Regulatory Commission, January 1983.

2. R. H. Bryan et al., *Quick-Look Report on Test of Intermediate Vessel V-8A-Tearing Behavior of Low Upper-Shelf Material*, ORNL/HSST-4, Union Carbide Corp. Nuclear Div., Oak Ridge Natl. Lab., August 25, 1982.

3. J. M. Bloom and S. N. Malik, *A Procedure for Assessment of the Integrity of Nuclear Pressure Vessels and Piping Containing Defects*, EPRI NP-2431, Electric Power Research Institute, Palo Alto, Calif., June 1982.

4. H. A. Domian and R. J. Futato, "J-Integral Test Results of HSST-ITV8A Low Upper Shelf Weld," Babcock & Wilcox Letter Report RDD:83:4083-01-01:01 to Oak Ridge Nat. Lab., February 25, 1983.

5. R. H. Bryan, Oak Ridge Nat. Lab., Load-Displacement Data From V-8A Weld Tensile Test, Letter to B&W, April 6, 1983.

6. H. A. Ernst, "Material Resistance and Instability Beyond J-Controlled Crack Growth," pp. 191—214 in *Elastic-Plastic Fracture: Second Symposium*, ASTM STP 803, Vol. II, American Society Testing and Materials, Philadelphia, 1983.

7. J. M. Bloom, "A Procedure for the Assessment of the Structural Integrity of Nuclear Pressure Vessels," *ASME J. Pressure Vessel Tech.* 105(1) (February 1983).

8. V. Kumar et al., *An Engineering Approach for Elastic-Plastic Fracture Analysis*, EPRI NP-1931, Electric Power Research Institute, Palo Alto, Calif., July 1981.

9. J. C. Newman and I. S. Raju, *Stress Intensity Factor Equation for Cracks in 3-D Finite Bodies*, NASA-TM-83200, National Aeronautics and Space Administration, Langley Research Center, Hampton, Va., August 1981.

10. G. G. Chell, *Elastic-Plastic Fracture Mechanics*, CEGB Report RD/L/R 2007, Central Electricity Generating Board, Berkeley Nuclear Laboratories, January 1980.

Appendix J

FORMULATION OF THE DEFORMATION PLASTICITY FAILURE ASSESSMENT DIAGRAM (DPFAD)

The Deformation Plasticity Failure Assessment Diagram (DPFAD) is a graphical method for solving the nonlinear equation $J_{mat} = J_{appl}$ for the load corresponding to the current crack length and tearing resistance. The diagram contains a curve, known as the DPFAD curve, relating the ratio of the elastically calculated value of K_I to the value of $\sqrt{E' J_{appl}}$, termed K_r, to the ratio of the applied load P to the fully plastic load of the flawed region P_0, termed S_r. For a given flawed structure, the coordinates

$$S_r' = \frac{P}{P_0} \tag{J.1}$$

and

$$K_r' = \frac{K_I}{\sqrt{E' J_{mat}}} \tag{J.2}$$

will increase linearly with the applied load P, producing a straight line radiating from the origin and intersecting the DPFAD curve when

$$J_{mat} = J_{appl} \, . \tag{J.3}$$

Because of the linearity of the S_r', K_r' coordinates with load, the load that satisfies Eq. (J.3) can be determined by locating the coordinates S_r', K_r' corresponding to an arbitrary load P and then multiplying P by the ratio of the radial distance along the loading line through S_r', K_r' to the DPFAD curve, divided by the distance to the load point S_r', K_r'.

The equation of the DPFAD curve is based on representing J as

$$J_{appl} = J_e + J_p \, , \tag{J.4}$$

so that

$$\frac{J_{appl}}{G} = \frac{1}{K_r^2} = \frac{J_e + J_p}{G} \, . \tag{J.5}$$

The difference between J_e and G in this formulation is that J_e includes a small-scale, yielding plastic zone size correction to the geometry factor

and the crack length and G does not. The plastic zone size corrected crack length is given by

$$a_e = a + r_Y \phi \ , \tag{J.6}$$

where

$$r_Y = \frac{1}{6\pi} \left(\frac{n-1}{n+1}\right) \left(\frac{K_I}{\sigma_0}\right)^2 \ , \tag{J.7}$$

$$\phi = \frac{1}{1 + S_r^2} \ , \tag{J.8}$$

$$S_r = \frac{P}{P_0} \ , \tag{J.9}$$

and n is the Ramberg-Osgood strain-hardening exponent. In Eq. (J.7) K_I is calculated on the basis of the uncorrected crack size, and σ_0 is the flow stress. Thus, writing

$$K_I(a) = C(a) P \left(\frac{\sigma}{P}\right) \sqrt{\pi a} \ , \tag{J.10}$$

where σ is a defined reference stress and P is the load, using Eqs. (J.6)—(J.10) gives

$$\frac{a_e}{a} = 1 + \frac{\left(\frac{\sigma}{P}\right)^2 \left(\frac{P_0}{\sigma_0}\right)^2}{6} \left(\frac{n-1}{n+1}\right) C^2(a) \frac{S_r^2}{1 + S_r^2} \ . \tag{J.11}$$

The terms in Eq. (J.4) are given by

$$J_e = \frac{K_I^2 (a_e)}{E'} = \frac{C^2(a_e) \ P^2 \left(\frac{\sigma}{P}\right)^2 \pi a \left(\frac{a_e}{a}\right)}{E'} \ , \tag{J.12}$$

$$J_p = \alpha \ \sigma_0 \ \varepsilon_0 \ a \left(1 - \frac{a}{t}\right) h_1 \left(\frac{P}{P_0}\right)^{n+1} \ , \tag{J.13}$$

and

$$G = \frac{K_I^2\,(a)}{E'} = \frac{C^2(a)\;P^2\left(\frac{\sigma}{P}\right)^2 \pi a}{E'}\,, \tag{J.14}$$

where

$$E' = \begin{cases} \dfrac{E}{(1-\nu^2)} & \text{(plane strain)} \\ E & \text{(plane stress)} \end{cases}\,, \tag{J.15}$$

$$\frac{\varepsilon}{\varepsilon_0} = \frac{\sigma}{\sigma_0} + \alpha\left(\frac{\sigma}{\sigma_0}\right)^n\,, \tag{J.16}$$

and

$$\varepsilon_0 = \frac{\sigma_0}{E}\,. \tag{J.17}$$

Using Eqs. (J.12)—(J.17), Eq. (J.5) becomes

$$\frac{1}{K_r^2} = \frac{C^2(a_e)}{C^2(a)}\,\frac{a_e}{a} + \frac{1}{\pi\left(\frac{\sigma}{P}\right)^2\left(\frac{P_0}{\sigma_0}\right)^2(1-\nu^2)}\;\frac{\left(1-\frac{a}{t}\right)\alpha\, h_1\, S_r^{n-1}}{C^2(a)}\,, \tag{J.18}$$

which is the equation of the DPFAD curve. The equation for a particular geometry is determined by specifying the equations for (σ/P) and (P_0/σ_0).

The source of the factors $\frac{n-1}{n+1}$ and ϕ in the small-scale, yielding plastic zone size correction to the crack length, Eqs. (J.6)—(J.9), are discussed in papers by Kumar and Shih[1] and McCabe and Ernst.[2] The factor $\frac{n-1}{n+1}$ appeared in a Mode III analysis derived by Rice,[3,4] and the factor ϕ is based on a paper by Edmonds and Willis.[5]

References 6—13 provide useful general background on the Failure Assessment Diagram approach to elastic-plastic fracture analysis.

References

1. V. Kumar and C. F. Shih, "Fully Plastic Crack Solutions, Estimation Scheme and Stability Analyses for the Compact Specimen," pp. 406–38 in *Fracture Mechanics*, ASTM STP 700, American Society Testing and Materials, Philadelphia, 1980.

2. D. E. McCabe and H. A. Ernst, "A Perspective on R-Curves and Instability Theory," pp. 561–84 in *Fracture Mechanics*, ASTM STP 791, Vol. I, American Society Testing and Materials, Philadelphia, 1983.

3. J. R. Rice, "Stresses Due to a Sharp Notch in a Work-Hardening Elastic-Plastic Material Loaded by Longitudinal Shear," *Trans, ASME, J. Appl. Mech.* 34, 287–98 (June 1967).

4. J. R. Rice, "Mathematical Analysis in the Mechanics of Fracture," pp. 191–311 in *Fracture*, Vol. 2, ed. H. Liebowitz, Academic Press, New York, 1968.

5. T. M. Edwards and J. R. Willis, "Matched Asymptotic Expansion in Nonlinear Fracture Mechanics," *J. Mech. Phys. Solids* 24, 205–25 (1976) and 25, 424 (1977).

6. V. Kumar, M. D. German, and C. F. Shih, "Elastic-Plastic and Fully Plastic Analysis of Crack Initiation, Stable Growth and Instability in Flawed Cylinders," pp. 306–53 in *Elastic-Plastic Fracture: Second Symposium*, ASTM STP 803, Vol. I, American Society Testing and Materials, Philadelphia, 1983.

7. G. G. Chell and I. Milne, "Ductile Tearing Instability Analysis: A Comparison of Available Techniques," pp. 179–205 in *Elastic-Plastic Fracture: Second Symposium*, ASTM STP 803, Vol. II, American Society Testing and Materials, Philadelphia, 1983.

8. J. M. Bloom, "Validation of a Deformation Plasticity Failure Assessment Diagram Approach to Flaw Evaluation," pp. 206–38 in *Elastic-Plastic Fracture: Second Symposium*, ASTM STP 803, Vol. II, American Society Testing and Materials, Philadelphia, 1983.

9. C. F. Shih, V. Kumar, and M. D. German, "Studies on the Failure Assessment Diagram Using the Estimation Method and J-Controlled Crack Growth Approach," pp. 239–61 in *Elastic-Plastic Fracture: Second Symposium*, ASTM STP 803, Vol. II, American Society Testing and Materials, Philadelphia, 1983.

10. I. Milne, "Experimental Validation of Resistance Curve Analysis," pp. 657–85 in *Elastic-Plastic Fracture: Second Symposium*, ASTM STP 803, Vol. II, American Society Testing and Materials, Philadelphia, 1983.

11. J. M. Bloom and S. N. Malik, *Procedure for the Assessment of the Integrity of Nuclear Pressure Vessels and Piping Containing Defects*, EPRI NP-2341, Electric Power Research Institute, Palo Alto, Calif., June 1982.

12. J. M. Bloom, "A Procedure for the Assessment of the Structural Integrity of Nuclear Pressure Vessels," *ASME J. Pressure Vessel Tech.* 105(1), February 1983.

13. J. M. Bloom, "Extensions of the Failure Assessment Diagram Approach — Semi-Elliptical Flaw in Pressurized Cylinder," presented at the 1983 ASME Winter Annual Meeting, Boston, preprint 83-WA/PVP-3, to be published in the *ASME J. Pressure Vessel Tech.*

Appendix K

EXAMINATION OF THE PARAMETERS J_D AND J_M AS MEASURES OF TOUGHNESS CONTROLLING THE DUCTILE TEARING RESISTANCE CURVE

The currently prescribed method for calculating the value of the J-integral for a compact specimen undergoing stable crack growth[1] is based on the assumptions of the deformation theory of plasticity. Thus, the value of J is assumed to be independent of the loading path, the variables of which are load, displacement, and crack length, and dependent only on the current values of those variables, as if the current crack length had existed since the start of loading. The value of J so calculated is termed J_D, where the subscript D stands for deformation theory. It is assumed that

$$J_D = \frac{\eta A}{bB} , \tag{K.1}$$

where b is the current ligament size, η corresponds to b, and A is the area under the load-displacement curve corresponding to a ligament of constant size b. Thus, A is not $\int P d\Delta$, and an adjustment must be made to calculate J_D.

Ernst et al.[2] outlined a procedure, which can be derived by differentiating J_D to obtain

$$dJ_D = \left(\frac{\partial J_D}{\partial \Delta}\right)_a d\Delta + \left(\frac{\partial J_D}{\partial a}\right)_\Delta da . \tag{K.2}$$

Then by using Eq. (K.1),

$$dJ_D = \frac{\eta \left(\frac{\partial A}{\partial \Delta}\right)_a d\Delta}{bB} + \frac{1}{B}\left[\frac{\partial \eta}{\partial a}\frac{A}{b} + \frac{\eta A}{b^2} + \frac{\eta}{b}\left(\frac{\partial A}{\partial a}\right)_\Delta\right] da . \tag{K.3}$$

Substituting for A in terms of Eq. (K.1) and recognizing that

$$\frac{1}{B}\left(\frac{\partial A}{\partial a}\right)_\Delta = - J_D , \tag{K.4}$$

Eq. (K.3) becomes

$$dJ_D = \frac{\eta P d\Delta}{Bb} - J_D\left(\eta - 1 - \frac{b}{W}\frac{\eta'}{\eta}\right)\frac{da}{b} . \tag{K.5}$$

Writing

$$dJ_f = \frac{\eta P d\Delta}{bB} \quad , \tag{K.6}$$

where J_f is termed the far field value of J, and defining

$$\gamma = \left(\eta - 1 - \frac{b}{W}\frac{\eta'}{\eta}\right) , \tag{K.7}$$

Eq. (K.5) becomes

$$dJ_D = dJ_f - \gamma J_D \frac{da}{b} . \tag{K.8}$$

For the compact specimen, it has been shown[3,4] that η can be represented by

$$\eta = 2 + 0.522 \left(\frac{b}{W}\right) , \tag{K.9}$$

so that using Eq. (K.7),

$$\gamma = 1 + 0.522 \left(1 + \frac{1}{\eta}\right)\left(\frac{b}{W}\right) . \tag{K.10}$$

Because γ turns out to be a slowly varying function of b/W, using the value of η near b/W = 0.45 as an approximation,[2]

$$\gamma = 1 + 0.76 \left(\frac{b}{W}\right) . \tag{K.11}$$

Because of the occasional occurrence of size effects and negative slopes in J_D-based R-curves, Ernst[5] subsequently suggested a modified J parameter, termed J_M, based on a suggestion of Rice, Drugan, and Sham,[6] that

$$\left(\frac{\partial J_p}{\partial a}\right)_{\Delta_p} = 0 . \tag{K.12}$$

Using this condition replaces the assumption of load path independence with the observation that plastic work cannot be recovered from a specimen and that, at least for a rigid plastic specimen, a crack cannot

extend in ductile tearing without an increase in the load point displacement. Thus, replacing the total area A in the second term of Eq. (K.3) with A_e leads to

$$dJ_M = dJ_f - \gamma\, G\, \frac{da}{b} \,. \tag{K.13}$$

An equation for converting J_D values to J_M can be obtained by combining Eqs. (K.8) and (K.13) to give

$$dJ_M = dJ_D + \gamma\, (J_D - G)\, \frac{da}{b} \,, \tag{K.14}$$

so that

$$J_M = J_D + \int_0^a \gamma\, J_D \left(1 - \frac{G}{J_D}\right) \frac{da}{b} \,. \tag{K.15}$$

Comparing Eqs. (K.14) and (K.8) shows that when G becomes small relative to J_D, J_M approaches J_f, the far field value of J with no correction for crack extension.

An alternate expression for J_M can be developed by separating J_M into elastic and plastic parts[7] and then differentiating to obtain

$$dJ_M = \left(\frac{\partial G}{\partial \Delta_e}\right)_a d\Delta_e + \left(\frac{\partial G}{\partial a}\right)_{\Delta_e} da + \left(\frac{\partial J_{M,p}}{\partial \Delta_p}\right)_a d\Delta_p + \left(\frac{\partial J_{M,p}}{\partial a}\right)_{\Delta_p} da \,. \tag{K.16}$$

According to Eq. (K.12), note that the last term in Eq. (K.16) is zero[7] and that the first two terms are a total differential, Eq. (K.16) becomes

$$dJ_M = dG + \left(\frac{\partial J_{M,p}}{\partial \Delta_p}\right)_a d\Delta_p \,. \tag{K.17}$$

Because

$$\left(\frac{\partial J_{M,p}}{\partial \Delta_p}\right)_a = \frac{\eta P}{bB} \,, \tag{K.18}$$

Eq. (K.17) becomes

$$dJ_M = dG + \frac{\eta P d\Delta_p}{bB} , \qquad (K.19)$$

so that

$$J_M = G + \int_0^{\Delta_p} \frac{\eta P d\Delta_p}{bB} , \qquad (K.20)$$

where G is calculated according to ASTM E399, using the current values of load and crack length. Equation (K.20) has recently been proposed by Ernst.[8] It should agree with Eq. (K.15) and appears to be a convenient expression for calculating J_M when the input is experimental data and values of J_D are not available or needed.

Using J_M as a resistance-curve parameter reduces or eliminates size effects on the R-curves and ensures non-negative R-curve slopes. However, with respect to methods of calculating J for toughness specimens and flawed structures, it creates a consistency problem that needs to be evaluated.

The difference between J_M- and J_D-based R-curves can be appreciable, at least in terms of slopes, as illustrated by Bloom's Fig. I.4 for the low-shelf weld metal of ITV-8A. These data provide a good example for illustrating the conversion of J_D to J_M values. A convenient rearrangement of Eq. (K.15) for calculational purposes is

$$J_M = J_D + \int_{\ln a_i}^{\ln a} \frac{\gamma J_D \left(1 - \frac{G}{J_D}\right)}{\left(\frac{b}{a}\right)} d \ln a . \qquad (K.21)$$

For specimen V8AJ2, W = 50.8 mm, and a_i = 31.37 mm. Approximate calculations can be made by using selected values from Table I.1 and the trapezoidal rule for estimating areas. Using the values listed in Table K.1 and the simplifying assumptions that $G/J_D \sim 0$ for $\Delta a > 1.27$ mm and $J_M \sim J_D$ for $\Delta a < 1.27$ mm,

$$J_M = 207 + \frac{205 + 389}{2}(0.082) + \frac{389 + 1190}{2}(0.176) = 370 \text{ kJ/m}^2 ,$$

which agrees well with the value of J_M at Δa = 10.95 mm given in Table I.1.

Table K.1. Values used for approximate conversion of J_D to J_M values at Δa = 10.95 mm for specimen V8AJ2

Δa (mm)	a (mm)	b (mm)	$\frac{b}{W}$	γ	J_D (kJ/m^2)	$\gamma J_D/(b/a)$ (kJ/m^2)	$\Delta \ln a$
1.30	32.8	18.3	0.36	1.27	90	205	
							0.082
4.14	35.6	15.2	0.30	1.23	136	389	
							0.176
10.95	42.4	8.4	0.17	1.13	207	1190	

References

1. ASTM Standard E813-81, "Standard Test Method for J_{Ic}, A Measure of Fracture Toughness," pp. 762–80 in *1983 Annual Book of ASTM Standards*, American Society Testing and Materials, Philadelphia, 1983.

2. H. A. Ernst, P. C. Paris, and J. D. Landes, "Estimations on J-Integral and Tearing Modulus T from a Single Specimen Test Record," pp. 476–502 in *Fracture Mechanics: Thirteenth Conference*, ASTM STP 743, American Society Testing and Materials, Philadelphia, 1981.

3. J. G. Merkle, Oak Ridge Natl. Lab., personal communication to G. A. Clarke, Westinghouse Research Laboratories, August 1978.

4. G. A. Clarke and J. D. Landes, "Evaluation of the J Integral for the Compact Specimen," *J. Test. Eval.* 7(5) (1979).

5. H. A. Ernst, "Material Resistance and Instability Beyond J-Controlled Crack Growth," pp. 191–213 in *Elastic-Plastic Fracture: Second Symposium*, ASTM STP 803, Vol. I, American Society Testing and Materials, Philadelphia, 1983.

6. J. R. Rice, W. J. Drugan, and T. L. Sham, "Elastic-Plastic Analysis of Growing Cracks," pp. 189–221 in *Fracture Mechanics: Twelfth Conference*, ASTM STP 700, American Society Testing and Materials, Philadelphia, 1980.

7. J. G. Merkle, Oak Ridge Natl. Lab., personal communication to H. A. Ernst, Westinghouse Research Laboratories, January 19, 1982.

8. H. A. Ernst, "Further Developments on the Modified J-Integral, J_M," draft 85-9D7-GUDAS-P1, Westinghouse Research Laboratories, February 25, 1985 (to be published).

Appendix L

PROPERTIES OF SPECIAL SEAM WELD IN VESSEL V-8A AND OF CHARACTERIZATION WELDS

The information in this appendix supplements that given in Sect. 2.3, "Materials Investigations."

Tables L.1 and L.2 present the results of chemical analyses and Charpy impact tests, respectively, of the characterization welds.[1] Chemical analyses were performed on welds V852 and V8102. Charpy impact tests were performed for all four characterization welds.

Table L.1. Chemical analyses of characterization welds V852 and V8102

Location	Element (wt %)											
	C	Mn	P	S	Si	Cr	Ni	Mo	Cu	Sn	V	Al
						Weld V852						
Top	0.06	1.53	0.030	0.016	0.67	0.04	0.63	0.46	0.17	0.018	0.008	0.004
Middle	0.06	1.58	0.036	0.016	0.77	0.04	0.64	0.48	0.28	0.020	0.009	0.004
Bottom	0.06	1.58	0.028	0.017	0.70	0.04	0.62	0.49	0.29	0.020	0.008	0.005
						Weld V8102						
Top	0.05	1.52	0.026	0.015	0.65	0.04	0.64	0.47	0.18	0.030	0.006	0.007
Middle	0.05	1.52	0.025	0.013	0.62	0.04	0.64	0.47	0.17	0.030	0.006	0.011
Bottom	0.07	1.52	0.022	0.013	0.58	0.04	0.61	0.47	0.17	0.027	0.005	0.045

All results of tests of material properties of the special seam weld cut from vessel V-8A after the test are reported either in Sect. 2.3 or in this appendix. Figure L.1 describes the locations of V-8A specimens. Charpy impact properties for the specimens identified in Fig. L.1(*c*) are given in Table L.3. Stress-strain data for the only specimen of special seam weld material for which such data were recorded are presented in Table L.4.

Results of tearing-resistance tests performed by the Babcock & Wilcox Company[2] for the Oak Ridge National Laboratory are presented in Table L.5 and a series of tables and plots for each specimen (Figs. L.2—L.11). Power-law parameters for each of the specimens are given in Table L.6.

Table L.2. Charpy V-notch impact test results for V-8A characterization welds[a]

Specimen No.	Test temperature (°C)	Energy[b] (J)	Lateral expansion (mm)				Shear (%)			
			Technician[b]			Average	Technician[b]			Average
			1	2	3		1	2	3	
			Weld V852							
C1	−73.3	2.6	0.03	0	0.03	0.02	1	0	0	0.3
C2	−17.8	19.7	0.38	0.36	0.36	0.36	10	0	5	5.0
C3	37.8	52.5	1.19	1.07	1.09	1.16	65	65	50	60.0
C4	65.6	62.5	1.40	1.37	1.35	1.37	85	90	80	85.0
C5	79.4	63.6	1.40	1.37	1.24	1.34	95	100	100	98.3
C6	93.3	60.7	1.42	1.24	1.24	1.30	99	97	98	98.0
C11	104.4	69.8	1.45	1.45	1.42	1.44	100	100	100	100.0
C12	104.4	76.6	1.68	1.63	1.45	1.58	100	100	100	100.0
C18	104.4	66.2	1.45	1.45	1.42	1.44	100	100	100	100.0
C19	104.4	64.7	1.42	1.40	1.35	1.39	100	100	100	100.0
C20	104.4	62.5	1.37	1.35	1.35	1.35	95	96	95	95.3
C7	107.2	61.1	1.42	1.40	1.37	1.40	100	100	100	100.0
C13	115.6	67.7	1.50	1.50	1.47	1.49	100	100	100	100.0
C14	115.6	70.0	1.55	1.50	1.52	1.52	100	100	100	100.0
C15	115.6	67.1	1.60	1.57	1.30	1.49	100	100	100	100.0
C16	115.6	67.7	1.42	1.40	1.37	1.40	100	100	100	100.0
C17	115.6	68.3	1.45	1.40	1.40	1.41	100	100	100	100.0
C8	121.1	60.5	1.40	1.37	1.30	1.35	100	100	100	100.0
C9	204.4	61.0	1.52	1.42	1.37	1.44	100	100	100	100.0
C10	260.0	60.5	1.40	1.37	1.55	1.44	100	100	100	100.0
			Weld V862							
C1	−73.3	5.0	0.18	0.18	0.15	0.17	1	0	5	2.0
C2	−17.8	19.3	0.41	0.41	0.41	0.41	10	5	10	8.3
C3	37.8	48.5	1.07	1.02	1.04	1.04	50	75	40	55.0
C4	65.6	56.7	1.24	1.24	1.22	1.24	85	80	70	78.3
C5	79.4	63.5	1.40	1.37	1.35	1.37	99	97	98	98.0
C6	93.3	62.4	1.27	1.40	1.37	1.35	99	99	100	99.3
C11	104.4	66.7	1.40	1.40	1.37	1.39	100	100	100	100.0
C12	104.4	63.9	1.37	1.35	1.40	1.37	100	100	100	100.0
C18	104.4	56.9	1.30	1.27	1.24	1.27	100	100	100	100.0
C19	104.4	63.6	1.37	1.27	1.24	1.30	100	100	100	100.0
C20	104.4	59.5	1.35	1.30	1.30	1.31	100	100	100	100.0
C7	107.2	62.6	1.37	1.35	1.24	1.32	99	100	100	99.7
C13	115.6	52.7	1.27	1.27	1.32	1.29	100	100	100	100.0
C14	115.6	61.8	1.50	1.47	1.50	1.49	100	100	100	100.0
C15	115.6	59.2	1.37	1.37	1.24	1.33	100	100	100	100.0
C16	115.6	59.7	1.40	1.35	1.40	1.38	100	100	100	100.0
C17	115.6	59.8	1.37	1.35	1.32	1.35	100	100	100	100.0
C8	121.1	61.0	1.37	1.37	1.35	1.36	100	100	100	100.0
C9	204.4	65.1	1.45	1.52	1.47	1.48	100	100	100	100.0
C10	260.0	55.9	1.42	1.40	1.40	1.41	100	100	100	100.0

Table L.2 (continued)

Specimen No.	Test temperature (°C)	Energy[b] (J)	Lateral Expansion (mm)				Shear (%)			
			Technician[b]			Average	Technician[b]			Average
			1	2	3		1	2	3	
			Weld V882							
C1	104.4	59.4	1.32	1.32	1.24	1.30	100	100	100	100.0
C2	104.4	67.8	1.50	1.50	1.47	1.49	100	100	100	100.0
C8	104.4	56.4	1.30	1.30	1.32	1.30	100	100	100	100.0
C9	104.4	55.6	1.30	1.24	1.19	1.24	100	100	100	100.0
C10	104.4	58.6	1.40	1.35	1.35	1.36	100	100	100	100.0
C3	115.6	59.7	1.42	1.40	1.35	1.39	100	100	100	100.0
C4	115.6	55.9	1.30	1.30	1.30	1.30	100	100	100	100.0
C5	115.6	60.9	1.35	1.32	1.35	1.34	100	100	100	100.0
C6	115.6	55.3	1.27	1.22	1.27	1.25	100	100	100	100.0
C7	115.6	59.7	1.35	1.30	1.17	1.27	100	100	100	100.0
			Weld V8102							
C1	148.9	52.1	1.27	1.24	1.22	1.24	100	100	100	100.0
C2[c]	148.9	54.9	1.32	1.32	1.32	1.32	100	100	100	100.0
C3	115.6	52.3	1.27	1.24	1.19	1.24	100	100	100	100.0
C4[c]	115.6	54.1	1.30	1.24	1.24	1.26	100	100	100	100.0
C5	148.9	50.2	1.19	1.19	1.17	1.19	100	100	100	100.0
C6[c]	148.9	54.2	1.27	1.27	1.24	1.26	100	100	100	100.0
C7	115.6	50.0	1.22	1.19	1.19	1.20	100	100	100	100.0
C8[c]	115.6	49.5	1.17	1.17	1.14	1.16	100	100	100	100.0
C9	148.9	48.9	1.14	1.14	1.09	1.13	100	100	100	100.0
C10[c]	148.9	50.8	1.24	1.22	1.22	1.23	100	100	100	100.0

[a]Orientation is CA, except as noted.

[b]Lateral expansion was measured and shear was estimated by three technicians. The absorbed energy was read by technician No. 1.

[c]Orientation is CR.

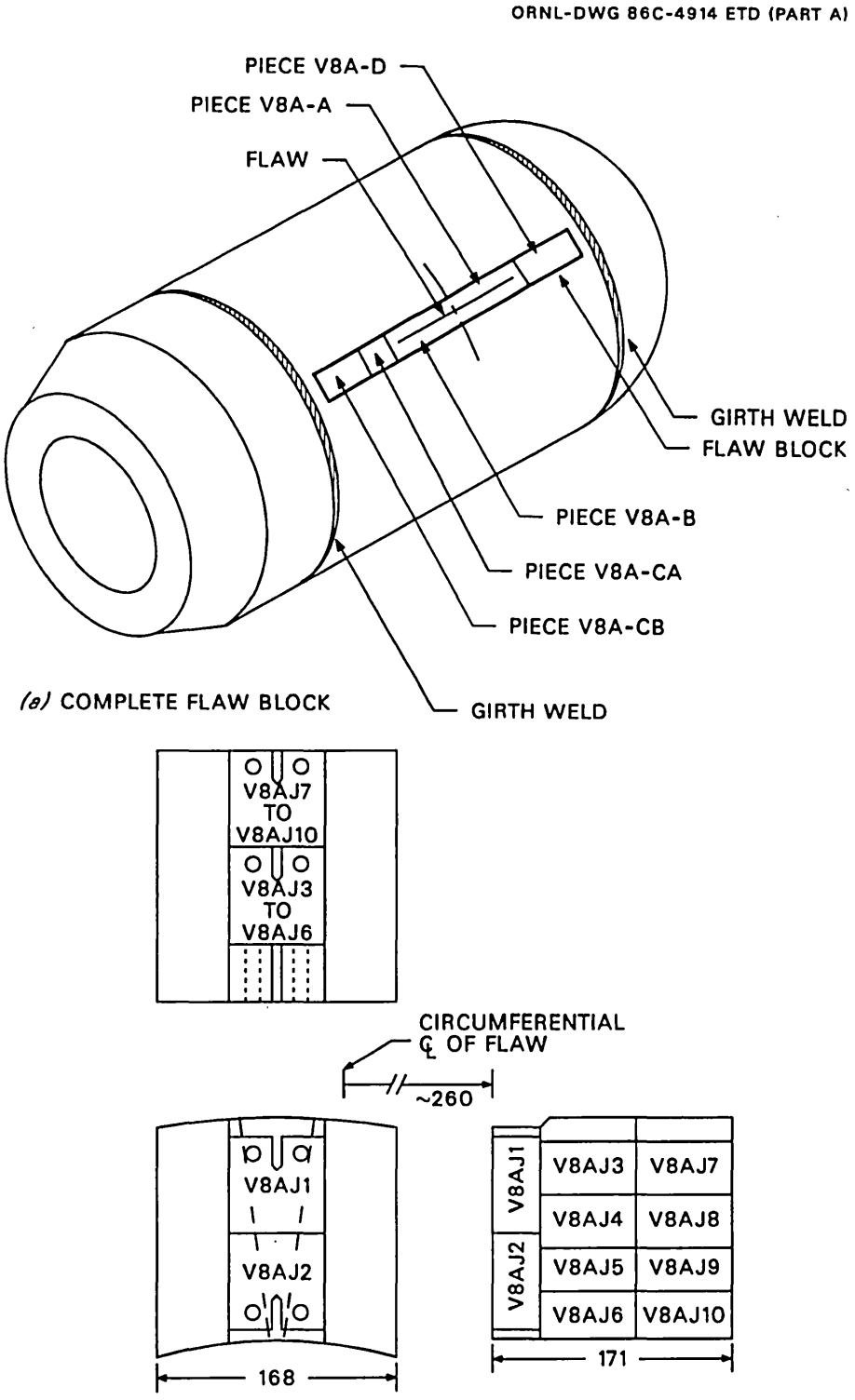

Fig. L.1. Plan for cutting the special seam weld from vessel V-8A after the test. (*a*) Location of pieces used for J-integral, Charpy impact, and tension tests; (*b*) location of blanks for J-integral specimens; and (*c*) location of blanks for Charpy impact and tensile specimens.

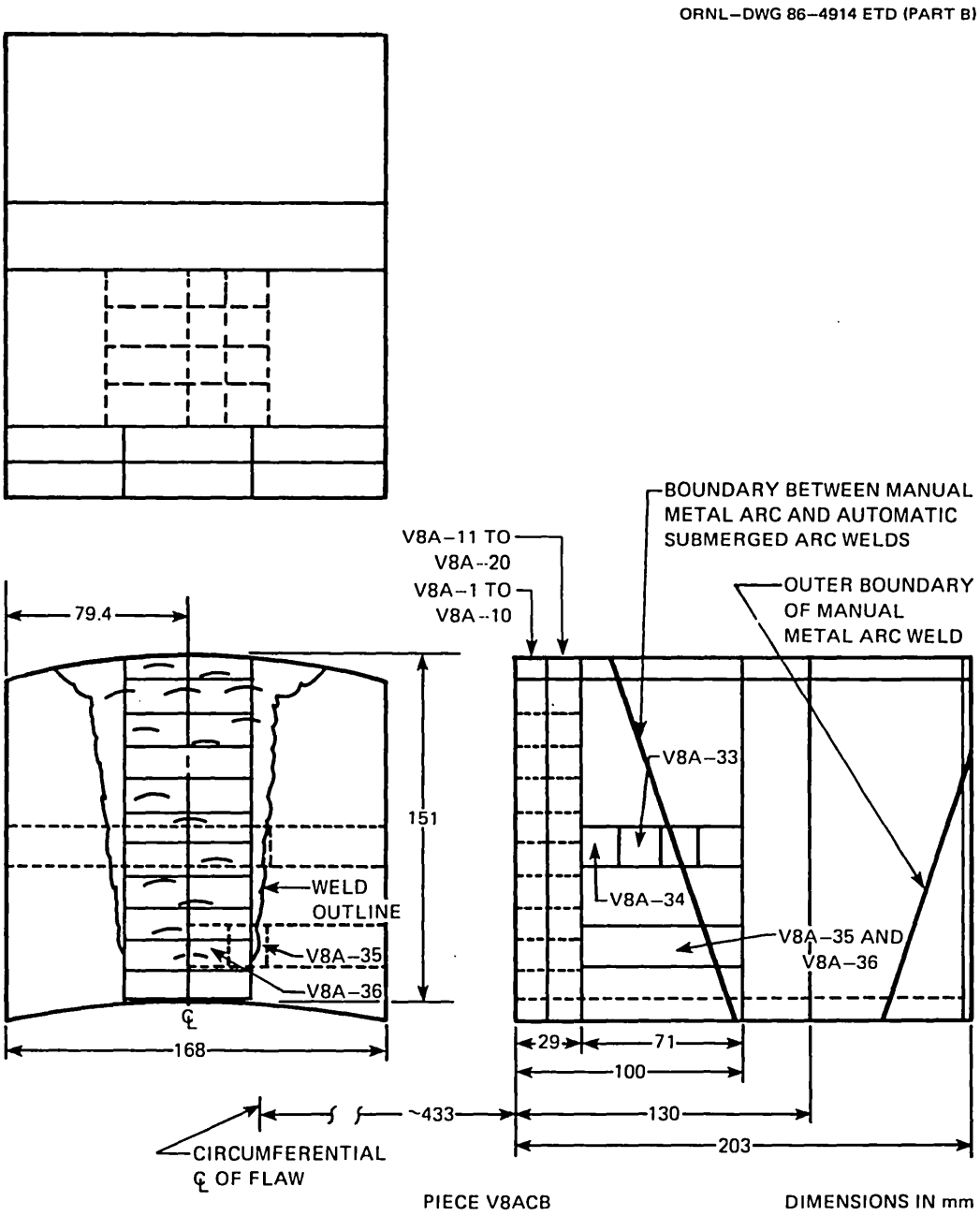

(c) LOCATION OF BLANKS FOR CHARPY AND TENSILE SPECIMENS

Fig. L.1 (continued)

Table L.3. Charpy V-notch impact test results from special seam weld material from vessel V-8A[a]

V8A specimen No.	Test temperature (°C)	Energy (J)	Lateral expansion (mm)	Shear (%)
1	−73.3	12.2	0.04	0
2	−17.8	7.7	0.10	15
3	37.8	31.9	0.64	42
4	65.6	43.0	0.87	69
5	79.4	53.6	1.12	97
6	93.3	50.4	1.04	82
7	107.2	56.3	1.17	100
8	121.1	55.9	1.18	100
9	204.4	56.3	1.18	100
10	260	56.7	1.34	100
11	−45.6	12.2	0.15	0
12	−17.8	5.4	0.01	5
13	−3.9	20.3	0.44	10
14	10.0	10.2	0.17	18
15	23.9	22.8	0.44	50
16	65.6	43.4	0.83	66
17	79.4	50.4	1.00	97
18	10.0	21.7	0.40	21
19	−3.9	17.6	0.30	9
20	−45.6	3.7	0.04	0

[a]Orientation of all specimens is CA; locations are shown in Fig. L.1(*c*).

Table L.4. Stress-strain data for specimen V8A-33 of special seam weld material from vessel V-8A

Engineering		True	
Strain	Stress (MPa)	Strain	Stress (MPa)
0.0	0.0	0.0	0.0
0.000300	70.286	0.000299	70.307
0.000610	140.571	0.000609	140.657
0.000910	210.857	0.000909	211.049
0.001235	281.142	0.001233	281.489
0.001415	316.285	0.001413	316.732
0.001645	351.428	0.001643	352.006
0.001840	371.811	0.001838	372.495
0.002040	385.165	0.002038	385.951
0.002540	400.628	0.002536	401.645
0.003040	405.548	0.003035	406.780
0.004040	406.954	0.004032	408.597
0.004540	406.954	0.004529	408.801
0.006040	412.576	0.006021	415.068
0.007040	415.388	0.007014	418.312
0.008040	418.902	0.008007	422.270
0.009040	421.714	0.008999	425.526
0.010040	424.525	0.009989	428.787
0.011040	427.336	0.010979	432.054
0.012040	430.148	0.011967	435.326
0.013040	432.959	0.012955	438.605
0.014040	435.771	0.013942	441.889
0.015040	438.582	0.014927	445.178
0.020040	451.234	0.019841	460.276
0.025040	462.128	0.024731	473.699
0.030040	471.616	0.029597	485.784
0.035040	477.239	0.034440	493.962
0.040040	484.268	0.039258	503.657
0.045040	488.485	0.044054	510.486
0.050040	493.405	0.048828	518.094
0.055040	497.271	0.053578	524.640
0.060040	499.731	0.058306	529.734
0.065040	502.542	0.063012	535.227
0.070040	505.354	0.067696	540.748
0.075040	506.056	0.072358	544.031
0.080040	506.759	0.076998	547.320
0.085040	507.111	0.081616	550.235
0.090040	506.056	0.086214	551.621
0.100040	505.354	0.095346	555.909
0.110040	499.028	0.104396	553.941
0.120040	492.702	0.113364	551.846
0.130040	482.862	0.122252	545.653

Table L.5. J-integral test results for specimens from the special seam weld in vessel V-8A[a]

V8AJ specimen No.	Thickness, B (mm)	Net thickness (mm)	Specimen depth (mm)	Initial crack length, A_0 (mm)	Maximum deviation from average A_0 (mm)	Initial ligament, $(w - A_0)$ (mm)	Corrected modulus (GPa)	J_{Ic} (kJ/m^2)
1[b]	25.43	20.47	50.80	31.32	−0.43	19.48	195.89	39.4
2[b]	25.45	20.37	50.80	31.39	−0.25	19.41	199.43	42.9
3	25.45	20.40	50.80	31.98	−0.58	18.82	200.58	38.0
4	24.89	20.07	50.77	30.78	−0.36	19.99	200.84	43.3
5	25.43	20.50	50.80	30.99	−0.28	19.81	200.50	43.6
6	25.45	20.45	50.77	30.96	−0.23	19.81	199.06	45.9
7	25.45	20.42	50.80	30.63	−0.23	20.37	201.07	47.8
8	25.32	20.22	50.77	30.78	−0.33	19.99	199.30	60.1
9	25.45	20.37	50.80	31.37	−0.41	19.43	200.53	57.4
10	25.43	20.35	50.80	31.39	−0.33	19.41	200.84	47.3

[a]Test temperature: 149°C; test loading rate (displacement at load line: 0.0051 mm/s; ultimate and tensile strengths are 420 and 510 MPa, respectively. Orientation is CA except as noted. Maximum precracking load and ΔK are 9.8 KN and 23 MPa$\cdot\sqrt{m}$, respectively.

[b]Orientation is CR.

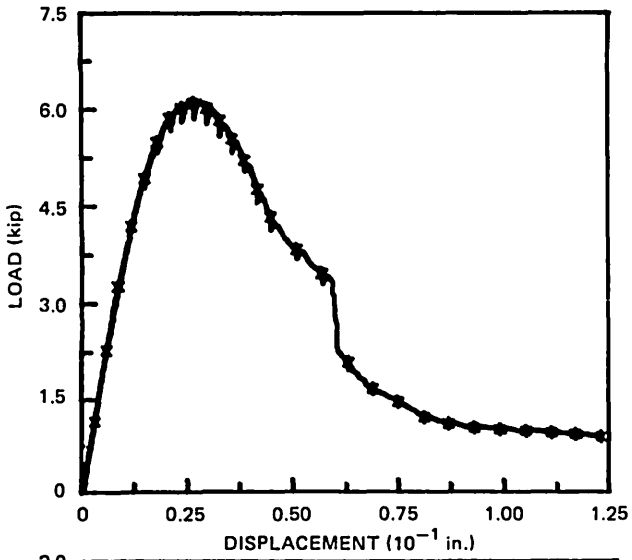

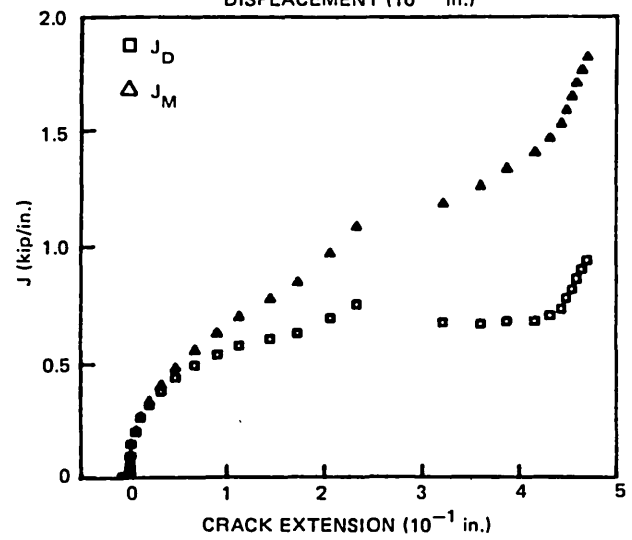

ORNL–DWG 86–4997 ETD

CRACK EXTENSION (in.)	J_D (kip/in.)	J_M (kip/in.)
−6.38628E−03	7.86864E−03	7.89126E−03
1.57237E−04	0.0274131	0.0279205
4.82798E−04	0.0567338	0.057291
7.00474E−04	0.101367	0.101982
1.40595E−03	0.151203	0.152091
5.86033E−03	0.206266	0.209455
0.0117475	0.267026*+	0.274053
0.020972	0.325158*+	0.33936
0.0327498	0.38419*+	0.40909
0.047713	0.444167*+	0.484632
0.0674347	0.496012	0.559475
0.0905113	0.541206	0.634351
0.113026	0.579846	0.704357
0.143689	0.608718	0.779166
0.172249	0.633939	0.850072
0.205481	0.696718	0.972511
0.2334	0.757018	1.08862
0.321993	0.678455	1.18565
0.360746	0.672944	1.26213
0.388146	0.683587	1.33524
0.416668	0.682932	1.40344
0.432055	0.705938	1.46626
0.443451	0.735639	1.52759
0.448543	0.77917	1.58626
0.454819	0.819866	1.64686
0.459372	0.863227	1.70559
0.46427	0.903024	1.76286
0.469315	0.942866	1.82169

• DENOTES POINTS USED FOR J_{Ic} DETERMINATION

+ DENOTES POINTS USED IN TEARING MODULUS CALCULATION

J_{Ic} = 0.225164 kip/in.

T = 30.9217

Fig. L.2. Load vs displacement and J vs crack extension for the V-8A vessel special seam weld corresponding to specimen V8AJ1. The graphics and data are from the Babcock & Wilcox Company.[2]

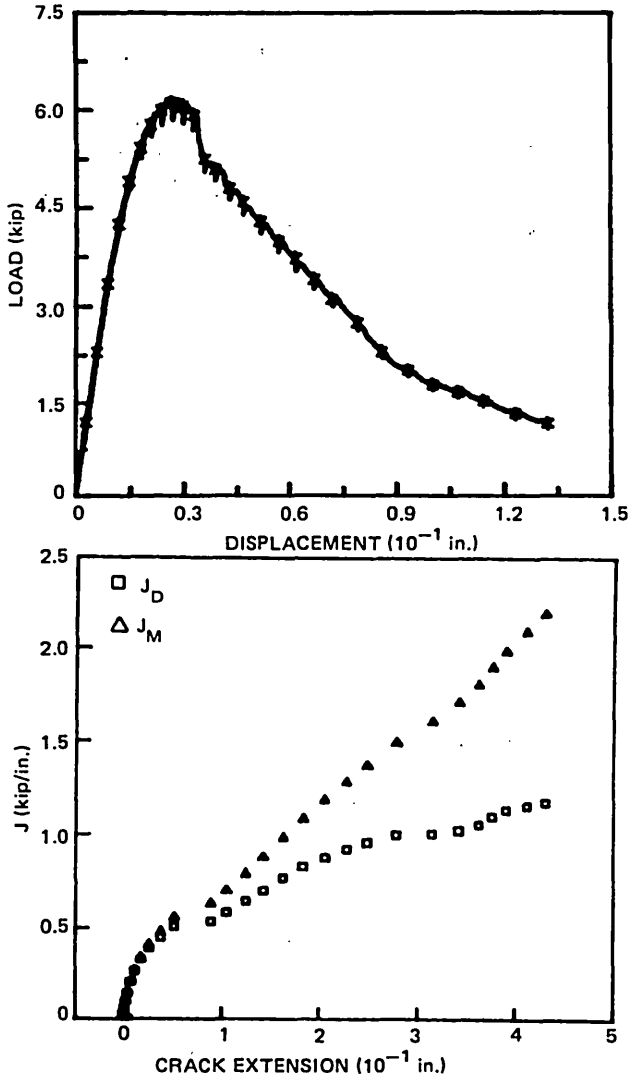

CRACK EXTENSION (in.)	J_D (kip/in.)	J_M (kip/in.)
2.57051E−03	8.62551E−03	8.85503E−03
−1.59466E−03	0.029767	0.0296683
−5.30005E−04	0.061859	0.0619357
1.44017E−03	0.106369	0.106994
2.85375E−03	0.152641	0.15382
5.91946E−03	0.211704	0.214492
9.77957E−03	0.271931*+	0.277247
0.0167395	0.334979*+	0.345795
0.0248731	0.396908*+	0.415207
0.0372171	0.453754*+	0.484893
0.0511315	0.51507*+	0.562534
0.0886803	0.543117	0.63785
0.104112	0.590911	0.706963
0.124311	0.649753	0.796636
0.142309	0.700312	0.885443
0.16276	0.774698	0.989775
0.182957	0.834573	1.09055
0.206042	0.885044	1.19187
0.228339	0.926675	1.28614
0.249046	0.964887	1.37644
0.278635	1.00632	1.49855
0.314628	1.01269	1.60914
0.341925	1.0307	1.71156
0.362203	1.05992	1.80765
0.376297	1.10332	1.90075
0.390402	1.13735	1.98746
0.411813	1.15944	2.09463
0.430989	1.17791	

* DENOTES POINTS USED FOR J_{Ic} DETERMINATION

\+ DENOTES POINTS USED IN TEARING MODULUS CALCULATION

J_{Ic} = 0.244943 kip/in.

T = 36.2609

Fig. L.3. Load vs displacement and J vs crack extension for the V-8A vessel special seam weld corresponding to specimen V8AJ2. The graphics and data are from the Babcock & Wilcox Company.[2]

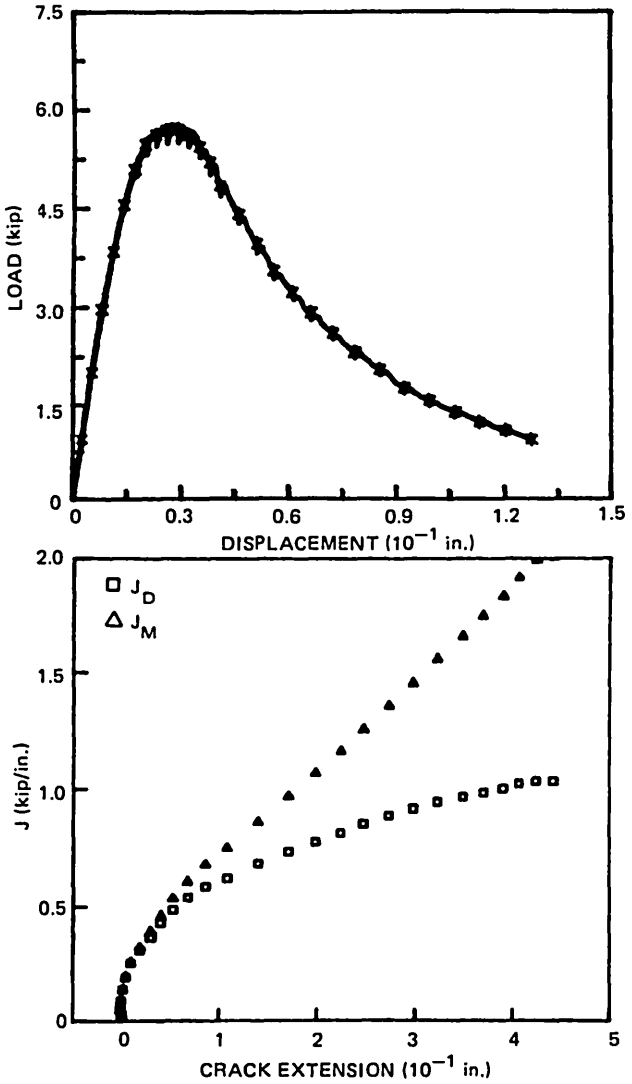

ORNL–DWG 86–4999 ETD

CRACK EXTENSION (in.)	J_D (kip/in.)	J_M (kip/in.)
1.16920E–03	6.63895E–03	6.84432E–03
1.70708E–04	0.0253339	0.0254703
–1.10638E–03	0.053242	0.0531917
–3.51667E–04	0.0933627	0.0935024
1.45137E–03	0.140781	0.141592
4.56274E–03	0.195915	0.198294
9.89544E–03	0.256749*+	0.262561
0.0190709	0.313421*+	0.326298
0.0298891	0.371472*+	0.394078
0.04029	0.431821*+	0.465173
0.0531243	0.489215*+	0.53748
0.0682389	0.540931	0.608578
0.0863671	0.587699	0.680722
0.108907	0.623775	0.750693
0.139279	0.686007	0.864084
0.170473	0.736039	0.971989
0.199094	0.777566	1.0712
0.224329	0.816303	1.16487
0.248062	0.853649	1.25783
0.27375	0.888776	1.35782
0.298307	0.919253	1.45484
0.323416	0.950497	1.55937
0.349317	0.969473	1.65902
0.371022	0.988579	1.75024
0.396544	1.00678	1.83724
0.407596	1.02486	1.91885
0.424488	1.03799	1.9984
0.442484	1.03745	2.07189

* DENOTES POINTS USED FOR J_{Ic} DETERMINATION
\+ DENOTES POINTS USED IN TEARING MODULUS CALCULATION

J_{Ic} = 0.216742 kip/in.
T = 34.2117

Fig. L.4. Load vs displacement and J vs crack extension for the V-8A vessel special seam weld corresponding to specimen V8AJ3. The graphics and data are from the Babcock & Wilcox Company.[2]

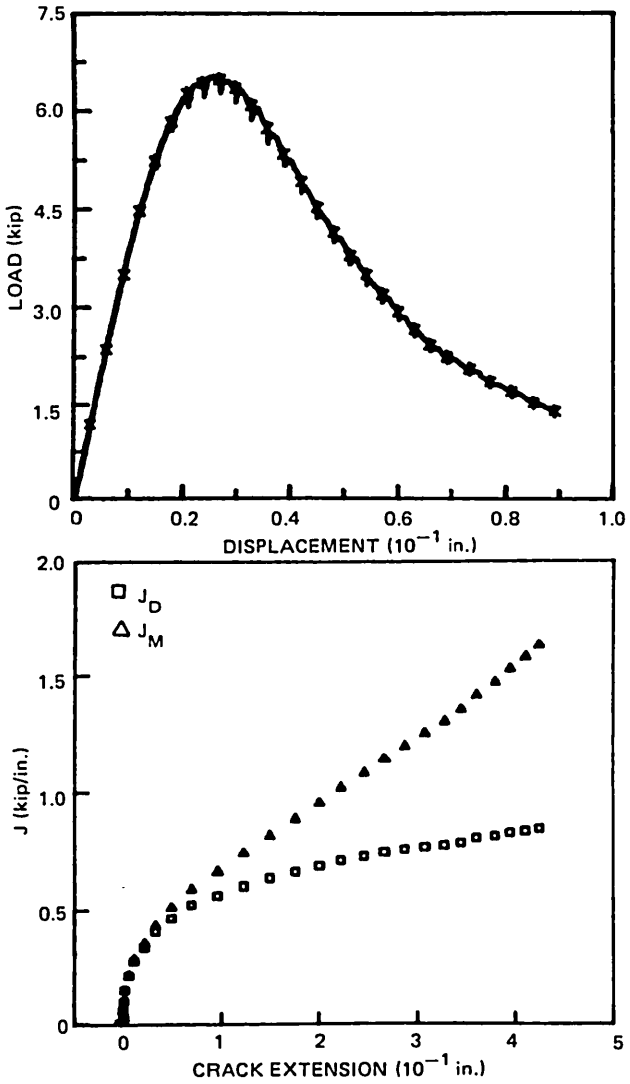

CRACK EXTENSION (in.)	J_D (kip/in.)	J_M (kip/in.)
−3.71850E−03	8.17902E−03	8.24461E−03
2.68817E−04	0.0287334	0.0290984
−3.80158E−04	0.0636564	0.0639142
4.61340E−03	0.107654	0.108029
1.35696E−03	0.157381	0.158274
5.29695E−03	0.217655	0.220647
0.0168166	0.282591*+	0.289308
0.0213795	0.343868*+	0.359109
0.0331699	0.410703*+	0.437112
0.0495373	0.46902*+	0.513004
0.0698658	0.523033	0.591333
0.0961986	0.56324	0.665987
0.122949	0.603564	0.744378
0.149619	0.638594	0.820259
0.175335	0.665829	0.889437
0.200916	0.690978	0.958891
0.223101	0.714904	1.02331
0.246777	0.731771	1.0857
0.267085	0.749673	1.14451
0.287585	0.760644	1.1985
0.308272	0.770807	1.25388
0.327312	0.777832	1.30404
0.344635	0.787162	1.35421
0.360239	0.810174	1.41597
0.380068	0.815355	1.47239
0.394585	0.831181	1.52744
0.411505	0.837553	1.58135
0.425854	0.845784	1.63153

* DENOTES POINTS USED FOR J_{Ic} DETERMINATION
\+ DENOTES POINTS USED IN TEARING MODULUS CALCULATION

J_{Ic} = 0.246568 kip/in.
T = 30.611

Fig. L.5. Load vs displacement and J vs crack extension for the V-8A vessel special seam weld corresponding to specimen V8AJ4. The graphics and data are from the Babcock & Wilcox Company.[2]

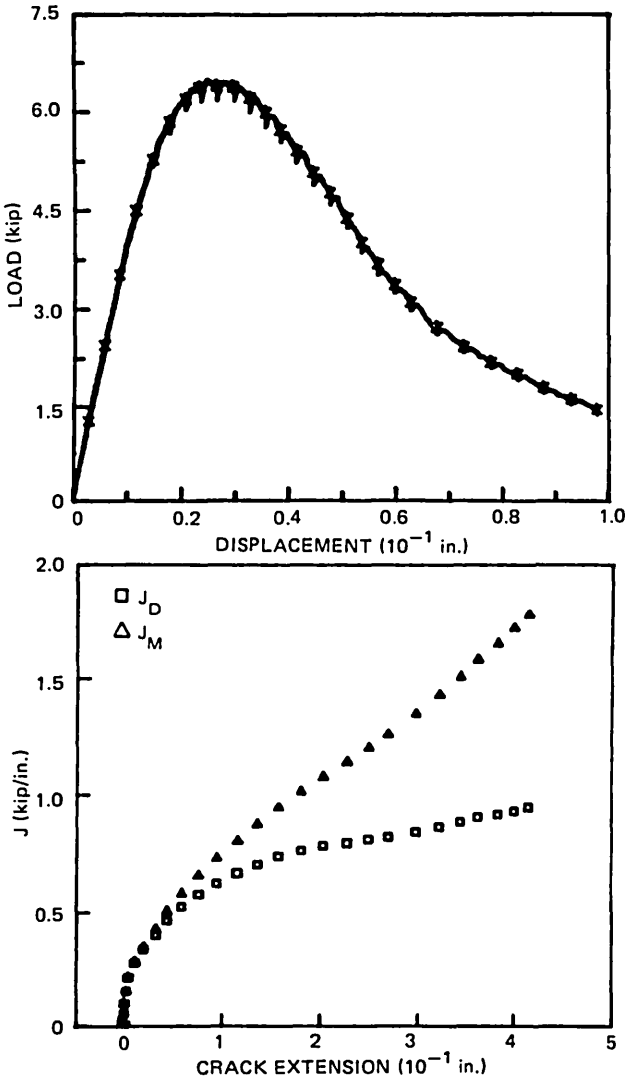

CRACK EXTENSION (in.)	J_D (kip/in.)	J_M (kip/in.)
1.44112E–03	8.77706E–03	8.97056E–03
–2.48694E–03	0.0298557	0.0297399
–4.38213E–04	0.0616803	0.0618986
–1.64986E–04	0.106514	0.106808
2.17819E–03	0.160111	0.161351
4.04894E–03	0.220842	0.223091
0.01033	0.282481*+	0.28895
0.019285	0.341432*+	0.355049
0.0317458	0.405103*+	0.431364
0.0432482	0.46914*+	0.506679
0.0588259	0.528849*+	0.585018
0.0762495	0.5803	0.659372
0.0948397	0.62729	0.732936
0.115077	0.670279	0.807129
0.136241	0.707926	0.879703
0.157197	0.742933	0.951622
0.180762	0.767686	1.02013
0.202873	0.786722	1.08212
0.228044	0.799964	1.14662
0.250013	0.814147	1.20752
0.269889	0.826173	1.26341
0.298136	0.847169	1.35101
0.322558	0.867157	1.43195
0.344033	0.889323	1.51102
0.362832	0.909474	1.58378
0.382399	0.922585	1.6544
0.400188	0.936358	1.72301
0.414249	0.951476	1.78335

* DENOTES POINTS USED FOR J_{Ic} DETERMINATION
\+ DENOTES POINTS USED IN TEARING MODULUS CALCULATION

J_{Ic} = 0.24868 kip/in.
T = 32.2289

Fig. L.6. Load vs displacement and J vs crack extension for the V-8A vessel special seam weld corresponding to specimen V8AJ5. The graphics and data are from the Babcock & Wilcox Company.[2]

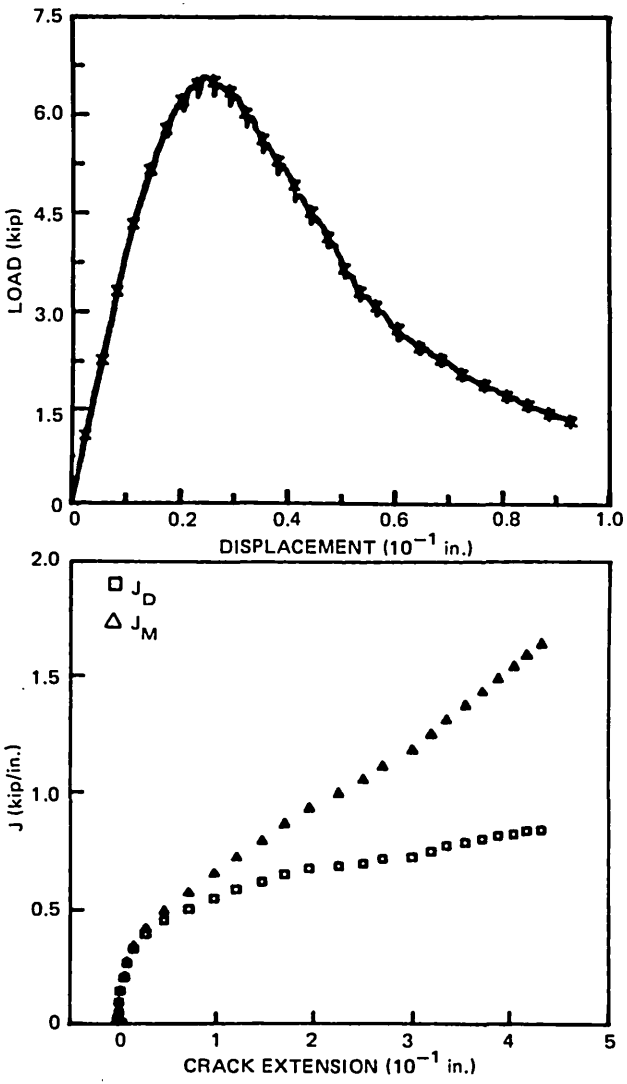

CRACK EXTENSION (in.)	J_D (kip/in.)	J_M (kip/in.)
3.37505E–03	6.84689E–03	7.04438E–03
–1.70374E–03	0.0266741	0.0265175
7.27177E–05	0.0558004	0.0559055
5.99980E–04	0.0984379	0.0986783
1.60158E–03	0.150686	0.15131
5.87463E–03	0.209604	0.212454
8.72695E–03	0.272988*+	0.277714
0.0154874	0.33573*+	0.345806
0.0274681	0.400059*+	0.421235
0.0468783	0.456756*+	0.498384
0.0719566	0.505448	0.576486
0.0985371	0.551318	0.656707
0.120237	0.590014	0.726556
0.146624	0.621991	0.797433
0.169598	0.655462	0.867768
0.195195	0.680099	0.935996
0.225411	0.689094	0.998741
0.250258	0.700915	1.05681
0.269865	0.720088	1.11453
0.299761	0.728027	1.18444
0.318841	0.752827	1.25108
0.334721	0.77747	1.31253
0.354424	0.791301	1.37422
0.371607	0.805696	1.4324
0.387911	0.81899	1.48916
0.40449	0.825548	1.54178
0.416881	0.83957	1.59162
0.431447	0.844221	1.63997

* DENOTES POINTS USED FOR J_{Ic} DETERMINATION
+ DENOTES POINTS USED IN TEARING MODULUS CALCULATION

J_{Ic} = 0.261695 kip/in.
T = 29.2143

Fig. L.7. Load vs displacement and J vs crack extension for the V-8A vessel special seam weld corresponding to specimen V8AJ6. The graphics and data are from the Babcock & Wilcox Company.[2]

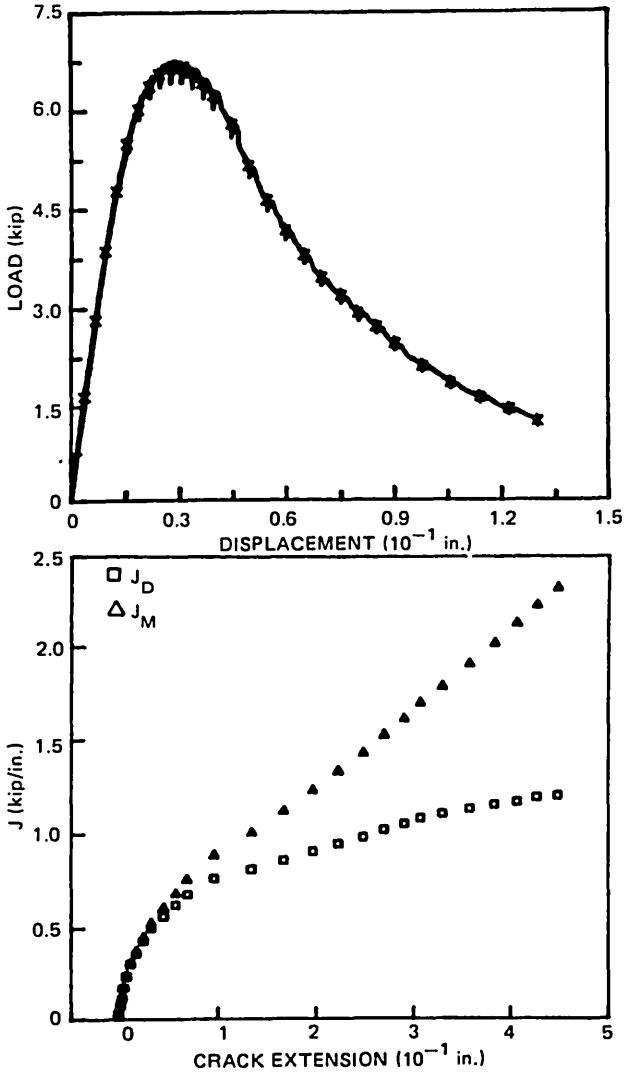

ORNL–DWG 86–5003 ETD

CRACK EXTENSION (in.)	J_D (kip/in.)	J_M (kip/in.)
−1.66249E−03	0.0144856	0.0146472
−1.34707E−03	0.0399773	0.0401714
4.91500E−04	0.0756428	0.0761945
2.17116E−03	0.122251	0.123323
3.27957E−03	0.178872	0.180431
6.61111E−03	0.241175	0.244649
0.0105602	0.307651*+	0.313938
0.0165252	0.36807*+	0.379338
0.0239173	0.436201*+	0.45464
0.0318323	0.506183*+	0.533374
0.0445571	0.56867*+	0.611596
0.0572058	0.629548*+	0.68972
0.0688751	0.687572	0.765047
0.0966095	0.768951	0.89281
0.13485	0.818739	1.01269
0.167445	0.867922	1.12696
0.197011	0.915434	1.23846
0.223552	0.954949	1.33966
0.249255	0.987626	1.43607
0.270094	1.02848	1.53213
0.290885	1.05753	1.61941
0.308	1.09188	1.70445
0.329219	1.11248	1.79112
0.357991	1.13862	1.91322
0.383754	1.15872	2.02496
0.407049	1.17894	2.13355
0.427009	1.1987	2.23355
0.447893	1.20709	2.33052

* DENOTES POINTS USED FOR J_{Ic} DETERMINATION
+ DENOTES POINTS USED IN TEARING MODULUS CALCULATION

J_{Ic} = 0.272966 kip/in.
T = 43.2901

Fig. L.8. Load vs displacement and J vs crack extension for the V-8A vessel special seam weld corresponding to specimen V8AJ7. The graphics and data are from the Babcock & Wilcox Company.[2]

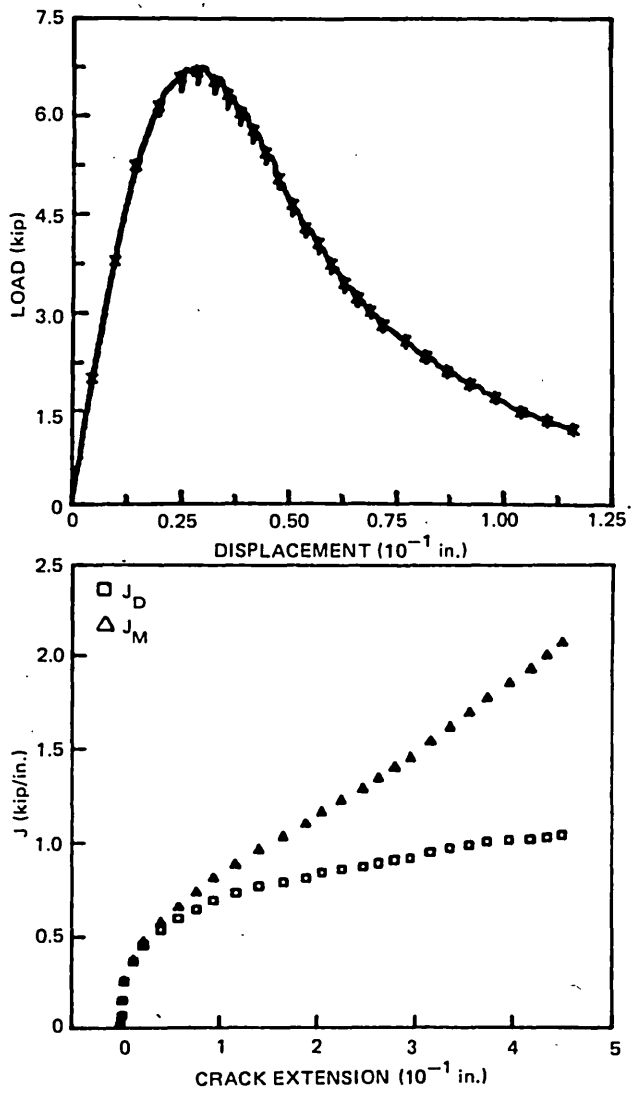

ORNL–DWG 86–5004 ETD

CRACK EXTENSION (in.)	J_D (kip/in.)	J_M (kip/in.)
−7.95960E−04	0.0207146	0.0208303
1.04368E−03	0.0740705	0.0745402
1.46806E−03	0.156953	0.15759
3.97193E−03	0.262658	0.26485
0.0129768	0.372603*+	0.382424
0.0231351	0.460394*+	0.480588
0.0413803	0.543925*+	0.585914
0.0591847	0.601558*+	0.667102
0.0778677	0.65277	0.745259
0.0947298	0.701105	0.819844
0.117561	0.73715	0.893863
0.014887	0.773243	0.971243
0.166298	0.796448	1.04195
0.189067	0.819518	1.10975
0.205763	0.848128	1.17287
0.226599	0.864872	1.23449
0.247958	0.879232	1.29684
0.264088	0.89911	1.3545
0.279783	0.916596	1.41025
0.295627	0.929362	1.46302
0.316162	0.959796	1.5485
0.336616	0.980053	1.62651
0.356145	0.997796	1.70224
0.374119	1.01722	1.77771
0.397384	1.02258	1.85933
0.418411	1.0283	1.93732
0.435507	1.03847	2.00914
0.450396	1.05222	2.07916

* DENOTES POINTS USED FOR J_{Ic} DETERMINATION
\+ DENOTES POINTS USED IN TEARING MODULUS CALCULATION

J_{Ic} = 0.342788 kip/in.
T = 30.4102

Fig. L.9. Load vs displacement and J vs crack extension for the V-8A vessel special seam weld corresponding to specimen V8AJ8. The graphics and data are from the Babcock & Wilcox Company.[2]

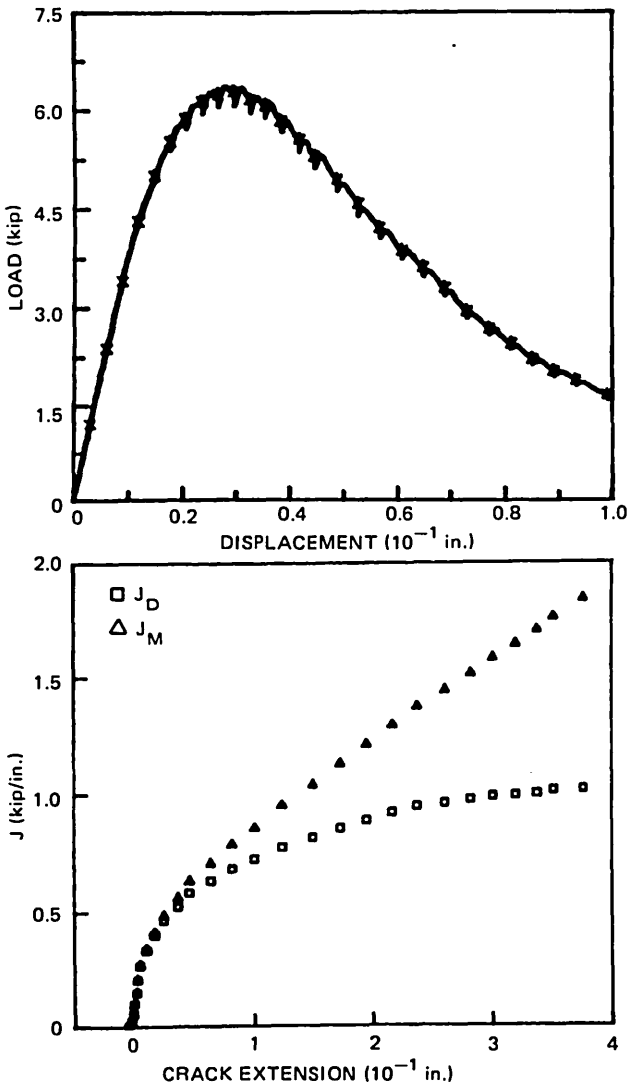

CRACK EXTENSION (in.)	J_D (kip/in.)	J_M (kip/in.)
−4.31335E−03	8.76265E−03	8.82286E−03
−2.84040E−03	0.030257	0.0304363
−3.36409E−04	0.0625691	0.0631689
3.37482E−04	0.106572	0.10736
2.28488E−03	0.157548	0.159122
3.06606E−03	0.213655	0.215641
5.49030E−03	0.275166	0.278748
0.0108558	0.341726*+	0.349587
0.0169449	0.40787*+	0.421399
0.0248598	0.471348*+	0.493264
0.0377854	0.533216*+	0.5705
0.0474106	0.591273*+	0.641154
0.0652961	0.639623*+	0.714966
0.0833629	0.689589	0.792813
0.101342	0.73077	0.863726
0.125434	0.782326	0.958602
0.150563	0.823637	1.04852
0.17412	0.860986	1.13441
0.195601	0.897427	1.21808
0.216867	0.92879	1.29903
0.237638	0.953959	1.37511
0.260901	0.966652	1.44715
0.282098	0.980812	1.51788
0.301168	0.99385	1.58406
0.320392	0.999141	1.64481
0.338112	1.00648	1.70531
0.351986	1.01979	1.76185
0.376497	1.02155	1.84379

* DENOTES POINTS USED FOR J_{Ic} DETERMINATION
+ DENOTES POINTS USED IN TEARING MODULUS CALCULATION

J_{Ic} = 0.328385 kip/in.
T = 34.0931

Fig. L.10. Load vs displacement and J vs crack extension for the V-8A vessel special seam weld corresponding to specimen V8AJ9. The graphics and data are from the Babcock & Wilcox Company.[2]

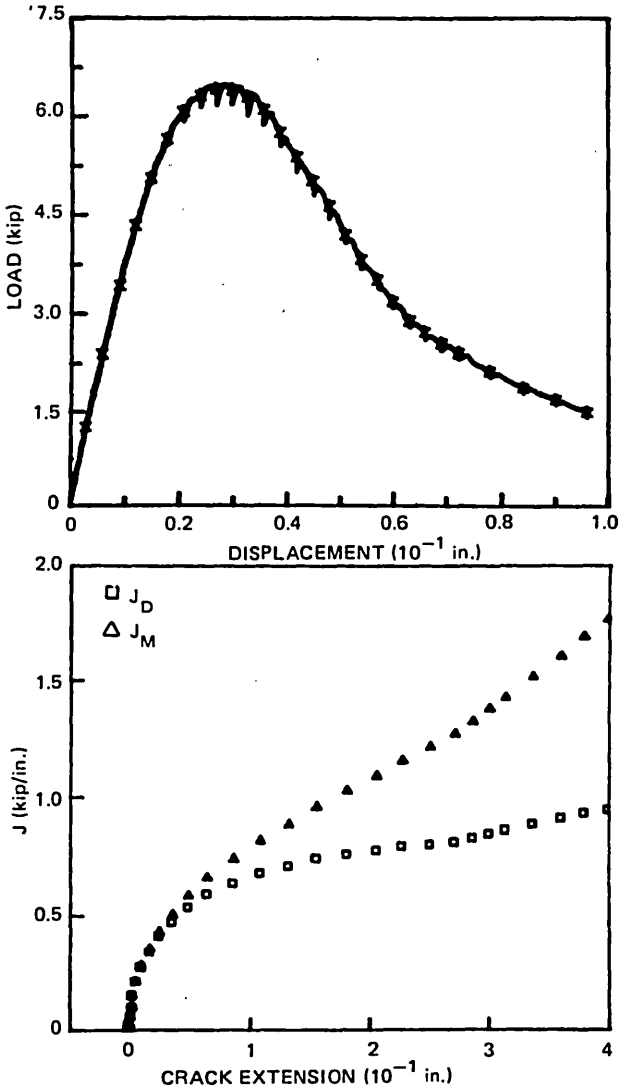

ORNL–DWG 86–5006 ETD

CRACK EXTENSION (in.)	J_D (kip/in.)	J_M (kip/in.)
−2.01464E−05	9.35677E−03	9.53790E−03
−1.05846E−03	0.031009	0.0311038
2.33412E−04	0.0649118	0.0652304
1.92714E−03	0.107002	0.107802
1.74427E−03	0.157863	0.158589
4.82655E−03	0.217722	0.220134
9.07397E−03	0.280671*+	0.286002
0.0164893	0.348681*+	0.3602
0.0241966	0.414441*+	0.433449
0.0351402	0.475525*+	0.506591
0.0487621	0.538871*+	0.58683
0.0644217	0.594072*+	0.663401
0.0859742	0.640559	0.741822
0.108819	0.682119	0.819887
0.131604	0.713577	0.890055
0.154716	0.744944	0.963129
0.180764	0.76455	1.03211
0.205378	0.779799	1.09624
0.227493	0.797184	1.15968
0.25031	0.805602	1.21745
0.270645	0.816219	1.27381
0.285488	0.834543	1.32701
0.299846	0.852069	1.37966
0.313301	0.866737	1.42856
0.336683	0.894576	1.51978
0.359279	0.917228	1.60768
0.379187	0.939354	1.69099
0.398695	0.953956	1.76882

* DENOTES POINTS USED FOR J_{Ic} DETERMINATION
+ DENOTES POINTS USED IN TEARING MODULUS CALCULATION

J_{Ic} = 0.269698 kip/in.
T = 35.2055

Fig. L.11. Load vs displacement and J vs crack extension for the V-8A vessel special seam weld corresponding to specimen V8AJ10. The graphics and data are from the Babcock & Wilcox Company.[2]

Table L.6. J-integral properties of special seam weld from vessel V-8A at 149°C[a]

V8AJ specimen No.	Orientation[b]	Power law parameters[c]					
		ASTM range[d]			Full range[d]		
		c	n	Points included	c	n	Points included
1	CR	0.072147	0.363066	7–10	0.071217	0.279183	7–28
2	CR	0.081745	0.385324	7–11	0.079360	0.387258	7–28
3	CA	0.074490	0.384070	7–11	0.074656	0.376149	7–28
4	CA	0.075656	0.336728	7–10	0.074644	0.292165	7–28
5	CA	0.078808	0.362074	7–11	0.079055	0.324751	7–28
6	CA	0.077038	0.306538	7–10	0.075217	0.277547	7–28
7	CA	0.094764	0.430137	7–12	0.092079	0.352084	7–28
8	CA	0.093536	0.313698	5–8	0.092990	0.283061	5–28
9	CA	0.096343	0.363408	8–12	0.094203	0.306349	8–28
10	CA	0.086966	0.391510	7–11	0.083590	0.300295	7–28

[a] All specimens are 25-mm-thick compact specimens with 20% total side grooves.

[b] C — circumferential, A — axial, R — radial.

[c] $J = c(\Delta a)^n$ with J in kJ/m^2 and Δa in mm (J-deformation, J_D, only).

[d] Data ranges: ASTM — only data between ASTM E813 exclusion lines; full — all data with Δa beyond lower exclusion line.

References

1. H. A. Domian, *Vessel V-8A Repair and Preparation of Low Upper-Shelf Weldment*, ORNL/Sub/81-85813/1, report prepared for Oak Ridge Natl. Lab. by the Babcock & Wilcox Company, Alliance, Ohio, June 1982.

2. H. A. Domian and R. J. Futato, *J-Integral Test Results of HSST-ITV8A Low Upper Shelf Weld — Final Report*, Babcock & Wilcox Company, Research and Development Division, Alliance, Ohio, Febraury 1983.

Appendix M

VESSEL V-8A TEST DATA

This appendix presents a complete record of test data recorded by the computer-controlled data acquisition system. The locations of strain and crack-mouth-opening-displacement (CMOD) sensors and the definition of the coordinate system for locating sensors are described in Figs. 4.4 and 4.5 and Table 4.2. Locations of thermocouples are given in Table M.1.

Pressure, CMOD, strain, and temperature data are presented in a series of plots of the measured parameter vs time (Figs. M.1—M.39). Data from strain gage XE66 are excluded because the gage was faulty.

Prefixes for sensor numbers are

Temperature	TE
Pressure	PE
Strain	XE
CMOD	ZT
Instability parameter, $\dot{v}$	XM

Table M.1. Location of thermocouples on vessel V-8A

TE	Surface[a]	θ	x	z
1	0	180		385
2	0	180		—15
3	0	180		—385
4	0	0		385
5	0	0		235
6	0		—50	15
7	0		50	15
8	0	0		—235
9	0	0		—385
10	0	90		0
11	0	270		0
12	Closure			
13	Hemisphere			
14	I	0		385
15	I		105	0
16	I		—105	0
17	I	0		—385

[a]Cylindrical test section: 0 — outside; I — inside.

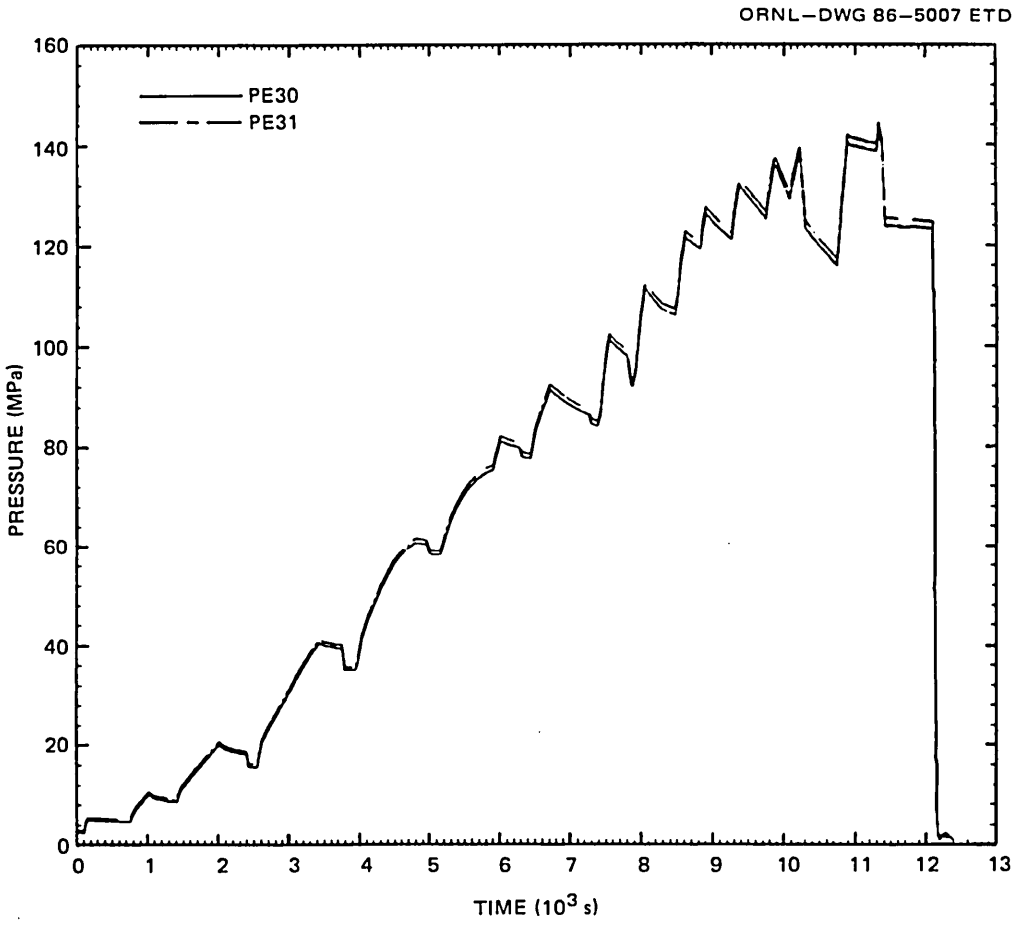

Fig. M.1. Pressure vs time.

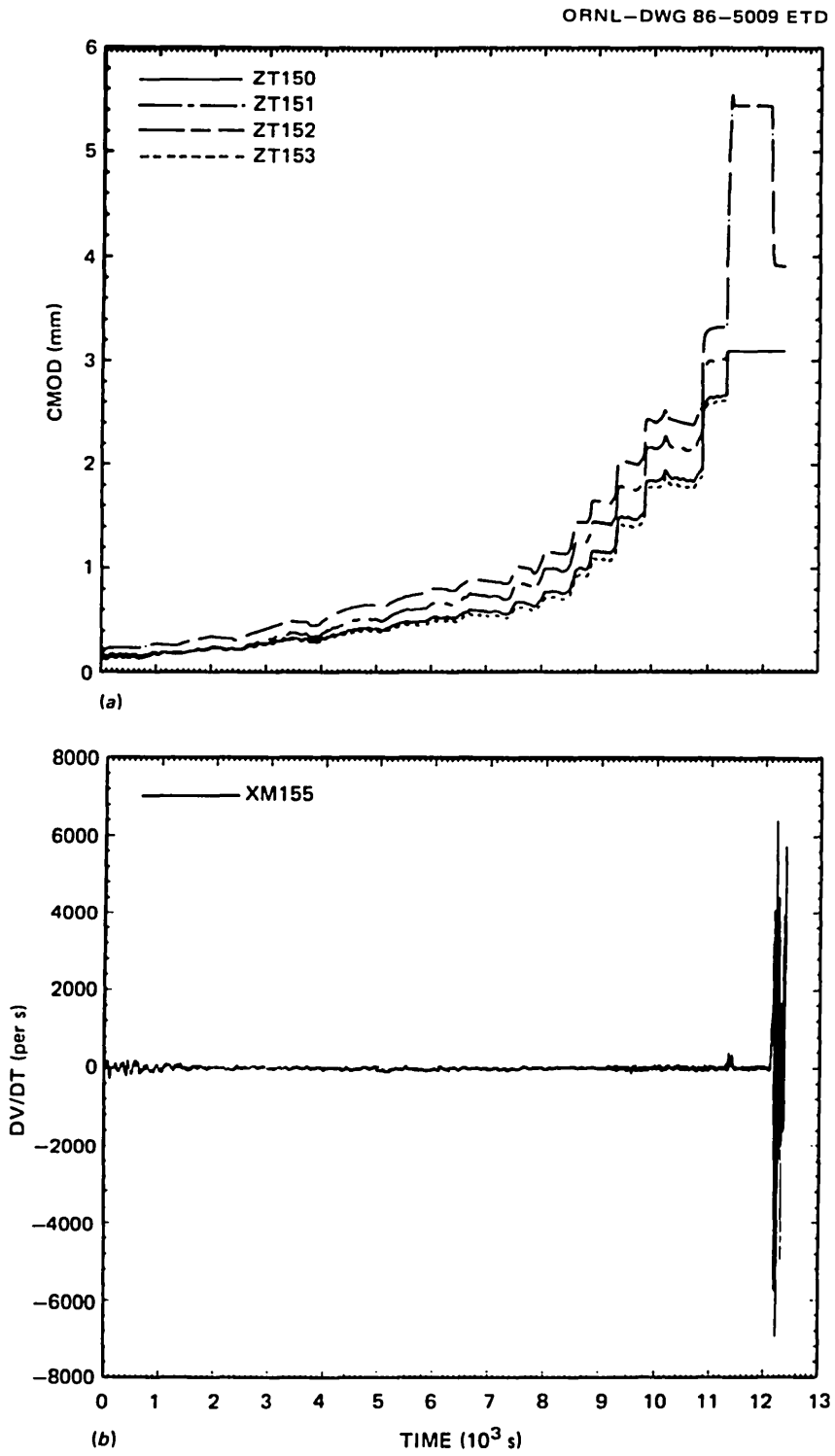

Fig. M.2. (*a*) CMOD vs time; (*b*) dv/dt vs time.

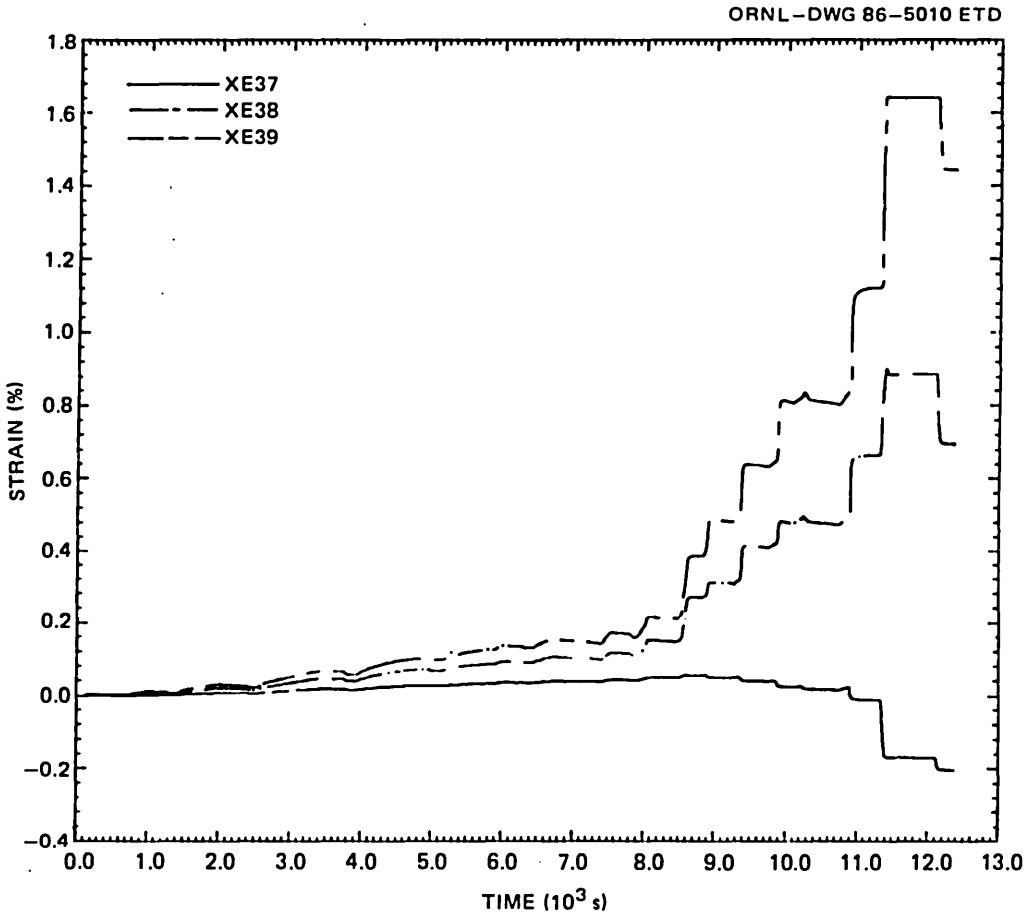

Fig. M.3. Strain vs time, XE37–39.

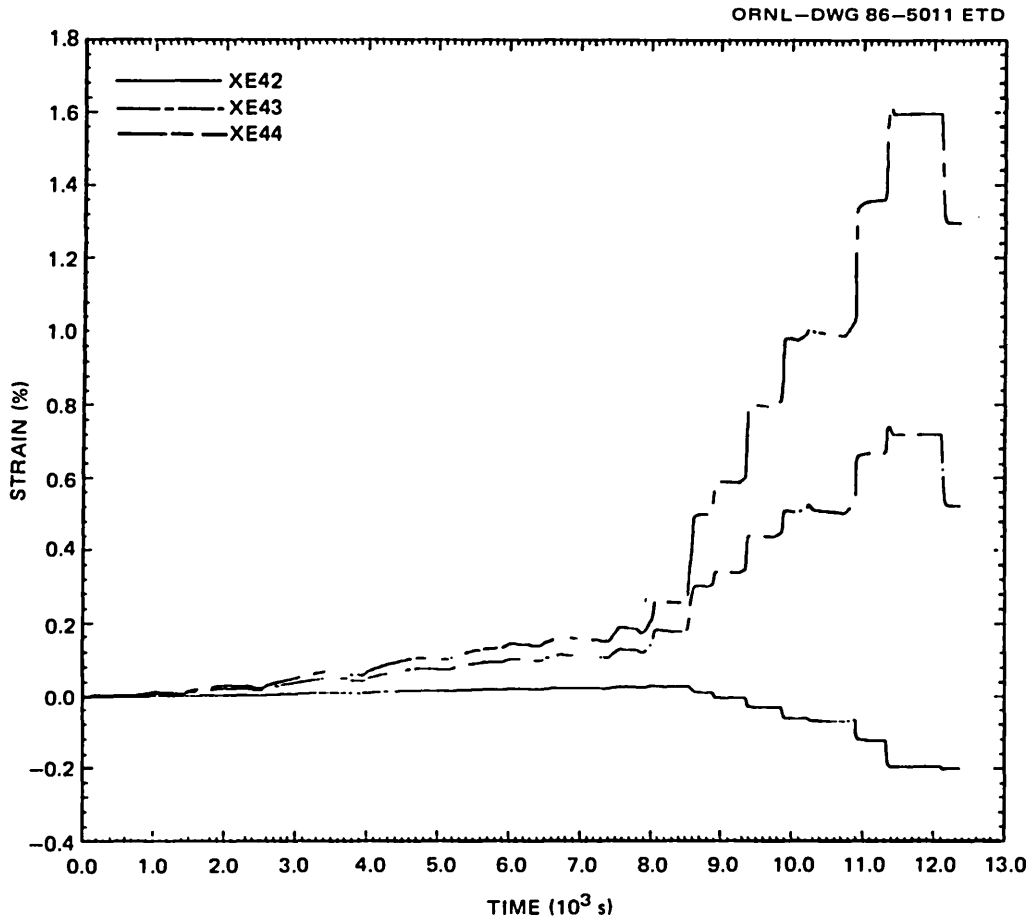

Fig. M.4. Strain vs time, XE42–44.

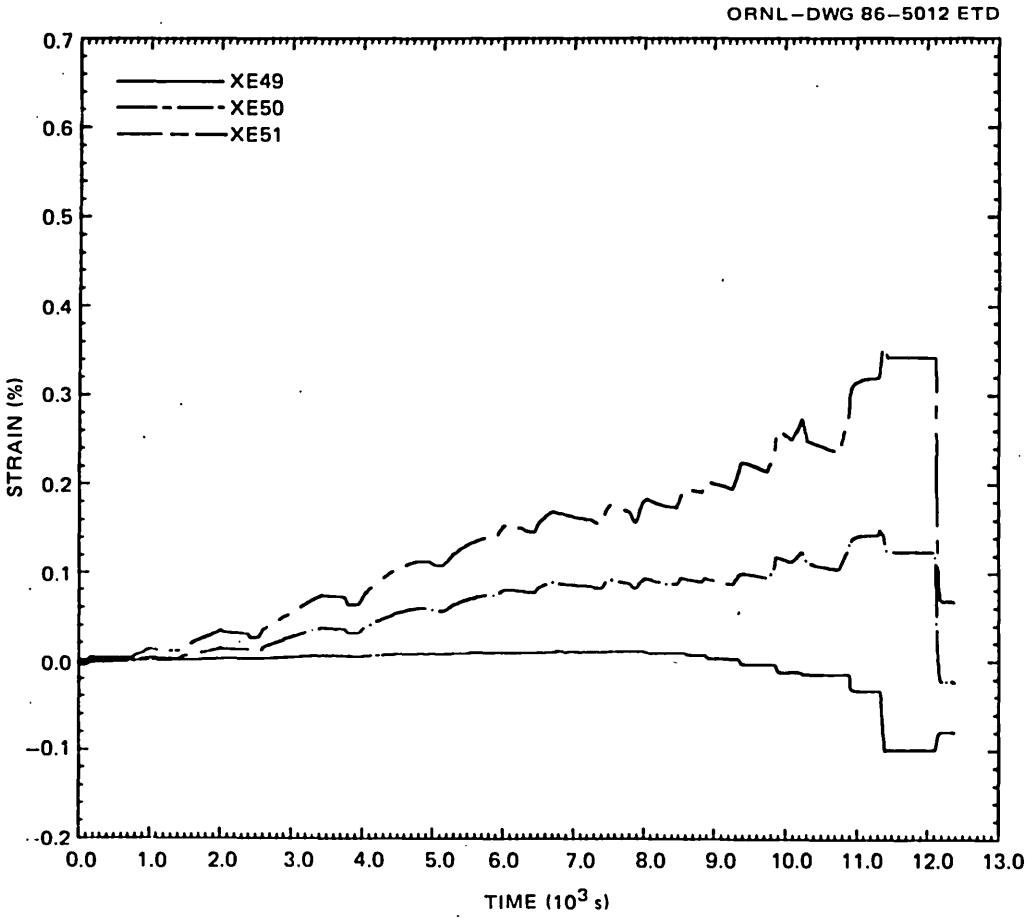

Fig. M.5. Strain vs time, XE49–51.

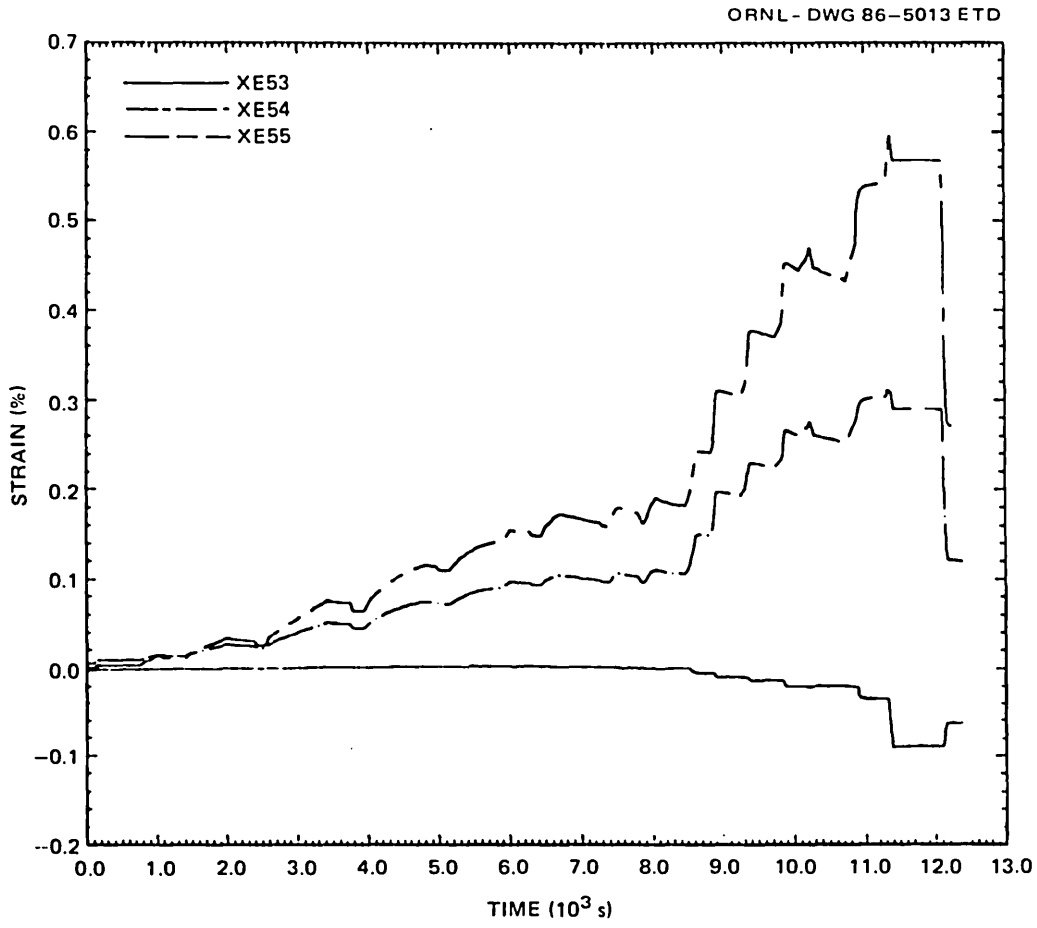

Fig. M.6. Strain vs time, XE53–55.

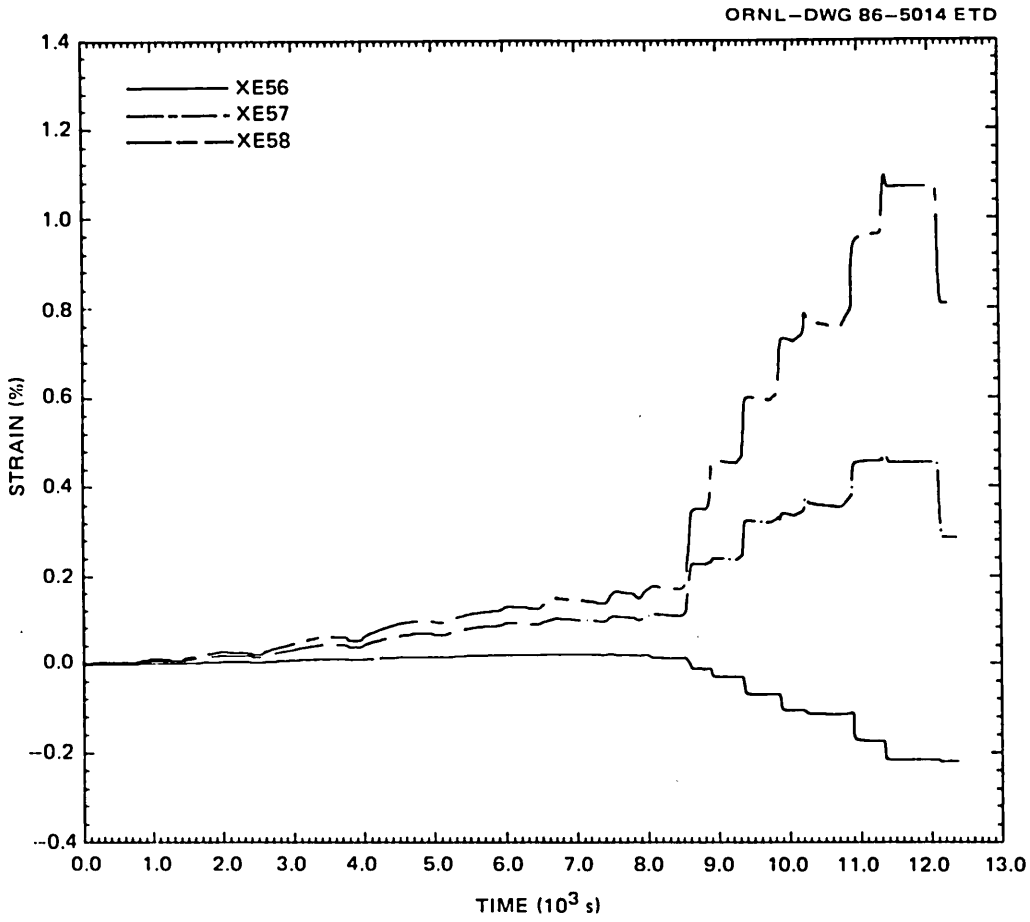

Fig. M.7. Strain vs time, XE57–59.

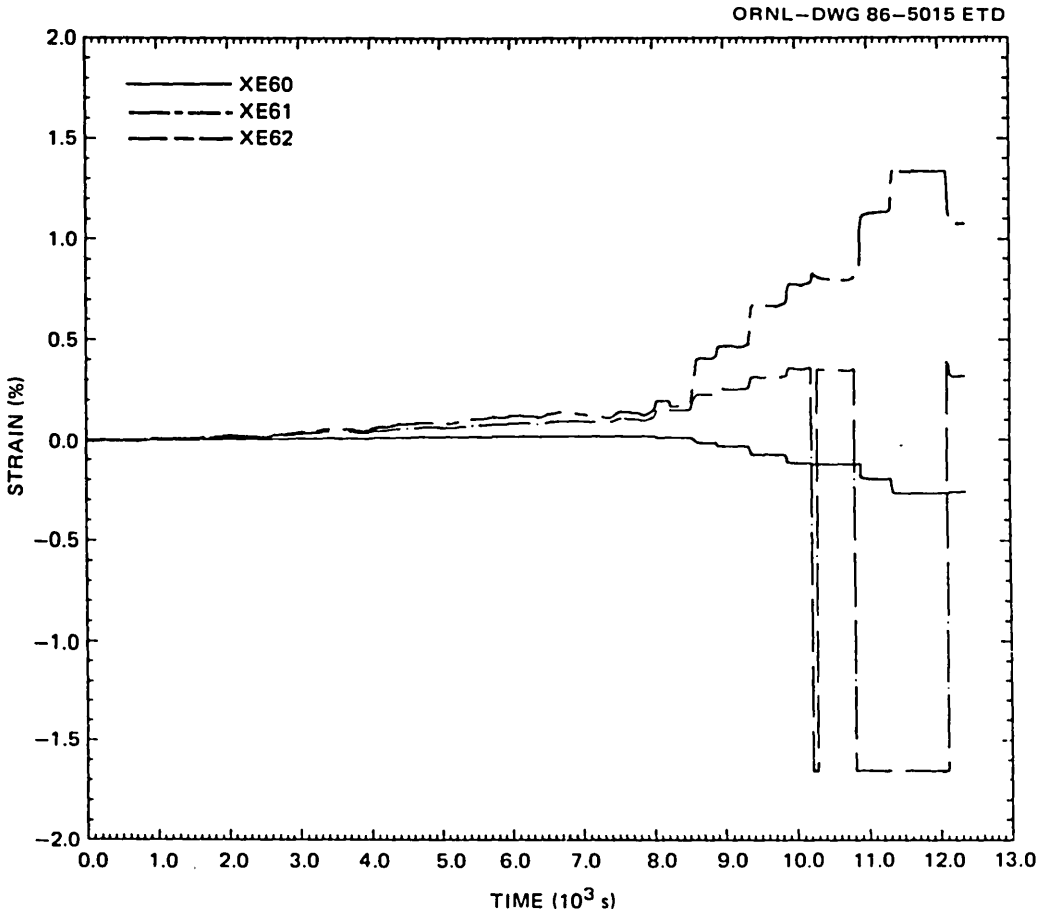

Fig. M.8. Strain vs time, XE60–62.

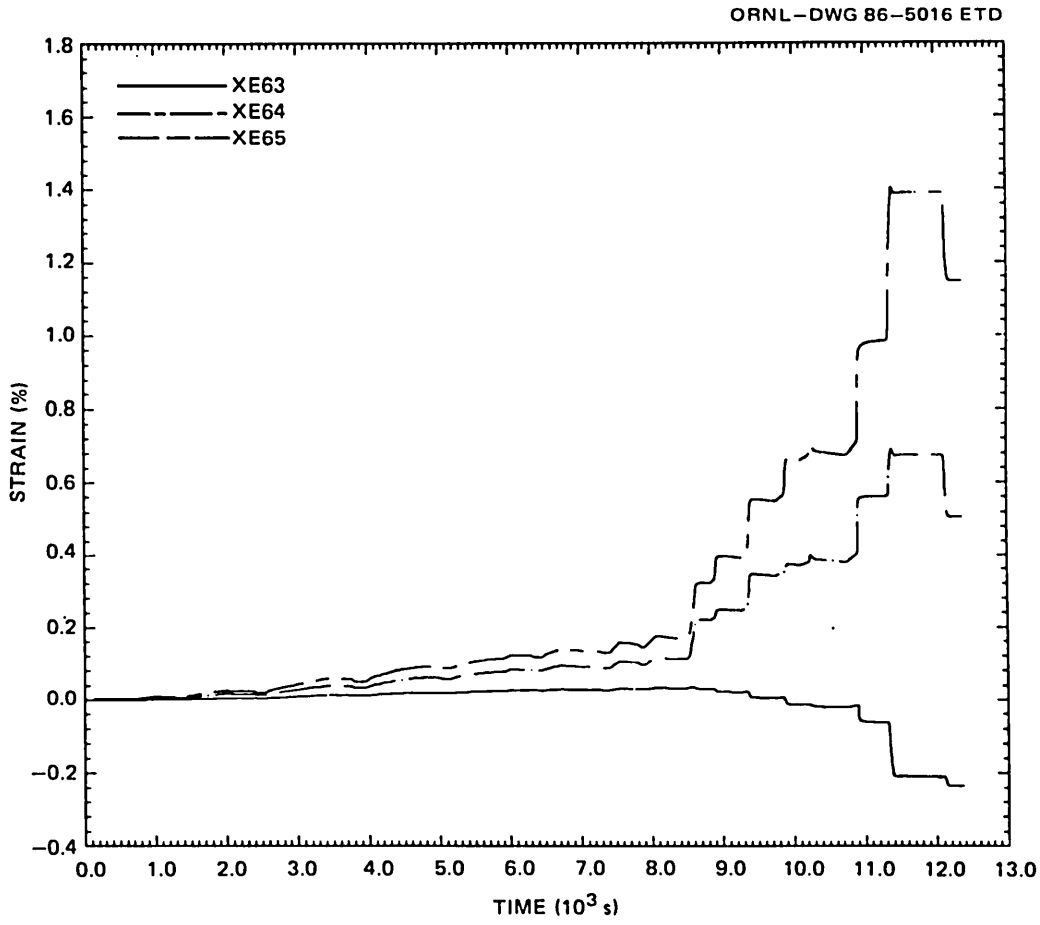

Fig. M.9. Strain vs time, XE63–65.

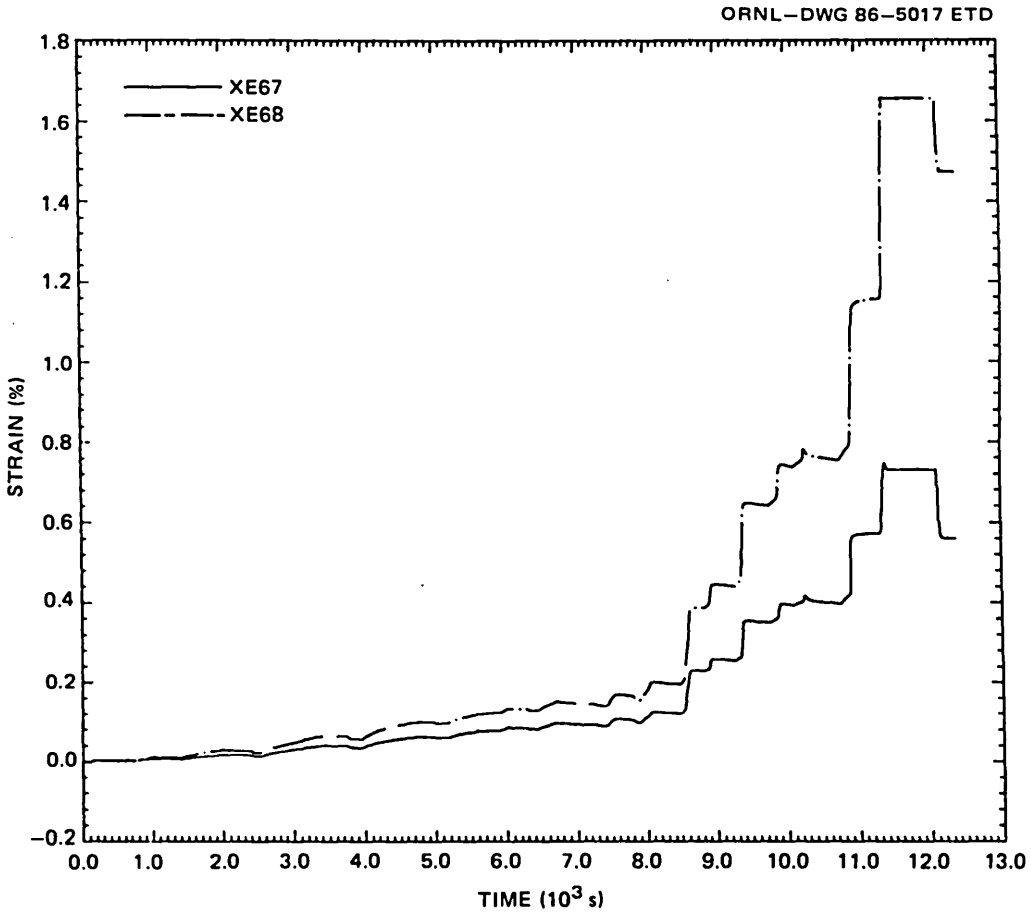

Fig. M.10. Strain vs time, XE67–68.

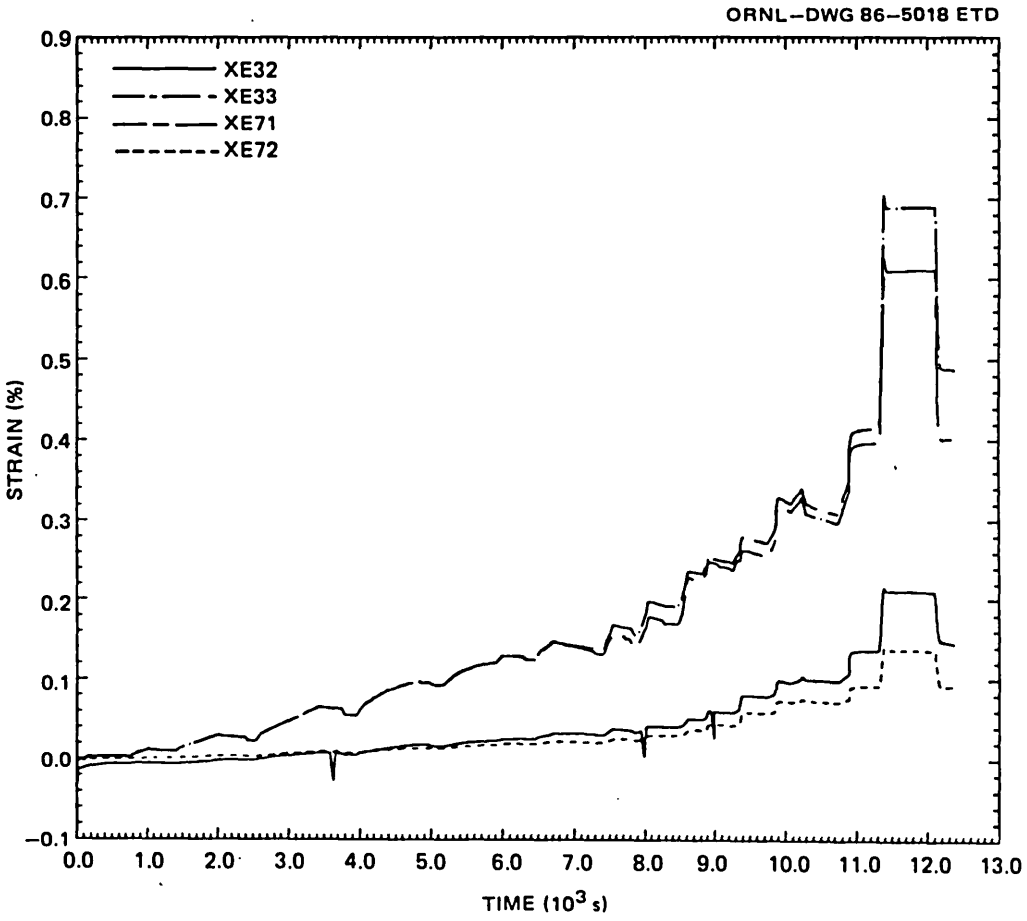

Fig. M.11. Strain vs time, XE32, 33, 71, and 72.

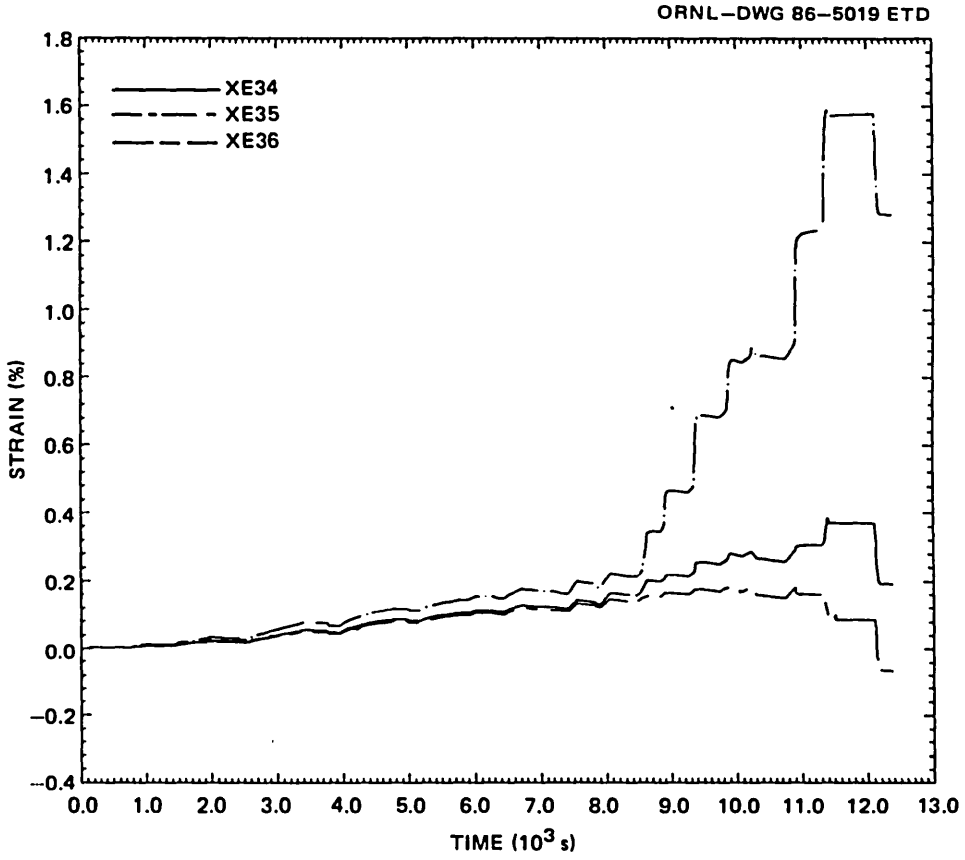

Fig. M.12. Strain vs time, XE34–36.

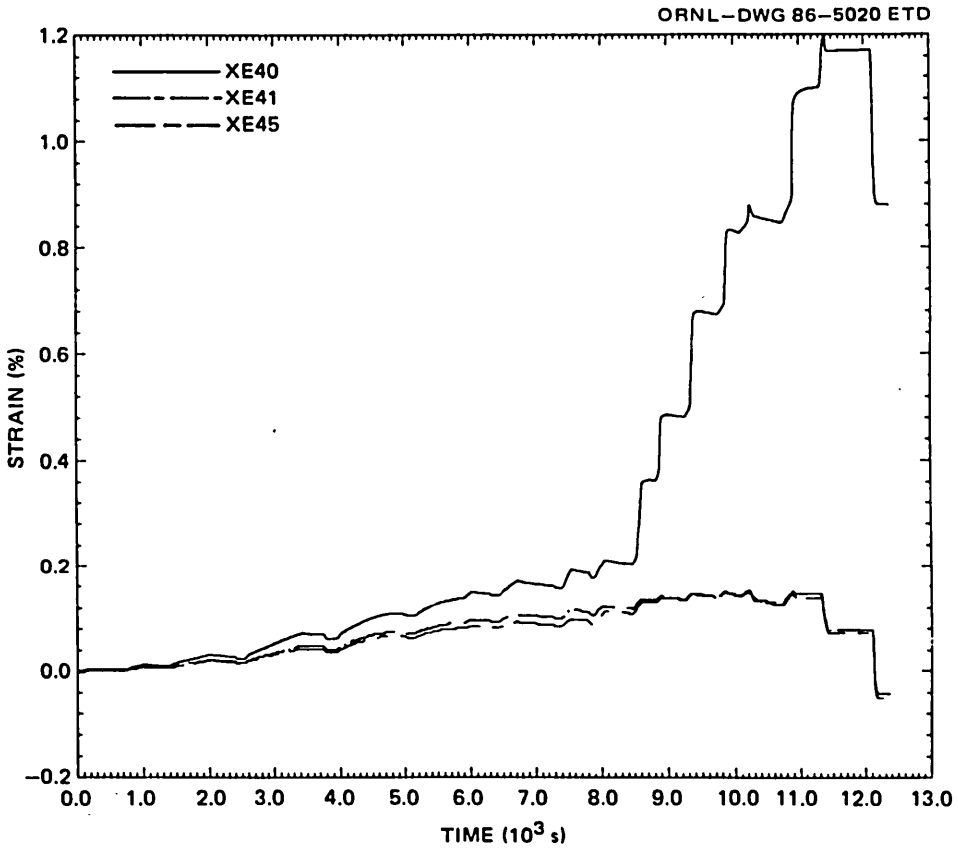

Fig. M.13. Strain vs time, XE40, 41, and 45.

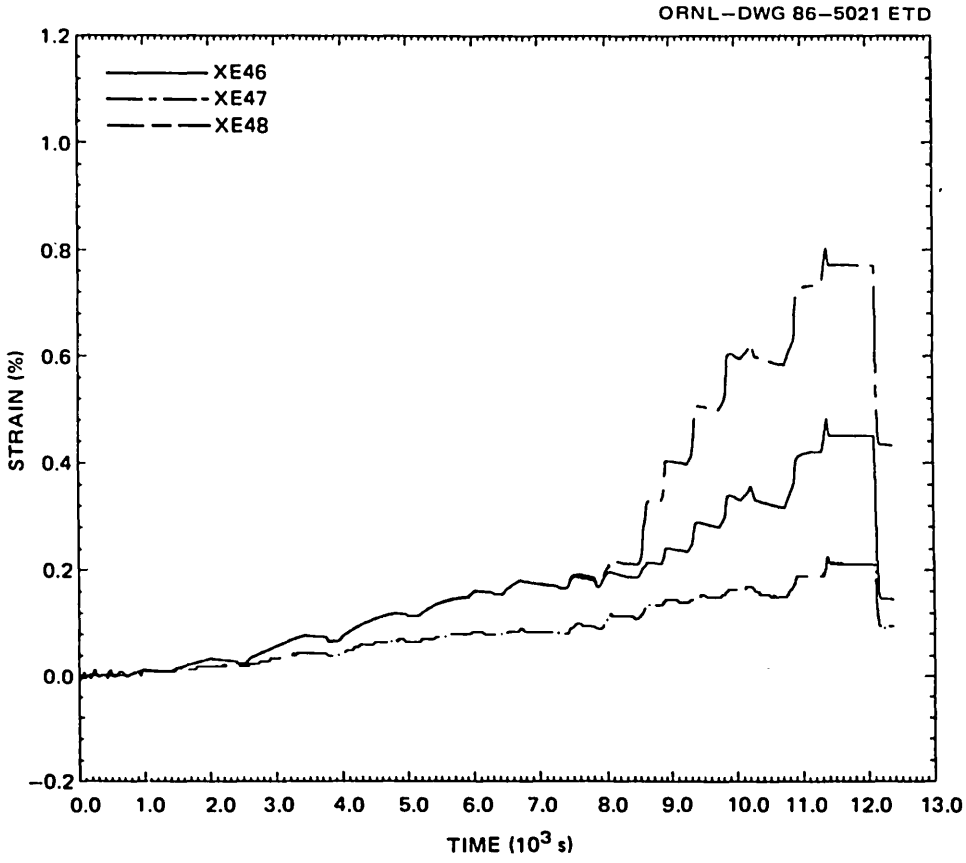

Fig. M.14. Strain vs time, XE46–48.

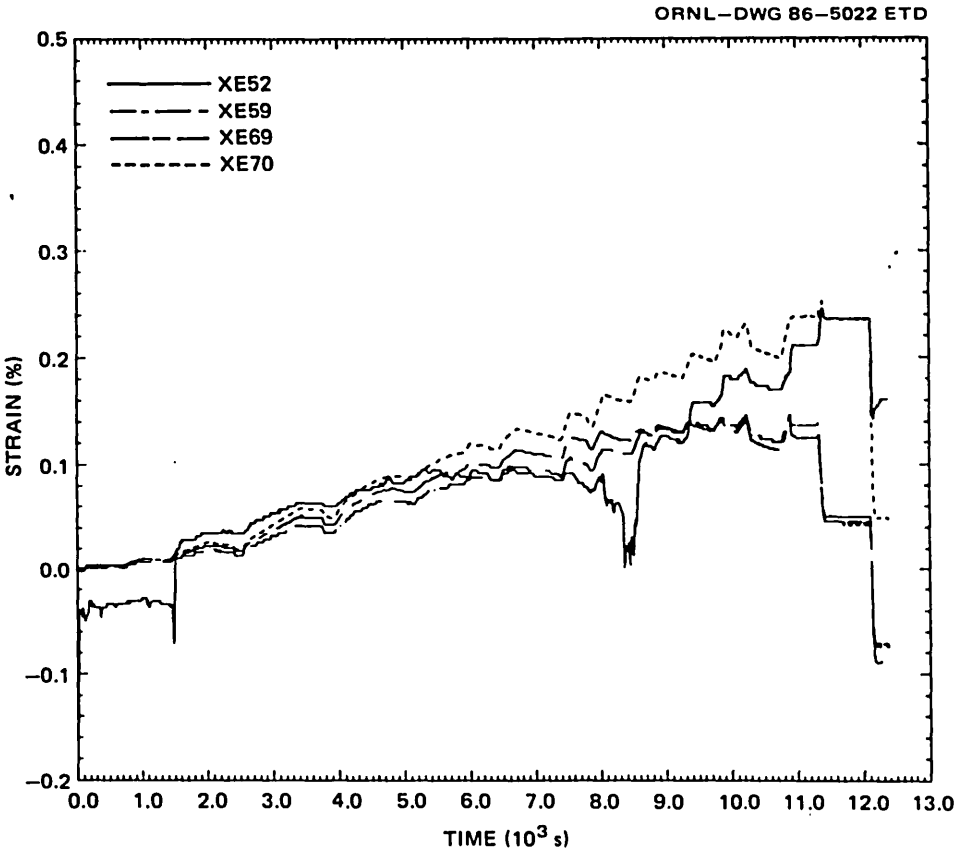

Fig. M.15. Strain vs time, XE52, 59, 69, and 70.

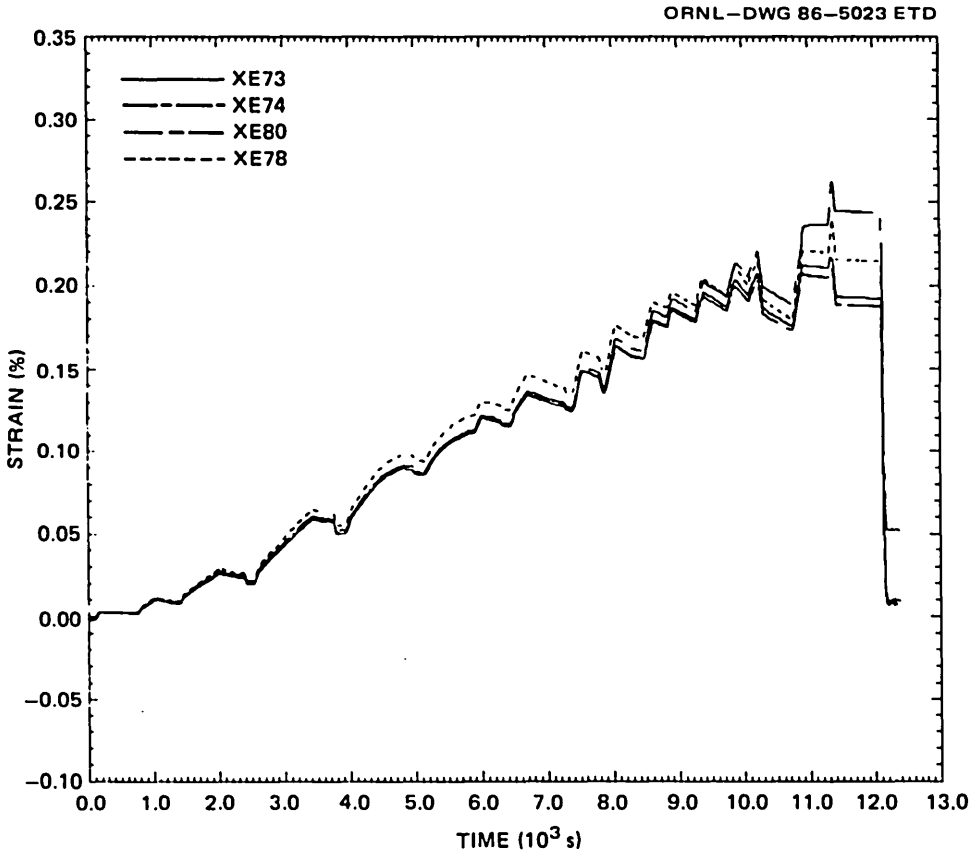

Fig. M.16. Strain vs time, XE73, 74, 79, and 80.

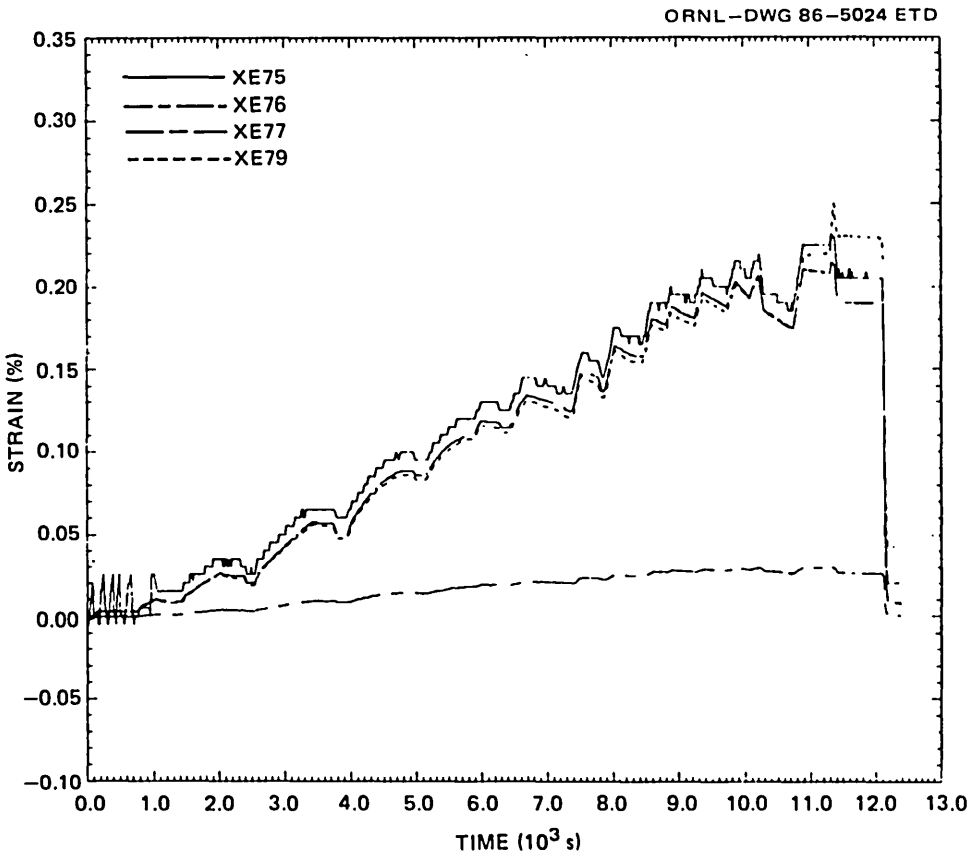

Fig. M.17. Strain vs time, XE75—77 and 79.

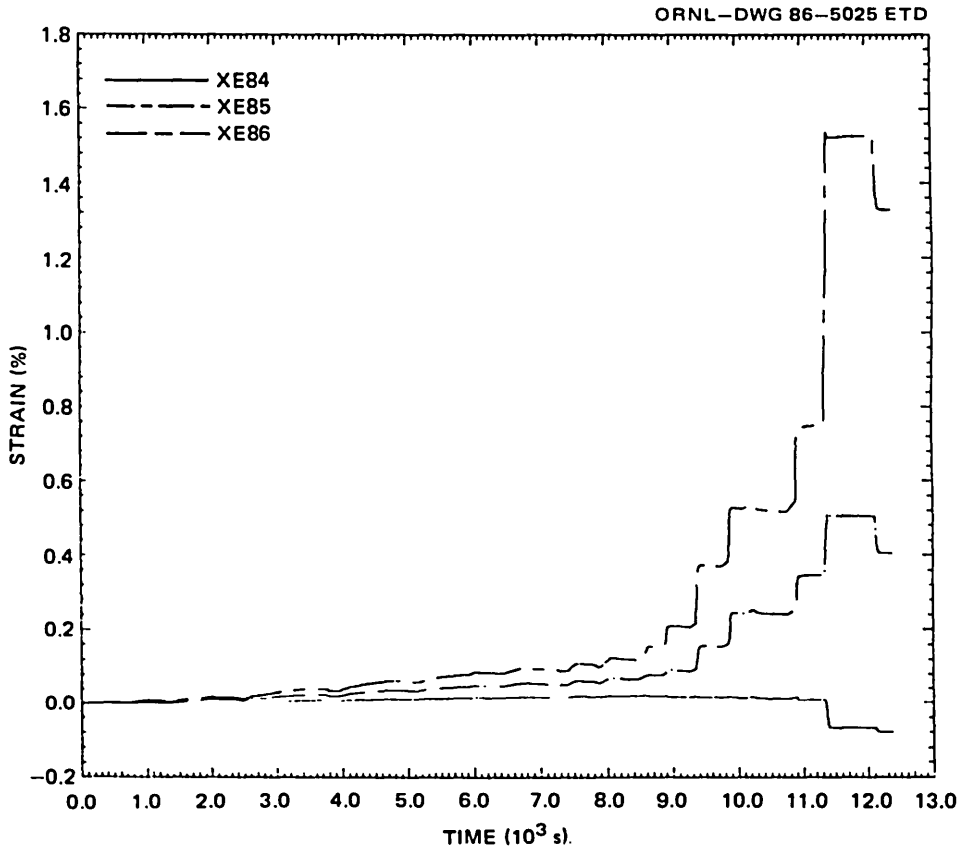

Fig. M.18. Strain vs time, XE84–86.

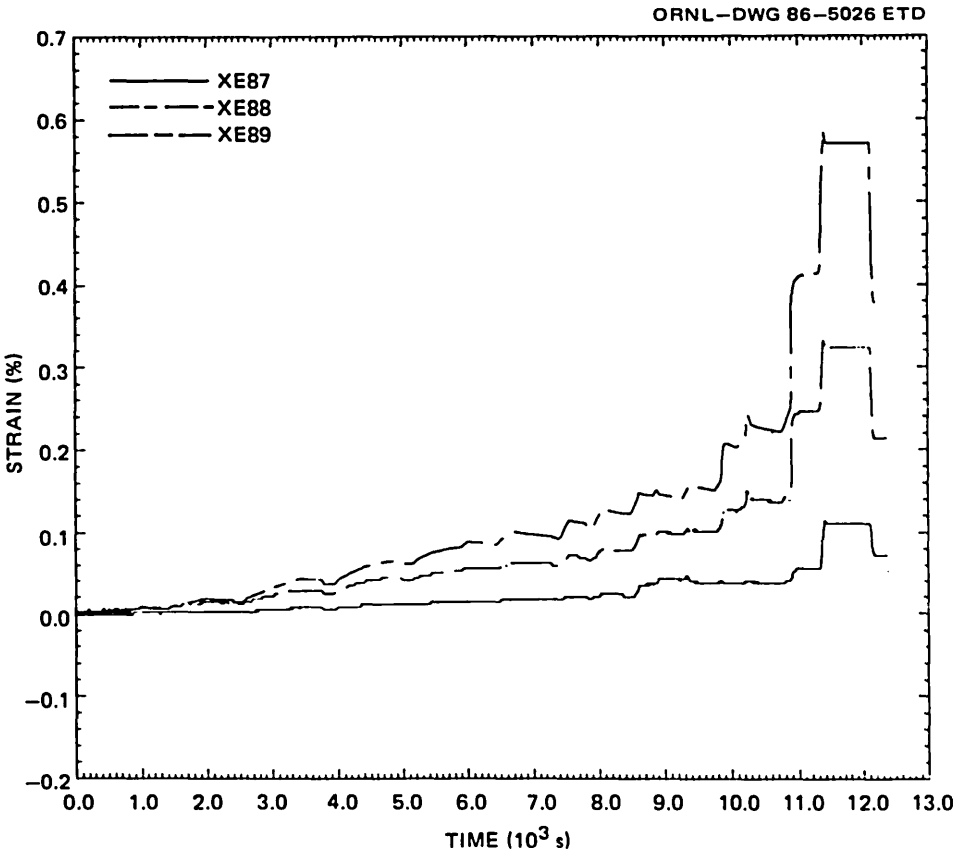

Fig. M.19. Strain vs time, XE87–89.

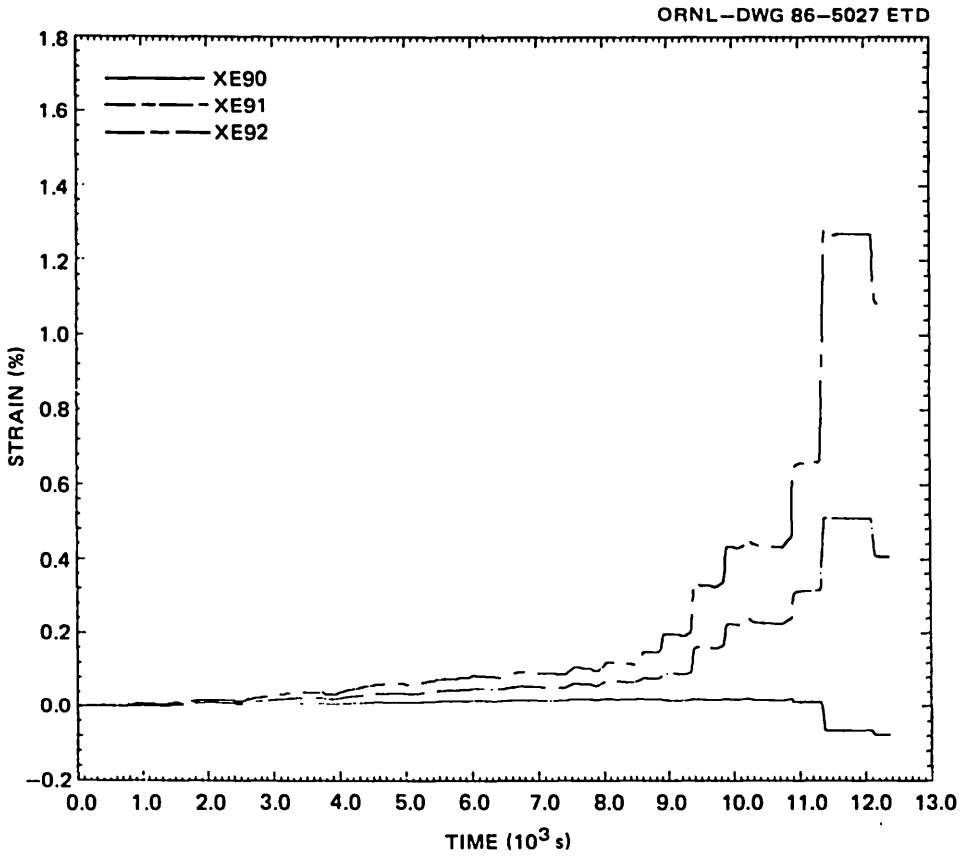

Fig. M.20. Strain vs time, XE90–92.

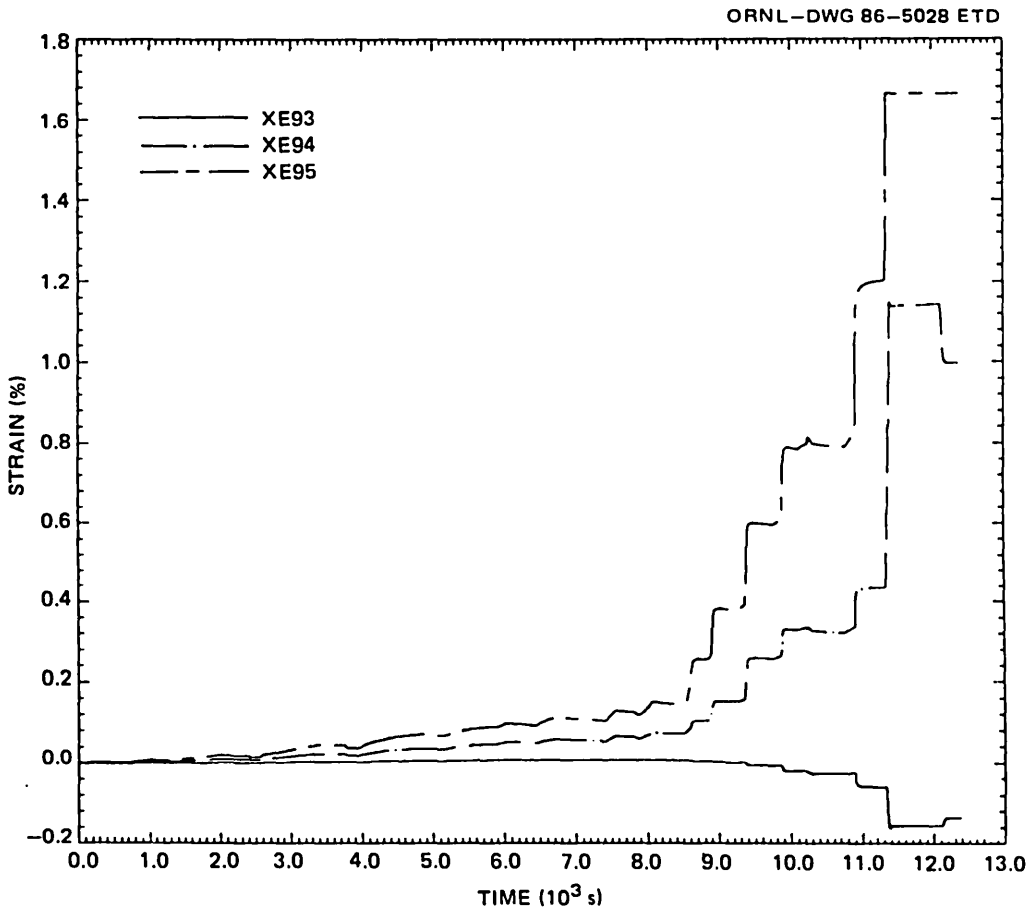

Fig. M.21. Strain vs time, XE93–95.

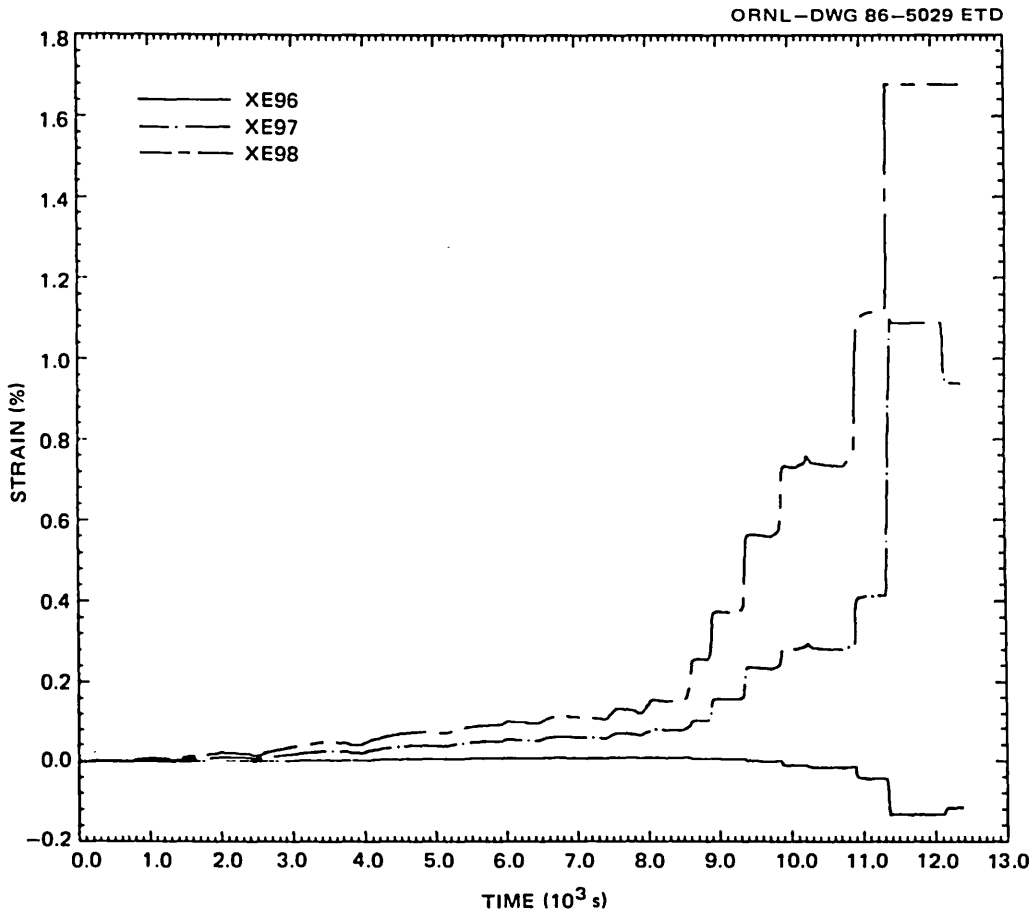

Fig. M.22. Strain vs time, XE96–98.

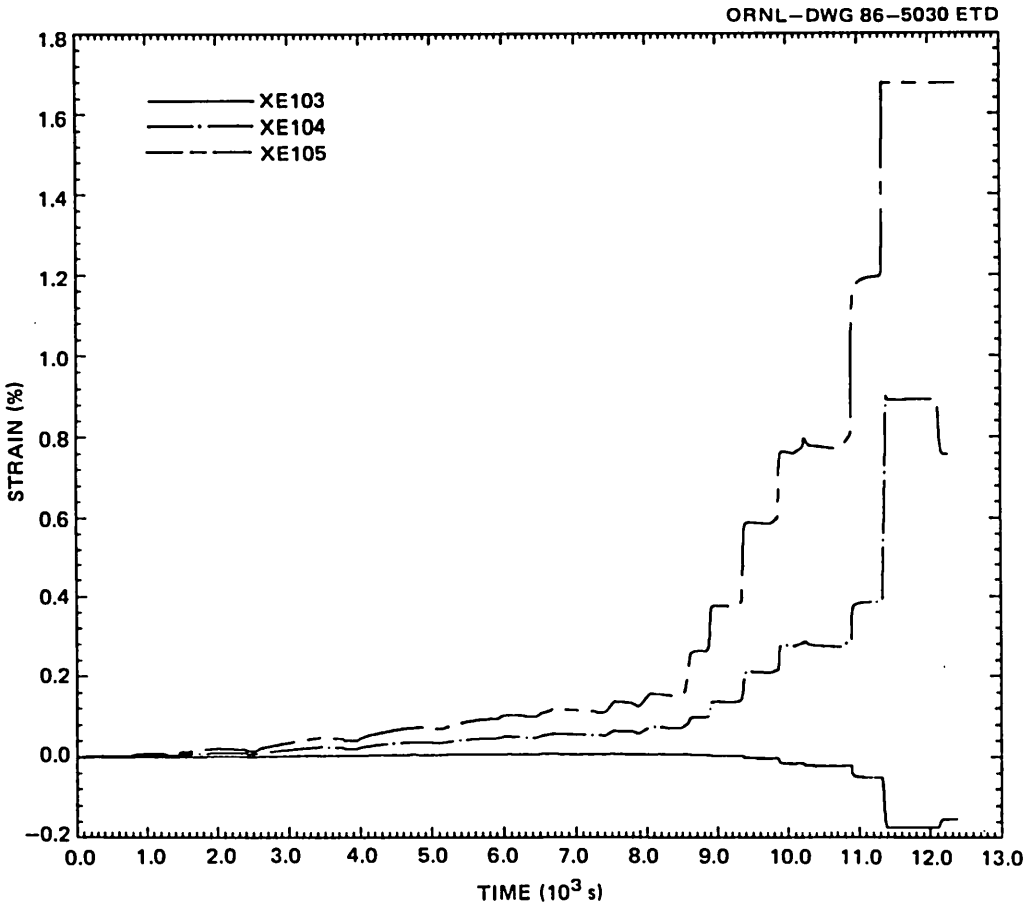

Fig. M.23. Strain vs time, XE103–105.

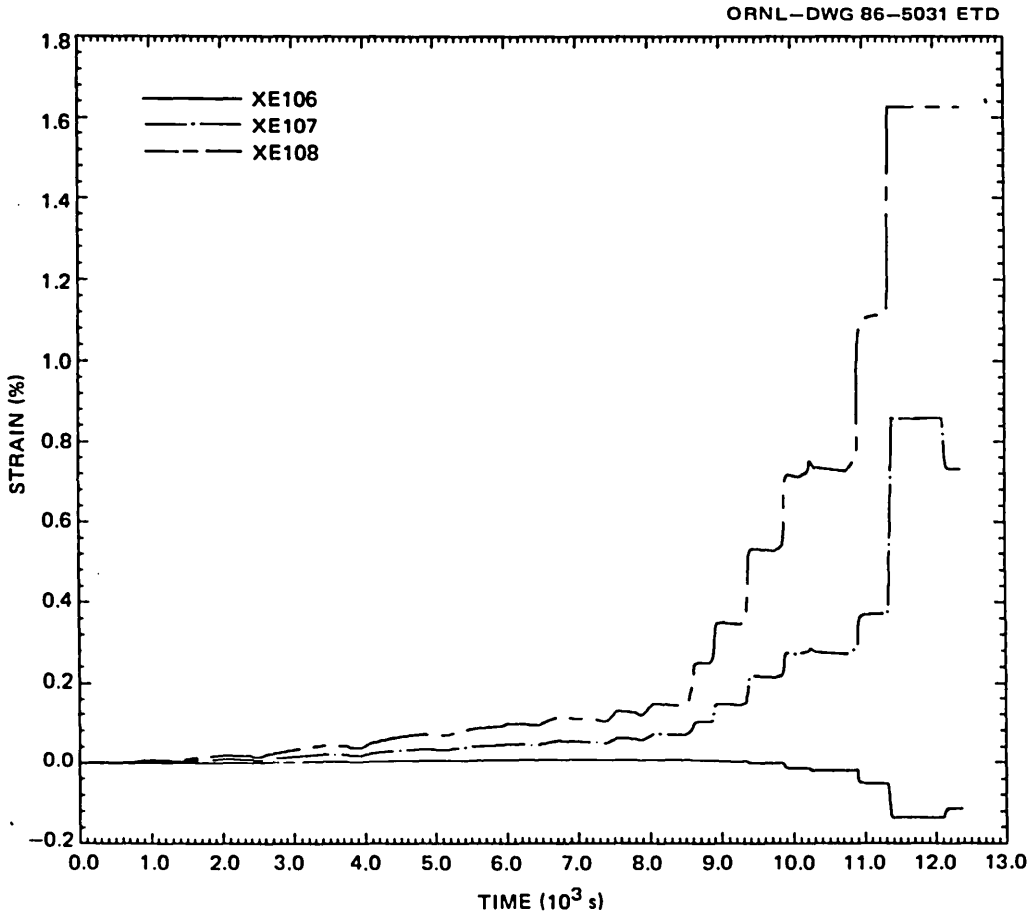

Fig. M.24. Strain vs time, XE106–108.

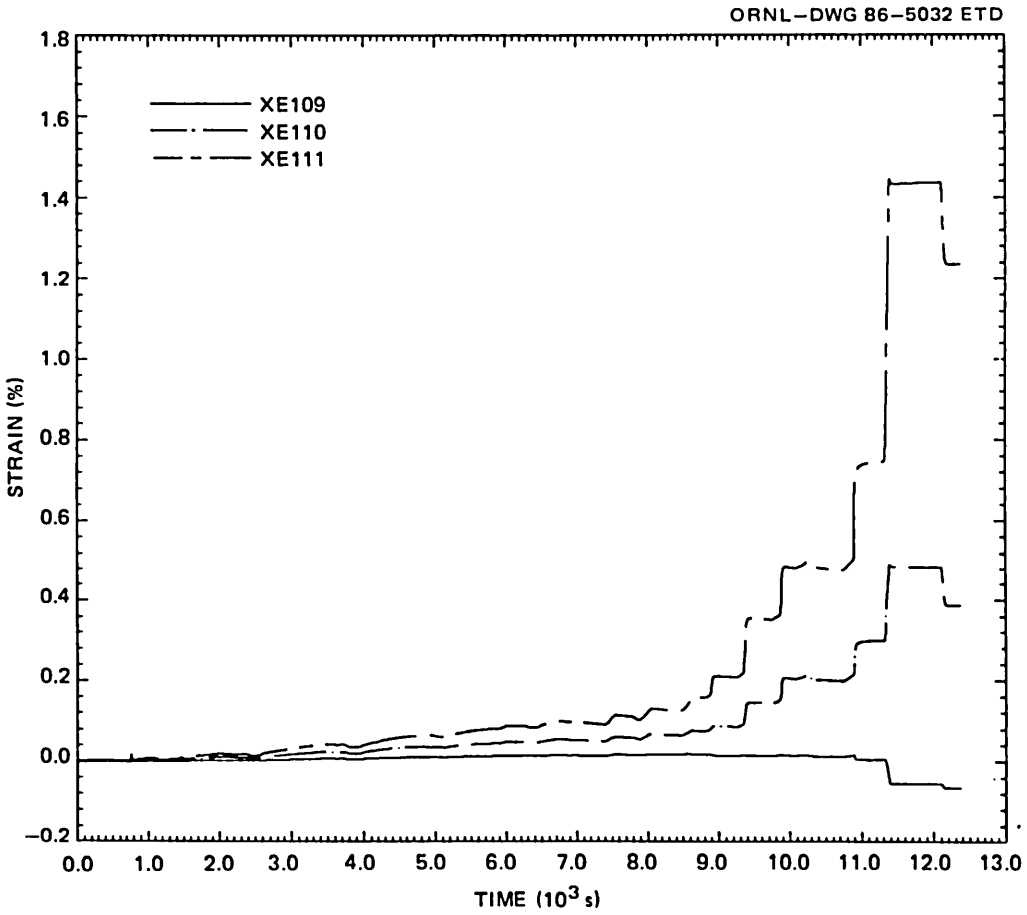

Fig. M.25. Strain vs time, XE109–111.

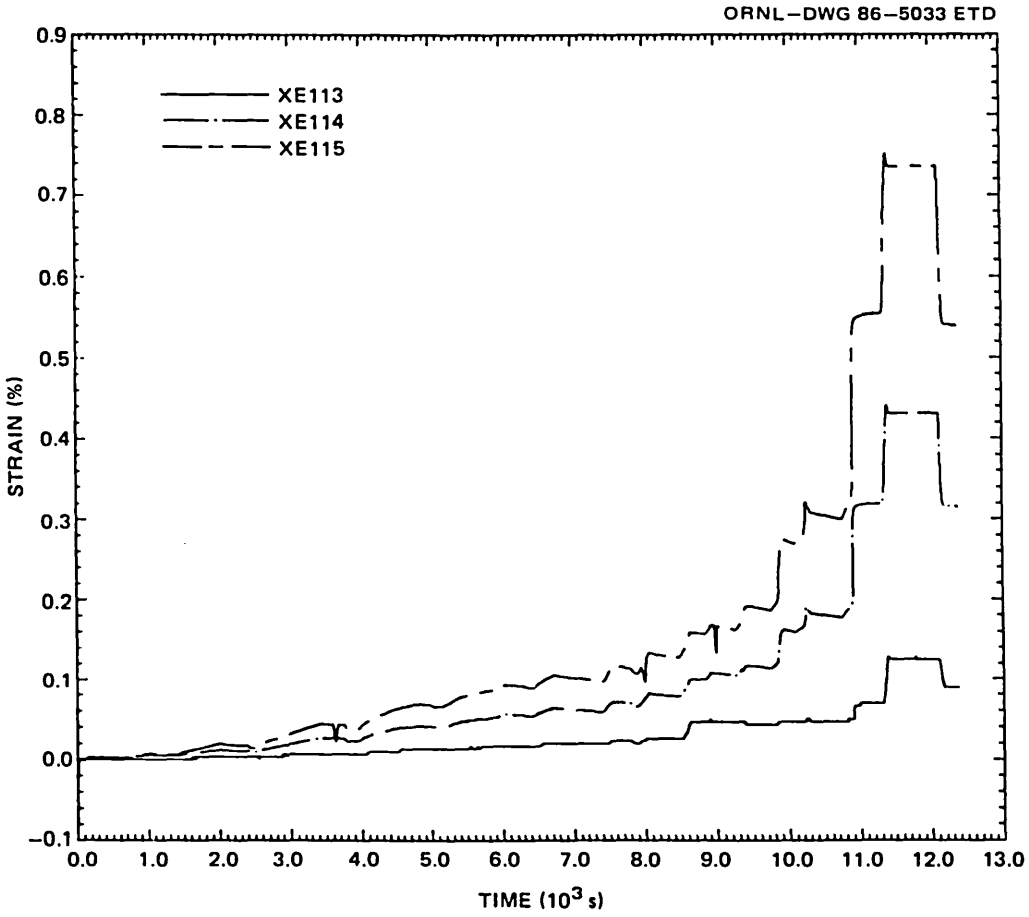

Fig. M.26. Strain vs time, XE113–115.

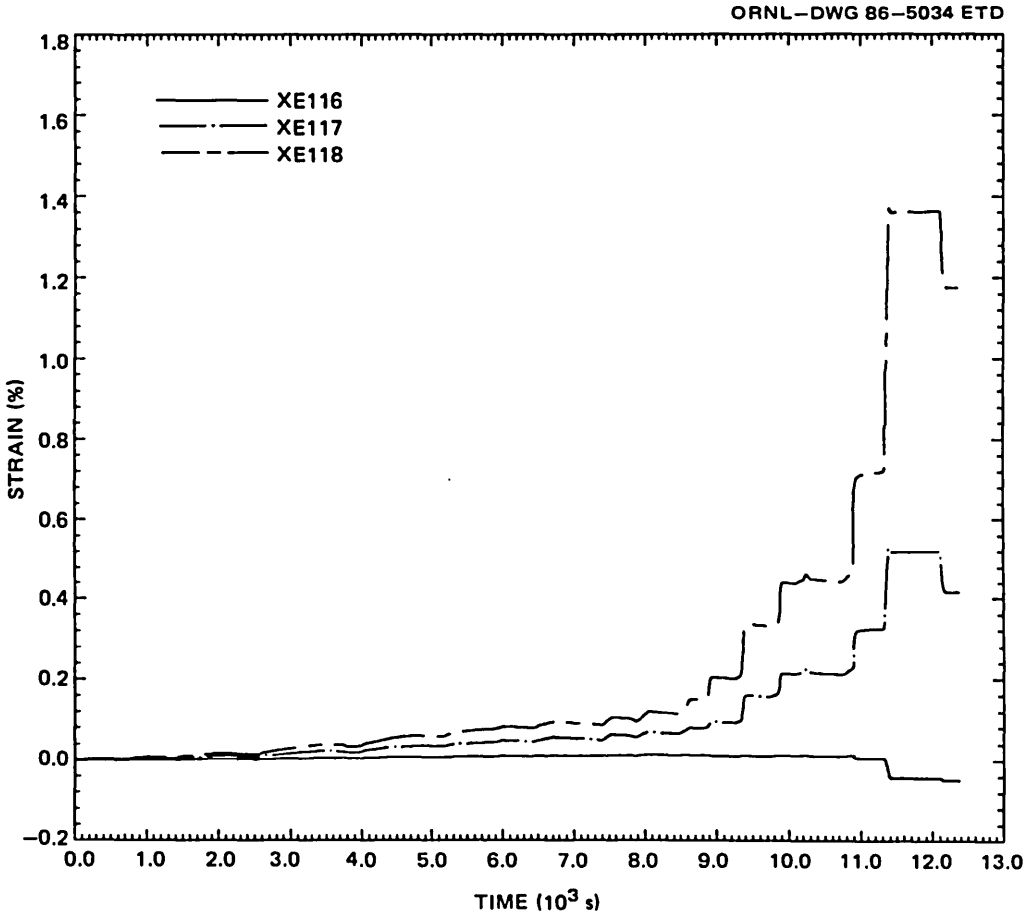

Fig. M.27. Strain vs time, XE116–118.

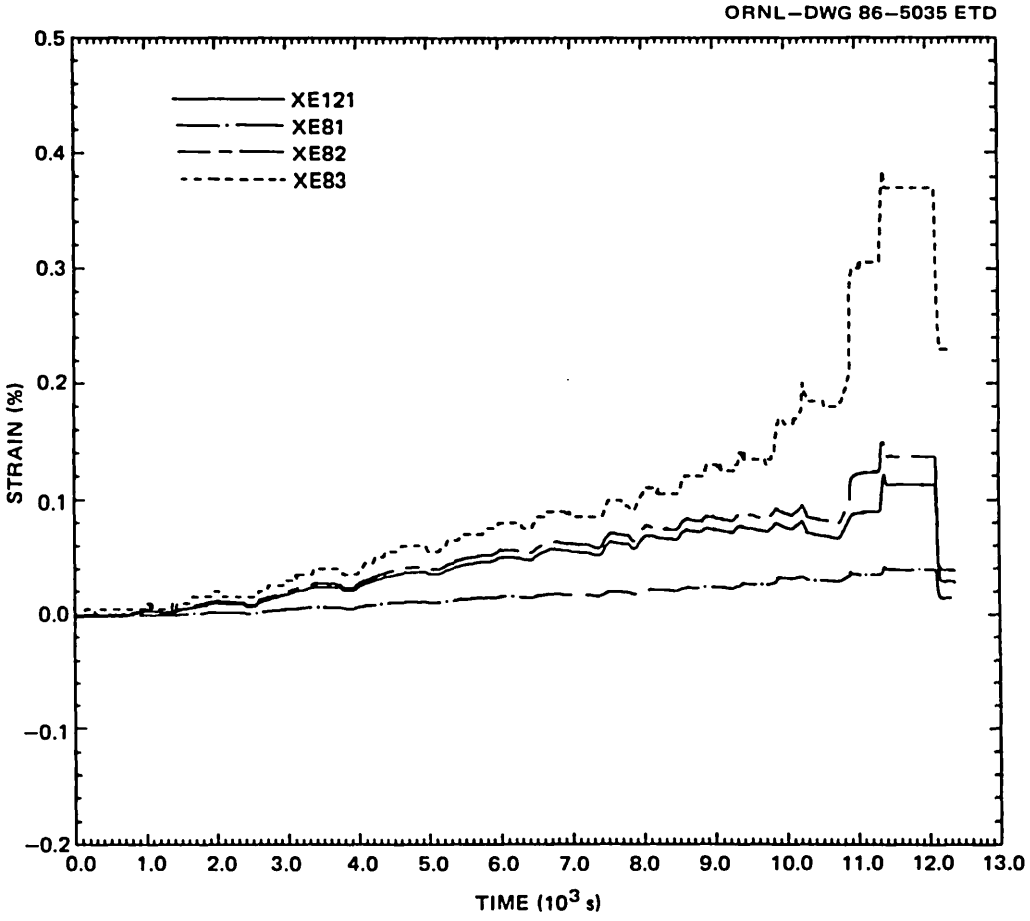

Fig. M.28. Strain vs time, XE81–83 and 121.

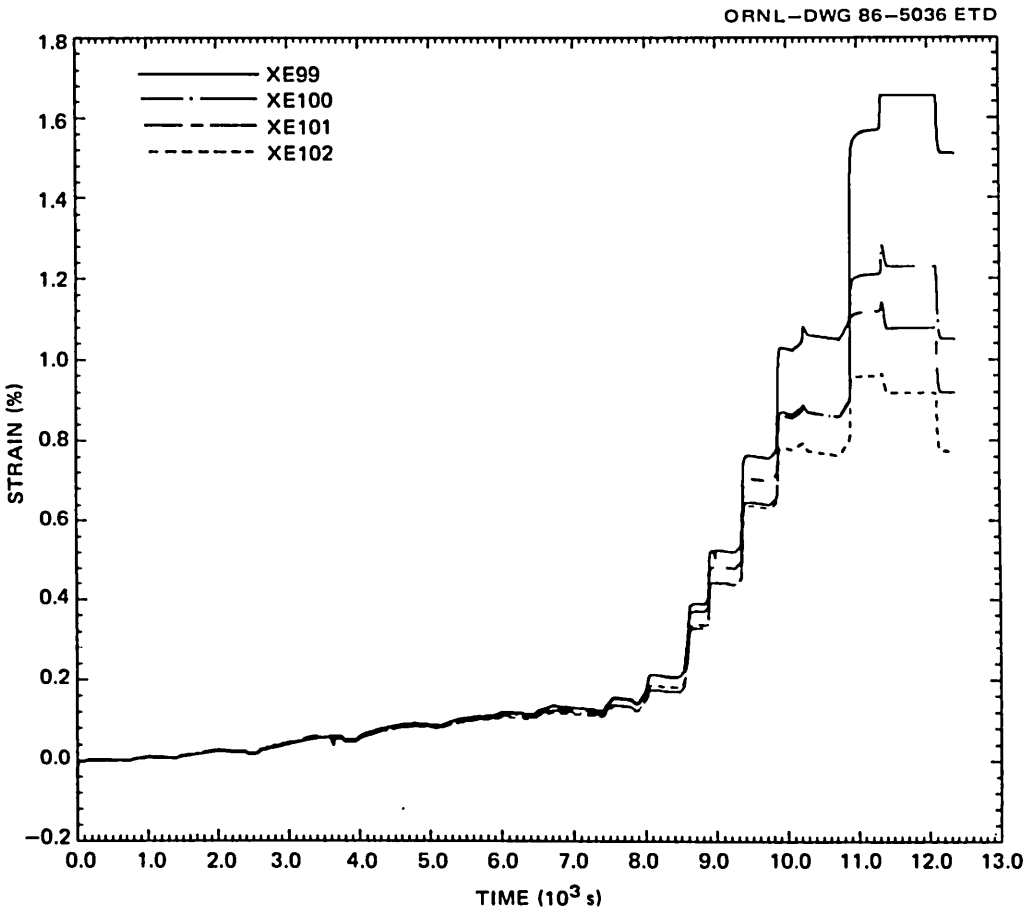

Fig. M.29. Strain vs time, XE99–102.

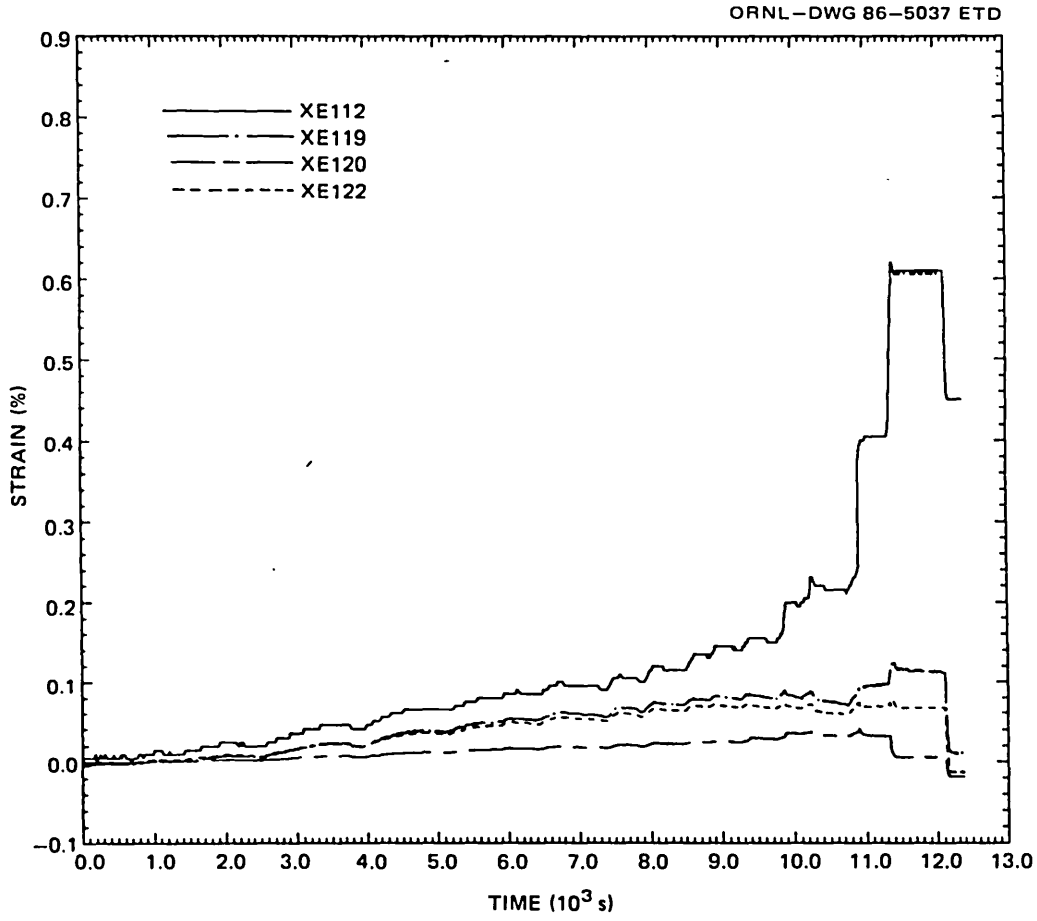

Fig. M.30. Strain vs time, XE112, 119, 120, and 122.

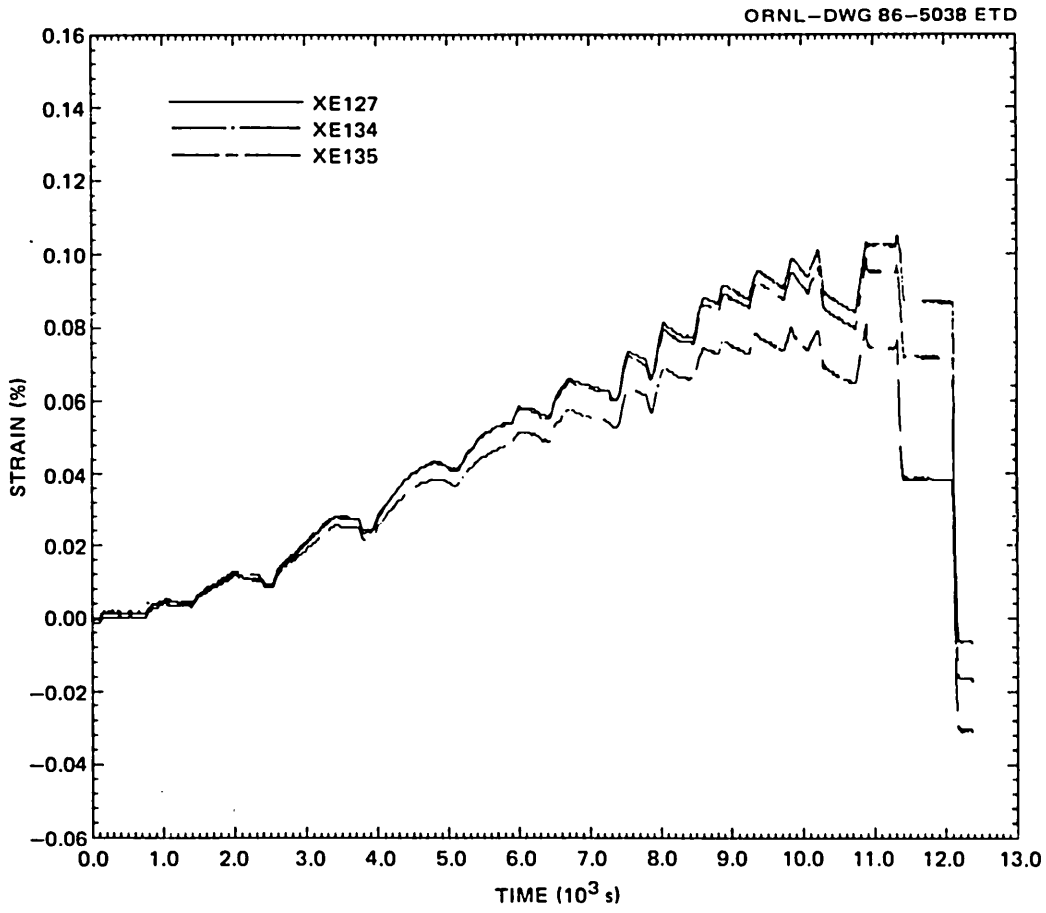

Fig. M.31. Strain vs time, XE127, 134, and 135.

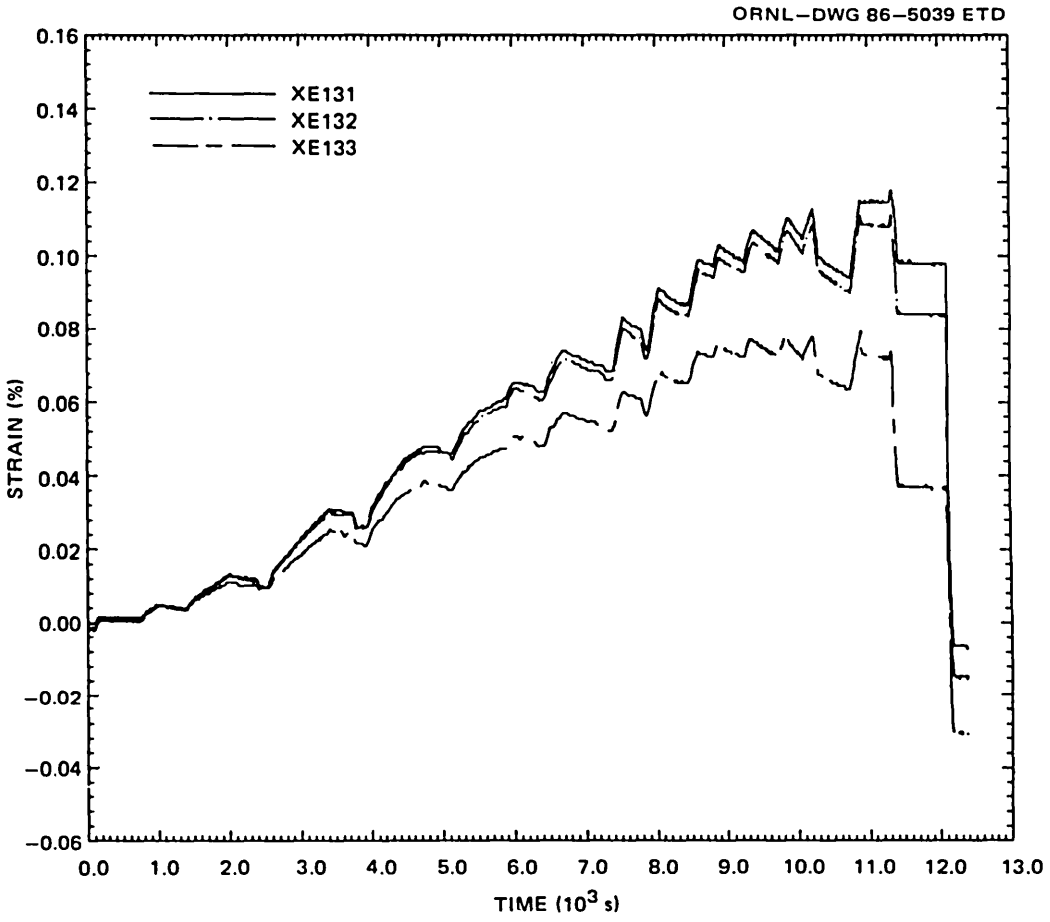

Fig. M.32. Strain vs time, XE131–133.

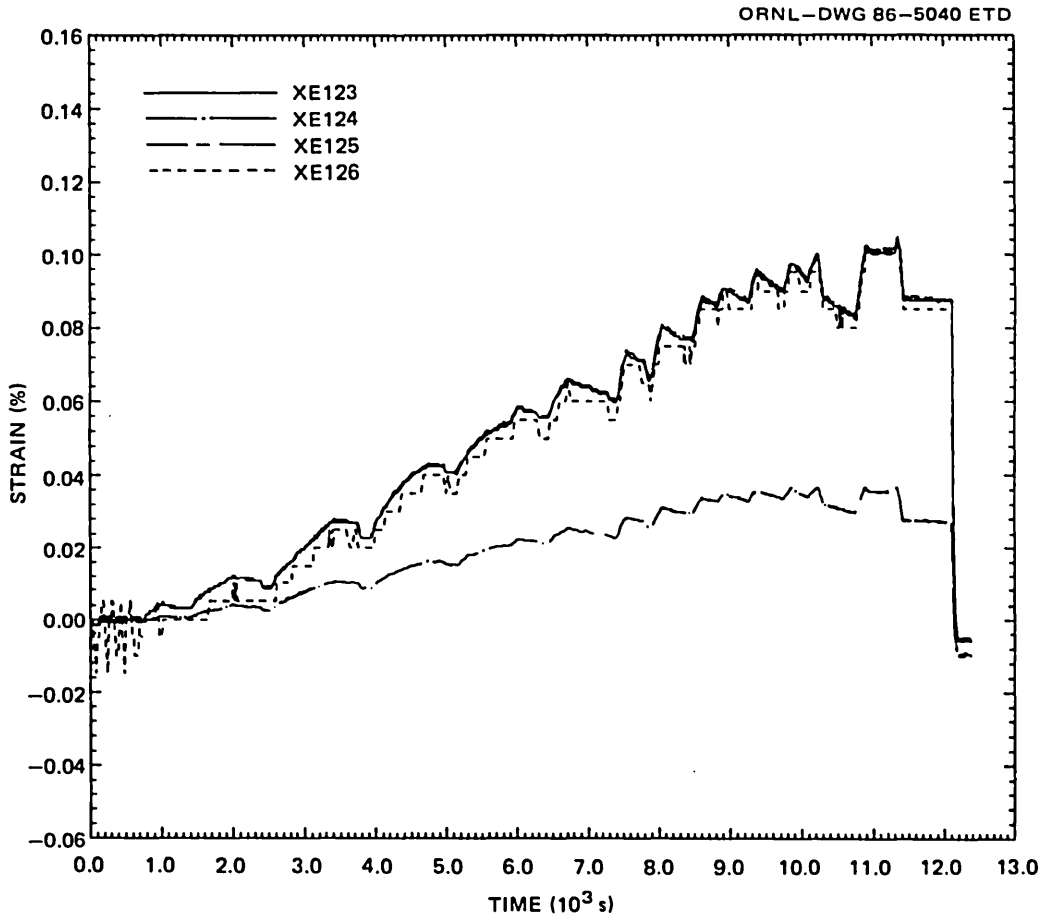

Fig. M.33. Strain vs time, XE123–126.

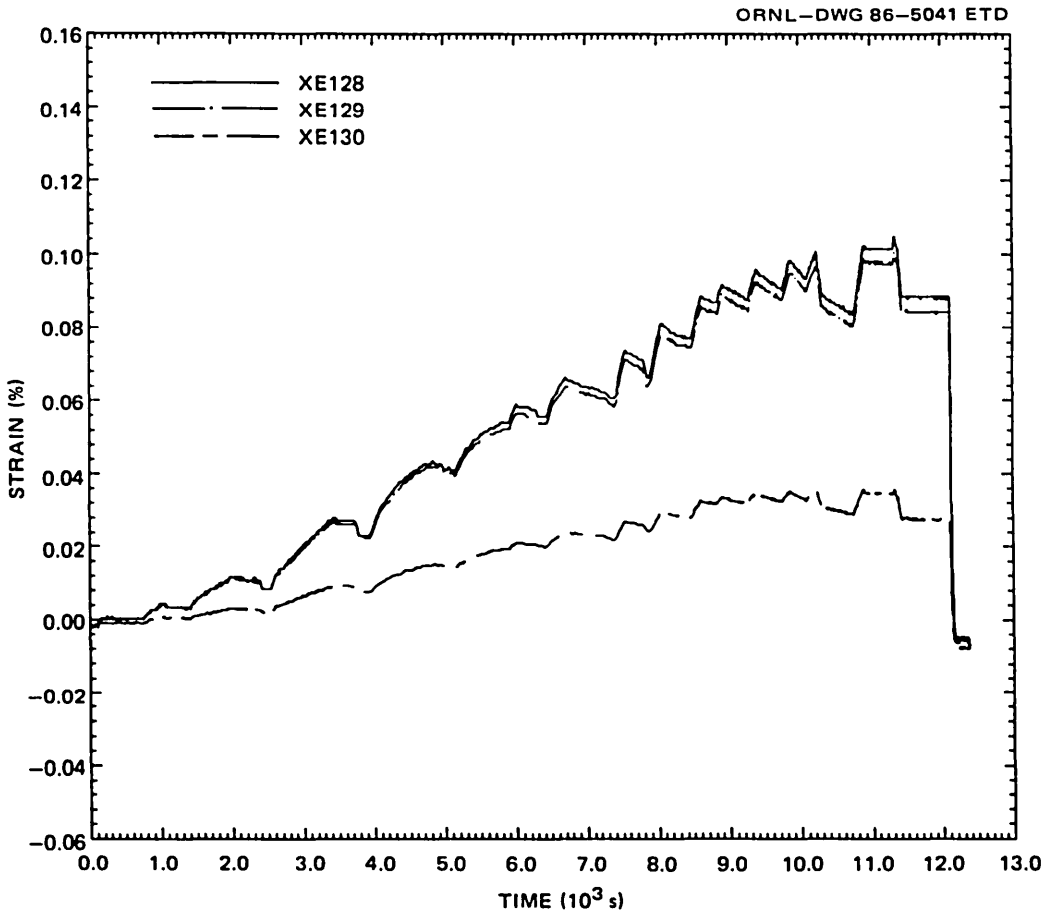

Fig. M.34. Strain vs time, XE128–130.

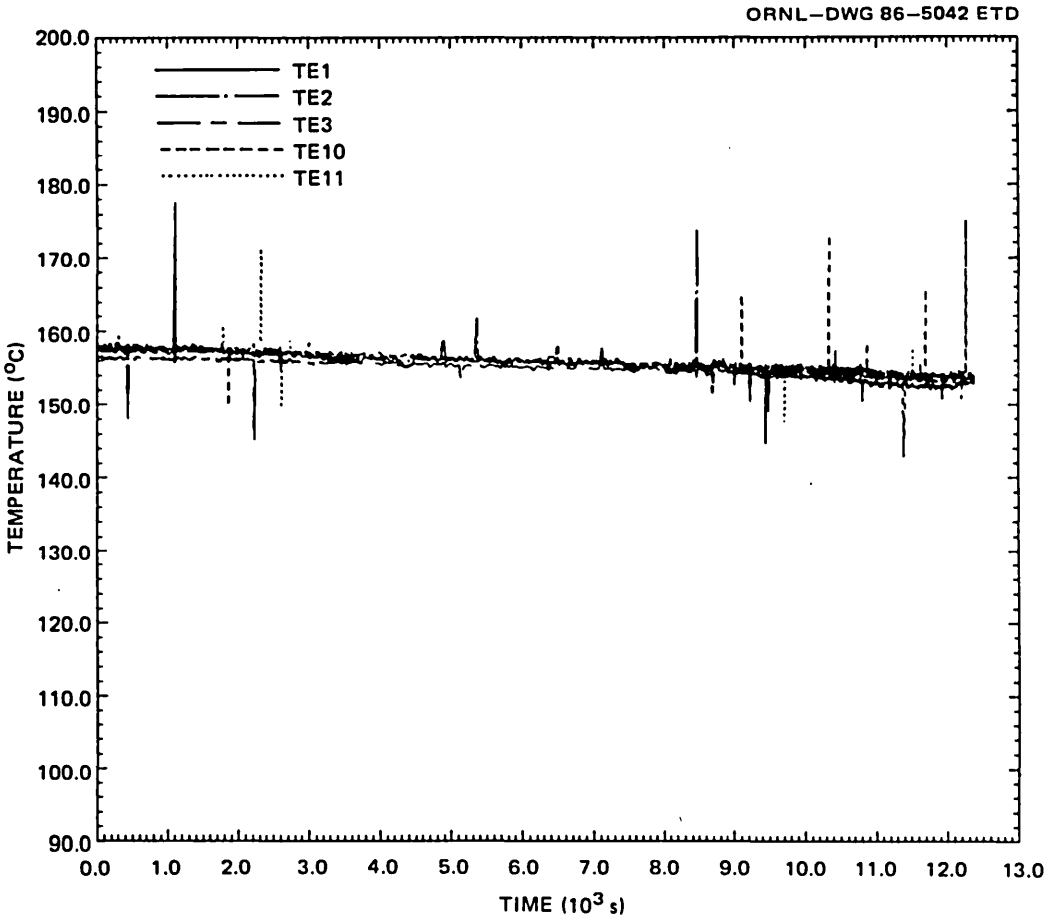

Fig. M.35. Temperature vs time, TE1, 2, 3, 10, and 11.

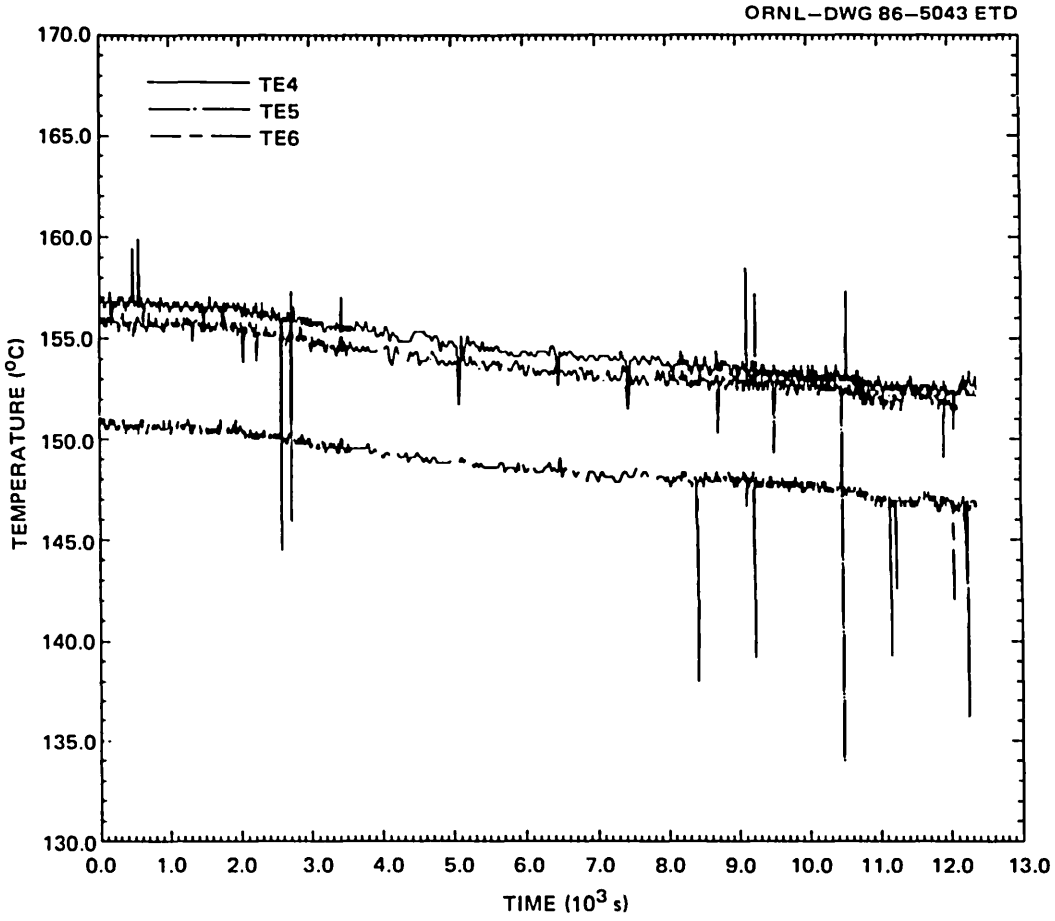

Fig. M.36. Temperature vs time, TE4–6.

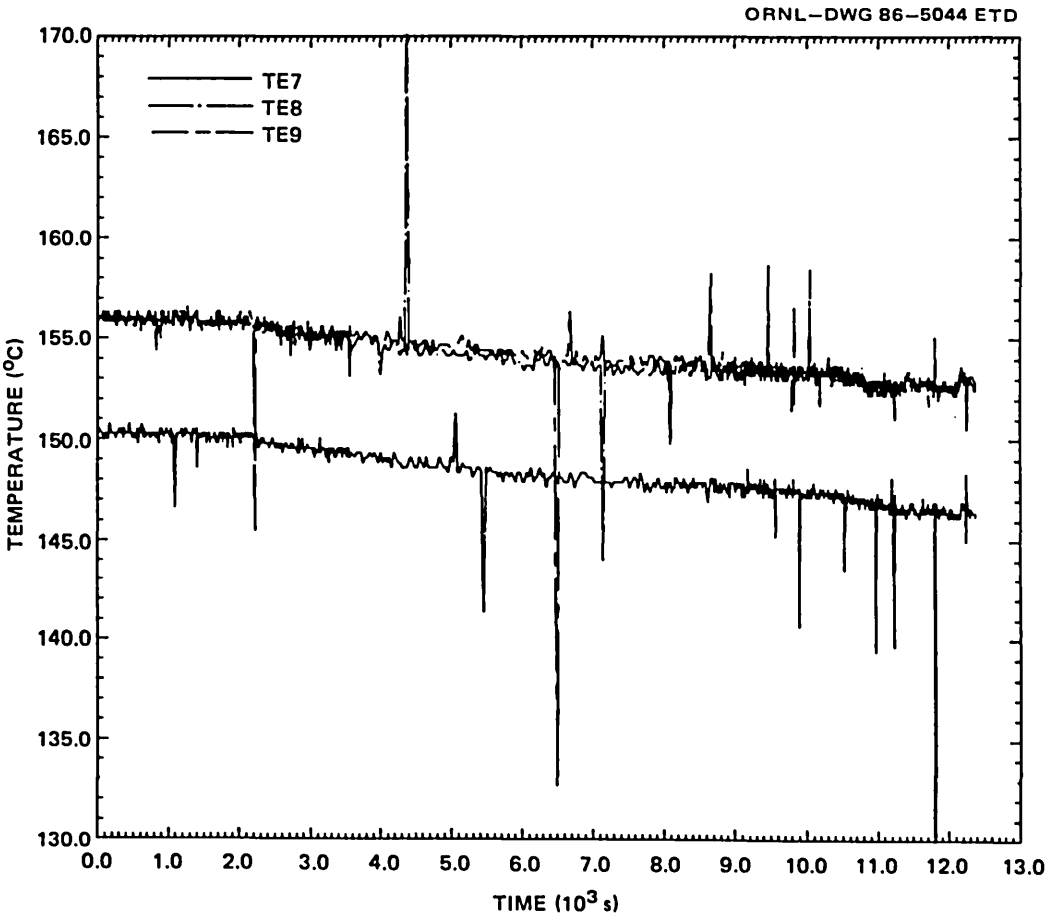

Fig. M.37. Temperature vs time, TE7–9.

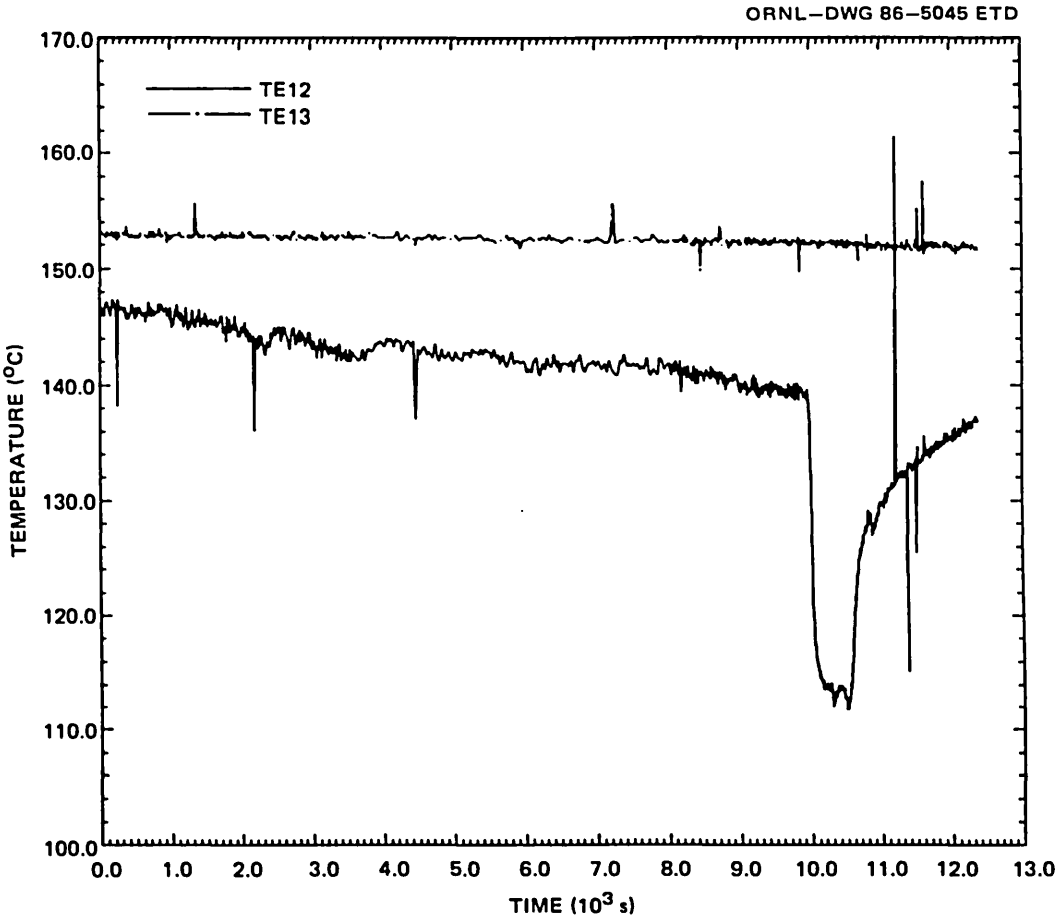

Fig. M.38. Temperature vs time, TE12 and 13.

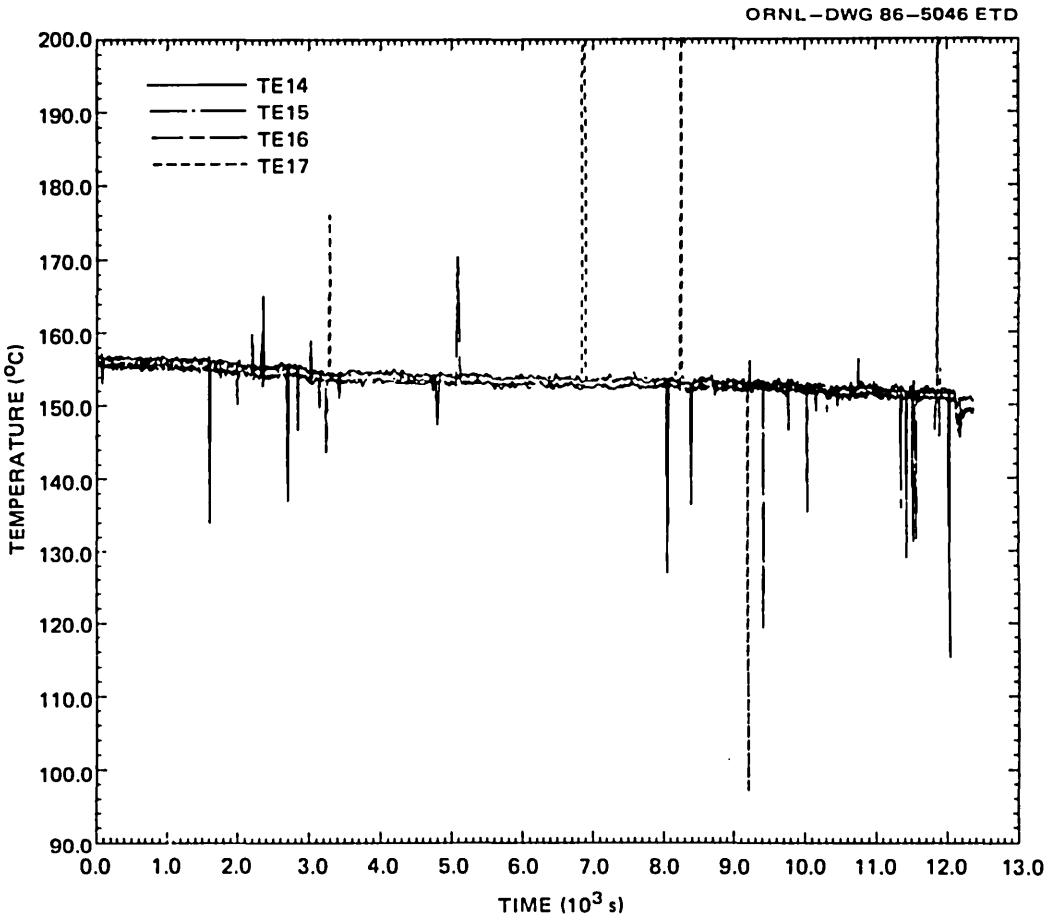

Fig. M.39. Temperature vs time, TE14–17.

Appendix N

PHOTOGRAPHS OF FLAW AND FRACTURE SURFACES

This appendix contains photographs of both fracture surfaces of the V-8A flaw. Figures N.1—N.3 show the outside surface of the vessel around the flaw. Figure N.4 identifies parts of the block containing the flaw as it was cut from the vessel. The two fracture surfaces are labeled "V8A-A" and "V8A-B" in this and succeeding figures. An orientation arrow pointing toward the closure flange of the vessel is shown with each fracture surface. A discussion of the fracture surface is in Sect. 4.4.6.

In Figs. N.5—N.20 the top edge of the block, if shown, is at the outside surface of the vessel, and the opposite edge, if shown, is at the inside surface. In Figs. N.5—N.14 the lighter gray areas next to the inner wall of the vessel and other light gray areas contiguous with them are surfaces developed by cooling the flaw block in liquid nitrogen and wedge-loading the machined notch. Figures N.5—N.7 and N.9—N.13 show only a portion of the fracture surfaces developed during the vessel test because the extreme ends of the surfaces were still hidden, after the initial chilling and wedging, by material that was subsequently removed by further cutting, chilling, and breaking.

Figures N.8 and N.14 show the two opposite fracture surfaces with all fragments assembled in proper order.

Features of fracture surface B are identified and described by Figs. N.21—N.29. Coordinates of features of this surface are given in Tables N.1 and N.2.

Table N.1. Coordinates of points along the tips of the machined notch, initial crack, and final crack

(See Fig. N.21 for definitions of coordinates and symbols)

Cross section No.	z (mm)	y (mm)				
		Crack fronts				Inside surface of vessel[a]
		MN	IC	FC	FC-P	
0	0.0	69.8	87.8	101.4		140.0
1	−15.2	69.7	82.2	100.7		
2	−29.4	69.8	86.2	99.5		139.2
3	−45.0	69.4	83.9	97.5		138.3
4	−62.3	66.4	78.9	95.9		138.7
5	−83.8	59.0	68.9	92.5		
6	−99.5	49.5	56.7	89.7		138.1
7	−109.3	42.6	49.6	88.8		138.2
8	−121.6	29.6	34.7	86.2		
9	−140.0	0	0	81.9	0.0	138.7
10	−154.5			80.9	15.5	
11	−177.5			77.0	28.7	
12	−193.5			75.5	34.5	
13	−209.6			68.7	40.7	
14	−223.1			58.5	43.0	
15	−233.0			46.0	46.0	
21	18.5	69.5	87.4	101.2		
22	30.2	69.5	86.8	101.0		139.2
23	45.8	69.1	84.6	99.6		
24	58.2	66.9	81.8	98.0		
25	74.4	62.0	77.0	97.8		138.0
26	86.2	56.7	72.0	94.0		138.0
27	99.8	48.2	63.9	91.2		139.2
28	109.8	40.0	56.2	89.8		140.8
29	123.6	24.5	41.1	86.0		141.3
30	137.7	0.0		84.0	0.0	
31	150.5			80.3	9.0	
32	162.5			75	19.8	
33	183.0			67	31.2	
34	208.8			53.5	38.3	
35	220			44.2	44.2	

[a]Additional measurements of the vessel thickness were precluded by fragmentation of parts of the flaw block, which made results uncertain. Actual unnecked thickness is probably slightly greater than the largest value measured.

Table N.2. Coordinates of features on fracture surface B

(See Fig. N.21 for definition of coordinates and Figs. N.22–N.29 for description of features)

Feature	Cross section No.	z (mm)	y (mm)
A	0	0.0	95.2
B	1	−15.2	94.3
C	1	−15.2	98.0
D	0	0.0	98.2
E	2	−29.4	94.5
F	2	−29.4	97.5
G		−34.6	85.5
H	3	−45.0	95.0
I	3	−45.0	85.5
J	3	−45.0	86.9
K	4	−62.3	81.5
L	4	−62.3	86.7
M	10	−154.5	15.5
N		−157.5	22.5
O	21	18.5	95.0
P	22	30.2	95.0
Q	23	45.8	87.7
R	23	45.8	95.0
S	23	45.8	98.2
T	24	58.2	87.3
U	24	58.2	94.5
V		135.4	7.0
W		145.5	0.0
X		−127.6	22.0
Y	25	74.4	80.5

ORDGP PHOTO 82–2750

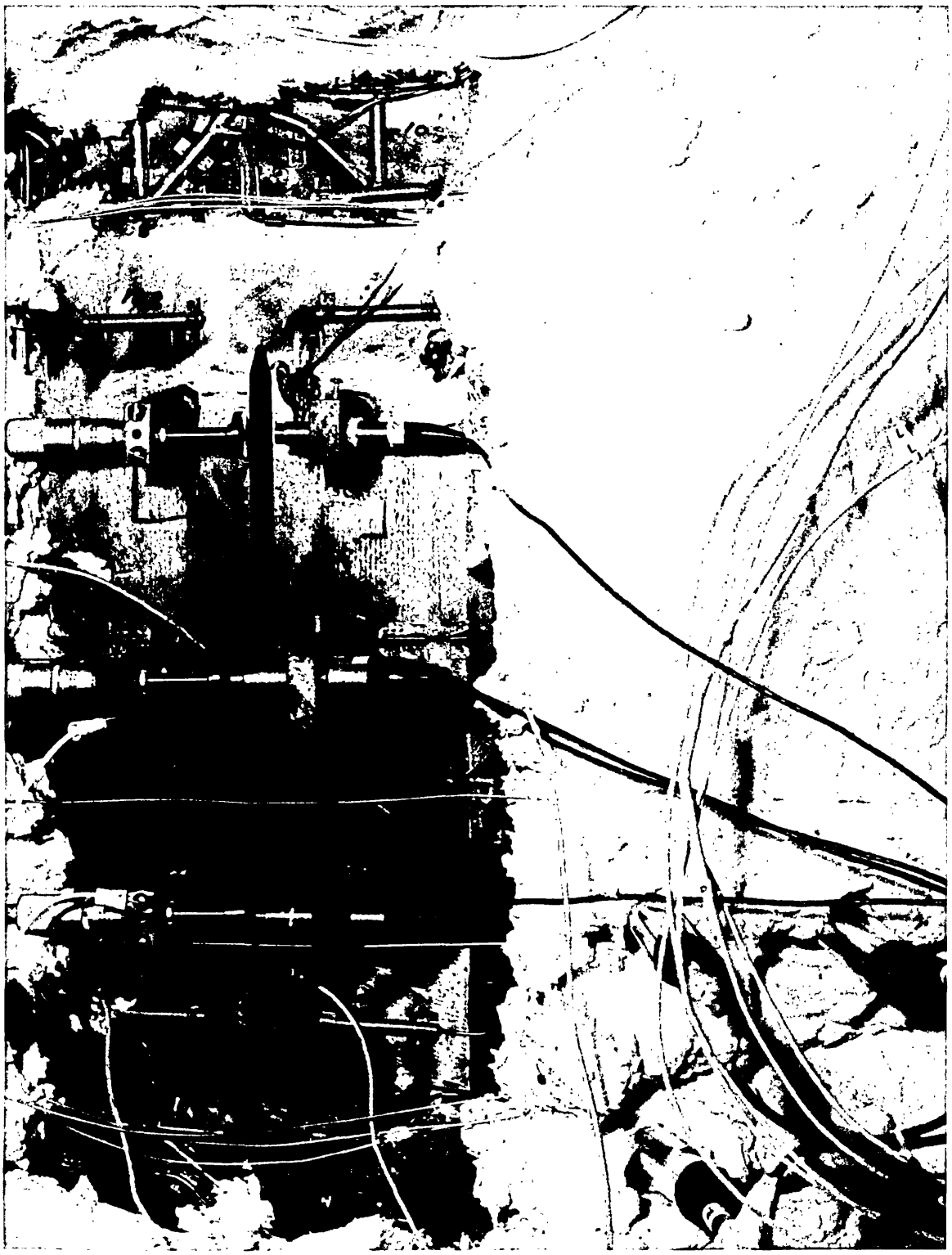

Fig. N.1. View of outside surface of vessel around the flaw. A short tear and surface deformation are visible at the upper end of the flaw.

ORDGP PHOTO 82–2749

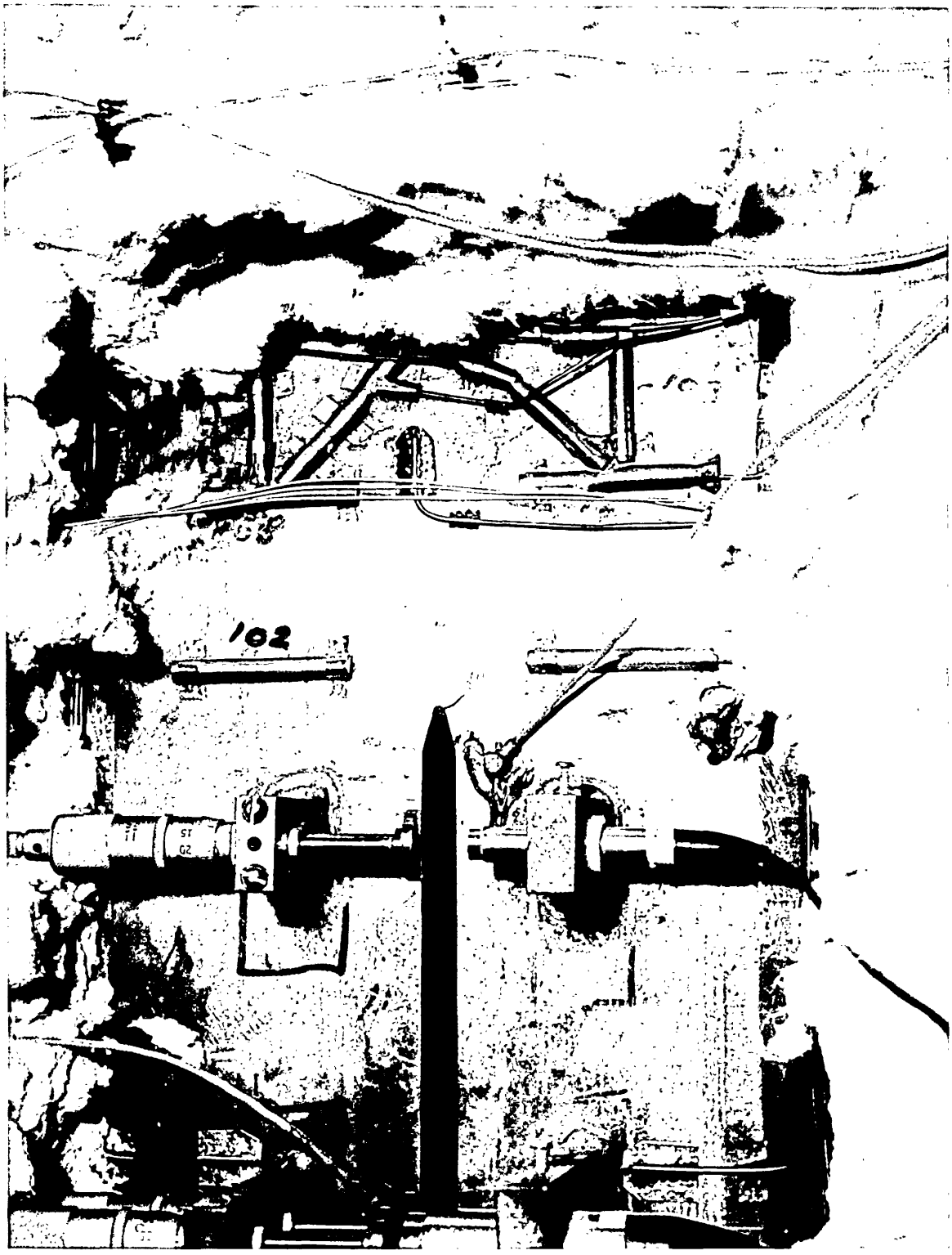

Fig. N.2. View of outside surface of vessel around the upper end of the flaw.

ORDGP PHOTO 82–2751

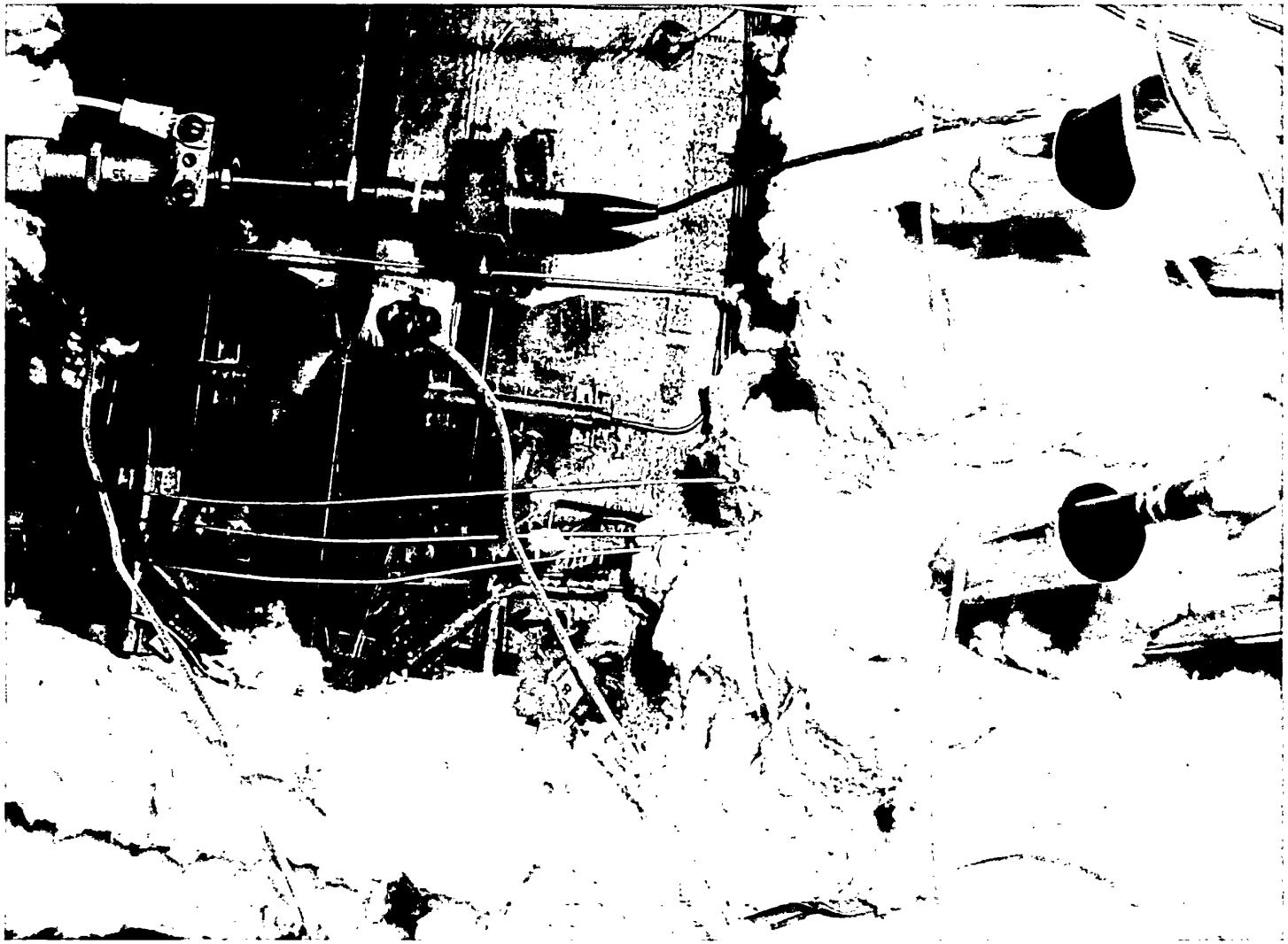

Fig. N.3. View of outside surface of vessel around the lower end of the flaw.

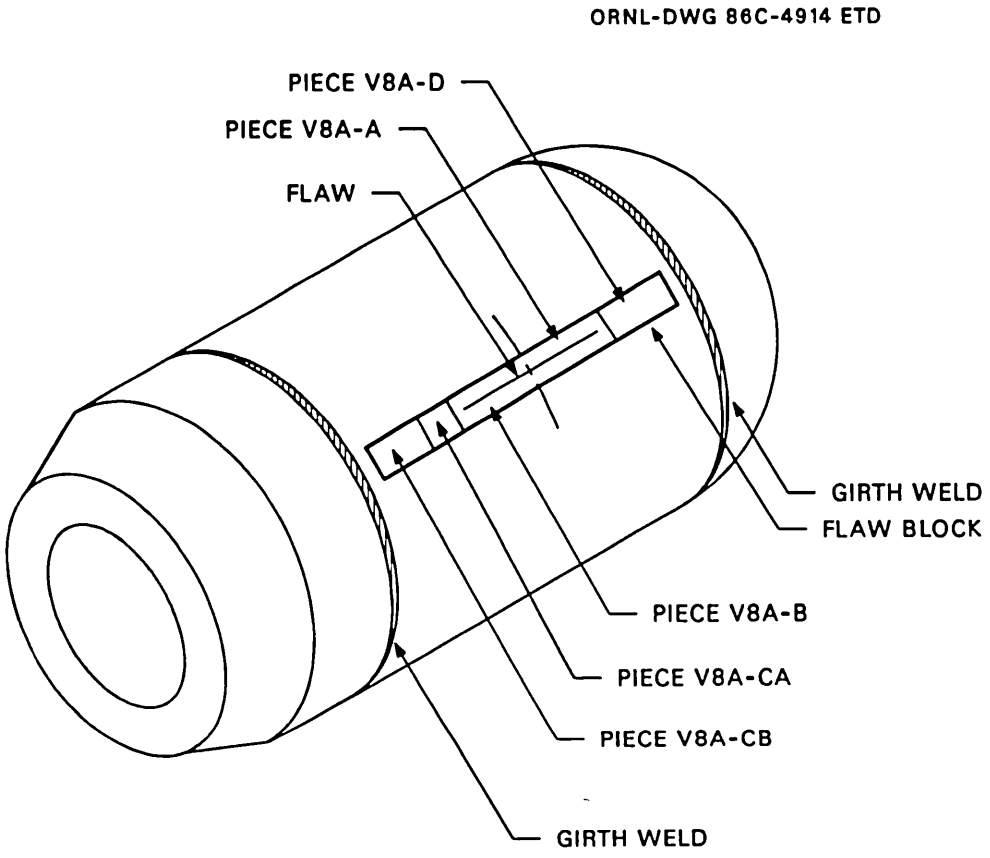

Fig. N.4. Diagram identifying parts of the block containing the flaw and defining orientations.

M&C PHOTO Y187552

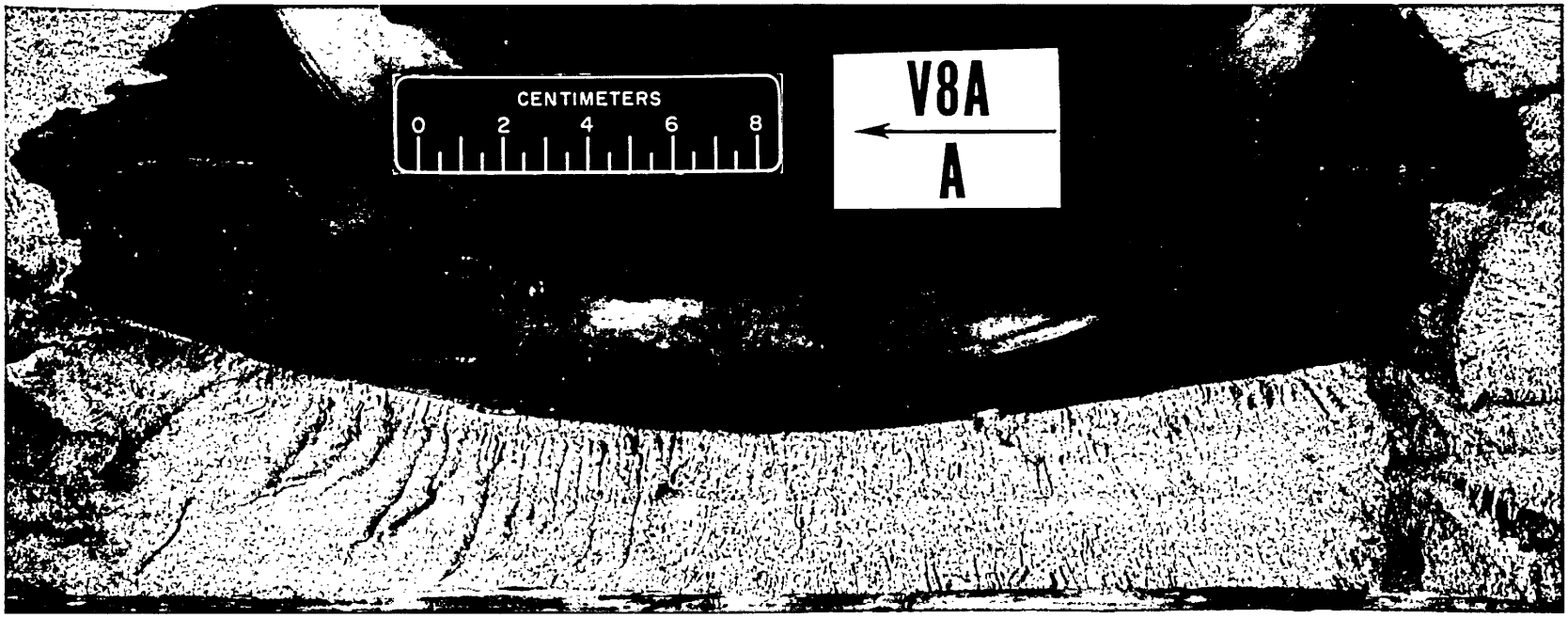

Fig. N.5. Fracture surface V8A-A as revealed by the initial cold fracture of the flaw block.

M&C PHOTO Y187555A

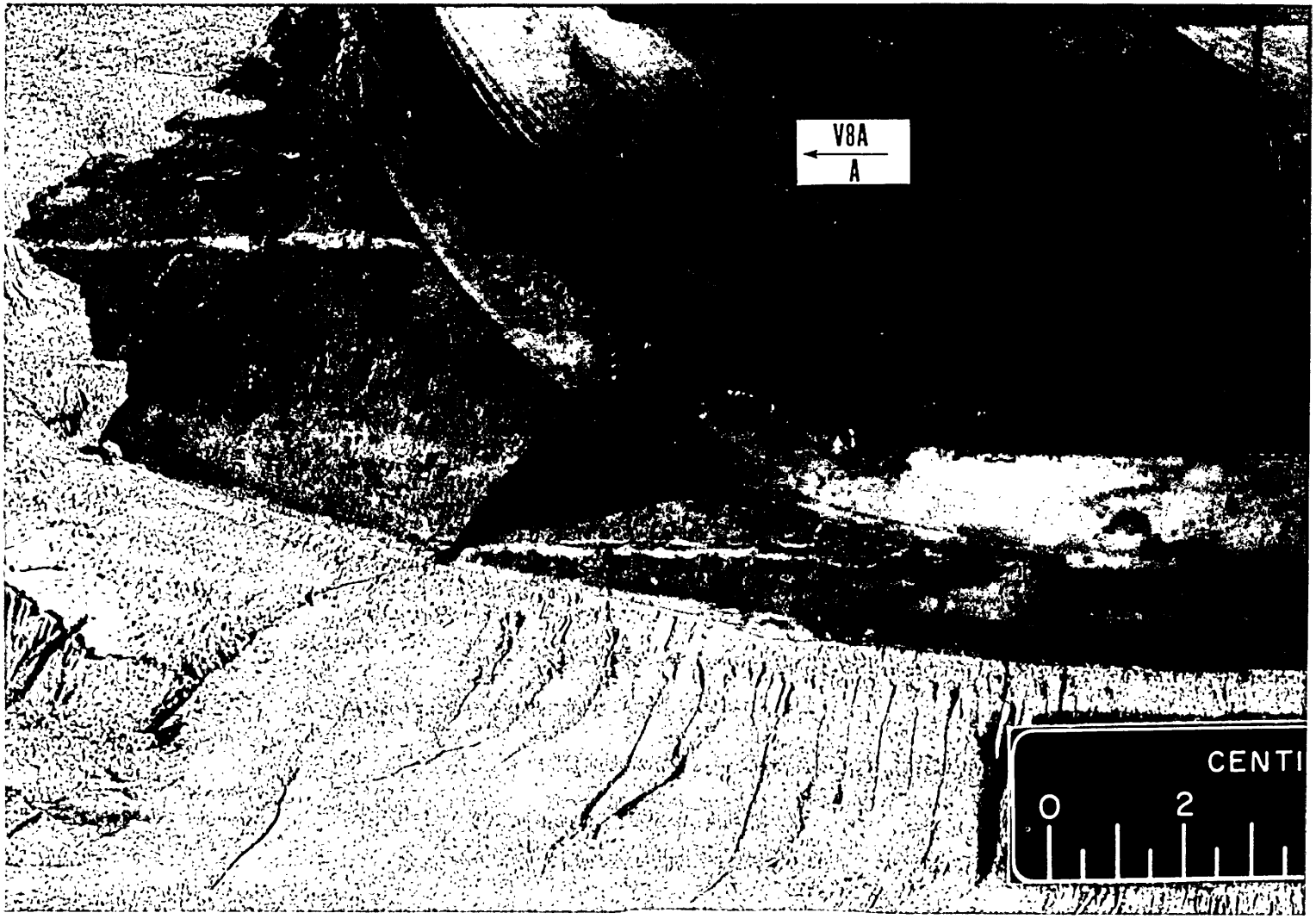

Fig. N.6. A portion of surface shown in Fig. N.5. This photograph shows details not visible in other views. The cracks crossing the fracture surfaces in this and subsequent figures were generated by the wedge-loading operation.

M&C PHOTO Y187554

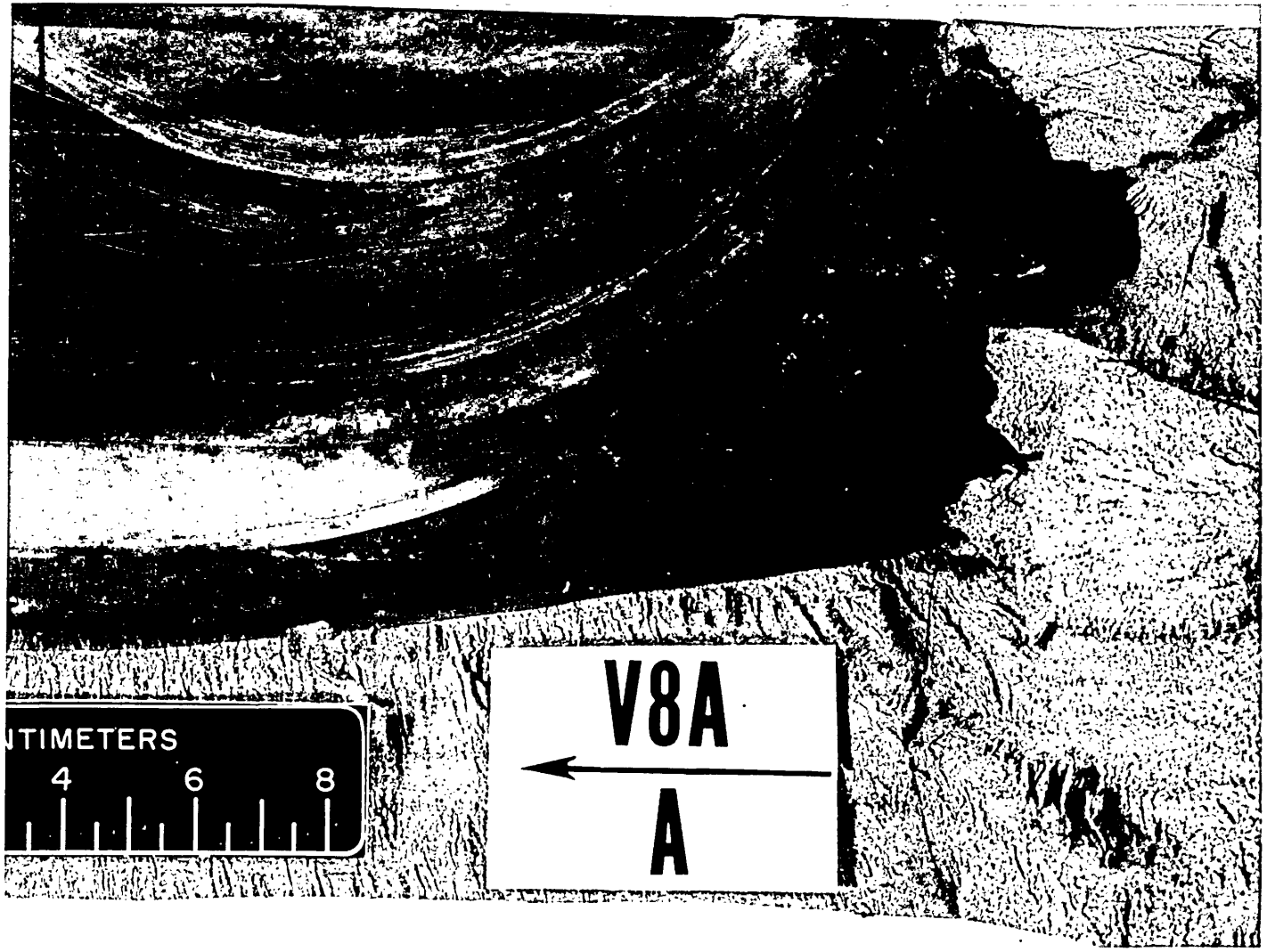

Fig. N.7. V8A-A fracture surface complementary to that shown in Fig. N.6.

ORNL PHOTO 6782–83A

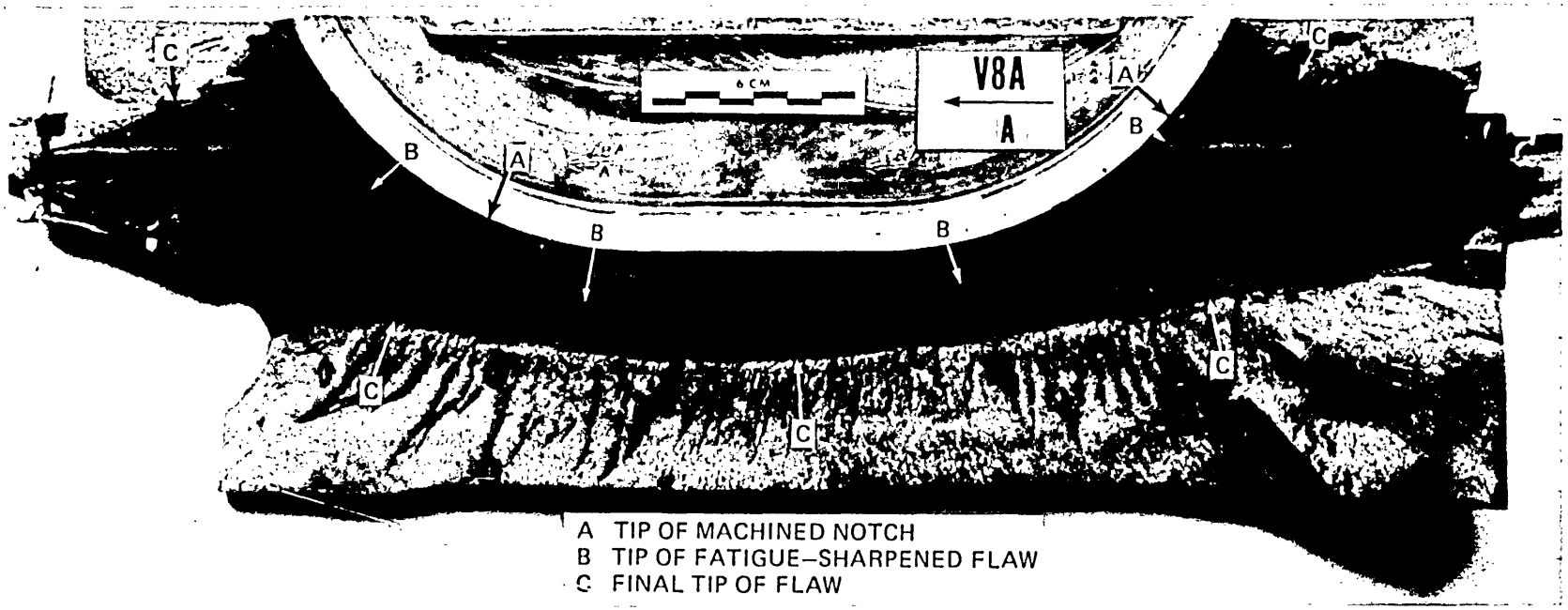

Fig. N.8. Entire fracture surface V8A-A.

M&C PHOTO Y187553

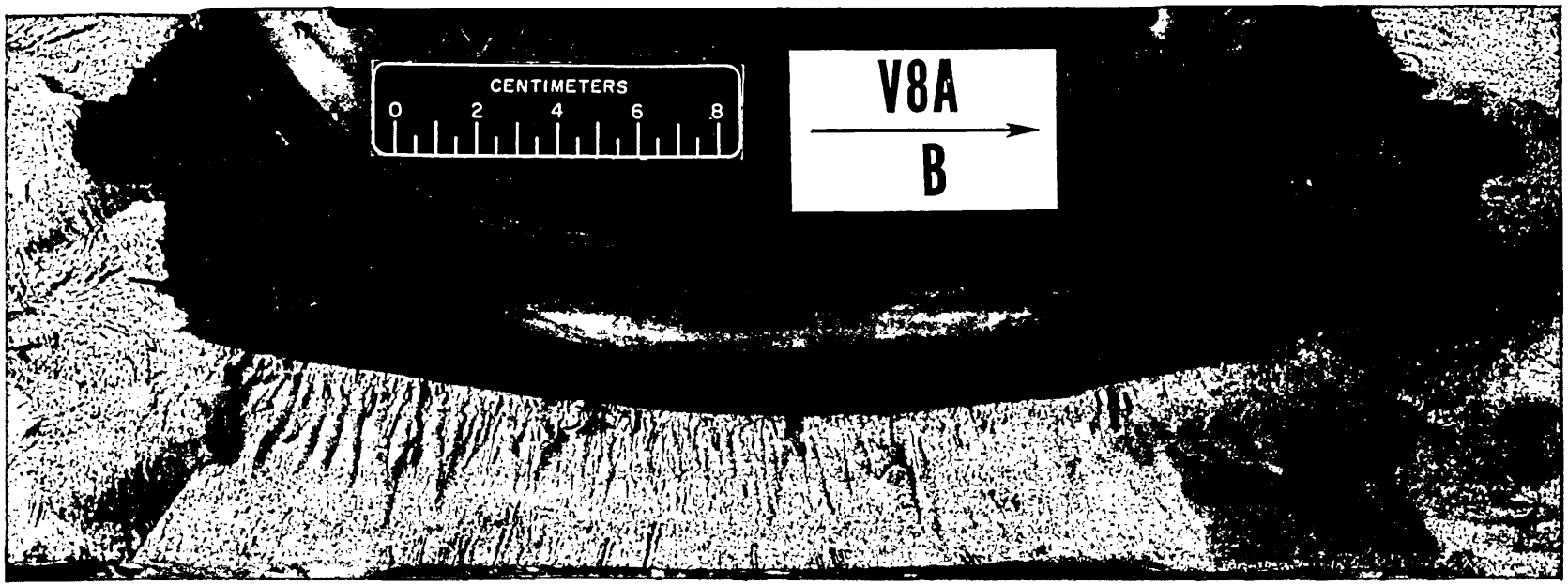

Fig. N.9. Fracture surface V8A-B as revealed by the initial cold fracture of the flaw block.

M&C PHOTO Y187557

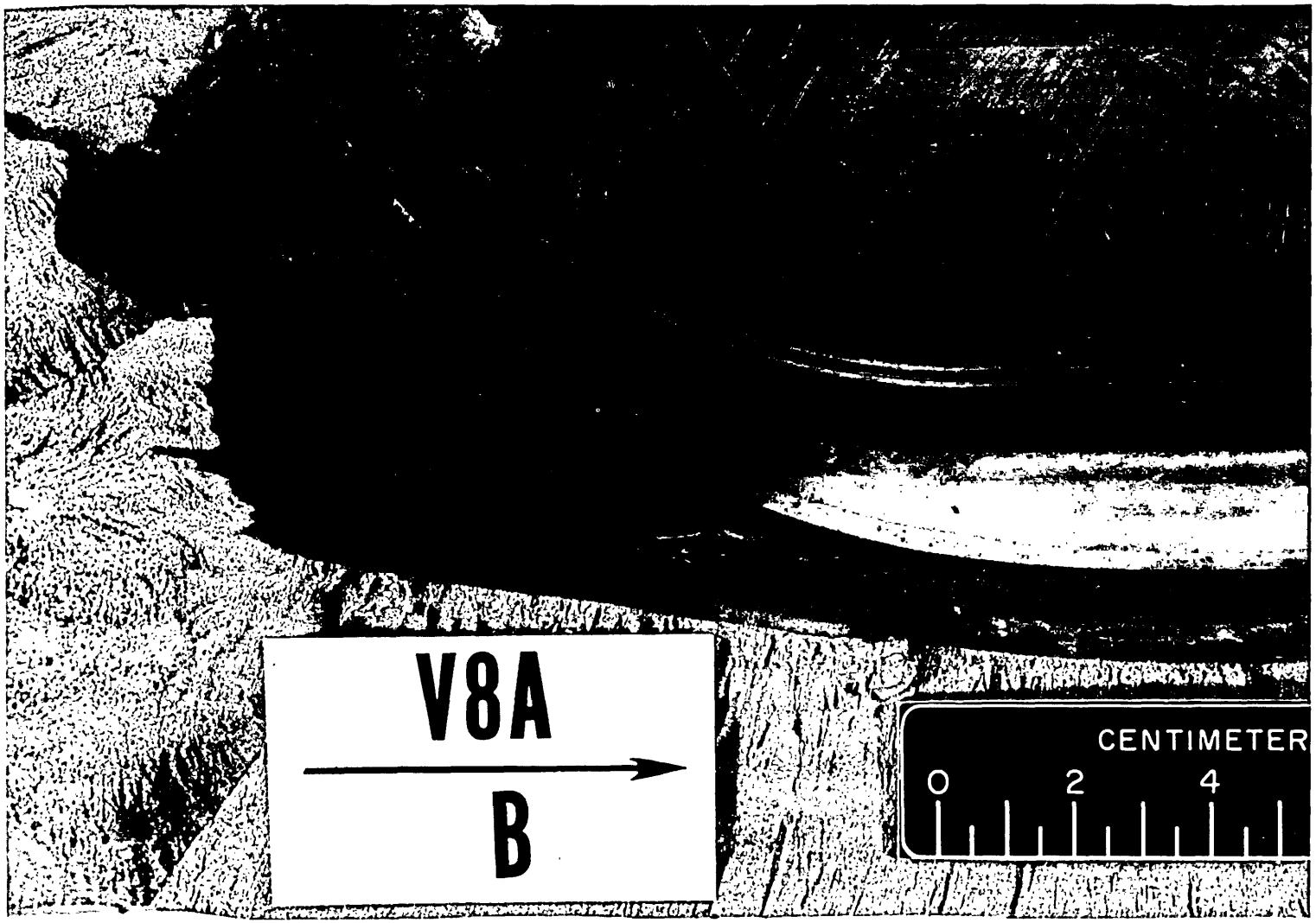

Fig. N.10. A portion of the surface shown in Fig. N.9. This photograph shows details not visible in other views.

M&C PHOTO Y187565

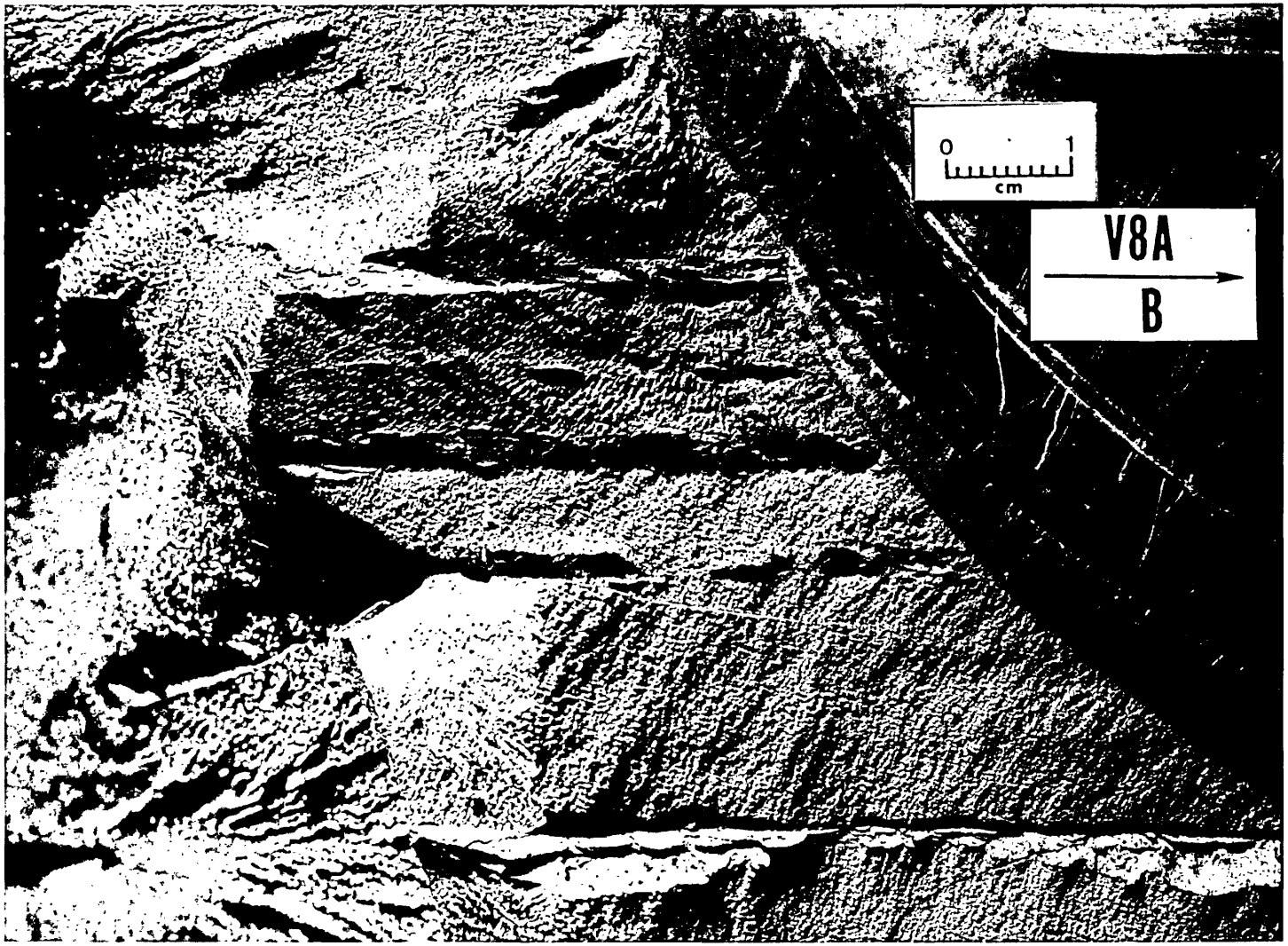

Fig. N.11. A portion of the surface shown in Fig. N.10. Oblique illumination accentuates features.

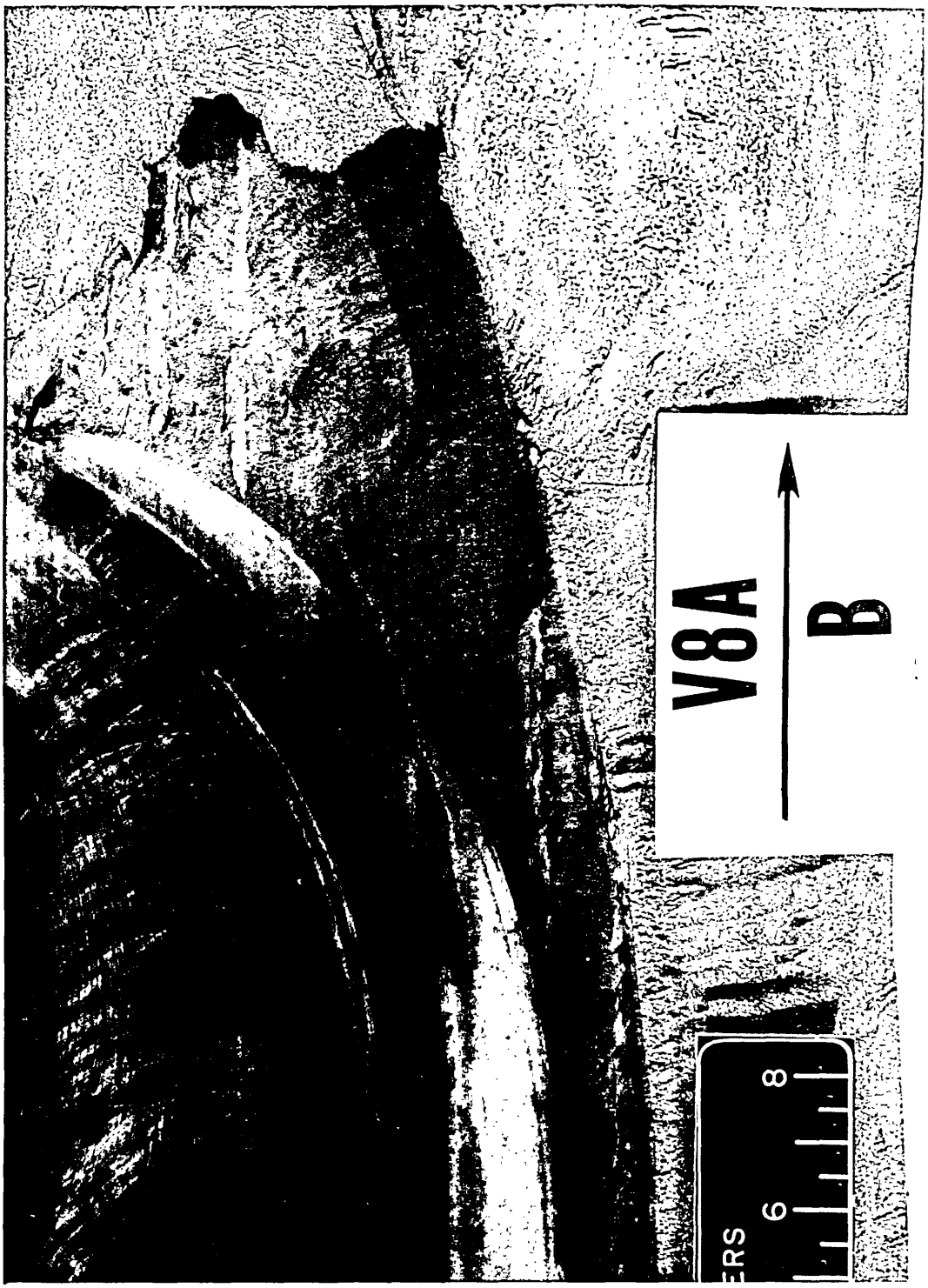

Fig. N.12. V8A-B fracture surface complementary to that shown in Fig. N.10.

M&C PHOTO Y187564

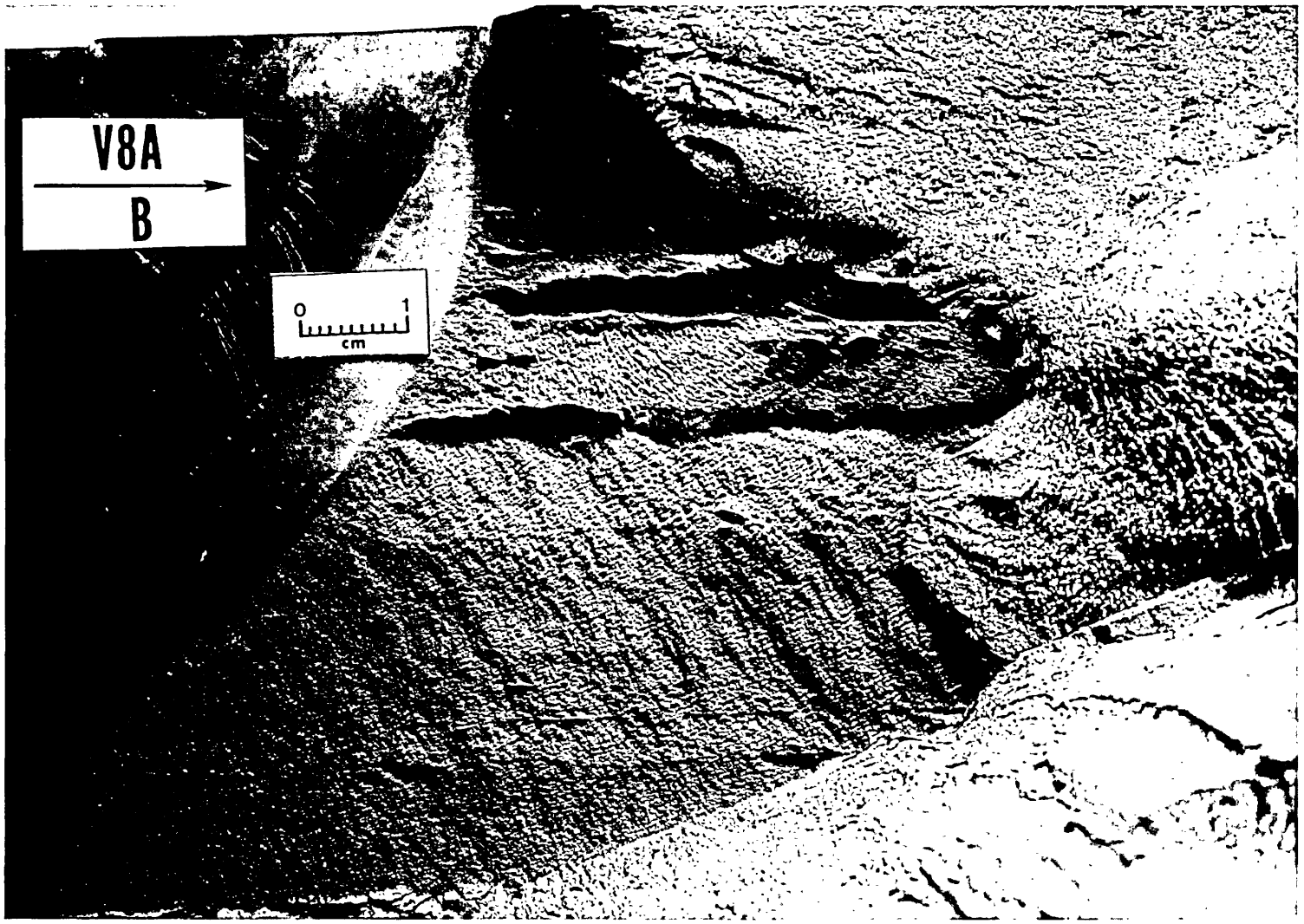

Fig. N.13. A portion of the surface shown in Fig. N.12. Oblique illumination accentuates features.

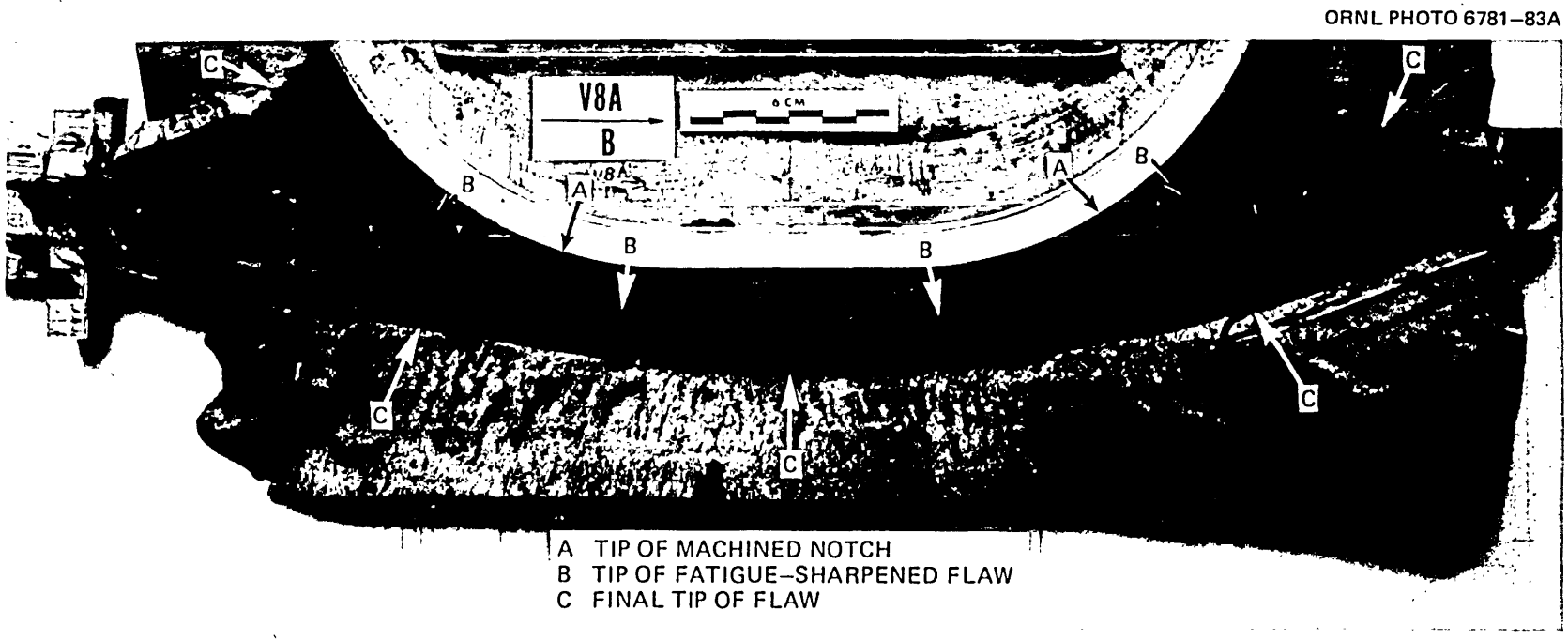

Fig. N.14. Entire fracture surface V8A-B.

M&C PHOTO Y187559A

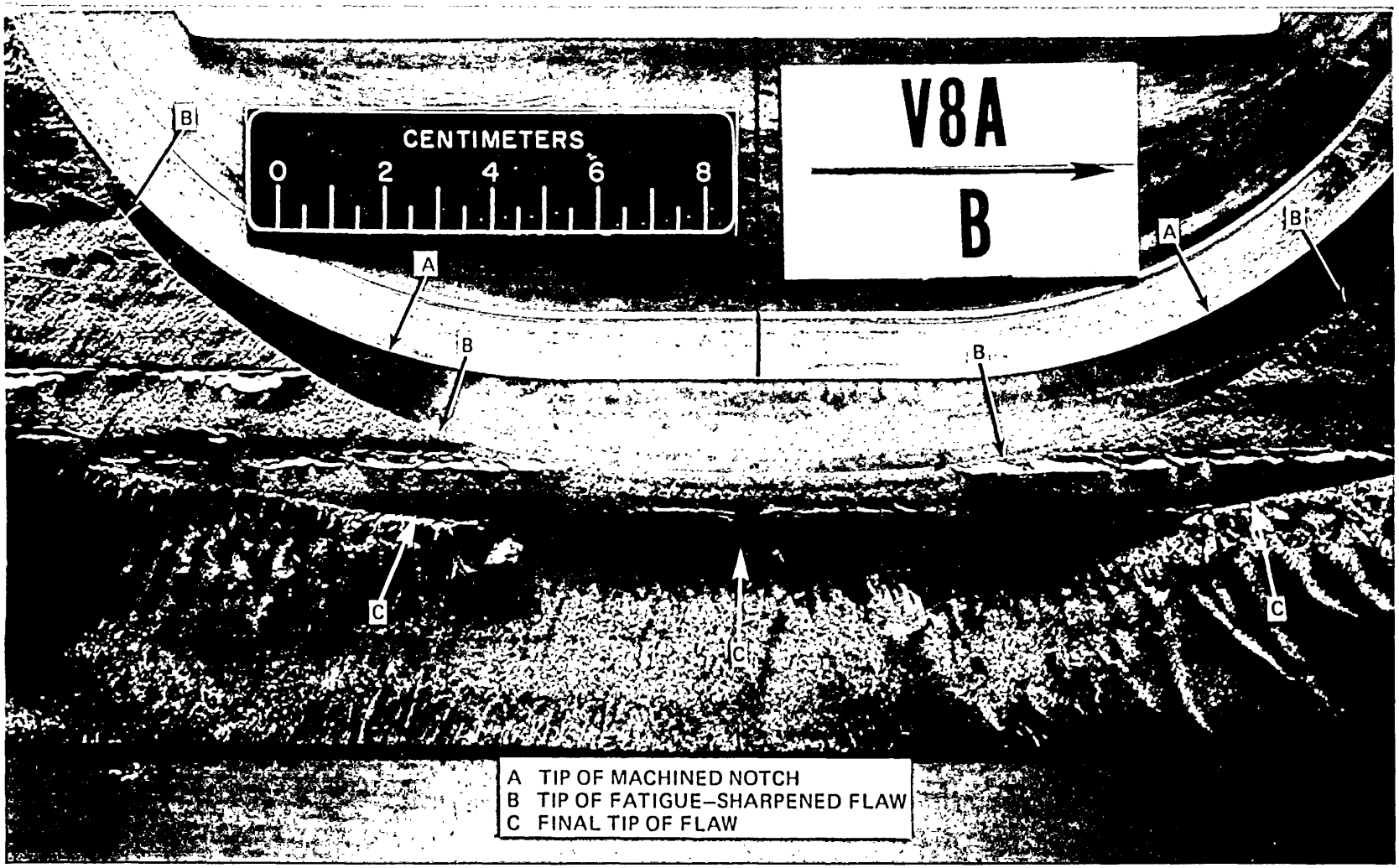

Fig. N.15. Central portion of fracture surface V8A-B with oblique illumination from top of photograph.

M&C PHOTO Y187558A

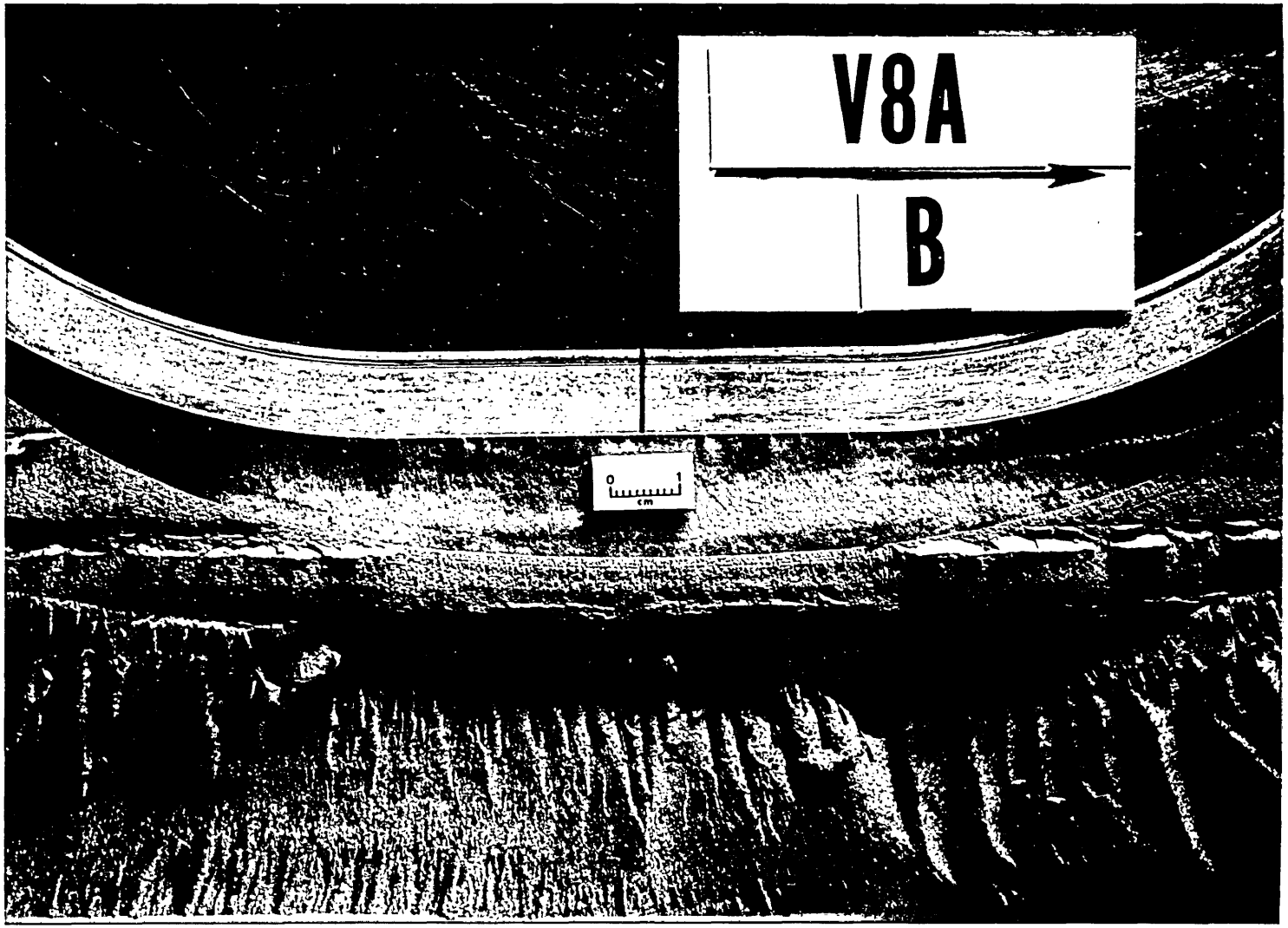

Fig. N.16. Central portion of fracture surface V8A-B with oblique illumination from top of the photograph. Smaller details are visible in this figure than in Fig. N.15.

M&C PHOTO Y187560A

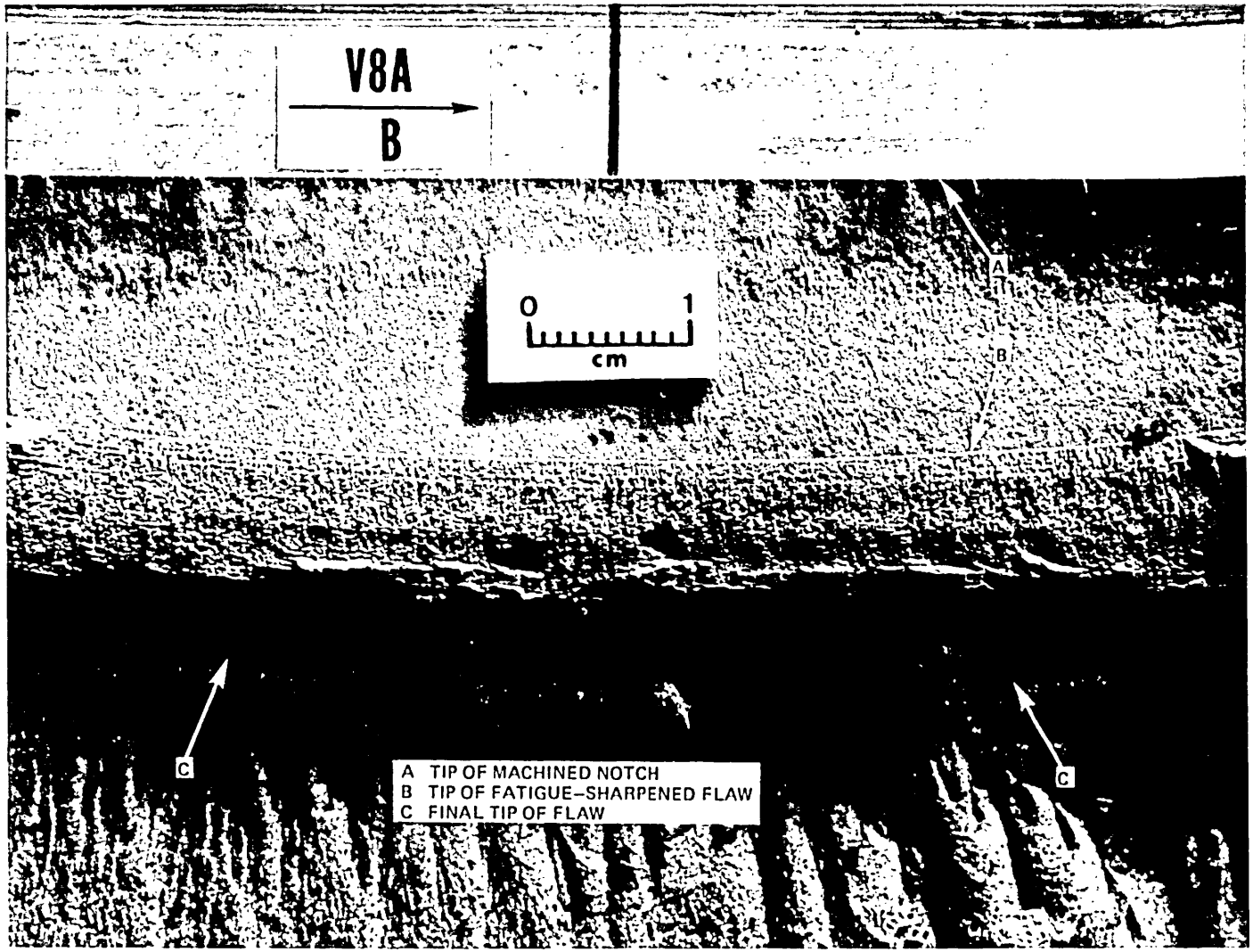

Fig. N.17. Central portion of fracture surface V8A-B with oblique illumination from top of photograph. Some details not clear in this photograph are accentuated in Fig. N.18.

M&C PHOTO Y187563A

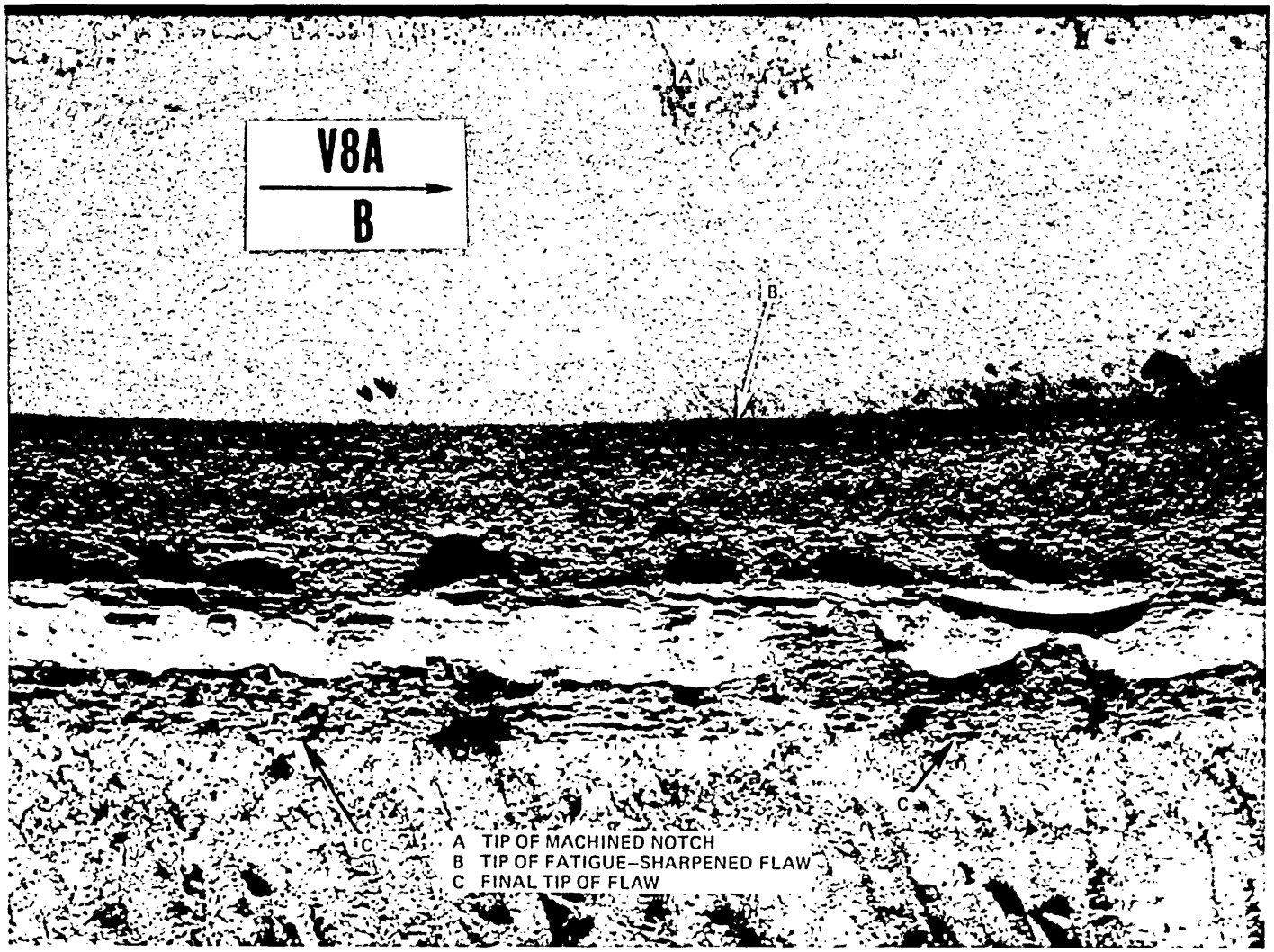

Fig. N.18. Central portion of fracture surface of V8A-B with oblique illumination from bottom of photograph.

M&C PHOTO Y187561A

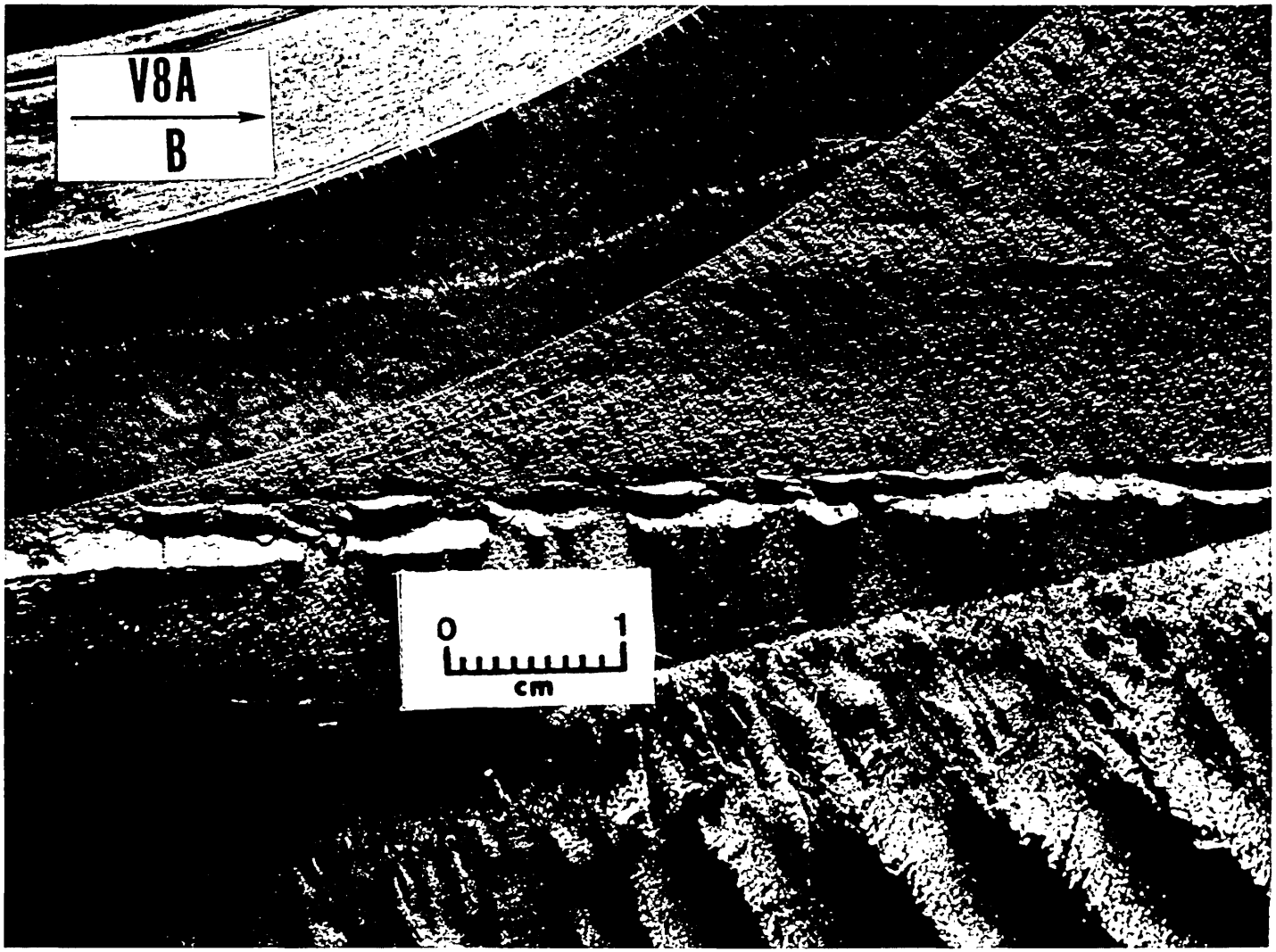

Fig. N.19. A deep portion of the V8A-B fracture surface situated above (toward the vessel closure) the center of the flaw. Oblique illumination is from the top of the photograph.

M&C PHOTO Y187562A

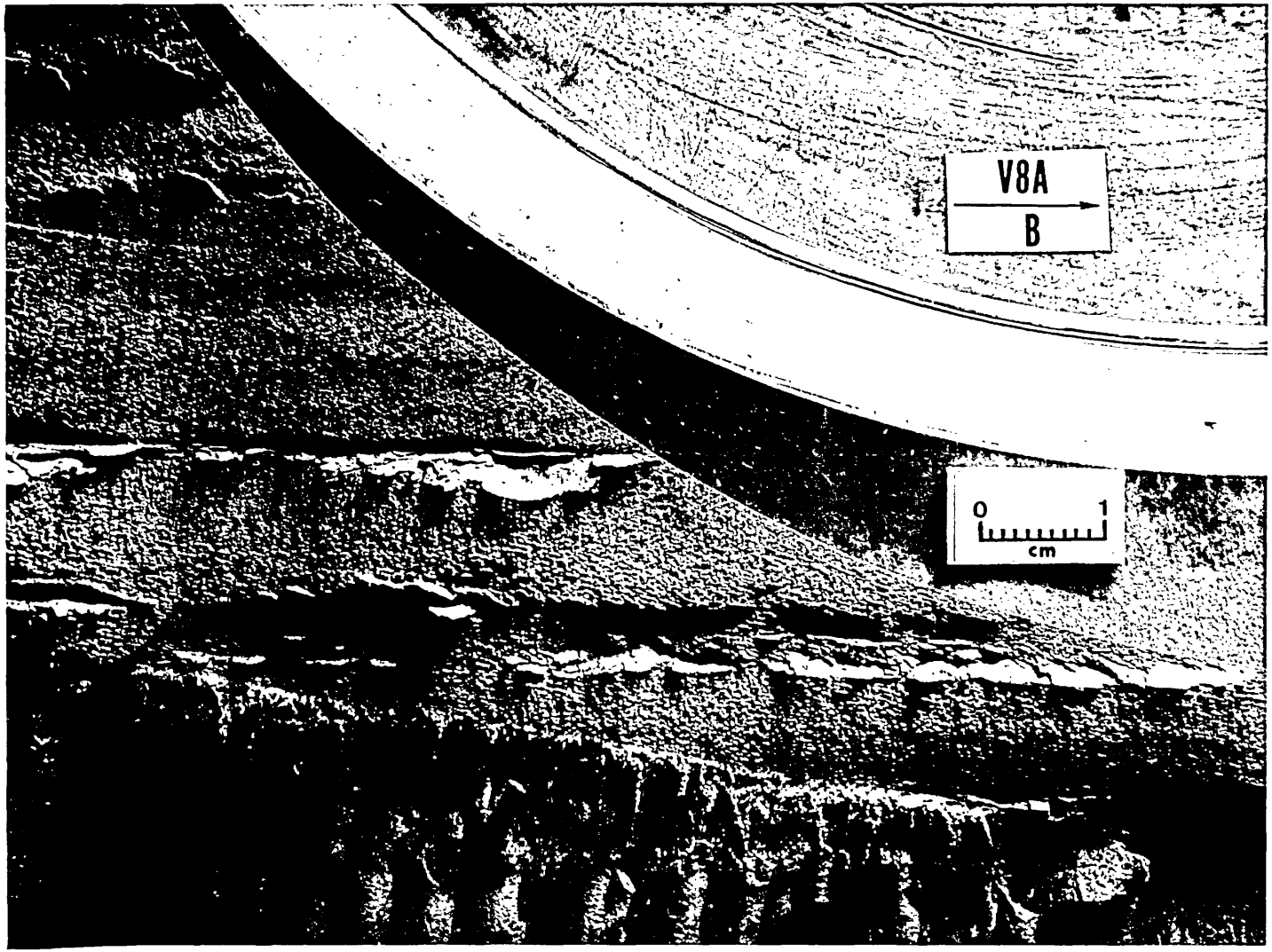

Fig. N.20. A portion of the V8A-B fracture surface from the opposite end of the flaw from that shown in Fig. N.19. Illumination is as in that figure.

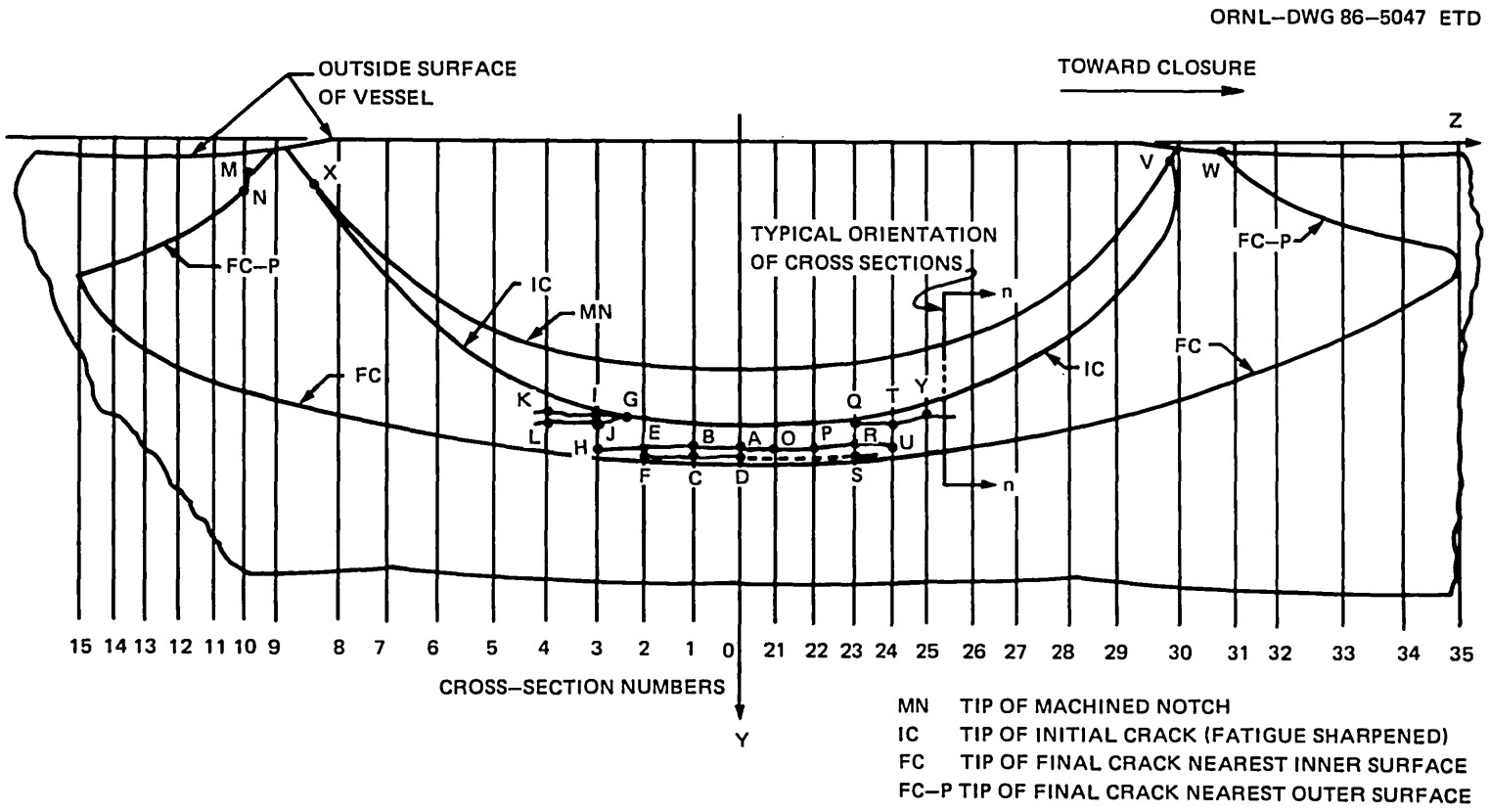

Fig. N.21. Plan of fracture surface B identifying cross sections, coordinates, and features described in Tables N.1 and N.2 and in subsequent figures.

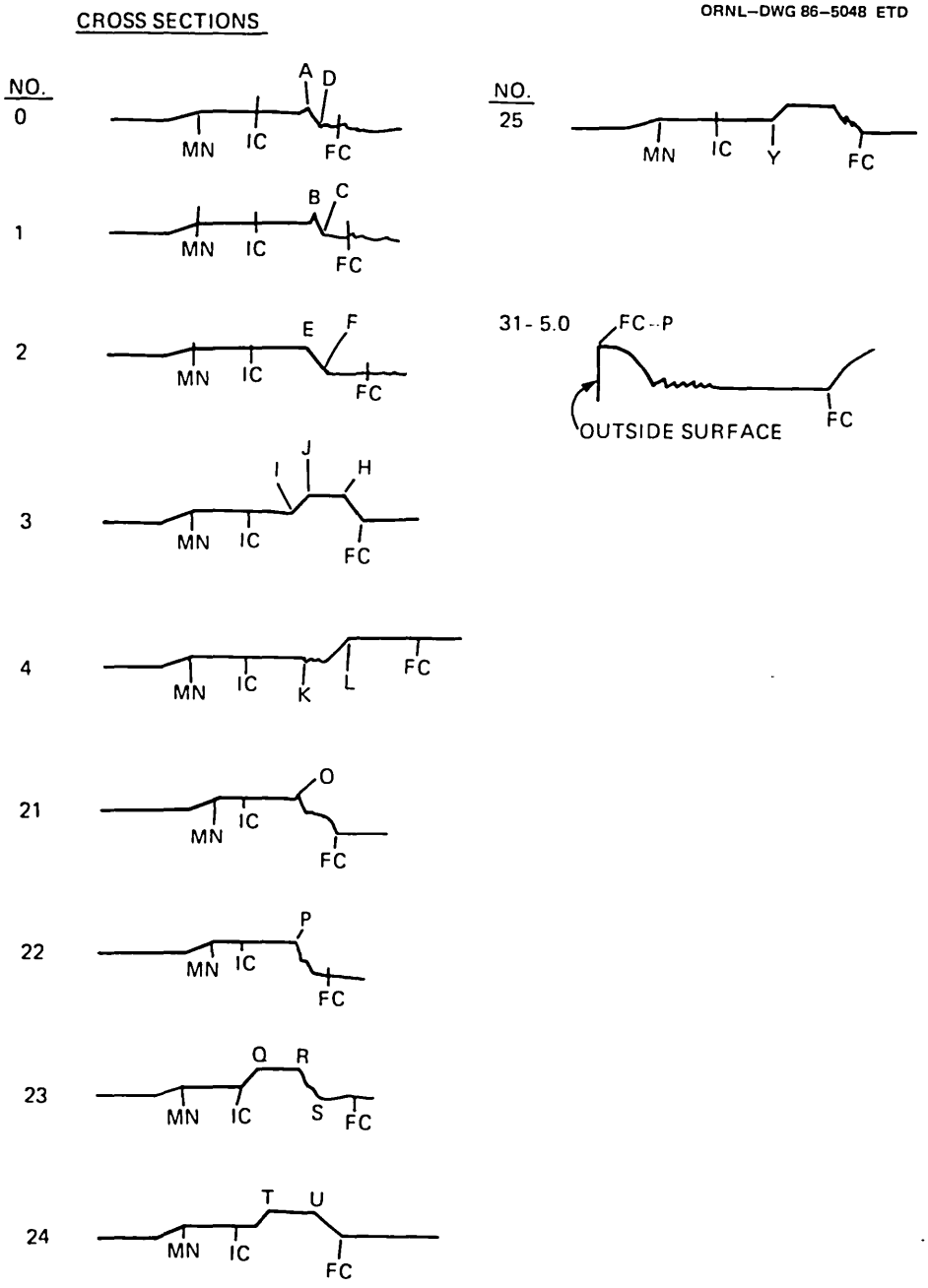

Fig. N.22. Cross sections of fracture surface B.

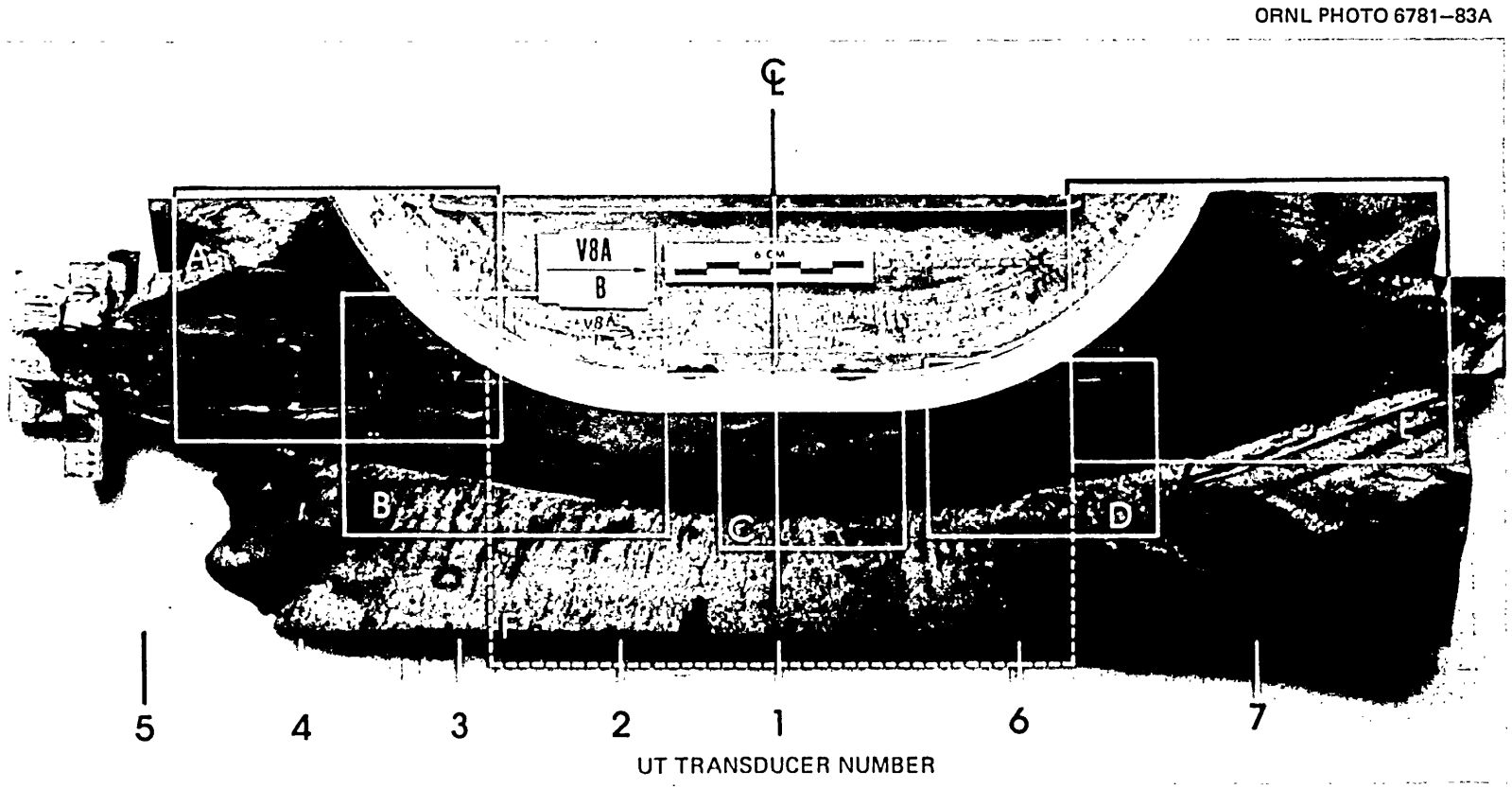

Fig. N.23. Photograph of fracture surface B identifying areas shown in subsequent figures.

M&C PHOTO Y187565

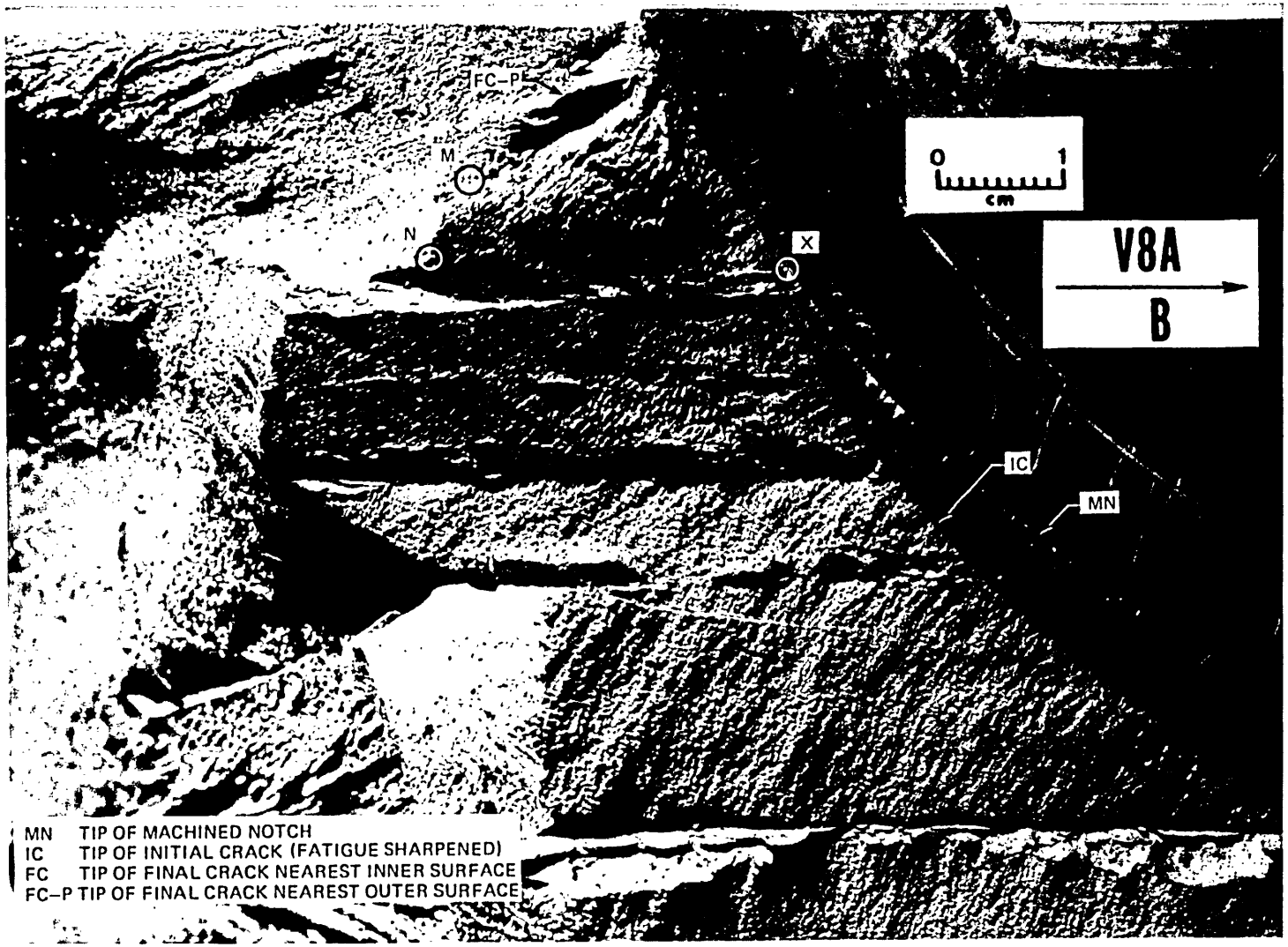

Fig. N.24. Area A.

M&C PHOTO Y187562B

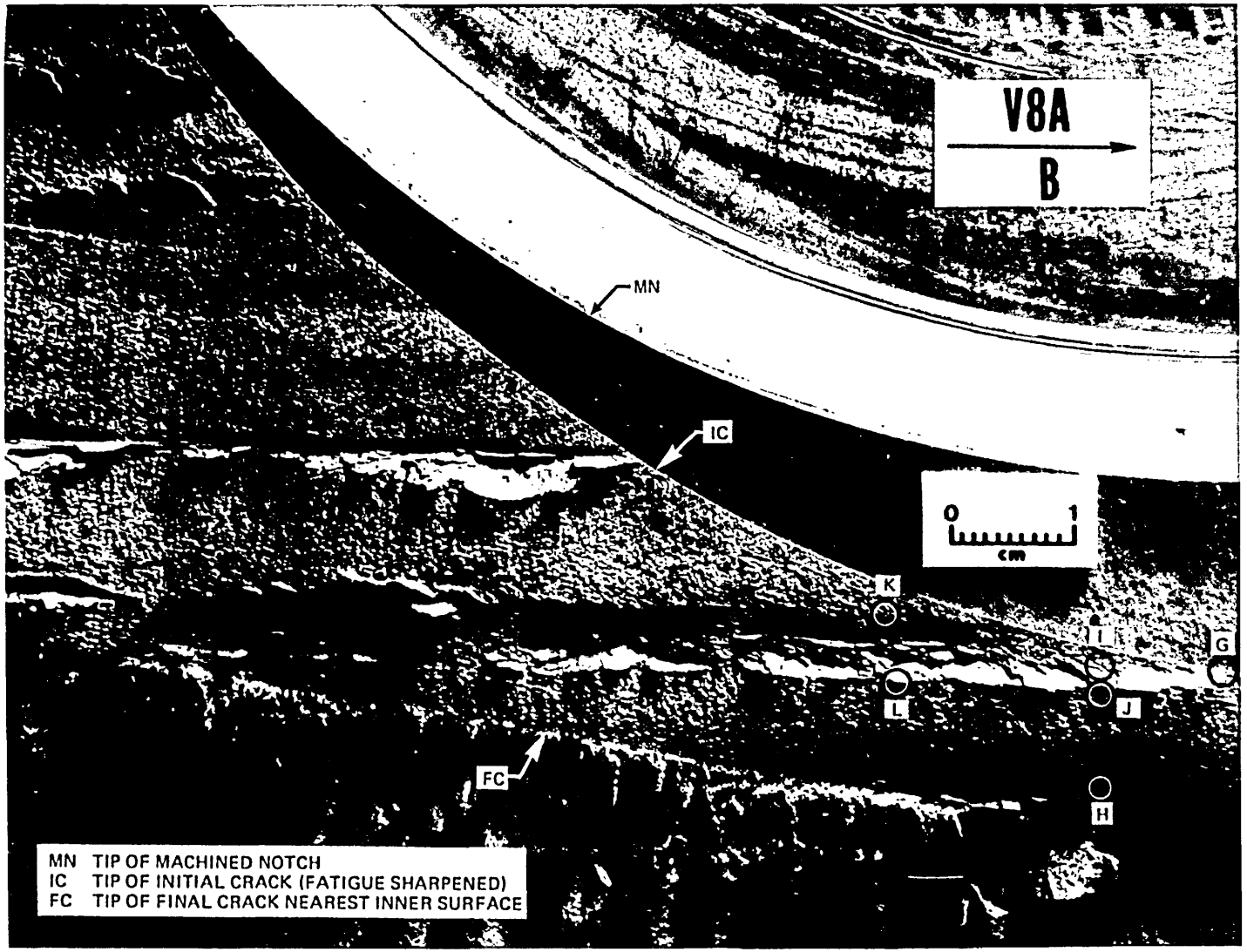

Fig. N.25. Area B.

M&C PHOTO Y187563B

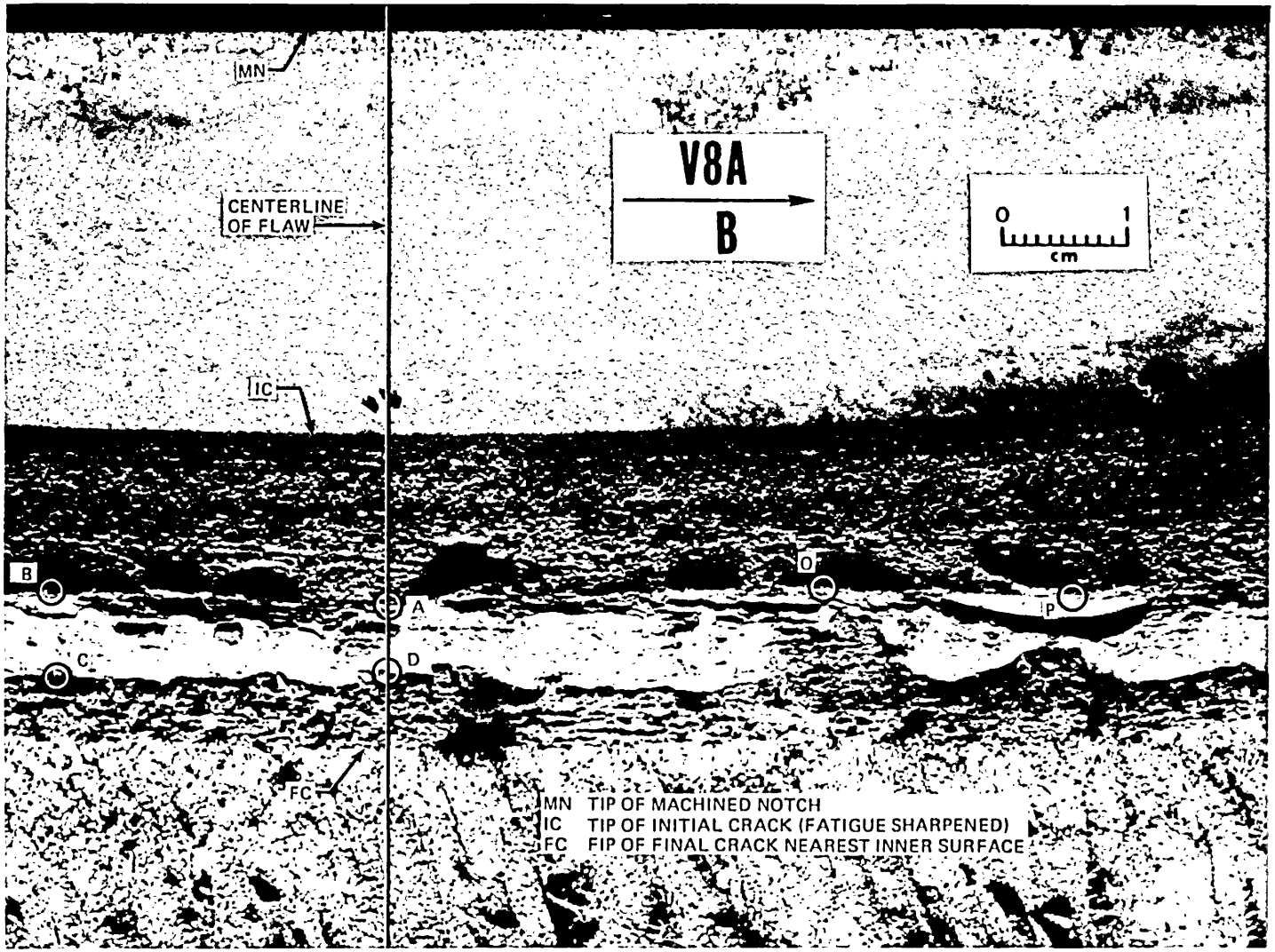

Fig. N.26. Area C.

M&C PHOTO Y187561B

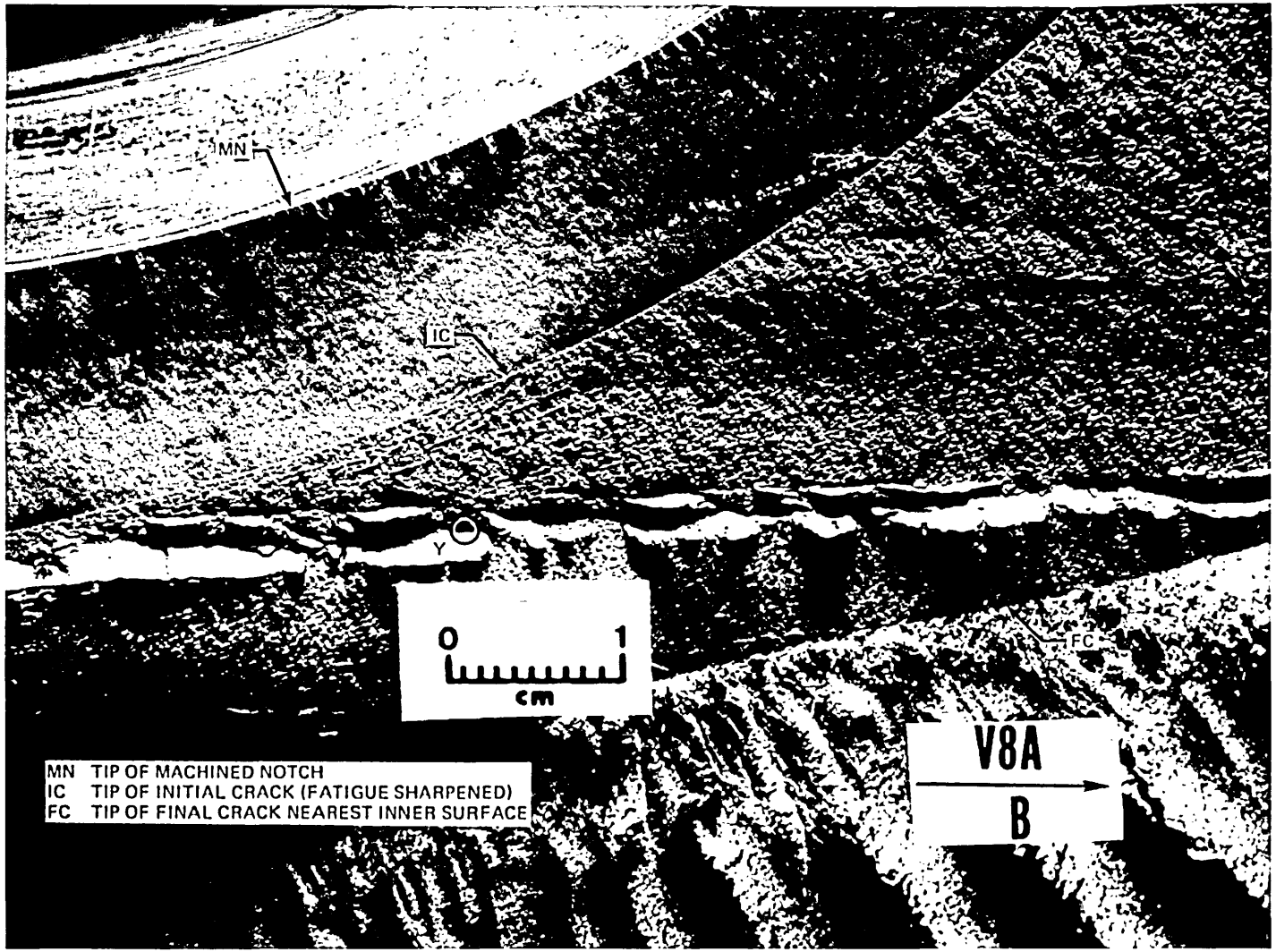

Fig. N.27. Area D.

M&C PHOTO Y187556A

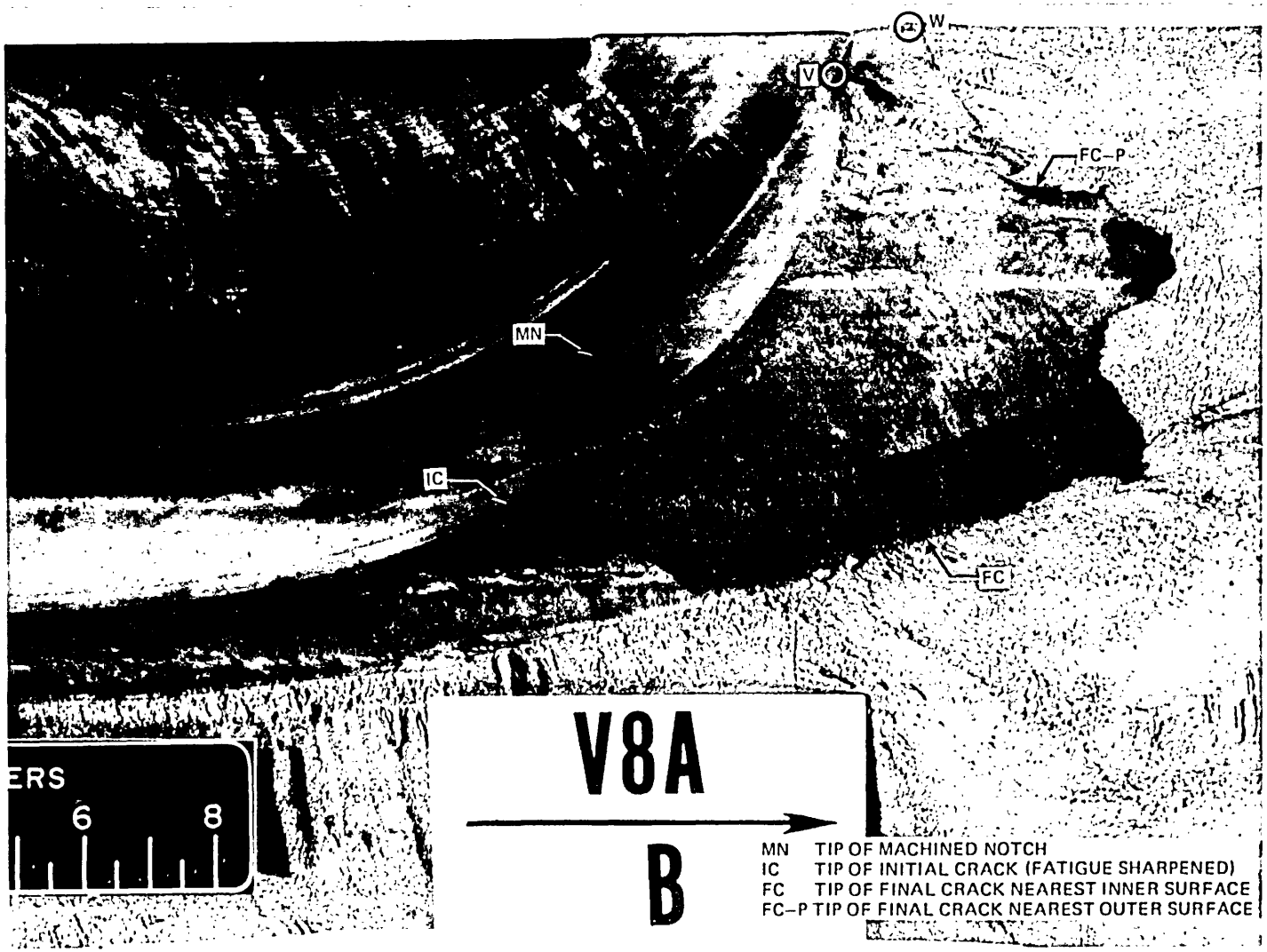

Fig. N.28. Area E.

M&C PHOTO Y187558A

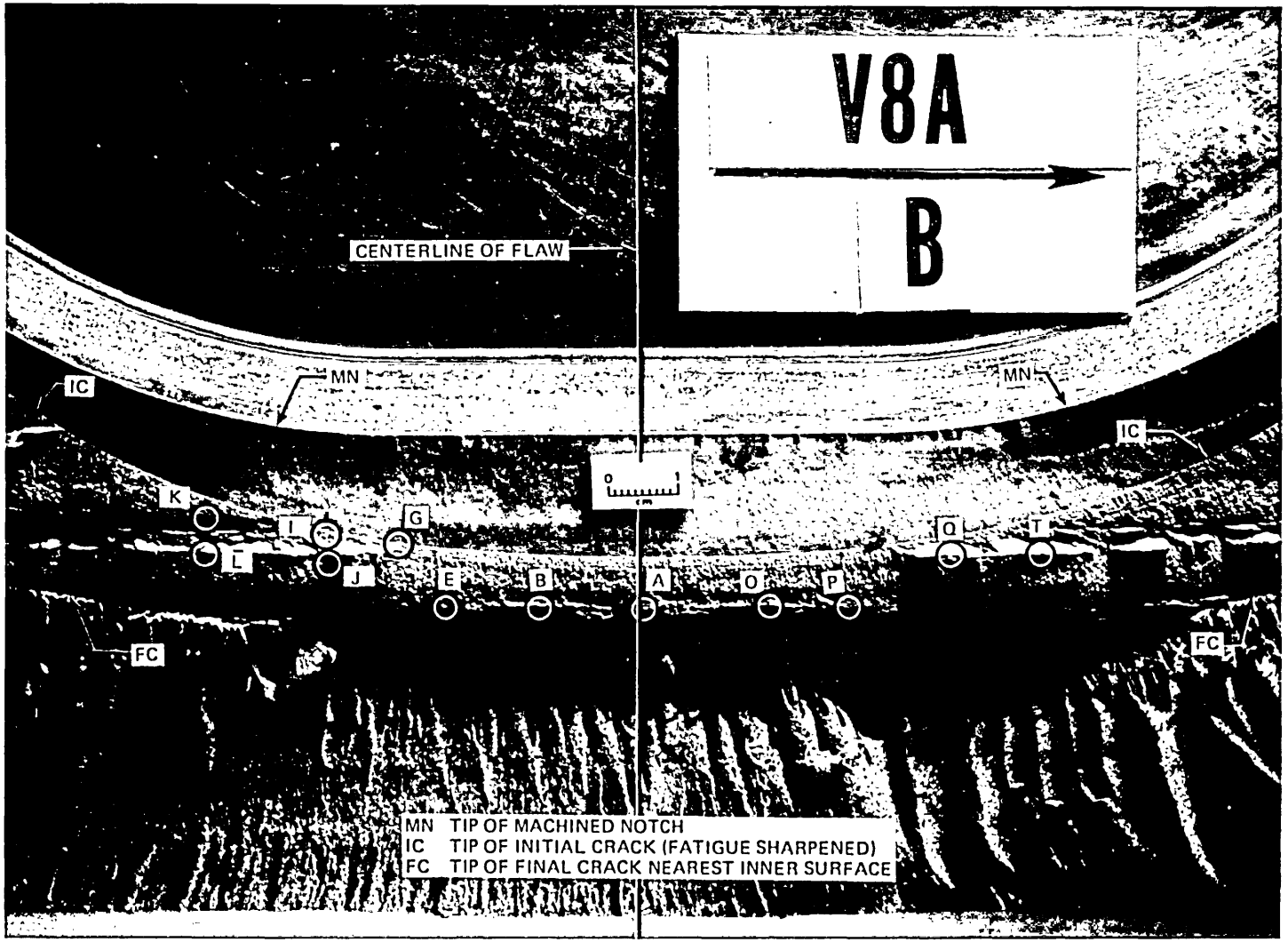

Fig. N.29. Area F.

CONVERSION FACTORS[a]

SI unit	English unit	Factor
mm	in.	0.0393701
m	ft	3.28084
m^3	gallon (U.S. liquid)	264.172
m^3/kg	ft^3/lb	16.0185
m^3/s	gpm	15,850.3
kN	lb_f	224.809
kPa	psi	0.145038
MPa	ksi	0.145038
$MPa \cdot \sqrt{m}$	$ksi \cdot \sqrt{in.}$	0.910048
J	ft•lb	0.737562
J/g	Btu/lb	0.429923
K	°F or °R	1.8
kJ/m^2	$in.-lb/in.^2$	5.71015
MJ/m^2	$in.-lb/in.^2$	5710.15
kg	lb	2.20462
T(°F) = 1.8 T(°C) + 32		

[a]Multiply SI quantity by given factor to obtain English quantity.

NUREG/CR-4760
ORNL-6187
Dist. Category RF

Internal Distribution

1. B. R. Bass
2. S. E. Bolt
3-7. R. H. Bryan
8-9. J. W. Bryson
10. T. M. Cate
11. R. D. Cheverton
12. J. M. Corum
13. W. R. Corwin
14. J. A. Getsi
15. R. C. Gwaltney
16. S. K. Iskander
17. A. P. Malinauskas
18-22. J. G. Merkle
23-25. R. K. Nanstad
26. D. J. Naus
27. N. Perrone
28. T. W. Pickel, Jr.
29-36. C. E. Pugh
37-38. G. C. Robinson
39. G. M. Slaughter
40. J. E. Smith
41. H. E. Trammell
42. ORNL Patent Office
43. Central Research Library
44. Document Reference Section
45-46. Laboratory Records Department
47. Laboratory Records (RC)

External Distribution

48. C. Z. Serpan, Division of Engineering Technology, Nuclear Regulatory Commission, Washington, DC 20555
49. M. Vagins, Division of Engineering Technology, Nuclear Regulatory Commission, Washington, DC 20555
50. Office of Assistant Manager for Energy Research and Development, Department of Energy, Oak Ridge Operations Office, Oak Ridge, TN 37831
51-52. Technical Information Center, DOE, Oak Ridge, TN 37831
53-302. Given distribution as shown in category RF (NTIS-10)

NRC FORM 335 (2 84) NRCM 1102, 3201, 3202

U.S. NUCLEAR REGULATORY COMMISSION

BIBLIOGRAPHIC DATA SHEET

SEE INSTRUCTIONS ON THE REVERSE

1 REPORT NUMBER (Assigned by TIDC add Vol No., if any)

NUREG/CR-4760
ORNL-6187

2 TITLE AND SUBTITLE

Test of 6-in.-Thick Pressure Vessels. Series 3: Intermediate Test Vessel V-8A - Tearing Behavior of Low Upper-Shelf Material

3 LEAVE BLANK

4 DATE REPORT COMPLETED

MONTH: April YEAR: 1987

5 AUTHOR(S)

R. H. Bryan, B. R. Bass, S. E. Bolt, J. W. Bryson, J. G. Merkle, R. K. Nanstad and G. C. Robinson

6 DATE REPORT ISSUED

MONTH: May YEAR: 1987

7 PERFORMING ORGANIZATION NAME AND MAILING ADDRESS (Include Zip Code)

Oak Ridge National Laboratory
P.O. Box X
Oak Ridge, Tennessee 37831

8 PROJECT/TASK/WORK UNIT NUMBER

9 FIN OR GRANT NUMBER

B0119

10 SPONSORING ORGANIZATION NAME AND MAILING ADDRESS (Include Zip Code)

U.S. Nuclear Regulatory Commission
Division of Engineering Technology
Office of Nuclear Regulatory Research
Washington, DC 20555

11a TYPE OF REPORT

b PERIOD COVERED (Inclusive dates)

12 SUPPLEMENTARY NOTES

13 ABSTRACT (200 words or less)

Tests of several 152-mm-thick vessels have been performed to study the behavior of flaws under stress states similar to those in full-scale reactor pressure vessels. The objective of the latest test, V-8A, was to provide accurate quantitative data concerning the growth by ductile tearing and final instability of a flaw in a low-upper-shelf toughness weld located in a cylinder of reactor vessel steel. This test is important because there are vessels in service that contain welds which, because of high copper content, may have their Charpy upper-shelf energy values reduced to relatively low levels by neutron irradiation. The results of the V-8A test are intended to provide an experimental basis for judging the accuracy of vessel fracture safety analysis procedures for low-upper-shelf toughness conditions. The objective of the V-8A test was attained, with a tearing instability observed at a pressure of ∿139 MPa (∿2 x design pressure). The flaw, which was initially a fatigue-sharpened notch with an approximately elliptical profile, grew in depth and length to 101.4 mm and 453 mm, respectively. Pretest and posttest fracture-mechanics and stress analyses were made by simplified methods, convenient for investigating a wide range of parameters, and by three-dimensional finite element methods, which modeled the material properties and geometry more precisely. Ductile flaw growth and instability predictions based upon measured J-resistance and tensile properties were made. Results of analyses based on J_R-controlled crack growth agree reasonably well with experimental observations.

14 DOCUMENT ANALYSIS - a KEYWORDS DESCRIPTORS

Ductile crack growth
Elastic-plastic fracture mechanics
Experiment
Fracture mechanics
Pressure vessel
Tearing resistance

b IDENTIFIERS OPEN ENDED TERMS

15 AVAILABILITY STATEMENT

Unlimited

16 SECURITY CLASSIFICATION

(This page) Unclassified

(This report) Unclassified

17 NUMBER OF PAGES

18 PRICE